UNIVERSITY OF LIVERPOOL

School of Engineering

Centre for Engineering Sustainability

Asphalt Fatigue Failure Analysis and Modelling: Experimental Studies and Theoretical Formulation

Thesis submitted in accordance with the requirements of University of Liverpool for the degree of Doctor of Philosophy

Taher Mahmood Ahmed

B.Sc., M.Sc.

August 2016

ABSTRACT

This thesis focused on the review and background theory of previous studies on fatigue failure criteria, experimental work and results' analysis. Several techniques are used for testing fatigue performance for both hot mix asphalt (HMA) and fine aggregate matrix (FAM), such as two-, three- and four-point bending, indirect tension and uniaxial tests. In recent years, a new technique has been introduced using the Dynamic Shear Rheometer (DSR). This technique is based on applying a sinusoidal deformation or loading onto small cylindrical samples, 12 mm diameter and 50 mm height, and the response is analysed to obtain phase angle and deformation data under any given circumstances, such as temperature, frequency, etc. The DSR is limited to test bitumen and fine aggregates matrix FAM samples only; nevertheless, no research efforts have been found that use a DSR to study the performance of full HMA samples.

In this work, a successful trial was proposed using a DSR for fatigue testing of HMA under controlled strain and stress modes. Two types of aggregates, limestone and granite with two binder grades, 40/60 and 160/220, were employed to prepare four different mixes of hot rolled asphalt (HRA) and dense bitumen macadam (DBM). A technical procedure was adopted to prepare the DSR samples (12 mm in diameter and 50 mm in height) and a statistical procedure based on histograms and modes for the bulk density of the DSR samples was used to select the samples to be tested for fatigue.

An approach was developed based on sweep strain/stress amplitude to arrive at a suitable strain and stress amplitude at the damage region to be used in the fatigue test. A new fatigue index (FI^R) parameter was derived from the dissipated pseudo-strain energy for the stress-pseudo-strain relationship to be used for evaluating fatigue performance. Results showed that there is a plateau value for FI^R which can be used to evaluate fatigue performance, and this value increases when the normalised shear modulus decreases to less than 0.35 and 0.20 for strain and stress test modes respectively. In addition, the FI^R results were in agreement with the results from other reliable approaches that have been used for evaluating fatigue performance, such as the energy ratio (ER) and the traditional approach

(TA). A two-point bending (2PB) test for trapezoidal samples was used to verify the DSR technique using FI^R, TA and ER approaches; the analysis of results revealed the same conclusions as the DSR technique. The variance in the results of the tested samples was studied using error bars in terms of standard of error for all approaches in both techniques: DSR and 2PB. This variance analysis revealed that FI^R has low variation in comparison with the TA and ER approaches in both test techniques.

A computational model based on artificial neural networks (ANNs) was used in this work for developing models to predict the fatigue performance of hot mix asphalt (HMA). The fatigue performance was defined according to the criteria of the TA, ER and FI^R approaches. The results revealed an excellent correlation between the predicted and experimental data. Bias analysis for ANN models involving average error, intercept and slope showed that the strain test mode was more accurate than the stress test mode.

A fracture mechanistic approach was also used to evaluate the fracture performance of HMA tested in DSR. A simple fracture model was developed based on a modified Paris' law and fatigue test parameters represented by relaxation test coefficient (m) and the dissipated pseudo-strain energy to calculate an internal damage parameter, namely the fracture damage index (FI_c). The analysis of the results for FI_c was in agreement with the FI^R, ER and TA approaches; also, it showed better performance analysis in terms of variation than the TA and ER approaches. The fracture model, FI_c, was used as a base for developing a model for predicting fatigue life of HMA in terms of number of cycles for strain and stress test modes. The bias analysis revealed that the strain model's prediction accuracy was better than that of the stress model.

Hysteretic behaviour represents the nonlinear relationship of the stress–strain response for HMA under cyclic loading during fatigue testing. In this regard, a successful trial introduced for modelling the hysteresis loops using Bouc-Wen model for HMA samples tested for fatigue under controlled strain mode using DSR. The nonlinear least squares algorithm was used to estimate the seven parameters for the Bouc-Wen model using experimental results for hysteresis loops of the HMA samples tested in DSR; these parameters control the shape and slope of the degraded hysteresis loops. The outcome of this work confirmed that

there is a good agreement between the modelled and experimental hysteresis loops. Due to the variation in the fatigue performance of HMA samples as a result of their properties, the Bouc-Wen model was not able to fully simulate the degradation for different samples when there were changes in the parameters. To improve the Bouc-Wen model's simulation performance, an ANN technique was used to develop models to predict its parameters; this technique improved the Bouc-Wen model's performance in Phase I, while its performance in Phase II-III was still poor, despite the degradation simulation being clear.

This work revealed the feasibility of using the DSR technique in evaluating the fatigue performance of full HMA according to the developed approaches for preparing and selecting DSR samples and performing fatigue tests. In addition, the work confirmed that limestone has a better fatigue performance for both HRA and DBM mixes than granite. On the other hand, the theoretical part included developing several models based on an ANN and constitutive equations showed the efficiency of these models in predicting the fatigue life of HMA samples tested in the DSR.

ACKNOWLEDGMENT

I would like to express my deep and sincere thanks to my primary supervisor, Dr Hussian Khalid, who led me to the right way and supported me in all the stages of this project. Also, I am very indebted to the second supervisor, Dr Peter Green, for his help and supportive comments to produce this work. Also, I am grateful to all the technical staff in the Highways Lab of Liverpool University.

I am very grateful to the Iraqi Government represented by the Iraqi Attaché in London for the award of a study scholarship to pursue this research.

Many thanks are due to the following industrial partners for the supply of materials: Aggregate Industry, Tarmac Ltd and Nynas Co. Also, I would like to give my appreciation to Pavement Testing Services Ltd (pts) for letting me use their lab facilities in the experimental work. I would like to express my gratitude to Dr. John Duffy from Malvern Co. for his attitude in supporting us during the training on the DSR. Moreover, I am grateful to all those who have helped me but have not been mentioned here.

Special thanks to the nearest persons to my heart and who have provided companionship on this journey and shared with me all the difficulties: my wife, **Marwah**; also, to my children, **Mustafa and Mohammed**, who filled my life with happiness when I felt bored. Exceptional thank to the spirits of my parents; I have never forgot them and ask Allah to give them joy in paradise.

Before and after all, the real thanks are to Allah, who gave me the knowledge and patience, and preferred us to all the creatures in the world.

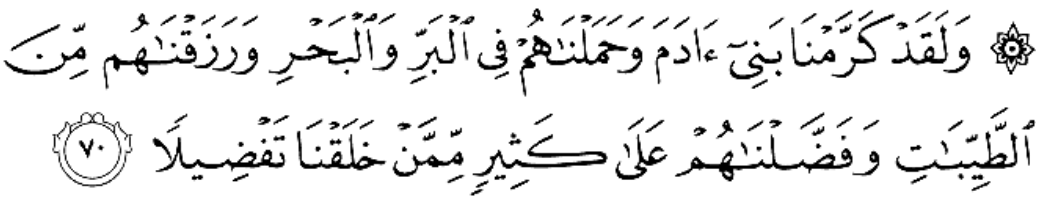

((And We have certainly honoured the sons of Adam and carried them on the land and sea and provided for them of the good things and preferred them above many of Our other creatures))

CONTENTS

LIST OF FIGURES

LIST OF TABLES

CHAPTER

I

CHAPTER I

1. INTRODUCTION

1.1. The Problem of Study

Fatigue cracking is one of the most common distresses in pavement structure when it subjected to repeated loading less than the ultimate strength of the materials. This repeated loading creates tensile stress at the bottom of the pavement layer; and as loading progressing more cracks are developing. Cracks development under repeated loadings pass into initiation and propagation phases to coalesce the micro cracks to create macro cracks; during this process materials loss the rigidity and strength and at the end leads to failure (Di Benedetto et al., 2004).

HMA is composite material where it is combined from different scales: aggregates gradations, varies asphalt film thickness, range of air voids sizes and bitumen binder. HMA behaves as viscoelastic material because of the visco property of bituminous materials and the composite nature of the full HMA; so, several factors such as temperature, time loading, amplitude loading; aging and healing phenomenon effect on the fatigue performance to be complex behaviour (Masad et al., 2008a). In this regards, several approaches were developed to define the fatigue performance for example: phenomenological approach (e.g. traditional and dissipated energy approaches); mechanistic approaches (e.g. continuum damage and fracture mechanics approaches); endurance limit approach and hysteresis loops distortion. These approaches are distributed between simple approach such traditional approach to complicated approach such as mechanistic approach.

In lab, fatigue test has been simulated using several techniques such as two-, three-, four-points bending, indirect tensile stress test and tension-compression test; all these devise are used for hot mix asphalt (HMA). Another technique is

called dynamic shear rheometer (DSR) has been used for fine aggregate matrix (FAM), mastic and binders. Fatigue life measured in lab depends on several parameters including: test modes (stress or strain), load configuration (sinusoidal or haversine) and frequency, sample geometry and mixture properties (Zeiada et al., 2013).

One of the challenges in the characterization fatigue performance is the high variance in the results among the tested samples under the same conditions due to the complex behaviour of the HMA, so more samples are required to overcome this problem which increase the cost in time and materials. Another issue was identified in the previous study represented in the criteria of fatigue test; which was performed without any criteria for selecting the stress and strain amplitude. Where, three stress or strain amplitudes have been used in fatigue test at three arbitrary levels: low, medium and high; (Tayebali et al., 1992;Rowe, 1993;Artamendi and Khalid, 2005).

In the last years, DSR has been used as a technique to characterize the fatigue performance of FAM mixes with maximum size aggregate 1.19 mm in controlled strain test mode (Kim et al., 2002;Kim et al., 2003). In the analysis results, authors used Schapery's works on elastic-viscoelastic principles to transform the real strain to pseudo strain. Three variables were selected to evaluate the fatigue damage included: loss of dynamic modulus, change in the dissipated strain energy and change of pseudo strain – stress slope (hysteresis loops). In other work DSR was used to study the moisture susceptibility of FAM damage tested in fatigue (Zollinger, 2005).

These studies were expanded more by Masad *et al*. (2007) to develop a unified method in characterization the fatigue performance of FAM using DSR. In this method, fatigue test was performed at high strain amplitude in controlled strain test mode; and the measured stress at 50% of the initial stiffness modulus was also used in fatigue test in controlled stress mode (Masad et al., 2008a;Branco, 2008). This study succeeded in reducing the variation of fatigue performance in the tested samples using a new parameter called crack growth index in comparing with other two criteria: number of cycles at failure and the cumulative dissipated energy. The problem highlighted from four issues: this method has been used for

FAM; no criteria for selecting the samples in test; selected strain amplitude was based on high value to insure that value was in damage, and crack growth index as a parameter for evaluating was based on the crack radius concept which still controversial.

Extensive works were achieved by researches to develop models for predicting the fatigue performance of HMA; these models were developed based on a traditional technique called least square error optimization for the regression models. These models started with early simple model developed by Monismith *et al*. (1961) based on the relationship between number of cycles and tensile strain and stress to intricate models included: volumetric and mechanical properties in addition to shift factors for correlating between lab and field observations (Bonnaure et al., 1980;Shook et al., 1982). The problem in these models are related to the correlation which sometimes is not satisfied based on the determination correlation (R^2); consequently, more effort still making by the researcher to improve the quality. In last years, a new technique called Artificial Neural Network (ANN) was developed and used by the researchers to develop new models for predicting or to enhance the predictability of existence models. ANN promises in a new vision and imagine for developing new models for predicting the fatigue performance of HMA irrespective of the correlation level between dependent and independent variables.

Hysteresis loops is one of the characteristics HMA, which highlighted in the stress and strain nonlinear relationship. The change in the shapes and slopes of the hysteresis loops reflects the degradation in materials (Sues et al., 1988;Kim et al., 2003). Modelling of hysteresis loops represents a challenge for researchers because of the complexity of this issue and the difficulty in modelling in HMA. Hysteresis loops have been modelled in other disciplines: ferromagnetism, brittle and elastic materials. For example, Preisach model is the oldest model used in the field of ferromagnetism (Preisach, 1935); and Bouc-Wen models was used widely in modelling the hysteric loops in brittle and elastic materials such as concrete, steel and soils (Bouc, 1967;Baber and Noori, 1986;Pires, 1996). These models are presented as first order differential equations; nevertheless, no works have been

done for modelling the hysteresis loops for viscoelastic materials such as HMA tested in fatigue using aforementioned models.

1.2 Research Scope

A considerable amount of work has been carried out on fatigue of HMA concerned with understanding the behaviour, improving the performance and developing new techniques or enhancing existing techniques. These efforts aimed to reduce the time and material costs while improving or at least maintaining the performance and evaluation quality.

The purpose of this research is to use the DSR technique to characterise the fatigue failure of full HMA under stress- and strain-controlled modes. Due to the DSR's limitations in capacity and size, this task requires the development of an approach for preparing and selecting samples to be tested in the DSR; also, these samples should be representative of the mixture properties at the same time.

In this work, four asphalt mixtures have been manufactured using two aggregate gradations, namely gap-graded and continuous; two aggregates, limestone and granite; and two binder grades, hard 40/60 and soft 160/220 Pen binders.

In addition, the study included developing models for predicting the fatigue performance using two techniques, artificial neural network (ANN) and fracture mechanics based on Paris' law. Additionally, an effort was made to model the hysteresis behaviour of HMA during fatigue tests using a Bouc-Wen model.

1.3. Objectives of the Research

The targets of this research can be summarised specifically according to the following:

- To understand the fundamental concepts of fatigue behaviour of viscoelastic materials under load repetitions.

- To develop a practical technique for preparing cylindrical samples from full HMA to be used in fatigue tests using the DSR technique or any further works.
- To develop an approach based on statistical concepts for selecting specific cylindrical samples from a large number of prepared samples to be used in fatigue testing by DSR. These selected samples should be representative of the full HMA properties.
- To develop an approach to test the selected cylindrical samples in fatigue using a DSR based on identifying the stress and strain amplitudes required to be adopted in fatigue testing under stress and strain test modes. It is also aimed to verify the validity of this approach using traditional test methods such as two-point bending (2PB).
- To develop an index based on the energy concepts criteria to be used in the results' analysis of the fatigue performance of HMA; which will help to ensure less scattering and variation in the results compared to the phenomenological approaches.
- To develop models for predicting the fatigue performance of HMA based on an Artificial Neural Network (ANN) technique using fundamental parameters of the fatigue test.
- Using the fracture mechanics concept based on Paris' law to analyse and predict fatigue performance of HMA tested in a DSR for both test modes.
- To model the nonlinear hysteretic behaviour for HMA samples tested in fatigue using a Bouc-Wen model.

1.4. Contents of Thesis

The thesis is organised into eight chapters:

Chapter I contains the summery, overview of the problems, scopes and objectives of the study.

Chapter II provides a literature review related to the fatigue performance of HMA. It includes background information such as test techniques, fatigue criteria for defying fatigue performance, mode tests and configuration of loading and viscoelastic behaviour.

Chapter III includes the fatigue performance of HMA under strain test mode. This chapter provides several aspects: the mixture properties and preparation, method of manufacturing cylindrical samples (DSR samples) and an approach for selecting DSR samples. In addition, Chapter III provides an approach for defining the strain amplitude based on the damage region and performing the fatigue test using the DSR technique. Fatigue analysis was made using a new fatigue index, which was developed based on dissipated pseudostrain energy in viscoelastic materials; also, the traditional approach and energy ratio approach were used in the analysis. A verification study was included using a 2PB technique with the method of preparing trapezoidal samples and testing; the analysis of results was completed using the same approaches as for the DSR.

Chapter IV comprises the details about the fatigue test in stress test mode; where the details include an approach for selecting the shear stress amplitude that will be used in fatigue testing using the DSR. The same approaches in Chapter III have been used in Chapter IV to analyse the fatigue performance results. Chapter IV also includes a variation study using the standard error to demonstrate the capability of the fatigue index in analysing the fatigue performance at low variation compared to the traditional and energy ratio approaches. In addition, this chapter introduces a simple model that was developed based on the damage rate (m_{II}) within Phase II to predict the fatigue life according to the criteria of the traditional approach for both strain and stress test modes.

Chapter V provides details on developing models for predicting the fatigue performance of HMA using an Artificial Neural Networks (ANN) technique. In this regard, the models were developed to predict the fatigue life in terms of number of cycles for traditional and energy ratio approaches and fatigue index as well in both test modes (strain and stress). Bias analysis was made for all ANN models to evaluate their prediction accuracy.

Chapter VI gives another view for analysing the fatigue performance of the tested samples in the DSR using fracture mechanics based on Paris' law (1963). In this regard, a simple fracture model has been developed based on the damage density concept, dissipated pseudo energy and relaxation test to be used in the analysis of the fatigue performance results for the HMA samples. The simple

fracture model was also used as a base for developing models to predict the fatigue performance in terms of number of cycles, as defined in the traditional and energy ratio approaches in both test modes. Similarly, a bias analysis was conducted to assess the prediction accuracy of these models.

Chapter VII contains details on the utilisation of a Bouc-Wen model for modelling the nonlinear hysteresis loops for the HMA samples tested in the DSR instrument. Details about the nonlinear optimisation for estimating the seven parameters of the Bouc-Wen model are available with the method of gathering stress-strain data. This model exhibited capability in modelling the hysteresis loops but it was poor in predicting the hysteresis loops for other different samples due to the variation in the fatigue results. An ANN was used as a technique to improve the prediction performance of the Bouc-Wen model, but the enhancement was only within Phase I while II-III still poor.

Chapter VIII is a short chapter and it contains on a comparison for all fatigue analysis approaches which were used in this work. In addition, an accuracy comparison for the developed models was presented to demonstrate the superiority of the models in prediction fatigue performance.

Conclusions and recommendations are presented in **Chapter VIIII**. Furthermore, this chapter includes a comparison of the developed models to demonstrate the best one.

CHAPTER II

CHAPTER II

2. Fatigue Performance of HMA: Techniques and Criteria

2.1. Introduction

Asphalt is the most commonly used material in pavement construction. Fatigue damage represents one of the main failure modes of asphalt pavements, which results in degradation of the pavement materials and eventually of the pavement structure. This damage occurs when asphalt pavements undergo repeated loading in the intermediate temperature range of about 10–30 °C (Al-Khateeb and Shenoy, 2004;Deacon et al., 1994). The tensile and compressive strain created by this repeated loading is usually less than the ultimate strength of the materials, but, if they are sufficiently high, the loading results in a loss of material rigidity and can, by accumulation in the long term, lead to structural failure (Di Benedetto et al., 2004). This fatigue failure appears as cracks in pavements which take different shapes as a longitudinal or hexagonal crack pattern in the wheel paths (Ghuzlan and Carpenter, 2006), and, at the final stage of fatigue life, pieces from the surface layer are removed under the action of traffic (Suh et al., 2010). Fatigue failure is also accelerated when the load is coupled with environmental factors, such as the presence of water, temperature cycles and inappropriate materials or poor construction quality.

2.2. Fatigue Test Techniques

Fatigue was recognised as a problem in the early 1800s when investigators in Europe observed cracks in metallic components of bridges and railroads subjected to repeated loading (Lampman, 1996). Researchers have taken great interest in asphalt pavement and mixture fatigue performance to understand and enhance its performance for several decades; the first test and experimental works were carried out by Pell in the 1950s at Nottingham University (Pell, 1962;Partl et al.,

2013). In this work, binders, mastics and mixtures were evaluated using a testing machine working on a bending method technique.

Several fatigue test devices were later used based on different mechanisms of testing and analysis. In this regard, RILEM TC 182-PEB introduced a study about the fatigue of bituminous mixtures, which used 11 different test methods under controlled stress and strain. The results were analysed using both the classical approach and the continuum damage mechanics approach. The findings can be concluded as the results of the tests are dependent on the modes and methods of testing (Di Benedetto et al., 2004).

There are several techniques to measure the fatigue performance of materials in the laboratory; Figure 2–1 shows the configurations of these techniques. The next sections will provide more details about these configurations, which are divided into two groups: classical and dynamic mechanical analysis.

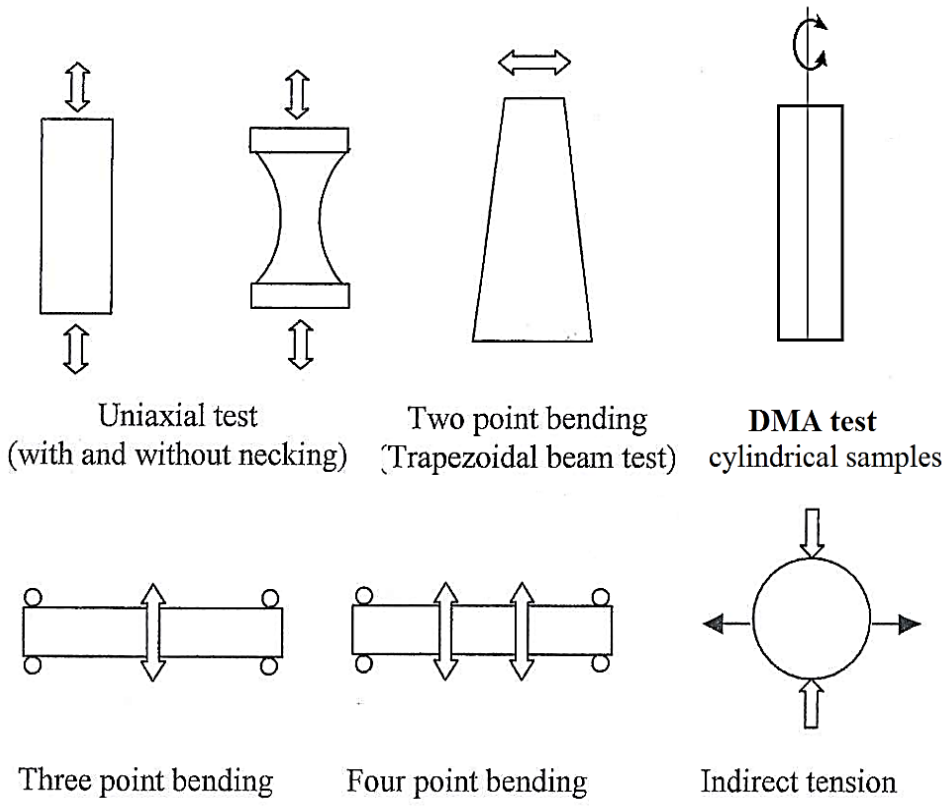

Figure 2- 1: Tests for performing fatigue properties.

2.2.1. Classical Fatigue Test

Classical fatigue test technique includes different devices what are commonly used and known by the researcher, such as those presented in Figure 2–1; these devices comprise homogeneous and non-homogeneous loading effect (Di Benedetto et al., 2004). In homogenous effect, the load or stress is distributed uniformly all over the loaded sample section, while in non-homogenous the load is concentrated in one location more than others.

2.2.1.1. Four-Point Bending (4PB) Test

4PB test is widely used to measure the stiffness modulus and evaluate fatigue resistance of pavement materials; this test is non-homogeneous because the maximum flexural stress is in the mid span and zero at the ends of the sample. The 4PB test is generally used more in the USA than in Europe (Rowe and Bouldin, 2000;Maggiore et al., 2012). The tests are conducted on prismatic beams, which are held horizontally, as shown in Figure 2–2. During the test, the specimen is subjected to sinusoidal or haversine loading for a wide range of frequencies, either under controlled stress or strain modes. The loading test is applied using servo-hydraulic technology, where two concentrated and symmetric loads are applied on the beam specimen, which is subjected to four-point bending with free rotation at all loading points; loads and deformation values are recorded by data acquisition software. The test lasts until a criterion is met, such as complete failure or 50% reduction in initial modulus (Thomas and Masad, 2008). Though this test is widely used and reliable, it is expensive in terms of time and materials: it takes about several days to test one sample based on strain and stress amplitudes, and a great deal of effort and high-quality fabrication is required to make perfect prismatic beams.

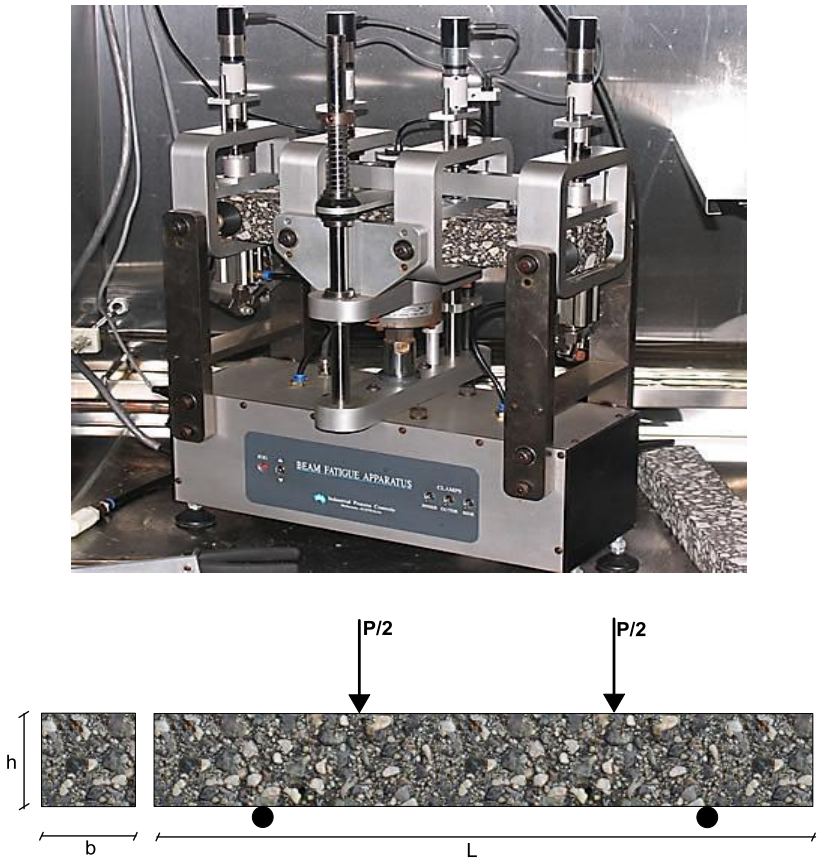

Figure 2- 2: Four-point bending testing machine and configuration.

2.2.1.2. Two-Point Bending (2PB) Test

2PB test is used to perform stiffness modulus and fatigue test on a trapezoidal specimen mounted vertically as a cantilever beam, as shown in Figure 2–1, according to European Standards (BS EN 12697-24, 2012;BS EN 12697-26, 2012); the sinusoidal loading configuration is applied at the top of the specimen while the bottom is fixed using a steel base plate. This test is commonly used and widespread in Europe (Maggiore et al., 2012); 2PB is characterised as a non-homogeneous test because the fracture usually happens in the first third of the specimen height from the bottom whereas the bending moment is maximum (Rowe, 1993;Cocurullo et al., 2008;Maggiore et al., 2012). The protocol of 2PB test in the European Standards BS EN 12697-24 characterises fatigue test only in strain test mode because the device is designed to apply a sinusoidal loading under controlled displacement; for stress test mode, another device uses an

electronic-magnetic actuator to apply constant sinusoidal loading waveform in addition to its usability in strain test mode (Rowe, 1993;Maggiore et al., 2012). The main advantage of 2PB is the ability to test two specimens at the same time and this ensures the same condition during the test. However, the difficulty highlights through producing a high-quality specimens.

2.2.1.3. Indirect Tensile Test (ITT)

ITT is performed on cylindrical samples to evaluate the fatigue performance in addition to the stiffness modulus of bituminous mixtures with a slight difference in the mechanism of testing between them. Where in fatigue test, displacement transducers (DTs) are used to measure the vertical displacement, in stiffness modulus the DTs measure the deformation in the horizontal diameter of the specimens. ITT is a non-homogeneous test because the tensile stress distributes irregularly under repeated compressive loading, where the maximum tensile stress is located in the centre of the cross-section sample and decreases outside (Hudson and Kennedy, 1968). Also, ITT is determined to operate in stress-testing mode (Brown, 1995;Di Benedetto et al., 2004;Cocurullo et al., 2008) which follows haversine configuration loading, as a consequence for this pattern of loading a localised deformation is observed at the edge of the loading strips, especially at a high temperature (Maggiore et al., 2012). So, this test is a combination of fatigue mechanism and permanent deformations (Cocurullo et al., 2008).

2.2.1.4. Uniaxial Test (Tension-Compression)

Tension-compression (TC) test is used for fatigue performance in addition to evaluating stiffness modulus of asphalt mixtures; also, TC is a homogeneous test (Di Benedetto et al., 2004) because the stress is distributed uniformly within the loaded cross-section of the specimen. TC test is performed on cylindrical specimens (Luo, 2012;Zeiada et al., 2013) and beam specimens (Qian et al., 2013). To apply a uniform loading, specimens are glued to a pair of end steel caps using high adhesive glue, and three axial linear variable differential transformers (LVDTs) are mounted on the middle part of the test specimen at 120° apart from

each other around the specimen surface to capture the axial deformation of the specimen. The specimens are sometimes necked, as shown in Figure 2–1, in order to reduce the probability of cracking close to the fixing point.

2.2.2. Dynamic Mechanical Analysis (DMA)

DMA is a technique whereby a small deformation or load is applied to a sample and the response is analysed to obtain phase angle and deformation data under any given circumstances, such as temperature, frequency, etc. (Menard and Bilyeu, 2008). The basic work of DMA is based on oscillatory loading by applying a sinusoidal deformation to a sample which has known geometric details. The sample is subjected to a controlled stress or strain which is generated by a force motor in a sinusoidal wave and transmitted to the sample by drive shaft. The first oscillatory work was done by Poynting in 1909 to measure the elastic properties of materials; later researchers became more interested in developing different techniques to do that (Menard, 1999). The first commercial DMA was developed in 1961 based on normal force and in 1967 work started on torsional loading (Menard, 1999). The revolution in computer technology played an important role in developing an advanced DMA with high sensitivity and performance, and became more useful and integration with the researchers.

Dynamic Shear Rheometer (DSR) is similar to DMA and works on the same concept but it has less capability and cheaper than DMA. DSR has been adopted and used commonly by researchers to study the rheological properties of liquid and semisolid materials, especially polymers and viscous materials. Figure 2–3 shows different DSR models. DSR has recently been used by many researchers to study the rheological properties and fatigue characteristics of asphalt binder, mastic and Fine Aggregates Matrix (FAM) (Airey et al., 2003;Kim et al., 2002;Tan et al., 2012;Kim and Little, 2004;Masad et al., 2008b;Woldekidan et al., 2013;Hintz, 2013;Johnson et al., 2009;Masad et al., 2008a). The results were valuable in evaluating rheological and fatigue properties.

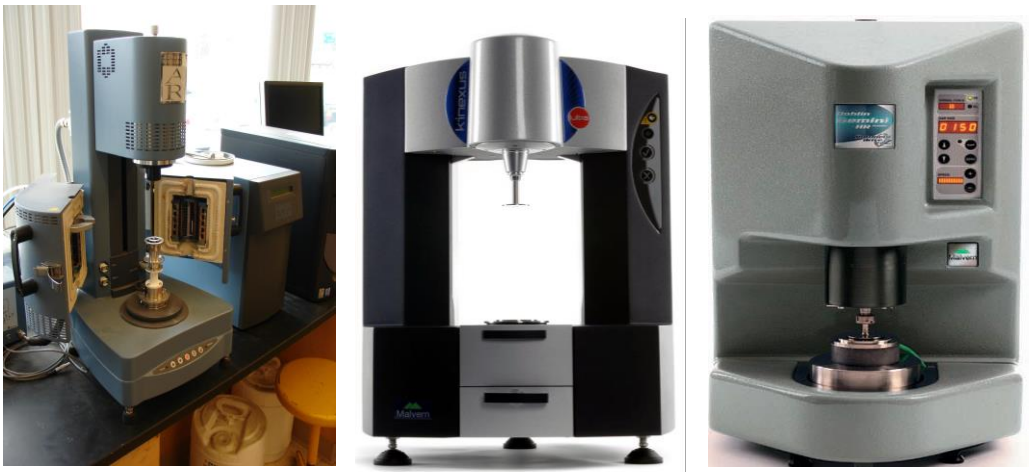

AR-2000 Kinexus Ultra Bohlen Gemini

Figure 2- 3: Different DSR models.

2.3. Fatigue Test Modes and Loading Configuration

Asphalt fatigue tests are carried out using two modes, either a constant applied load (controlled stress) or constant displacement (controlled strain). With controlled stress, the stress amplitude is kept constant and the strain response increases during the fatigue test. In contrast, a constant strain is maintained in the controlled strain mode and the stress response decreases during the test, as illustrated in Figures 2–4 and 2–5. The controlled stress test mode is generally applicable to thick asphalt pavement layers, usually thicker than 200 mm, where high stiffness is the fundamental parameter used to assess the fatigue life; in contrast, the controlled strain test mode is considered to be more suitable for thin asphalt pavement layers, usually thinner than 50 mm, where the elastic properties of the materials have a fundamental impact on the fatigue life (Pell 1973, Thom 2008, Yu 2013).

Additionally, fatigue life in terms of number of cycles is longer in the controlled strain test than in the controlled stress test (Branco 2008). This can be explained based on Paris' law for modelling crack propagation in Equation 2–1 (Paris and Erdogan 1963), where the crack length (r) is a function of stress intensity factor (K) and material properties (a, b); also, K is a function of stress (σ) and (r) in addition to specimen geometry factor (Ω), as shown in Equation 2–2.

$$\frac{d\Gamma}{dN} = a(\Delta K)^b \quad (2–1)$$

$$K = \Omega\sigma\sqrt{\pi\Gamma} \quad (2–2)$$

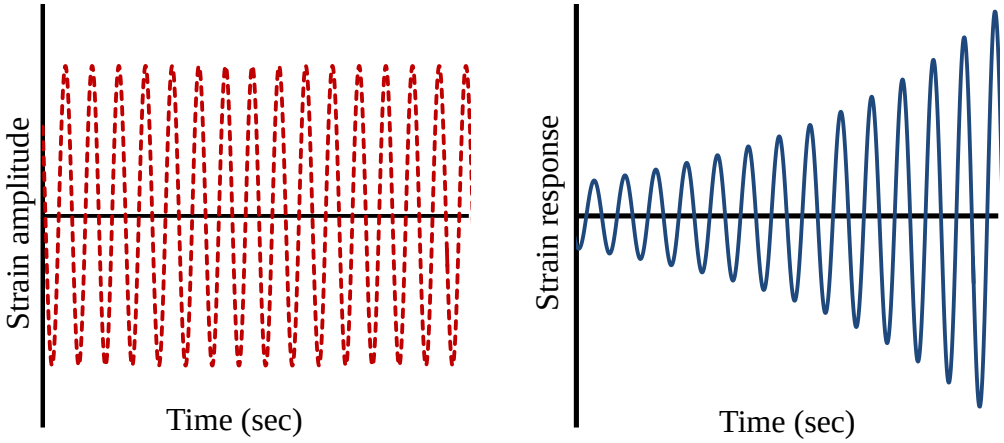

Figure 2-4: Controlled stress test mode.

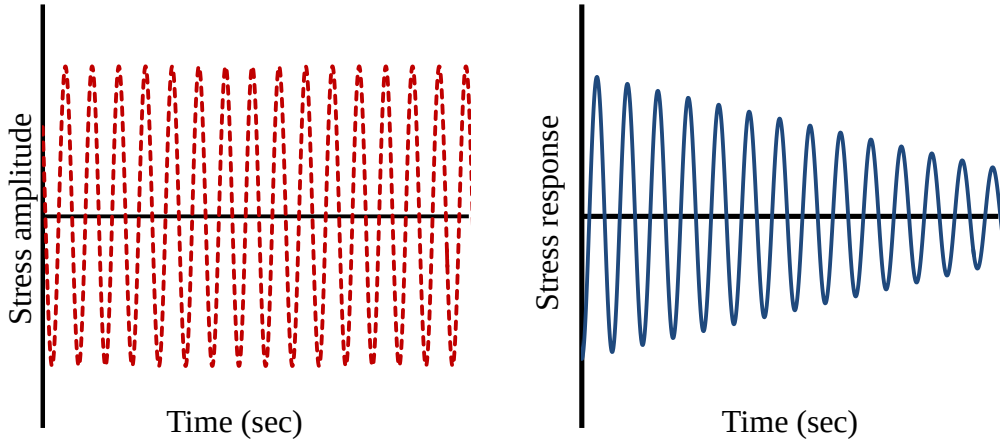

Figure 2-5: Controlled strain test mode.

It is clear that the crack propagation basically depends on the stress intensity, and stress intensity decreases in the controlled strain test mode because the stress decreases as the fatigue test progresses, and it is sometimes below a value at which the material can withstand this damage to continue to a high or infinite number of cycles, which is sometimes called the endurance limit (Bhattacharjee *et al.* 2009, Witczak *et al.* 2013). In contrast, the stress intensity is constant along the test in the controlled stress test mode, and the materials with crack propagation become weaker and quicker to damage. Thus, if we proposed that the test in both

modes starts at the same stress intensity, the fatigue life as a number of cycles in the strain mode is definitely longer than the stress mode under the same test conditions.

In the fatigue test there are two main configurations of loading, either haversine waveform (ASTM D7460-2008) or sinusoidal waveform (AASHTO T321-2007), as well as British Standards (BS EN 12697-24 2012). The main difference between the two configurations is that the load in a haversine waveform bends the beam downward in one direction, while in a sinusoidal waveform the load bends the beam in both upward and downward directions with half the magnitude of the haversine waveform, as shown in Figure 2–6. Typically, this can be characterised by the ratio (R), which is the ratio of the minimum force or displacement to the maximum force or displacement; thus, a pure sinusoidal waveform is characterised by R=-1 while R=0 for a haversine waveform.

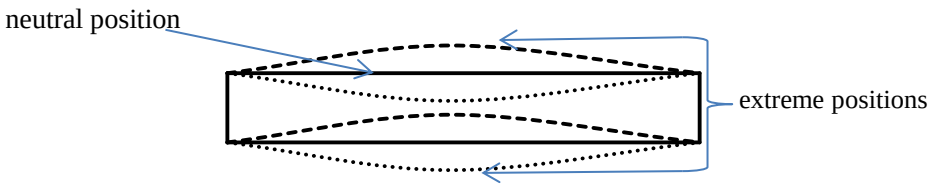

(a) Sinusiodal (AASHTO T321)

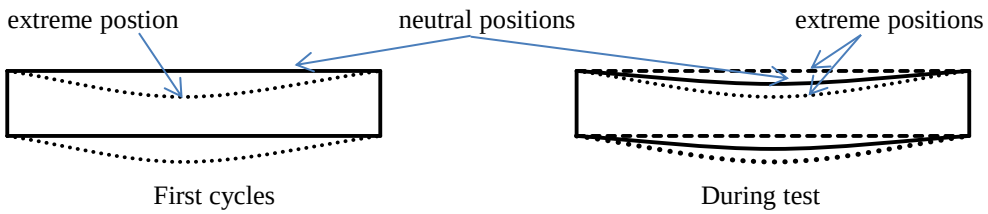

(b) Haversine (ASTM D-7460)

Figure 2- 6: Bending direction for both configurations of loading (a) sinusoidal and (b) haversine.

It is clear that stress and strain in sinusoidal loading follow the sinusoidal waveform throughout the fatigue test, as shown in Figure 2–7; also, the neutral position of the beam remains in the same position, halfway between the extreme positions, as shown in Figure 2–6a. In contrast, in the haversine waveform stress, strain and deflection follow the haversine waveform during the first cycles; as the test progresses, the behaviour changes from haversine to sinusoidal waveform for

strain and stress while the deflection remains haversine waveform, as detailed in Figure 2–8. Therefore, an initial permanent deformation (creep) occurs during the first cycles due to the viscose character as a relaxation response of the beam during the loading/unloading within the initial cycles, where the stress builds up because of the HMA's nature but then relaxes because of its ability to undergo viscous flow. During this process, the neutral position moves downward, which is located halfway between the extreme positions, as shown in Figure 2–6b.

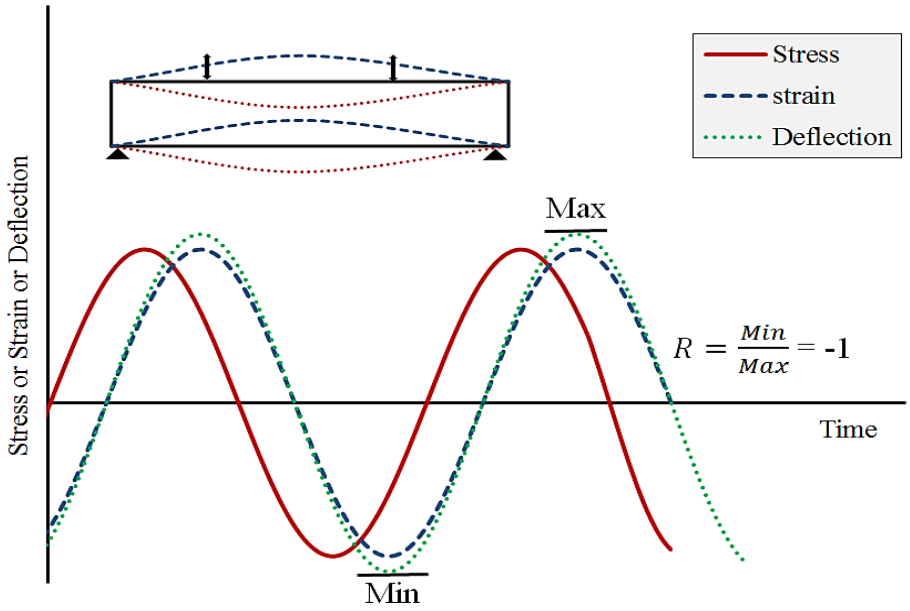

Figure 2- 7: Stress and strain vs time for sinusoidal waveform loading (BS EN 12697-24 and AASHTO T321).

Additionally, the R value of the haversine waveform during cyclic loading is not the same as at the beginning, i.e. R=0, (Pronk and Erkens 2002). The stress and strain signals change into a sinusoidal form in strain test modes and the R factor will change from 0 to -1; also, a new neutral axis for the beam will be created because of the permanent deformation (creep), as shown in Figure 2–6b, and this axis continues to the end of the test, so at the end of the test the beam has been bent. However, the deflection form remains haversine along the test, as shown in Figure 2–8. In stress mode, immediately after creating the permanent deformation, the stress-strain signals convert into a sinusoidal form (R=-1) but there is an increasing R factor (R>0) in the deflection signal. This is because the load is not influenced by the permanent deformation, and the beam is subjected to the same load as in the undamaged specimen, causing progressive curvature of the beam

due to the cumulative permanent deformation; thus, the neutral axis is changing as loading progresses. Thus, the haversine loading form comprises two types of damage to components: fatigue damage and creep damage, but creep damage in the stress mode is more than in the strain mode as a result of the increased permanent deformation (creep) (Pronk and Erkens 2002).

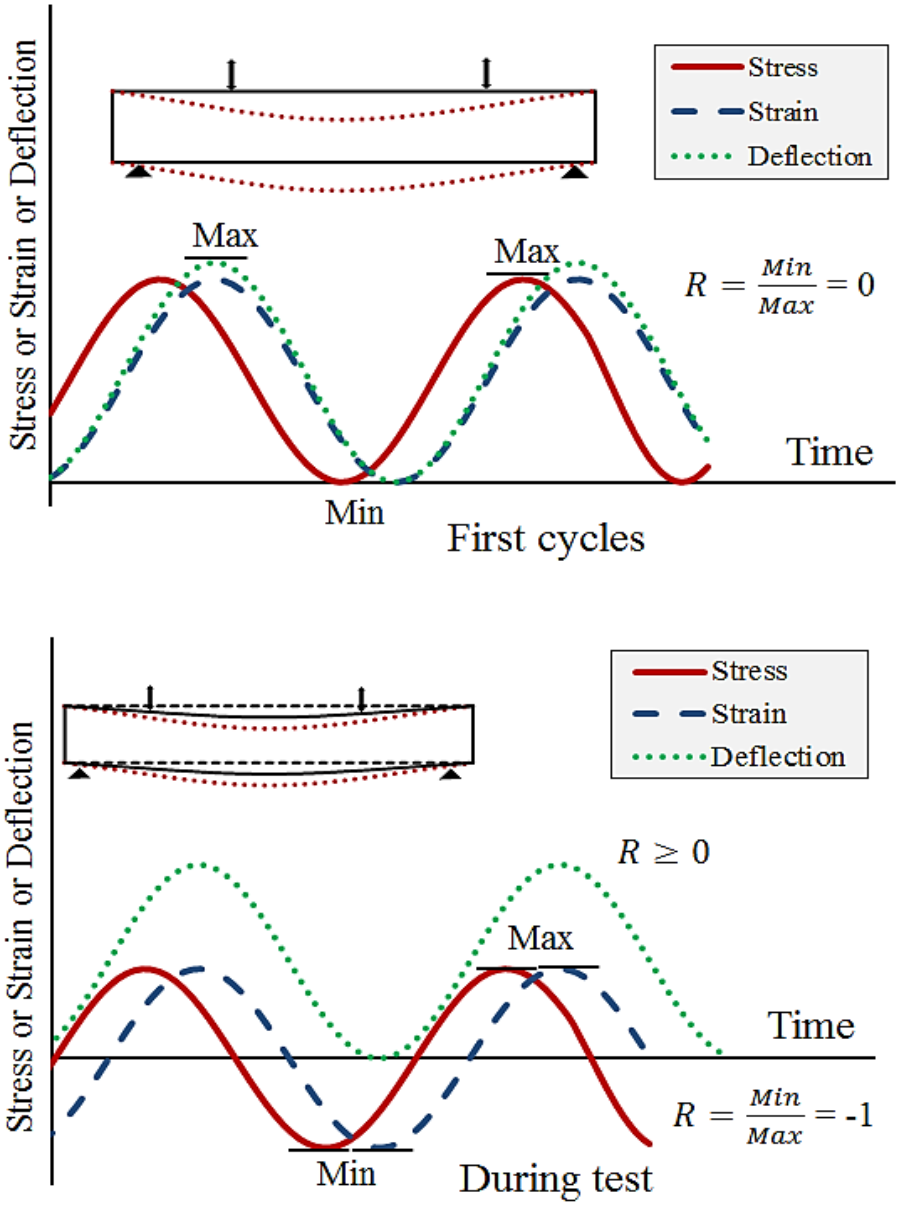

Figure 2- 8: Stress, strain and deflection vs time for haversine waveform loading (ASTM D-7460).

The developed stress and strain during sinusoidal loading generate reversible tension and compression on the top and bottom of the beam during cyclic loading. In contrast, the movement to one direction in haversine loading creates tension at

the bottom and comparison on the top of the beam during the first cyclic loading; later the developed stress and strain change to sinusoidal waveform, causing changeable tension and comparison with half stress magnitude at the beginning of the test. So, at the end of the haversine test and after removing the loading the sample remains bent downward while in sinusoidal loading the sample remains straight (Pronk et al., 2010;Witczak et al., 2013).

Mamlouk *et al.* (2012) revealed that the haversine loading gave unexpected results in a healing study in compression with sinusoidal waveform loading. Whereas the fatigue life with rest period in haversine loading was shorter than without rest period and this result was unexpected, in contrast, fatigue life in sinusoidal waveform loading produced consistent and expected results (Mamlouk et al., 2012). This effect was justified in the same study (Mamlouk et al., 2012); where, the developing stress and strain during sinusoidal loading with and without rest period creates reversible tension and compression to the top and bottom of the beam. In contrast, the haversine waveform loading with rest period is more harmful where it creates higher tension stress because the beam being bent double time than sinusoidal, consequently high tension at the bottom of the beam is generated. As is known, tension stress reduces fatigue life while compression stress helps to heal the micro cracks to extend fatigue life. So, the recommendation of this study was adopting sinusoidal waveform AASHTO T-321 in studying the healing instead of haversine. While in ASTM D7460 haversine was used because the loading shape is similar to the nature of loading on the pavement surface (Pronk et al., 2010).

2.4. Fatigue Life Criteria

Fatigue life of asphaltic pavement is defined as the number of standard axle loads passing until the failure, i.e. cracking on the pavement surfaces, occurs. In the lab, fatigue life is defined as a number of repeated stress or strain cyclic loadings on prepared samples to failure, according to standard defined criteria. During fatigue life under repeated loading, materials exhibit three phases, as shown in Figure 2–9: phase I, or the adaptation phase, is characterised by a rapid decrease in stiffness due to heat generation and thixotropy in addition to fatigue damage

(Carpenter and Shen, 2006;Ghuzlan and Carpenter, 2006); phase II, or the quasi-stationary phase, is where the steady decrease in stiffness predominates fatigue life, and the degradation in the material is very slow over a number of load cycles; and phase III, or the failure phase, is where macro cracks begin to develop and failure completely sets into the material at the end of this phase. Phases I and II are associated with crack initiation, while phase III is associated with crack propagation (Di Benedetto et al., 2004).

In the literature, various approaches have been found as criteria to define fatigue life of HMA; more details are provided in the next section.

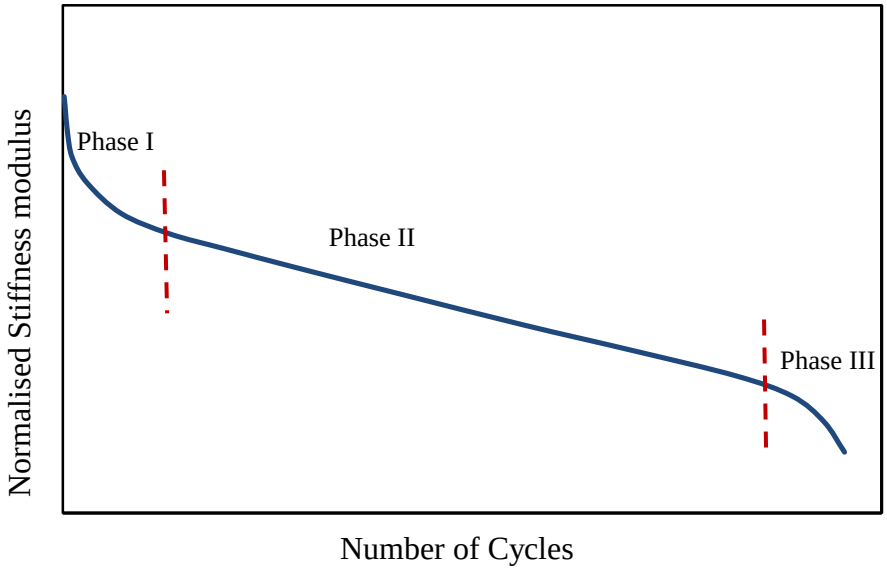

Figure 2- 9: Typical fatigue curve

2.4.1. Traditional Approach Criteria

Traditional approach (TA) is the approach most commonly used by researchers in evaluating fatigue performance of HMA. In this approach, fatigue failure is defined based on the mode of loading. For example, in the controlled strain mode, fatigue failure is defined as the number of cycles needed to reach 50% reduction in the initial stiffness modulus (Kim et al., 2003;Daniel et al., 2004;Artamendi and Khalid, 2005;Dondi et al., 2013); however, another study recommended that fatigue testing under the controlled strain mode should be continued until the modulus has dropped to 20% of the initial stiffness value, because a 50% stiffness

reduction is often reached before crack initiation has occurred (Rowe and Bouldin, 2000). While, in the controlled stress mode, failure is defined either as the complete fracture of the sample (Tayebali et al., 1992;Ghuzlan and Carpenter, 2006), or reduction in stiffness modulus of the sample to 10% of its initial value (Rowe, 1993). The American Association of State Highway and Transportation Official (AASHTO) adopted the traditional approach in evaluating fatigue performance of asphalt pavements (AASHTO, 2002).

2.4.2. Energy Concepts Criteria Approach

Applying a stress to a material creates a strain, and the area under the stress–strain curve represents the energy being put into the material. For elastic materials without any damage, the strain is recovered directly when the stress is removed and the stress–strain curve coincides, meaning the energy is recovered completely without losses. If the two curves for loading and unloading do not coincide, this indicates there is a difference between the amount of energy put into the material and the amount of energy recovered from the material, and this difference in energy loss is called dissipated energy, as shown in Figure 2–10. This dissipated energy transforms into damage in materials including any structural changes in the system such as micro-crack propagation and coalescence, void growth, plastic flows, etc.

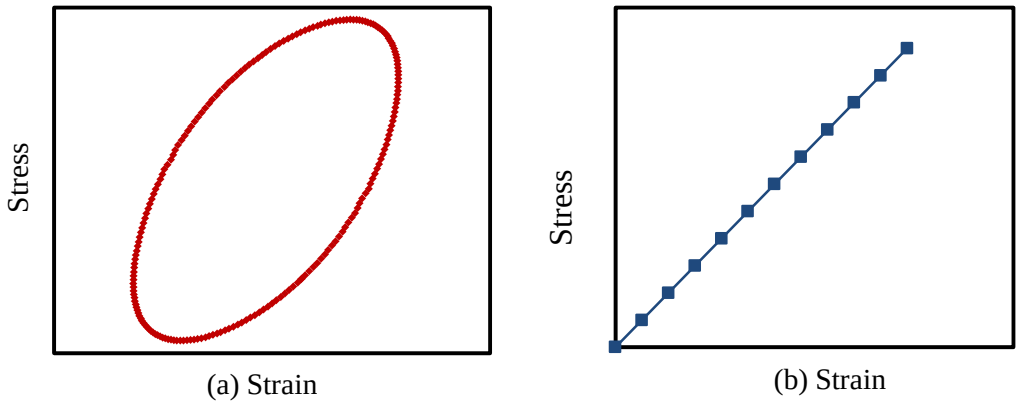

Figure 2- 10: Stress–strain curve: (a) with energy losses (damage); (b) without energy losses (no damage).

In this regard, an approach related to the dissipated energy concept was introduced by Van Dijik (Van Dijk and Visser, 1975;Van Dijk and Visser, 1977) to characterise the fatigue performance of HMA. He proposed that the total dissipated energy at failure is the same irrespective of fatigue testing mode. Van Dijik's (1975) defined a unique relationship between numbers of load cycles with the total dissipated energy per unit volume to the fatigue points. Rowe (1993) defined dissipated energy ratio (ER) as a function of the number of cycles and stiffness modulus for both strain and stress modes, as in Equations 2–3 to 2–5, and used in characterisation fatigue performance.

$$ER = \frac{n(\pi\sigma_o\varepsilon_o \sin\delta_o)}{(\pi\sigma_i\varepsilon_i \sin\delta_i)} \quad (2–3)$$

$$R_\sigma = nE_i^* \quad (2–4)$$

$$R_\varepsilon = \frac{n}{E_i^*} \quad (2–5)$$

Where: n = cycle number; ε = strain amplitude; σ = stress amplitude; δ = phase angle; R_σ = equivalent energy ratio for controlled stress mode; R_ε = equivalent energy ratio for controlled strain mode; E^* = complex stiffness modulus; and 0, i = initial and i^{th} cycle.

In Rowe's study (1993), Fatigue life was defined using a graphic method where, in the stress mode, was the number of cycles (N_1) at the point when the ER reaches the peak point in the relationship of ER vs n as shown in Figure 2–11a; while in the strain mode it was defined as the point when the ER slope deviates from a straight line in the same relationship, as demonstrated in Figure 2–11b.

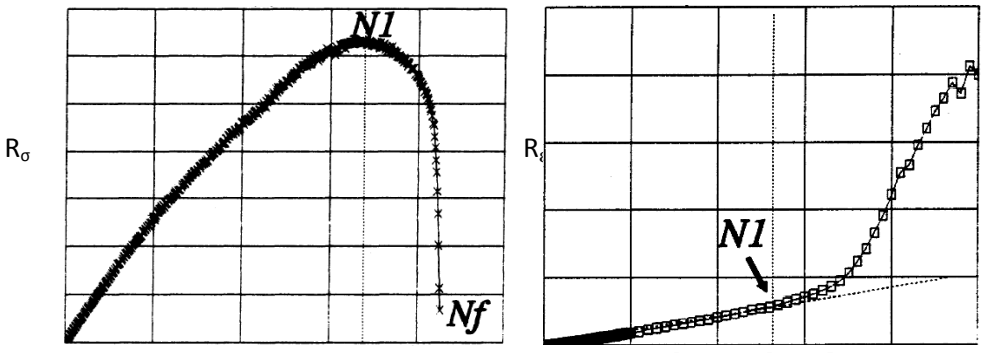

(a) Load cycles (b) Load cycles

Figure 2- 11: Energy ratio criteria for (a) controlled stress (b) controlled strain (Rowe, 1996).

The results in the graphical method are subjective because it depends on the accuracy and calculations of the person, as well as on the number of points obtained from the test. This case is more highlighted in the use of Equation 2–5 to define N_1 in strain mode. In this regard, Rowe and Bouldin (2000) introduced a practical solution represented by applying Equation 2–4 to produce a similar graph of stress mode, as shown in Figure 2–11a; and the peak point in the relation of R_ε vs n was used to define N_1 (Rowe and Bouldin, 2000). Herein, N_1 represents the number of cycles at the beginning of micro-crack formation (where phase II starts) and this will lead to misleading results because the real fatigue life is within phase II which sometimes takes longer or shorter than expected value depending on the test and material conditions. Also, using Equation 2–4 to calculate N_1 in strain gives less than N1 which is calculated using Equation 2–5 (Partl et al., 2013).

The variations in results that are related to number of cycles such as the traditional approach and ER are relatively high (Masad et al., 2008a); therefore, to reduce the scattering in the results, more samples are required.

Another approach related to energy concepts, called the dissipated energy ratio (DER), was introduced as a fatigue criterion. DE in viscoelastic material is calculated by the area inside the hysteresis loop for each loading cycle, and the total dissipated energy for the whole fatigue test is the sum of the DE for all the cycles of loads, as shown in Equations 2–6 and 2–7 (Daniel et al., 2004;Ghuzlan and Carpenter, 2006).

$$W_i = \pi \sigma_i \varepsilon_i \cos \delta_i \quad (2–6)$$

$$W_{tot} = \sum_{i=1}^{N} W_i \quad (2–7)$$

Where: W_i = dissipated energy in load cycle i; W_{tot} = total dissipated energy during test; σ_i = stress amplitude for load cycle i; $\mathcal{E}_i$ = strain amplitude for load cycle i and δ_i = phase angle for load cycle i.

DER is defined as the difference between the DE for load cycle i+1 and load cycle i divided by the DE in load cycle i (Equation 2–8) (Ghuzlan and Carpenter, 2000;Daniel et al., 2004;Al-Khateeb and Shenoy, 2004;Ghuzlan and Carpenter, 2006).

$$DER = \frac{W_{i+1} - W_i}{W_i} \quad (2–8)$$

DER was calculated approximately every 100 cycles and the values of DER against the number of load cycles were plotted as shown in Figure 2–12. This plot is called the damage curve (DC). Fatigue failure was defined as the point where the DER begins to increase rapidly (Ghuzlan and Carpenter, 2000). Before this rapid change, the changes in the DER with number of load cycles were an approximately constant value, and this value is called the plateau value (PV), as shown in Figure 2–12. The DC can be divided into three stages. In stage I DER decreases with the number of cycles; in stage II the energy input is approximately constant and this period is called the plateau value (PV); extending this stage leads to stage III, which is a dramatic increase in DER, indicating failure of the material (Carpenter and Shen, 2006).

The weakness of using DER in characterisation of fatigue performance for HMA is that there is no physical meaning to this parameter; also, DER values do not have a limited range.

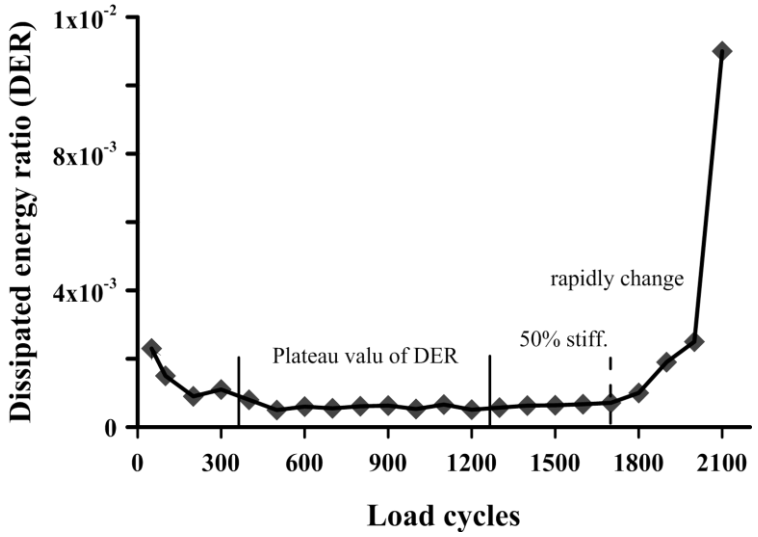

Figure 2- 12: The dissipated energy ratio (DER) against number of load cycles (Ghuzlan and Carpenter, 2006).

Another energy-related approach, referred to as dissipated pseudostrain energy (DPSE) (Masad et al., 2008a;Bhasin et al., 2008), has been used in evaluating the fatigue performance of HMA. In this approach, real strain amplitude is converted

to an equivalent pseudostrain to remove the viscoelastic contribution to dissipated energy and used to quantify the damage growth using mechanistic approaches, as detailed in the next section.

There have been attempts to separate the DPSE into different components during fatigue testing. Masad *et al.* (2008), who tested fine aggregate matrix (FAM) asphalt mixtures under cyclic torsion in a dynamic shear rheometer (DSR), divided DPSE into three components: the first is related to material damage due to increase in the phase angle; the second is due to permanent deformation caused by loading and unloading within each cycle; and the third component is associated with the difference between the pseudo-stiffness before and after damage; however, in this study there is no hint that the sum of this energy is equal to the total energy. In contrast, in another work where cylindrical samples were tested in tension/compression fatigue with samples remaining under only tensile strain during each load cycle (Luo et al., 2012), the DPSE was separated into only two components: DPSE for fatigue cracking and DPSE for permanent deformation. However, both methods tried to split the energy into two main components: permanent deformation and fatigue cracking. As presented from both studies, the final result has gone to different components; and this causes confusion about which one is closest to the real case.

2.4.3. Mechanistic Approaches

The previous approaches are known as the phenomenological and energy approaches: tensile stress or strain or dissipated energy is correlated with the number of load repetitions to failure. The mechanistic approaches are more complicated than those for the phenomenological and energy approaches, as differential equations and experimental results are matched together to develop a model to describe fatigue performance. Continuum damage mechanics (CDM) is one of the mechanistic approaches; it was based on Schapery's work on crack growth in viscoelastic media (Schapery, 1984). This approach was developed by Lee and Kim (Kim et al., 1997;Lee et al., 2000;Park et al., 1996) to characterise the damage in asphalt due to fatigue. The damage was quantified by a non-dimensional internal state variable (S), and this variable represents an indicator of the change in the pseudo-stiffness modulus (C), as shown in Equation 2–13.

$$S_{N+\Delta N} \cong S_N + \left(\Delta N/_f\right)^{\alpha/_{1+\alpha}} \left[-0.5 I \varepsilon_N^{R^2} (C_{N+\Delta N} - C_N)\right]^{\frac{1}{1+\alpha}} \quad (2\text{–}13)$$

α = a parameter depends on the relaxation test and fatigue mode; f = frequency and ε_N^R = pseudo strain.

Fatigue is considered to have occurred when the pseudo-stiffness drops to 50% of the initial value.

Another mechanistic approach is called fracture mechanics; it is based on a well-known power function called Paris' law (Paris and Erdogan, 1963), which correlates the crack growth per cycle (*dc/dN*) with the stress intensity factor (*K*) using two regression coefficients, *A* and *n*, as shown in Equation 2–14.

$$\frac{dc}{dN} = AK^n \quad (2\text{–}14)$$

This model is a reliable approach to investigate the fracture behaviour of brittle or quasi-brittle material within linear elastic fracture mechanics (LEFM). Essentially, Paris' law was derived from the analysis of a single crack growth in metallic specimens, which are homogenous materials. This represents a major problem when studying crack growth in non-homogeneous and viscoelastic materials such as hot mix asphalt (HMA), as numerous cracks appear in the specimens under repeated loading conditions (Mull et al., 2002;Walubita et al., 2006;Mun and Lee, 2010). Based on Schapery's extended work on viscoelastic materials, a modification was made to Paris' law, which was to use the *J*-integral instead of *K* for fracture analysis of viscoelastic materials, as shown in Equation 2–15 (Schapery, 1984). This modification is more appropriate to describe the fracture resistance of asphalt mixtures (Mull et al., 2002;Rice, 1986;Mun and Lee, 2010;Walubita et al., 2006).

$$\frac{dc}{dN} = AJ^n \quad (2\text{–}15)$$

DPSE has been used to develop a model for measuring fatigue cracking resistance using a parameter called the crack growth index (Masad et al., 2008a;Bhasin et al., 2008), as shown in Equation 2–16, which is based on Paris' law for crack growth and the J-integral. The results of the crack growth index were found to be consistent with field observations and independent of fatigue test mode (Bhasin et

al., 2008). However, these techniques used the so-called 'crack radius' as it is practically impossible to measure the cracking radius because the crack always creates new surfaces with an increase in the crack mouth opening displacement.

$$\Delta R = \left[\left(\frac{2n+1}{nb+1}\right)^{n+1}\left(\frac{G_R bc}{4\pi G_1 \Delta G_f}\right)^{n} N^{nb+1}\right]^{\frac{1}{2n+1}} \quad (2\text{–}16)$$

Where ΔR is the fracture radius; b and c are regression coefficients for dissipated pseudo-strain energy vs N (number of cycles); G_R is the reference modulus; G_1 is the relaxation coefficient; ΔG_f is the adhesive bond energy; and n depends on the relaxation coefficient and test mode.

Mechanistic approaches are characterised as complex and require stress–strain data for the whole fatigue test in calculations, in addition to relaxation test parameters.

2.4.4. Endurance Limit Approach

A technique related to the properties of HMA is called the endurance limit (EL), which is defined as a strain level at or below which no fatigue damage is expected to accumulate in materials. The EL concept was introduced early in 1870 by Wöhler to define the stress level below which no failure damage will occur in metals (Zeiada et al., 2013). The researchers in this regard tried to define EL; for example, EL defined 70 μs as HMA because there was no fatigue damage (Monismith and McLean, 1972); however, this study did not have sufficient data; while another study revealed that, when the tensile strain at the bottom of the pavement was less than 200 μs, no fatigue cracks appeared (Nishizawa et al., 1997). All these works were based on experimental works and examine the fatigue damage without analytical criteria. In other sophisticated works, EL was identified using an approach based on elastic-viscoelastic principles to define the strain level at which stress–pseudostrain loops begin to form (Bhattacharjee et al., 2009); however, in this work the EL was determined as a range value depending on the strain values at which the loops were formed. In further works, EL has been determined as the strain level at which the fatigue-damaged material recovered completely, when there is a balance between loading damage and recovery, which is a rest period during testing (Witczak et al., 2013;Zeiada et al.,

2013). In this work, a method was developed based on pseudo stiffness ratio for HMA samples tested in 4PB and T-C techniques to estimate EL and developing mathematical models to predict the EL. Several parameters were taken into account in this work, such as air voids, binder contents, initial stress, and strain amplitude and rest period, which gave a wide range of EL based on the conditions of the mixes and tests. However, this study was limited to one binder grade, PG 64-22, so it needs to be expanded to include more binder grades to give better idea of EL.

2.4.5. Distortion of the Load-Deformation (Hysteresis Loops)

Al-Khateeb and Shenoy (2004) suggested that the fatigue life failure is revealed directly from raw data by observing the distortion of load-deformation hysteresis loops or response waveform of load and deformation. The study showed that, before fatigue failure, the stress and strain signals are strongly correlated with time and, as the test progresses; they are no longer correlated, as shown in Figure 2–13. This marks a very significant and clear definition of the point of fatigue failure.

Basically, this approach is based on monitoring the changes in the raw data of the response materials to load and deformations. However, an attempt was introduced using a standard error (σ_s) to quantify the distortion in the hysteresis loops between the measured raw data and the best-fit sinusoid for the same raw data, as shown in Equation (2–17) (Kutay et al., 2008). The criterion defined the fatigue failure in the plot of σ_s against number of cycles, when there is a sudden increase from plateau value.

$$\sigma_S = \sqrt{\frac{\sum_{i=1}^{n}(Y_f - Y_m)^2}{n-4}}\ \frac{100}{|Y_f^*|} \qquad (2–17)$$

Where: Y_m and Y_f are measured and fit data points.

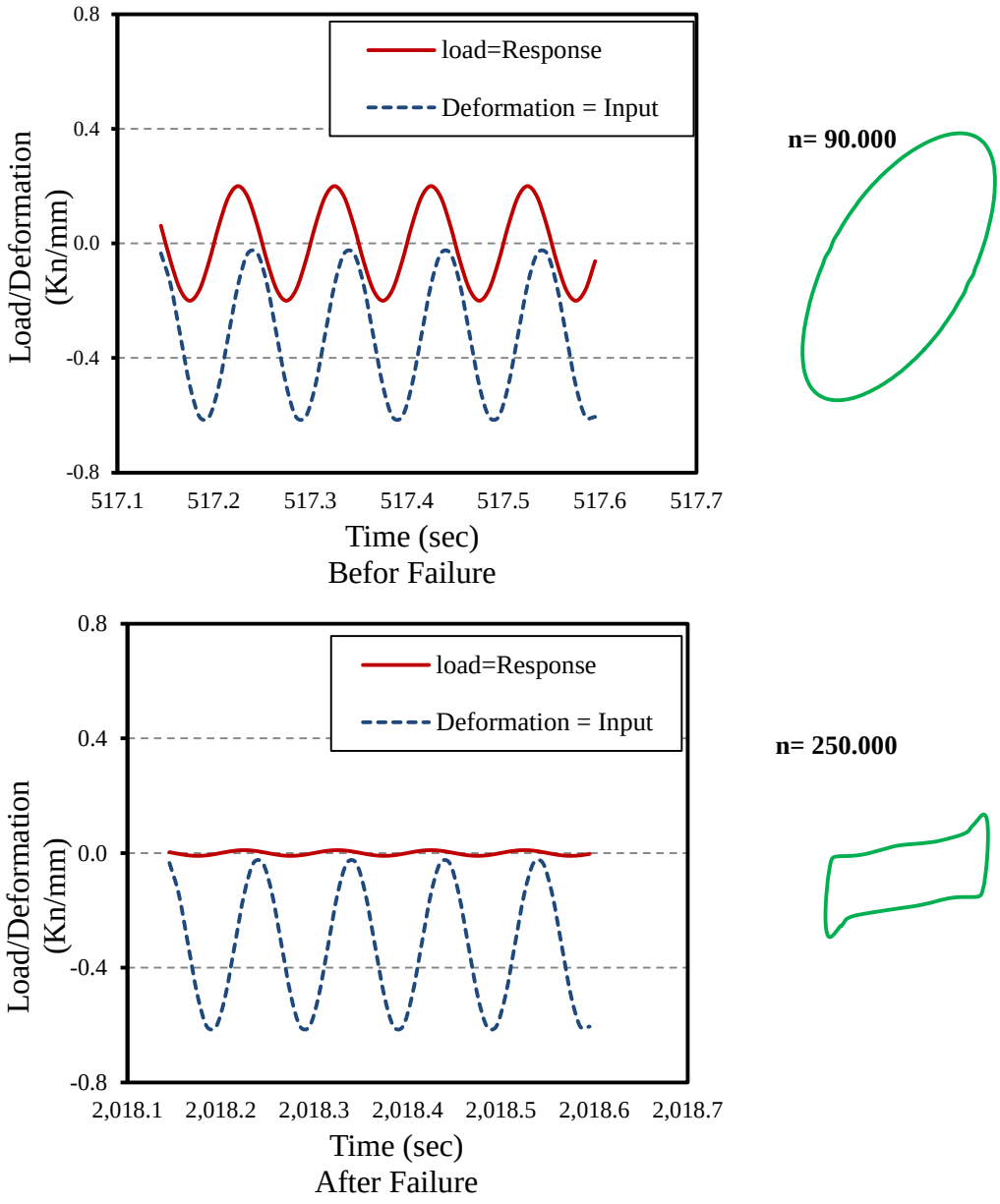

Figure 2- 13: Load-Deformation and hysteresis loops response fatigue test (Al-Khateeb and Shenoy, 2004).

2.4.5. The DGCB Approach

All the previous approaches deal with fatigue as bulk damage created by loading and unloading effects irrespective of test modes and test techniques, i.e. homogenous and non-homogenous test. However, these approaches still valid and used extensively in interpret the outputs of fatigue results.

A new approach was developed by Di Benedetto et.al (1996) at the ((Département Génie Civil et Bâtiment)) in ENTPE so is called DGCB approach; this approach was submitted to analysis the fatigue performance as a pure fatigue damage to avoid the main problems of the classical approach (ε vs N). The authors proposed that the damage in HMA created by loading-unloading test is not only pure fatigue damage but also there are another thinks occur during the test: self-heating and thixotropy; and these thinks were nominated as artefacts or biased (Di Benedetto et al., 1996;Di Benedetto et al., 2004). From this hypothesis, the authors tried to separate these artefacts from the fatigue results to produce pure fatigue damage.

Heating represents the main problem in fatigue due to the dissipated energy (DE) after each cycle, transforming the DE to heat increases the temperature of samples and this reduces the stiffness modulus of samples, where $1^{\circ}C$ variation in the sample's temperature leads to 10 percent variation in the modulus. The authors found the temperature of sample is increases higher than the temperature of test in Phase I due to heating and fatigue, but heating has the predominate effect; while the temperature is stabilized during phase II which is quasi-stationary phase and the fatigue is predominate on this phase as decreasing in the stiffness modulus. The recommendation was using Phase II in characterisation the fatigue damage rate where the heating effect at least and making the correction on fatigue damage rate on this phase to eliminate the artefacts effect (Di Benedetto et al., 1996;Di Benedetto et al., 2004;Baaj et al., 2003).

Di Benedetto *et al*. corrected the experimental damage rate parameter, Equation 2–18, from the artefacts to estimate the true rate of damage per cycle, Equation 2–19, within Phase II, as shown in Figure 2–14a.

$$D_{exp} = 1 - \frac{E_0 - E_N}{E_0} \tag{2–18}$$

$$a_T = a_F + a_B \tag{2-19}$$

Where: D_{exp} is the experimental damage parameter; E_0 and E_N are initial stiffness modulus and current modulus respectively, a_T is the damage slope of Phase II, a_F is the true fatigue damage slope and a_B is the stiffness variation due to artefact

effects (heating and thixotropy). a_B in Phase II is considered to be related to the variation in the dissipated energy as shown in Figure 2–14b (Di Benedetto et al., 1996;Di Benedetto et al., 2004;Baaj et al., 2005).

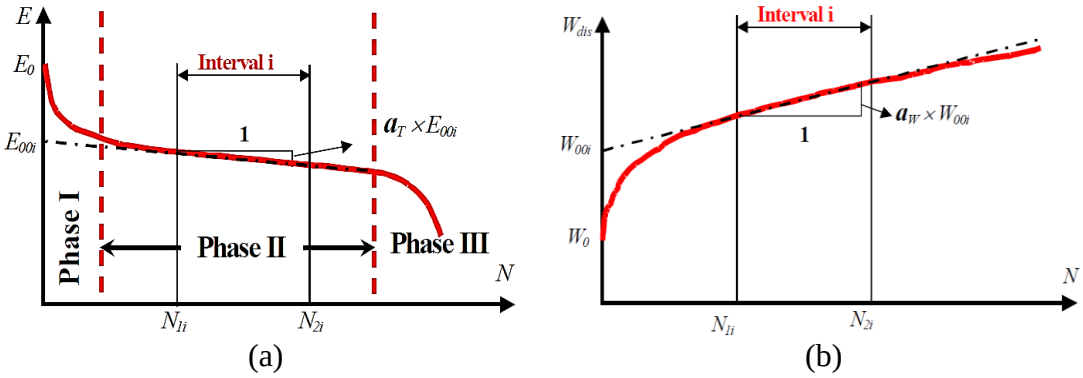

Figure 2- 14: Corrections factors: (a) determination of E_{00i} and a_T from the stiffness evolution curve (b) determination of W_{00i} and a_W from the dissipated energy curve(Baaj et al., 2005).

The final proposed equation for calculating the corrected true fatigue damage slope a_F is shown in Equation 2–20.

$$a_F = a_T + a_w \frac{C_i(E_0 - E_{00i})}{E_{00i}} \qquad (2–20)$$

Noteworthy, a_w represents the slope of the linear regression of the dissipated energy within Phase II; based on the test modes, a_w may have positive or negative effect where the DE increases in stress mode and digresses in strain mode with time. Due to the non-linearity of the Phase II, the DGCB approach considers two particular intervals of cycles during Phase II to calculate the true fatigue damage slope a_{Fi} , these intervals are: first interval, $i = 1$ for 50000 to 150000 cycles, and second interval, $i = 2$ for 150000 to 300000 cycles. Then the fatigue law can be derived from the relationship of the ε_i against a_{Fi}.

This approach was applied by researchers to study the fatigue damage for a wide range of asphaltic mixes and different tests techniques (Baaj et al., 2003;Di Benedetto et al., 2004;Baaj et al., 2005;Artamendi and Khalid, 2005). All the studies confirmed the efficiency of this approach in describing fatigue damage and ranking order of the mixes when the results compared with the classical approached. Also, the main advantage of this approach is represented by the short

period of test, where it could be stooped at 300000 cycles which is enough to calculate the fatigue damage rate. However, this need to make sure it is within Phase II to make this approach applicable.

2.5. Summary

Hot mix asphalt is a viscoelastic material and it is affected by several factors such as binders, aggregates, volumetric properties, loads and environmental conditions. Consequently, the fatigue performance is a complex behaviour, so several approaches were developed to define the fatigue life to overcome this complexity, as discussed earlier.

Although all these approaches are still adopted and valid, there are problems present in: high variance, cost, consumed time and complexity.

Energy during loading and unloading is dissipated because of the viscoelasticity properties of HMA. In this work, more attention was paid to this property to develop a new index for evaluating fatigue performance of HMA.

In the following chapters, expanded works based on the concept of dissipated pseudo-strain energy are presented; in addition, an approach was developed to use the DSR technique in fatigue testing of HMA.

CHAPTER III

CHAPTER III

3. Fatigue Performance in Strain Test Mode

Fatigue performance of HMA is a complex issue due to the nature of these materials which is dealt as viscos material. The external, internal parameters and test conditions such as temperature, time of loading, load, displacement amplitude, frequency and material properties play a role in determine the response of this material to behave from elastic to plastic passing in viscoelastic behaviour in addition to linear-nonlinear behaviour. On the other hand, HMA is composite material; it compromises on coarse, fine aggregates, filler and binder, so the verity in the mechanical properties is highly probable. However, several techniques were developed to simulate the fatigue damage in the HMA to be close as much as can to what is happening in the field, more details for these techniques are presented in Chapter II.

3.1. Introduction

Traditionally, asphalt fatigue tests involve the manufacture of relatively large-size beams or cylinders, which are then conditioned and tested in flexure, tension–compression or diametrically to determine their fatigue properties. These tests may take a considerable amount of time to finish, thus rendering them time-consuming and inefficient. At typical strain or stress levels adopted in classical laboratory fatigue test techniques, the duration can be anything from one day to several days (or even more), which ties up resources and leads to considerable delays in arriving at the required results. In a move to rationalise test procedures and ensuing analyses for asphalt mixtures, a white paper by Christensen *et al*. (D. Christensen et al., 2009) advocated the standardisation of test and analysis protocols, which would lead to a significant reduction in material quantities and test duration; this protocol suggested fatigue testing and analysis based on a reduced cycle and viscoelastic continuum damage mechanical analysis.

In recent years, DSR has been successfully used in performing fatigue tests in addition to rheological properties of binder, mastic and fine aggregate matrices

(FAM) (Airey et al., 2003;Kim et al., 2002;Tan et al., 2012;Kim and Little, 2004;Masad et al., 2008b;Woldekidan et al., 2013;Hintz, 2013;Johnson et al., 2009;Masad et al., 2008a). DSR technique has been improved with time in the ability and accuracy, which enhanced the quality of results and the flexibility of using in several tasks such as fatigue test , relaxation test, creep test , sweep test, thixotropy test, etc. However, the DSR technique has not been used in evaluating the fatigue performance for a full HMA yet because of the limitations in the DSR capacity and sample sizes.

Several criteria were developed and used as approaches to evaluate fatigue performance of HMA as detailed in Chapter II. In this regard, phenomenological approaches such as the traditional approach (TA), energy ratio (ER) and dissipated energy ratio (DER) were correlated with the number of cycles at failure; as detailed in Chapter II. Other approaches are more complicated and advanced called mechanistic approaches such as continuum damage mechanics and fracture mechanics were used to quantify the damage growth, these approach needs to further work such pseudostrain calculation and relaxation test; more details about these approaches are presented in Chapters II and VII.

Alternative prediction tools, however, have been developed based on short fatigue tests to evaluate performance. For example, a model was developed based on the ratio of the initial dissipated energy at the 50th load repetition for samples tested in 4PB, to the total fracture energy from an indirect tension test (IDT) to predict fatigue life in accordance with the traditional approach, i.e. 50% of initial modulus value (Qiang et al., 2012). This model was independent of binder type, content, strain level and volumetric properties. Another technique takes the form of a new direct tensile test called the Fénix test. It is similar to the monotonic test but the applied load is perpendicular to the notch, and has been used to estimate the fatigue behaviour of asphalt samples tested by three-point bending through finding the parameters of the fatigue curve that are related to Fénix test parameters (Pérez-Jiménez et al., 2012).

In this work, an approach based on energy concept by calculating applied and recovered energies to develop a new index; which is used in evaluating fatigue performance of HMA tested in DSR. This approach ensured acceptable

performance evaluation with lower variation and scattering; also, reduced test duration and materials compared to traditional test techniques.

3.2. Objectives of Study

This study in this chapter aims to:

1. Develop an approach for producing small cylindrical samples, i.e. 12 mm in diameter and 50 mm in height, were fabricated from full HMA to be used in fatigue test. This approach requires developing a method for selecting DSR samples reflects the same properties to the full HMA.
2. Introduce a new index called, Fatigue Index (FI^R), based on pseudostrain energy to be used in evaluating the fatigue performance of asphalt mixtures tested using DSR.
3. Verify the ability of the proposed index to rank the mixtures in respect of their fatigue performance; this verification was achieved using an established fatigue performance evaluation tools called TA and ER approaches as discussed above.
4. Verify the DSR technique using the 2PB test technique using the same approaches: FI^R, TA and ER.

The verification process involved the manufacture of four asphalt mixtures including two aggregates gradations, namely gap-graded and continuous; two aggregates, limestone and granite; and two binder grades, hard 40/60 and soft 160/220 Pen binders. The FI^R was evaluated for all the adopted mixtures in the study to evaluate their efficiency in ranking the mixtures tested under the controlled strain mode using DSR and 2PB techniques.

3.3. Methodology

3.3.1. Data Acquisition and Analysis

The DSR technique is non-homogenous test, where the stress and strain are not the same at every point. The DSR mechanism works based on applying a torsion force or torque at the top of the sample while the other end is fixed, as shown in Figure 3–1a. The torque (T) applied to the sample will twist the sample in the

direction of torque, and during that the whole sample's body is deformed according to the direction of torque, for example, the sample will rotate from BA to BA' or BA". However, this rotation is not the same throughout the sample; it varies along the height of the sample from 0 at the bottom, point B, to Ø at the top, points A' or A", as shown in Figure 3–1.

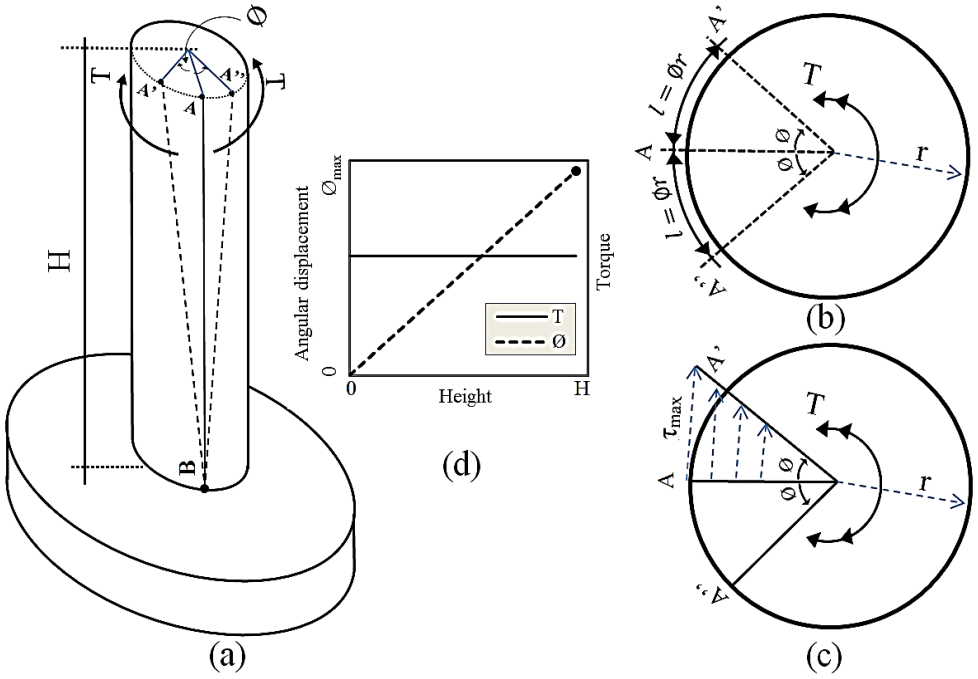

Figure 3-1: (a) the whole sample under torsion load, (b) cross section with angular displacement, (b) cross section with shear stress and (d) variation T and Ø with H.

The main difference between the homogenous and non-homogenous tests is that, in the first test, the mechanical properties of the test (load and deformation) are given directly without needing to postulate a law to calculate them, while the non-homogenous test needs further calculations (Di Benedetto *et al.* 1996). Additionally, in the non-homogenous test, these mechanical properties are calculated at the worst point in the samples during the test, for example: in 4PB and 3PB, they are calculated at the bottom in the mid span of the sample, while in 2PB they are calculated at the top of the first third of the specimen's height from the bottom where the fractural bending is high (Rowe and Bouldin 2000, Maggiore *et al.* 2012). In the DSR technique, the maximum deformation is at the top of the sample, as shown in Figure 3–8d, and is in proportion to the torque, radius (r) and height of the sample (H); so the maximum displacement (*l*) is at the

top which is equivalent to the arc length opposite to the rotation (angular displacement in rad) (Ø); and it is equal to ($\emptyset \times r$). Thus, the maximum shear strain at the top of the sample is calculated using Equation 3–1 (Gere 2004) .

$$\gamma_{max} = \frac{\emptyset r}{H} \tag{3–1}$$

Torque is constant along the sample, as shown in Figure 3–1d, but the maximum shear stress (τ_{max}) for a cylindrical sample under torsion force is at the outer surface of the sample, as shown in Figure 3–1c, and it can be calculated using Equation 3–2 (Gere 2004) .

$$\tau_{max} = \frac{16T}{\pi(2r)^3} \tag{3-2}$$

The cyclic load configuration in the DSR technique is sinusoidal, and, due to the viscous property of the material, the strain lag delays then the stress lag, and this difference is called the phase angle ($\delta=2\pi\Delta t$), as shown in Figure 3-2.

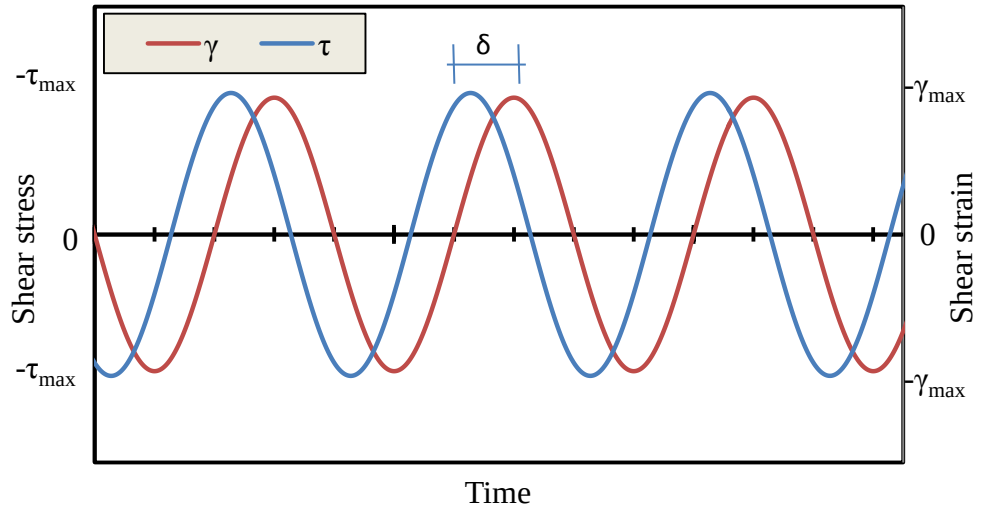

Figure 3- 2: Load configuration in DSR instrument.

In cyclic load laboratory testing, the dynamic complex shear modulus $|G^*|$ is calculated by dividing maximum shear stress amplitude from the stress signal by maximum shear strain amplitude of the strain signal, Equation 3–3.

$$|G^*| = \frac{\tau_0}{\gamma_0} \tag{3-3}$$

Where: $|G^*|$ is dynamic shear modulus, and τ_0 and γ_0 are shear stress amplitude and shear strain amplitude respectively.

$|G^*|$ in viscoelastic materials comprises two components: storage modulus due to the elastic characteristic and loss modulus due to the viscous property; these components can be calculated as shown in Equations 3–4 and 3–5.

$$G' = |G^*| \cos \delta \quad (3–4)$$

$$G'' = |G^*| \cos \delta \quad (3–5)$$

Where: G*'* and G*''* are elastic and loss modulus respectively.

The mechanical parameters: G*, δ, τ, γ and time, are the base for evaluating the fatigue performance in all approaches, as detailed in Chapter II. In this work, an approach based on an energy concept was developed, as shown in the following section, to be used in evaluating the fatigue performance of HMA samples tested in DSR and 2PB techniques.

The question then arises as to the possibility of using the DSR technique in a fatigue test for HMA using small cylindrical samples, 12 mm in diameter by 50 mm in height, i.e. a DSR sample; and these small samples should be representative for the full HMA. An answer to this question can be found by interpreting through the basic concept of the damage growth mechanism during fatigue test. This damage, which is represented by the formation of cracks, i.e. micro and macro cracks, within the matrix due to its stiffness, is much lower than in the aggregates. This concept was used in developing an approach for evaluating fatigue performance based on fracture mechanics (Luo *et al.* 2013). On the other hand, an X-ray CT study with continuum mechanics was used to characterise the damage in the DSR samples tested in fatigue, and showed that the damage developed as cracks and started from the air voids and spread within the matrix (Song *et al.* 2005). Matrix components are: fine aggregates passing through a 2.36 mm sieve, filler and bitumen; this is also called a fine aggregate matrix (FAM). The FAM surrounds the coarse aggregates in the full mixtures and the fatigue damage occurs within it. However, as the DSR samples have a small diameter, and in this study the nominal maximum size of aggregate is 10 mm,

enough FAM can surround the aggregates' DSR sample, ensuring that the samples will simulate the full HMA, as shown in Figure 3–3; also, the damage growth will develop within the FAM. Furthermore, verification that the DSR samples simulate the full HMA was achieved by selecting DSR samples with volumetric properties similar to the full HMA properties, as detailed in the following section.

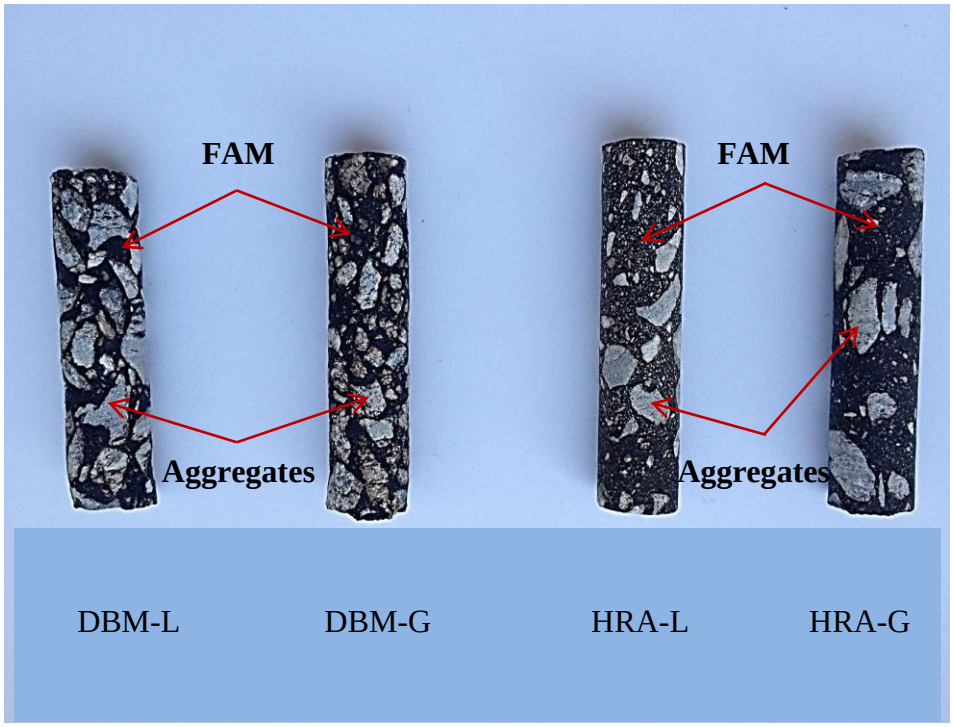

Figure 3- 3 : The aggregates and FAM distribution within DSR samples.

3.3.2. Background and Theory

In fatigue tests using sinusoidal loading and unloading, two types of energy are produced: applied energy during loading and recovered energy during unloading. The difference between both energies is called the dissipated energy, which is equal to the hysteresis loop area (Daniel et al., 2004;Ghuzlan and Carpenter, 2006). A sinusoidal wave was used in this work for fatigue testing to calculate the applied strain energy (ASE) and recovered strain energy (RSE). Figure 3–4 shows the typical sine wave of one cycle loading for time loading t_0 to t_6. Because the calculations are based on the DSR test, the time for one cycle is split into two parts: T_R (right direction of loading) and T_L (left direction of loading). Figure 3–5 is a stress–strain graph representing energy components (ASE and RSE) on a typical hysteresis loop for a viscoelastic material. As shown in Figures 3–4 and

3–5, there are two intervals for loading t_0 to t_1 and t_3 to t_4 in T_R and T_L, respectively, as well as t_1 to t_3 and t_4 to t_6, which are unloading periods in T_R and T_L, respectively. However, strain increases during unloading in periods t_1 to t_2 and t_4 to t_5 because of the viscoelastic behaviour of the material, this interval being the phase angle (δ). As shown in Figure 3–5, there are two parts to ASE: the first one, ASE_1, is under the curve $t_0t_1t_2$, and the second part, ASE_2, is above the curve $t_3t_4t_5$; while, RSE_1 is the area under the curve t_2t_3 and RSE_2 is the area within the region t_5t_6 as details in the energy components graph.

A useful technique to calculate ASE and RSE is to use the integration over the periods [t_0, t_6] as tabulated in Table 3–1 with the basic equation of the energy formula, as in Equation 3–6 (Larson, 1999;Schapery, 1990):

$$W = \int_{t_d}^{t_u} \tau(t) \frac{d\gamma(t)}{dt} dt \quad (3–6)$$

Where W is the strain energy and $\tau(t)$ and $\gamma(t)$ are shear stress and strain, respectively. Equations 3–7 and 3–8 are the sinusoidal shear stress and strain functions.

$$\tau = \tau_0 \sin(\omega t) \quad (3–7)$$

$$\gamma = \gamma_0 \sin(\omega t - \delta) \quad (3–8)$$

Where τ is shear stress, τ_0 is shear stress amplitude, γ is shear strain, γ_0 is shear strain amplitude, δ phase angle, t is loading time and ω is angular frequency in rad/s.

To calculate the pseudostrain energy (PSE), the pseudostrain relationship in the formula below (Equation 3–9) has been used to calculate the pseudostrain energy (Masad et al., 2008a). The final formulations for applied pseudostrain energy and recovered pseudostrain energy are in Equations 3–11 and 3–12.

$$\gamma^R = \frac{G_{lve}\gamma_o}{G_R} \sin(\omega t - \delta_N + \delta_{lve}) \quad (3–9)$$

$$W = \int_{t_d}^{t_u} \tau(t) \frac{d\gamma^R(t)}{dt} dt \quad (3–10)$$

$$W_A^R = \frac{G_{lve}\tau_0\gamma_0}{G_R}\left[\begin{array}{c}\frac{\cos(\delta-\delta_{lve})}{2}\left(\sin^2\left(\frac{\pi+2\delta}{2}\right)+\sin^2\left(\frac{3\pi+2\delta}{2}\right)\right)\\+\frac{\sin(\delta-\delta_{lve})}{4}(2\pi+4\delta-\sin(\pi+2\delta)-\sin(3\pi+2\delta))\end{array}\right] \quad (3\text{–}11)$$

$$W_R^R = \frac{G_{lve}\tau_0\gamma_0}{G_R}\left[\begin{array}{c}\frac{\sin(\delta-\delta_{lve})}{4}(2\pi+4\delta+\sin(\pi+2\delta)+\sin(3\pi+2\delta))\\+\frac{\cos(\delta-\delta_{lve})}{2}\left(\sin^2\left(\frac{\pi}{2}+\delta\right)+\sin^2\left(\frac{3\pi+2\delta}{2}\right)\right)\end{array}\right] \quad (3\text{–}12)$$

Where: γ^R = pseudostrain; G^*_{lve} is dynamic modulus at linear viscoelastic; G_R is reference modulus; δ_N is phase angle; δ_{lve} is phase angle at linear viscoelastic; $W_A{}^R$, $W_R{}^R$ are applied and recovered pseudostrain energy.

Table 3- 1: Integration limits of the strain energy formula

Strain energy	t_l	t_u	Period
ASE_1	0	$\frac{\pi}{2\omega}+\frac{\delta}{\omega}$	$[t_0,t_2]$
ASE_2	$\frac{\pi}{\omega}$	$\frac{3\pi}{2\omega}+\frac{\delta}{\omega}$	$[t_3,t_5]$
RSE_1	$\frac{\pi}{2\omega}+\frac{\delta}{\omega}$	$\frac{\pi}{\omega}$	$[t_2,t_3]$
RSE_2	$\frac{3\pi}{2\omega}+\frac{\delta}{\omega}$	$\frac{2\pi}{\omega}$	$[t_5,t_6]$

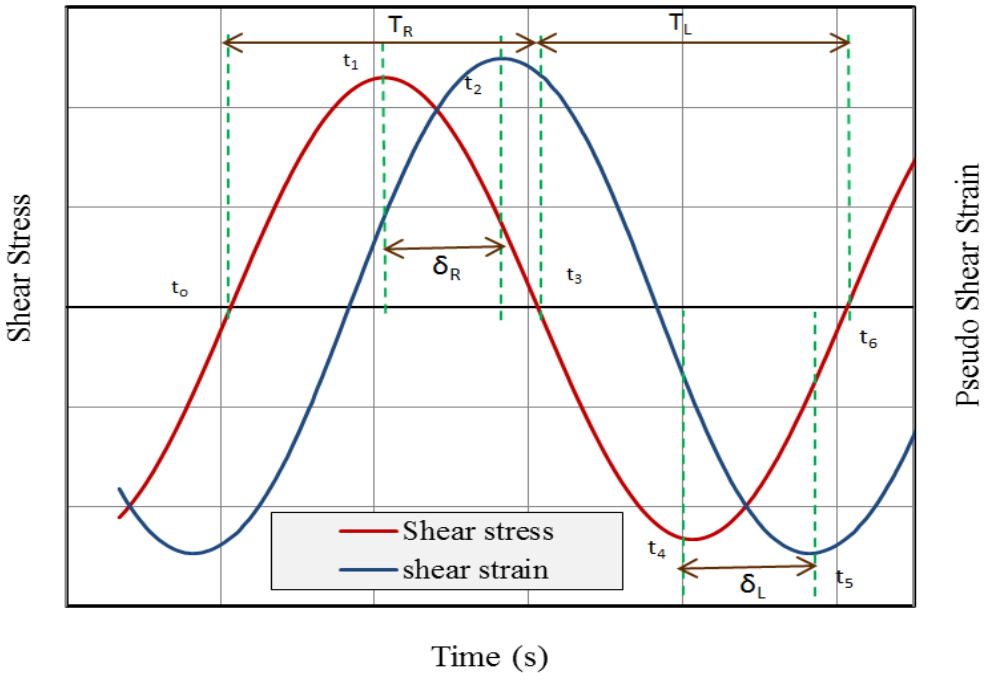

Figure 3- 4: Typical one cycle loading.

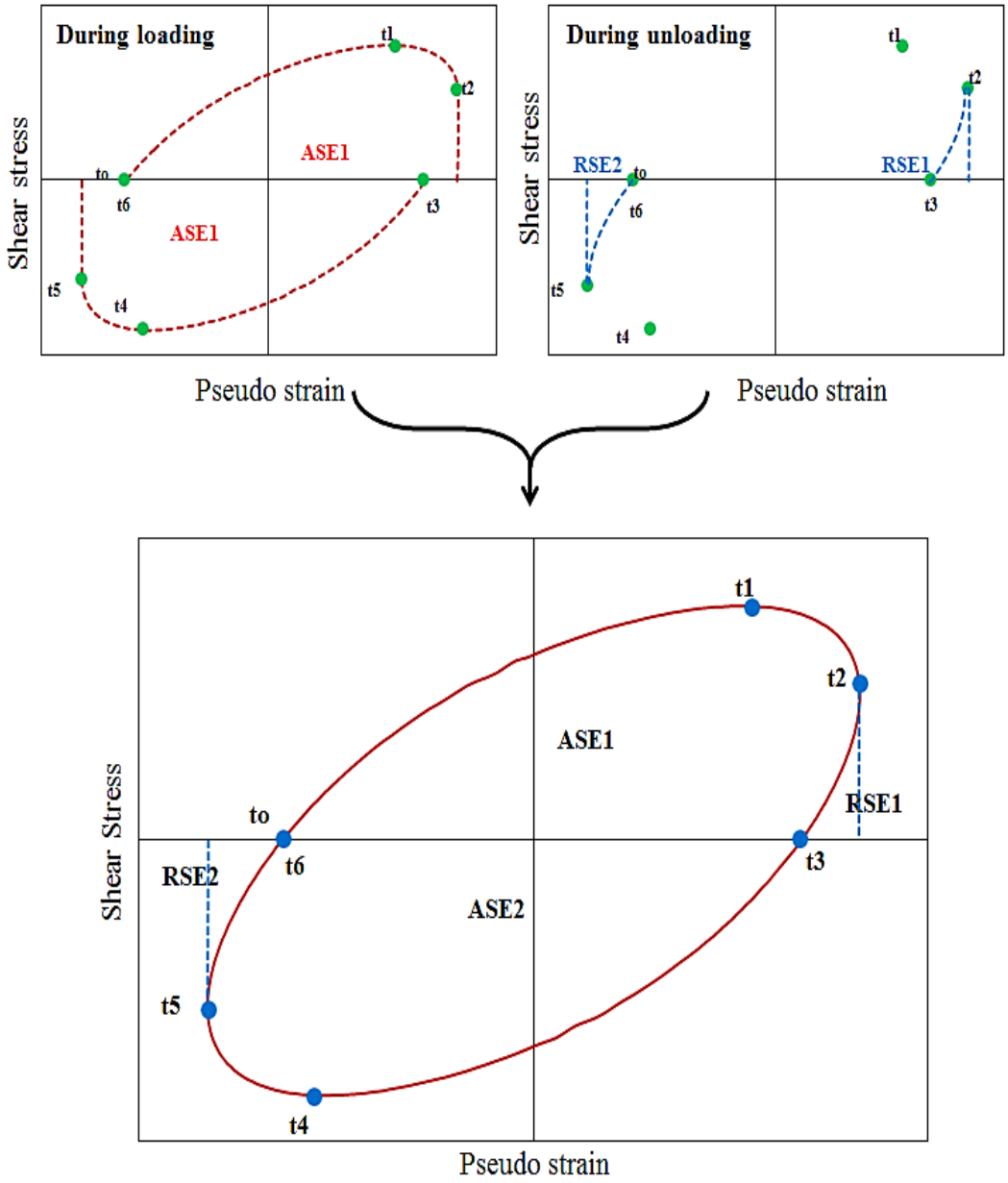

Figure 3- 5: Components of pseudo strain energy on a typical hysteresis loop.

3.3.3. Dynamic Shear Rheometer (DSR)

Dynamic Shear Rheometer-Kinexus (DSR-Kinexus) was used in this work. The DSR Kinexus rheometer was developed by the Malvern Instrument Company. It is an advanced rotational rheometer platform, integrating innovative instrument design with advanced software to provide accurate and precise measurements with ultimate flexibility and ease of use. The specifications of the DSR-Kinexus are shown in Table 3-2. Modifications have been made to the DSR Kinexus in order to enable it to be used for testing cylindrical HMA samples. These modifications

included design and manufacturing end alterations and adjusting the holder connections that are used to hold and set up samples in the proper position for testing. To control the sample temperature during testing, a temperature controller unit (TCU) has been designed and added to the DSR as an essential part. End connections, the holder and the TCU were manufactured in the Liverpool University workshop. As well as, and to monitor the samples temperature itself, data acquisitions unit (instruNet®), has been used to measure the temperature at three points on the samples: at middle and ends of the sample. Figure 3–6 to 3–10 shows the end connections, holders, TCU and whole systems of the test including DSR apparatus and other assessors. Geometrical details of end connections and holders are presented in Appendix A.

Table 3- 2: DSR-Kinexus specifications (Malvern)

Item	**Specification**
Torque range	0.05–200 mNm (0.1 nNm resolution)
Angular velocity range	10 μrads^{-1} to 500 rads^{-1}
Position resolution	<10 nrad
Normal force range	0.001–20N
Normal force response time	<10 ms
Vertical lift speed	0.1 μm/s to 35 mm/s
Plate environmental controller	–40 to 200°C (0.01°C resolution)
Frequency range	1 μHz to 150 Hz
Gap resolution	0.1 μm
Environmental conditions	15–40 C 35–80% non-condensing

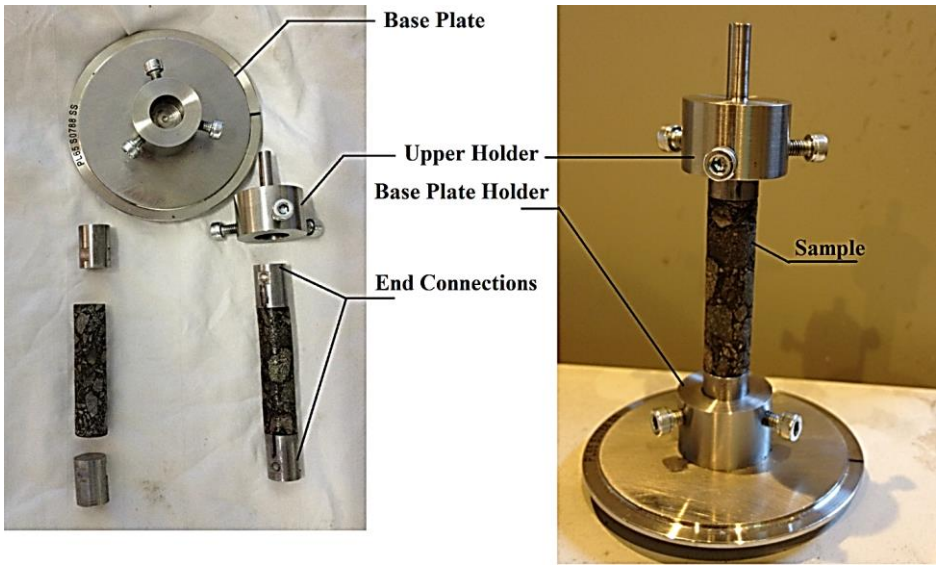

Figure 3- 6: End connections and holders with DSR samples

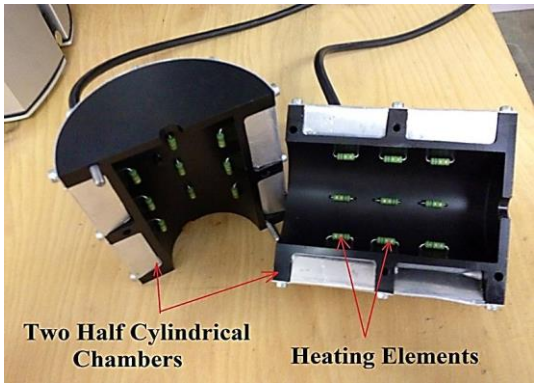

Figure 3- 7: Temperature controller unit (TCU).

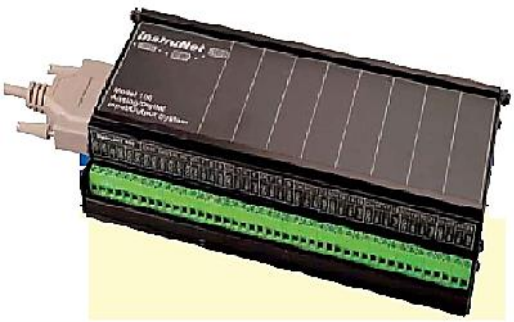

Figure 3- 8: Data acquisition unit (instruNet®)

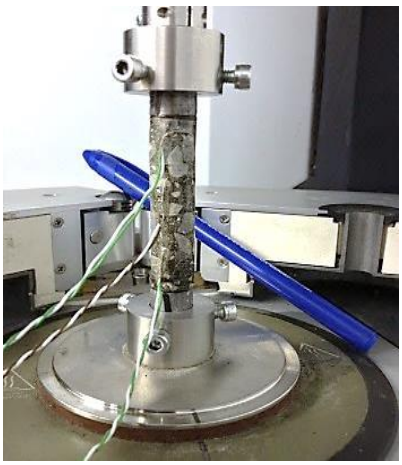

Figure 3- 9: samples with three thermocouples

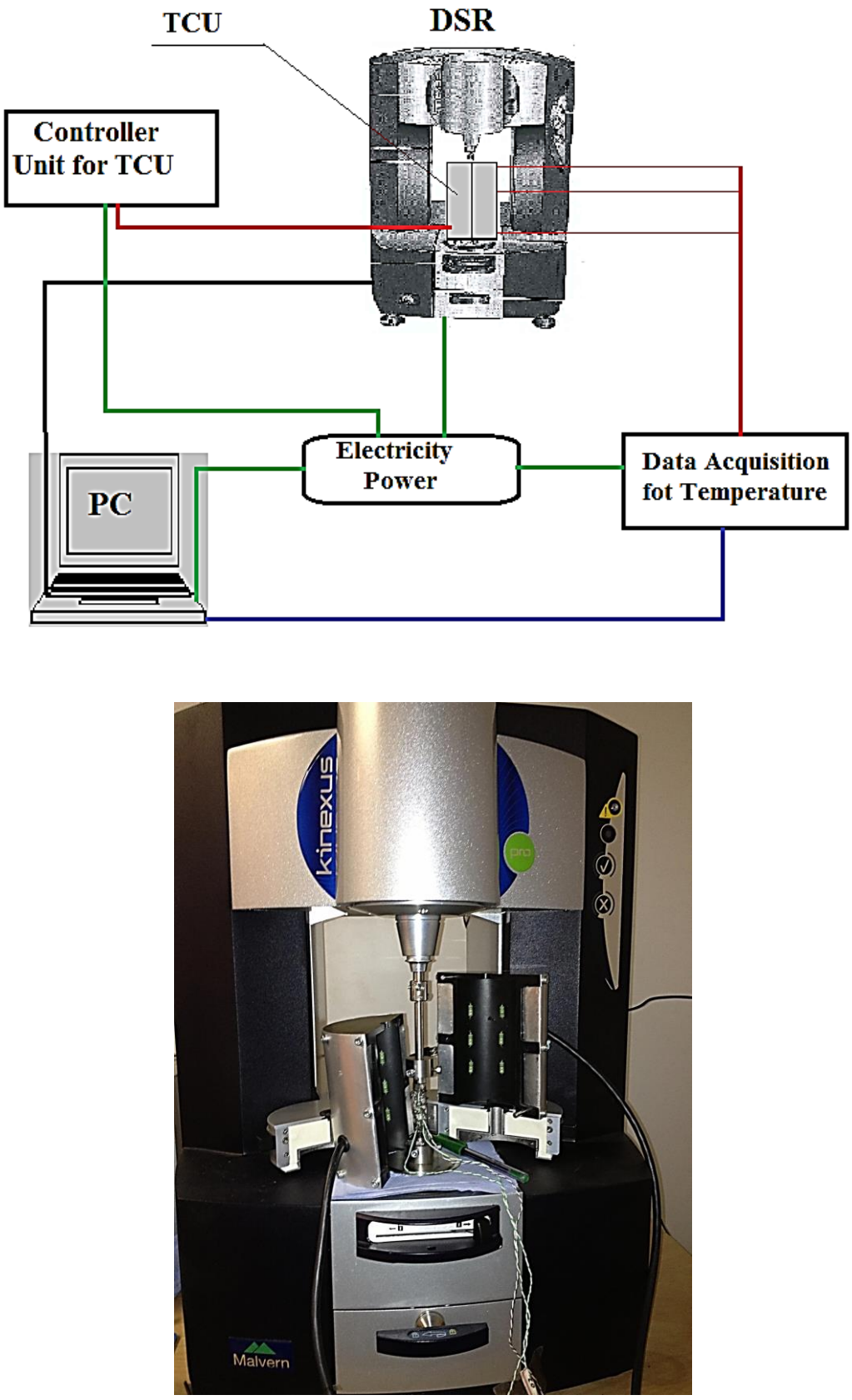

Figure 3- 10: The system of testing including DSR apparatus and accessories

3.3.4. Experimental Work

The experimental works included several aspects: preparation the materials for making the mixes to be used in manufacturing the DSR cylindrical samples (12 mm in diameter and 50 mm high) and trapezoidal beams. As well as, the experimental work included fatigue testing in two techniques DSR and two point bending (2PB); this stage needs to prepare the samples for testing and selecting the appropriate strain amplitude in fatigue test.

3.3.4.1. Materials

In this work, two aggregate types limestone (L) was supplied by Tarmac and granite (G) also supplied by Aggregates Industries, as well as two binders 40/60 and 160/220 penetration grades supplied by Nynas were used to prepare the mixes. The physical and chemical properties of aggregate are shown in Table 3-3 as received from the suppliers.

Table 3- 3: Physical and chemical properties

Properties	Limestone	Granite
Apparent particle density	2.70 Mg/m^3	2.69 Mg/m^3
Compacted bulk density	1.51 Mg/m^3	---
Water absorption	0.3 %	1.7%*, 0.6%**
Los Angeles Coefficient	23	27
Aggregate Abrasion Value	2.1	2.9
pH Value	7.9	---
Oxidisable Sulfides	0.03 %	0.02%*, 0.41%**
Acid Soluble Sulfate	0.02 %	0.02%*, 0.05%**
Water Soluble Sulfate	15 mg/l	<0.01*, <0.001**
* Coarse aggregate ** Fine aggregate		

3.3.4.2. Mix Design

In this work, two kinds of hot mix asphalt (HMA) were produced: gap-graded hot rolled asphalt (HRA) using 40/60 bitumen grade; and continuously graded dense bitumen macadam (DBM) using 160/220 bitumen grade. The recipe specification method was adopted in the design of mixes; this method provides details for the aggregate type and gradations and binder grades for a particular mixes. Also, composition of each component together with laying and compaction are detailed for producing the mixes. In this regard, two types of DBM and two types of HRA were produced in lab according to British standards (BS 4987-1, 2005;BS 597-1, 2005;BS PD 6691, 2010) and denoted as: DBM-L, DBM-G, HRA-L and HRA-G,. Figure 3-11 and 3-12 show the particle size distribution of the aggregates for HRA and DBM mixes respectively.

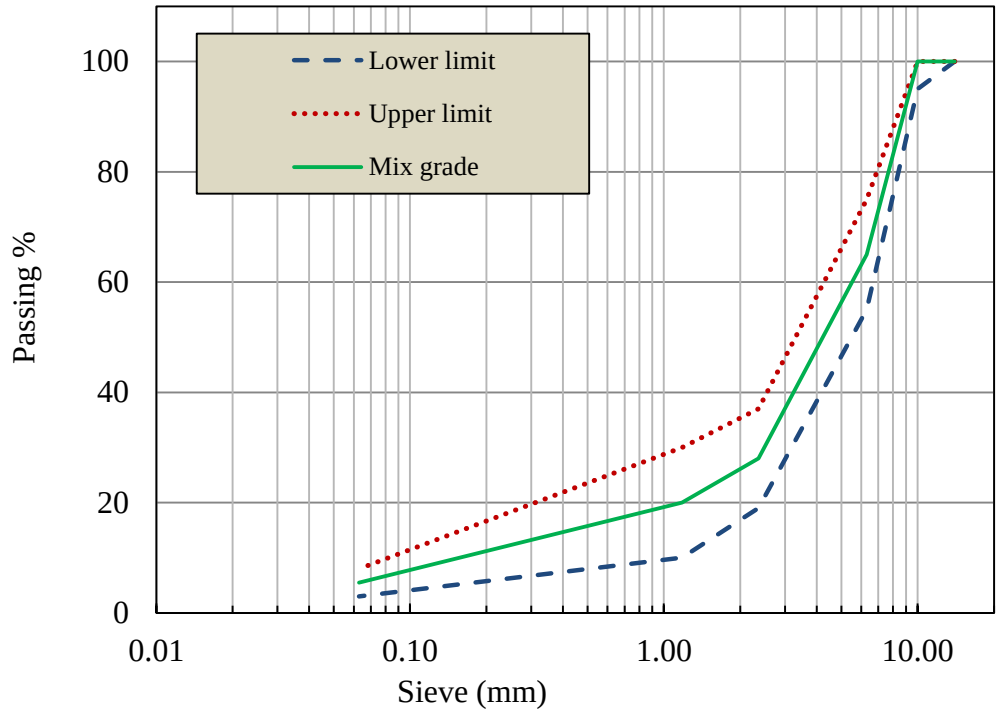

Figure 3- 11: Particle size distribution curves for HRA mix

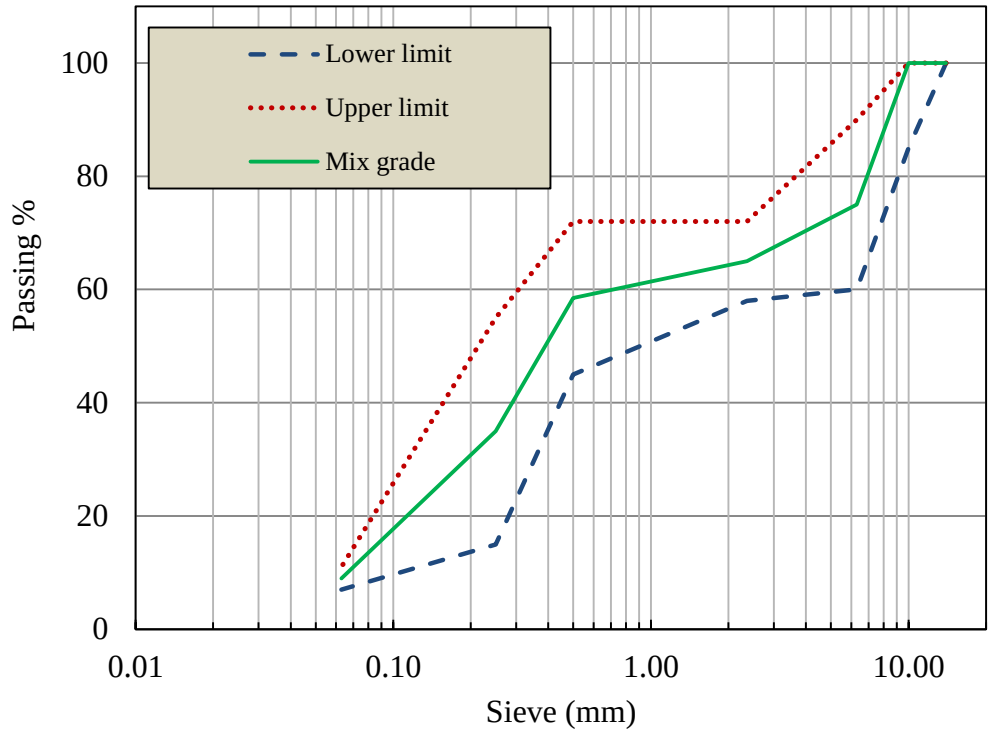

Figure 3- 12: Particle size distribution curves for DBM mix

To manufacture specimens, a laboratory asphalt mixer shown in Figure 3-13 was used. Before mixing, the aggregates and bitumen were heated at the same mixing temperature which was 160°C. Aggregates were heated overnight while bitumen was heated prior to mixing for four hours. After mixing, mixtures were poured into steel moulds 305 × 305 × 100 mm^3 sprayed with silicon grease to prevent adhesion and, then, covered with oiled papers to prevent the adhesion with the compactor. Then, the laboratory roller compactor (BS EN 12697, 2003), shown in Figure 3-14, was used for compaction in a slabs 305 × 305 × 65 mm^3 at four pressures levels 25, 40, 50, and 72 psi; each pressure was applied for 10 passes over the slab according to (BS EN 12697, 2003). The roller compactor was heated to a very high temperature to prevent sudden cooling of mixtures. The compacted slabs were left for 24 hours, to cool at ambient temperature, before de-moulding. The slabs were then cut into two types of beams: prismatic beams (TB) (305 × 65 × 50 mm) and trapezoidal beams for 2PB. TB was cored with an electric coring machine to obtain the cylindrical DSR samples. Table 3-5 shows the mixes details.

Figure 3- 13: The laboratory asphalt mixture.

Figure 3- 14: The laboratory roller compactor

Table 3- 4: Mix ID and material details

Mix type		Aggregate	
		Type	Apparent density (Mg/m^3)
Dense bitumen macadam (DBM)		Limestone (L)	2.71
Dense bitumen macadam (DBM)		Granite (G)	2.67
Hot rolled asphalt (HRA)		Limestone (L)	2.71
Hot rolled asphalt (HRA)		Granite (G)	2.67
Mix properties			
Mix ID	Bulk density (Mg/m^3)	Air voids (%)	Binder grade
DBM-L	2.374	4.9	160/220
DBM-G	2.290	7.5	160/220
HRA-L	2.343	2.2	40/60
HRA-G	2.298	4.0	40/60

3.3.4.3. Preparation of DSR Samples

In the literature, two techniques have been used to prepare DSR samples: Kim *et al.* (Kim et al., 2002;Kim et al., 2003) prepared 15 g individual samples using a steel cylindrical mould 12 mm in diameter and 50 mm in height compacted by using a cylindrical rod at both ends. Zollinger (Zollinger, 2005) prepared cylindrical samples 152 mm in diameter and 85 mm in height using the Superpave gyratory compactor (SGC) and then cored them to obtain small samples. Both techniques, however, have been used only with fine aggregate matrix (FAM) mixtures. In this study, full asphalt mixtures were produced whose properties are more representative than FAM mixtures of the material in the field. In this regards, prismatic beams are the source of the DSR samples for HMA and an electric drill was used to obtain these samples. Briefly, the procedure begins by supporting the beam on a timber plate and tying it tightly using PVC foil or tape to prevent any gap between them and to prevent any movement, this ensures that

damage is minimised when the coring pet punches from the top to the bottom face of the beam and it also reduces vibration. The drill has three speeds, the first speed was chosen for coring and the time required for punching the beams from top to bottom (50 mm) was 35–45 s. Water was used during the coring. The number of DSR samples for each beam was 43–46 samples; these samples were put in an oven for 24 h at 25°C to dry and kept in PVC tubes after coding them, and then stored in a fridge at 10°C. Figure 3–15 shows the steps in this process.

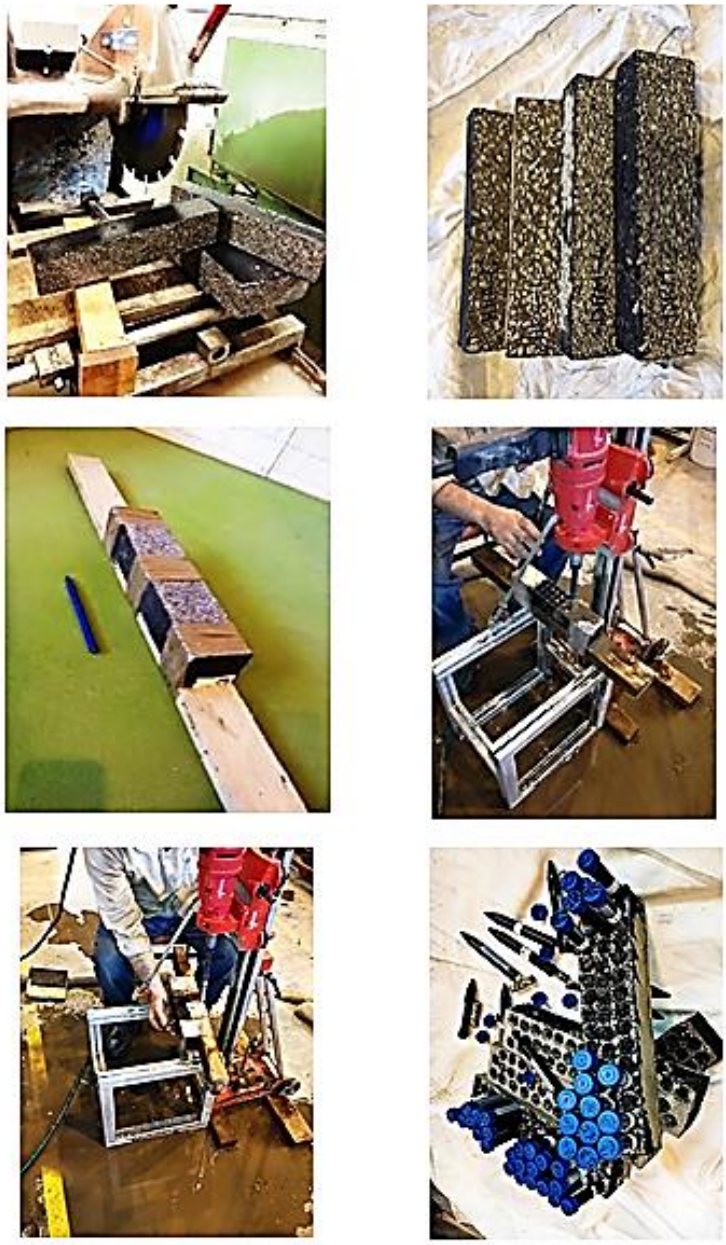

Figure 3- 15: Steps for preparing DSR samples.

3.5. Procedure for Selection DSR Samples

Scattering in the fatigue data is common; therefore, it is necessary to test large number of samples to enhance the reliability of the results (Di Benedetto et al., 2004). In this study, an approach was used to select prepared samples for further use that would reduce the variability within the total number of samples prepared. This approach is based on measuring the sample's bulk density in according with the procedure in the British Standards (BS EN 12697, 2004). The measured bulk density varied according to aggregate grading, shape, type and binder content, among other factors. The approach starts by finding the mode 'M_o' of the measured sample's bulk density, i.e. the value with the highest frequency. This value, M_o, was used to calculate the standard deviation, σ, of the bulk density data using Equation 3–13. A range, R, was then calculated, using Equation 3–14, which is one σ value on either side of M_o. Thus, only those samples whose bulk density value fell within R were chosen for further use in the project, thereby ensuring the least variability. Table 3-5 summarises the values of bulk density and range limits for all the mixtures in the study as shown in Figure 3–16 to 3–19, together with the corresponding air voids.

$$\sigma = \sqrt{\sum_{i=1}^{N} \frac{(X_i - M_o)^2}{N}} \quad (3–13)$$

$$R = M_o \pm \sigma \quad (3–14)$$

Where σ is the standard deviation with respect to the mode, M_o is the mode value (highest frequency), X_i is a single bulk density measurement, N is the number of measurements and R is the range of bulk density of selected DSR samples.

It is worth noting that DBM-G mix has two modes and the differences between them is relatively small as shown in Figure 3–17; therefore, the average of the two modes was taken in calculation the standard deviation and the range (R) using above equations. In contrast, the other mixes had only one mode; maybe DBM-G has high air voids which effect on the mode of bulk density.

Table 3- 5: Bulk density and air void range of DSR samples.

Mix ID	Bulk density range limits (Mg/m^3)			
	Upper	Mode	Lower	$\sigma_{(Mo)}$
DBM-L	2.413	2.398	2.383	0.015
DBM-G	2.373	2.350	2.327	0.023
HRA-L	2.368	2.356	2.344	0.012
HRA-G	2.327	2.311	2.295	0.016
Mix ID	Air voids range limits (%)			
	Upper	Upper	Upper	
DBM-L	4.486	3.872	3.259	
DBM-G	6.023	5.101	4.179	
HRA-L	2.153	1.641	1.130	
HRA-G	4.150	3.487	2.824	

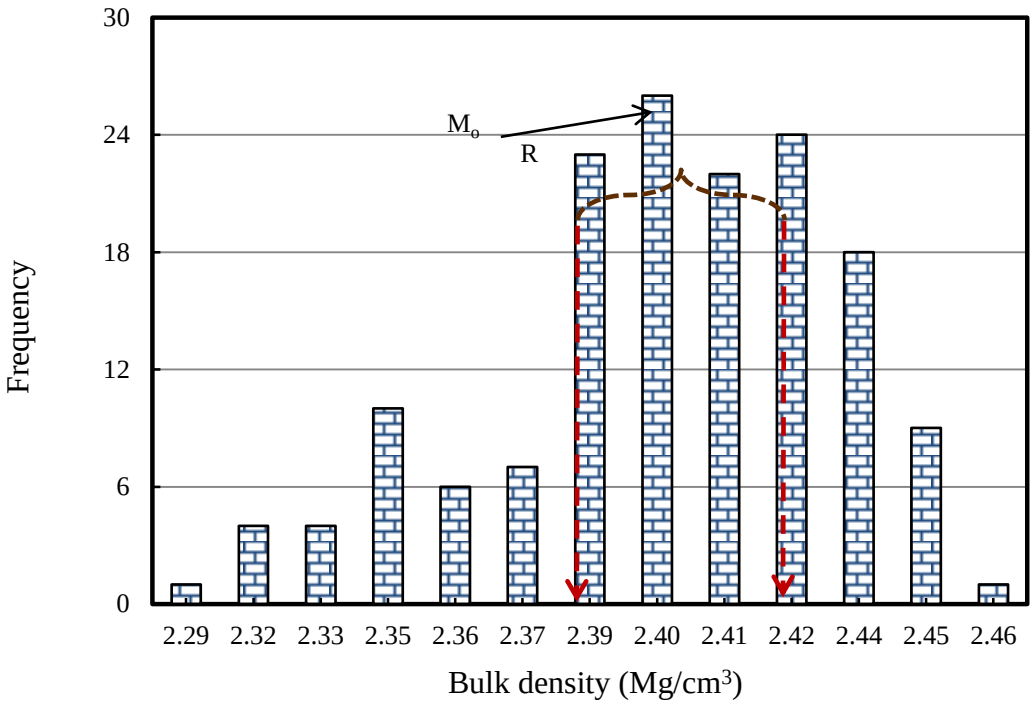

Figure 3- 16: Bulk density histograms for DSR samples of DBM-L mix.

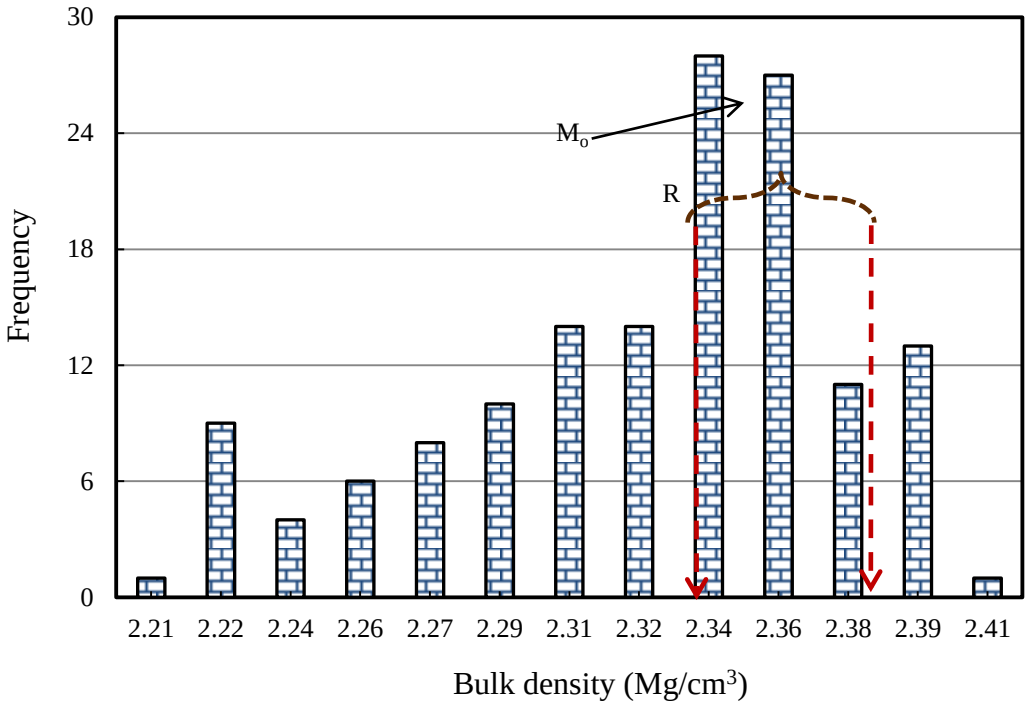

Figure 3- 17: Bulk density histograms for DSR samples of DBM-G mix.

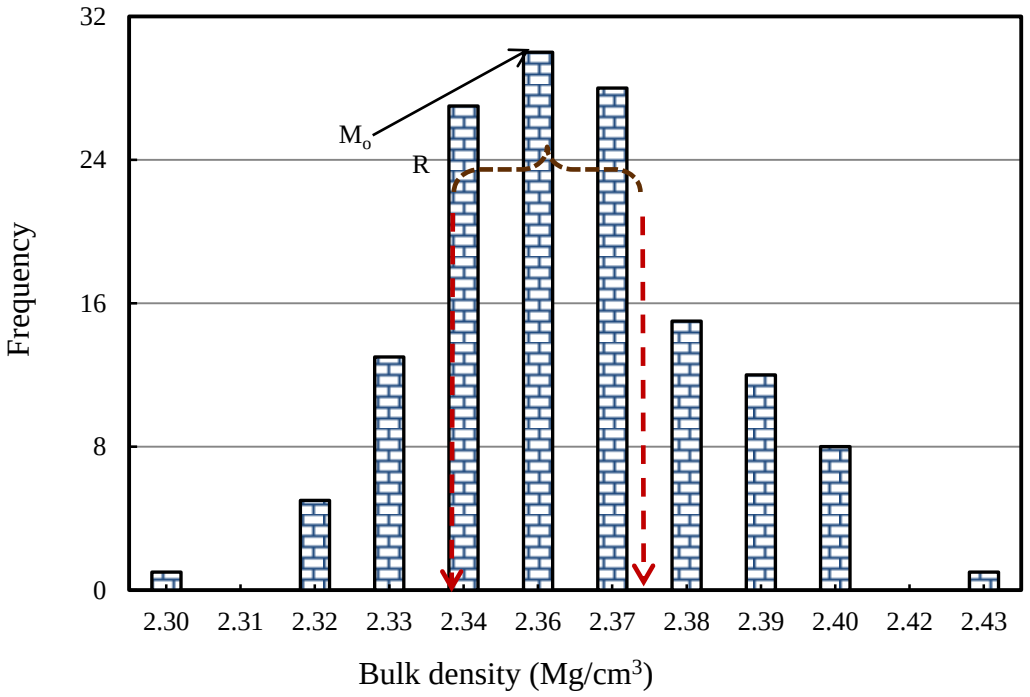

Figure 3- 18: Bulk density histograms for DSR samples of HRA-L mix.

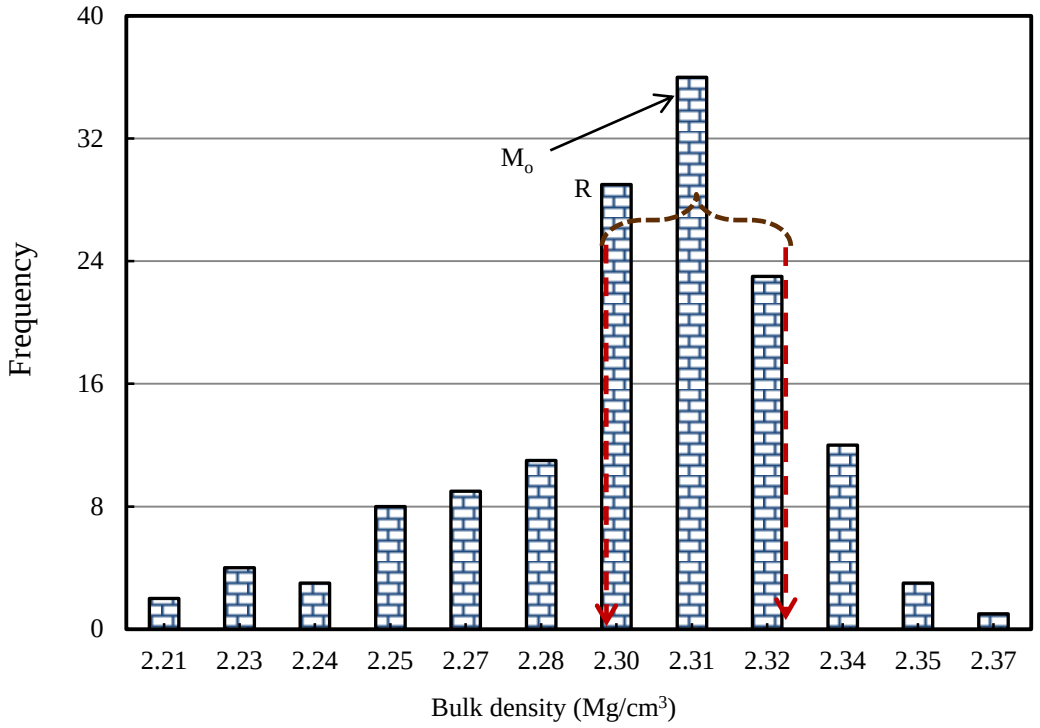

Figure 3- 19: Bulk density histograms for DSR samples of HRA-G mix.

The bulk density and air voids of beams are used for coring DSR samples and trapezoidal specimens were compared with their mode values of bulk density and air voids of DSR samples as shown in Figure 3–20 and 3–21. The variation in bulk density for DSR, beams and trapezoidal specimens was not noteworthy as shown in Figure 3–20; but air voids of DSR samples were slightly lower than 2PB and prismatic beams as shown in Figure 3–21.

On the other hand, it can be seen that the variation of the samples in each mix is very low as revealed from the error bores which are presented using the standard deviations of the samples as shown in Figure 3–20. This will insure that the selected DSR samples are more representative and have similarity to the HMA which are used as resources for DSR samples.

Also, noteworthy was that the bulk densities of the mixes with limestone are slightly higher than the granite mixes for all specimens because the apparent density of the limestone was higher than granite as detailed in Table 3-4. In addition, air voids in the granite mixes were greater in number than the limestone mixes, possibly because the surfaces of granite aggregates rougher than that of

limestone and this helps to keep some voids in between the aggregates during compaction. On the other hand, it is clear that there is not significant variance between beams and trapezoidal specimens as is in the DSR samples.

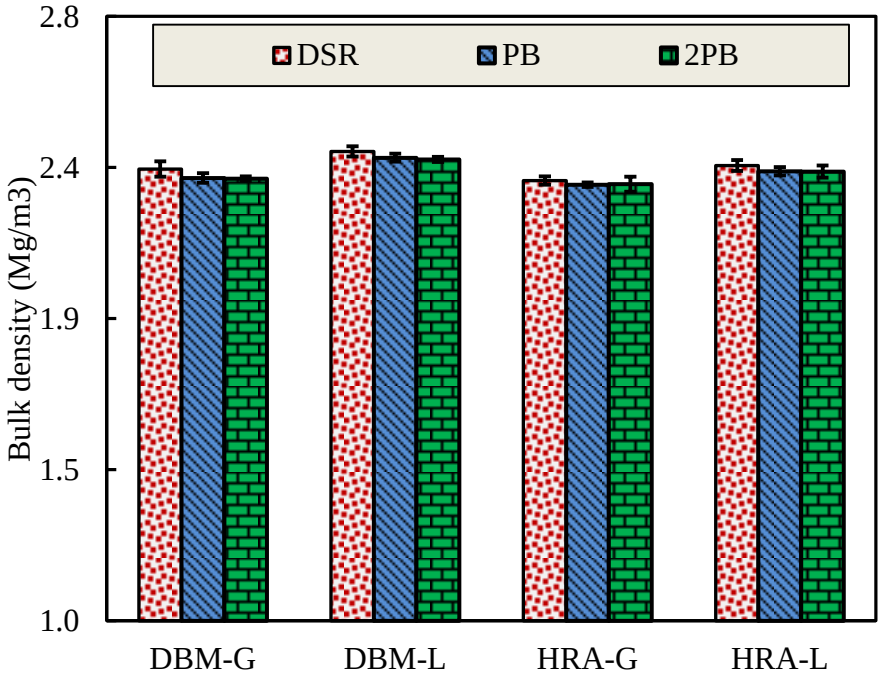

Figure 3- 20: Bulk density for DSR, PB and 2PB samples

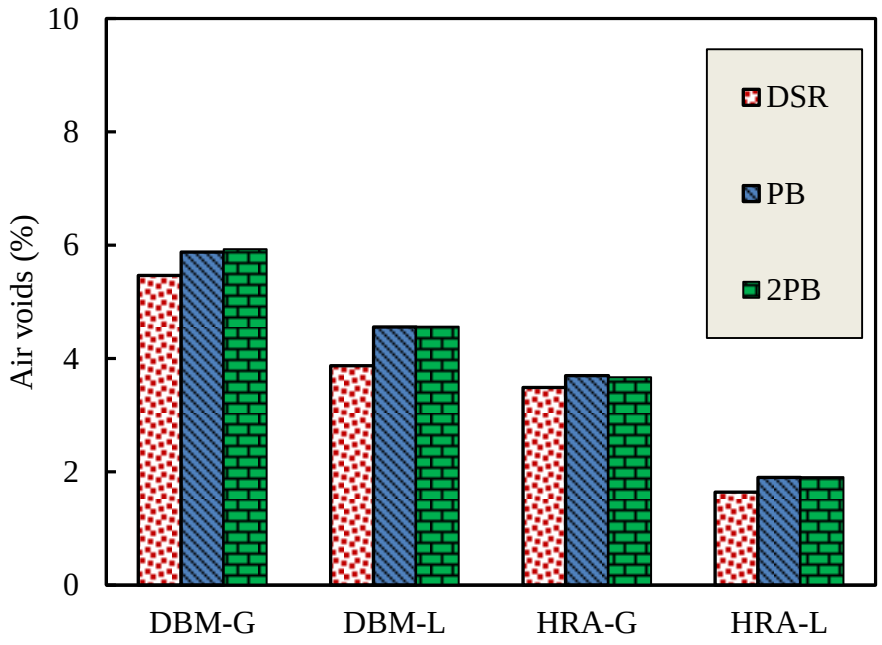

Figure 3- 21: Air voids for DSR, PB and 2PB samples.

3.6. Two-point Bending Fatigue Test

3.6.1. Preparation Trapezoidal Specimens

In this work the same trapezoidal specimen as used by the Laboratoire Central des Ponts et Chaussées (LCPC) has been used. Specimens were prepared and treated according to British Standards (BS EN 12697-24, 2012); the dimensions of the specimens were: major base 56 mm, minor base 25 mm, thickness 25 mm and length 250 mm. The same method that was used for preparing asphalt slabs (305 × 305 × 65 mm) for DSR samples has been used for preparing slabs for trapezoidal specimens. Initially, a masonry saw was used for cutting beams (305 × 65 × 25 mm) as shown in Figure 3–22, later a trapezoidal steel mould was used to print the same shape on the wide face (305×65 mm), then the masonry saw was used to cut the beam to obtain trapezoidal specimens with dimensions (250 × 56 × 25 × 25 mm) as shown in Figure 3–23. These specimens have been marked and stored on their flat faces at atmosphere temperature to eliminate any moisture, then were stored in a dry controlled temperature cabinet at 10˚C to prevent any distortion or ageing; to be ready later for volumetric measurements and fatigue testing.

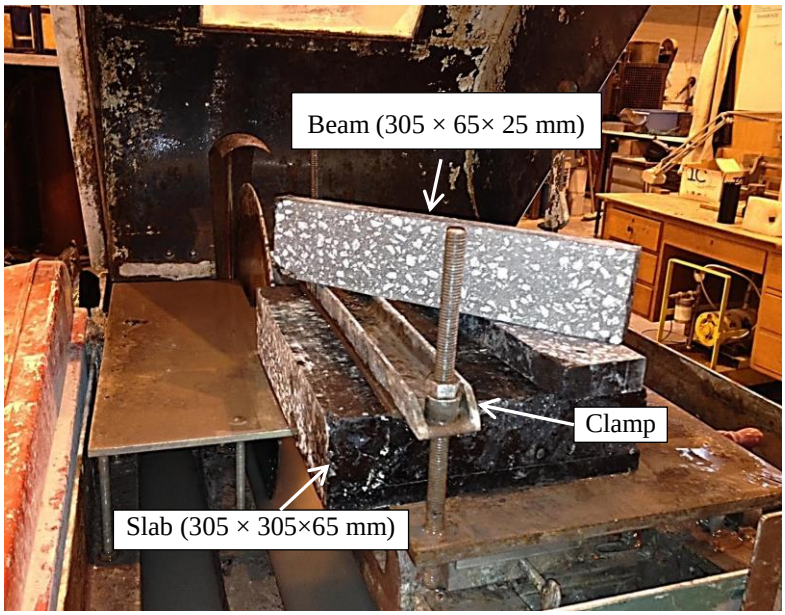

Figure 3- 22: Sawing trapezoidal specimens for compacted asphalt slabs

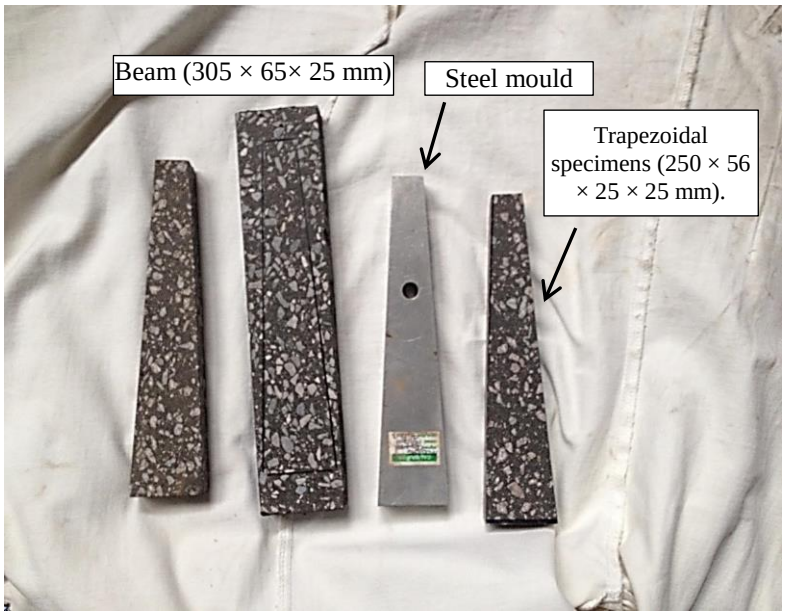

Figure 3- 23: trapezoidal specimens

3.6.2. Specimen Gluing and Conditioning

Specimens for testing were removed from the controlled environment chamber to be bonded to the steel end plates using epoxy resin to allow them to be fitted in the 2PB test machine according to British Standards (BS EN 12697-24, 2012). The large base of the trapezoidal specimen was glued to a groove 2 mm deep manufactured from a steel base 20 mm thick. In this case, a special jig was used to carry out this operation to ensure the correct position of the specimen on the base plate during the resin hardening process, as shown in Figure 3–24.

The Epoxy resin film was applied as thinly as possible and allowed to harden for at least 24 h at room temperature. Later, the glued trapezoidal specimens were brought to the environmental chamber of the 2PB machine and set into a suitable position to be left for 2 h for conditioning before testing.

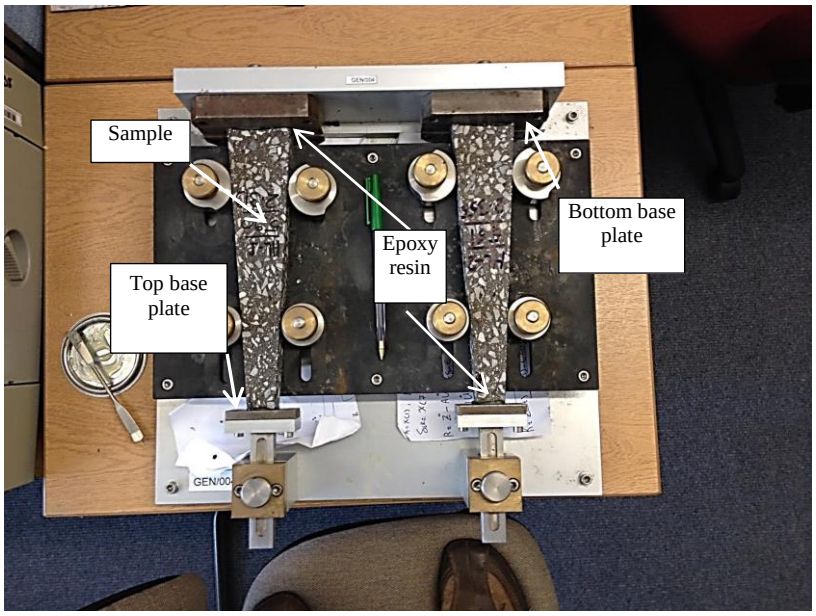

Figure 3- 24: Jig for gluing specimens.

3.6.3. 2PB test and Data Collection

This test is a non-homogenous test where the beam is cantilevered and the flexural bending is not constant along the specimen. Additionally, the section modulus (S) of the trapezoidal beam is not constant as in the prismatic beam due to the variety in the beam's sections along its height, as shown in Figure 3–25. Consequently, we cannot assume that the maximum stresses occur at the cross section with the largest bending moment – sometimes the maximum stresses occur elsewhere; therefore, this makes the analysis more complicated.

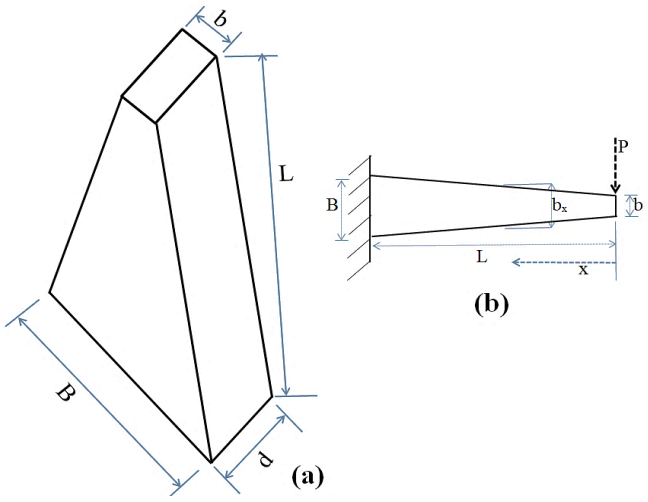

Figure 3- 25: Geometry of a typical trapezoidal beam

Conventional bending theory has been used to analyse the trapezoidal cantilever beam (Gere 2004). Bending stress can be determined using the flexure formula (Equation 3–15); this formula shows that the stresses are directly proportional to the bending moment and inversely proportional to the section modulus.

$$\sigma = \frac{M}{S} \tag{3–15}$$

$$S = \frac{I}{c} \tag{3–16}$$

Where: σ is the bending stress, M is the bending moment, S is the section modulus, I is the moment of inertia and c is the distance from the numeral axis; in this case, c is at the neutral axes.

The depth of the trapezoidal beam (b_x) at any cross section of the beam can be expressed as a function of the distance x measured along the beam's axes from the free end, as shown in Figure 3–25b and Equation 3–17. The cross section of the trapezoidal beam is rectangular, so the moment of inertia (I) can be calculated using Equation 3–18.

$$b(x) = \frac{B-d}{L}x + b \tag{3–17}$$

$$I(x) = \frac{bh^3}{12} = \frac{b\left(\left(\frac{B-d}{L}\right)x+b\right)^3}{12} \tag{3–18}$$

Substituting Equations 3–17 and 3–18 into Equations 3–15 and 3–16 yields:

$$\sigma(x) = \frac{6Px}{d\left(\left(\frac{B-d}{L}\right)x+d\right)^2} \tag{3–19}$$

In this work, an LCPC specimen was used, so the dimensions in mm are: B=56, d=25, b=25 and L=250. Figure 3–27 shows the plot of Equation 3–19 using the geometric properties of the LCPC with one unit load (1 KPa); it is clear that the maximum stress is above the bottom base of the sample. This point can be found by differentiating the bending stress equation (Equation 3–19) and setting the derivative equal to zero to determine the location of the maximum stress.

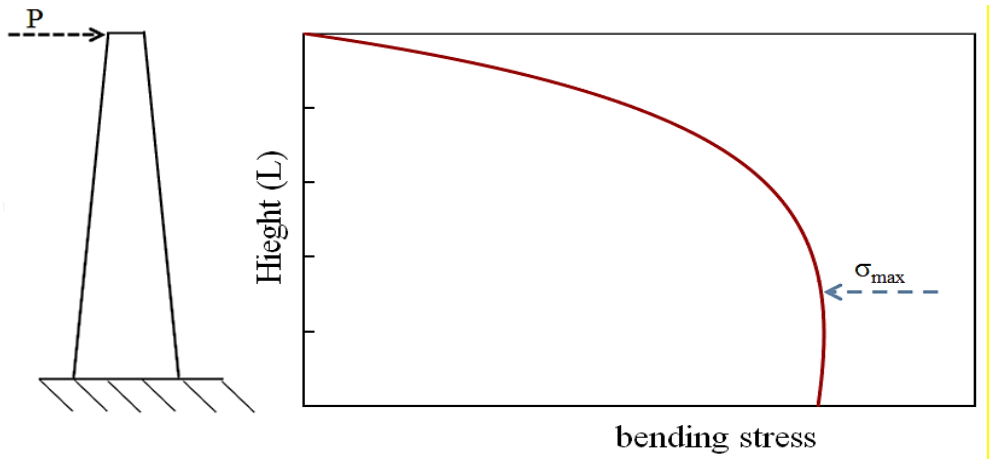

Figure 3- 26: Stress distribution in a Two-Point bending trapezoidal specimen

Stiffness modulus can be calculated at the maximum stress using the expression in Equation 3–20 (Cocurullo *et al.* 2008).

$$E = \frac{PL}{\Delta bd}\left[K_1 \frac{L^2}{d^2} + K_2(1+\mu)\right] \quad (3–20)$$

Where: Δ is the deflection at the top of the beam, b is the width of sample, K_1 is the deflection coefficient from bending, K_2 is the deflection coefficient from shear and μ is Poisson's ratio. For the LCPC trapezoidal sample, K_1 and K_2 are 0.389 and 1.301 respectively (Rowe 1996). Strain in 2PB follows the stress response, being at maximum when the stress is maximum; thus, the maximum strain can be calculated using formula 3–21.

$$\varepsilon_{max} = \frac{\sigma_{max}}{E} \times 100 \quad (3–21)$$

In this project, the controlled strain test mode was used to test all trapezoidal specimens using the two-point bending test machine, as shown in Figure 3–27. Under loading, the trapezoidal specimen was subjected to a sinusoidal displacement that was measured by an LVDT displacement transducer at the top of the trapezoidal specimens. The stress amplitude was measured by a force transducer at the top of the specimens, as detailed in Figure 3–27. In this work, three trapezoidal specimens from each mix were tested under the following conditions:

a) Controlled strain test mode 200 μstrain

b) Test temperature 20°C
c) Frequency 10 Hz.

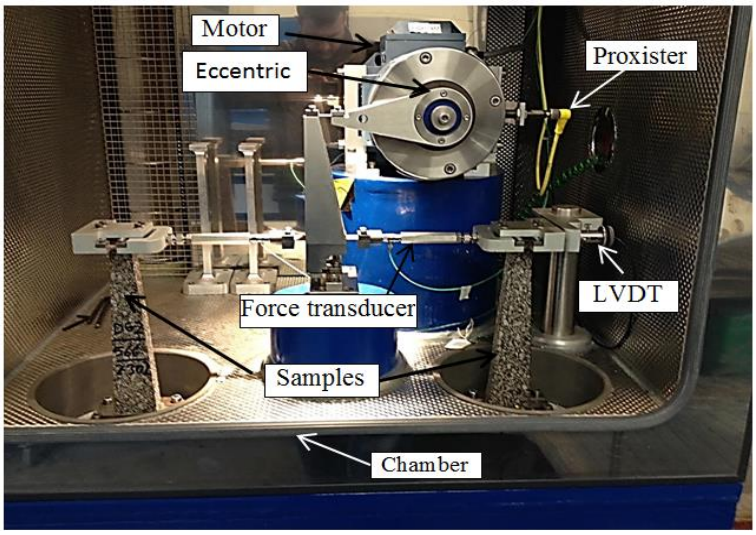

Figure 3- 27: Two-point bending apparatus.

3.7. Analysis and Discussion of Results

3.7.1. Determination of strain amplitude

Fatigue testing in the DSR requires the identification of the strain or stress level in the damage zone to be used later as the stress/strain amplitude for fatigue testing. In the literature, different techniques have been applied. Kim *et al.* (Kim et al., 2003;Kim et al., 2002) used amplitude sweep strain to find the maximum stress value that could be applied to the sample before causing damage. Masad *et al.* (2008) used high strain amplitude value 0.2% in fatigue testing for DSR samples prepared from fine aggregate matrix (FAM), and the stress corresponding to a 50% reduction of initial complex shear modulus (G^*) was used for fatigue testing in the stress test mode. This selection was arbitrary and the authors proposed this selected value in fatigue test is in the damage region without any clue, also this approach was applied on FAM only.

In this work, and to determine the strain amplitude in fatigue testing, sweep strain amplitude was used and the changes in the slope of the strain–stress curve at each point were calculated using Equation 3–22. At the instant when the slope changed from positive to negative, the value of the strain amplitude at the damaged region was identified.

$$\frac{\Delta\tau}{\Delta\gamma} = \frac{\tau_{i+1} - \tau_i}{\gamma_{i+1} - \gamma_i} \quad (3\text{–}22)$$

Where τ_i and τ_{i+1} are shear stresses at shear strains γ_i and γ_{i+1}, respectively.

In this study, three samples were arbitrarily selected within the range *R* in Table 3-5, and sweep strain amplitude was conducted in the DSR using the detailed DSR sequence in Appendix B-1. Linear increments of 65 points were chosen for sweep strain amplitudes from 0.001 to 0.7% for 100 cycles applied at each strain level. The slope changes plotted against strain amplitude for the sweep strain test for the DBM and HRA mixes are shown in Figures 3-28 and 3-29. It is clear that the damage occurs earlier in DBM-G and the amplitude range (0.2–0.3%) is shorter than that of DBM-L (0.3–0.45%). This is possibly due to that air voids in DBM-G is higher than air voids in DBM-L as detailed in Table 3-4, so, the damage in DBM-G is earlier than DBM-L. In HRA, the damaged regions for both granite and limestone were equal, perhaps because both mixes are homogenous. Information is given in Table 3-6 on the strain range at which damage begins and, hence, the selected values for fatigue testing. To compare between the fatigue performances of the mixes, 0.3 and 0.25% strain levels were selected for DBM and HRA, respectively. This is sensible because the DBM includes a softer binder that requires a higher movement level to incur any damage. Table 3-6 provides details about the strain amplitudes for fatigue testing. In this study, strain amplitudes were selected using the same value for fatigue testing in the same mix kind to take into account the effect of the aggregates types; also, DBM-G was tested at shear strain amplitude 0.25 in addition to 0.3 in order to consider the effect of mix type when compared with HRA-G.

Table 3- 6: Strain/stress amplitude test results

Mix ID	Shear strain (%)	
	Strain @ damage	Strain for fatigue test
DBM-L	0.30–0.45	0.30
DBM-G	0.20–0.30	0.30, 0.25
HRA-L	0.25–0.35	0.25
HRA-G	0.25–0.35	0.25

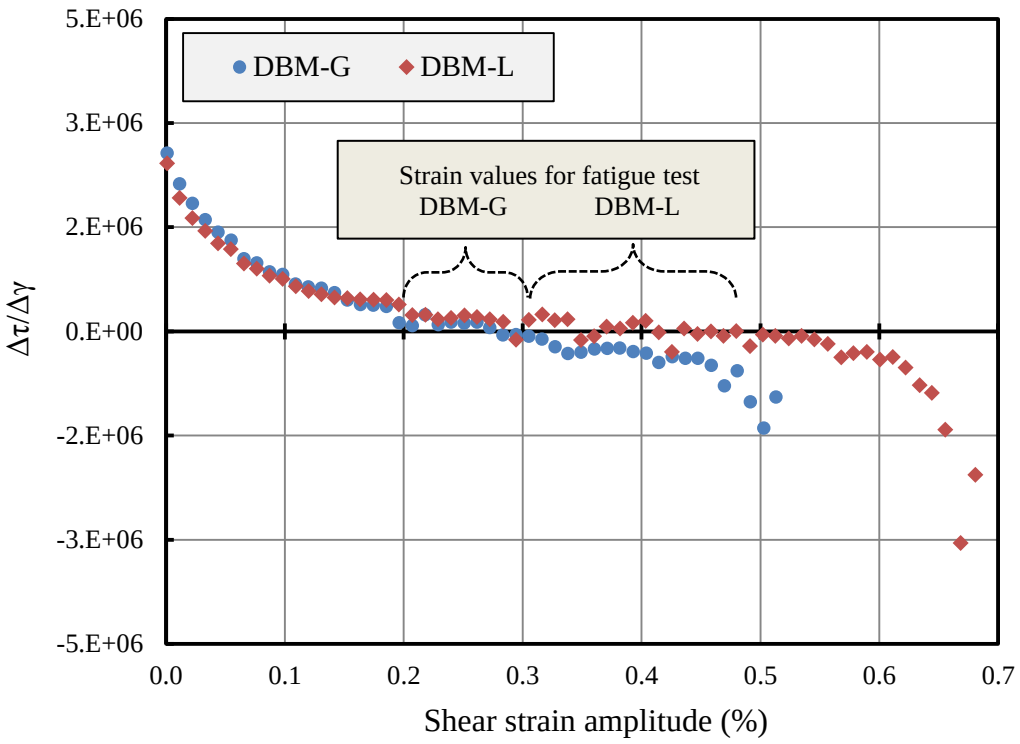

Figure 3- 28: Sweep strain amplitude for DBM mixes

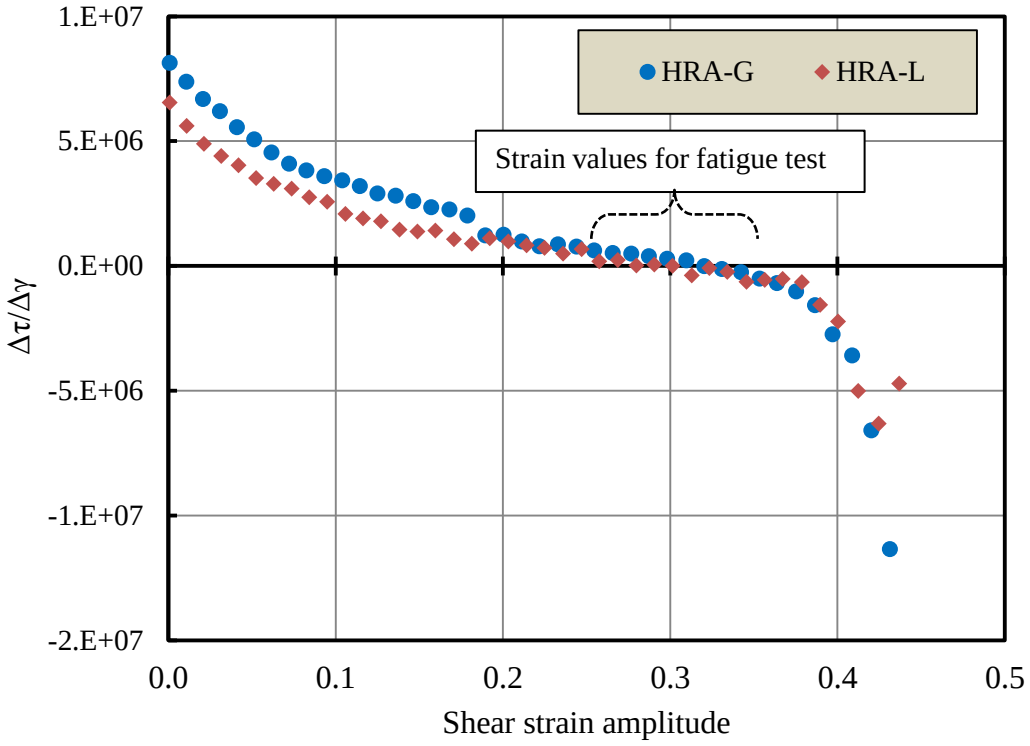

Figure 3- 29: Sweep strain amplitude for HRA mixes

3.7.2. Fatigue Performance Using Fatigue Index (FI^R)

Herein, an approach was developed to analysis the fatigue performance of asphalt mixtures. First, we arbitrarily selected nine samples within the range R to be tested in fatigue using the shear strain values in Table 3-6. Fatigue test was performed in DSR using the detailed sequence in Appendix B-3. A new fatigue index (FI^R) was formulated based on the energy concept as a function of the ratio of pseudo strain recovered energy to pseudo strain applied energy (Equation 3–23). Logically, when W_R^R is equal to W_A^R, then the fatigue index equals zero, which means no damage has occurred in the material. Otherwise, when the W_R^R is equal to zero, then the fatigue index equals one, which means that the sample is completely damaged. So, the value of FI^R should be between one and zero.

$$FI^R = 1 - \frac{W_R^R}{W_A^R} \tag{3–23}$$

Figure 3-30 shows the relationship of FI^R plotted against the normalised shear modulus. It is clear that there are plateau values for all mixes where the FI^R is barely constant between 0.85 to 0.35 of normalised shear modulus; and increases sharply after that. This trend is similar to the one shown in the dissipated energy ratio approach (Daniel et al., 2004). Figure 3-30 demonstrates that FI^R reflects the performance of HRA fatigue is higher than DBM and this is consistent with a previous study (Brown, 1995) and limestone is better than granite. On the other hand, the maximum FI^R value is about one, which means the sample is completely damaged, and this is the closest to the reality, as the majority of tested samples were completely damaged at the end of testing.

Figure 3-31 summarises the fatigue results as a fatigue index value within plateau region. It is clear that the fatigue performance as an FI^R for mixes with limestone aggregates is better than the granite mixes. This is due to the fact that the number of air voids in the mixes with granite is higher than in the limestone mixes as detailed in Table 3-4 and presented in Figure 3-32. Maybe the main advantage for using FI^R is revealed from the variation in the results, which was low as shown by the error bars, i.e. standard deviation, in Figure 3-31, this property was compared with other two approaches as shown later.

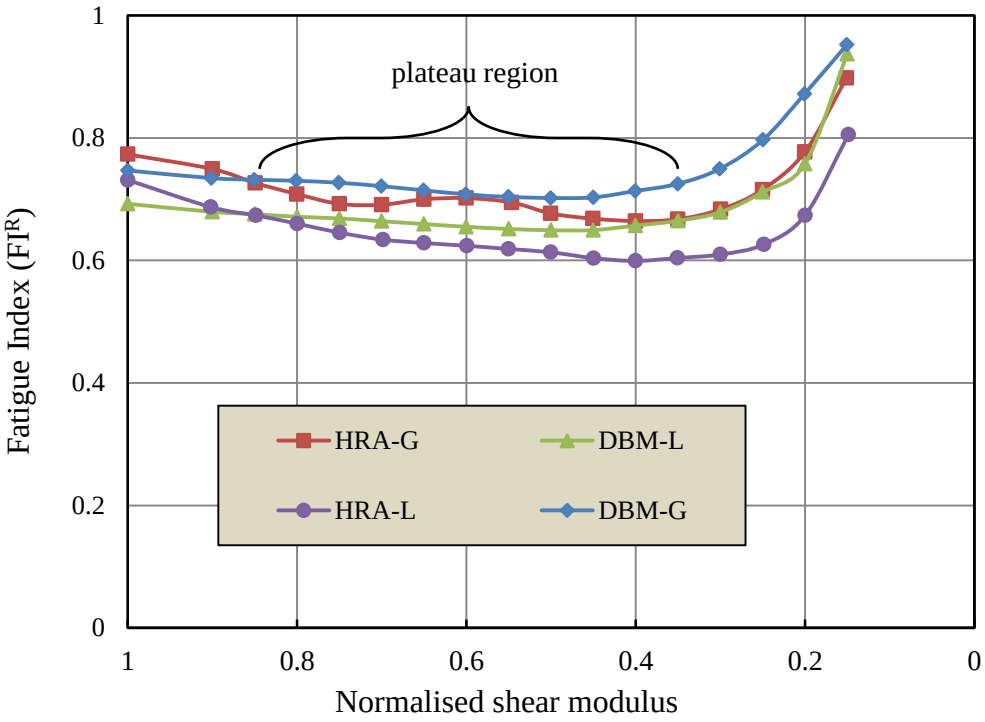

Figure 3- 30: Fatigue index against normalised shear modulus

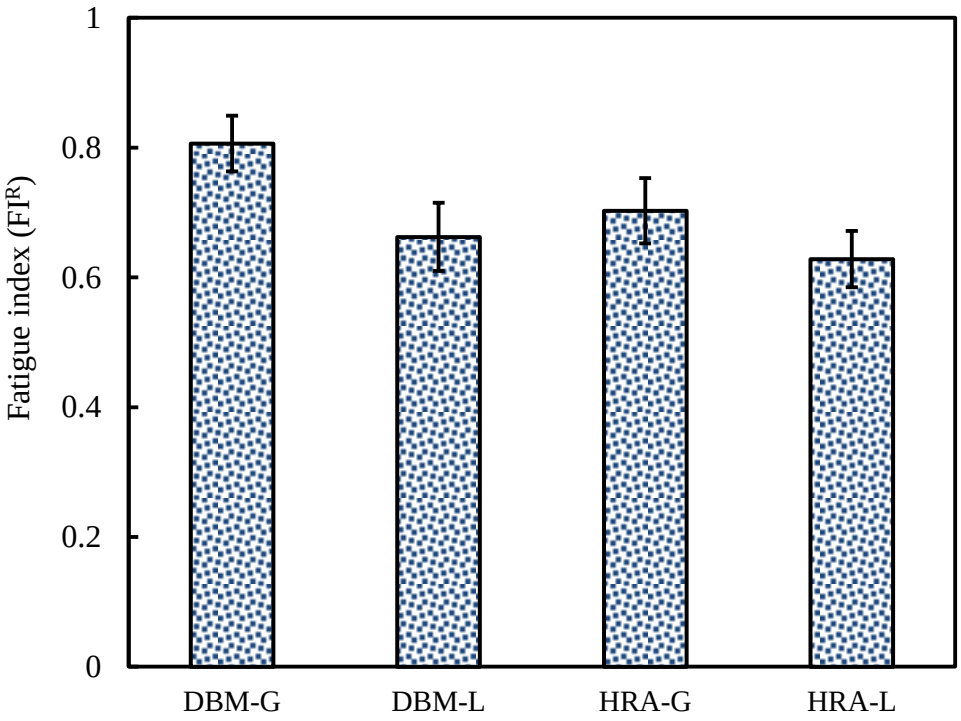

Figure 3- 31: Fatigue index at plateau region for different mixes.

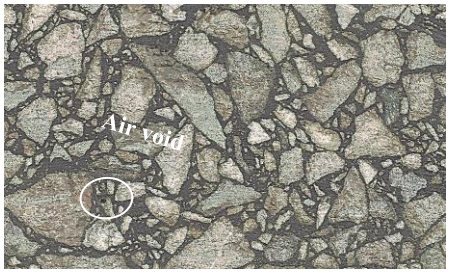

DBM-L

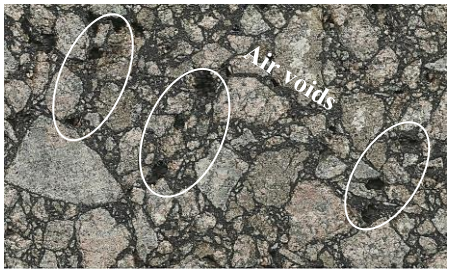

DBM-G

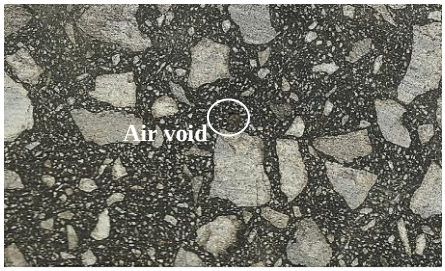

HRA-L

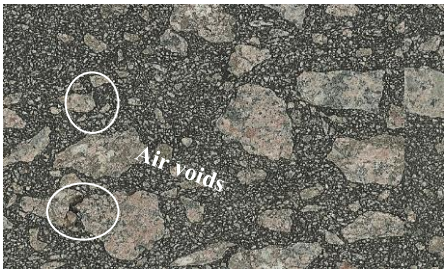

HRA-G

Figure 3- 32: photos of different mixes

3.7.3. Verification with Other Approaches

3.7.3.1. Traditional approach

The traditional approach (Kim et al., 2003;Daniel et al., 2004;AASHTO, 2002) represents the changes in a material's modulus and phase angle, and has been used in this work to study fatigue performance as shown in Figures 3-33 and 3-34. In this study, fatigue performance was defined in terms of number of cycles at a 50% reduction in the normalised shear modulus. The outcomes from these figures are in agreement with the results of FI^R in the performance as a ranking order, where HRA performed better than DBM and limestone performed better than granite in both mixes. It can also be seen that the phase angle begins to decrease quickly when the normalised shear modulus drops below 0.35. This behaviour is similar to the behaviour of FI^R. This level, i.e. 0.35, represents the second inflection point in the fatigue curve where the initiated cracks start to coalesce to produce macro cracks (Kim et al., 2003;Kim et al., 2002).

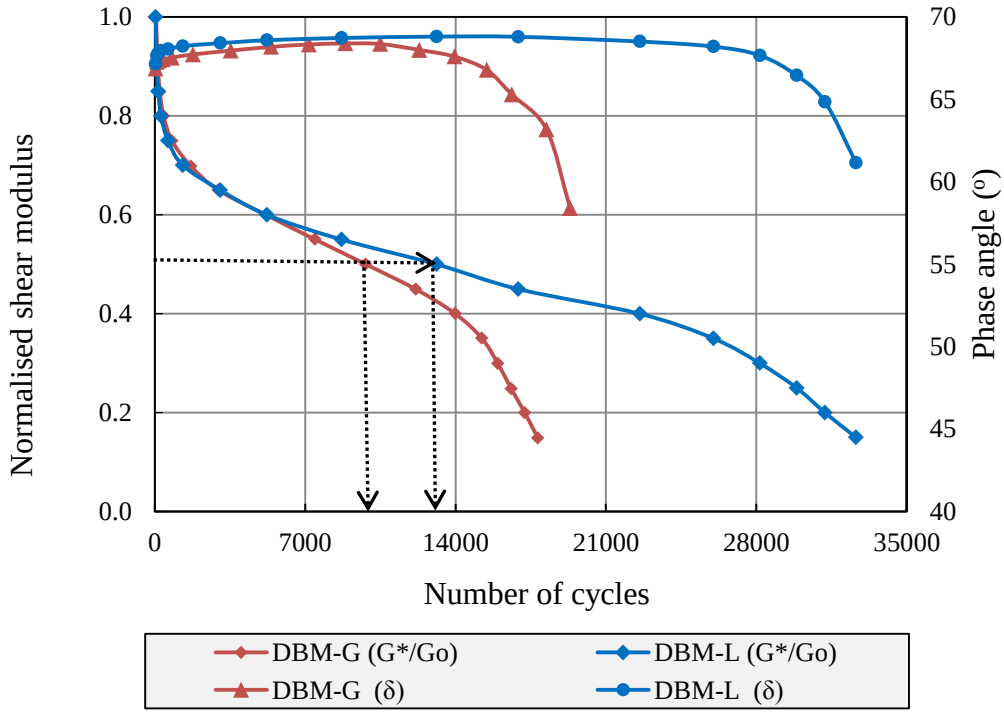

Figure 3- 33: Number of cycles against normalised shear modulus and phase angles for DBM mixes

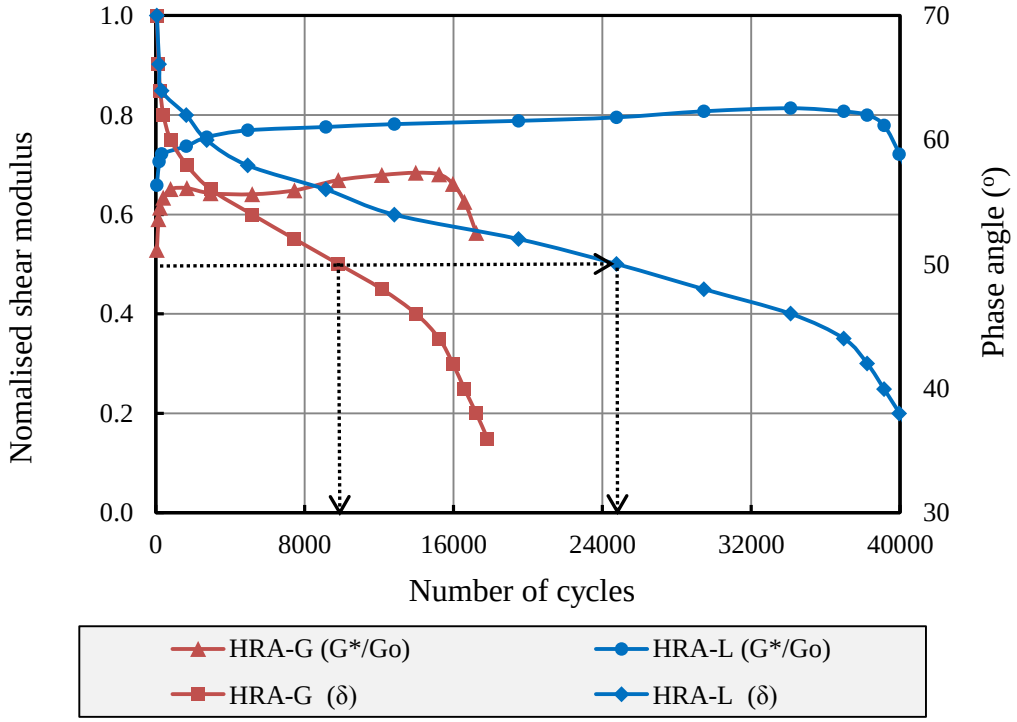

Figure 3- 34: Number of cycles against normalised shear modulus and phase angles for HRA mixes

3.7.3.2. Energy ratio approach

The energy ratio (ER) approach (Rowe, 1993) was also used to study the validity of the FI^R parameter in evaluating fatigue performance. Figures 3-35 and 3-36 show the relationship of energy ratio against the number of cycles for different mixes; from these figures, numbers of cycles (N_1) was located at the point when the slope deviates from a straight line in the same relationship as shown by the dashed lines. Figures 3-35 and 3-36 demonstrate the same outputs of the FI^R, whereas limestone mixes fatigue performance are better than granite mixes also, HRA is better than DBM. The main conclusion is that the TA and ER approaches emphasise the feasibility of using the FI^R parameter to evaluate fatigue performance as summarised in the Table 3-7.

Table 3- 7: Summary results of fatigue testing for all approaches

Mix	FI^R	Traditional approach	Energy approach
DBM-G	0.731	8,466	≈8,200
DBM-L	0.662	14,716	≈13,100
HRA-G	0.717	9,808	≈8,900
HRA-L	0.625	24,753	≈22,800

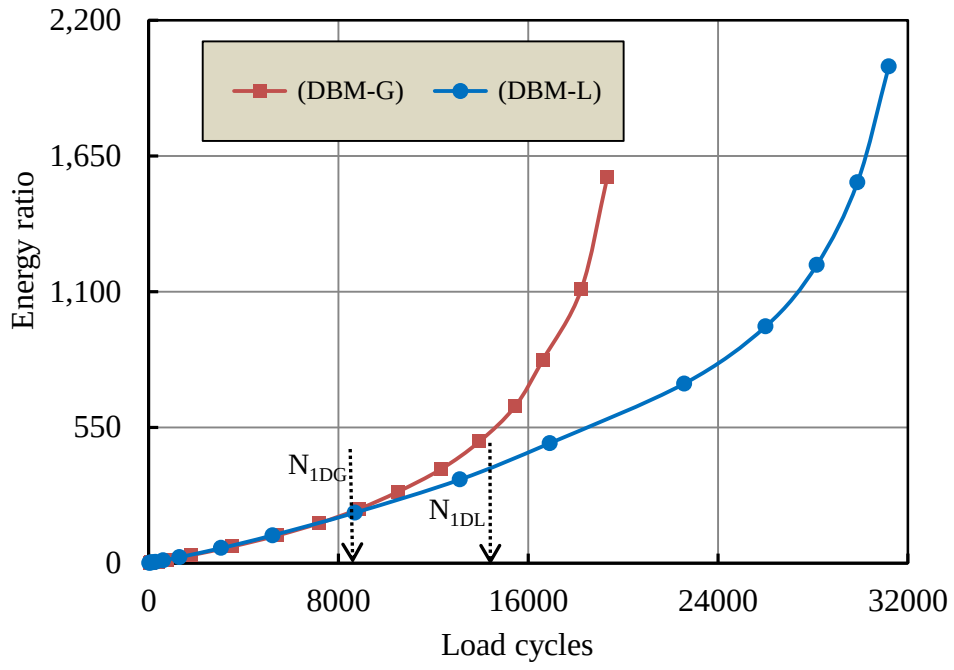

Figure 3- 35: Energy ratio approach at controlled strain test mode for DBM mixes

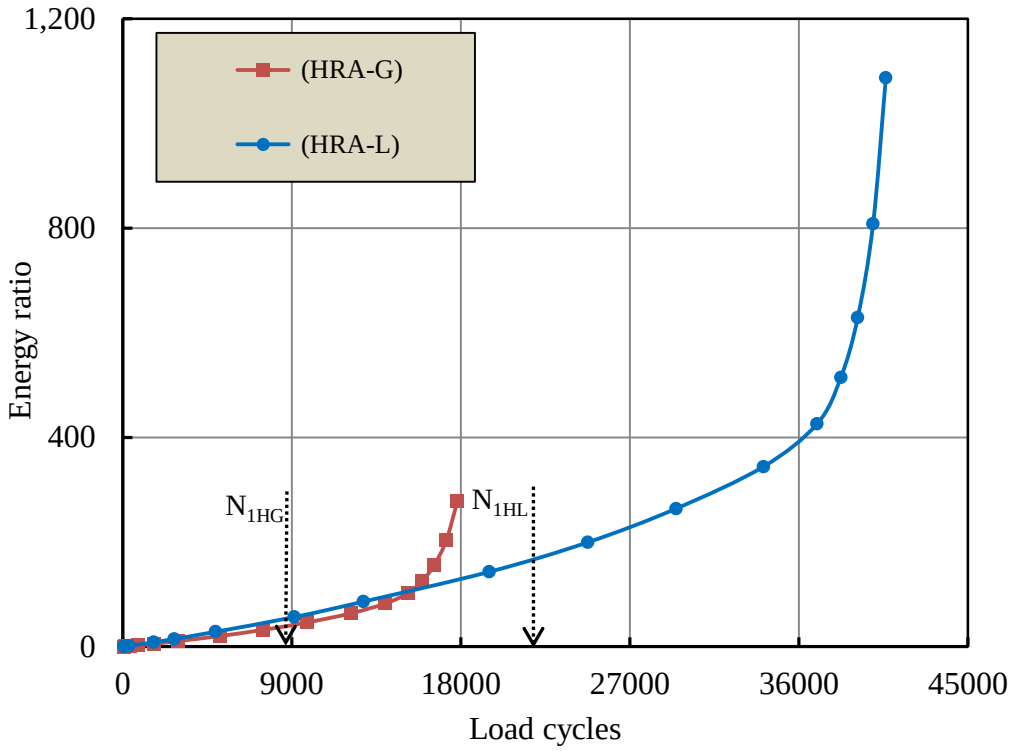

Figure 3- 36: Energy ratio approach at controlled strain test mode for HRA mixes

3.7.4. Fatigue Test at the Same Strain Amplitude

In the previous discussion, fatigue test was performed at different strain level: 0.3% and 0.25% for DBM and HRA mixes respectively as detailed in Table 3–6; herein the fatigue test was made using the same strain level to give better verification and more reliability for the adopted approach. In this regard, DBM-G and HRA-G were chosen to perform fatigue test at strain level 0.25% because they were sharing in the same strain level as shown in Table 3–6. The results were analysed using the same approaches FI^R, TA and ER as demonstrated in Figures 3–37 and 3–38. It can be seen that the damage level as FI^R for DBM-G at 0.25% is less than at 0.3%; also in HRA-G is less than at DBM-G 0.25% as shown in Figure 3–37. This conclusion was the same as in in TA and ER approaches that are presented in Figure 3–38.

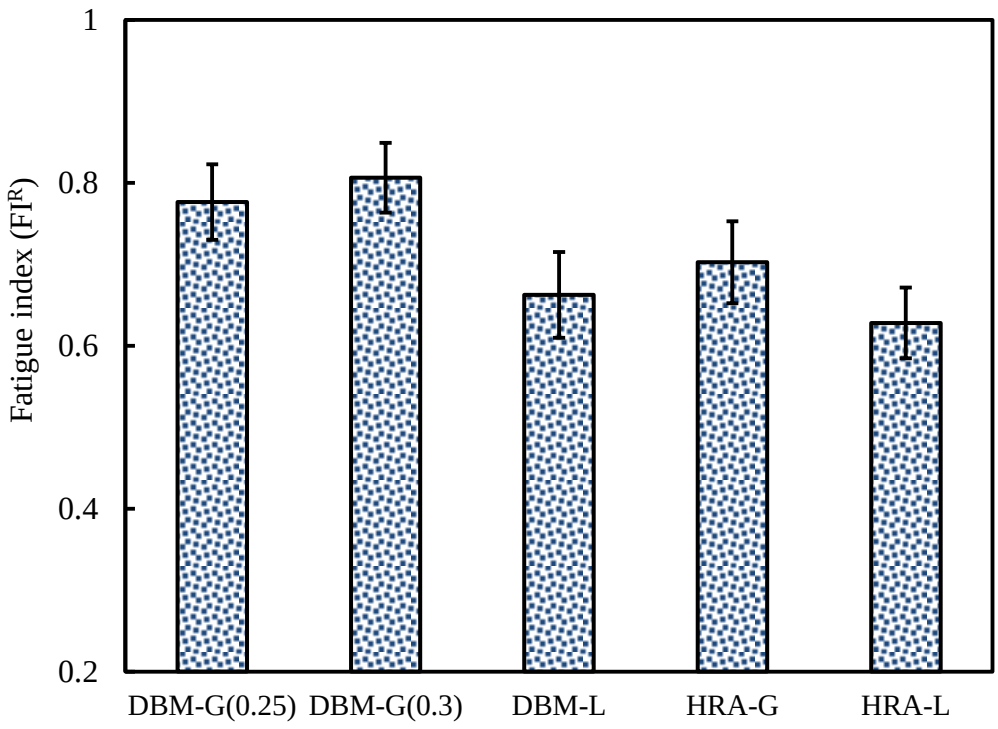

Figure 3- 37: Fatigue index at plateau region for different mixes tested at different strain levels.

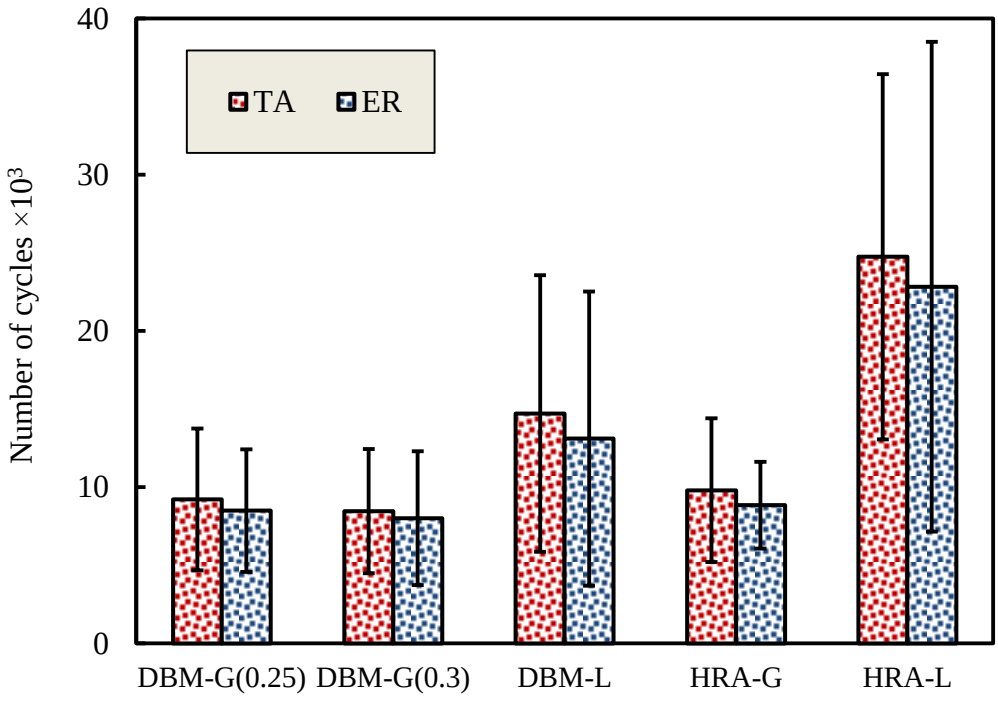

Figure 3- 38: Traditional and energy ratio approaches for different mixes tested at different strain levels.

On the other hand, it can be seen that the variation in the TA and ER approaches results is significantly very high in comparison to the FI^R, as shown in Figures 3-37 and 3-38; this emphasises that the FI^R approach is a powerful one by which to evaluate and analyse the fatigue performance results at low variance. This may be because the FI^R interprets the result as average values of FI^R within the plateau region, while, in the TA and ER approaches, the interpretation was based on the number of cycles which are selected at a single point, and there are different variables such as volumetric properties, in addition to the duration of the test playing a role in the variation of the results.

3.7.5. Validation of DSR Technique Using the 2PB Test

In this work, DSR technique results according to the previous discussion gave a reliable indication where, the results are compatible in outcomes through the comparison between the fatigue index (FI^R) with others approaches: traditional and energy ratio approaches. Despite that, DSR technique needs to verification with a traditional technique test to give high reliability for this technique; for this purpose 2PB test was adopted because it was available as a facility in lab. In this case, and to remove any bias, the same approaches: FI^R, traditional approach and energy ratio were used in the analysis results of 2PB test. FI^R approach requires identifying the viscoelastic linear region (LVE) to fined viscoelastic parameters: phase angle and stiffness modulus, for calculating: W_A^R and W_R^R as defined in Equations 3–11 and 3–12. In this regards, stiffness modulus test according to British Standards (BS EN 12697-26, 2012) was performed on the trapezoidal samples at strain level less than (50 μm/m), because of this strain level insures that the behaviour of bituminous mixtures being within LVE region; and to prevent any fatigue damage (BS EN 12697-26, 2012).

The fatigue results of the investigated samples were analysed using three approaches: FI^R, TA and ER approaches. The relation between FI^R and normalised shear modulus was plotted in Figure 3–39. It is clear there is a plateau region for FI^R located between 0.85 to (0.35-0.3) of the normalised shear modulus as similar to DSR samples as presented in Figure 3–30. It can be seen there is some distortion in FI^R vs normalised shear modulus of 2PB technique as shown in

Figure 3–39, in compare to the DSR tested samples as shown in Figure 3–30. This is due to the mechanism of 2PB machine, where electronic motor used for applying the loading on the sample and this causes noising because of the vibration. However, the results of FI^R of 2PB are fully in agreement with the DSR techniques, whereas HRA mixes are better performance than DBM mixes; and limestone mixes are better performance than granite mixes as demonstrated in Figures 3–39

In the traditional approach, the normalised stiffness modulus was plotted against the number of cycles as presented in Figures 3–40 and 3–41. These figures confirmed the same trend as a typical fatigue curve, whereby the stiffness modulus decreases with progressing cyclic loading at three rates: a sharply decreasing rate in the beginning and at the end of curve during phases I and III, and a lower rate of decreasing with phase II as shown in Figures 3–40 and 3–41. In phase II, where the traditional approach is defined, it is clear that the rank orders of the mixes are compatible with the same rank that is recognised by using the DSR test technique.

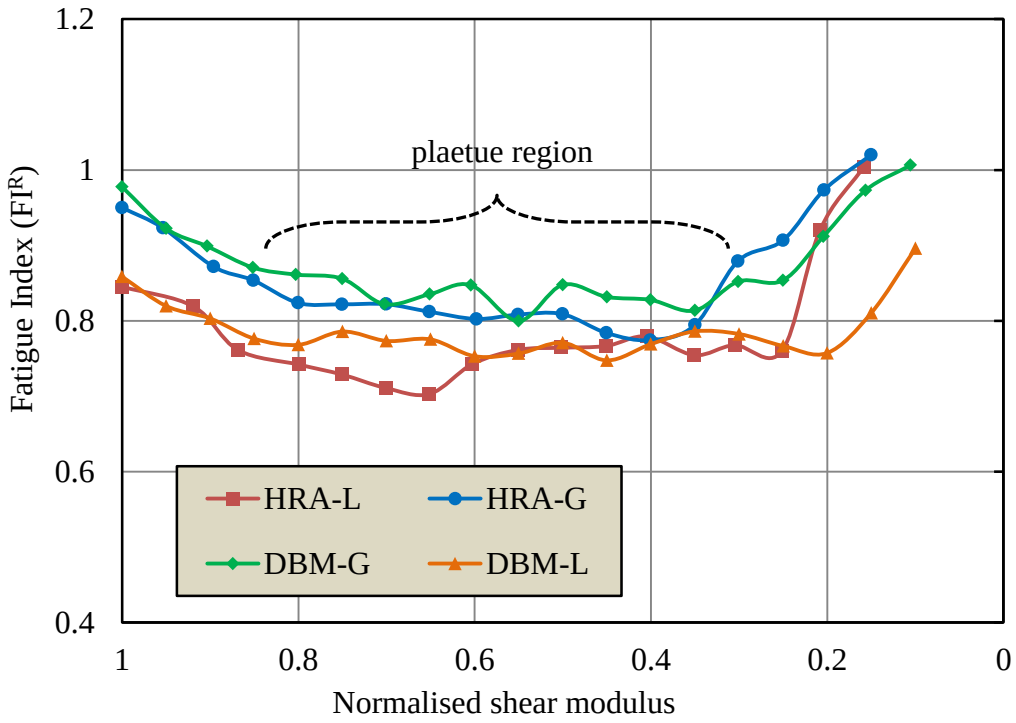

Figure 3- 39: Fatigue index against normalised shear modulus for trapezoidal samples tested in 2PB.

Also, the phase angle is fairly constant within phases I and II and drops sharply after reaching the peak point. The dropping in phase angle is within phase III as presented in Figures 3–40 and 3–41; and this behaviour emphasises the same response for the phase angle with number of cycles as for the samples that were tested using DSR. This peak phase angle value has been successfully used as an indication for fatigue failure point in previous studies (Reese, 1997;Lee et al., 2003;Cocurullo et al., 2008). In addition, the phase angle dropped suddenly when the normalised stiffness modulus decreased to less than about 0.35, which is the value for the tested samples in DSR techniques.

Another approach is ER, which is presented as the number of cycles (N_1) at the point when the ER slope deviates from a straight line in the relationship of energy ratio to number of cycles as described in Figure 3–42. This figure also revealed the same results as presented using DSR technique. This emphasises that the DSR technique gives the same conclusion in compare to a tradition technique as 2PB test.

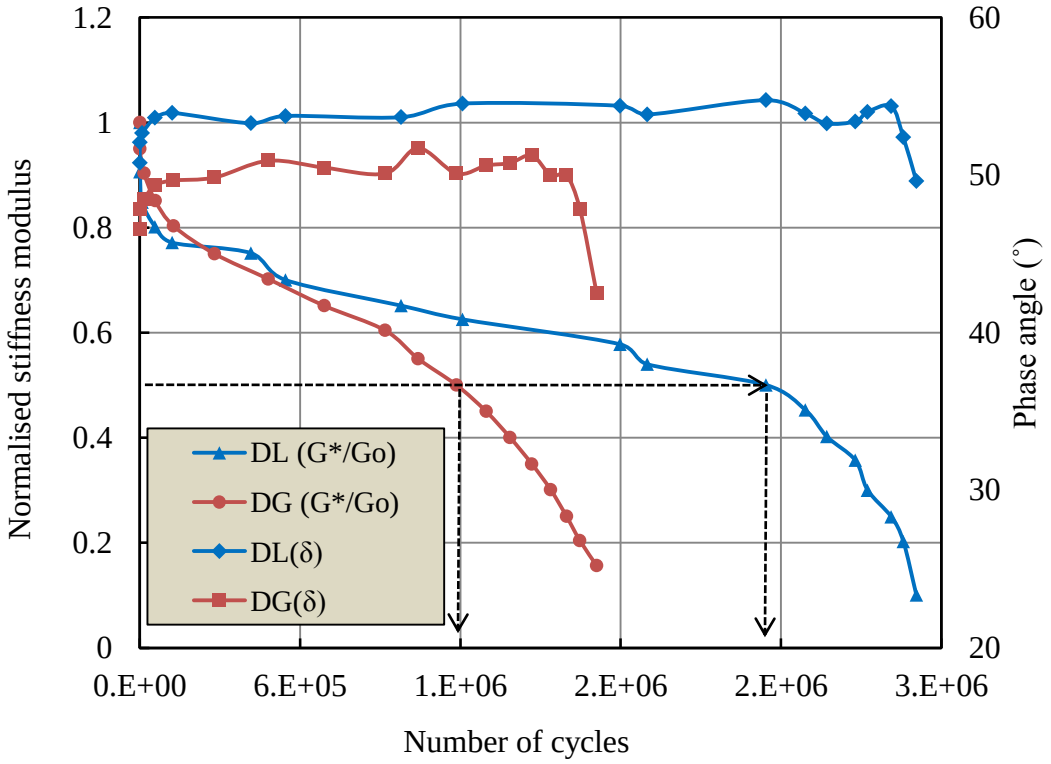

Figure 3- 40: Traditional approach of controlled strain test mode for DBM mixes.

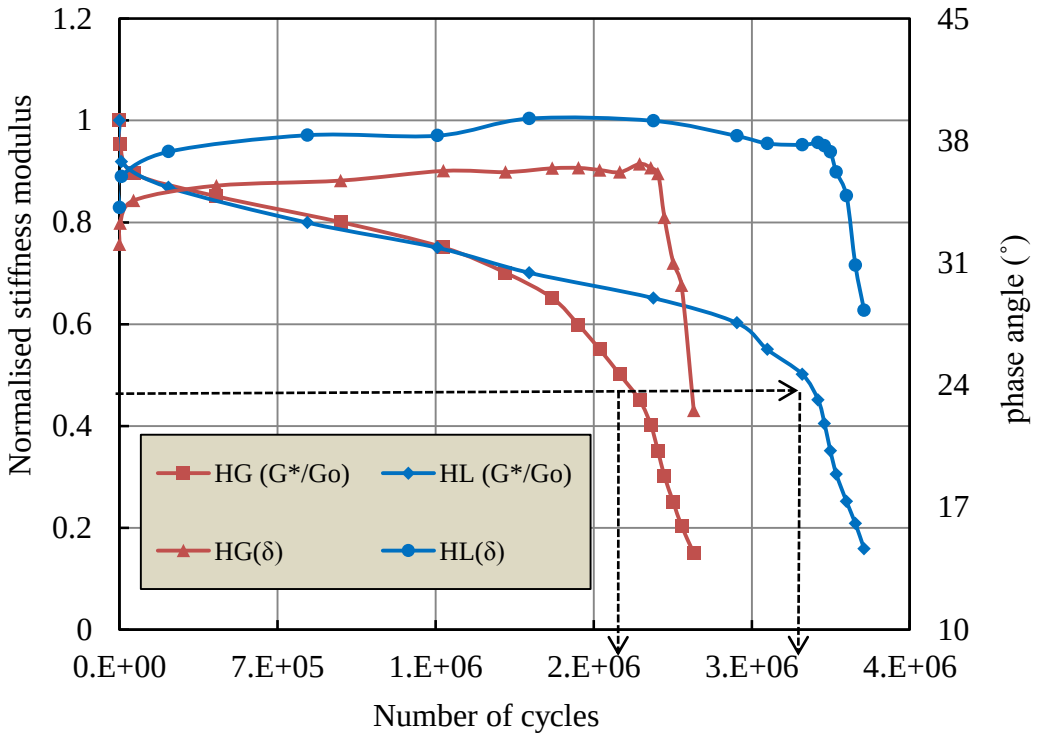

Figure 3- 41: Traditional approach of controlled strain test mode for HRA mixes.

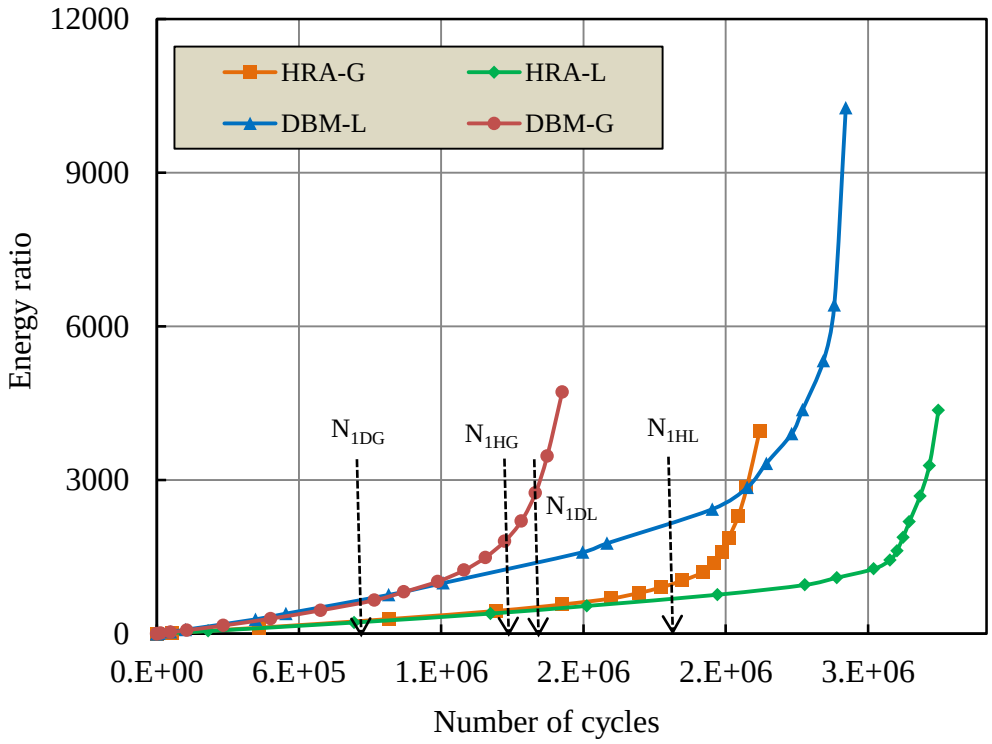

Figure 3- 42: Energy ratio approach at controlled strain test mode for different mixes.

Figure 3–43 and 3–44 represent the summarised results for the overall outcomes of the tested samples for DSR and 2PB techniques using three approaches: FI^R, TA and ER. The consistency between the two techniques is presented and demonstrated in these figures through the ranking order in the mixes. In addition, the variation represented by error bars shows the same trends in both techniques for all approaches, and it can be seen that FI^R displayed low variance in comparison to the other approaches. It is worth noting that the same trend is visible in the TA and ER approaches for DSR and 2PB, but the essential difference appears from the big differences in the fatigue life in terms of number of cycles. This may be due to several factors, for example: the strain amplitude in 2PB was not in the damage region, so it requires a long time to create the damage according to the criteria of the fatigue life definition; or maybe it is due to the geometry of the samples, where the DSR samples are cylindrical and the 2PB are trapezoidal beams.

Overall, the above discussion highlights that the response of small cylindrical samples which are tested in a DSR is similar to the trapezoidal beams that were tested in 2PB; and this emphasises the feasibility of using the DSR technique and FI^R approach in fatigue tests: performance and analysis.

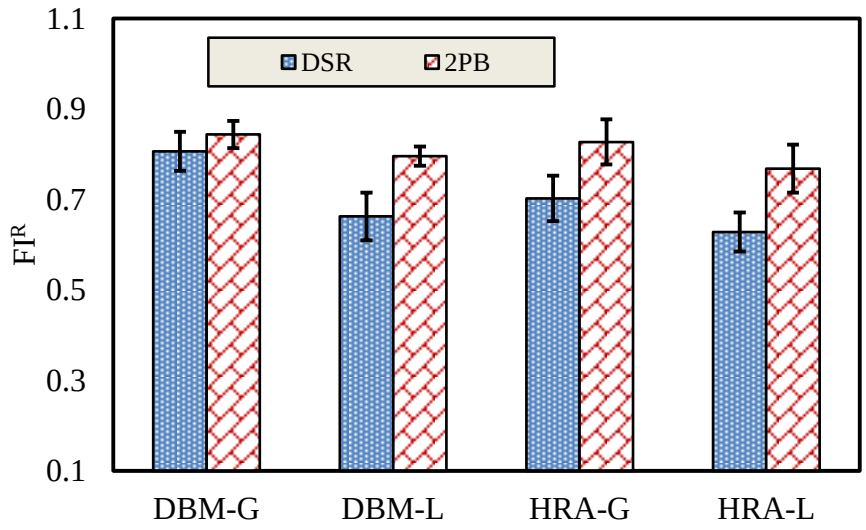

Figure 3- 43: Fatigue index at plateau region for DSR and 2PB samples.

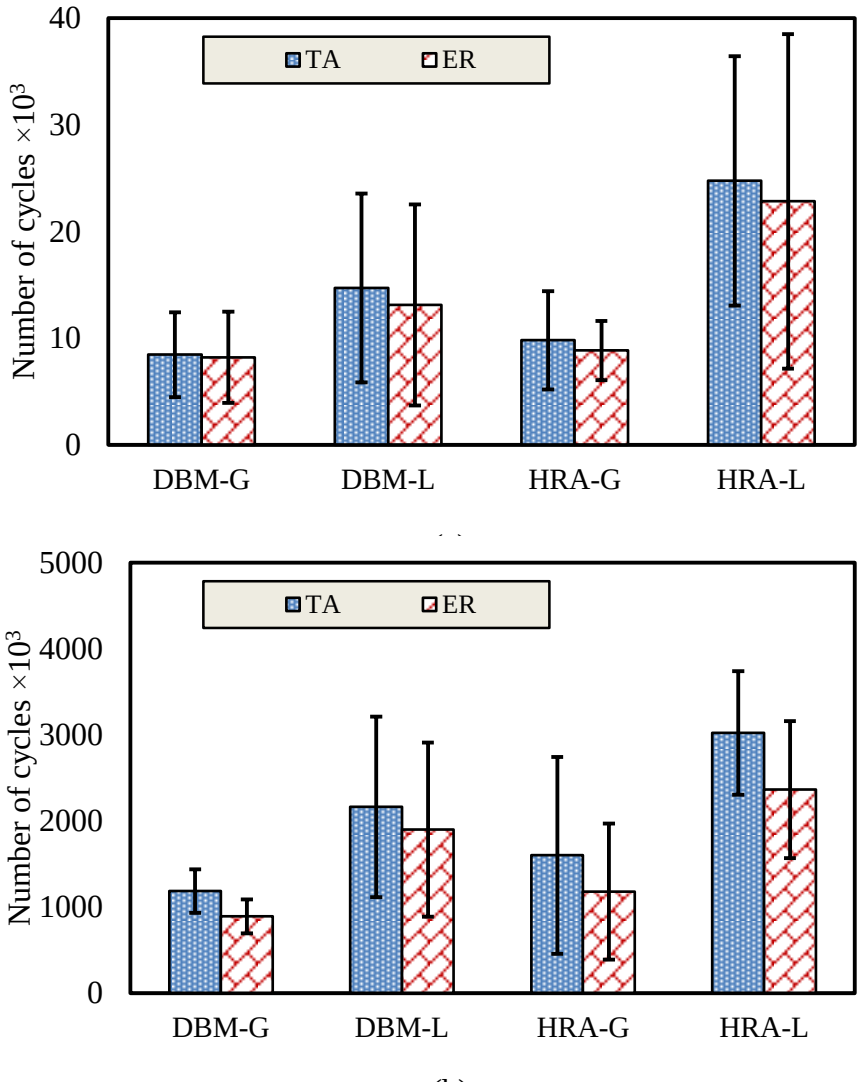

Figure 3- 44: TA and ER approaches for samples tested in: (a) DSR and (b) 2PB.

So, using the DSR technique to evaluate the fatigue performance of asphalt mixes according to the approach described in this project will provide the following advantages:

1. Savings in the cost of materials, as fewer materials are used for preparing DSR samples than for traditional techniques.

2. The DSR technique is based on selecting the strain amplitudes for fatigue testing at the damaged region, while, in the traditional technique, the strain amplitudes are selected arbitrarily without any criterion.

3. The developed approach offers a time saving, and this is very important while studying the fatigue performance of HMA.

However, there is a shortcoming in using the DSR approach, as this was applied for aggregate maximum for aggregate with a maximum nominal size of up to 10 mm due to the limitations of the DSR's capacity, as the maximum torque is 0.2 N.m. However, with time it should be possible to develop this device to increase the capacity.

3.8. Summary

From the results presented in this Chapter, the following conclusions have been made.

1. An approach has been developed and used effectively to prepare full hot mix asphalt DSR samples of 12 mm in diameter and 50 mm in height.

2. A selection method for DSR samples was used based on determining the mode and standard deviation of the sample's bulk density, which ensured the least variability with the high amount of samples to be used in fatigue testing. On the other hand, there is not noteworthy difference between the mode of the bulk densities of the DSR samples with bulk density of the beams and trapezoidal specimens.

3. A simple method was devised to arrive at the strain level that should be adopted in conducting fatigue tests in the DSR; this method was based on evaluating the slope of the strain–stress relationship. When the slope changed from positive to negative, the value of the strain amplitude was identified as the strain amplitude for fatigue test.

4. A new fatigue index, FI^R, was developed based on the pseudostrain energy concept of applied and recovered energy to evaluate the fatigue performance of HMA. This index revealed an agreement with the results from other reliable approaches, namely the energy ratio and traditional approaches. In addition, FI^R was verified in evaluation the fatigue performance of trapezoidal samples tested using traditional techniques called 2PB; the results emphasise the same outcomes of DSR technique.

5. DSR technique was verified using a traditional technique called the 2PB test, which was performed on trapezoidal samples, and two approaches: the traditional and energy ratio approaches in addition to FI^R approach were used in the analysis results. The results of the 2PB test agreed with the results of the DSR samples in terms of the rank orders of mixes.

6. The variance of the results in this study was presented using error bars in terms of standard error for all approaches in both techniques: DSR and 2PB. The analysis revealed that FI^R displayed a significantly low variation in comparison to the TA and ER approaches for the DSR samples; and this behaviour was emphasised in the 2PB technique too. This confirms the efficiency of using the DSR technique and FI^R approach in fatigue test and performance analysis, and that they are reliable and acceptable.

7. The study confirmed that limestone has a better fatigue performance for both HRA and DBM mixes than granite for both techniques: DSR and 2PB in all approaches: FI^R, TA and ER.

CHAPTER IV

CHAPTER IV

4. Fatigue Performance in Controlled Stress Test Mode

4.1. Introduction

Asphalt fatigue tests are performed using two modes, either a controlled stress mode or controlled strain mode. Chapter III described an approach for fatigue test using DSR instrument in strain test mode and analysed the results using a new parameters was named fatigue index (FI^R) and another approaches: traditional and energy ratio. Herein, in this chapter, the work was extended using the same approach to evaluate the fatigue performance of HMA samples tested in DSR in controlled stress mode.

4.2. Objectives of Study

The objectives of this chapter are to use the same approach that has been used in controlled strain test mode, Chapter III, in stress test mode. Where, DSR and FI^R were used in fatigue test and for evaluating fatigue performance of HMA respectively. The work involved using cylindrical samples (12 mm in diameter and 50 mm in high) prepared from HMA and selected according to the same method as in strain test mode. As well as, TA and ER approaches were also used in verification of the FI^R.

4.3. Results and Discussion

4.3.1. Determination of Stress Amplitude

An amplitude sweep stress test was performed on DSR samples and the strain responses were collected, and then strain response - time slopes were calculated for each stress value was applied on sample for several cycles, as shown in Figure 4–1. The strain response against time was plotted and fitted linearly for each stress amplitude value. The slopes of strain-time ($d\gamma/dt$) were evaluated from the fitted equations and also plotted against stress amplitude. At the instant when the slope

(dγ/dt) increased dramatically, the stress amplitude was taken as stress value for the fatigue test.

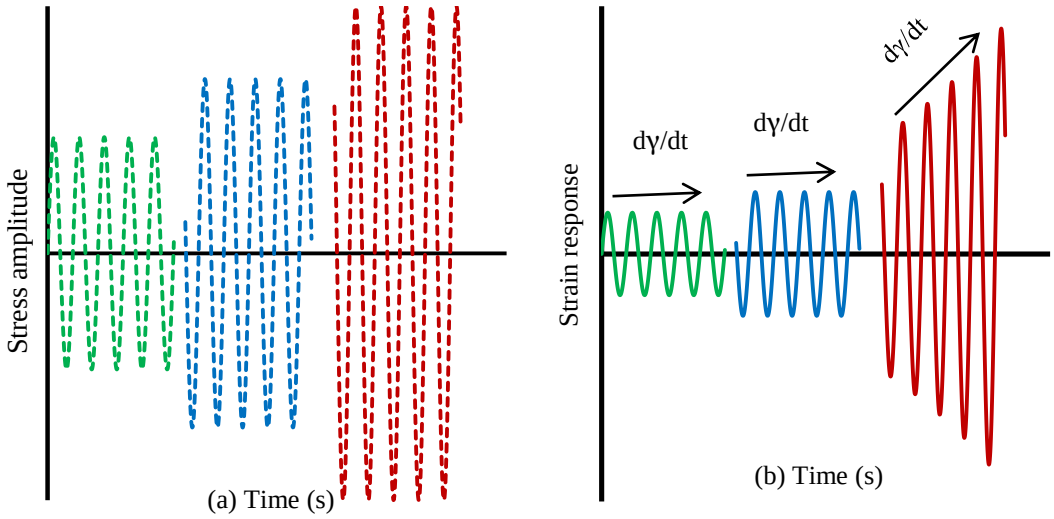

Figure 4- 1: (a) applied stress-time (b) strain-time response.

Three DSR samples were selected within the range *R* from Table 3–5 in Chapter III to perform an amplitude sweep test using DSR. Sweep stress increased linearly from 1 KPa to 600 KPa and distributed along 25 points; stress amplitude was applied for 100 cycles at each stress value at frequency 2.5 Hz; more details about the DSR sequence which was used in the sweep stress are presented in Appendix B-2. The maximum applied stress was 600 KPa because the maximum torque which can be applied using DSR is 0.2 N.m, which is equal to 600 KPa. The final result of the sweep test included collecting 40 point for each applied stress value, then the strain response was fitted using linear regression model as a function of time, i.e. $\gamma = A_0+A_1t$; the slopes of the strain response with time were determined using the regression model ($d\gamma/dt = A_1$). Figures 4–2 to 4–5 demonstrate a typical plot for the shear strain response with time for DBM and HRA samples. The strain response with time increased with increasing shear stress amplitude; it is clear that the failure of DBM mixes was earlier than HRA mixes, where the maximum shear stress for DBM mixes was 325 KPa and 350 KPa for DBM-G and DBM-L respectively; while it was 600 KPa for HRA mixes because HRA mixes are stiffer.

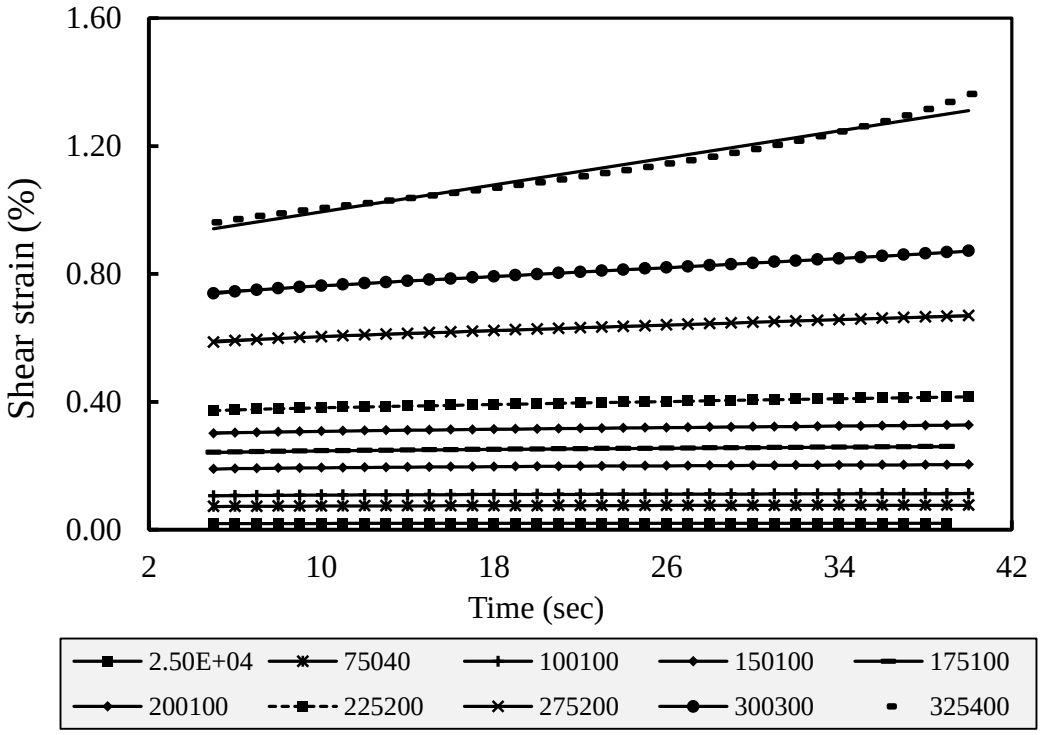

Figure 4- 2: Shear strain response against time for DBM-G sample.

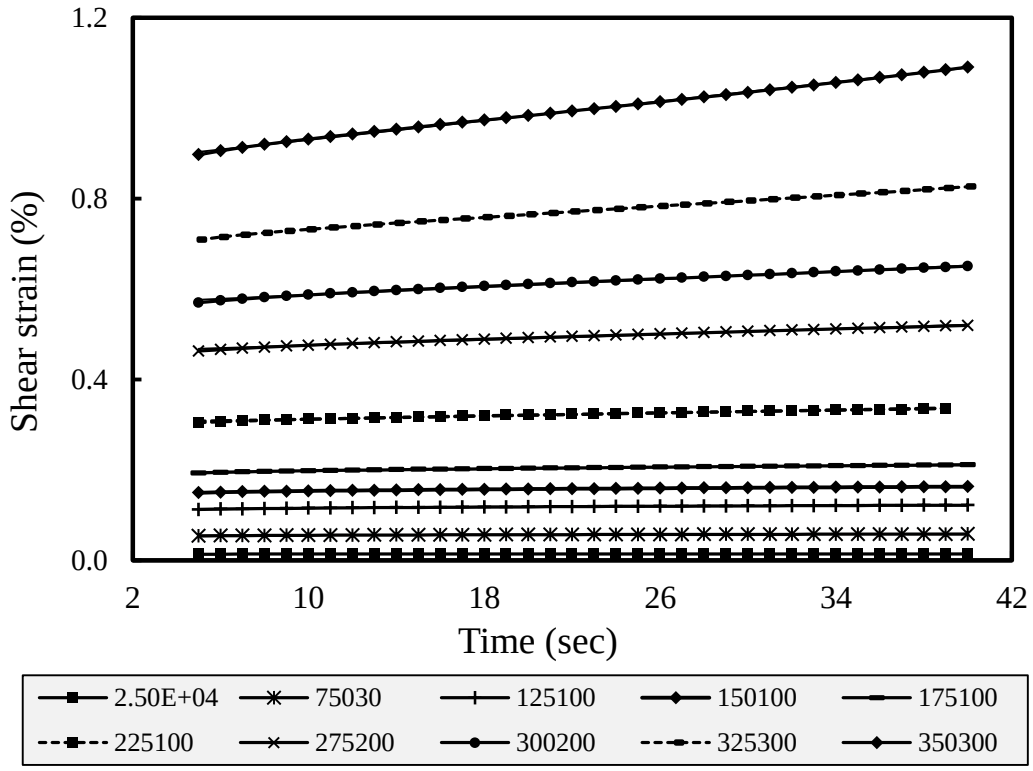

Figure 4- 3: Shear strain response against time for DBM-L sample.

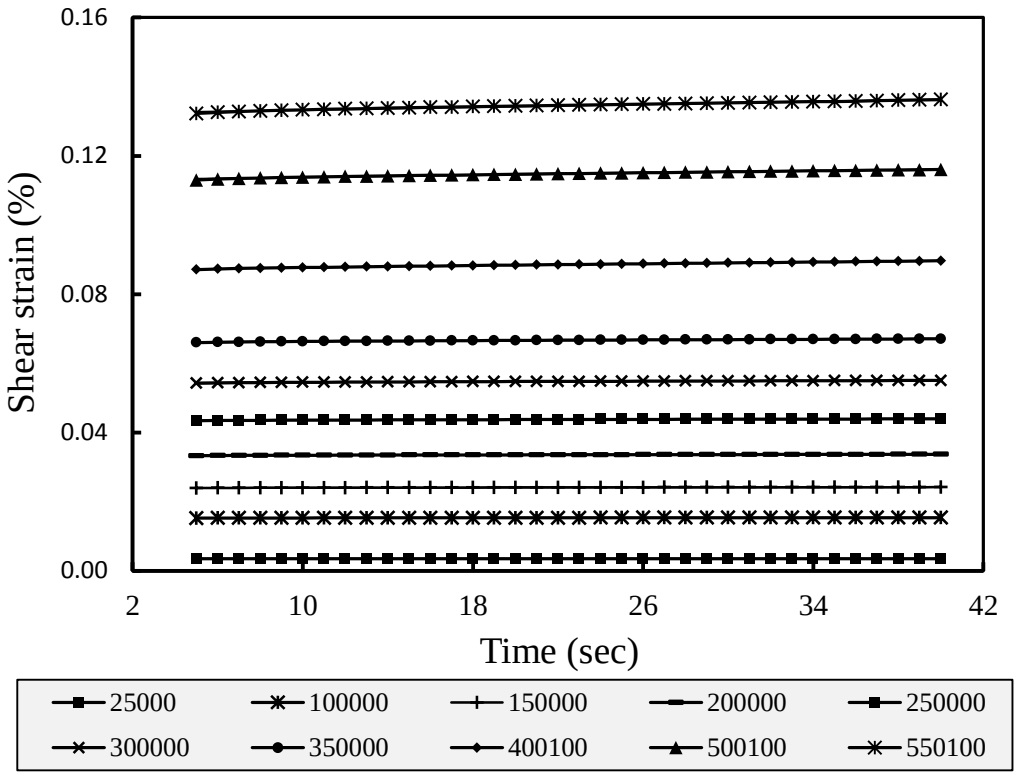

Figure 4- 4: Shear strain response against time for HRA-G sample.

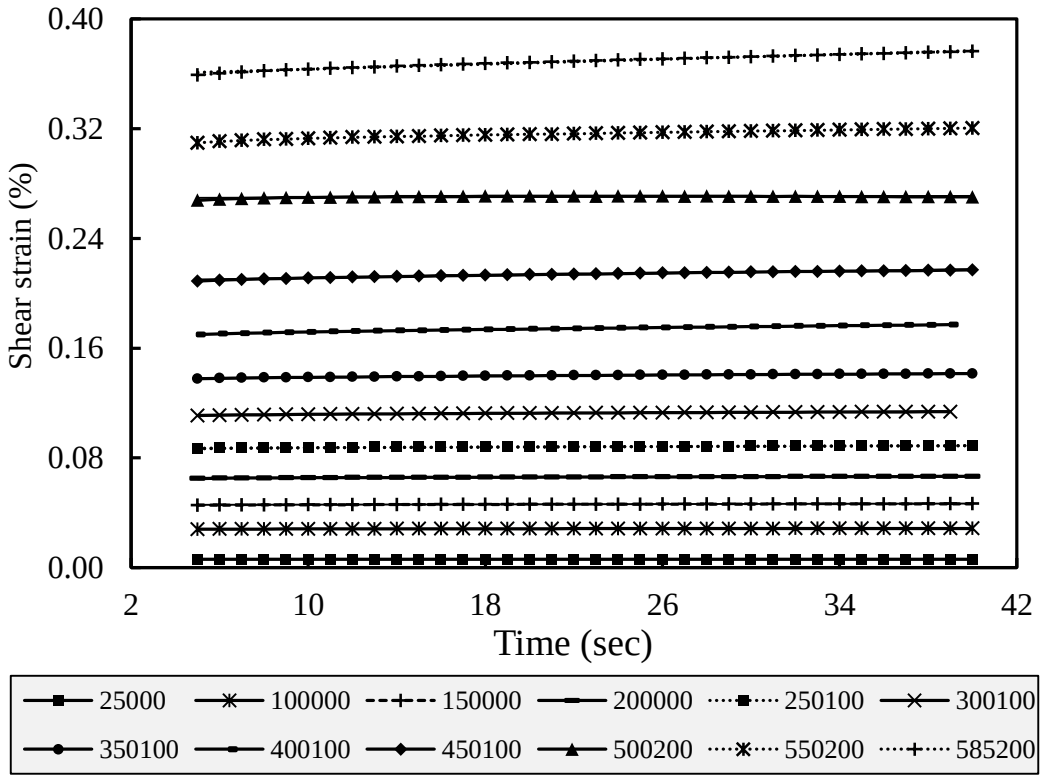

Figure 4- 5: Shear strain response against time for HRA-L sample.

The slope of strain response (dγ/dt) for each stress amplitude was evaluated from the linear fitting equation of the data in Figures 4–2 to 4–5 and plotted against shear stress amplitude as shown in Figures 4–6 and 4–7. These figures revealed a marked increase in the strain response slopes starting at definite shear stress value; this value can be defined at the point when there is divergence from the straight line in the relationship of strain response slope against shear stress amplitude, as demonstrated in Figures 4–6 and 4–7. These points are considered as start damage in materials, whereas it was about 150 KPa for DBM mixes and about 250 KPa and 400 KPa for HRA-L and HRA-G respectively, as shown in Figures 4–6 and 4–7.

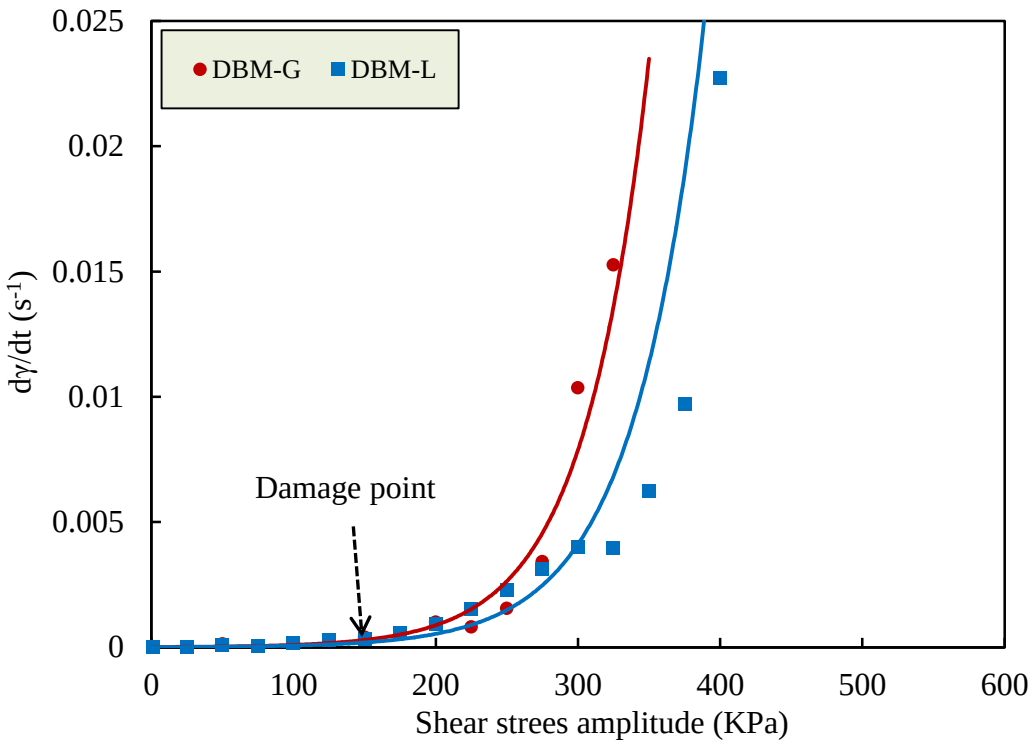

Figure 4- 6: Shear strain response slope against shear stress amplitude for DBM mixes.

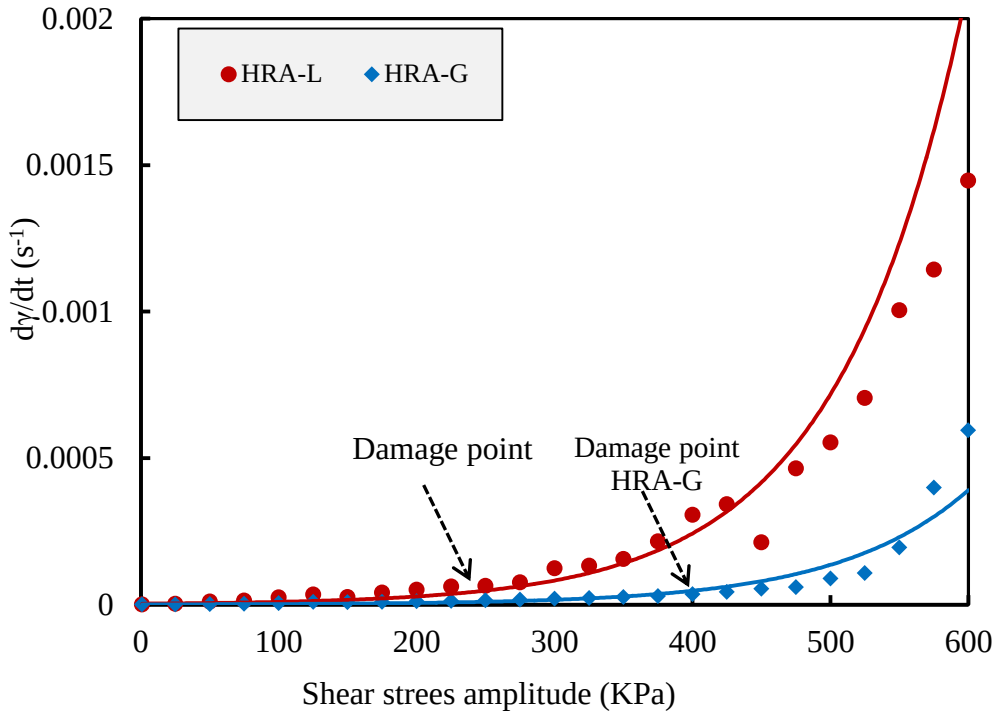

Figure 4- 7: Shear strain response slope against shear stress amplitude for HRA.

4.3.2. Fatigue Analysis

The same approach of strain test mode in Chapter III was used here in stress test mode. Where, nine DSR samples were selected according to the same criteria to perform fatigue tests using the DSR technique, more details in Appendix B-4. FI^R was used in fatigue analysis; also, TA and ER approaches were adopted in the analysis of verification.

4.3.2.1. Fatigue Index

FI^R against the normalised shear modulus is plotted in Figure 4–8. It is noticed that the plateau region (PR) is not as clear as in the strain test mode, because the dissipated energy increases in stress test mode and causes heating in the sample during fatigue testing (Di Benedetto et al., 1996;Baaj et al., 2005). However, FI^R increased sharply beyond 0.2 of normalised shear modulus; this behaviour was found to be the same for the relationship of DER vs n (Ghuzlan and Carpenter, 2006). The PR was defined between 0.85 and 0.2 of normalised shear modulus, and FI^R was calculated as average within PR. Figure 4–8 demonstrates that the performance of HRA fatigue is higher than DBM and limestone is better than

granite in both mixes. It is worth mentioning that the fatigue test in stress mode lasted up to 10% of initial stiffness; therefore, it can be seen that the maximum FI^R value is approximately one, which means that samples were possibly completely damaged, and this is the reality because the majority of tested samples were completely damaged at the end of test.

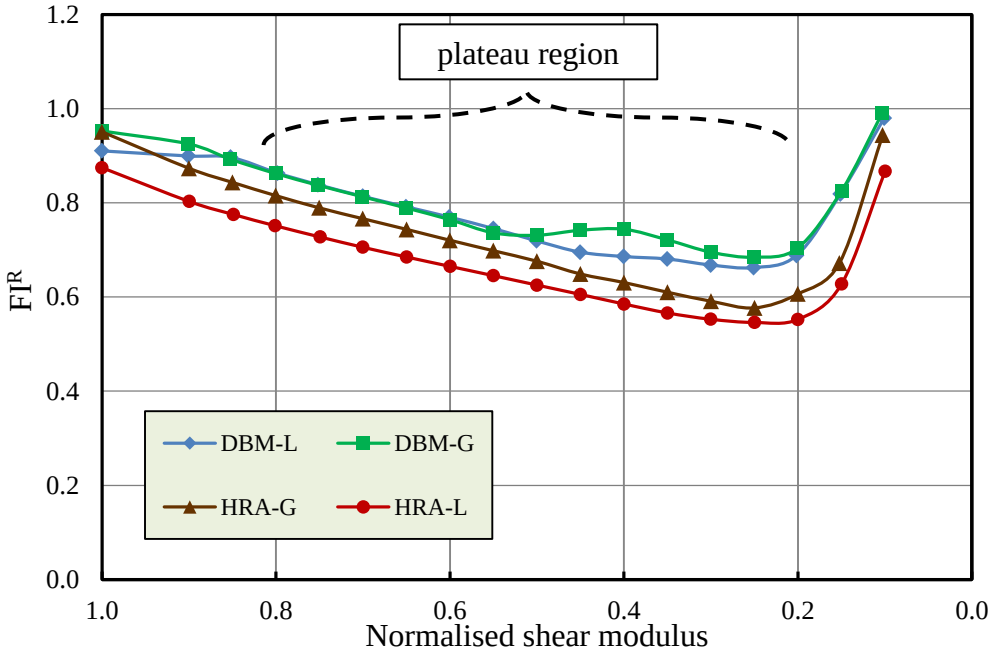

Figure 4- 8: Fatigue index against normalised shear modulus.

4.3.2.2. Verification of Fatigue Index Approach

The same approaches, i.e. TA and ER, which were used for verification the FI^R in strain test mode (Chapter III), were adopted here in stress test mode. In the first approach, TA, fatigue performance was defined in terms of number of cycles at 10% reduction in the normalised shear modulus (Rowe, 1993). The set of data was presented in Figures 4–9 and 4–10; it is clear from the figures that the performance as a number of cycles for HRA mixes is better than DBM, and limestone is better than granite as well, this ranking in order is the same as in FI^R. Also, phase angle decreases sharply when the normalised shear modulus decreases below 0.20, as shown in Figures 4–9 and 4–10, and this point represents the second infliction points in fatigue curve, whereas the damage accelerated quickly because the macro cracks started forming (Kim et al., 2002;Kim et al., 2003).

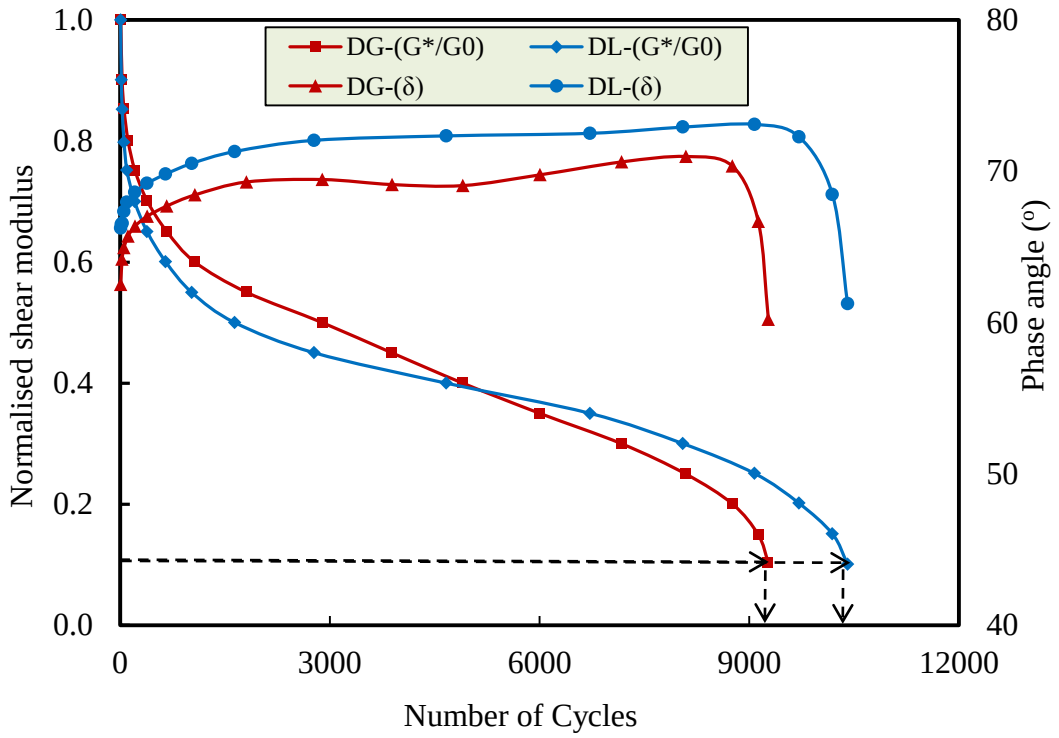

Figure 4- 9: Number of cycles against normalised shear modulus and phase angles of DBM mixes.

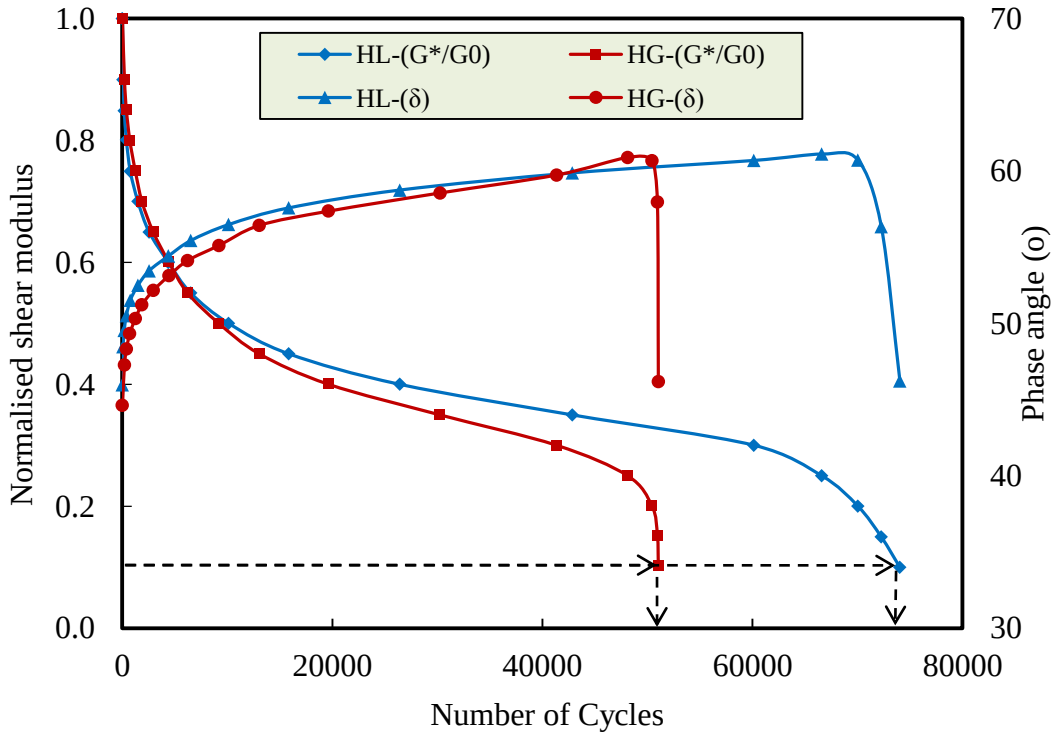

Figure 4- 10: Number of cycles against normalised shear modulus and phase angles of HRA mixes.

The second approach, ER, (Rowe, 1993) was also used to study the validity of the FI^R in evaluating fatigue performance, and the results of this approach are presented in Figures 4–11 and 4–12 for DBM and HRA mixes respectively. The ER approach defines fatigue life (N_1) in the stress mode as the number of cycles at the point when the ER reaches the peak point in the relationship of ER vs number of cycle, as located by the dished lines on Figures 4–11 and 4–12. The ER approach results are completely in agreement in terms of order of magnitude with the FI^R and TA approach results, as shown in Figures 4–11 and 4–12.

Overall, Table 4-1 summarises the results of all the approaches and consistency can be seen in the results among these approaches. Furthermore, the analysis included the variation, where the error bars in terms of standard deviation were also used to study the variation in the results for the three approaches, as presented in Figures 4–13 and 4–14.

It can be noticed that FI^R exhibited lower variation while there is significantly high variation in the TA and ER approaches as shown by the error bars; this performance was as in the strain test mode in Chapter III. Therefore, the main conclusion is that the TA and ER approaches emphasise the DSR technique for fatigue testing in the stress model, in addition to the FI^R approach for analysing fatigue test results of HMA with low variation.

Table 4- 1: Summary results of fatigue testing for all approaches.

Mix	FI^R approach	Traditional approach	Energy approach
DBM-G	0.777	9,200	≈6,950
DBM-L	0.752	10,380	≈8,300
HRA-G	0.694	51,920	≈45,200
HRA-L	0.631	74,460	≈61,500

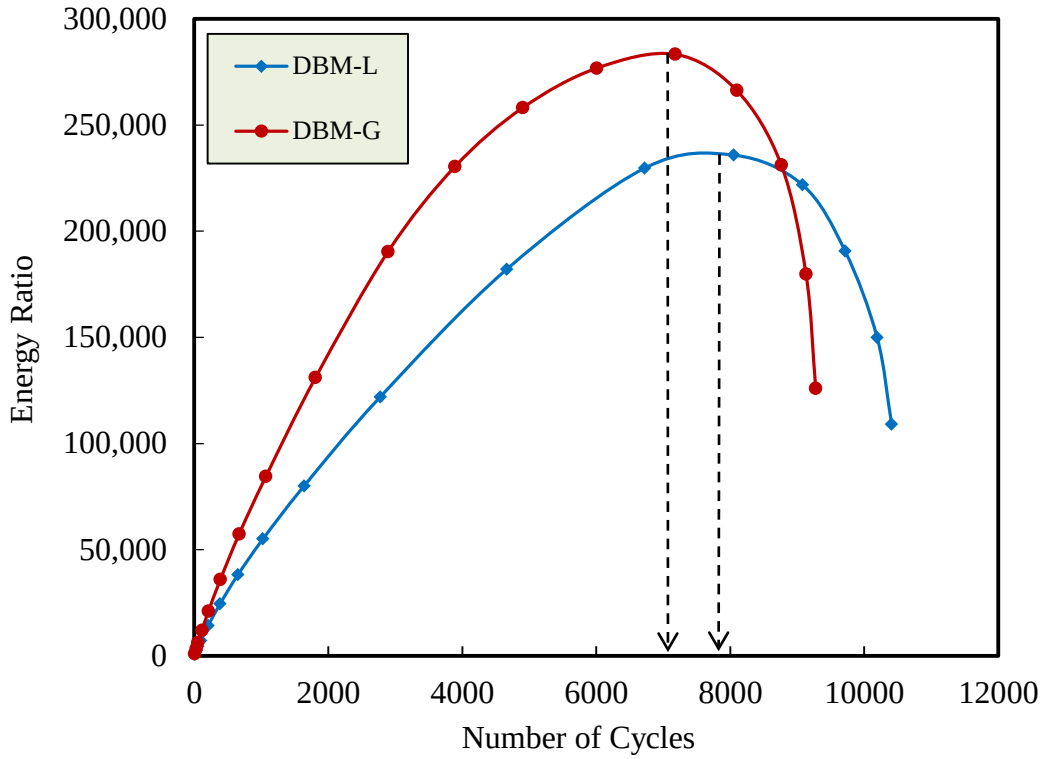

Figure 4- 11: Energy ratio approach for DBM mixes.

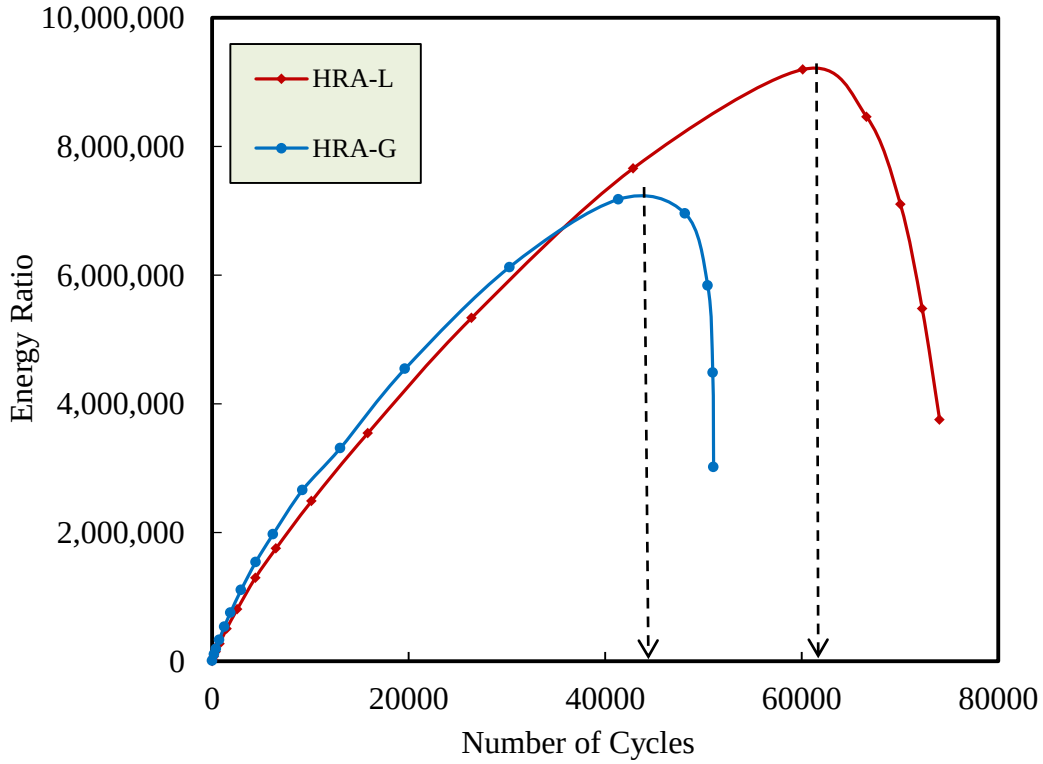

Figure 4- 12: Energy ratio approach for HRA mixes.

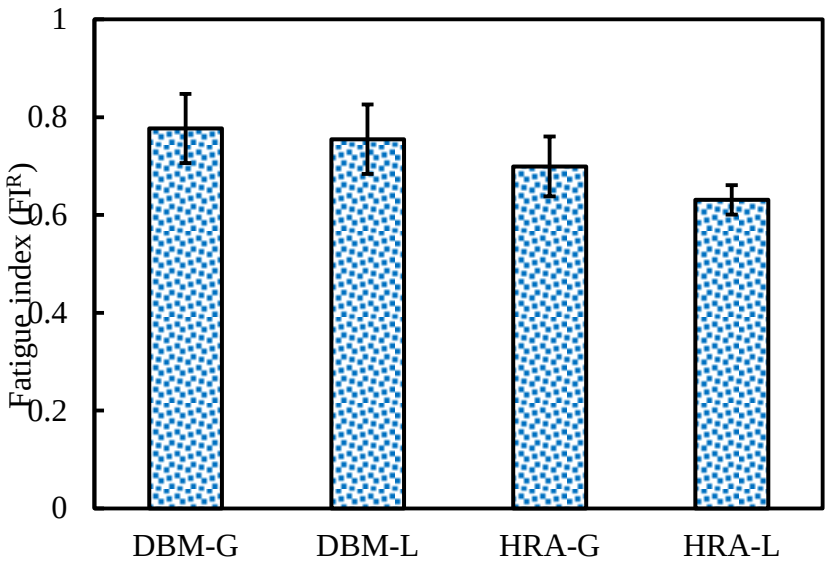

Figure 4- 13: FI^R approach for DBM and HRA mixes.

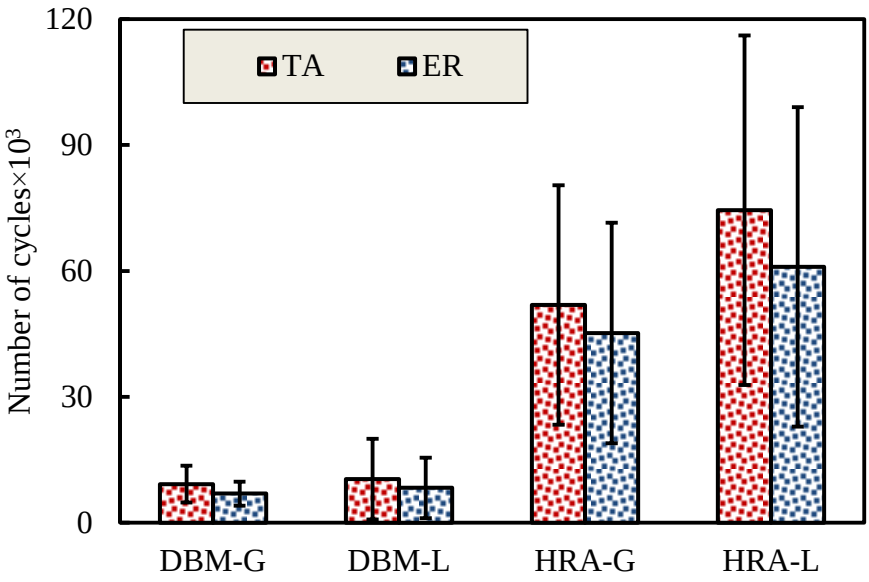

Figure 4- 14: TA and ER approaches for DBM and HRA mixes.

4.4. Comparison between Strain and Stress Test Modes

In strain test mode, the stress response decreases as the number of cycles progresses, while, in stress test mode, the strain increases as the number of cycles progresses, as shown in Figure 4–15. In stress mode, the fatigue test is usually performed either arbitrary stress amplitudes or the stress response at 50% of initial

stiffness modulus from strain test mode to ensure high stress value during the test (Rowe 1993, Artamendi and Khalid 2005, Bhasin *et al.* 2008, Masad *et al.* 2008).

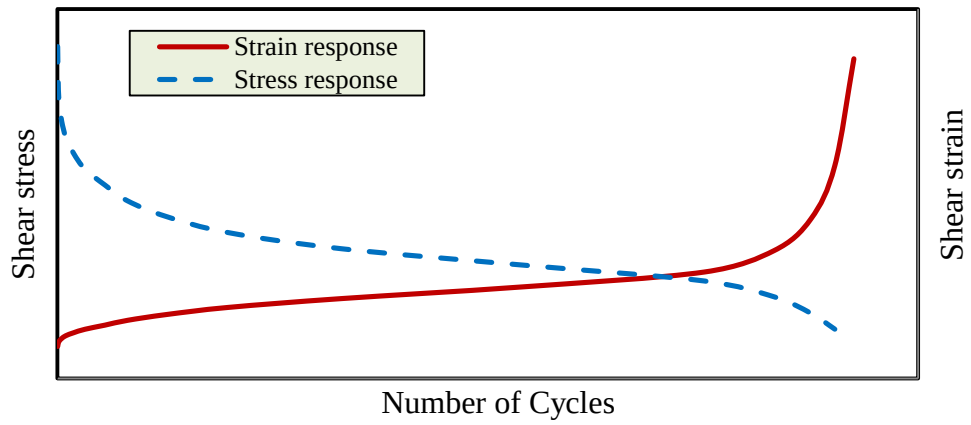

Figure 4- 15: Shear strain and shear strain response against number of cycles.

In this regard, the strain and stress amplitudes used in the fatigue test were compared with the stress and strain responses at 50% of normalised shear modulus; in other words, using the TA of the strain test mode. This comparison revealed there is compatibility between the strain/stress responses with strain/stress amplitudes in ranking order, as shown in Figures 4–16 and 4–17; but a significant difference was noticed among these values. This possibly indicates that either the values in response to the strain and stress modes are less than the damage values or they are higher than the damage values.

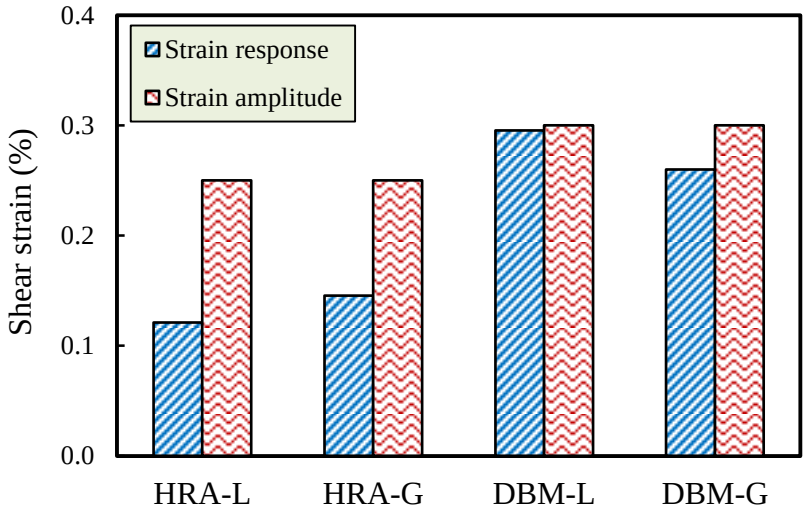

Figure 4- 16: Shear strain amplitude and shear strain response at 50% G* for mixes.

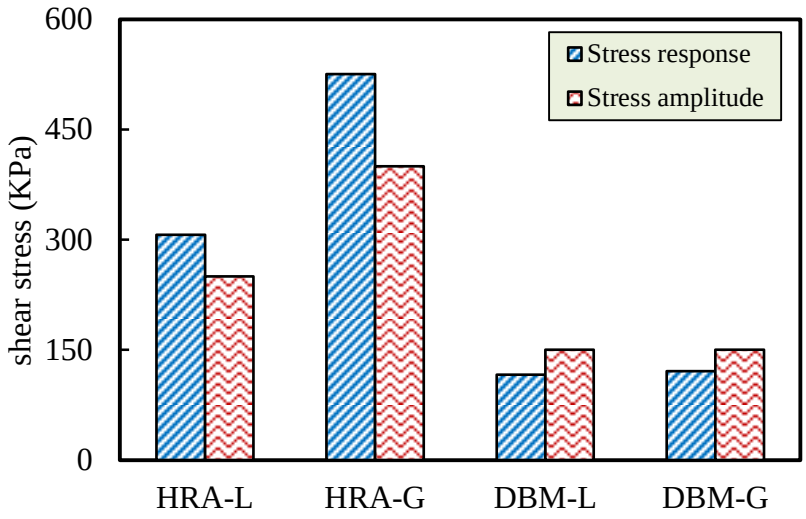

Figure 4- 17: Shear stress amplitude and shear stress response at 50% G* for mixes.

Shear stress response was plotted against normalised stiffness modulus for all the mixes tested in strain mode, as shown in Figures 4–18 and 4–19. The shear stress amplitudes of the fatigue test in stress mode corresponded to about 0.62 and 0.64 for the DBM-G and DBM-L mixes respectively, say around 0.6; and this was 0.41 and 0.38 for HRA-L and HRA-G respectively, say around 0.4, as shown in Figures 4–18 and 4–19. The shear stress response from the TA approach, i.e. $0.5G_o^*$, for the DBM mixes was around 120 KPa; and this means it was less than the damage value in stress test mode, which was 150KPa. In contrast, the shear stress responses of the HRA mixes were 306 KPa and 525 KPa for HRA-L and HRA-G respectively, and these values are higher than the shear stress amplitudes in the fatigue test, which were 250 and 400 KPa respectively. The conclusion is that the response values are not consistent with the amplitude values in the fatigue test from a damage and non-damage region perspective, and this is clear where, in the DBM mixes, the shear stress response was less than the damage value while, in HRA mixes, the responses were extremely in the high damage region, as shown in Figures 4–18 and 4–19. Thus, using the shear stress responses from the TA approach does not create the same damage because these values are higher or lower than the damage amplitude values, and this does not offer a fair comparison.

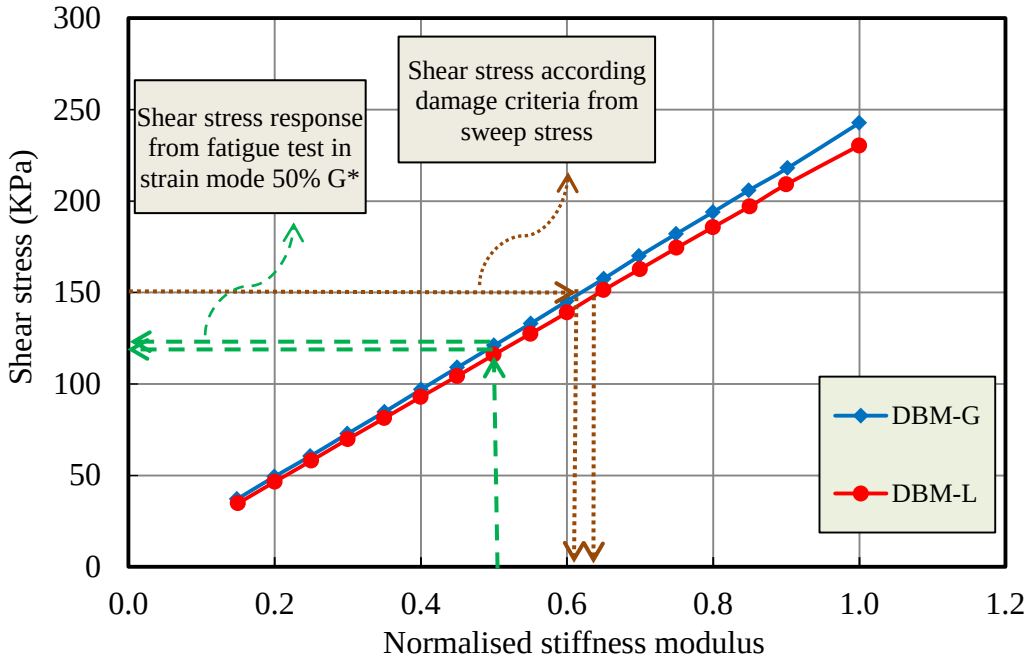

Figure 4-18: Shear stress aginst normalised stifness modulus for DBM samples tested in strain mode.

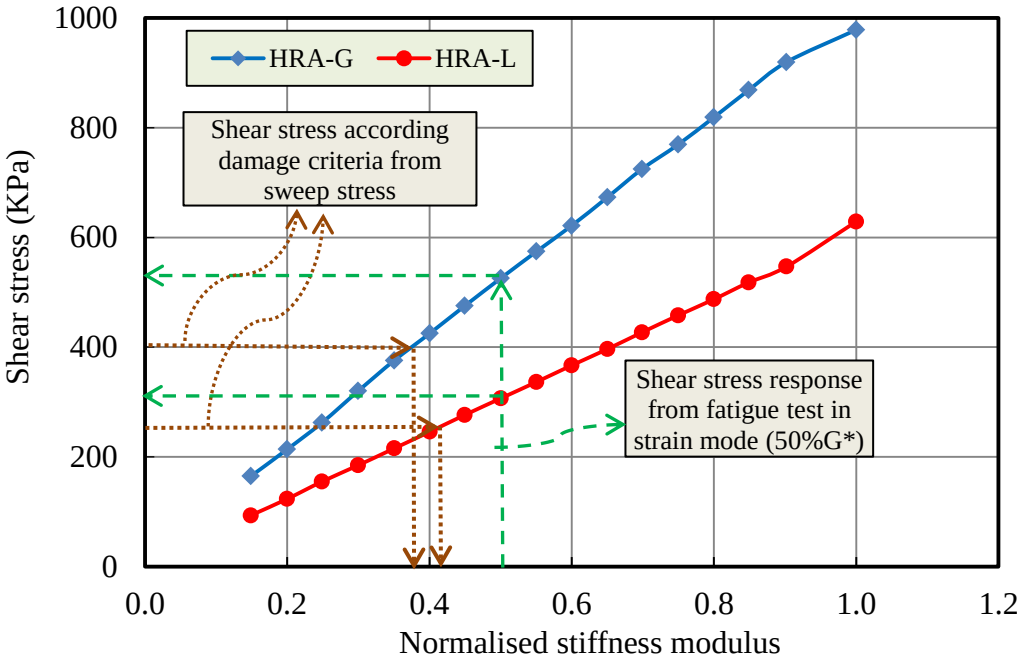

Figure 4-19: Shear stress against normalised stiffness modulus for HRA samples tested in strain mode.

4.5. FI^R and Number of DSR Samples

Due to the high scattering and variation in the fatigue results, it is essential to test more samples to minimise this imperfection. In this study, nine samples from each mix were selected and tested according to the criteria in Chapters III and IV; however, a presentation was made to highlight the efficiency of FI^R as a parameter in evaluating the fatigue performance, and the number of samples was considered in this analysis. In the previous discussion, the presentation of results included all the tested samples, and it can be seen there was a significant variation in the results of TA and ER, as revealed by the error bars, as shown in Figures 3–33 and 4–14; while the variation in FI^R was significantly low, as shown in Figures 3–32 and 4–13.

Figures 4–20 demonstrates the response of FI^R for different numbers of DSR samples in strain and stress test modes. As shown by the error bars, it can be seen that there is little variation in results for all mixes in both test modes; also, the order rank maintained the same trends irrespective of the number of samples, as shown in Figure 4–20. This behaviour reflects a main conclusion highlighted through the efficiency of FI^R in evaluating the fatigue performance even with a low number of DSR samples; while, in the case of the TA and ER approaches, testing more samples maybe helps to reduce the scattering in results.

4.6. Rate of Damage within Phase II

It is known that the fatigue life of HMA passes through three phases during its lifetime performance: Phases I, II and III as detailed in Chapter II; Phase II is the quasi-stationary phase, where the degradation in materials under loading passes hardly has a linear relationship with the number of cycles, i.e. fatigue curve (G* against number of cycles). Within this phase, fatigue life is defined based on the fatigue criteria such as traditional approach, energy ratio, and continuum mechanics approaches (Kim *et al.* 1997, Lee *et al.* 2000, Rowe and Bouldin 2000, Kim *et al.* 2003, Daniel *et al.* 2004, Artamendi and Khalid 2005, Dondi *et al.* 2013).

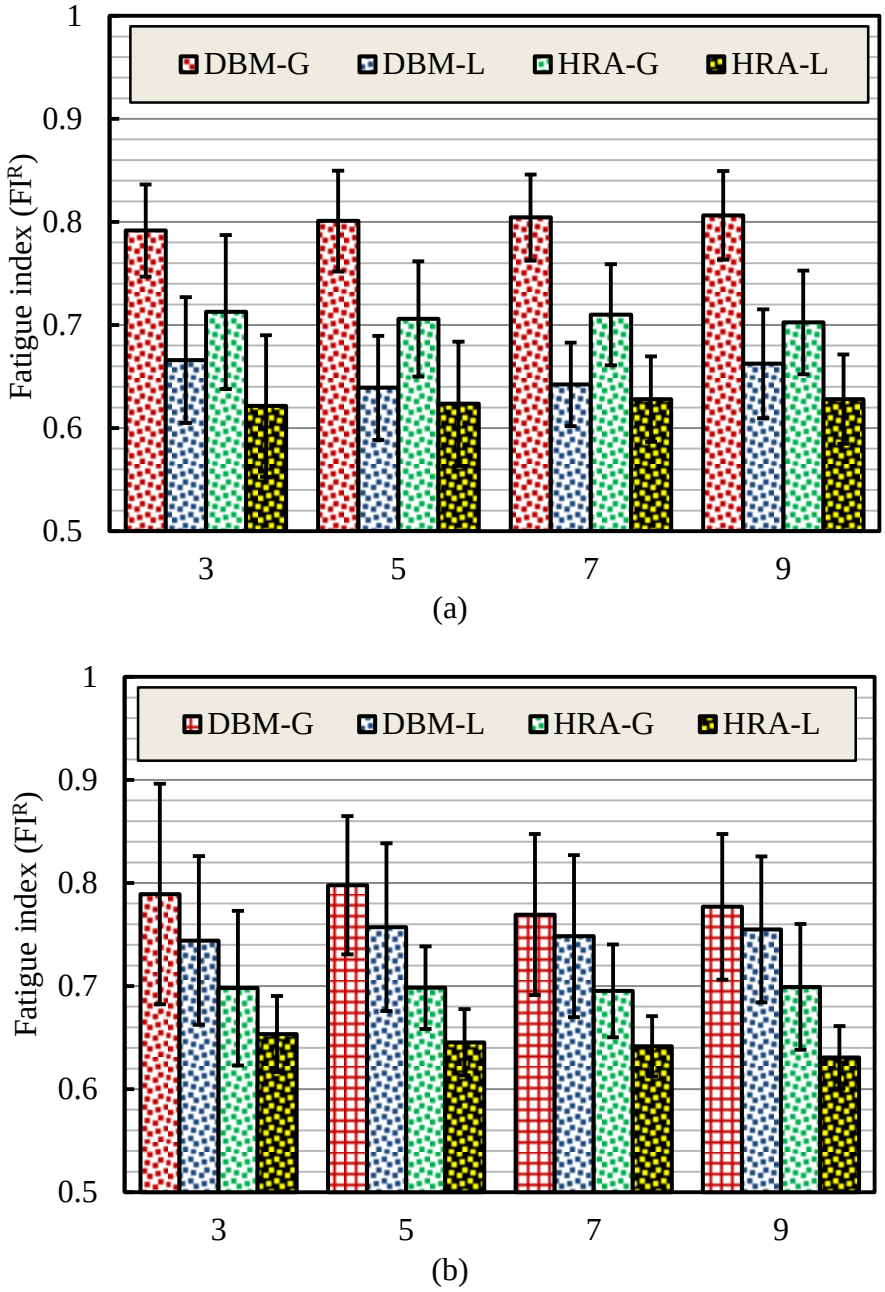

Figure 4- 20: FI^R for different numbers of DSR samples tested in: (a) strain mode and (b) stress mode.

In other works, Phase II was used to eliminate any artefacts accompanying the loading and unloading during HMA fatigue test to produce a pure fatigue damage rate (Di Benedetto *et al.* 1996, Di Benedetto *et al.* 2004).

Herein, the rate of damage within Phase II (m_{II}) was calculated from the experimental works to be used for predicting the fatigue life of HMA using a phenomenological approach (Traditional approach). Rate of damage within Phase

II was calculated from the experimental works for the relationship of complex stiffness modulus against number of cycles, as shown in Figure 4–21.

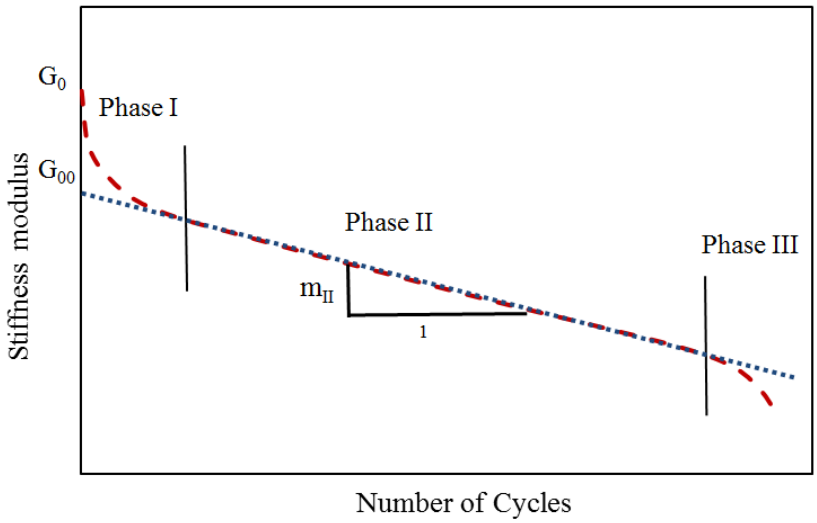

Figure 4- 21: Complex modulus against number of cycles for all phases.

However, the correlation between number of cycles to failure (N_f) and absolute rate of damage within Phase II ($|m_{II}|$) is poor, as shown in Figures 4–21 and 4–22; the trends is clear where fatigue life decreases as $|m_{II}|$ increases. The correlation increased significantly when the initial complex stiffness modulus (G_0^*) was considered to calculate the ratio of N_f/G_0^*, as shown in Figure 4–24; it is clear that the ratio of N_f/G_0^* decreased as the $|m_{II}|$ values increased.

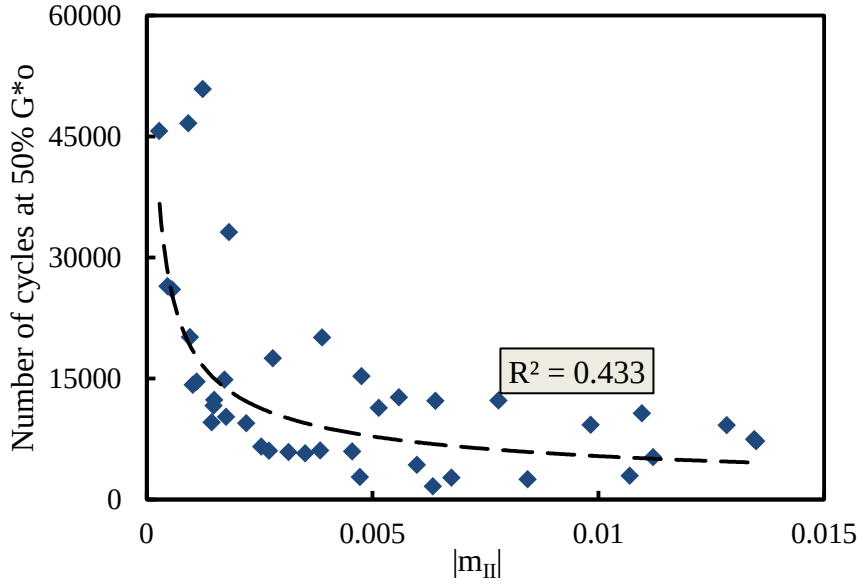

Figure 4- 22: Number of cycles against $|m_{II}|$ for strain test mode.

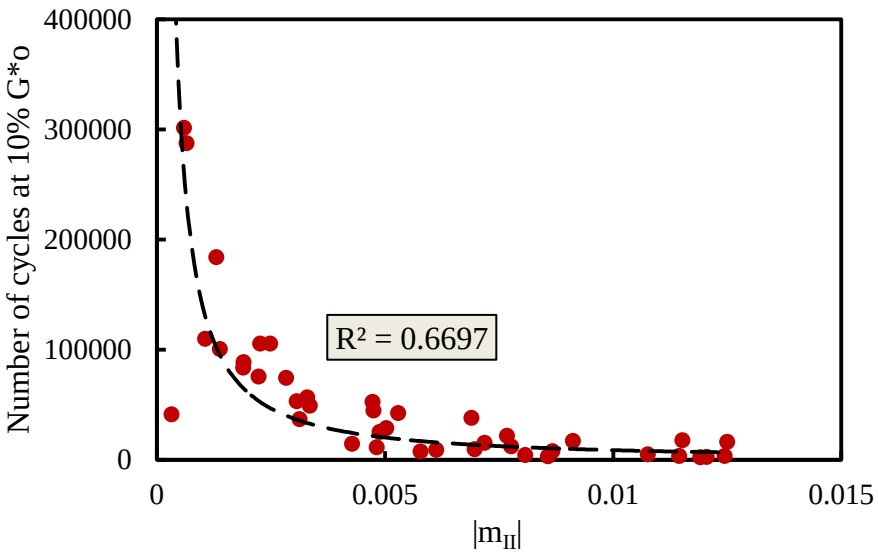

Figure 4- 23: Number of cycles against $|m_{II}|$ for stress test mode.

From Figure 4–24, the relationships between number of cycles and $|m_{II}|$ can be concluded as given in Equations 4–1 and 4–2 for strain and stress test modes respectively.

$$N_{f\gamma} = G_0^*(0.299(|m_{II}|)^{-0.966}) \quad (4–1)$$

$$N_{f\tau} = G_0^*(0.520(|m_{II}|)^{-0.957}) \quad (4–2)$$

Where: $N_{f\gamma}$ and $N_{f\tau}$ are number of cycles at failure in strain and stress test modes respectively.

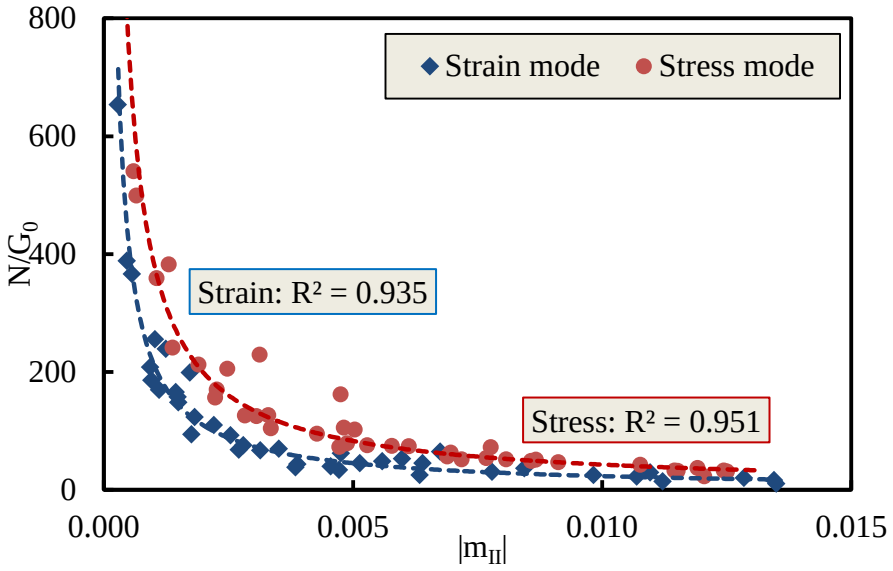

Figure 4- 24: Relationship between N_f/G_0 and $|m_{II}|$ for stress and strain test modes.

Clearly, the number of cycle was defined at 50% and 10% of the initial complex modulus for strain and stress modes respectively. $|m_{II}|$ represents one of the mix fatigue performance properties and it is affected by the mix properties and test conditions; therefore, it could be used to estimate the fatigue life of HMA if there is a good relationship between $|m_{II}|$ and its mix properties.

Fatigue performance of HMA, as other mechanical properties, is affected by mix properties and test conditions. In this work, SPSS Statistics software version 22 was used to analyse the correlation of several parameters with damage rate (m_{II}); these parameters were: initial values of complex modulus (G_0^*), phase angle (δ_0), inverted bulk density ($1/G_{bulk}$), air voids (AV%) and square initial dissipated pseudo strain energy ($(W_{d0}^R)^2$). Table 4–2 contains the correlation matrix for the data of these parameters; it can be seen that the most significant parameter that might be correlated with m_{II} was the square $of\ (W_{d0}^R)$ for strain mode and initial phase angle for stress test mode. In addition, inverted bulk density ($1/G_{bulk}$) has a correlation in the second rank with m_{II} for both test modes, while the other parameters have poor correlation with m_{II}, as detailed in Table 4–2.

Table 4- 2: Correlation matrix.

Strain test mode						
R^2	m_{II}	G_0^*	δ_0	$1/G_{bulk}$	Av%	$(W_{d0}^R)^2$
m_{II}	1.000	0.473	0.356	0.663	0.001	0.831
G_0^*	0.473	1.000	0.945	0.333	0.134	0.735
δ_0	0.356	0.945	1.000	0.245	0.216	0.647
$1/G_{bulk}$	0.663	0.333	0.245	1.000	0.014	0.624
Av%	0.001	0.134	0.216	0.014	1.000	0.072
$(W_{d0}^R)^2$	0.831	0.735	0.647	0.624	0.072	1.000
Stress test mode						
R^2	m_{II}	G_0^*	δ_0	$1/G_{bulk}$	Av%	$(W_{d0}^R)^2$
m_{II}	1.000	0.152	0.697	0.552	0.001	0.023
G_0^*	0.152	1.000	0.751	0.445	0.064	0.070
δ_0	0.697	0.751	1.000	0.377	0.032	0.028
$1/G_{bulk}$	0.552	0.445	0.377	1.000	0.134	0.014
Av%	0.001	0.064	0.032	0.134	1.000	0.017
$(W_{d0}^R)^2$	0.023	0.070	0.028	0.014	0.017	1.000

Thus, a multiple linear regression analysis was used to find the relationships of m_{II} with the parameters that had the highest correlation, as shown previously. This gave two relationships, one for strain and the other for stress test mode, as shown in Equations 4–3 and 4–4 respectively.

$$m_{II} = 4.555 \times 10^{-2} - 4.405 \times 10^{-8}(W_{D0}^{R})^2 - 1.107 \times 10^{-1}\frac{1}{G_{bulk}} \qquad (4–3)$$

$$m_{II} = -2.465 \times 10^{-3} - 3.311 \times 10^{-4}(\delta_0)^2 + 3.427 \times 10^{-2}\frac{1}{G_{bulk}} \qquad (4–4)$$

The determination coefficients, i.e. R^2, are: 0.864 for strain mode (Equation 4–3) and 0.700 for stress mode (Equation 4–4). It is clear that R^2 for stress was lower than for strain due to the low correlation of the independent variables with m_{II}, as detailed in Table 4–2. Now, the prediction models for m_{II} in Equations 4–3 and 4–4 can be used with Equations 4–1 and 4–2 to predict the fatigue life (N_f). Figures 4–25 and 4–26 demonstrate the relationship between the predicted numbers of cycles using the above equations against the actual fatigue life from experimental works. It is clear that the correlation between the actual and predicted fatigue life in strain test mode is much higher than in stress test mode, and this was justified previously due to correlation of the independent variables with m_{II}.

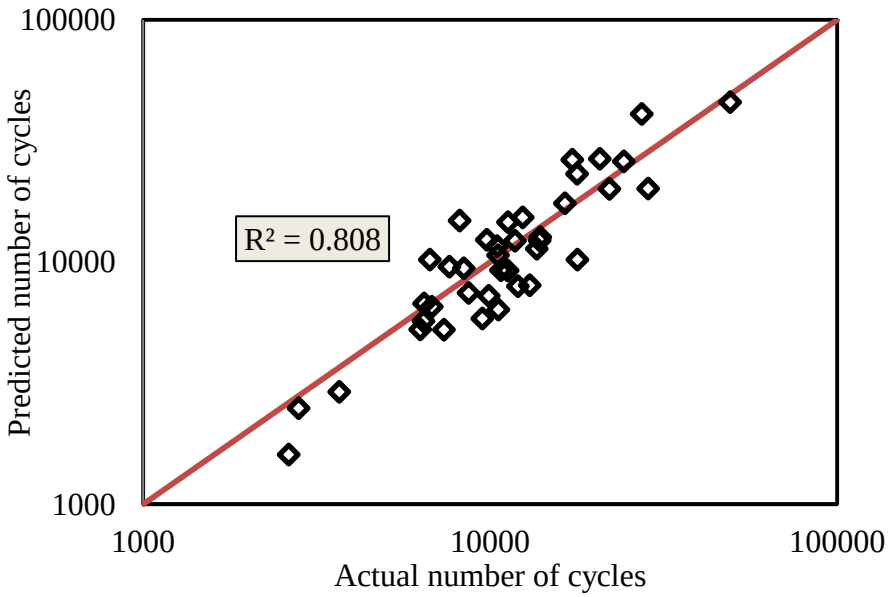

Figure 4–25: Actual against predicted number of cycles in strain test mode.

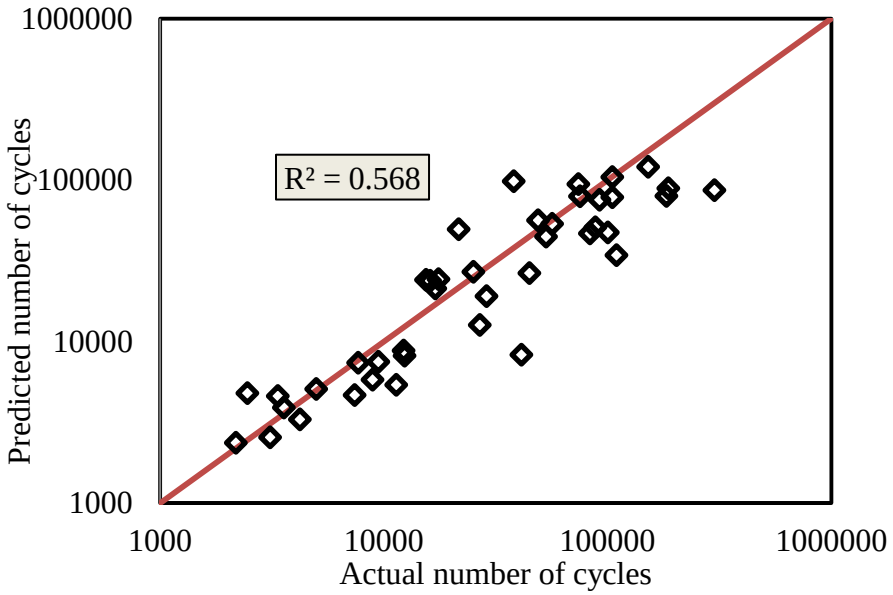

Figure 4–25: Actual against predicted number of cycles in stress test mode.

4.6. Summary

From the results presented in this chapter, the following conclusions have been made:

1. The developed approach which was used successfully for preparing and selecting DSR samples for fatigue testing in strain mode (Chapter III) was also used successfully in stress test mode. The results revealed the efficiency of this approach for adoption in stress test mode in addition to strain mode.

2. A method was adopted based on evaluating the slope of the strain response with time at different stress amplitudes to arrive at an appropriate stress level that should be used to perform fatigue tests using a DSR.

3. A comparison study between strain and stress response with stress and strain amplitude derived from the TA approach at 50% of initial stiffness revealed that there is compatibility between them. However, the study showed that the response values are not consistent with amplitude values in fatigue test from a damage and non-damage region perspective, and this is clear where, in the DBM mixes, the shear stress response was less than the damage value while, in the HRA mixes, the response were at high

damage region. Using the shear stress response from the TA approach does not give a fair comparison.

4. Fatigue performance analysis was made based on TA, ER and FI^R approaches; the analysed results showed that all approaches are in agreement according to the ranking order for all mixes; also, these results were compatible with the outcomes of the strain test mode in Chapter III.

5. A standard error was used to study the variation in results for all approaches, FI^R, TA and ER, in both test modes; this variance analysis revealed that FI^R has low variation in comparison to the TA and ER approaches. In addition, the variance in FI^R results was similar, irrespective of the number of samples and maintained the same order in the mixes. This means that FI^R is efficient in evaluating the fatigue performance of HMA with a low number of DSR samples, compared to the TA and ER approaches which are required more samples to reduce the variation.

6. Rate of damage (m_{II}) was calculated from fatigue curve, G^* vs N, within Phase II; the absolute values of m_{II} demonstrated a trend with N_f, where N_f decreases as $|m_{II}|$ decreased in both test modes; but the correlation of $|m_{II}|$ increased significantly when the ratio of N_f to initial G^* was considered. Based on the correlation analysis of m_{II} and several variables from fatigue test and volumetric properties, initial dissipated energy, initial phase angle, and bulk density were selected to develop a model for predicting m_{II}. The predicted m_{II} was used for predicting N_f using N_f/G_0^* relationship for both test modes. The analysis showed that the strain mode model gives a more satisfactory prediction than the stress test mode.

7. The study confirmed that limestone has a better fatigue performance for both HRA and DBM mixes than granite, and the strain test mode gave the same conclusion (Chapter III).

CHAPTER V

CHAPTER V

5. Predicting Fatigue Performance of Hot Mix Asphalt Using Artificial Neural Networks

5.1. Introduction

Hot mix asphalt (HMA) is a composite material with compounds from different scales: coarse and fine aggregates, filler and bitumen as a binder. Because of its composite nature, in addition to other factors such as environmental, test conditions and the properties of the material itself, the performance behaviour of HMA, e.g. fatigue, rutting and cracking, is complex and difficult to predict (You and Buttlar, 2004;Xiao et al., 2007). This complex behaviour is due to the response of these components under loading – the stiffness of the aggregates is several times higher than that of the binder, and deformation occurs in the binder leading to non-linear behaviour in the HMA. In addition, rotation, slippage and interaction between aggregates all contribute to this non-linear behaviour (Masad and Somadevan, 2002;Huang et al., 2007).

5.2. Regression Models for Fatigue Life

Despite the complex behaviour of HMA, several attempts have been made to develop regression models to predict the performance of HMA. The earliest model was introduced during the 1960s based on the relationship between HMA fatigue life in terms of number of cycles and horizontal tensile strain and tensile stress at the bottom of the asphalt layer using the basic formula in Equations 5–1 and 5–2 (Monismith et al., 1961;Pell, 1962).

$$N_f = k_1 \left(\frac{1}{\varepsilon_t}\right)^{k_2} \quad (5–1)$$

$$N_f = k_3 \left(\frac{1}{\sigma_t}\right)^{k_4} \quad (5–2)$$

where: N_f is the number of cycles at failure, ε_t, σ_t are the magnitudes of tensile strain and stress repeatedly applied and k_1, k_2, k_3 and k_4 are regression constants.

Later, studies were extended on models 5–1 and 5–2 in order to take into account mix properties represented by the stiffness modulus to develop the final model as shown in equations 5–3 and 5–4 (Monismith, 1969;Monismith, 1985).

$$N_f = a_1 \left(\frac{1}{\varepsilon_t}\right)^{b_1} \left(\frac{1}{S_m}\right)^{c_1} \quad (5–3)$$

$$N_f = a_2 \left(\frac{1}{\sigma_t}\right)^{b_2} \left(\frac{1}{S_m}\right)^{c_2} \quad (5–4)$$

where: S_m is the stiffness modulus of the asphalt mixture.

Extensive efforts were made to develop new regression models to predict the fatigue life of HMA based on large experimental works; in these cases several variables related to the mix properties were represented in these models in order to take into account the variability in the mix properties as well as the test conditions. For example, Bonnaure *et al*. (1980) developed regression models to predict the fatigue life of HMA for the controlled strain and stress test modes. These models were more comprehensive than the previous models; in addition to stiffness modulus, volumetric binder content (V_b) and temperature effect presented by the penetration index (PI) were involved in these model as shown in Equations 5–5 and 5–6 for the strain and stress mode tests, respectively:

$$N_f = A_f(0.17PI - 0.0085PI.V_b + 0.045V_b - 0.112)^5 \varepsilon_t^{-5} S_m^{-1.8} \quad (5–5)$$

$$N_f = A_f(0.0252PI - 0.0012PI.V_b + 0.0067V_b - 0.0167)^5 \varepsilon_t^{-5} S_m^{-1.4} \quad (5–6)$$

Also, for simplicity a Nomo-graph was developed based on these models (Bonnaure et al., 1980). The Shell International Petroleum Company (1978) also developed a model using the formula in Equation 5–3 for predicting the fatigue life of HMA, but in this case the volume of binder (V_b) was included in the model as shown in Equation 5–7 (Shell, 1978). Asphalt Institute developed another relationship using the same formula in Equation 5–3, but the voids filled with asphalt (VFA) were used in this model as shown in Equation 5–8 (Shook et al., 1982).

$$N_f = \left(\frac{\varepsilon_t}{(0.856V_b+1.08)S_{mix}\times 0.36}\right)^{-5} \quad (5–7)$$

$$N_f = A_f \times 10^{(4.84(VFA-0.69))}\varepsilon_t^{-3.291}S_{mix}^{-0.845} \quad (5–8)$$

In practice, the use of these regression models to predict the actual life performance of pavement is a complex problem. This is due to the nature of fatigue performance in the laboratory as opposed to the field: in the field there is no continuity in loading repetitions, which gives opportunities for rest periods that have a healing effect, and the effect of environmental conditions also has to be taken into account. However, some studies have tried to use an adjustment factor (A_f) to transfer laboratory results to the field as shown in equations 5–5, 5–6 and 5–8 above.

Energy approach was used in several studies to predict the fatigue performance of HMA (Van Dijk and Visser, 1977;Tayebali et al., 1992;Rowe, 1993;Ghuzlan and Carpenter, 2006). This approach is based on the amount of energy dissipated being proportional to the number of cycles during cyclic loading testing, as presented in Equation 5–9:

$$W = A\left(N_f\right)^z \quad (5–9)$$

where: W is cumulative dissipated energy to failure, and A *and* z are regression constants.

All these regression models are used by researchers; and efforts are still being made to improve their performance by adding new parameters or deriving new models. But, the problem lies in the goodness of fit (quality) of these regression models, which is evaluated through the correlation between the actual and predicted values using the determination coefficient (R^2). Since 1980s, a mathematical technique called artificial neural networks (ANNs) has been used widely to improve the performance of models for predicting; and the outcomes have been good in terms of closeness of fit and the high correlation between actual and predicted results (Adeli, 2001).

5.3. Artificial Neural Networks (ANNs)

An artificial neural network (ANN) is a computational model based on the structure and functions of the central nervous system. The information flowing through the network affects the structure of the ANN because it changes and learns based on those inputs and outputs (Adeli, 2001;Priddy and Keller, 2005).

An ANN consists of a large class of different architectures – multilayer neural networks are among the most widely used and consist of three layers: input layers, where the input parameters are simulated; hidden layers, which represent the layers for transforming the input from input layers to output in the output layers; and output layers which represent the output parameters of the models. In the hidden layers, there are a number of nodes called neurons, which represent the processing element of the ANN. Each neuron has two parts: one deals with the sets of adaptive weight and the other provides a transfer function to process to output as illustrated in Figure 5–1. The outputs of the three layers of the ANN in Figure 5–1 are calculated as in Equation 5–10 (Priddy and Keller, 2005).

$$Y = \theta\left\{\beta_o + \sum_{j=1}^{n}\left[V_j.\theta_j\left(b_j + \sum_{i=1}^{m} X_i W_{ij}\right)\right]\right\} \quad (5-10)$$

where: β_o is bias at output; W_{ij} is the weight connection between neuron j in the hidden layers and input layers i; V_j is the weight connection between neuron j in the hidden layers and the output layer; b_j is bias at neuron j in hidden layers; and θ is a transfer function.

In ANN transfer function is used to correct the error during the training; to enable that must be deferential and continuous to use the back propagation in training (Priddy and Keller, 2005). Figure 5–2 displays different transfer functions used by the ANN designers. The most common transfer function is called sigmoid function; Equation 5–11 represents the formula of a sigmoidal logistic function; this function has nice mathematical properties such as continuity and differentiability that are very important during the training.

$$\theta(u) = \frac{1}{1+e^{-u}} \quad (5–11)$$

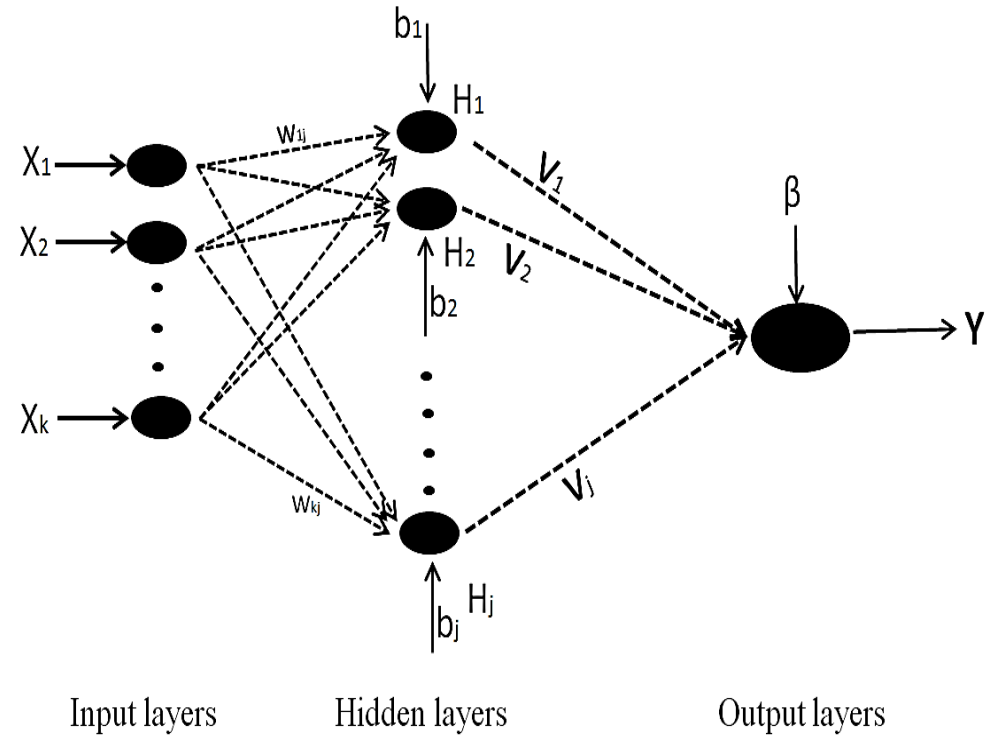

Figure 5- 1: Three layered neural network architecture.

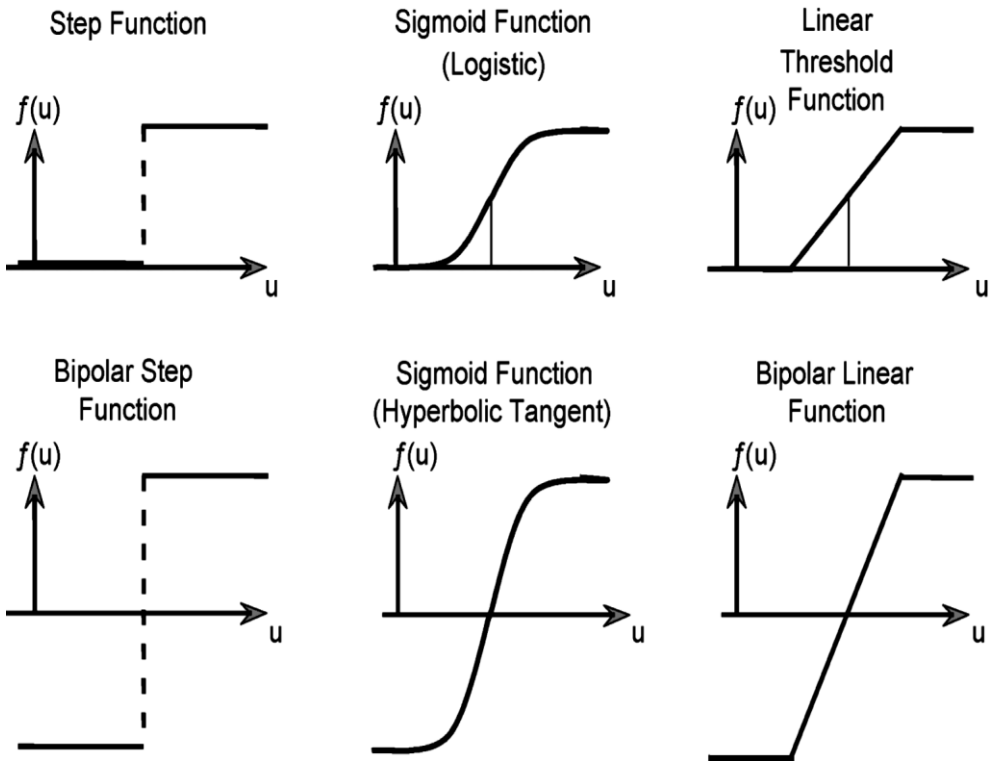

Figure 5- 2: Different types of transfer function (Priddy and Keller, 2005)

The working principle of ANNs is based on supervised or unsupervised learning. In supervised learning, a simple error back-propagation (BP) training algorithm is

used to train the neural networks. During the training, information is propagated forward through the neural network, this means finding the weight and bias in the link connections of neurons using a set of data. The output response is compared to the actual outputs (or target) data and the error is computed and propagated backward through the network neurons and used to make adjustments in the weights and biases. In unsupervised learning, ANNs are often more complicated than supervised, where the inputs are provided to the ANN without outputs and the ANN must organise and adapt itself based on the inputs and the function of the network. The network is trained through iterating the BP algorithm until the sum of the squares errors between the actual and predicted is minimised (Adeli, 2001;Priddy and Keller, 2005;Haykin, 1999)

5.4. Utilisation of ANNs

ANNs have been used successfully by researchers in prediction, classification and noise reduction in different disciplines of civil engineering; more details about the use of ANNs in civil engineering are available in the review paper by Adeli 2001. There are numerous studies to enhance predictive models for HMA performance. For example, Xiao *et al.* (2009) used a three-layered ANN to predict the fatigue life of rubberized asphalt concrete (RAC) and compared this with two regression models. The two regression models that were used to predict the fatigue performance of RAC were: the strain-dependent model, which is a function of initial flexural strain, initial stiffness modulus and VFA or air voids (AV); and the energy-dependent model, which is a function of VFA or AV and initial dissipated energy (Xiao, 2009). Analysis results for these two models stated there is poor fit between the predicted and actual result with low determination coefficients and high coefficients of variation (CV). At the same time, the same independent variables for the two regression models have been used as inputs in the three layers of ANNs (input–hidden–output) to predict the fatigue life of RAC. The outcome was high correlation between the actual and predicted results as shown by the high determination coefficients ($R^2 > 0.91$); however, there are no details given about the numbers of neurons in the hidden layers and the data size was limited.

Celyan *et al*. (2009) used ANNs with two hidden layers (20 neurons in each) to enhance the accuracy of the Witczak 1999–2006 models (Andrei et al., 1999;Bari and Witczak, 2006) for predicting the dynamic modulus |E*| of HMA. In this study, the same input parameters as used by Witczak were used as inputs in the ANN. These parameters included binder viscosity, loading frequency, aggregate gradation characteristics and mixture volumetric properties from a comprehensive laboratory database containing 7400 data records (Ceylan et al., 2009). The study demonstrated there was significant improvement in the ANN predictive model compared to regression models: Witczak-1999 and Witczak-2006; the improvement was evaluated using R^2 and S_e/S_y (standard error/standard deviation). For ANN-1999, R^2 increased to 0.98 and S_e/S_y decreased to 0.14, in contrast, R^2 was 0.68 and S_e/S_y was 0.57 for Witczak-1999; while R^2 for ANN-2006 increased to 0.96 and S_e/S_y decreased to 0.21, but R^2 for Witczak-2006 was 0.77 and S_e/S_y was 0.48.

Subsequently, an ANN with four layers (input–hidden–hidden–output) has been used to predict the stiffness modulus |E*| of HMA. In this study the same input parameters as used in an empirical model called the Hirsch model were used (e.g. VFA; voids in mineral aggregate (VMA); complex modulus of binder |G*|; phase angle; and contact factor) (Ceylan, 2008). The ANN model showed a remarkably high performance in predicting the stiffness modulus of HMA compared with the Hirsch model; this was observed from the increase in R^2 from 0.25 to 0.86 and the decrease in S_e/S_y from 0.88 to 0.38.

5.5. Objectives of Study

The following objectives have been determined for modelling using an ANN:

1. Predicting the fatigue performance of asphalt mixes tested in DSR and evaluated according to three approaches: traditional approach (TA), energy ratio approach (ER) and fatigue index (FI^R). Fatigue test parameters such as initial stiffness modulus, initial phase angle, shear strain amplitude, shear stress amplitude and relaxation test coefficients (G_1, m) in addition to volumetric properties (bulk density and air voids) were nominated as input parameters for

developing ANN models. In this study, fatigue test parameters and volumetric properties are called fundamental parameters.

2. Developing ANN models for predicting fatigue performance of HMA irrespective of fatigue test modes.

3. Bias analysis of ANN models; in this regards average error, intercept and slope are used to study and compare the accuracy of ANN models.

5.6. Materials and Experimental Work

Experimental work includes performing fatigue tests using DSR on HMA samples. More details for the materials and experimental work are available in Chapters III and IV.

5.7. Results and Discussion

According to the aims that are specified in the objectives of this chapter, the discussion included the development of ANN models as detailed in the next sections.

In this study, fatigue performance was defined using three approaches:

1. The TA defines fatigue life (N_f) as a number of cycles at 50% and 10% of initial stiffness modulus for strain and stress test modes, respectively as detailed in Chapters II, III and IV.

2. The ER approach defines fatigue life (N_1) in the stress mode as the number of cycles at the point when the ER reaches the peak point in the relationship of ER vs number of cycle, while in the strain mode it is defined as the point when the ER slope diverges from a straight line in the same relationship as detailed in Chapters II, III and IV.

3. Pseudostrain energy – in this case, fatigue index (FI^R) was calculated based on the ratio of recovered pseudostrain energy (W_R^R) to applied pseudostrain energy (W_A^R) as shown in Equation 3–23 and detailed in Chapter III.

5.7.1. ANN Model Based on Fundamental Parameters

The majority of the regression models that have been developed for predicting fatigue performance are based on two categories of variables: mechanistic variables such as stress, strain and stiffness modulus; and volumetric properties such as air voids, void fields with asphalt or voids of binders (Monismith, 1969;Bonnaure et al., 1980;Shook, 1982;Monismith, 1985). Fatigue performance in terms of number of cycles was also evaluated using the parameters of the fatigue test outputs represented by stiffness modulus and phase angle as used in the traditional and energy ratio approaches (Tayebali et al., 1992;Rowe, 1993;AASHTO, 2002;Kim et al., 2003). Based on these works, all fundamental parameters were selected for developing ANN models to predict the fatigue performance in terms of number of cycles according to the traditional and energy ratio approaches and fatigue index. These parameters are: initial stiffness modulus (G_o^*), initial phase angle (δ_o), shear strain amplitude (γ), shear stress amplitude (τ), relaxation test coefficients (G_1, m), bulk density (G_{bk}) and air voids (AV%). The ANN model is a function of these variables as shown in Equation 5–12 and the multi-layered general architecture shape presented in Figure 5–3.

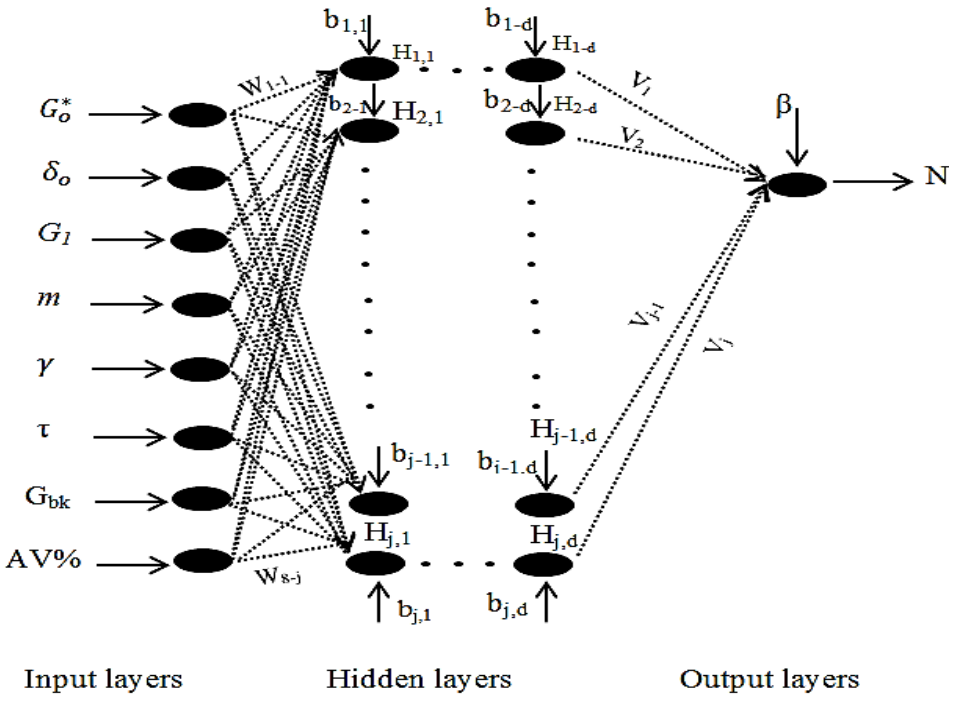

Figure 5- 3: General architecture shapes for multi-layered ANN.

$$ANN_{model} = f(G_o^*, \delta_o, \gamma, \tau, G_1, m, G_{bk}, AV\%) \quad (5–12)$$

The total data for training and testing were collected from 46 DSR-samples tested in strain and 46 DSR-samples tested in stress test modes; the data were divided randomly into two different groups: 85% of the data for training and 15% for testing.

The developed ANNs in the following sections have been classified according to fatigue performance approaches.

5.7.1.1. Traditional Approach (N_f)

Multi-layered ANNs consisting of input layers, two hidden layers and an output layer, as shown in Figure 5–3, were used for modelling fatigue life. These included single and double hidden layers with 10, 15 and 20 neurons. The coefficient of determination (R^2) was employed to investigate the correlation between the actual and predicted fatigue life. The chosen architecture of the neural network was based on the highest R^2; it was found that the best ANN architecture for this purpose consisted of double hidden layers with 15 neurones in each layer. For simplicity, the multi-layered ANN was denoted as [N_{Input}-$15_{HiddenI}$-$15_{HiddenII}$-$\dot{N}_{Output}$], where N is the number of input parameters and $\dot{N}$ is the number of output parameters; this definition will be used with all other ANNs in this Chapter.

The input parameters for the ANN of controlled strain test mode are seven parameters, i.e. $G_o^*, \delta_o, \tau_o, G_1, m, AV\% \; and \; G_{bk}$, while in stress test mode are the same parameters except using γ_o instead of the stress amplitude τ_o; this is because the strain amplitude in strain test mode is constant while in stress test mode the stress amplitude is constant. So the multi-layered ANN that was used in modelling the fatigue life (N_f) was denoted as [7_{Input}-$15_{HiddenI}$-$15_{HiddenII}$-1_{Output}] for both test modes. In this work, the MATLAB-2013a Neural Network Toolbox was used to create the ANN; the BP is a supervised learning algorithm that was used to train the neural network. For training, the Levenberg-Marquart algorithm was adopted for its efficiency in training networks (Demuth, 2009).

The relationships between the actual and predicted number of cycles by ANN are demonstrated in Figures 5–4 and 5–5 for the strain and stress test modes, respectively. The predicting performance of the trained neural network is considered satisfactory and a high correlation in terms of R^2 between actual and predicted values for the tested ANN is existed. It is noticed from R^2 that there is no significant differences between both ANN models for stress and strain test modes; where the correlation in both test modes are excellent where it is higher than 0.98 as shown in Figures 5–4 and 5–5.

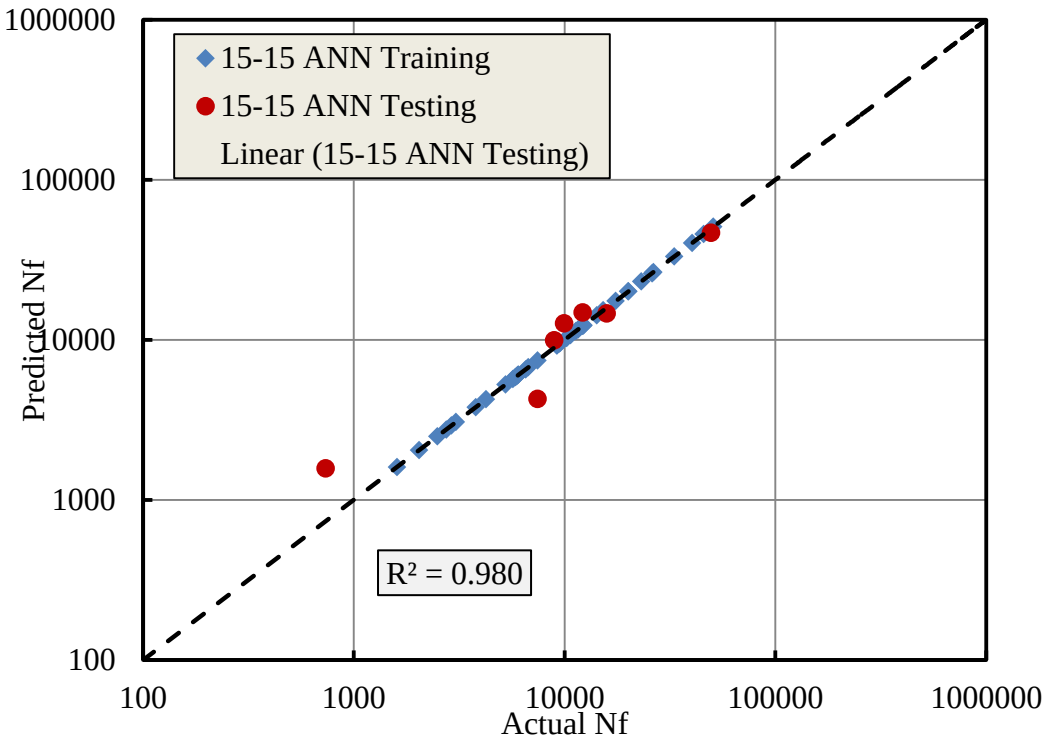

Figure 5- 4: Actual against predicted number of cycles (Nf) of ANN model for strain mode.

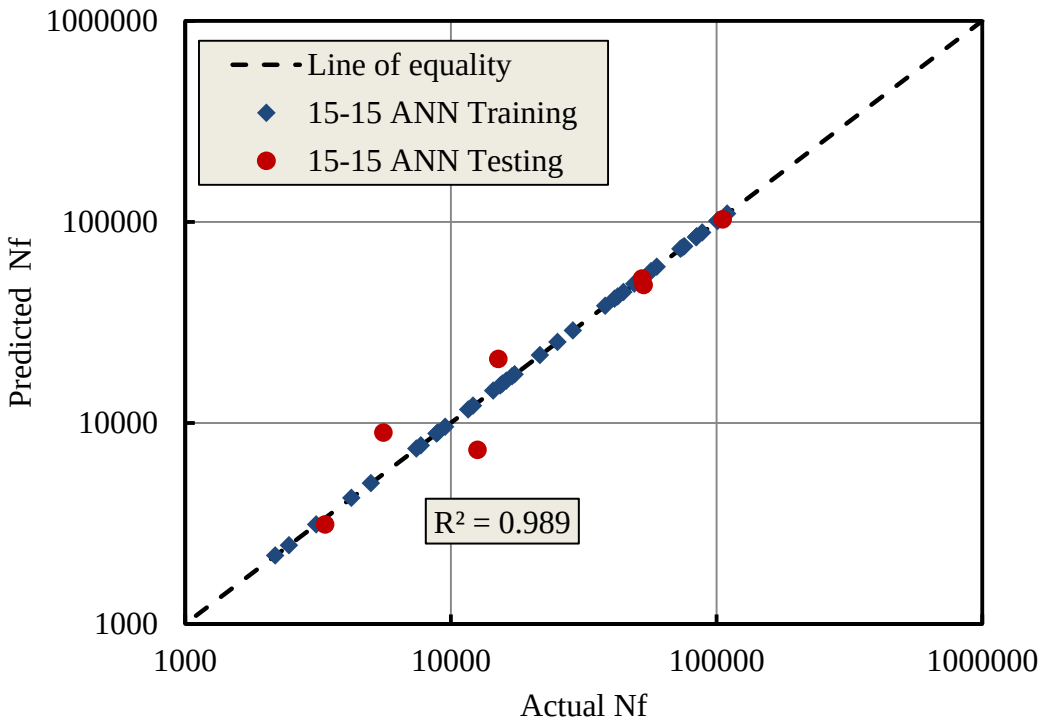

Figure 5- 5: Actual against predicted number of cycles (Nf) of ANN model for stress mode.

5.7.1.2. Energy Ratio Approach (N_1)

The same neural network [7_{Input}-$15_{HiddenI}$-$15_{HiddenII}$-1_{Output}] as was used for the traditional approach (N_f) was chosen to model the number of cycles (N_1) for the energy ratio approach because it resulted in the highest R^2 value. The results revealed there is high correlation between the actual and predicted number of cycles of the trained neural network in both test modes as presented in Figures 5–6 and 5–7. Again, in the stress test mode the correlation was slightly higher than in the strain test mode as was found with the traditional approach. This may be because the correlation between independent variables and number of cycles is better in the stress mode than the strain mode; however the correlation in both test modes are still excellent where higher than 0.95 and 0.98 for strain and stress test mode respectively as shown in Figures 5–6 and 5–7.

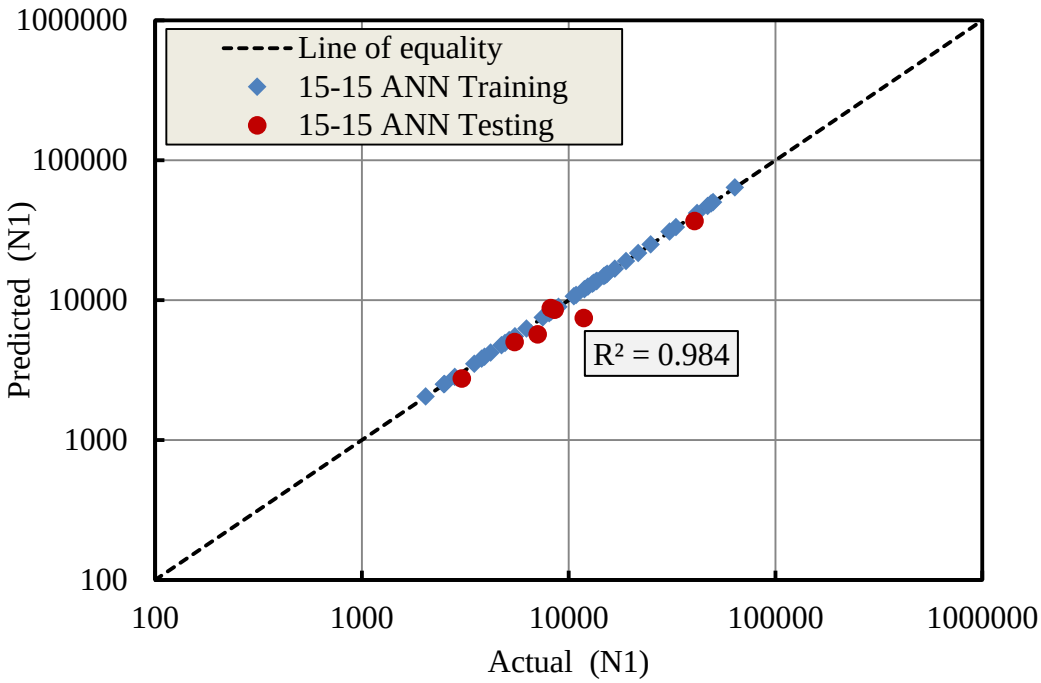

Figure 5- 6: Actual against predicted number of cycles (N1) of ANN model for strain mode.

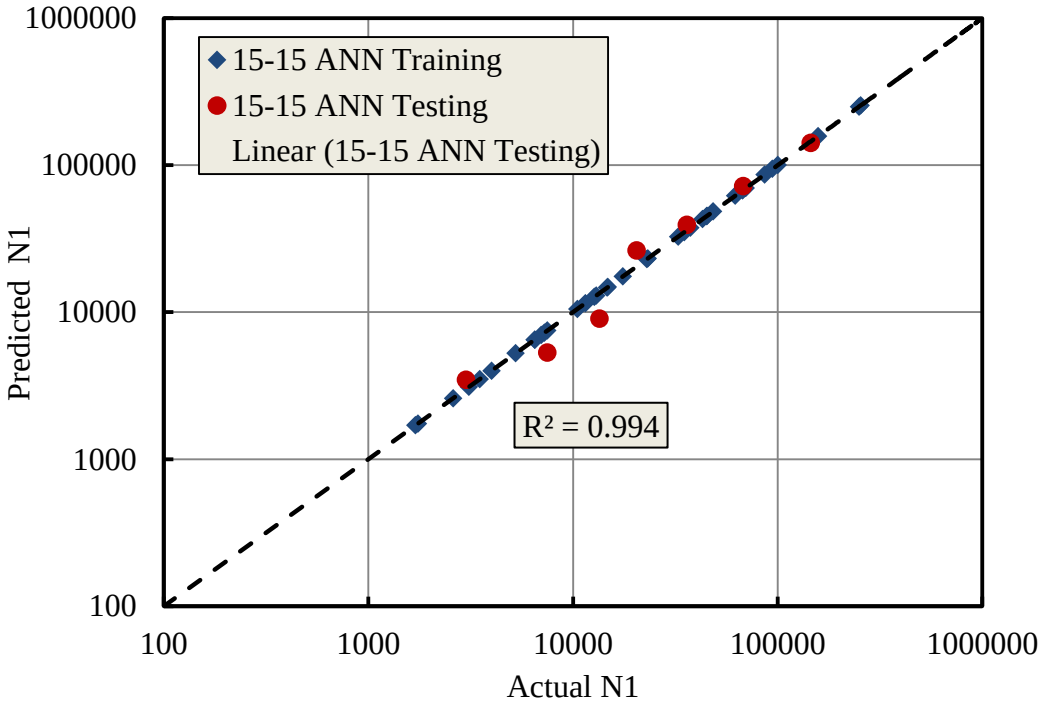

Figure 5- 7: Actual against predicted number of cycles (N1) of ANN model for stress mode.

5.7.1.3. Pseudostrain Energy (FI^R)

Fatigue performance was defined as FI^R using Equation 3–23. The ANN [7_{Input}-$15_{HiddenI}$-$15_{HiddenII}$-1_{Output}], was also used for modelling FI^R using the same input variables as in the traditional and energy ratio approaches in the input layer. The results revealed there is excellent correlation between the actual and predicted results using ANN models; also there is no significant difference in R^2 between both modes, where about 0.97 and 0.99 for strain and stress test modes respectively as shown in Figures 5–8 and 5–9.

The quality analysis of the all previous ANN models are required to evaluate according to a perfect model which is represented by line of equality, this will be demonstrated in a section related to bias analysis at the end of this chapter.

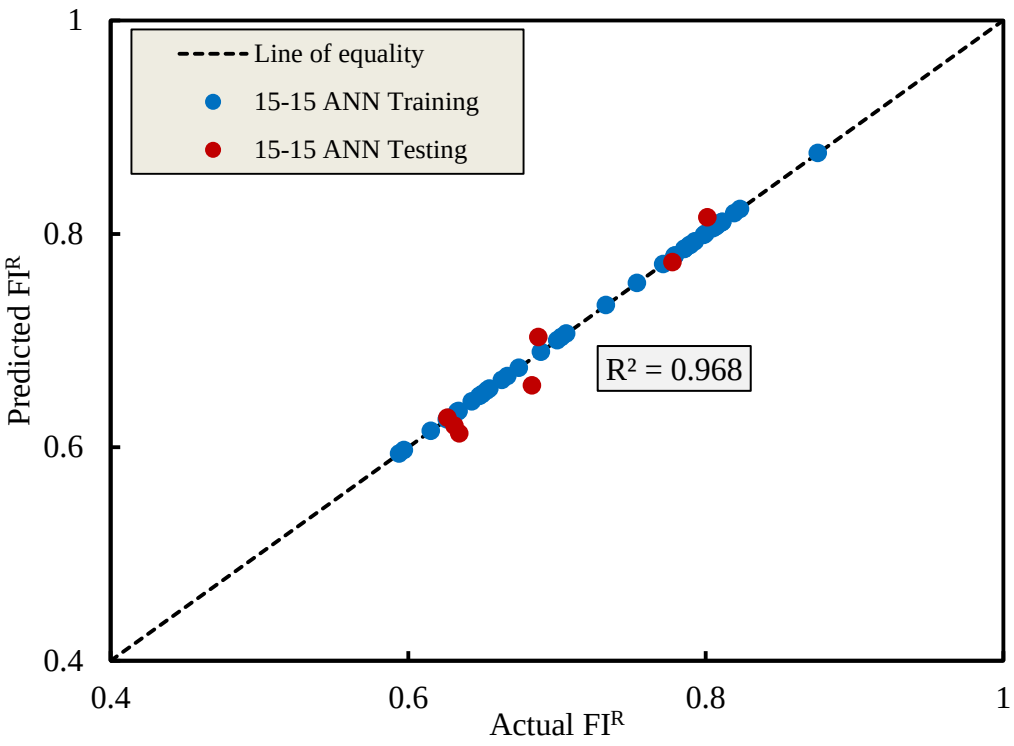

Figure 5- 8: Actual against predicted FI^R of ANN model for the strain test mode.

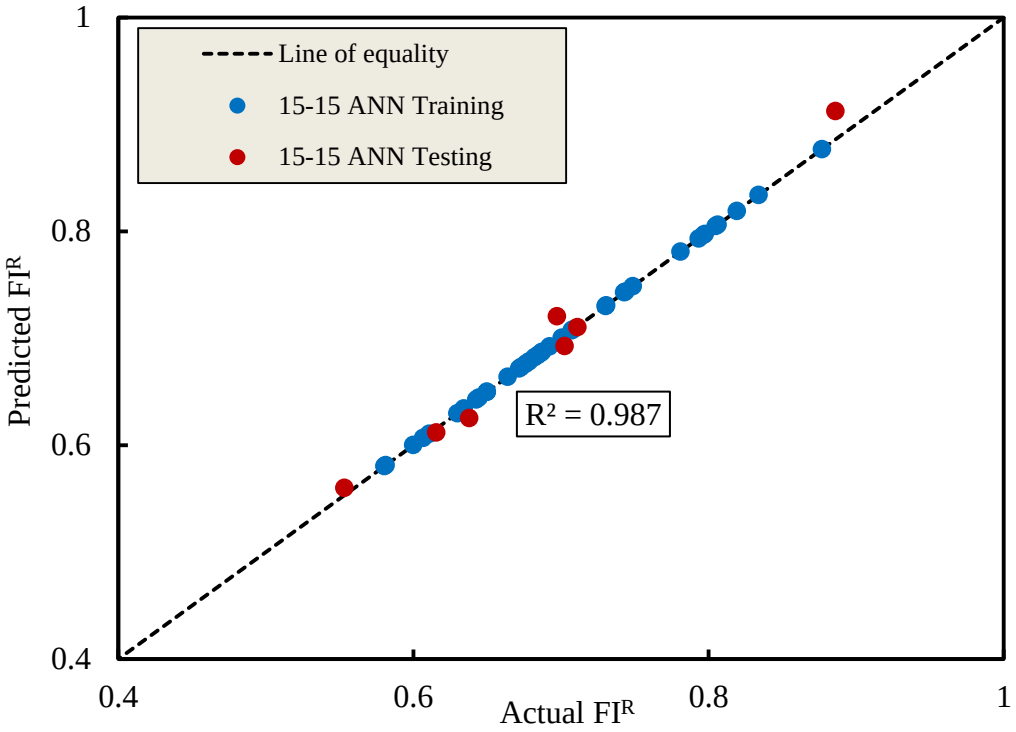

Figure 5- 9: Actual against predicted FI^R of ANN model for the stress test mode.

5.7.2. ANN Model for Independent Fatigue Mode Test

In this section of this chapter, a successful attempt was made to develop an ANN model to predict fatigue performance independent of test mode. The results of fatigue performance for two approaches were selected for modelling, the TA and FI^R approaches. ER approach was excluded because the definition of life as a number of cycles takes different criteria depending on the test mode where the relation between energy ratio and number of cycles are different for both test modes as detailed in Chapter II. In the TA, the neural network was trained using the date of the fatigue life as a number of cycles at 50% and 15% of initial stiffness modulus irrespective of test of mode.

The input parameters for training neural network are six parameters, i.e. $G_o^*, \delta_o, G_1, m, AV\% \; and \; G_{bk}$, while shear stress amplitude, τ_o, and shear strain amplitude, γ_o, have been excluded from the input parameters because the intention is to develop ANN model irrespective of test mode, so the architecture of ANN is [6_{Input}-$15_{HiddenI}$-$15_{HiddenII}$-1_{Output}]. The total data for training and testing were collected from 92 DSR-samples tested in strain and stress test modes; the

data were divided randomly into two different groups: 85% of the data for training and 15% for testing.

5.7.2.1. Traditional Approach ($N_{f,50\%,15\%}$)

The number of cycles in TA was modelled using neural network at 50% and 15% of initial G* as detailed previously. Figures 5–10 and 5–11 show the relationship between the predicted and actual N_f at 50% and 15% of initial G* respectively. The predicting performance of the trained neural network is considered acceptable as clear from the high correlation in terms of R^2 between actual and predicted values for the tested ANN models; where the correlation as R^2 values were 0.93 and 0.94 for 50% and 15% of initial G* respectively. This emphasises the feasibility of using the ANN model for predicting the fatigue performance as a number of cycle irrespective of test of modes at a high reliability.

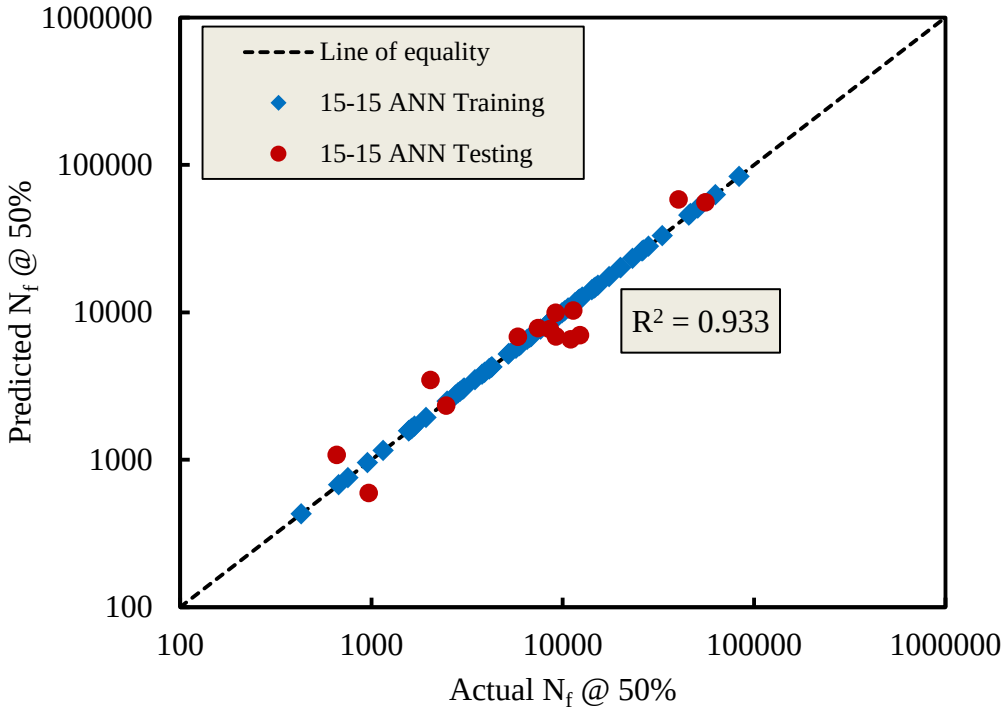

Figure 5- 10: Actual against predicted number of cycle (N_f) at 50% of initial stiffness modulus for independent test modes.

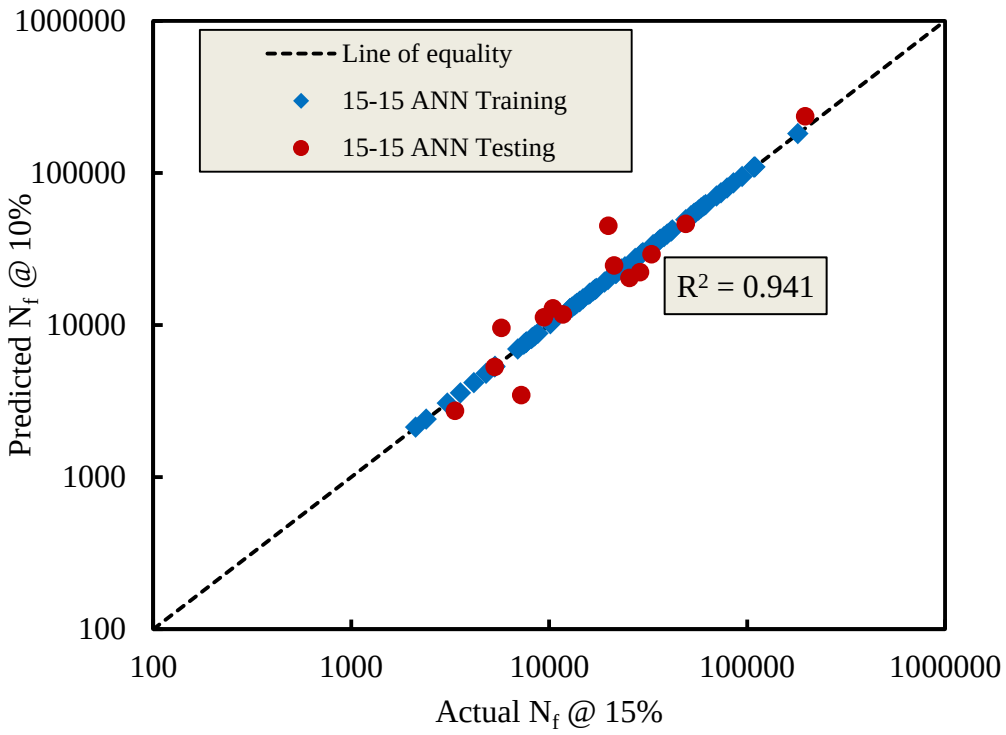

Figure 5- 11: Actual against predicted number of cycle (N_f) at 15% of initial stiffness modulus for independent test modes.

5.7.2.2. Pseudostrain Energy Approach (FI^R)

Figures 5–12 represents a set of data for training and testing the neural network [6_{Input}-$15_{HiddenI}$-$15_{HiddenII}$-1_{Output}] for modelling the fatigue index (FI^R) independent fatigue test modes. The correlation is excellent, as demonstrated from the high R^2 (0.93) values between the actual and predicted FI^R for the tested set of data as shown in Figure 5–12. This also emphasises the possibility of using the ANN models for predicting the fatigue performance as a FI^R irrespective of test of modes at a high reliability. More study was related to bias analyses for these models presented in the next section to give more features for these ANN models.

5.7.3. The Bias Analysis of ANN Models

In the previous sections, R^2 was used to evaluate the accuracy of the ANN models for all the approaches; however overall goodness-of-fit statistics such as R^2 does not necessarily tell the entire story regarding model accuracy.

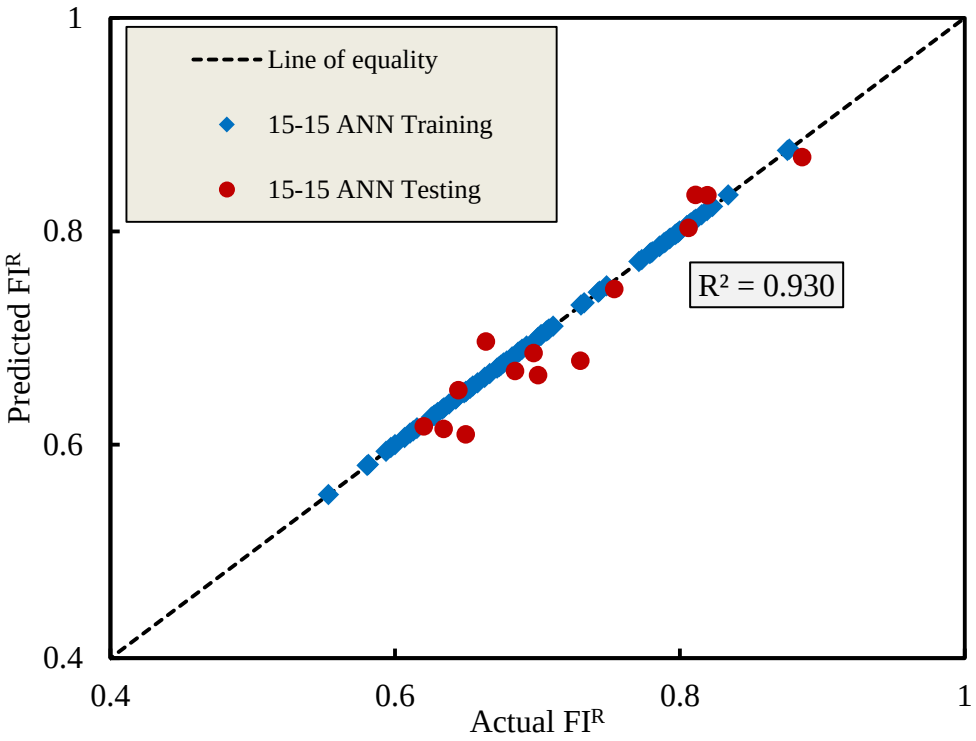

Figure 5- 12: against predicted FI^R value of independent test modes.

There may be overall biases in the predictions that can cause significant reduction in accuracy under certain conditions. Herein, the discussion was extended to study widely the bias of ANN models through the use of regression parameters. In this regard, three parameters were calculated based on the outcomes from the set of data for the testing ANN, these parameters are: average error (AE) between predicted and actual results, evaluated by using Equation 5–15 (Ceylan et al., 2009), slope and intercept of the relationship between predicted and actual values.

$$AE = \frac{\sum_{i=1}^{N}(\varphi_p - \varphi_a)}{N} \qquad (5\text{–}15)$$

where: φ_p and φ_a are predicted and actual values for the set of tested data.

These three parameters will be compared with the optimum values that are presented by the line of equality (LQ). LQ was selected as a perfect model because the predicted values are equal to actual results and LQ passes through the origin, therefore the average error, intercept and slope are 0, 0 and 1, respectively. The model results in over-prediction if the average error is positive or under-

prediction if the average error is negative. The model is close to the LQ when the slope and intercept approach 1 and 0, respectively.

The discussion here comprised the bias analysis of the two categories of ANN models: ANN models based on fundamental parameters for the stress and strain test mods and ANN models for independent test of modes.

5.7.3.1. ANN models of Fundamental Parameters

The ANN models in this case were developed based on the test of modes, i.e. strain and stress, for all the approaches: FI^R, N_f and N_1; therefor the bias analyses were divided into two categories: stress and strain test modes.

Figure 5–13 summarises the average error for ANN models for all approaches: FI^R, N_f and N_1 in both mode tests. It can be noticed that ANN models under-predict in the strain mode for FI^R and N_1 but over-predict in the stress test mode as shown from the negative and positive average error values while the behaviour was reversed in N_f. Also, the ANN model prediction for stress has a lower tendency towards this bias than for the strain mode if it was compared with the perfect value of the LQ, 0, due to the lower average error irrespective of the sign as shown in Figure 5–13.

Figure 5-14 demonstrates the intercept values of the three approaches; for FI^R, ANN model of stress mode is the smallest prediction bias for intercept than the strain test mode as demonstrated in Figure 5–14a, where stress's intercept is lower than strain mode. The intercept ranges for the N_f and N_1 approaches are about 1100 to 100 cycles as demonstrated in Figures 5–14b and 5–14c for both test modes. It is clear that the ANN model for N_1 approach in strain test mode is the closest to LQ because its intercept is slightly higher than 100 cycles; while for the stress mode it was higher than 750 cycles, as shown in Figure 5–14c. In contrast, there is no significant difference in N_f approach for both test modes where the intercept was approximately 1100 cycles, so there is no clear tendency bias.

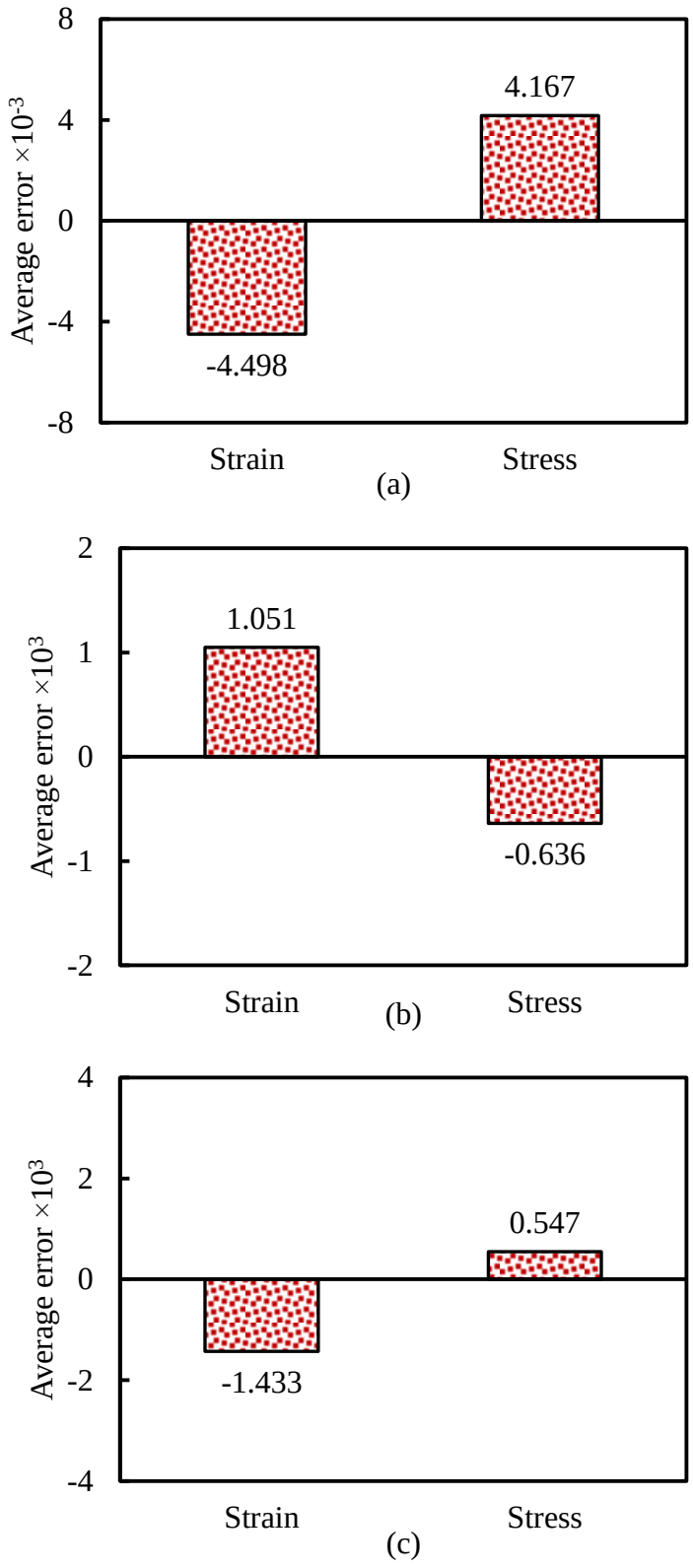

Figure 5- 13: Average error of ANN models for different approaches in strain and stress test modes: (a) FI^R, (b) N_f and (c) N_1.

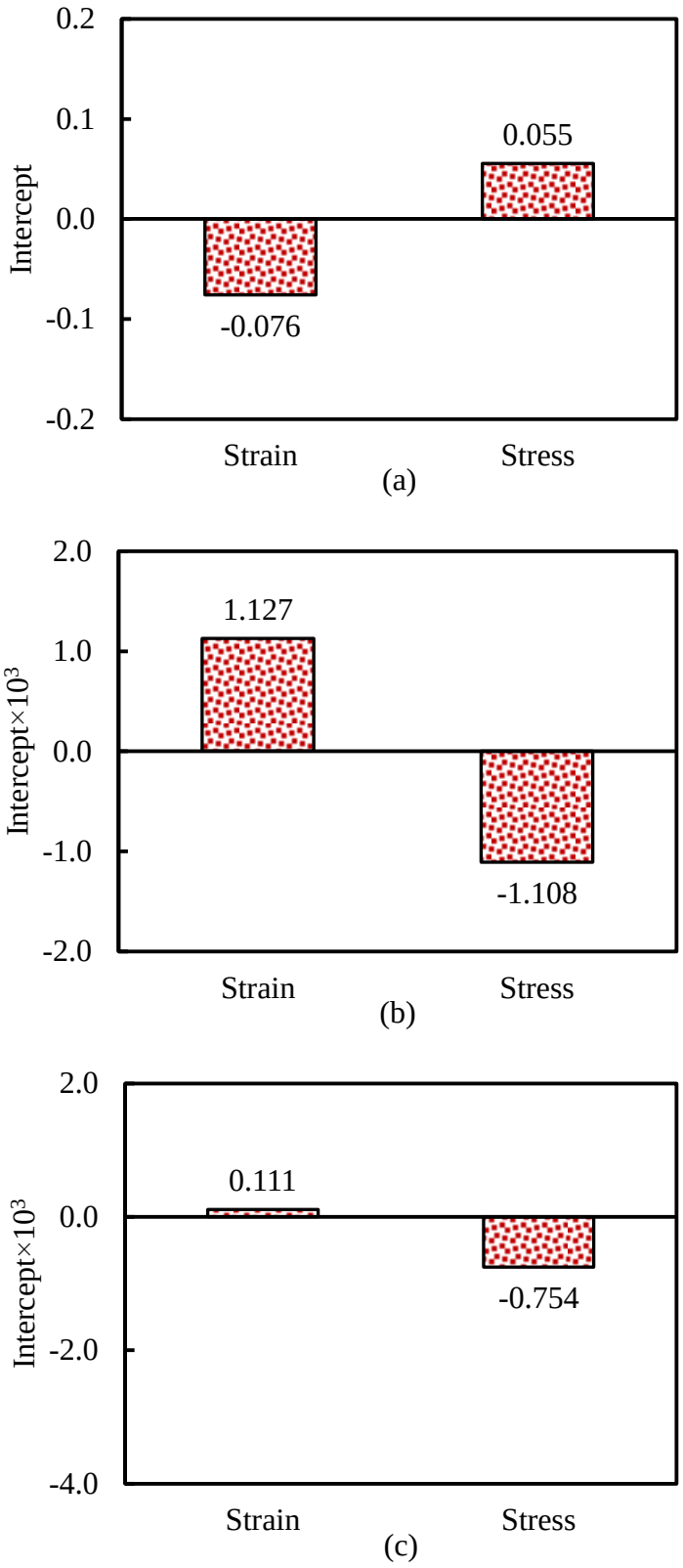

Figure 5- 14: Intercept of ANN models for different approaches in strain and stress test modes: (a) FI^R, (b) N_f and (c) N_1.

The third bias parameter is the slope which is presented in Figure 5–15; the smallest prediction bias ANN model is the closest to unity slope. Despite, the slopes of all ANN models are in range 1.1 to 0.9 which is accepted value, but it can be seen that the stress test mode model is the smallest prediction bias than the strain mode for all approaches because the slope of stress models are close to unity than strain models as presented in Figure 5–15.

Overall, it is clear that the ANN models of stress test mode have a lower prediction bias than the ANN models of strain test mode which means more accurate.

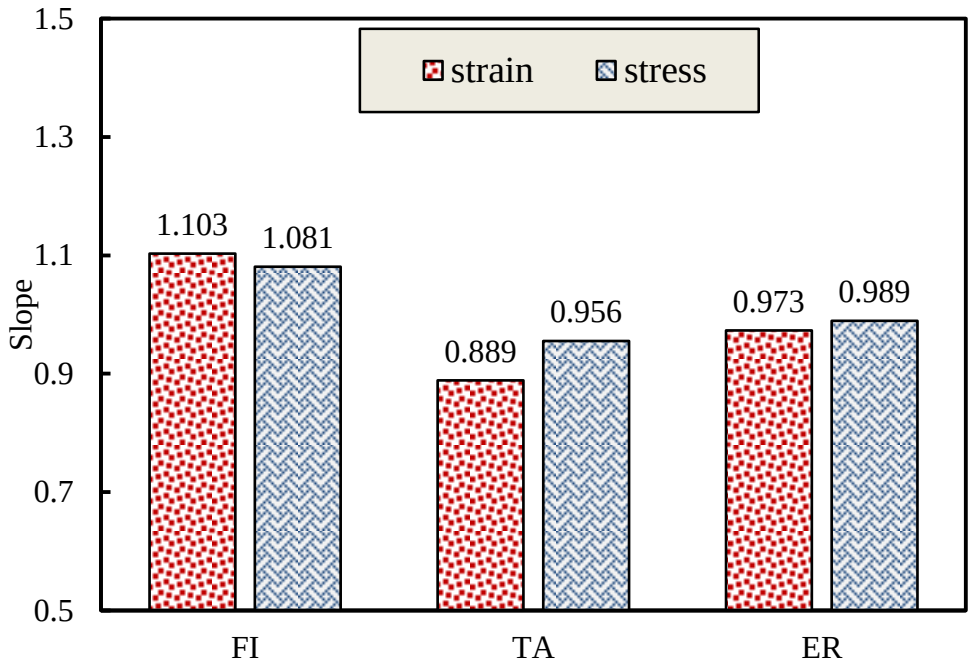

Figure 5- 15: Intercept of ANN models for different approaches in strain and stress test modes.

5.7.3.2. ANN models of Independent Test Modes

Herein, ANN models were developed irrespective to the test of modes, i.e. strain and stress, for FI^R and N_f approaches. Because of, the measurement unit of N_f approach is the number of cycles while FI^R without measurement unit, therefor the bias analyses were presented into two categories: N_f and FI^R for average error and intercept whereas the slope was dealt with N_f and FI^R at the same time.

Figure 5–16 exhibits the average error and intercept for N_f approach at 50% and 15% of initial stiffness modulus; noticeably, that the ANN models for N_f at 50% and 15% are over-predicting where the average error is positive. On the other hand, N_f at 50% model is also less bias than 15% model in terms of intercept as shown in Figure 5–16.

Figure 5–17 displays the average error and intercept for the ANN model of FI^R. It is clear, that the ANN model is under-predicting where the average error is negative despite its very small value. Also, it can be seen that the intercept is small value and approaches from the 0 but there is no model in the same class to make a comparison.

The slope of the three ANN models is presented in Figure 5–18; it can be seen that the ANN models of FI^R and N_f at 50% have the same bias because they have the same different (i.e. 0.04) then the slope of LQ (i.e. 1) as shown in Figure 5–18. In contrast, ANN model of N_f at 15% is the highest bias where it's slope the worst in compare with LQ.

Overall, it is clear that the ANN model of N_f at 50% is the smallest prediction bias than the the ANN models of FI^R and N_f at 15% models.

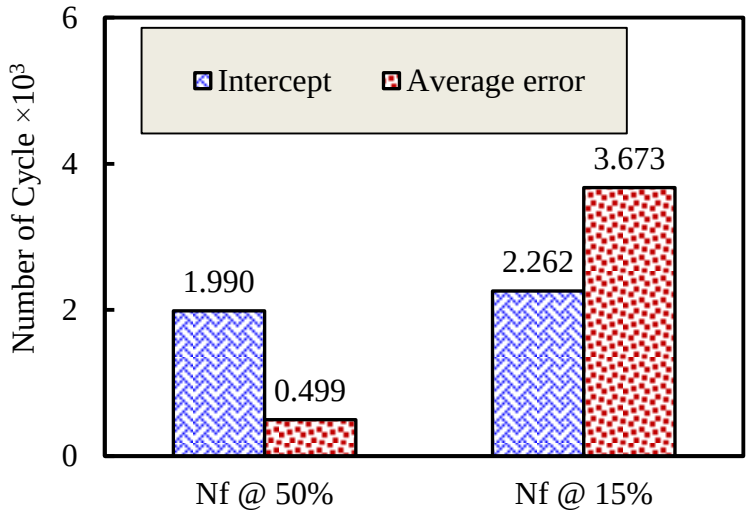

Figure 5- 16: Average error and intercept for ANN independent mode models for predicting fatigue performance at 50% and 15% of initial G*.

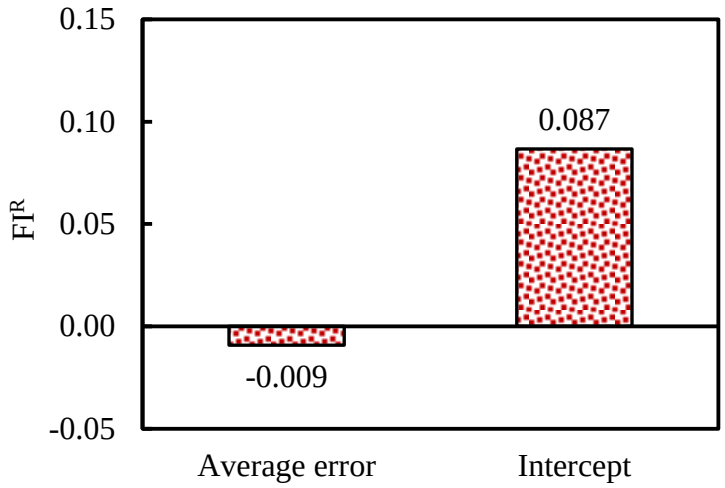

Figure 5- 17: Average error and intercept for ANN independent mode models for predicting FI^R.

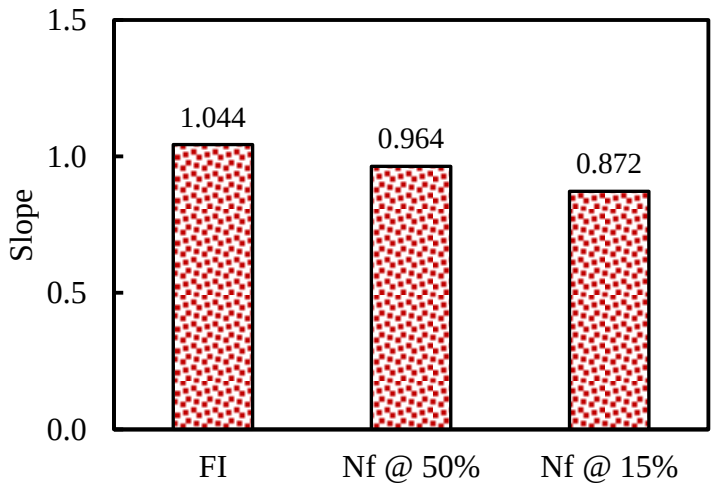

Figure 5- 18: Slope for ANN independent mode models for predicting fatigue performance as FI^R and number of cycles at 50% and 15% of initial G*.

5.8. Summary

The following outcomes were reached based on the results and discussions:

1. The ANN approach, as a new fatigue modelling method was used in this study to create an effective predictive model. The established ANN-based models were able to predict the fatigue life accurately, as evidenced by high R^2 values for the test set of data.

2. Experimental data from fatigue tests of cylindrical samples tested in DSR were used to train the neural networks to develop models for predicting the fatigue performance of HMA in terms of number of cycles (N_f and N_1) and FI^R. ANN models were based on parameters from fatigue tests (i.e. initial stiffness modulus, initial phase angle, shear strain amplitude, shear stress amplitude and relaxation test coefficients in addition to volumetric properties (i.e. bulk density and air voids)) of HMA to be the input variables for the ANN.
3. The first objective of neural networks was developing ANN models based on the fatigue test of modes (strain and stress) to predict fatigue performance. The results revealed a high correlation between predicted and actual data for all approaches (N_f, N_1 and FI^R) where the R^2 was about 0.9 to 0.99.
4. In the second objective, the ANN approach was used to develop models independent of test mode for predicting fatigue performance in terms of N_f at 50% and 15% of initial stiffness modulus and FI^R. The same parameters of fatigue testing and volumetric properties were also used as input parameters for training the neural networks. The results showed the capability of the ANN model to predict fatigue performance with high correlation regardless of test mode.
5. Bias analysis for all ANN models was evaluated based on the typical values of the line of equality because it is considered a perfect model, where average error and intercept are zero and the slope is unity. The analysis result stated that the ANN model for the stress test mode is a lower prediction bias than the ANN models of strain test mode; while in the independent test mode models, the ANN model of N_f at 50% is the smallest prediction bias than the ANN models of FI^R and N_f at 15%.
6. The ideal architecture of ANN models was determined after investigating several architectures containing one to two hidden layers with 10, 15 and 20 neurons in each hidden layer. The best ANN model was two hidden layers with 15 neurons based on the high determination coefficient (R^2) between the actual and predicted data.

CHAPTER VI

CHAPTER VI

6. A Simple Fracture Model for Evaluating and Predicting Fatigue Performance

6.1. Introduction

Crack growth due to fatigue brought on by repeated loading has been recognized as an important problem in asphalt pavements. Fatigue cracking models have used several approaches to describe the performance of asphalt concrete; generally these approaches can be classified into the following groups: the phenomenological approach, the energy-based approach and mechanistic approaches such as continuum damage and fracture mechanics approaches. In studies taking the phenomenological approach, tensile stress or strain were correlated with the number of load repetitions to failure (Pell, 1962;Monismith et al., 1961). In the energy approach, fatigue performance was characterised through a regression model of the relationship between dissipated energy and number of loadings to failure (Van Dijk and Visser, 1975;Tayebali et al., 1992;Ghuzlan and Carpenter, 2000;Ghuzlan and Carpenter, 2006). These models are simple and the regression was based on experimental data, which were used to determine the regression coefficients. These regression coefficients are therefore limited by the test conditions and material properties: if there is any change in these parameters, the coefficients need to be updated according to the changed conditions. The models used in mechanistic approaches are more complicated than those for the phenomenological and energy approaches, as differential equations and experimental results are matched together to develop a model to describe fatigue performance. In addition, non-traditional variables are used to characterise fatigue performance, such as damage density, internal damage, cracking radius, etc., rather than the traditional variables such as number of loadings, stiffness modulus and phase angle.

6.2. Mechanistic Models

Two main mechanistic models have been examined in detail: the continuum damage and fracture mechanics. The continuum damage mechanics has been used widely by researchers in evaluating the fatigue performance of viscoelastic materials. This model was based on Schapery's work on crack growth in viscoelastic media (Schapery, 1984) and was developed by Lee and Kim (Kim et al., 1997;Lee et al., 2000;Park et al., 1996) to characterise the asphalt damage caused by fatigue. In this model, a viscoelastic problem is transformed to an elastic case by replacing strain with pseudo-strain. The damage is quantified by a non-dimensional internal state variable (*S*), and this variable represents an indicator of the change in the pseudo-stiffness modulus (*C*).

The fracture mechanics model is based on the well-known Paris law (Paris and Erdogan, 1963) Equation 2–14, and detailed in 2.4.3. Basically, Paris' law was developed based on the analysis of propagation of a single crack in homogenous materials, which were metallic specimens. This represents a major problem when studying crack growth in non-homogeneous and viscoelastic materials such as hot mix asphalt (HMA) as numerous cracks appear in the specimens under repeated loading conditions (Mull et al., 2002;Walubita et al., 2006;Mun and Lee, 2010). A modification based on Schapery's work (1984) was made to Paris' law by replacing the K parameter with J-integral, as shown in Equation 6–1.

$$\frac{d\alpha}{dN} = AJ^n \qquad (6–1)$$

where: A and n are constants which depend on the material and the test conditions; J-integral is derived from dissipated pseudo-strain energy, and can be defined as the rate of change of loading dissipated pseudo-strain energy per unit of mean crack growth area. This modification enhanced the model in describing the fracture resistance of asphalt mixtures (Mull et al., 2002;Rice, 1986;Mun and Lee, 2010;Walubita et al., 2006).

Various researchers have used a modified Paris law (Equation 6–1) to develop new models. For example, a model was developed based on the modified Paris

law using the *J*-integral (Si et al., 2002). This model is detailed in Equation 6–2.

$$N_i = \frac{\frac{n+1}{2n+1} {C_R}^{2n+\frac{1}{n+1}}}{A^{1/n}\left(\frac{b}{4\pi}\right)^{\frac{n}{n+1}}} \quad (6–2)$$

where N_i is the i^{th} number of cycles, C_R is the crack radius in mm, A and b are constants and n is a parameter that depends on the relaxation coefficient.

Si *et al.*(2002) used this model (Eq. 6–2) in evaluating fatigue life in terms of the number of cycles required to create a crack of radius 7.5 mm in cylindrical samples (100 mm diameter and 150 mm height) prepared from four different mixes and tested in a strain controlled mode under repeated cyclic uniaxial loads. The model was based on the assumption that the micro-crack is circular in shape with a mean radius, and is used to calculate the number of loadings necessary to create a selected crack radius. Basically, under repeated loading damage growth increases due to the creation of more micro-cracks; however, it is practically impossible to measure the cracking radius because the crack always creates new surfaces with increase in the crack mouth opening displacement.

Masad *et al*. (2008) derived a model based on the modified Paris law to evaluate the fracture performance of cylindrical samples (12 mm diameter and 50 mm height) prepared from fine aggregate matrix (FAM) and fatigue tested under stress and strain test modes using a Dynamic Shear Rheometer (DSR). This model is more sophisticated than the previous one, as a parameter related to the adhesive bond energy was included to calculate the fracture radius, as shown in Equation 6–3.

$$\Delta R = \left[\left(\frac{2n+1}{nb+1}\right)^{n+1}\left(\frac{G_R bc}{4\pi G_1 \Delta G_f}\right)^{n} N^{nb+1}\right]^{\frac{1}{2n+1}} \quad (6–3)$$

where: ΔR is the fracture radius; b and c are regression coefficients for dissipated pseudo-strain energy vs N (number of cycles); G_R is the reference modulus; G_1 is the relaxation coefficient; ΔG_f is the adhesive bond energy; and n is constant materials (Equation 6–2). Parameter (n) as a function was predicted from a simple

test such as relaxation test based on Schapery's work for crack growth in viscoelastic materials (Schapery, 1975;Schapery, 1978;Schapery, 1984).

The development of this model was based on the same concept of the crack radius, which again represents a weak point for the same reasons as stated in the previous model. Another flaw in the model is that all the cracks that are proposed to occur in the sample under loading are represented by an equivalent crack with equivalent radius. However, ΔR was used as a crack growth index in evaluating the fatigue performance for different FAM mixes, and the variation in the results was at least comparable with other approaches, e.g. number of cycles at failure and cumulative dissipated energy (Masad et al., 2008a). Also, the results of the crack growth index were found to be consistent with field observations and independent of the fatigue test mode (Bhasin et al., 2008).

A concept by Kachanov (1958) called damage density was introduced as method of evaluation in continuum damage mechanics based on effective stress as shown in Equation 6–4.

$$\hat{\sigma}_{ij} = \frac{\sigma_{ij}}{1-\emptyset} \qquad (6\text{–}4)$$

where Ø is damage density (micro-cracks and micro voids per unit area); $\hat{\sigma}$ is the undamaged stress, σ is the damaged stress.

Abu Al-Rub *et al.* (2010) and Darabi *et al.* (2012) developed a micro-damage healing constitutive model on the basis of continuum damage mechanics for predicting the nonlinear visco-elastic, visco-plastic, and visco-damage of HMA. Numerical algorithms were implemented into the well-known finite element code Abaqus to develop this model. The model was validated by comparing the predictions output with experimental data of HMA specimens tested in single and repeated creep-recovery at different loading times, temperatures and rest periods in both tension and compression. Basically, these models were developed on Kachanov's damage model and the concept of effective stress for damage density without healing in Equation 6–4 and with healing as shown in Equation 6–5.

$$\hat{\sigma}_{ij} = \frac{\sigma_{ij}}{1-\emptyset(1-h)} \qquad (6\text{–}5)$$

Where: *h* is the micro-damage healing.

These models were complicated; however, they succeeded to predict the nonlinear visco-elastic and visco-plastic deformations; and the predictability of model was better in the single creep-recovery than repeated creep-recovery in comparing with experimental results. Also, the calculations of the visco-damage density were logical, where, the damage without healing was higher than the damage with healing for both single and repeated creep recovery. However, these models need to apply on a real fatigue data to evaluate the damage response.

In further work on the damage density concept was also used to evaluate fracture damage in HMA and was incorporated into a model using modified Paris' law instead of using the crack length or crack radius as shown in Equation 6–6 (Xue Luo et al., 2013).

$$\emptyset = (ab)^{\frac{1-d}{b-d}} \left(\frac{2\theta}{cd}\right)^{\frac{1-d}{b-d}} \left(\frac{dc}{2\theta}\right)^{\frac{1}{n+1}} \left(\frac{n+1}{cn+1}\right) N^{\frac{dn+1}{n+1}} + \emptyset_o \qquad (6–6)$$

where: a, b, c, d are material constants; $\emptyset_0$ is the initial damage, i.e. air voids; and *n* depends on the relaxation coefficient and test mode.

The model was based on the so-called energy balance between the apparent measurement of the bulk asphalt mixture specimen and the true measurement of the intact material and crack surface area within the cross-section of the sample. The crack surface area (θ) was calculated using damage density multiplied by the cross-sectional area of the specimen. It is perhaps better to calculate the crack surface area for the matrix only because the aggregate is stronger than the matrix and damage or cracks will occur in the matrix. The matrix represents the FAM components within the full HMA as explained later.

Bearing this in mind, a simple fracture model was developed in this chapter using the modified Paris law and based on the fundamental parameters of fatigue testing and the damage density concept. This model has been used to characterise fracture performance without using crack radius and crack surface concepts. As well as, a model was developed based on this fracture model to be used in predicting fatigue life of HMA as detailed in the following sections.

6.3. Objectives of Study

This chapter aims to develop a simple fracture model based on the fundamental fatigue parameters represented by the dissipated pseudo-strain energy for matrix volume and the relaxation test. Damage density was used to simulate the internal fracture damage in HMA samples. This model was used to evaluate the fracture performance for the same mixes which were tested in fatigue as presented in detail in Chapters III and IV. Also, a fatigue life model was developed based on this fracture model to be used for predicting fatigue performance in terms of number of cycles for HMA tested in DSR instrument.

6.4. Basic Concepts of Fracture Model

6.4.1. Energy calculations

During repetitive loading tests, two kinds of energy are created: applied energy and recovered energy. The difference between these two energies indicates the damage in material, as there is a net loss of energy due to heat generation or damage in the form of crack generation, which prevents the material from returning to its original state. This loss in energy is called dissipated energy, and it can be calculated by the area inside the hysteresis loop for each loading cycle (Daniel et al., 2004;Ghuzlan and Carpenter, 2006).

To calculate the dissipated pseudo strain energy (W_D^R), the difference between the applied pseudo-strain energy (W_A^R) and recovered pseudo-strain energy (W_R^R) was calculated as shown in the formula below.

$$W_D^R = W_A^R - W_R^R \quad (6–7)$$

where: (W_A^R) is applied pseudo-strain energy and (W_R^R) recovered pseudo-strain energy. It is worth noting, W_A^R and W_R^R are calculated using Equations 3–11 and 3–12 as detailed in Chapter III.

6.4.2. Fracture model

In this study, modified Paris' law (Equation 6–1) was adopted because it is more efficient for nonlinear fracture mechanics analysis of materials such as HMA (Mull et al., 2002;Rice, 1986;Mun and Lee, 2010;Walubita et al., 2006). Also, damage density (Ø) was used for the simulation of the internal damage as crack growth in materials. Equation 6–8 was adopted for this purpose. Equation 6–8 accounts for the cumulative damage density in materials under repeated loading where the damage starts from $Ø_o$, i.e. initial damage, which is represented by the air voids and increases in rate $\dot{\emptyset} = \frac{d\emptyset}{dN}$ Therefore, the damage rate can be written as shown in Equation 6–9.

$$\emptyset = \emptyset_o + \dot{\emptyset}N \tag{6–8}$$

$$\dot{\emptyset} = \frac{\emptyset - \emptyset_o}{N} \tag{6–9}$$

Damage accumulates as cracks occur within the matrix because it is weaker than aggregates and can be calculated as shown in Equation 6–10. The damage rate in materials is represented by a derivative of Equation 6–10 as shown in Equation 6–11.

$$D = \emptyset \times \alpha_v \tag{6–10}$$

$$\frac{dD}{dN} = \frac{d\emptyset}{dN}\alpha_v \tag{6–11}$$

where D is cumulative damage in a material and α_v is the matrix volume of the sample.

The pseudo J_R-integral in modified Paris' law represents the dissipated energy rate to damage rate in materials, and is calculated as shown in Equation 6–12.

$$J_R = \frac{\frac{dW_D^R}{dN}}{\frac{dD}{dN}} \tag{6–12}$$

The power law formula shown in Equation 6–13 was used to describe the relationship between cumulative dissipated pseudo-strain energy and number of

cycles; and the derivative of this equation represents the dissipated pseudo-strain energy per load cycle as shown in Equation 6–14.

$$W_{DC}^{R} = bN^{c} \tag{6–13}$$

$$\frac{dW_{DC}^{R}}{dN} = bcN^{c-1} \tag{6–14}$$

where W_{DC}^{R} is cumulative dissipated pseudo-strain energy; N is the number of cycles; and b and c are constant regression.

Substituting Equations 6–9, 6–11 and 6–14 into Equation 6–12 and combining with the modified Paris' law (Equation 6–1) yields:

$$\frac{\emptyset-\emptyset_{o}}{N} = \frac{A}{(\alpha_v)^{n}} \frac{(bc)^{n} N^{cn-n}}{\left(\frac{\emptyset-\emptyset_{o}}{N}\right)^{n}} \tag{6–15}$$

Simplifying and rewrite equation 6–15 produces:

$$\frac{\emptyset_{N}-\emptyset_{o}}{A^{\frac{1}{n+1}}} = \left(\frac{bc}{\alpha_v}\right)^{\frac{n}{n+1}} (N_i)^{\frac{cn+1}{n+1}} \tag{6–16}$$

Equation 6–16 represents the fracture index (FI_c), so the final model is in the following formula:

$$\mathrm{FI}_{c} = \left(\frac{bc}{\alpha_v}\right)^{\frac{n}{n+1}} (N_i)^{\frac{cn+1}{n+1}} \tag{6–17}$$

where $n = 1/m$ (controlled strain); $n = 1 + (1/m)$ for controlled stress; and m is the exponent of time in the power law equation of the relaxation modulus based on Schapery's works for crack propagation in viscoelastic media (Lee and Kim, 1998;Masad et al., 2008a).

6.5. Materials and Experimental Work

Experimental work includes performing relaxation test and fatigue test using the DSR on cylindrical samples of 12 mm in diameter and 50 mm in height prepared from HMA. More details on the materials and experimental work are available in Chapters III and IV.

6.6. Results and Discussion

6.6.1. Relaxation Test

The relaxation modulus is the ratio of stress response to constant strain input. This test was carried out to determine the relaxation moduli as a function of time according to the power law formula $G(t) = G_\infty + G_1 t^{-m}$ to determine the linear viscoelastic properties represented by the parameters: G_1 and m.

According to the criteria that were adopted in the Chapter III and IV, cylindrical samples were selected to be used in relaxation and fatigue tests. Relaxation testing was performed at low shear strain amplitude of 0.002% within the linear viscoelastic region, and test duration of 140 s; more details for the DSR sequence of relaxation test is presented in Appendix B-5. Atypical relaxation moduli against time for different mixes are shown in Figures 6–1 and 6–2. Table 6–1 presents the regression coefficients of the relaxation test, which have been fitted using the power law model for the samples that were tested later in fatigue under strain and stress test modes. It is clear from the high R-square values that there is a good correlation between the experimental and fitted data.

Table 6– 1: A typical relaxation coefficients of relaxation moduli test.

Mix ID	Controlled strain		
	Relaxation coefficients		R^2
	G_1	m	
DBM-G	51235812	–0.513	0.935
DBM-L	31923580	–0.525	0.908
HRA-G	773280068	–0.509	0.976
HRA-L	327954621	–0.523	0.959
Mix ID	Controlled Stress		
	Relaxation coefficients		R^2
	G_1	m	
DBM-G	70958608	–0.559	0.936
DBM-L	55629776	–0.661	0.915
HRA-G	649562520	–0.797	0.978
HRA-L	452975126	–0.616	0.942

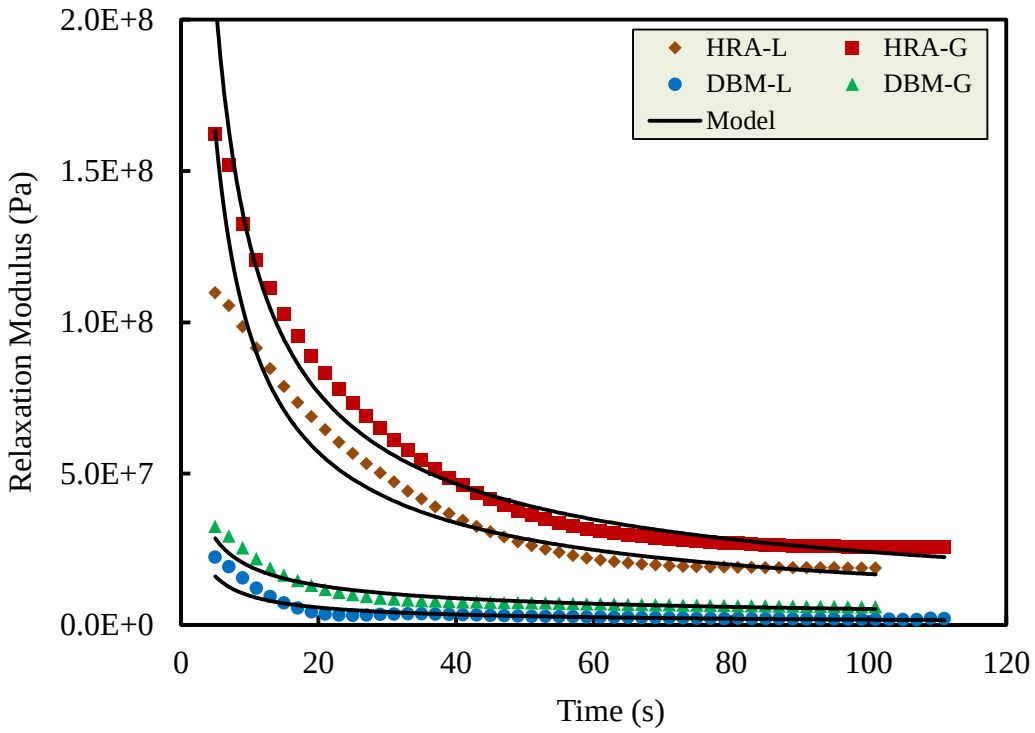

Figure 6- 1 A typical relaxation modulus against time for DSR samples will be tested in fatigue under controlled stress mode.

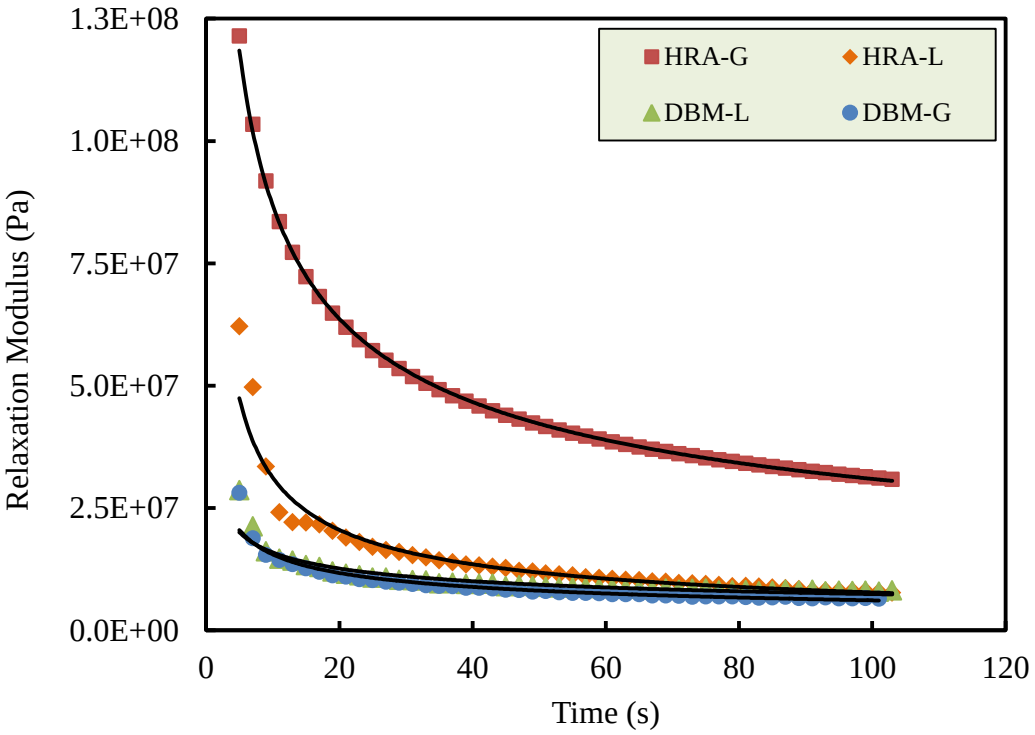

Figure 6- 2: A typical relaxation modulus against time for DSR samples will be tested in fatigue under controlled strain mode.

6.6.2. Dissipated Pseudo-strain Energy

The same samples that were tested for relaxation were also used for fatigue testing in strain and stress modes after giving them a rest time of about 15 min to remove any initial damage caused by the relaxation test (Branco, 2008). Test conditions are presented in Chapters III and IV. Fatigue testing provides the necessary variable values, e.g. shear stress, shear strain and phase angle, to be used for calculating W_A^R, W_R^R and W_D^R, using Equations 3–11, 3–12 and 6–7.

The cumulative dissipated pseudo-strain energy (DPSE) was divided by the matrix volume to calculate the DPSE per unit volume (DPSEv) of the damaged part of the mix, because cracks predominantly occur in the matrix which is weaker than aggregates. The matrix represents the volume of fine aggregates passing through a 2.36-mm sieve, filler and binder; these components were calculated depending on the volumetric properties of the HMA. Then, DPSEv was fitted using Equation 6–13 as a function of number of load cycles. Table 6–2 shows a set of data for the fitted results of DPSE for both test modes, and it can be seen that the results obtained using the power formula are of good quality as confirmed by the high R^2 values in the table.

A typical relationship between cumulative DPSE and number of cycles is presented in Figure 6–3 for both experimental and modelling results using the power model for DBM-L samples tested in strain and stress controlled modes respectively. Clearly, a high correlation is existed between modelling and experimental results; however the power model of stress mode does not capable for modelling the DPSE at the end of fatigue life as shown in Figure 6-3; and this defect has an effect on the accuracy of the developed fatigue model as well be seen later.

Figure 6–4 demonstrates the relationship between cumulative DPSE and number of cycles for the strain test mode. Obviously, the rate of cumulative DPSE for DBM-G and HRA-G is higher than for DBM-L and HRA-L because the fatigue life of limestone mixes is longer than that of the granite mixes; consequently the

cumulative DPSE is distributed over a longer period in limestone mixes than granite mixes.

Table 6– 2: Power law fitting parameters from Eqn. 6-13 for different mixes.

Mix ID	Controlled strain		R^2	Controlled stress		R^2
	b	*c*		*b*	*c*	
DBM-G	0.0817	0.307	0.961	0.0125	0.453	0.968
DBM-L	0.109	0.265	0.930	0.043	0.368	0.959
HRA-G	0.117	0.308	0.949	0.00924	0.414	0.989
HRA-L	0.0791	0.288	0.976	0.00562	0.381	0.979

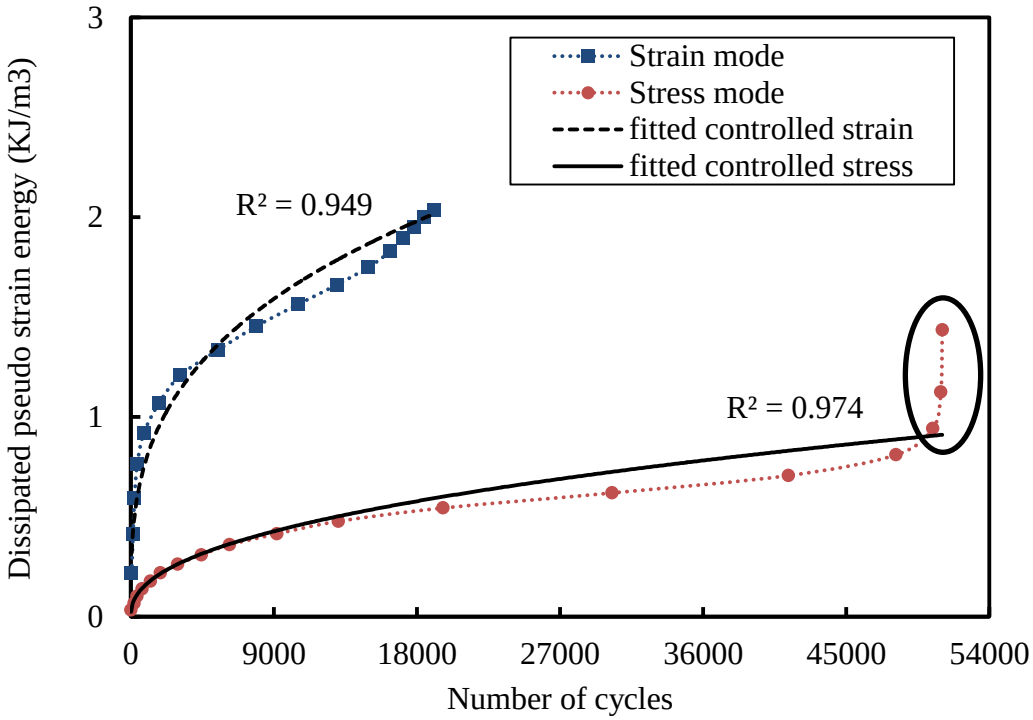

Figure 6- 3: A typical dissipated pseudo-strain energy against number of cycles for HRA-G sample tested in strain and stress controlled modes.

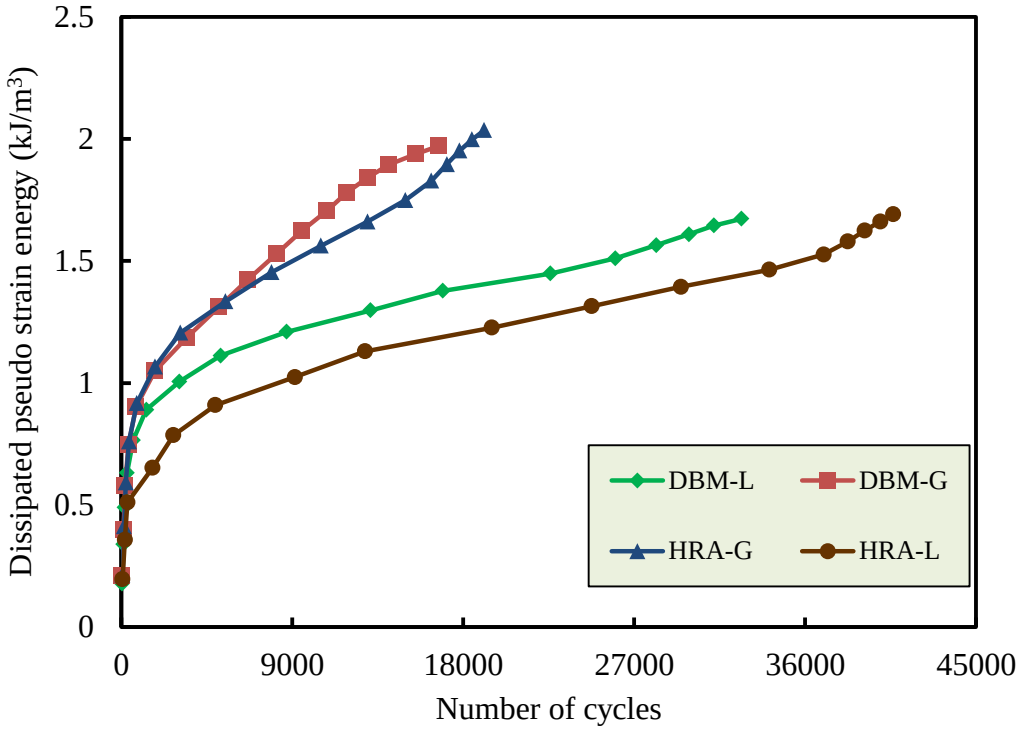

Figure 6- 4: Dissipated pseudo-strain energy against number of cycles for different mixes tested in strain mode.

The relationship between cumulative DPSE and number of cycles for the stress test mode is presented in Figure 6–5. It is notable that the rate of cumulative DPSE for DBM mixes are faster than for HRA mixes because the fatigue life for DBM mixes is shorter than for HRA mixes. Also, the DPSE increases sharply at the end of life because in stress mode, shear strain response increases with load repetitions, thus the energy increases according to the strain response.

Figure 6–6 was derived from Figures 6–4 and 6–5, wherein the ratio of cumulative DPSE to the number of cycles was calculated at 50% and 10% of the normalised shear modulus for the strain and stress test modes, respectively; in other words, using the traditional approach. This was to evaluate the rate of change in the DPSE with number of cycles. The conclusion was that higher DPSE/N values indicate quicker onset of damage and shorter fatigue life as demonstrated in Figure 6–6.

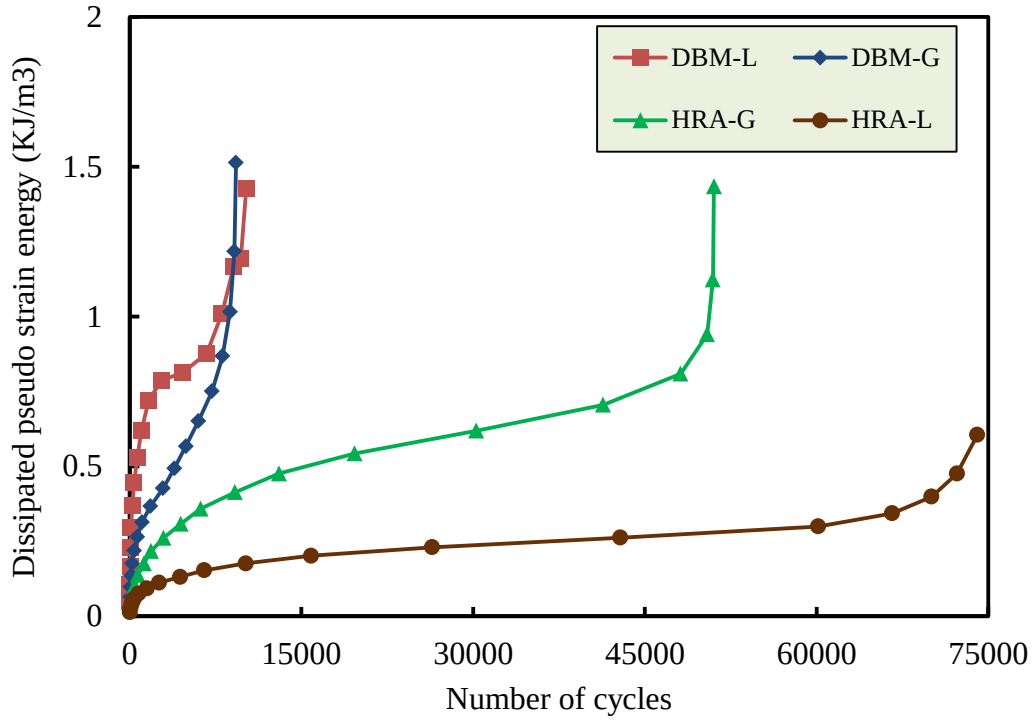

Figure 6- 5: Dissipated pseudo-strain energy against number of cycles for different mixes tested in stress mode.

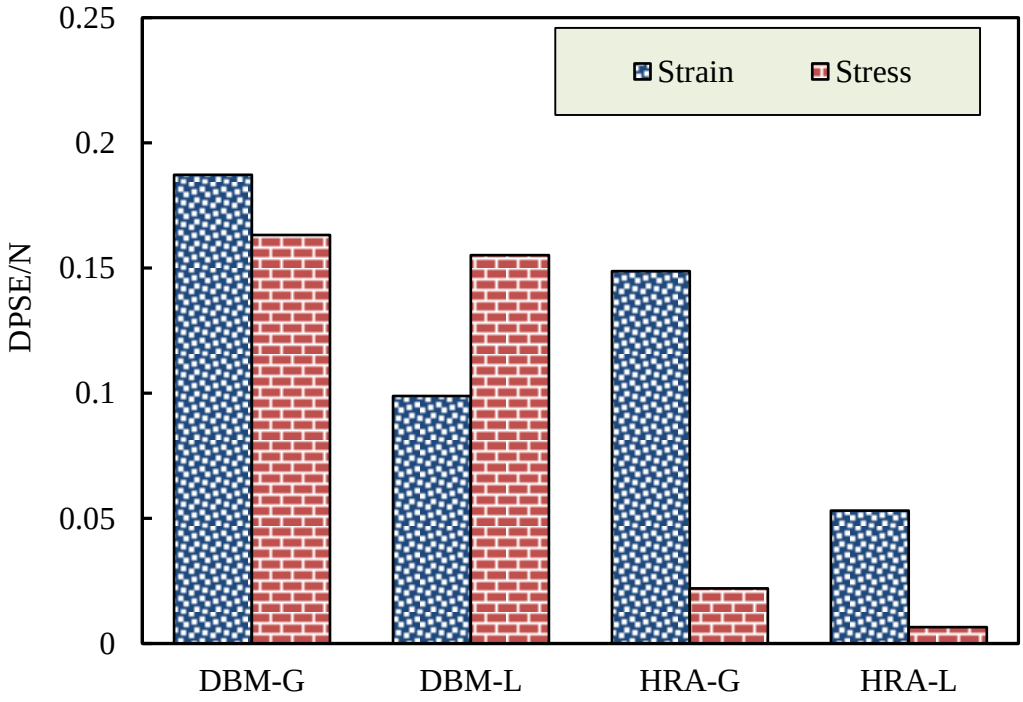

Figure 6- 6: DPSE/N ratio at traditional approach for different mixes tested in strain and stress test modes.

6.6.3. Fracture Damage

In order to demonstrate the changes in FI_c at different normalised stiffness moduli, FI_c was calculated using Equation 6–17 at a number of cycles equivalent to 50% and 15% of the initial stiffness modulus in strain test mode and 50% and 10% of the initial stiffness modulus in stress test mode. On the other hand, the fatigue performance was evaluated as a number of cycles at the same normalised stiffness modulus to present a comparison between the results.

Figure 6-7 shows the FI_C results for the mixes tested in strain mode; FI_c increases as the normalised stiffness modulus decreases for each mix; this indicates that the fracture damage increases as the fatigue testing progresses. It can be seen that an agreement is available in the order ranking for the mixes between the FI_c and number of cycles, as presented in Figures 6-7 and 6-8, where the higher FI_c values display lower fatigue performance as a number of cycles.

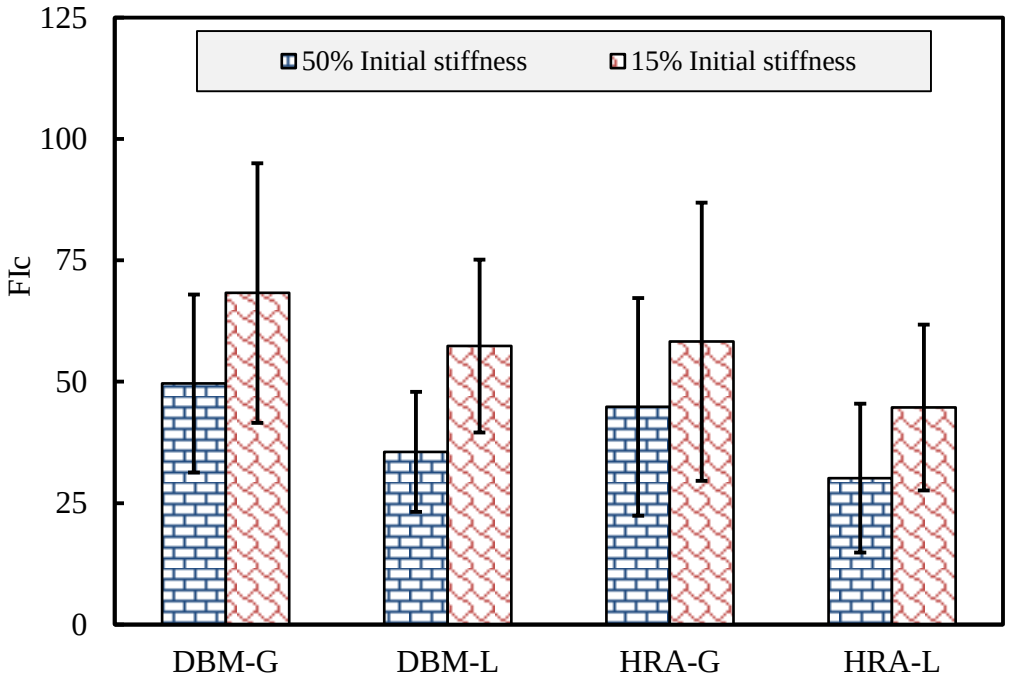

Figure 6-7: FI_C at different normalised stiffness modulus for different mixes tested in strain mode.

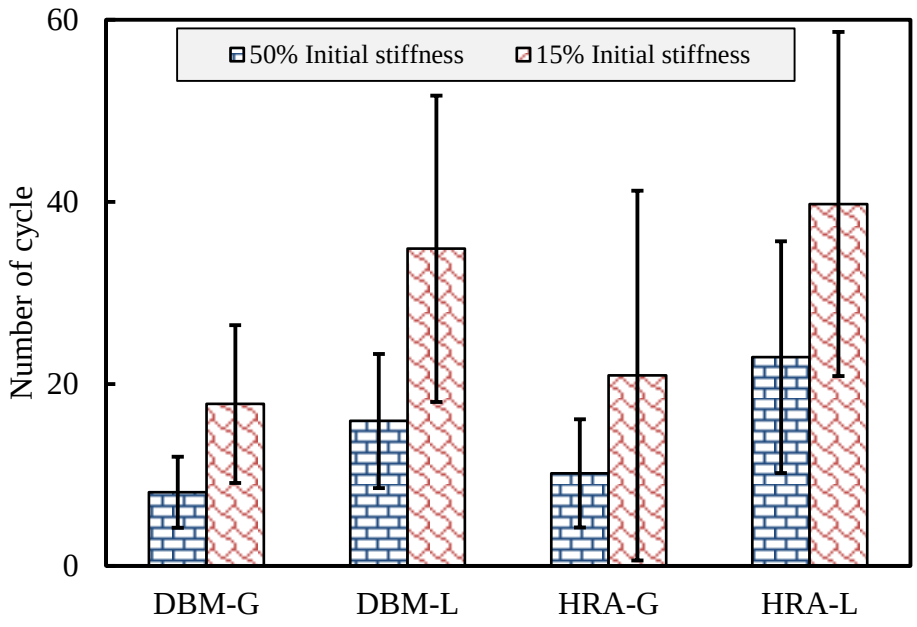

Figure 6- 8: Number of cycles at different normalised stiffness modulus for different mixes tested in strain mode.

Figures 6-9 and 6-10 present the outcomes for the stress test mode; also, it is clear that the FI_c trend was the same as in the strain mode, where FI_c increases as normalised stiffness decreases in all mixes. On the other hand, there is compatibility between the FI_c and fatigue life in a number of cycles, where a high FI_c results in a lower fatigue life, as presented in Figures 6-9 and 6-10. In both test modes, limestone mixes display better performance than granite mixes, and this is clear for both FI_c and number of cycles. Remarkably, FI_c revealed lower variation than number of cycles, as shown by the error bars, i.e. standard deviation, in Figures 6.7 to 6.10, which show significant differences between them. It is also noteworthy that the FI_c value for the stress test mode is higher than that for the strain test mode. This is due to the nature of the model itself; in other words, the *n* value. The *n* value in the strain test mode, $n = 1/m$, is lower than in the stress test mode, $n = 1 + 1/m$.

These outcomes emphasise the conclusions presented in Chapter III where DSR was used in fatigue testing, which alluded that limestone mixes in both DBM and HRA had better fatigue performance than granite, as demonstrated through the results of FI^R, TA and ER approaches. Additionally, they are compatible with the

DPSE/N results discussed in the previous section. Thus, FIc can be used in evaluating the fatigue performance based on fracture mechanics and is also reliable and has less variation.

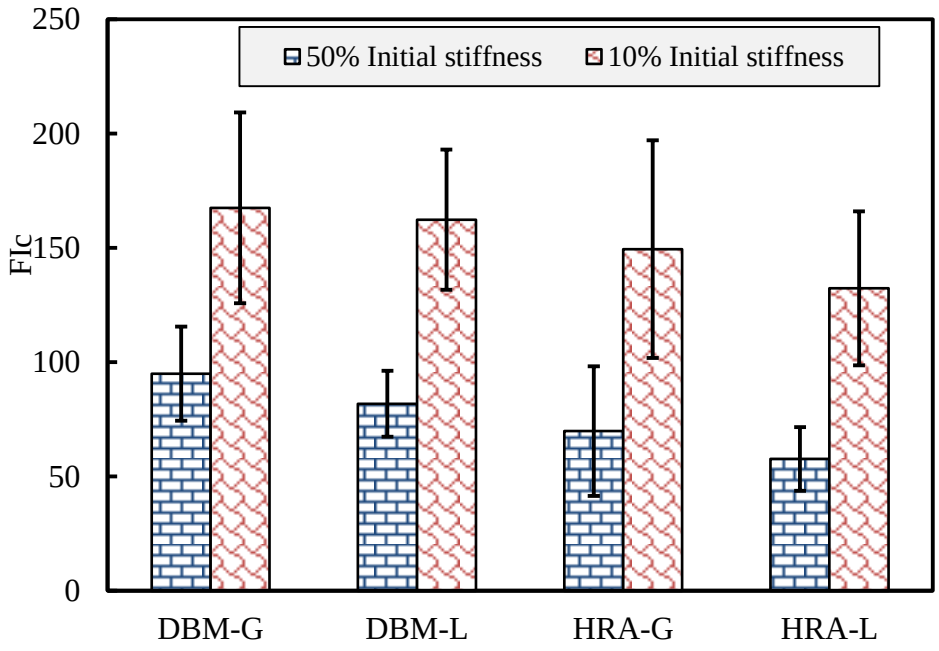

Figure 6-9: FI_C at different normalised stiffness modulus for different mixes tested in stress mode.

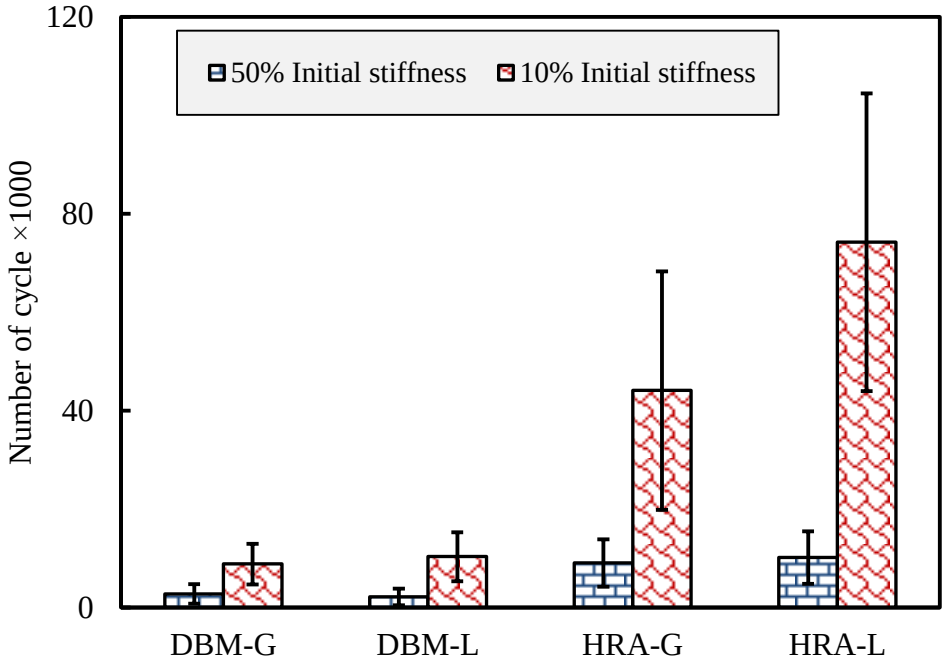

Figure 6-10: Number of cycles at different normalised stiffness modulus for different mixes tested in stress mode.

6.7. Predicting Fatigue Performance

In the next section, a model is developed to predict the fatigue performance in terms of a number of cycles, where the simple fracture model (Equation 6–17) in the previous section is the base for developing this model.

6.7.1. FI_c versus Normalised Stiffness Modulus

The normalised stiffness modulus (C_N) represents the ratio of the initial stiffness modulus to the stiffness modulus at number (i), as shown in Equation 6–18.

$$C_N = \frac{G_i^*}{G_o^*} \tag{6–18}$$

where: G_o^* is initial stiffness and G_i^* is stiffness modulus at number of cycles, i.

As detailed in Equation 6–17, FI_c is a function of number of cycles in addition to other factors derived from energy and relaxation. To enlist this model for use in predicting fatigue performance, a correlation between C_N and FI_c should exist; and Figures 6-7 and 6-9 have revealed this fact. Several mathematical models were examined to find the best formula that can be used for correlating the FI_c with the C_N. The formula in Equation 6–19 was the best one which gave a high correlation between FI_C and C_N, as evaluated from the high R^2 values and presented in Figures 6-11 to 6-14.

$$FI_c = \frac{1}{A + e^{(C_N)^B}} \tag{6–19}$$

where: A and B are regression coefficients of the model.

Substituting Equation 6–19 into Equation 6–17 yields Equation 6–20.

$$N_i = \left[\left(\frac{bc}{\alpha_v} \right)^{\frac{n}{n+1}} \left(A + e^{(C_N)^B} \right) \right]^{-\frac{n+1}{cn+1}} \tag{6–20}$$

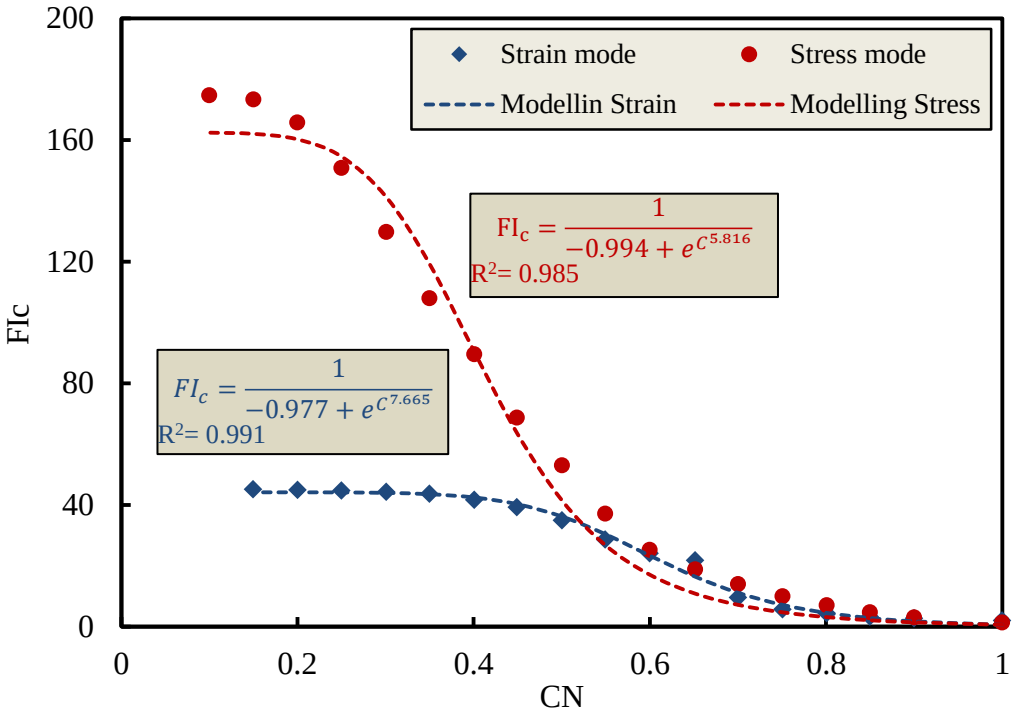

Figure 6- 11: A typical relationship between FI_c and C_N of HRA-L samples tested in strain and stress modes.

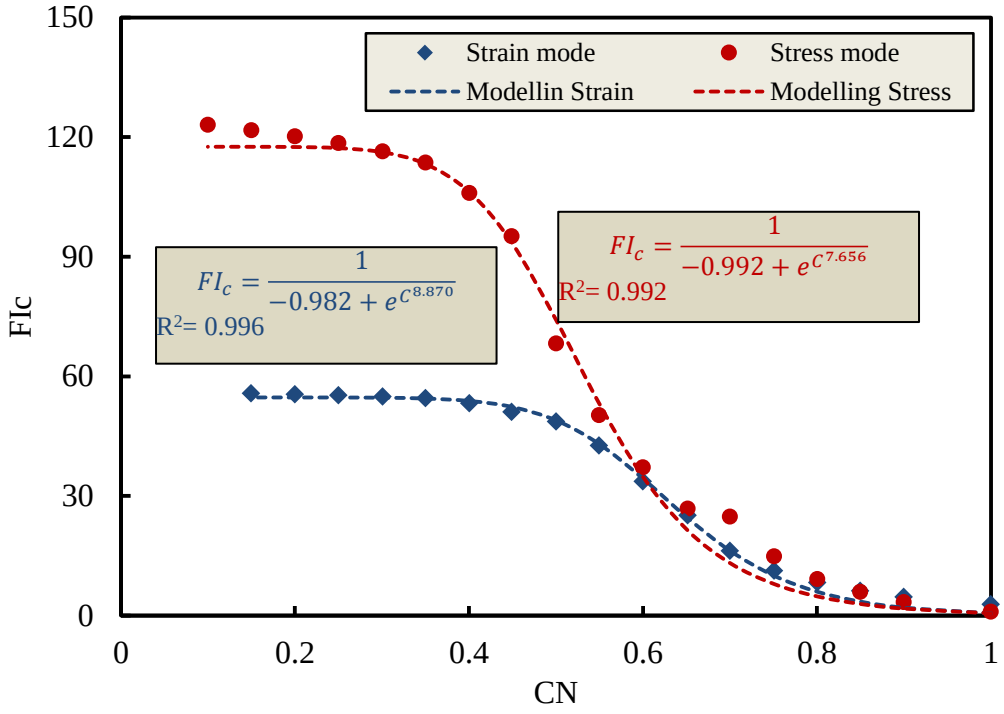

Figure 6- 12: A typical relationship between FI_c and CN of HRA-G samples tested in strain and stress modes.

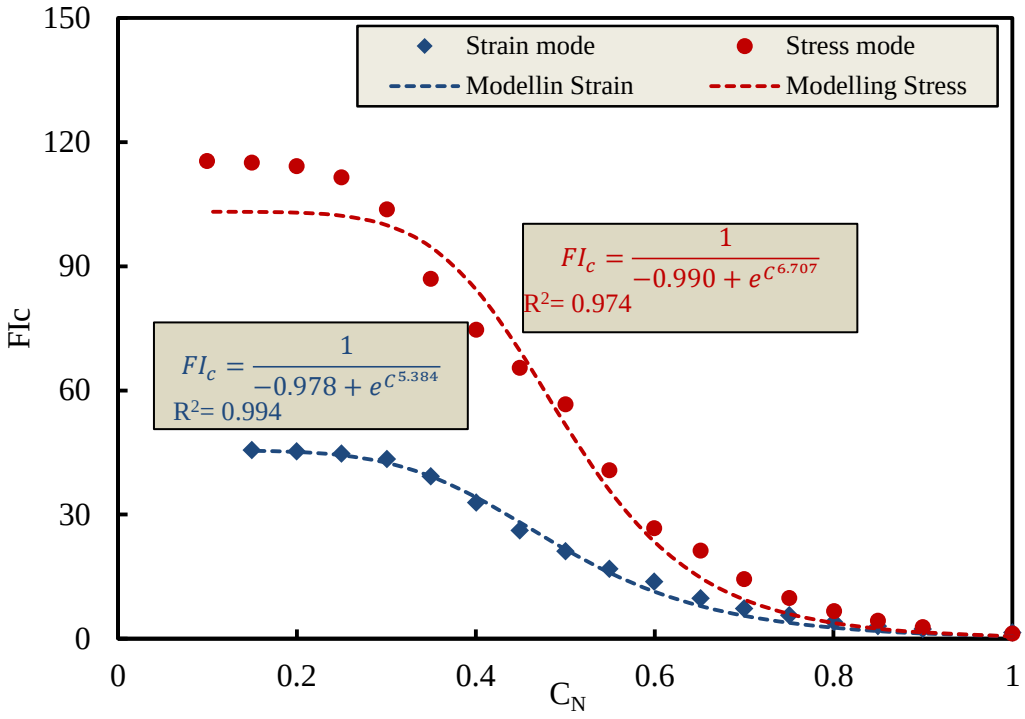

Figure 6- 13: A typical relationship between FI_c and C_N of DBM-G samples tested in strain and stress modes.

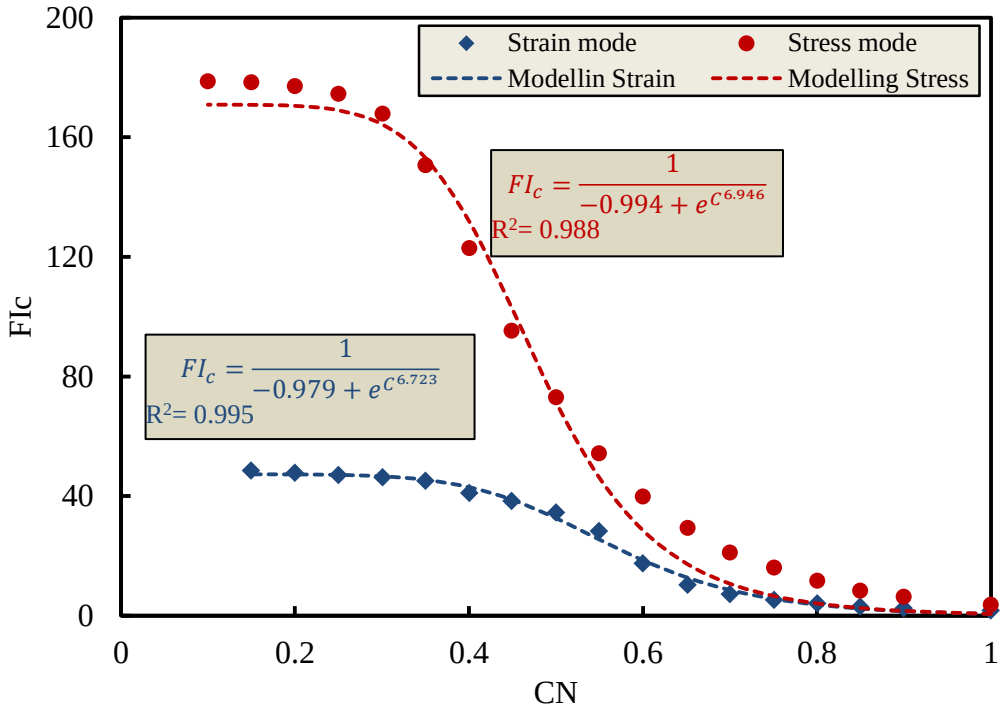

Figure 6- 14: A typical relationship between FI_c and CN of DBM-L samples tested in strain and stress modes.

Equation 6–20 is the general model for predicting the fatigue performance in terms of the number of cycles. This model is a function of normalised stiffness modulus (C_N) and its regression coefficients (A and B) and the properties of the tested samples represented by the relaxation and dissipation of energy regression coefficients (n, b and c). To make this model applicable, the coefficients (A, B, b and c) need to be defined using the properties of the mixes such as volumetric properties (i.e. air voids and bulk density) and mechanical properties such as initial stress, strain and phase angles.

6.7.2. Defining the Model's Parameters

6.7.2.1. Parameters A and B

A and B were correlated with several parameters selected from the fatigue test and volumetric properties in addition to relaxation coefficients (m and G_1). The results revealed there is a poor correlation between A and all these parameters, except for two parameters (m and n-1/n+1) where the correlation of A was higher than 0.9 in strain mode but was less in stress mode, as presented in the correlation matrix in Table 6-3. In addition, the correlation of B with all parameters was also poor, except for two parameters (m and n-1/n+1), but this correlation was not as strong as it was in parameter A, as shown in Table 6-3. According to the results in Table 6-3, parameter A was selected as a function of $(\frac{n-1}{n+1})$ and parameter B as a function of (m) due to the high R^2, as written in Equations 6–21 to 6–24 and plotted along with data obtained from experimental work for both test modes, as shown in Figures 6–15 and 6–16.

$$A_\gamma = -0.074\,(\frac{n-1}{n+1}) - 0.948 \quad (6–21)$$

$$A_\tau = -0.013\,\ln(\frac{n-1}{n+1}) - 1.004 \quad (6–22)$$

$$B_\gamma = -9.661\,m_1 + 12.090 \quad (6–23)$$

$$B_\tau = -2.616\,\ln(m_1) - 6.063 \quad (6–24)$$

where: A_γ and B_γ are parameters of the strain mode, and ; A_τ and B_τ are parameters of the stress mode.

Table 6– 3: Correlation matrix.

Strain mode									
R^2	A	B	G_o^*	δ_o	G_{bulk}	AV%	G_1	m	(n-1)/(n+1)
A	1.000	0.465	0.013	0.018	0.004	0.012	0.042	0.889	0.911
B	0.465	1.000	0.018	0.033	0.181	0.006	0.052	0.673	0.642
G_o^*	0.013	0.018	1.000	0.945	0.119	0.134	0.548	0.013	0.024
δ_o	0.018	0.033	0.945	1.000	0.118	0.216	0.471	0.011	0.019
G_{bulk}	0.004	0.181	0.119	0.118	1.000	0.031	0.006	0.042	0.014
AV%	0.012	0.006	0.134	0.216	0.031	1.000	0.088	0.061	0.048
G_1	0.042	0.052	0.548	0.471	0.006	0.088	1.000	0.257	0.242
m	0.889	0.673	0.013	0.011	0.042	0.061	0.257	1.000	0.949
(n-1)/(n+1)	0.911	0.642	0.024	0.019	0.014	0.048	0.242	0.949	1.000
Stress mode									
R^2	A	B	G_o^*	δ_o	G_{bulk}	AV%	G_1	m	(n-1)/(n+1)
A	1.000	0.481	0.041	0.078	0.051	0.006	0.235	0.673	0.713
B	0.481	1.000	0.053	0.127	0.026	0.106	0.199	0.667	0.641
G_o^*	0.041	0.053	1.000	0.751	0.319	0.064	0.190	0.035	0.035
δ_o	0.078	0.127	0.751	1.000	0.556	0.032	0.751	0.056	0.067
G_{bulk}	0.051	0.026	0.319	0.556	1.000	0.177	0.219	0.014	0.016
AV%	0.006	0.106	0.064	0.032	0.177	1.000	0.001	0.056	0.071
G_1	0.235	0.199	0.190	0.751	0.219	0.001	1.000	0.346	0.253
m	0.673	0.667	0.035	0.056	0.014	0.056	0.346	1.000	0.937
(n-1)/(n+1)	0.713	0.641	0.035	0.067	0.016	0.071	0.253	0.937	1.000

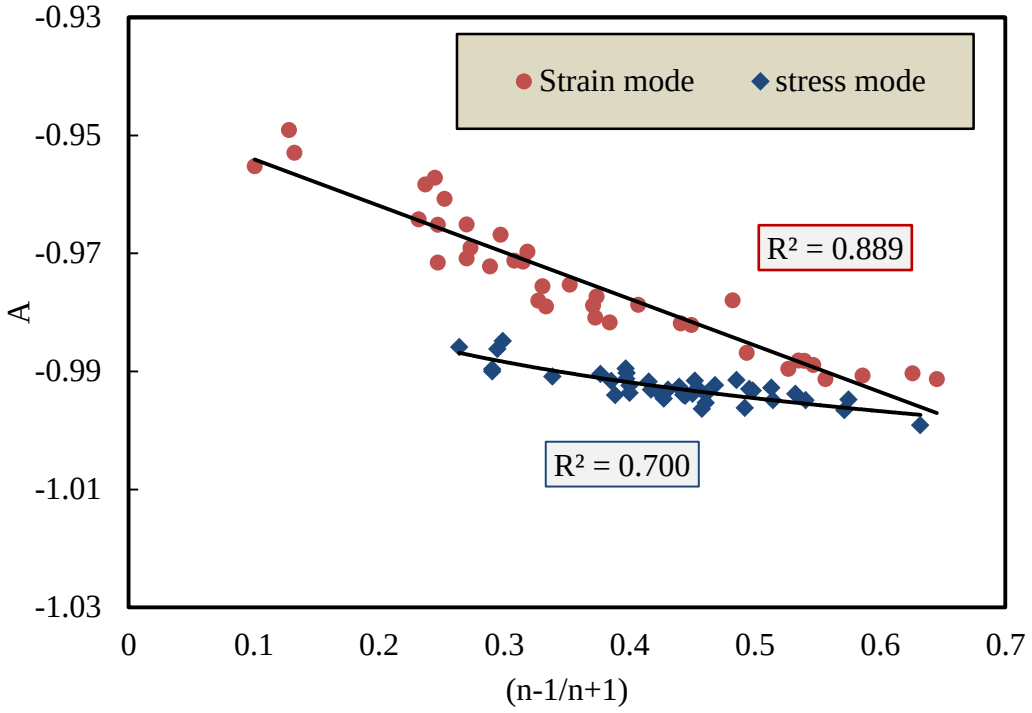

Figure 6- 15: Relationships between parameter (A) and (n-1)/(n+1).

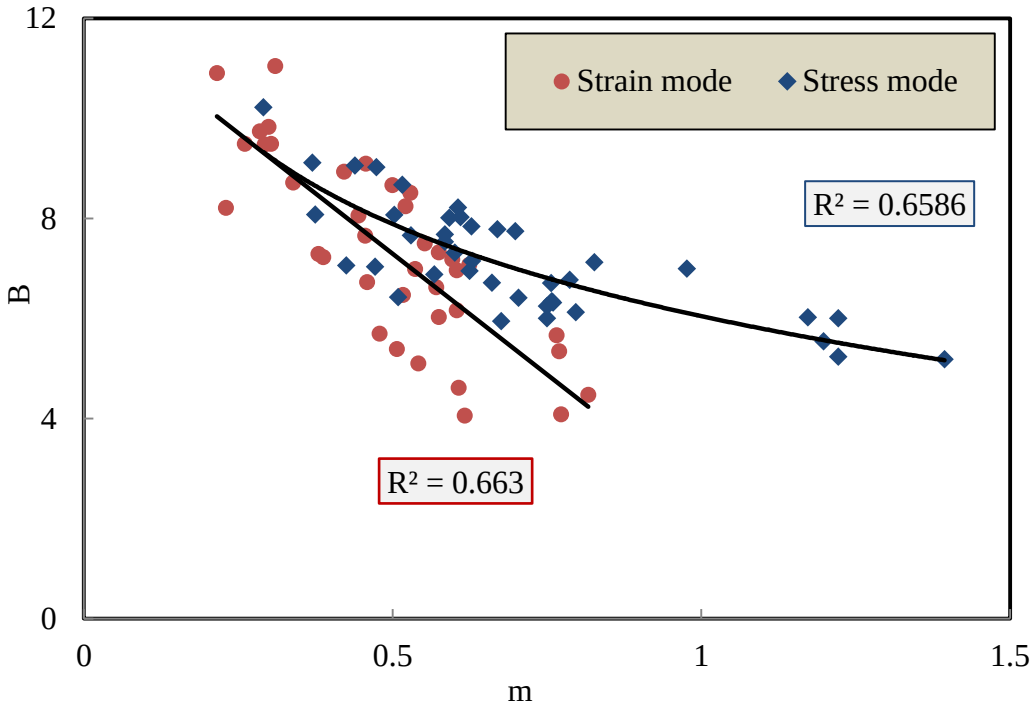

Figure 6- 16: Relationships between parameter (B) and (m).

6.7.2.2. Parameters b and c

The same variables that were used in correlation with parameters A and B were correlated here with the dissipated pseudo-strain energy parameters (b and c). The analysis results revealed that parameter (b) has the best correlation with the logarithm value of initial stiffness modulus ($\log G_o^*$) in strain mode, while in stress mode its best correlation was with the air voids, as presented in Figures 6–17 and 6–18 and shown in Equations 6–25 and 6–26. Meanwhile, parameter (c) has a good correlation with bulk density in controlled strain and initial stiffness modulus in stress test modes, as shown in Figures 6–19 and 6–20 and displayed in Equations 6–27 and 6–28.

$$b_\gamma = 140.328 \log(G_o^*) - 196.165 \quad (6–25)$$

$$b_\tau = 415.864 - 217.353 \ln(AV) \quad (6–26)$$

$$c_\gamma = 3373.529 G_b^{-10.926} \quad (6–27)$$

$$c_\tau = 0.515 e^{-1.080 \times 10^{-3} G_o^*} \quad (6–28)$$

where: b_γ and c_γ are parameters for strain mode; b_τ and c_τ are parameters for stress mode; G_b is bulk density; AV is air voids and G_o^* is initial stiffness modulus.

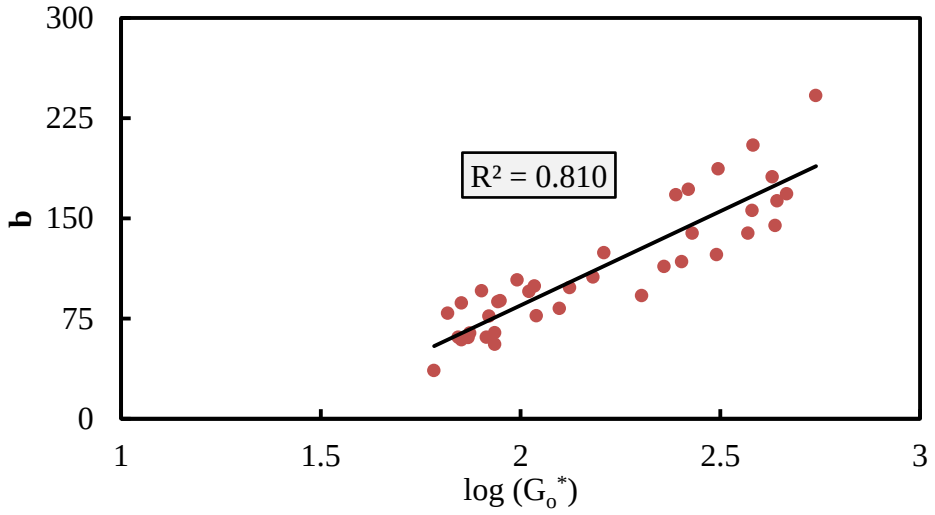

Figure 6-17: Relationship between parameter (b) and initial stiffness modulus for strain test mode.

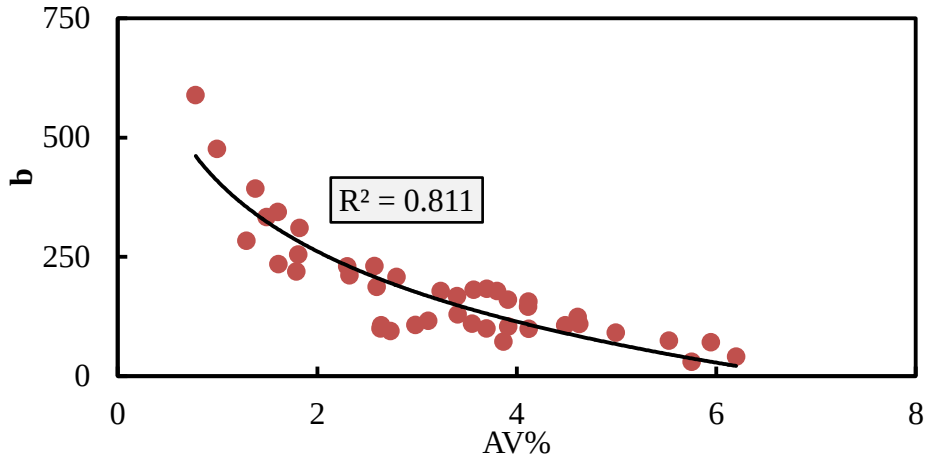

Figure 6-18: Relationship between parameter (b) and air voids for stress mode.

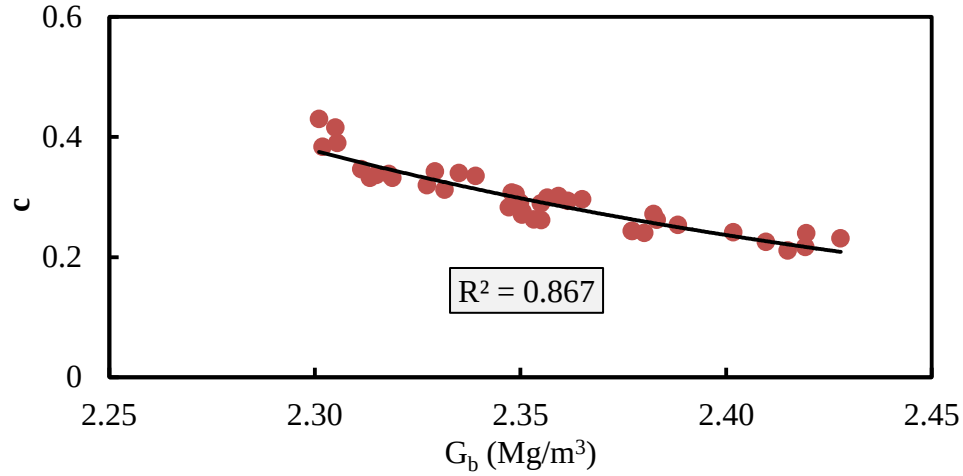

Figure 6-19: Relationship between parameter (c) and bulk density for strain mode.

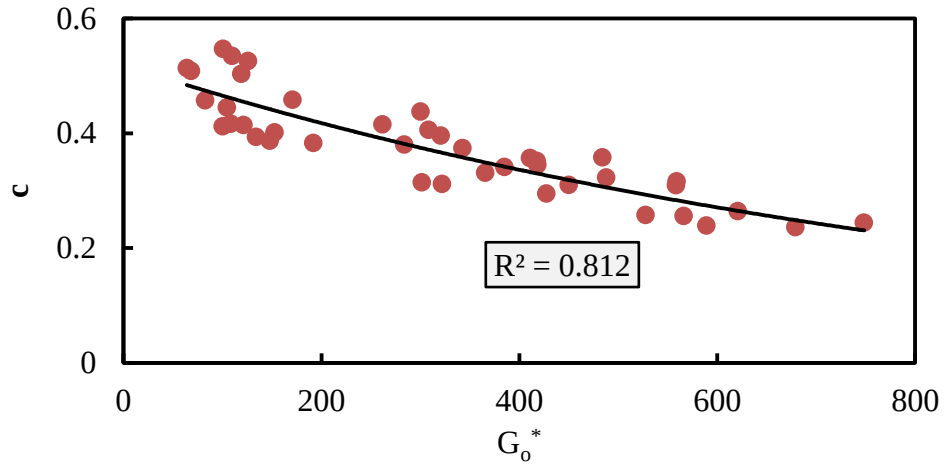

Figure 6-20: Relationship between parameter (c) and $\boldsymbol{G_o^*}$ for stress test mode.

6.7.3. Predictive Fatigue Model Formula

Now substituting the equations 6–21, 6–23, 6–25 and 6–27 into Equation 6–20 yields the final predictive model for controlled strain mode, as shown in Equation 6–29, while Equation 6–30 is the predictive model of controlled stress which has emerged from substituting Equations 6–22, 6–24, 6–26 and 6–28 into Equation 6–20.

$$N_{i_\gamma} = \left[\frac{\left(\frac{G_b^{-10.926}(473400.6 \log(G_o^*) - 661768.3)}{\alpha_v} \right)^{\frac{n}{n+1}}}{\left(\left(-0.074 \left(\frac{n-1}{n+1} \right) - 0.948 \right) + e^{(C_N)^{(-9.661\, m_1 + 12.090)}} \right)} \right]^{-\frac{n+1}{3373.529 n G_b^{-10.926} + 1}} \quad (6\text{–}29)$$

$$N_{i_\tau} = \left[\left(\frac{e^{-1.080 \times 10^{-3} G_o^*}(214.336 - 112.024 \ln(AV))}{\alpha_v} \right)^{\frac{n}{n+1}} \left(-(0.013 \ln\left(\frac{n-1}{n+1} \right) + 1.004) + e^{(C_N)^{-(2.616 \ln(m_1) + 6.063)}} \right) \right]^{-\frac{n+1}{n(0.961 - 0.106 \ln G_O^*) + 1}} \quad (6\text{–}30)$$

6.7.4. Modelling Results

The models in equations 6–29 and 6–30 were developed for predicting the fatigue performance in terms of number of cycles according to the traditional approach (N_f) and the energy ratio approach (N_1).

6.7.4.1. Traditional Approach (N_f)

In the traditional approach, fatigue life was defined as a number of cycles (N_f) when the stiffness modulus drops to 50% and 10% of initial stiffness modulus for strain and stress test modes respectively. Thus, C_N in models 6–29 and 6–30 is 0.5 and 0.1 for strain and stress test modes respectively.

Figure 6-21 shows the data set for the measured N_f against predicted N_f for controlled strain test mode; it is clear that there is a significant correlation between both, as displayed by the high R^2; also, the data are distributed along the line of quality.

In controlled stress, the model (Equation 6–30) was not good at predicting the fatigue life (N_f), and this is clear from the poor R^2, as presented in Figure 6–22. This may be due to the cumulative error in the model, which is coming from the parameters A, B, b and c, where the power law models in fitting DPSE against number of cycles are not capable of modelling at the end of fatigue life, as shown in Figure 6–3. Furthermore, this problem is repeated in the case of parameters A and B, as presented in the typical Figures 6–11 to 6–14. However, predicting fatigue life (N_f) was examined using the stress mode model (Equation 6–30) at normalised stiffness modulus (C_N= 20%). The results revealed that there is a satisfactory correlation between the measured and predicted N_f, as presented in Figure 6-23. This confirms this model's capability in predicting the fatigue life, but only well before the end of the fatigue test.

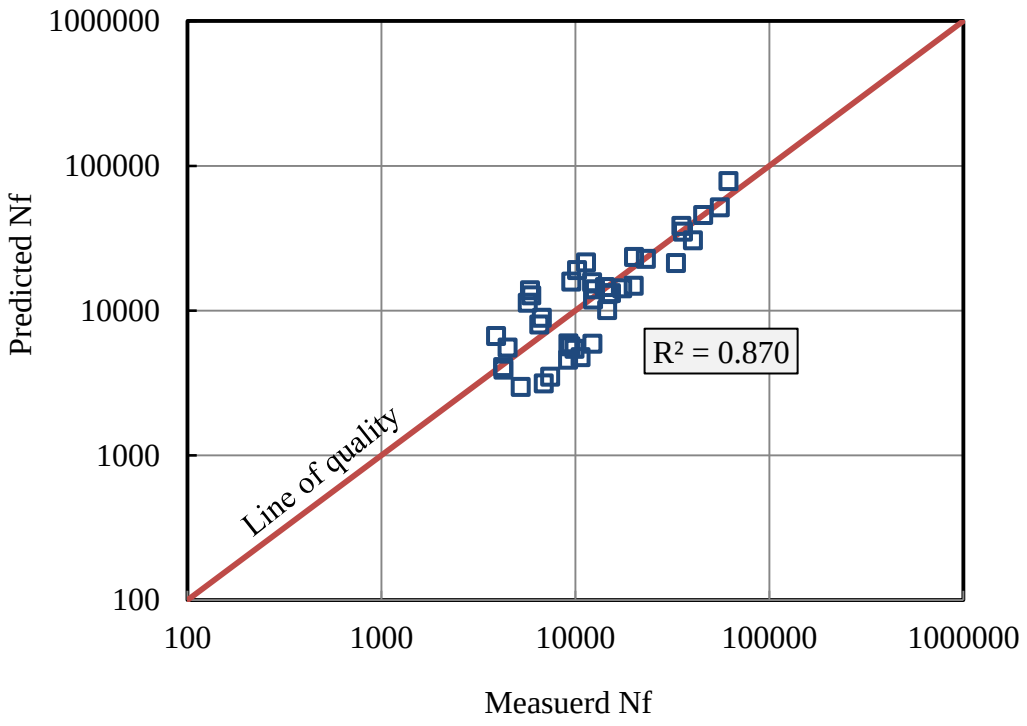

Figure 6- 21: Measured N_f against predicted N_f at 50% $\boldsymbol{G_o^*}$ in strain mode.

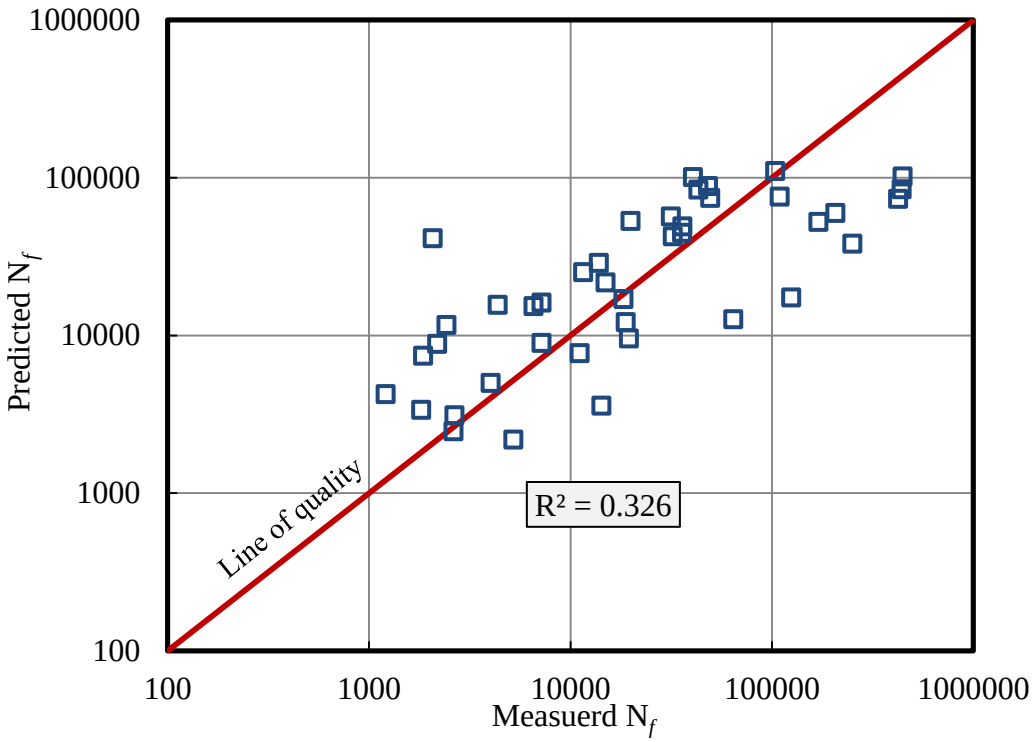

Figure 6- 22: Measured N_f against predicted N_f at 10% $\mathbf{G_o^*}$ in stress mode.

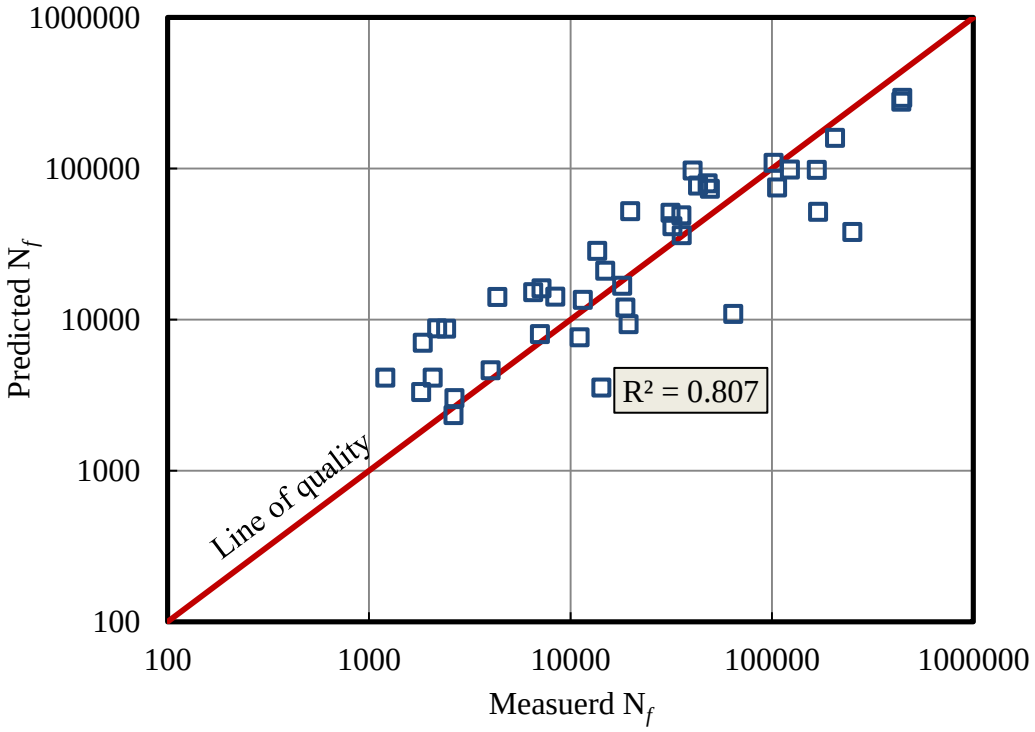

Figure 6- 23: Measured N_f against predicted N_f at 20% $\mathbf{G_o^*}$ in stress mode.

6.7.4.2. Energy Ratio Approach (N_1)

In the energy ratio approach, fatigue life has been defined as a number of cycles (N_1) in the relationship of energy ratio (ER) against number of cycles. Additionally, this definition is based on testing the modes, where in strain mode N_1 is the point at which ER diverges from the linear part, while in stress mode N_1 is the point at which ER reaches its maximum value. Therefore, there is no clear relationship between the number of cycles (N_1) as defined in the energy ratio approach and FIc as in the case of C_N. Thus, it is difficult to find relationships to use for developing a general model for predicting N_1 as in N_f. In spite of that, a relationship at high correlation does exist between N_1 and N_f for both test modes, as shown in Figures 6-24 and 6-25 and displayed in Equations 6–31 and 6–32 for strain and stress test modes respectively. It is worth noting that Figure 6-25 and Equation 6–32 are for the relationship between N_1 and N_f at C_N = 20%. Now, substituting Equations 6–31 and 6–32 into Equations 6–29 and 6–30, the models will produce a fatigue performance in terms of N_1 for both strain and stress test modes.

$$N_1 = 0.896\, N_f - 192.825 \qquad (6–31)$$

$$N_1 = 0.891\, N_f - 223.089 \qquad (6–32)$$

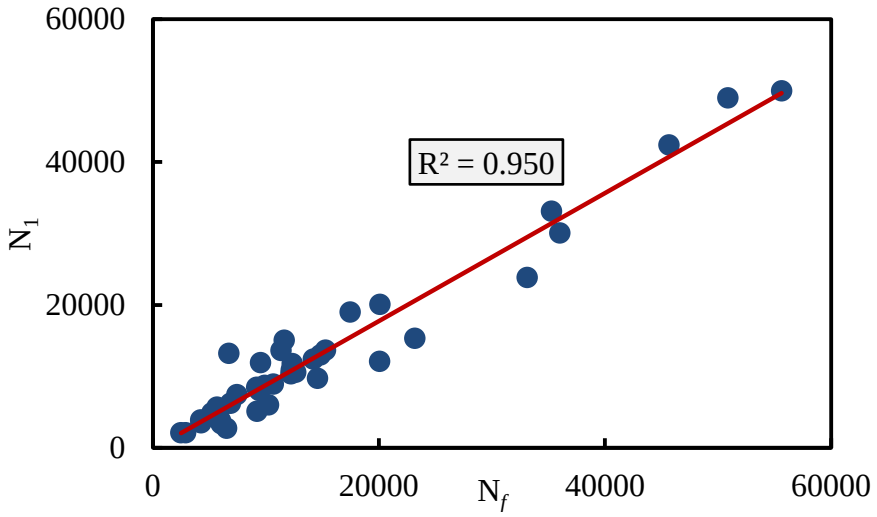

Figure 6-24: N_f against N_1 in strain mode.

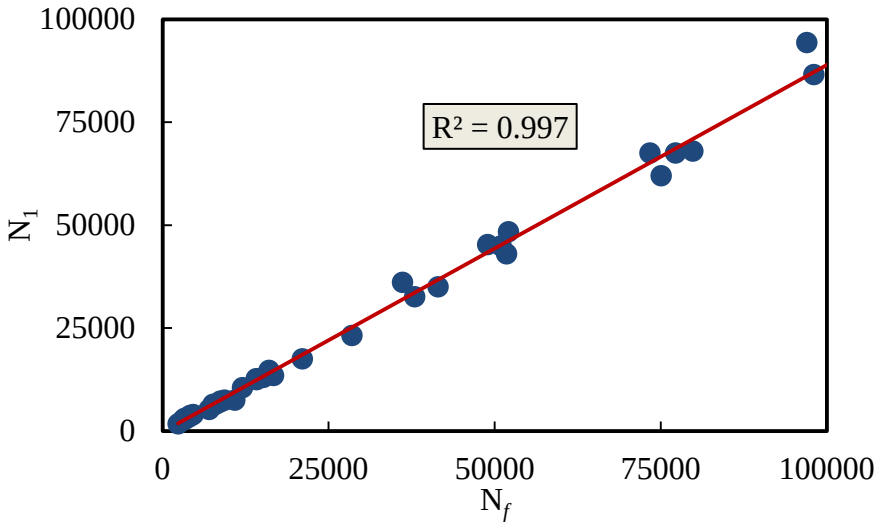

Figure 6-25: N_f against N_1 in stress mode.

Figures 6-26 and 6-27 demonstrate a good correlation is available between the measured and predicted N_1 for both test modes.

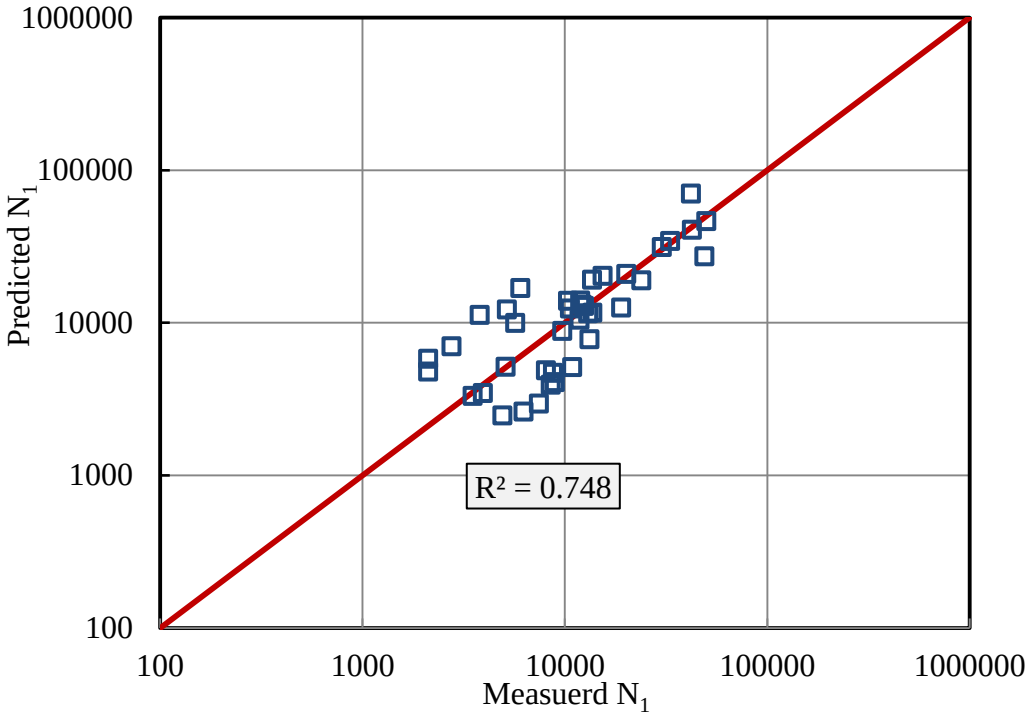

Figure 6-26: Measured N_1 against predicted N_1 in strain mode.

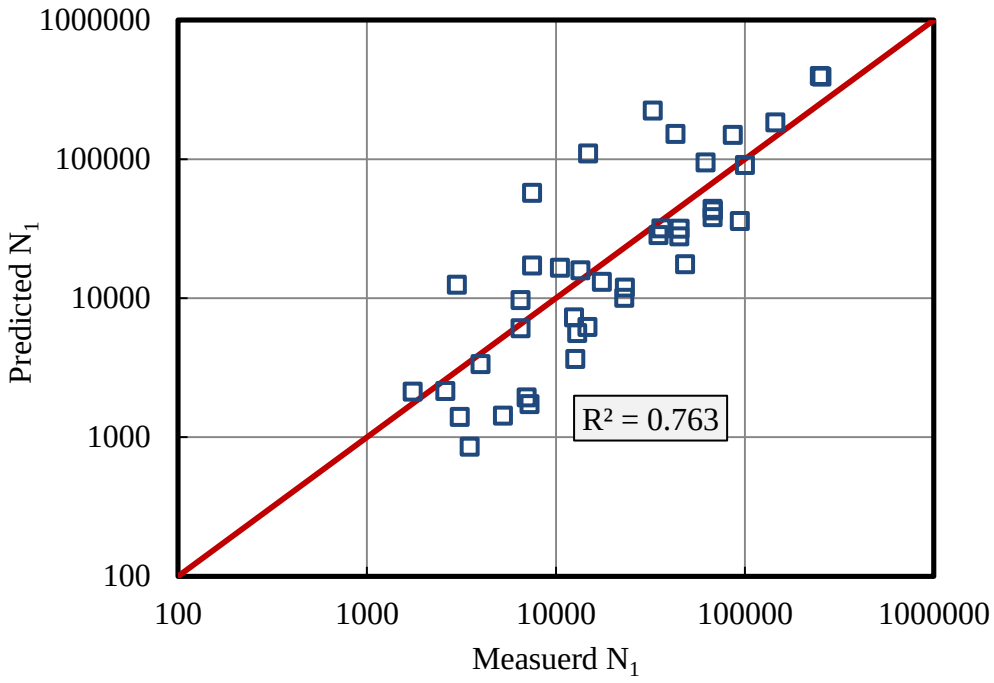

Figure 6- 27: Measured N_1 against predicted N_1 in stress mode.

6.7.4.3. Biases Analysis of Fatigue Models

However, although these models demonstrated their capability to predict the fatigue performance in terms of number of cycles (N_f and N_1), as shown by the high R^2, this does not definitely indicate their accuracy. There may be overall biases in the predictions that can cause significant reduction in accuracy. In this regard, three parameters were calculated based on the prediction outcomes of the models including: average error, slope and intercept of the relationship between predicted and actual values. More details about bias calculations are provided in Chapter V. These three parameters will be compared with the optimum values that are presented by the line of equality (LQ). LQ was selected as a perfect model because the predicted values are equal to actual results and LQ passes through the origin; therefore, the average error, intercept and slope are 0, 0 and 1 respectively. The model results in over-prediction if average error is positive or under-prediction if the average error is negative. The model is close to the LQ when the slope and intercept approach 1 and 0 respectively.

Figures 6-28 and 6-29 demonstrate a simple compression in accuracy between the predictive models of strain and stress mode using AE and intercept.

It is clear that the strain test mode model was a better predictive model than the stress test mode model; the average error and intercept in the stress model were much higher than the strain test modes in both approaches, N_f and N_1. On the other hand, both approaches (N_f and N1) are under-predicted where AV is a negative value. Additionally, slope emphasises the same outcomes, where the slope of the strain model was closer to the slope of LQ than that of the stress model for both approaches as shown in Figure 6-30. Overall, it is clear that, with regard to prediction, the strain model performs better than the stress model.

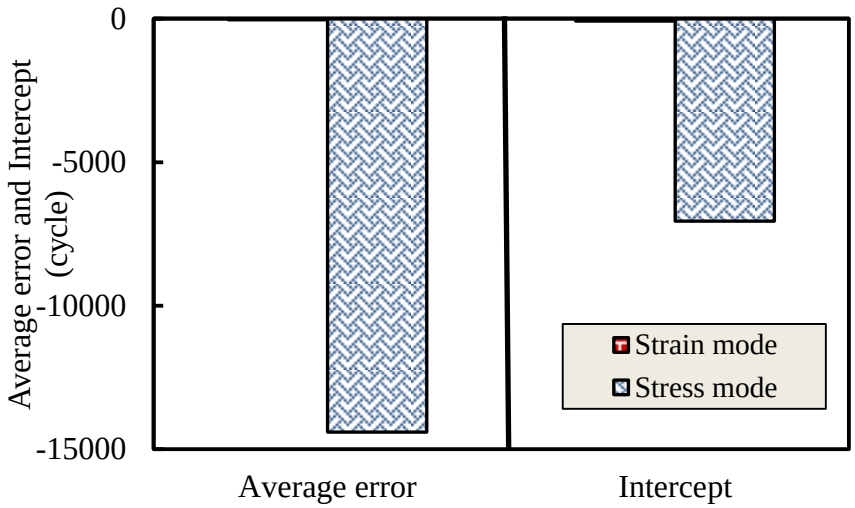

Figure 6- 28: Average error and intercept for predicting number of cycles (N_f) in strain and stress test modes.

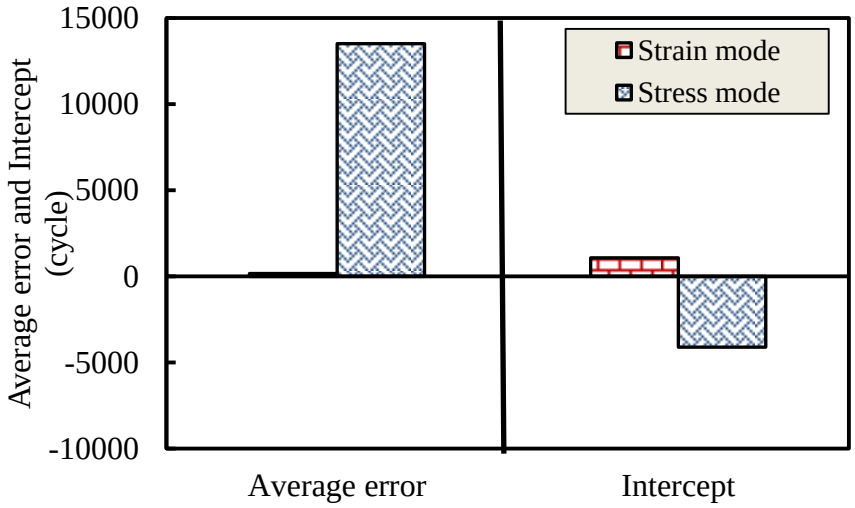

Figure 6- 29: Average error and intercept for predicting number of cycles (N_1) in strain and stress test modes.

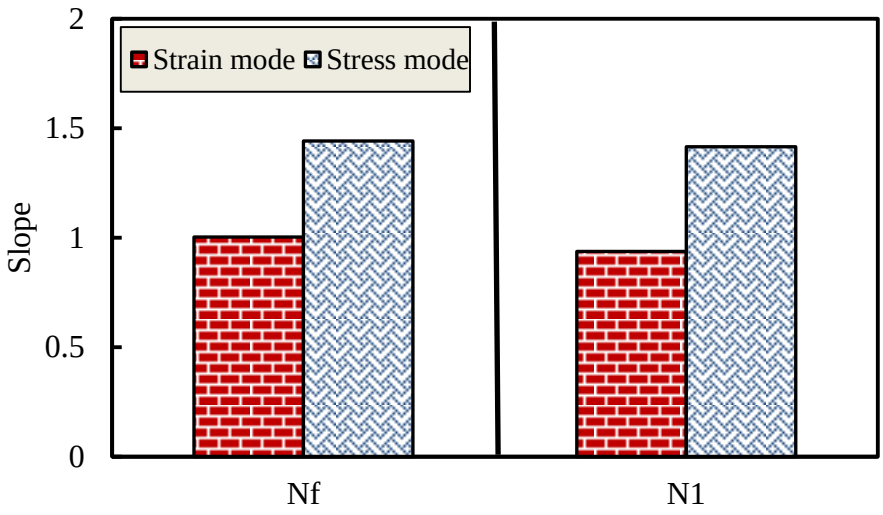

Figure 6- 30: Slope for predicting number of cycles (N_f and N_1) in strain and stress test modes.

6.8. Summary

Based on the results and discussion that are presented in this chapter, the following conclusions can be reached:

1. The Paris' law model has been used as an approach to investigate the fracture behaviour of materials within linear elastic fracture mechanics; a vital modification was carried out on this model to make it reliable and more accurate in simulating the fracture analysis of non-linear viscoelastic material by introducing the *J*-integral. Based on this modification, several approaches were developed to analyse the fracture performance of HMA. The majority of these models were based on the so-called crack radius, which is a flawed approach, while other models characterised fracture performance based on an internal damage parameter called damage density, which mimics the crack density inside materials.
2. Dissipated pseudo-strain energy was calculated based on the differences between applied and recovered pseudo-strain energies for cylindrical samples prepared from a variety of asphalt mixes and examined in fatigue using a DSR instrument under strain and stress mode testing. Analysis of the results revealed that a higher DPSE/N ratio indicates lower fatigue life and greater damage.

3. A simple fracture model based on a modified Paris' law was introduced and used successfully in evaluating fracture performance of different asphalt mixes. This model was derived based on the fundamental fatigue parameters represented by the exponential relaxation coefficient (*m*) and the cumulative dissipated pseudo-strain energy for the matrix, where cracks occur because it is weaker than aggregates in HMA samples.
4. The results showed that there is compatibility between the fatigue performance analysis using fracture mechanics represented by fracture index (FI_c) with other analyses presented in Chapters III and IV using FI^R, TA and ER approaches. In addition, the FI_c results showed better performance analysis in terms of variation than number of cycles.
5. Results showed the same conclusions as the previous study (Chapters III and IV): that limestone mixes perform better than granite mixes in both DBM and HRA mixes.
6. Models were developed for predicting fatigue performance in terms of number of cycles defined according to traditional (TA) and energy ratio (ER) approaches for HMA samples tested in DSR. These models were based on estimating four parameters (A, B, b and c) extracted from the relationships of FI_c with normalised stiffness modulus (C_N) and DPSE against number of cycles for strain and stress test modes, which were correlated with volumetric and mechanistic properties for developing fatigue models for both test modes, strain and stress.
7. The results revealed that the strain model's ($N_{i\gamma}$) prediction accuracy was better than that of the stress model ($N_{i\tau}$), as demonstrated by the bias analysis parameters, which are represented by average error, intercept and slope, where these parameters were closer to the line of quality for the strain model than for the stress model.

CHAPTER VII

CHAPTER VII

7. Hysteresis Characteristics and Modelling of HMA Tested by Dynamic Shear Rheometer

7.1. Introduction

Over the course of their life HMA materials suffer from degradation due to repeated traffic loading, a process known as fatigue. This degradation is estimated by measuring the loss of the stiffness modulus of these materials, and can be observed as a longitudinal or hexagon crack patterns on road or pavement surfaces (Ghuzlan and Carpenter, 2006). When sustaining fatigue loading, as a viscoelastic material, HMA takes different paths during loading and unloading cycles in stress-strain relationship and hysteresis loops are created, the areas inside these loops represent dissipated energy (Carpenter and Shen, 2006). The changes in the area and the slope of the hysteresis loops with an increasing number of loading cycles reflect the amount of internal damage in the materials (Kim et al., 2003;Kim et al., 2002). This concept has been used as a criterion in evaluating fatigue performance of HMA (Al-Khateeb and Shenoy, 2004;Kutay et al., 2008). Whereas, fatigue life failure was revealed directly from raw data by observing the distortion of load–deformation hysteresis loops or the response waveform of load and deformation. The distortion was quantified by the standard error (S_e) between the measured strain points and the best fit sinusoids to the raw data. Fatigue failure was defined at the point when S_e increases suddenly from the plateau value, which is produced by plotting S_e vs number of cycles.

7.2. Hysteresis Loops

The term hysteresis refers to a large class of non-linear systems in which, the restoring force depends not only the instantaneous deformation but also on the history of deformation. This phenomenon has been attracting the attention of

researchers for a long time because of its relevance to many scientific fields. Examples of hysteresis can be found in magnetic, ferroelectric, mechanical, optical and economic systems, as well as during the deformation of some materials in response to a varying force. In a hysteretic system, the output is a function of the current input and previous or initial input. Several models have been developed in order to describe non-linear hysteretic system input–output relationships (Macki et al., 1993).

The Duhem model is one of the earliest models, it was developed since 1897. This model uses the phenomenological approach postulating an integral operator or differential equation for modelling the relation between input and output signal (Macki et al., 1993). This model is suitable for application in the electromagnetic fields because the function and parameters of this model can match the experimental results (Coleman and Hodgdon, 1986). Another model is called the Ishlinskii model 1944, which was proposed for modelling the hysteresis loops of the plasticity-elasticity behaviour (Ikhouane and Rodellar, 2005); and used widely in the symmetric hysteresis loops of Piezoceramic actuator (Macki et al., 1993;Al Janaideh et al., 2009). Preisach model was suggested by Ferenc Preisach in 1935 (Preisach, 1935), since that time it has become commonly used in hysteresis loop modelling. This model was originally used in the field of ferromagnetism (Ktena et al., 2001;Mayergoyz, 2003), but was later adopted in other scientific disciplines such as shape-memory alloys ,i.e. strain vs. temperature, (Ktena et al., 2001). All these models are based on operator and differential equations (Al Janaideh et al., 2009). Another model is based on differential equations is the Bouc-Wen model 1967-1976 (Bouc, 1967;Wen, 1976), which was developed for simulating degrading materials under seismic loading. Bouc used the integral operator of the Duhem model in a particular case (Macki et al., 1993;Oh and Bernstein, 2005). Generally, these models may vary from sophisticated complex models, which can capture diverse behaviours, e.g. Preisach formalism, to versatile, easy to implement models, which can be defined via concise and explicit differential expressions, e.g. Bouc Wen formalism.

Stress-strain relationships in HMA samples that are tested under repeated loads have been presented as hysteresis loops, and these loops develop in shapes, sizes

and slopes with cyclic loading (Al-Khateeb and Shenoy, 2004). This development in loops is an indication of the deterioration in materials against time because of cracks that have occurred with loading and is expressed as reduction in the stiffness modulus of materials (Kim et al., 2002;Kim et al., 2003). The area inside the loops represents the energy being put into the materials, and is called dissipated energy which is used widely as a criterion in the definition of fatigue failure in HMA (Ghuzlan and Carpenter, 2000;Al-Khateeb and Shenoy, 2004;Daniel et al., 2004;Carpenter and Shen, 2006;Ghuzlan and Carpenter, 2006).

In other works (Al-Khateeb and Shenoy, 2004;Kutay et al., 2008), the distortion in the hysteresis loops was monitored under cyclic loading to be used as a criterion for fatigue failure, and when there is clear distortion in loops at a specific number of cycle, this point was defined as fatigue life, as detailed in Chapter II. However, no mathematical models are available to evaluate this behaviour. A mechanistic approach for HMA samples tested under uniaxial tensile cyclic loading was used for developing constitutive equation for accounting the damage of HMA samples under cyclic loading (Lee and Kim, 1998). This constitutive equation was used for predicting the stress-pseudostrain (hysteresis loops) behaviour of HMA under stress and strain mode tests; in spite of the predicted loops being in good agreement with the experimental results for controlled strain test mode, but in stress mode test, the prediction was poor with a considerable shift between experiment and model loops.

This study aims to model the degraded hysteresis loops for HMA samples tested in fatigue under stress and strain test modes using Bouc-Wen model. The simplicity and versatility of this model encouraged its use in this work.

7.3. Objectives of Study

The Bouc–Wen model has been used extensively to study the degradation of the hysteretic restoring force in structures subjected to extreme dynamic loads such as earthquakes where there are random vibrations (Baber and Wen, 1981;Sues et al., 1988) for a short time period of several seconds or minutes. Due to its simplicity, versatility and its high potential for practical applications (Spanos and Kougioumtzoglou, 2011) , the Bouc–Wen model is selected herein to model

degraded hysteretic behaviour over long periods of time (hours) in fatigue tests for asphalt mixtures tested with a Dynamic Shear Rheometer (DSR) in controlled strain mode. The goodness of fit between experimental fatigue and Bouc–Wen model data was also evaluated. In addition, a method based on the stress-strain relationship in viscoelastic materials has been used for creating calculated hysteresis loops due to the limitation in the software capacity of the DSR machine to save the stress-strain data. Also, a standard non-linear least squares algorithm was employed to identify the model's parameters (Wright and Nocedal, 1999).

7.4. The Bouc–Wen model

The Bouc–Wen hysteresis model is a first-order non-linear differential equation that relates to the input as displacement and output as a restoring force. This model was originally introduced by Bouc (Bouc, 1967) and later developed by Wen (Wen, 1976), so it is called the Bouc–Wen model. Previously, this model was used mainly with regard to wood and structural joints and was largely unknown among researchers, perhaps because of the absence of an analytical study for this model (Ikhouane et al., 2004). In the past 20 years, an extensive interest in this model has encouraged many researchers to study it, and there have been many books and publications brought out dedicated exclusively to this model (Ismail et al., 2009). The introduction of the versatile Bouc–Wen hysteretic model was followed by its successful application to numerous structural dynamics-related fields; for instance, this model has been used for modelling the hysteresis loops of dampers that interconnect to structural members, subjected to the seismic excitation (Basili and De Angelis, 2007); and for the response analysis of nonlinear hysteretic shear stress – strain relation of the soil subjected to cyclic loading (Pires, 1996). One of the reasons for the popularity of the model, besides its versatility in efficiently capturing a wide range of hysteretic behaviours, whereas, the model was extended to account for structural degradation (Baber and Wen, 1981;Sasani and Popov, 2001), pinching effects (Baber and Noori, 1985;Foliente and Noori, 1996) and asymmetric hysteresis (Dobson et al., 1997;Song and Der Kiureghian, 2006). A detailed presentation of the applications and the extensions of the Bouc–Wen model can be found in

review papers and books (Wen, 1986;Wen, 1989;Ikhouane and Rodellar, 2007;Ismail et al., 2009).

7.5. Bouc–Wen Model Formulation

The Bouc–Wen model is a first order non-linear differential equation and the general form is presented in the following equations:

$$\varphi = \alpha k u_{(t)} + (1-\alpha) k z_{(t)} \tag{7-1}$$

$$\dot{z} = A\dot{u} - \beta|\dot{u}||z|^{n-1}z - \psi\dot{u}|z|^{n} \tag{7-2}$$

Where $\dot{z} = \frac{dz}{dt}$, $\dot{u} = \frac{du}{dt}$,

φ is restoring force, i.e. is the force that brings the system back to the equilibrium state, *A*, β, ψ and *n* are non-dimensional parameters controlling the shape of hysteresis loops.

$$\alpha = \frac{k_f}{k_i} = \frac{post-yield\ stiffness}{pre-yield\ stiffness\ (elastic)}\ , k_i = \frac{P_y}{\varepsilon_y} = \frac{yield\ forces}{yield\ displacement}\ ,$$

z(t) is hysteresis forces, *u(t)* is hysteresis displacements.

Dividing Equation (7–2) by $\dot{u}$ yields Equation (7–3).

$$\frac{dz}{du} = A - \beta\frac{|\dot{u}|}{u}|z|^{n-1}z - \psi|z|^{n} \tag{7-3}$$

Equation 7–3 is the Bouc–Wen model for the non-degrading case (Baber and Wen, 1980;Baber and Wen, 1981;Baber and Noori, 1985;Sues et al., 1988), and identifying the parameters *A*, β, ψ and *n* and solving this model yields the stress–strain non-linear relationship for initial hysteresis loops of the non-degrading case. In the degrading case, the model is capable of reproducing the degradation behaviour of material as hysteresis loops, but some modifications (in the form of adding more parameters) to the original model are necessary. In this regards, Baber and Wen (1980) added some modification to the original Bouc-wen model to be as a function of dissipated hysteretic energy, strain rate and degrading

parameters; dissipated hysteretic energy is calculated by Equation 7–4 and degrading parameters are as a function of dissipated energy as shown in Equation 7–5. The Bouc-Wen model for degrading case is presented in Equation 7–6 and Equation 7–7 is the final Bouc-Wen model for degrading case. More details about these modifications are presented in (Baber and Wen, 1980;Sues et al., 1988).

$$\epsilon = (1-\alpha)k\int_{t_o}^{t_f} z\,\dot{u}dt \tag{7–4}$$

$$A(\epsilon) = A_0 - \delta_A\epsilon$$

$$\eta(\epsilon) = 1.0 + \delta_\eta\epsilon$$

$$\upsilon(\epsilon) = 1.0 + \delta_\upsilon\epsilon \tag{7–5}$$

$$\frac{dz}{du} = \frac{A-\delta_A\epsilon-(1.0+\delta_\upsilon\epsilon)\left(\beta\frac{|\dot{u}|}{\dot{u}}|z|^{n-1}z+\psi|z|^n\right)}{1.0+\delta_\eta\epsilon} \tag{7–6}$$

$$\dot{z} = A\frac{1}{1+\delta_\eta\epsilon} - \delta_A\frac{\epsilon}{1+\delta_\eta\epsilon} - \delta_\upsilon\frac{\epsilon\left(\beta\frac{|\dot{u}|}{\dot{u}}|z|^{n-1}z+\psi|z|^n\right)}{1+\delta_\eta\epsilon} - \frac{\beta\frac{|\dot{u}|}{\dot{u}}|z|^{n-1}z+\psi|z|^n}{1+\delta_\eta\epsilon} \tag{7–7}$$

Where δ_A, δ_η and δ_υ are degradation parameters and ϵ is dissipated hysteretic energy.

7.6. Identification of Bouc–Wen Parameters

In simple terms, all the methods to identify Bouc–Wen parameters are based on adjusting the parameters for a given set of experimental data (force-displacement) until the output of the model matches the experimental data. These identified parameters will be adopted when modelled output converge from the target values which are represented by experimental results. There are several methods in the literature for identifying Bouc–Wen parameters. For example, the least-square method has been used widely by researchers to identify the parameters of the model (Sues et al., 1988;Shih and Sung, 2005;Zhu and Lu, 2011), and the results were highly consistent with experimental data. Other methods such as the Kalman filter, the genetic algorithm, the Gauss–Newton iterative and the bootstrap filter have been used to deal with a large number of parameters, non-symmetrical

hysteresis loops, noise and corrupted input–output data; more details about these methods are presented in (Ismail et al., 2009).

In this work, a standard Trust-region-reflective non-linear least squares algorithm has been employed (Nocedal and Wright, 2006) to solve Equation 7–7 and determine the unknown parameters A, β, ψ, n, δ_A, δ_η and δ_v. To simplify the solution, the measured hysteresis loops were used to find the hysteresis shear stress rate ($\dot{z}$), hysteresis displacement rate ($\mathring{u}$) and energy (ϵ) as shown in the equations below.

$$\dot{z}_i = \frac{dz}{dt} = \frac{\Delta z}{\Delta t} = \frac{z_{i+1} - z_i}{t_{i+1} - t_i} \tag{7–8}$$

$$\dot{u}_i = \frac{du}{dt} = \frac{\Delta u}{\Delta t} = \frac{u_{i+1} - u_i}{t_{i+1} - t_i} \tag{7–9}$$

$$\epsilon_i = (1 - \alpha) k \sum_{i=1}^{i=n} z_i \times \dot{u}_i \times \Delta t_i \tag{7–10}$$

Where z_i, z_{i+1}, u_i, u_{i+1} are shear stress rate and shear strain at time i and i+1, respectively, n is the number of points that are used in identification and ϵ_i is cumulative dissipated energy at time i. as shown in Figures 7–1 and 7–2.

The non-linear least squares algorithm (Wright and Nocedal, 1999) was used to estimate the parameters of Equation 7–7. After several iterations, the Bouc–Wen parameters will be captured by the solver when there is a good convergence between the experimental and modelling results as demonstrated in Figure 7–3. In this regard, an algorithm solver code of nonlinear least squares was developed using MATlab 2013a to optimize the solution of Equation 7–7 as detailed in Appendix C-1. It is worth noting that, K_i is the initial stiffness at the initial time of the fatigue test, while K_f corresponds to the stiffness at the time (t_n) where the last point has been used for identification parameters from the results.

7.7. Materials and Experimental Work

The same materials that were used in strain and stress test modes have been used here; more details about mix design and selecting DSR samples are available in Chapter III. The experimental work included fatigue testing using DSR according to the criteria that were detailed in Chapters III and IV.

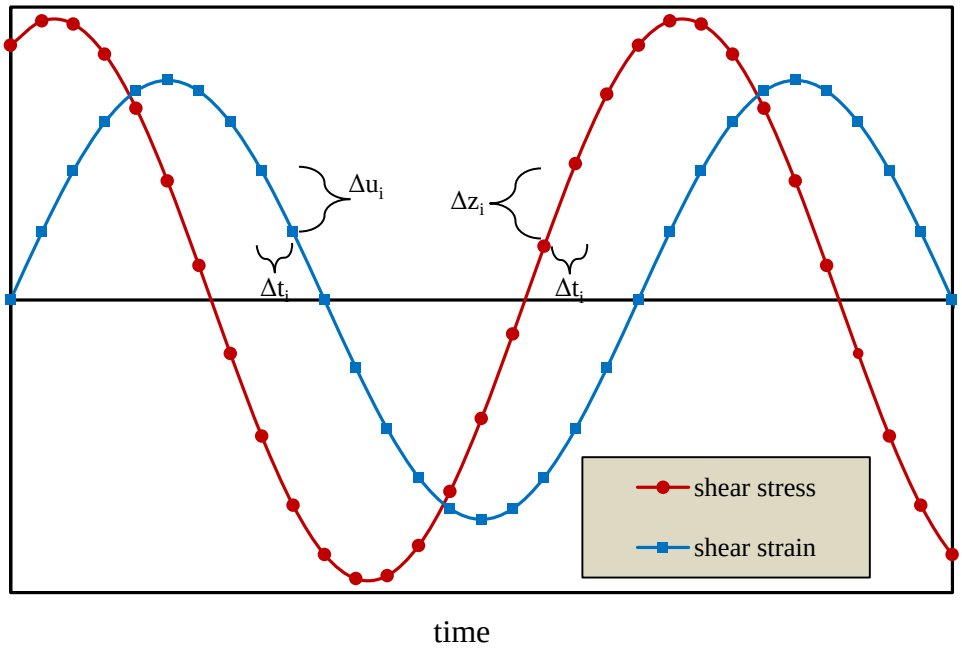

Figure 7- 1: Shear stress and shear strain vs. time

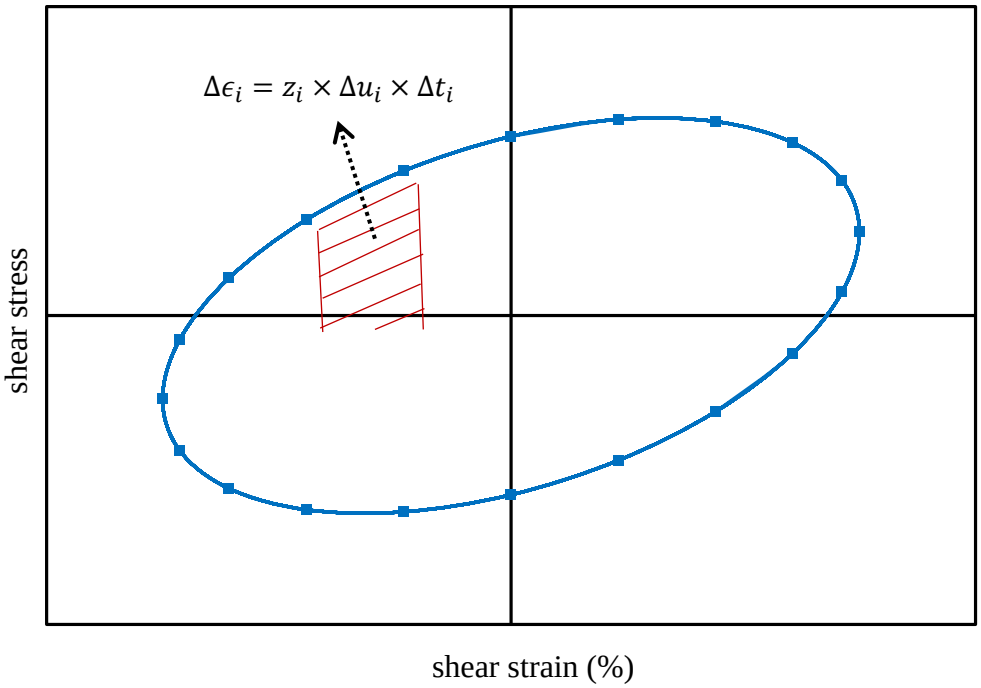

Figure 7- 2: Hysteresis loops and dissipated energy.

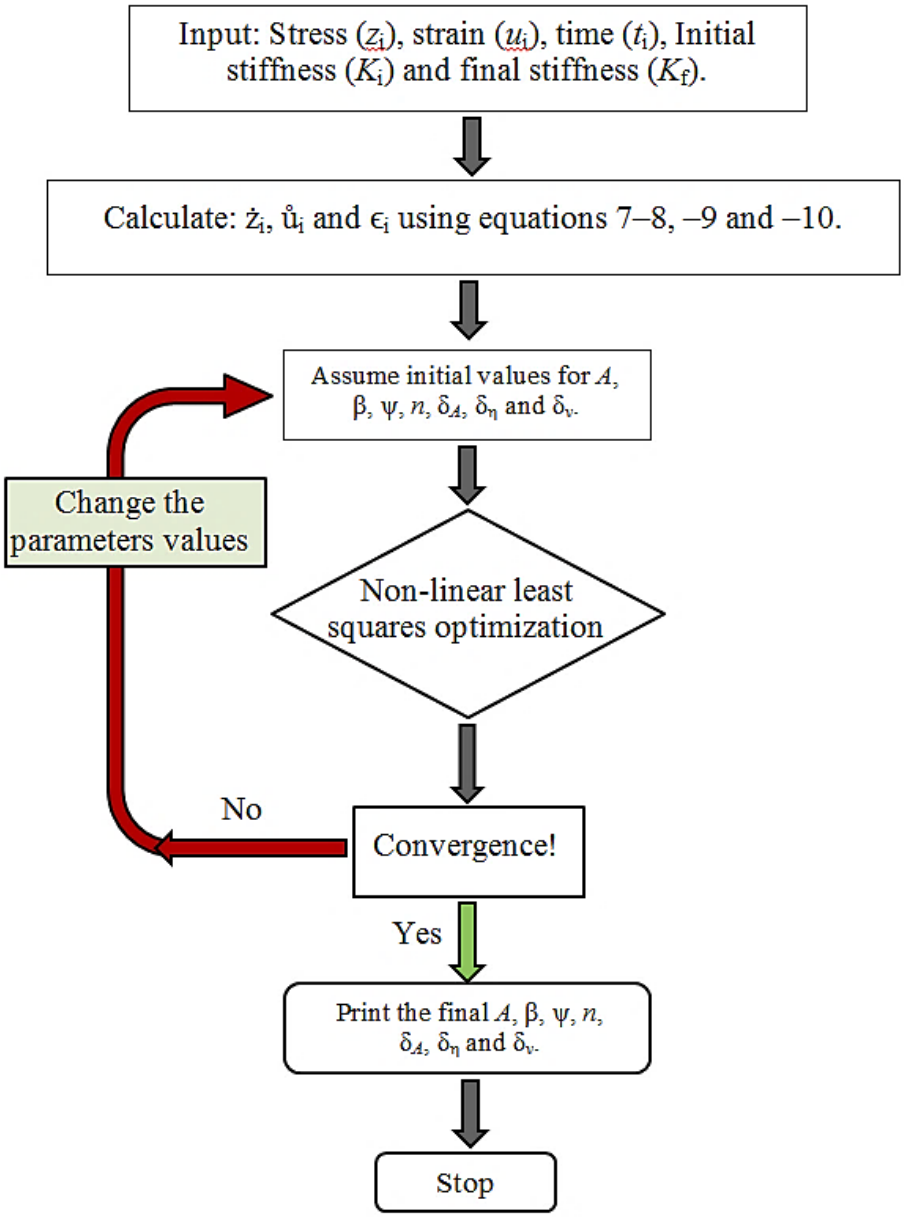

Figure 7- 3: Flow chart for identifying the Bouc-Wen parameters

7.8. Results and Discussion

7.8.1. Fatigue evaluation

The degrading during fatigue testing is evaluated using several approaches. One of the approaches that are commonly used in research is called the traditional approach (Kim et al., 2003;Daniel et al., 2004;AASHTO, 2002). In this approach, the normalized stiffness modulus and phase angles are plotted against number of

cycles; and fatigue life is evaluated as the number of cycles when the stiffness modulus is reduced to 50% and 10% of the initial stiffness value for controlled strain and stress, respectively, as demonstrated in Figure 7–4. It is clear that there are sharp drops in the phase angle when the normalized shear modulus is less than about 0.35 and 0.2 for strain and stress mode tests, respectively, more discussions for this issue was explained deeply in Chapters III and IV. This behaviour can be further explained by the changes in the hysteresis loops as shown in Figure 7–5 and 7–6.

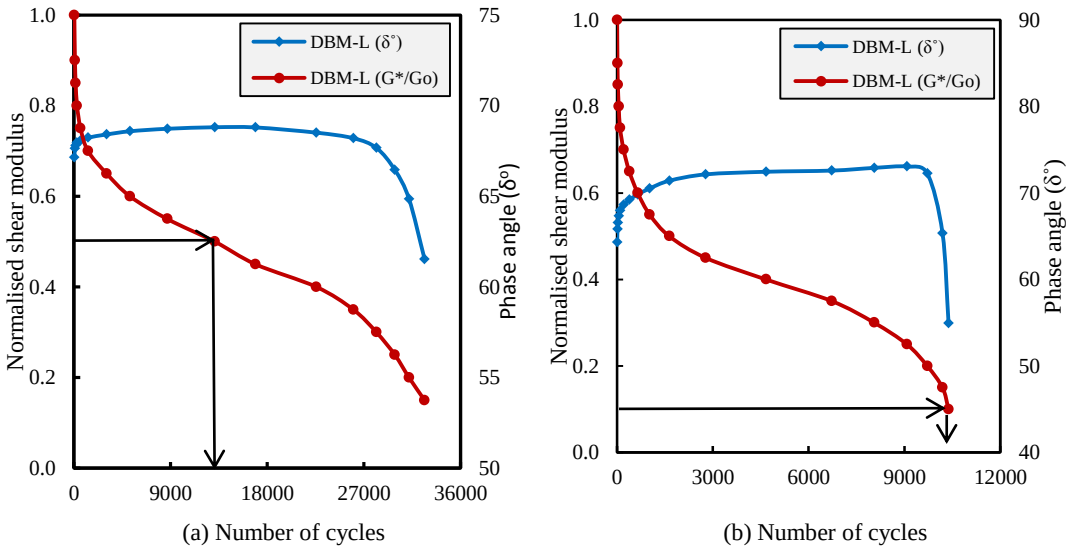

Figure 7- 4: Number of cycles against normalized shear modulus and phase angles for DBM-L mixes (a) controlled strain; and (b) controlled stress.

The loops became distorted from the original shape (ellipse) when the normalized shear modulus decreased to less than approximately 0.35 and 0.2 for both test modes as shown in Figure 7–4. These values (0.35 and 0.2) represent the second infliction point (Kim et al., 2002;Kim et al., 2003), where the tested samples become damaged rapidly after these limits are reached, as is clear from the rapid decrease in the normalized shear modulus as shown in Figure 7–4. Consequently, the fatigue test comes to an end when the normalized shear modulus reaches these values.

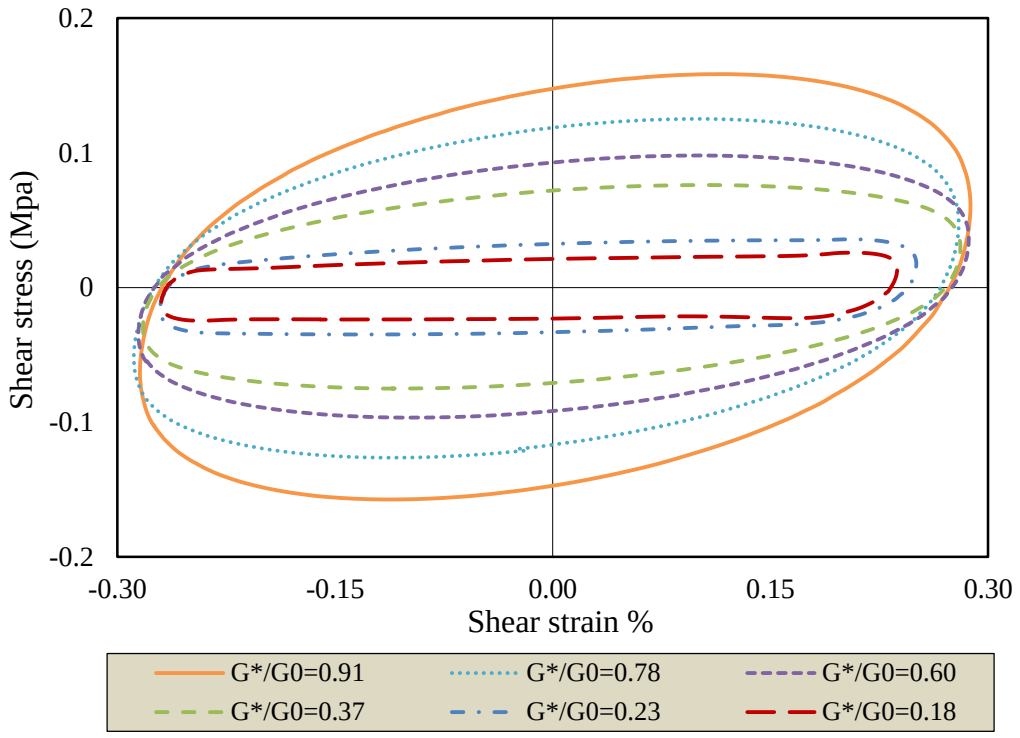

Figure 7- 5: Real hysteresis loops (strain–stress) at different normalised shear modulus for DBM-L mix tested in strain mode.

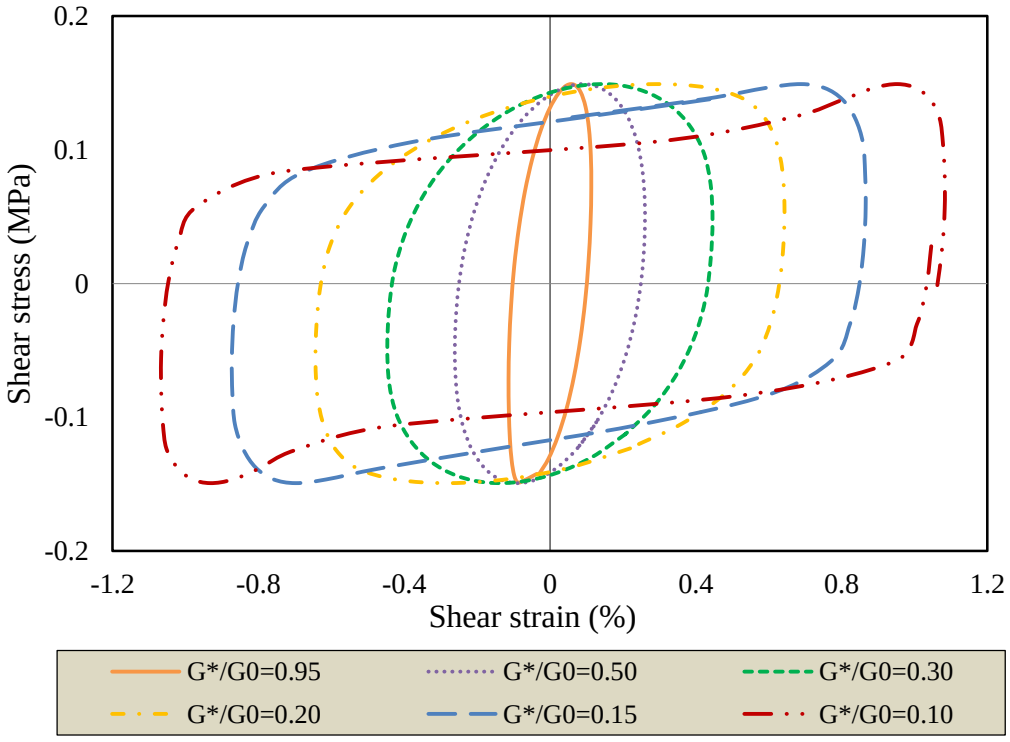

Figure 7- 6: Real hysteresis loops (strain–stress) at different normalised shear modulus for DBM-L mix tested in stress mode.

7.8.2. Data Preparation for Bouc–Wen Model

The Bouc–Wen model solution requires the hysteresis loop data from the beginning to the end of degradation. Because fatigue testing takes place over a long period, it is impossible to save all the hysteresis loop data due to the limitation of DSR software capacity. To solve this problem, a calculation method was adopted to obtain the hysteresis loops. This technique has been used for all DBM and HRA samples tested in controlled strain test mode due to lengthy test duration. Generally, in the controlled strain mode test, the response in stress is a function of time as shown in Equations 7–11 and 7–12 (Bhasin et al., 2008;Branco, 2008).

$$\gamma_h = \gamma_0 \sin(\omega t) \tag{7–11}$$

$$\tau_h = \tau(t) \sin(\omega t + \delta(t)) \tag{7–12}$$

where: τ_h and γ_h are shear stress and shear strain values in hysteresis loops, γ_0 is shear strain amplitude and $\tau(t)$ is shear stress response as a function of time, $\delta(t)$ is phase angle as function of time, $\omega = 2\pi f$ is angular frequency in rad and f is frequency in Hz. Polynomial models were used to fit the experimental data for shear stress (τ) and phase angle (δ) against time. Figures 7-7 and 7-8 represent an example of the data for shear stress and phase angle, it is clear from R-square there are a good correlations between the experimental and modelling data as shown in Figures 7-7 and 7-8.

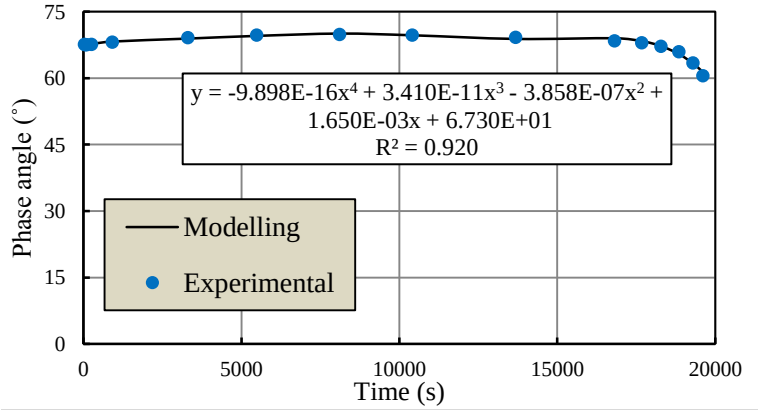

Figure 7- 7: Typical example for fitting phase angle against time for DBM-L sample tested in controlled strain.

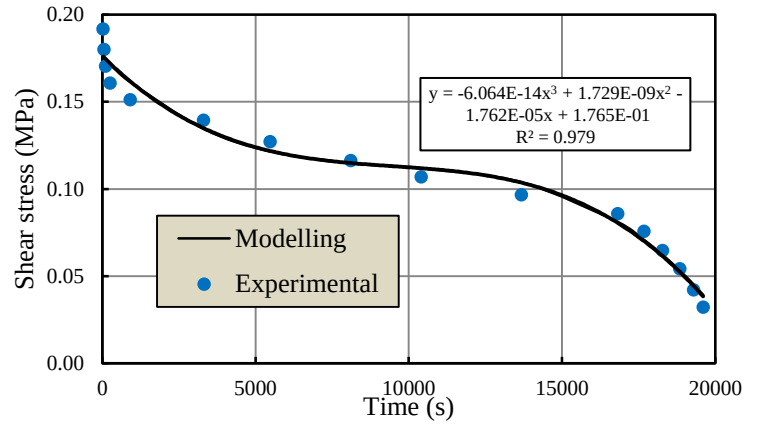

Figure 7- 8: Typical example for fitting shear strain against time for DBM-L sample tested in controlled strain.

It is worth noting that the number of points in each calculated loop was chosen as 32 to 16 points, and the interval (*dt*) between two points was 0.0125 to 0.25 s when the frequency was 2.5 Hz, depending on the fatigue life. This simplifies the calculation of the loops and the identification of Bouc–Wen parameters. The plots of functions 7–11 against 7–12 produces the hysteresis loops as shown in Figure 7-9. The degrading is clearly from the decreasing in stress as shown in Figures 7-9.

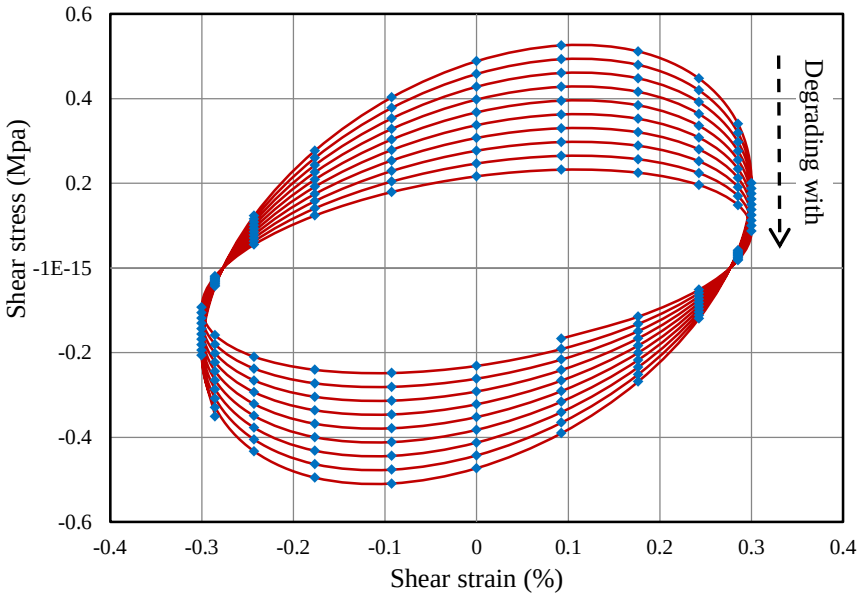

Figure 7- 9: A typical calculated hysteresis loops in strain mode for HRA-G sample.

7.8.3. Modelling the Hysteresis Loops Using Bouc-Wen Model

Over the course of repeated loading, materials exhibit three phases: phase I, or the adaptation phase, is characterised by a rapid decrease in stiffness due to heat generation and thixotropy; phase II or the quasi-stationary phase, is where the steady decrease in the stiffness predominates, and the degradation in material is very slow as the number of load cycles increases; and phase III, or the failure phase, is where macro cracks begin to develop and failure completely sets in to the material at the end of this phase, as demonstrated in Figure 7-10 (Di Benedetto et al., 2004;Carpenter and Shen, 2006;Ghuzlan and Carpenter, 2006). In the next sections, the Bouc-Wen model was applied in two strategies: the first strategy, strategy–1, applied the Bouc-Wen model for the set of data from phase I to phase III, while the second strategy, strategy–2, was for two sets of data: phase I separately and phases II and III together. This processing improved the capability of the Bouc-Wen model for modelling the hysteresis loops, as shown in the following sections.

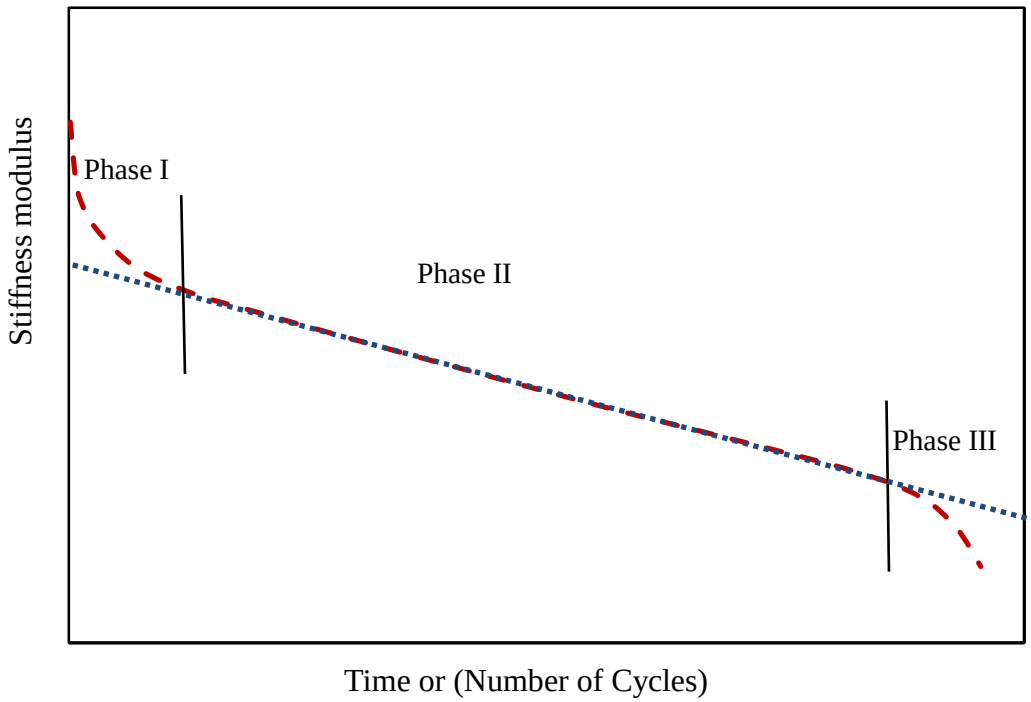

Figure 7- 10: Shear stiffness modulus against time or number of cycles.

7.8.3.1. Hysteresis Loops for Phases I-III (strategy–1)

To identify the Bouc-Wen parameters, stress-strain data were created using the calculation method for one DSR sample chosen from each mix, as detailed previously. Later, stress-strain (hysteresis loop) data were used to identify the model parameters using the non-linear least squares algorithm (Wright and Nocedal, 1999), as detailed in Figure 7–3. All parameters are listed in Table 7–1 for the hysteresis loops from phase I to phase III.

Table 7– 1: Bouc-Wen model parameters for stratigy-1

Mix ID	G_o^*	A	β	ψ	n	δ_A	δ_μ	δ_ν
DBM-L	65.685	1.153	15.544	-9.468	0.916	6.188×10^{-4}	8.651×10^{-5}	-2.004×10^{-5}
DBM-G	74.121	1.083	85.485	-74.793	1.380	9.066×10^{-4}	-2.282×10^{-4}	2.833×10^{-5}
HRA-L	212.115	2.452	46.258	-37.650	1.530	1.259×10^{-4}	-2.172×10^{-5}	6.833×10^{-6}
HRA-G	305.569	3.351	42.200	-34.754	1.717	3.384×10^{-4}	-8.956×10^{-5}	-6.929×10^{-5}

Figures 7–11 and 7–12 are representative data sets for the actual and modelled results. It can be seen from the figures that the Bouc-Wen model is incapable of capturing the hysteresis loops during the initial test time, while it does begin to capture the hysteresis loops beyond this point; also, the modelled loops underestimate the experimental loops, as shown in Figures 7–11 and 7–12. However, the degradation in the material is clear through the changes in the hysteresis loops where the loop size and shear stress decrease as the time progresses, and this is a good indication that the model predicts the degrading of the materials.

To verify this solution, the predicted stiffness modulus (G^*_z) was calculated using the modelled shear stress values (Z_τ) as in Equation 7–13, and the differences between the experimental and predicted shear modulus were calculated using Equation 7–14.

$$G_z^* = \frac{Z_\tau}{\gamma_0} \quad (7–13)$$

$$D = 100 \times \frac{G^* - G_Z^*}{G^*} \quad (7–14)$$

where: D is the differences between modelled and experimental results as a percentage (%).

The predicted stiffness modulus (G^*_z) was plotted against time and is presented in Figure 7–13. It can be seen the predicted stiffness modulus is always less than the actual stiffness modulus; and the differences fluctuated in behaviour, with decreases at the beginning (Phase I) and increases later, to a decrease at the end of the test, but, in general, they are less than 30%, as shown in Figure 7–14. Generally, the Bouc-Wen model is capable of modelling the hysteresis loops within Phases II and III but performed poorly within Phase I. In addition, the complex shear modulus decreases as test time increased in both the predicted and modelled results, and this is a good indication that the Bouc-Wen model can mimic the degradation in material. To enhance the modelling performance of the Bouc-Wen model, the next step is modelling the hysteresis loops in two stages: Phase I and Phase II-III together; in other words, using strategy-2.

7.8.3.2. Hysteresis Loops for Separated Phases (strategy–2)

The hysteresis loops in strategy-1 were split into two groups: first group Phase I and second group Phase II-III together, as detailed previously in Figure 7–10. The loop data of each group were then used to identify the Bouc-Wen parameters. The same procedure as used in strategy–1 was used to identify the Bouc-Wen parameters in strategy–2 and tabulated in Table 7–2 for Phase I and Phase II-III.

It can be seen that the initial parameters *A* and n for HMA mixes are higher than for DBM mixes; also, they have the same trends as initial stiffness modulus(G_o^*) where they increase as G_o^* increases. In contrast, the trends are not clear for initial parameters β and ψ and the degradation parameters (δ_A, δ_μ and δ_ν).

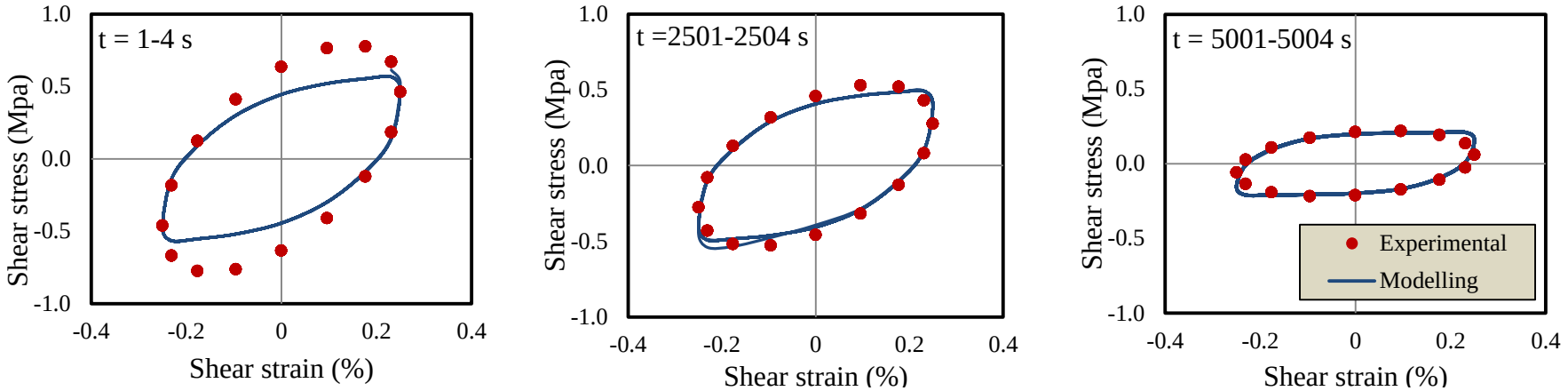

Figure 7- 11: : Experimental and modelled hysteresis loops of HRA-G9 for corresponding time- shear stress.

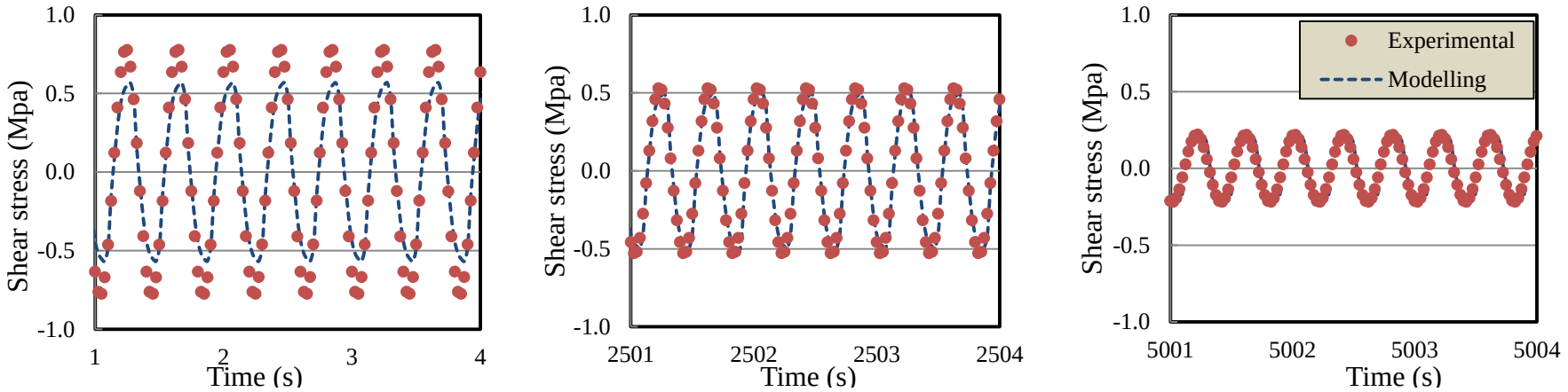

Figure 7- 12: Experimental and modelled stress amplitude at different times for HRA-G9.

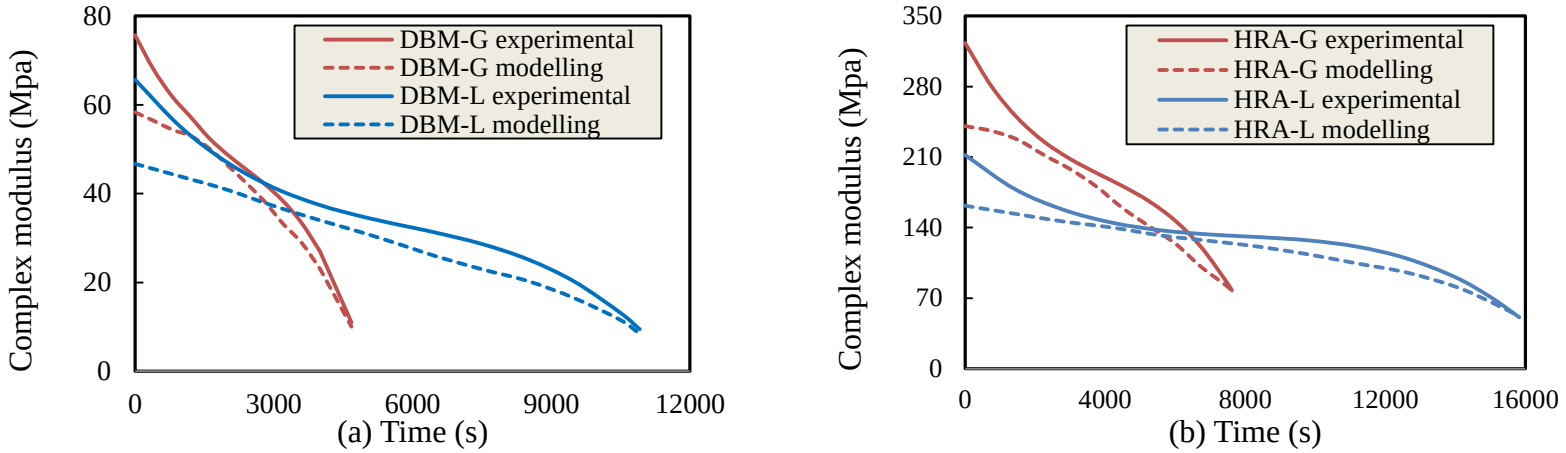

Figure 7- 13: Complex shear modulus against time for experimental and modelling of different mixes: (a) DBM mixes (b) HRA mixes.

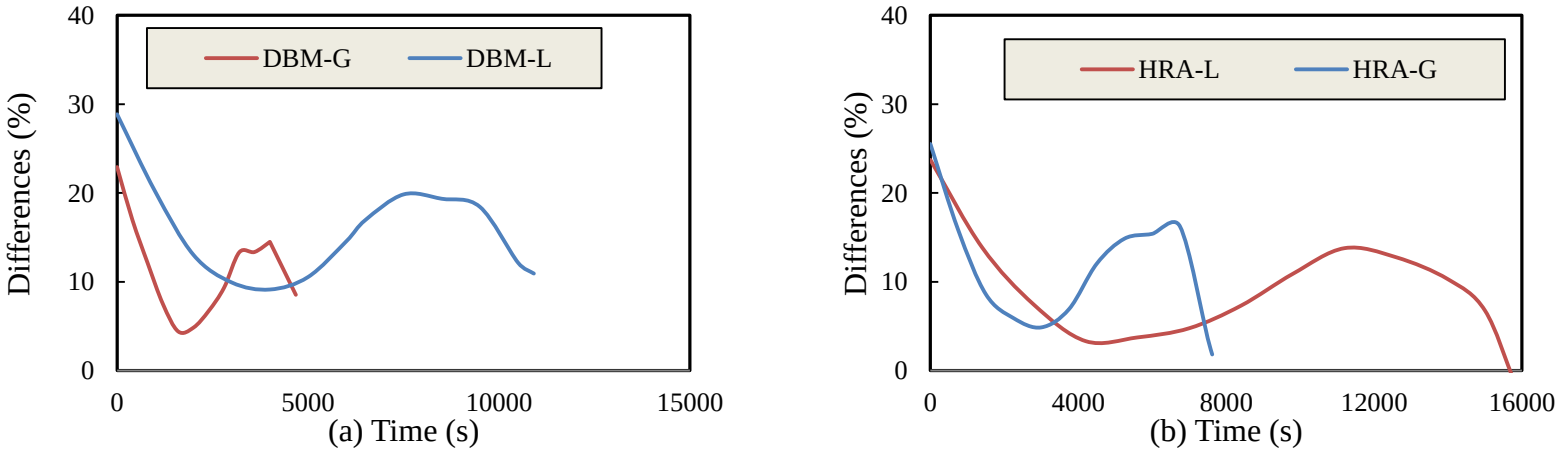

Figure 7- 14: Differences against time of different mixes: (a) DBM mixes (b) HRA mixes.

Table 7– 2: Bouc-Wen model parameters for stratigy-2.

Phase - I								
Mix ID	G_o^* (MPa)	A	β	ψ	n	δ_A	δ_μ	δ_ν
DBM-L	65.685	1.182	17.949	-11.249	0.993	1.369E-03	1.122E-03	1.249E-03
DBM-G	74.121	1.211	62.668	-52.813	1.327	2.097E-03	9.670E-04	2.749E-03
HRA-L	212.115	2.782	50.432	-41.392	1.672	1.137E-05	2.015E-04	5.049E-04
HRA-G	305.569	3.978	46.027	-38.775	1.911	-7.299E-04	5.411E-04	1.158E-03
Phase II-III								
Mix ID	G_o^* (MPa)	A	β	ψ	n	δ_A	δ_μ	δ_ν
DBM-L	44.494	0.777	15.477	-9.424	0.929	1.424E-03	-1.263E-03	-1.302E-03
DBM-G	49.035	0.738	81.902	-70.146	1.314	1.875E-03	-2.107E-03	-1.968E-03
HRA-L	146.389	1.898	64.131	-52.577	1.605	3.460E-04	-1.706E-04	-1.542E-04
HRA-G	233.233	2.975	59.778	-50.385	1.858	6.549E-04	-2.063E-04	-1.785E-04

The consistency between the experimental and modelled loops is demonstrated in Figures 7–15 to 7–18 for phases I and II-III respectively; the Bouc-Wen model is clearly performing better in capturing the hysteresis loops in strategy–2 than in strategy–1. Furthermore, the degradation in the material is clearly shown through the reduction in the sizes and slopes of the hysteresis loops and the decreasing in the shear stress response as test time progresses, as shown in Figures 7–16 and 7–18.

In addition, the verification was highlighted through the relationship of the complex shear modulus with time for the experimental and modelled results, as demonstrated in Figure 7–19. The percentages of differences for all phases were calculated using Equation 7–14 and plotted in Figure 7–20 to demonstrate the variation between modelled and experimental results. This figure shows that the

differences are about 6–12%, and this range is fair compared with the differences resulting from using strategy–1.

Overall, this study emphasises the capability of the Bouc-Wen model in modelling the hysteresis loops for viscoelastic materials tested in fatigue. It is noticeable that each sample has different identified parameters, as shown in Tables 7–1 and 7–2; this is because each sample has different properties, i.e. stiffness modulus and volumetric properties. However, all the identified parameters are within the acceptable ranges as detailed in the references (Ikhouane and Rodellar, 2005;Ismail et al., 2009). Now, this represents a challenge in the prediction or simulation of the hysteresis loops for other samples with different properties using the same identified parameters.

7.8.4. Bouc-Wen Model in Simulation for Strategy–2

In this section, the Bouc-Wen models of strategy–2 were used for simulating the degraded hysteresis loops for other samples tested in fatigue. This aims to test the capability of the Bouc-Wen model to predict the degraded hysteresis loops of the samples tested in fatigue irrespective of the fatigue performance; in other words, to discover whether the fatigue life is long or short. As is known, the variation in the fatigue results of HMA is common, and this is clear from Figure 7–16. Consequently, for this response in fatigue, the Bouc-Wen parameters will differ, as shown in Table 7–3.

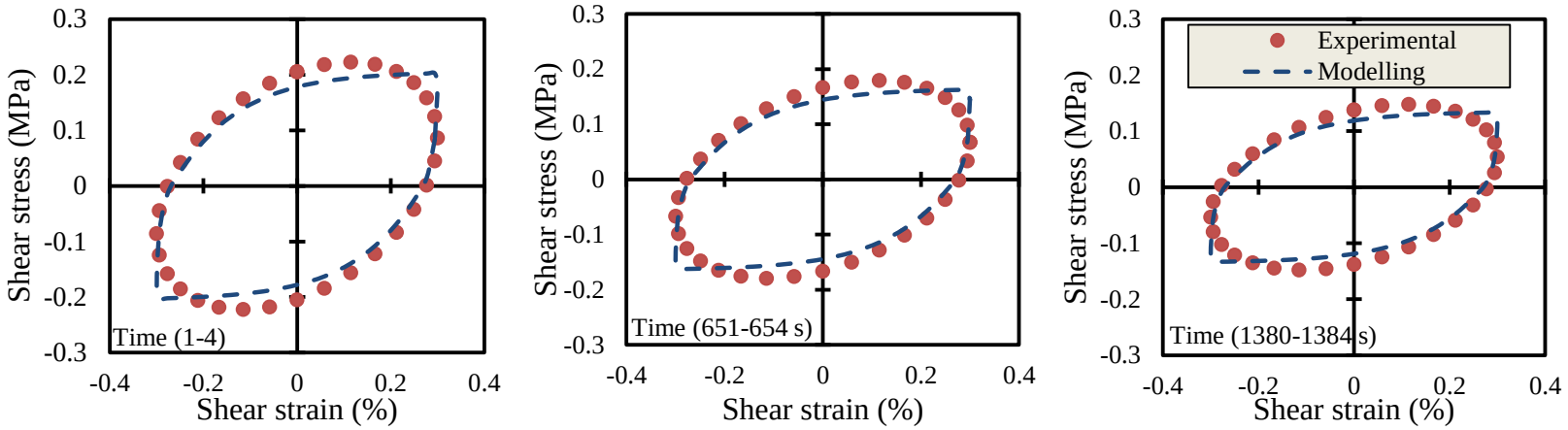

Figure 7- 15: Typical experimental and modelled hysteresis loops of Phase I for DBM-G at corresponding time.

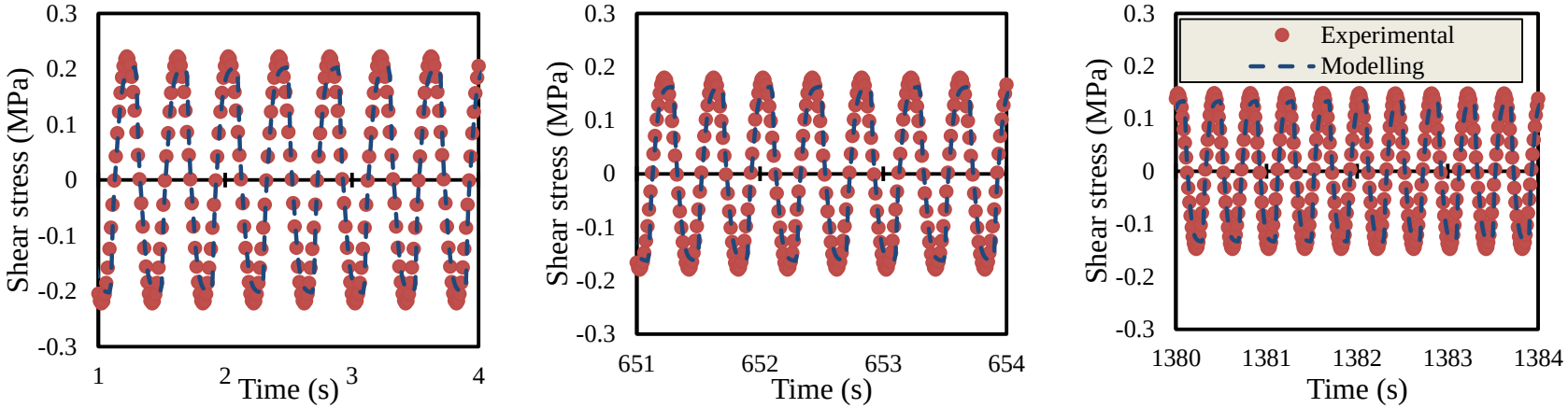

Figure 7- 16: Typical experimental and modelled stress amplitude for Phase I at different times for DBM-G.

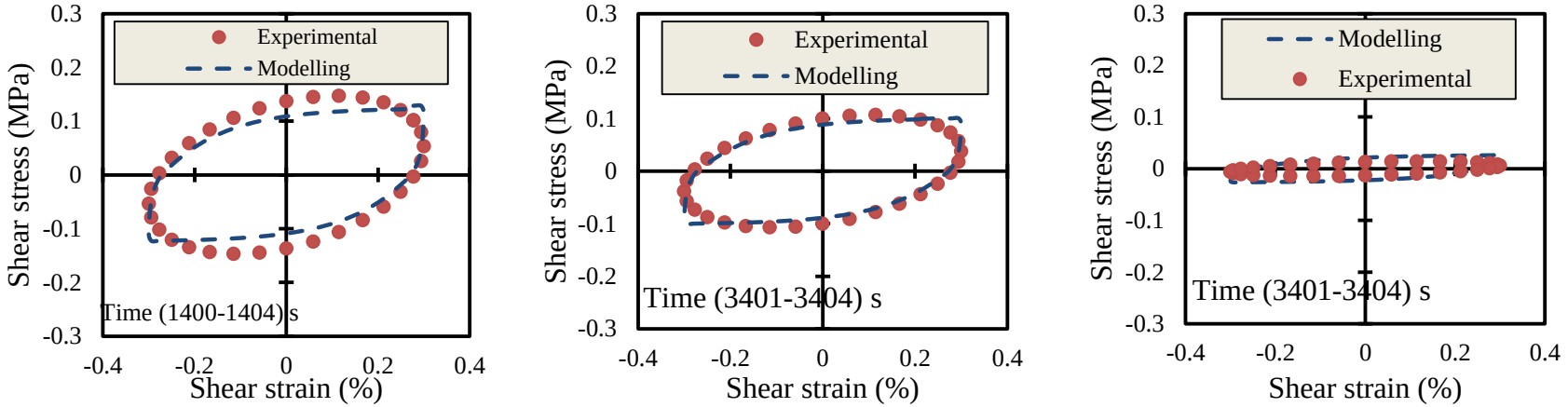

Figure 7- 17: Typical experimental and modelled hysteresis loops of Phase II-III for DBM-G at corresponding time.

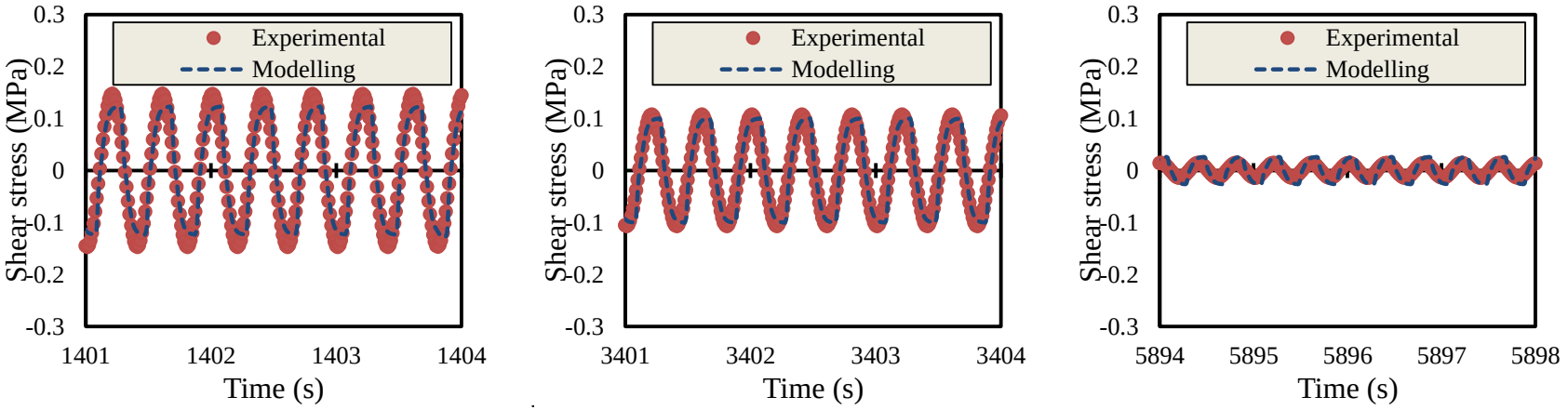

Figure 7- 18: Typical experimental and modelled stress amplitude for Phase II-III at different times for DBM-G.

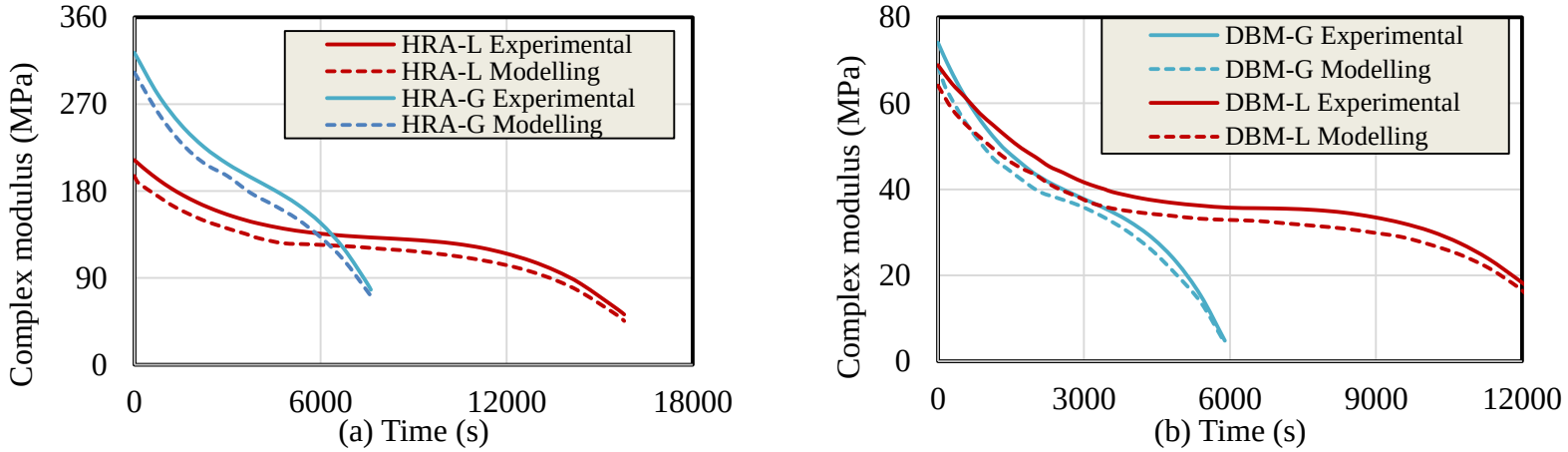

Figure 7- 19: Complex shear modulus against time for experimental and modelling of different mixes: (a) HRA mixes; (b) DBM mixes.

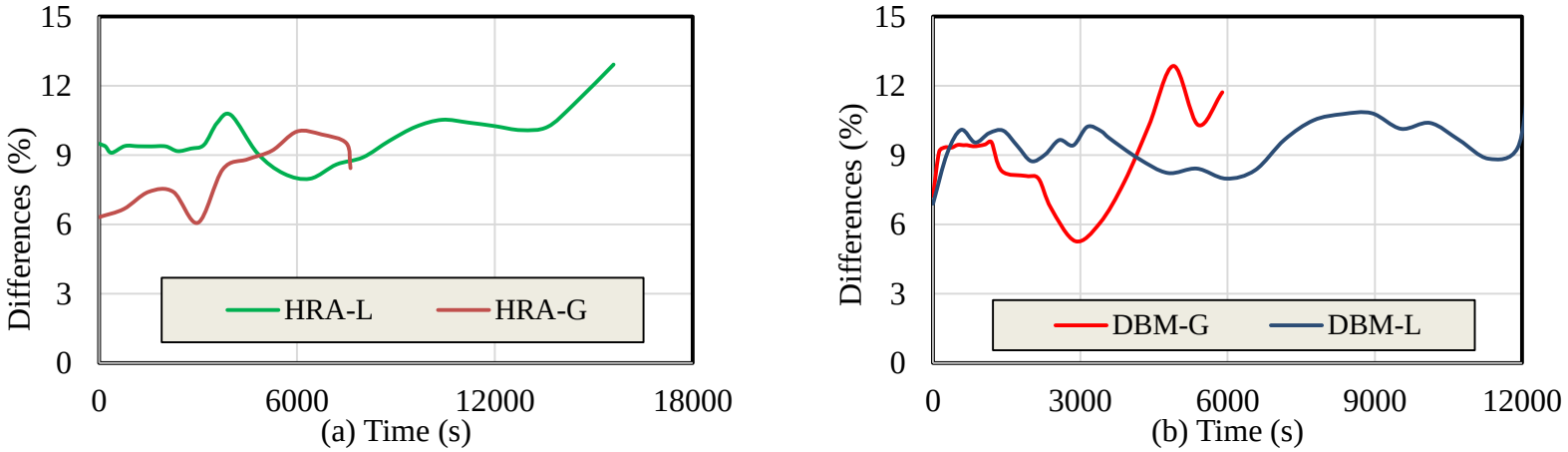

Figure 7- 20: Differences against time of different mixes: (a) HRA mixes; (b) DBM mixes.

Table 7– 3: Bouc-Wen parameters for DBM-G samples

Phase - I								
Sample ID	G_o^* (MPa)	A	β	ψ	n	δ_A	δ_μ	δ_ν
DG-1	78.021	1.268	53.941	-44.384	1.329	3.006E-04	3.839E-03	5.860E-03
DG-2	74.121	1.211	62.668	-52.813	1.327	2.097E-03	9.670E-04	2.749E-03
DG-3	48.464	0.820	77.166	-66.773	1.262	1.704E-04	4.081E-03	6.228E-03
DG-4	73.281	1.197	58.038	-48.265	1.321	2.171E-03	3.401E-04	1.660E-03
DG-5	67.155	1.110	67.873	-57.448	1.330	1.882E-04	2.464E-03	3.854E-03
DG-6	73.092	1.190	55.307	-45.741	1.309	1.143E-03	7.665E-04	1.926E-03
DG-7	75.702	1.247	60.792	-51.346	1.306	2.655E-03	2.585E-03	4.944E-03
DG-8	81.050	1.290	45.294	-36.570	1.289	6.027E-04	6.452E-04	1.493E-03
DG-9	71.514	1.177	83.397	-70.732	1.324	4.619E-05	2.312E-03	3.764E-03
Phase II-III								
Sample ID	G_o^* (MPa)	A	β	ψ	n	δ_A	δ_μ	δ_ν
DG-1	51.552	0.855	63.329	-52.363	1.303	2.201E-03	-2.412E-03	-2.351E-03
DG-2	49.035	0.738	81.902	-70.146	1.314	1.875E-03	-2.107E-03	-1.968E-03
DG-3	37.795	0.619	87.483	-75.571	1.275	1.735E-03	-2.288E-03	-2.190E-03
DG-4	42.091	0.669	78.822	-66.421	1.319	2.359E-03	-2.281E-03	-1.942E-03
DG-5	52.584	0.830	84.480	-72.822	1.329	1.011E-03	-1.066E-03	-1.009E-03
DG-6	48.678	0.775	68.255	-56.681	1.288	1.168E-03	-1.270E-03	-1.280E-03
DG-7	57.165	0.921	65.228	-54.953	1.274	3.400E-03	-2.845E-03	-2.675E-03
DG-8	46.243	0.752	49.208	-39.404	1.219	1.379E-03	-1.717E-03	-1.675E-03
DG-9	46.021	0.751	99.604	-85.011	1.308	1.719E-03	-2.098E-03	-1.999E-03

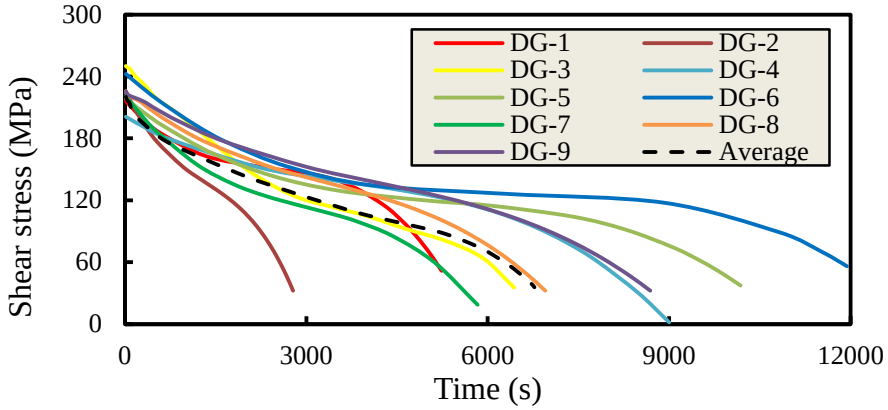

Figure 7- 21: Typical fatigue curves for different DBM-G samples tested in DSR instrument

To study the effect of the changes in the Bouc-Wen parameters, three samples from Figure 7–21 were selected to be used in a simulation. These samples were selected based on the average fatigue curve, where the first selected sample was the closest to the average curve and the other two samples were the extreme samples at the upper and lower points than the average curve, as shown in Figure 7–22. These samples were nominated as (Mid) for the sample closest to average and (U.Mid) and (O.Mid) for the lower and upper samples respectively, as shown in Figure 5–17(a). It is worth noting that there are no trends between the initial complex stiffness modulus (G^*) and fatigue life, as demonstrated in Figure 7–22; there are significant differences in fatigue life among these three samples while the differences in those G* are noteworthy; also, the trends in Phase I defers than in Phase II-III, as shown in Figure 7–22

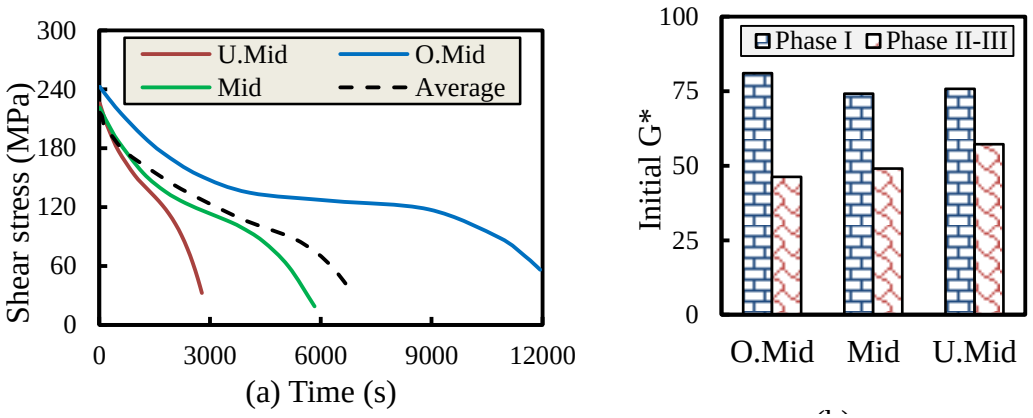

Figure 7- 22: Typical three samples selected for predicting: (a) fatigue curves; (b) initial stiffness modulus.

The identified Bouc-Wen parameters for Mid, O.Mid and U.Mid samples have been plotted in Figures 7–23 and 7–24 for Phase I and Phase II-III. The non-degraded parameter, A, behaves as the initial G* in both Phases I and II-III, as shown in Figure 7–23(a); in contrast, the random behaviour of the other non-degraded parameters, n, ψ and β, is clear, as shown in Figure 7–23. Regarding the degraded parameters δ_A, δ_μ and δ_ν, it is clear these deltas have an inverse relationship with fatigue life for Phase I and δ_A for Phase II-III; for example, the sample O.Mid has the longest fatigue life and the deltas are the lowest while U.Mid has the shortest fatigue life and the deltas are higher values, as demonstrated in Figure 7–24. At the same time, δ_μ and δ_ν in Phase II-III behave inversely to those in Phase I; for example, O.Mid has the longest life is the higher values than U.Mid, as shown in Figure 7–24. This random behaviour in some parameters will reflect on and effect the simulation, as shown in the next sections.

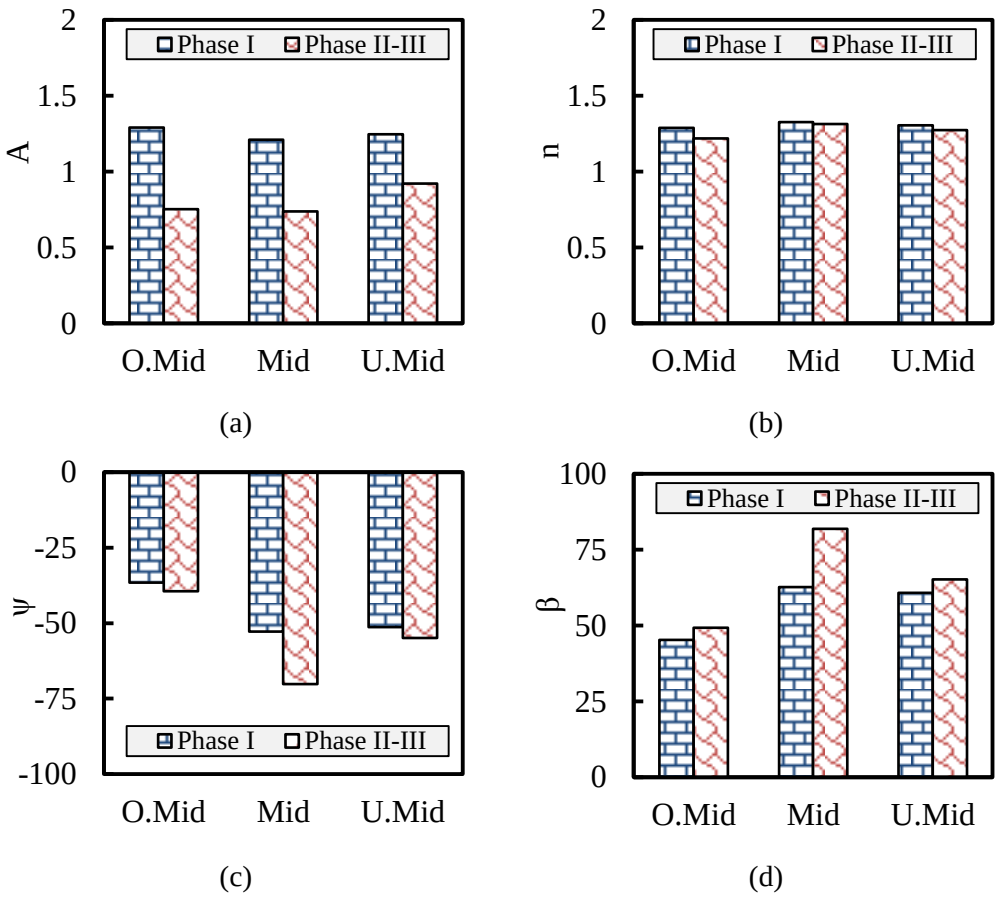

Figure 7- 23: The non-degraded identified Bouc-Wen parameters for Mid, U.Mid and O.Mid samples.

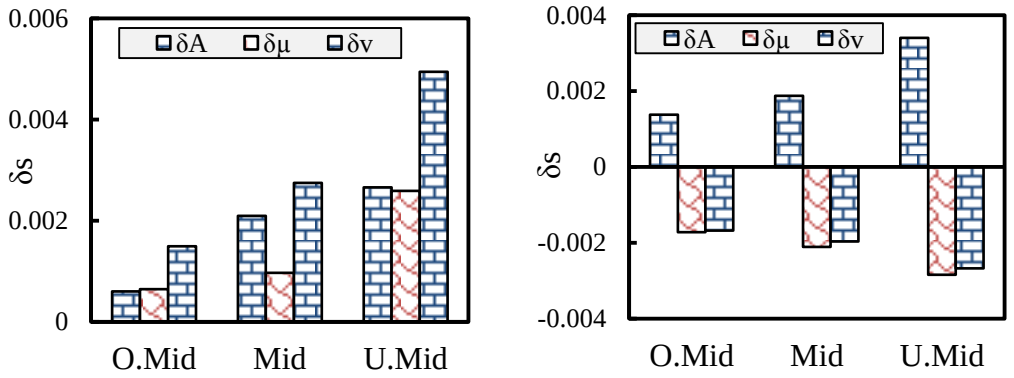

(a) (b)

Figure 7- 24: The degraded identified Bouc-Wen parameters for Mid, U.Mid and O.Mid samples: (a) Phase I and (b) Phase II-III.

In the simulation, the Bouc-Wen model of the Mid sample was used to simulate the degraded hysteresis loops of the U.Mid and O.Mid samples, and the method was repeated for the U.Mid and O.Mid samples, as explained in the following sections.

7.8.4.1. Simulation Using the Mid Model

The Bouc-Wen model of the Mid sample was used in the simulation with the U.Mid and O.Mid samples. Figure 7–25 demonstrates the experimental and simulated hysteresis loops of the U.Mid sample with their corresponding stress responses at different times for Phase I and Phase II-III. It is clear that there is a convergence between the experimental and simulated hysteresis loops in Phase I, but this convergence changed to divergence as time progressed, to make the simulation overestimation than the experimental, especially in Phase II-III, as shown in Figure 7–25. This is expected because the Mid sample is longer than the U.Mid sample, so the Bouc-Wen model will simulate the U.Mid loops to be closest to the Mid sample, which has a longer life than the U.Mid sample. However, the significant difference between the simulated and experimental results in Phase I was at minimum because the fatigue performance of both samples is the same within this phase, as shown in Figure 7–25. Figure 7–26 shows the simulated and experimental hysteresis loops of the O.Mid sample with their stress response at the corresponding time for Phase I and Phase II-III.

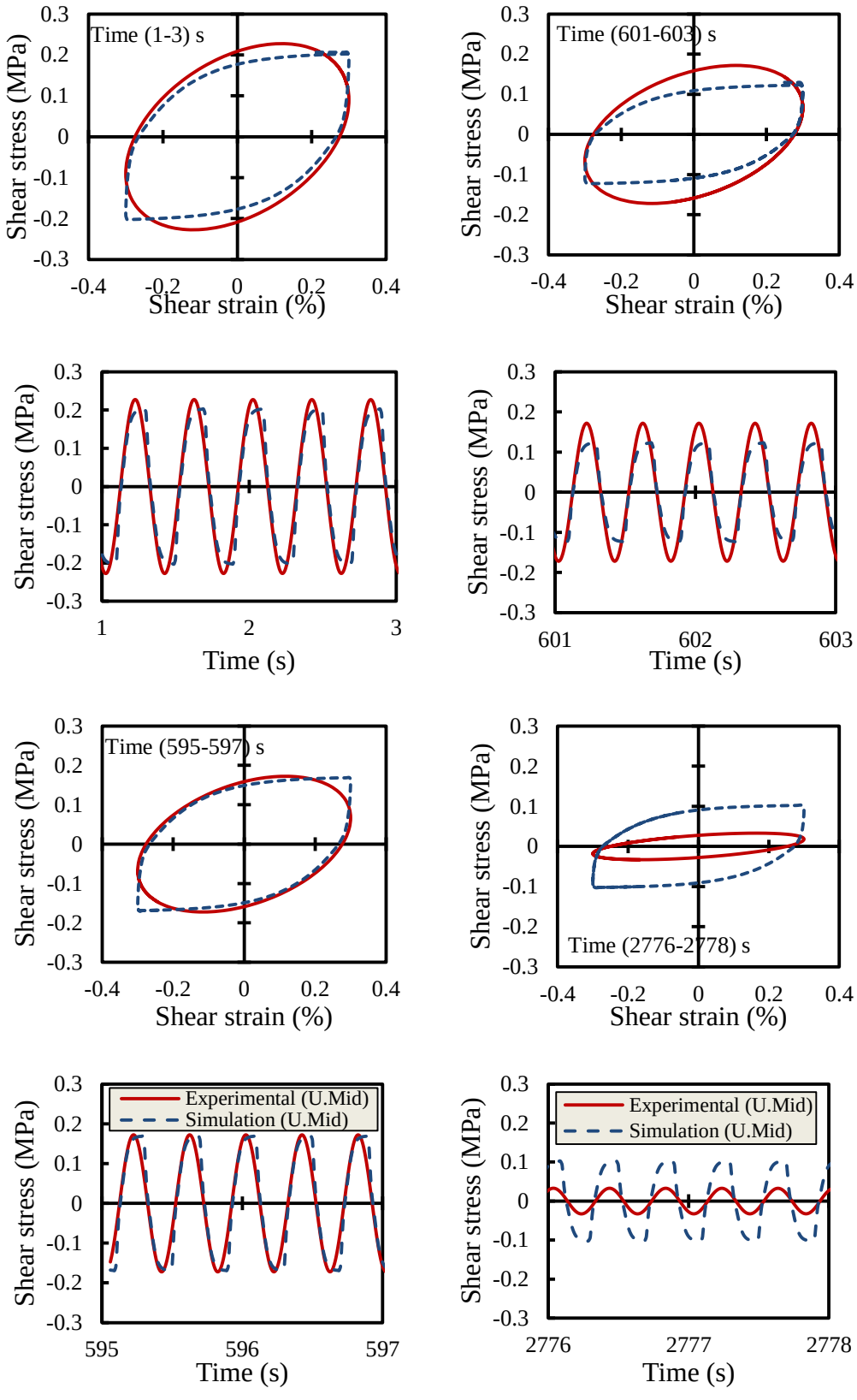

Figure 7- 25: U.Mid sample simulation using Bouc-Wen model of Mid sample for: (a) Phase I and (b) Phase II-III.

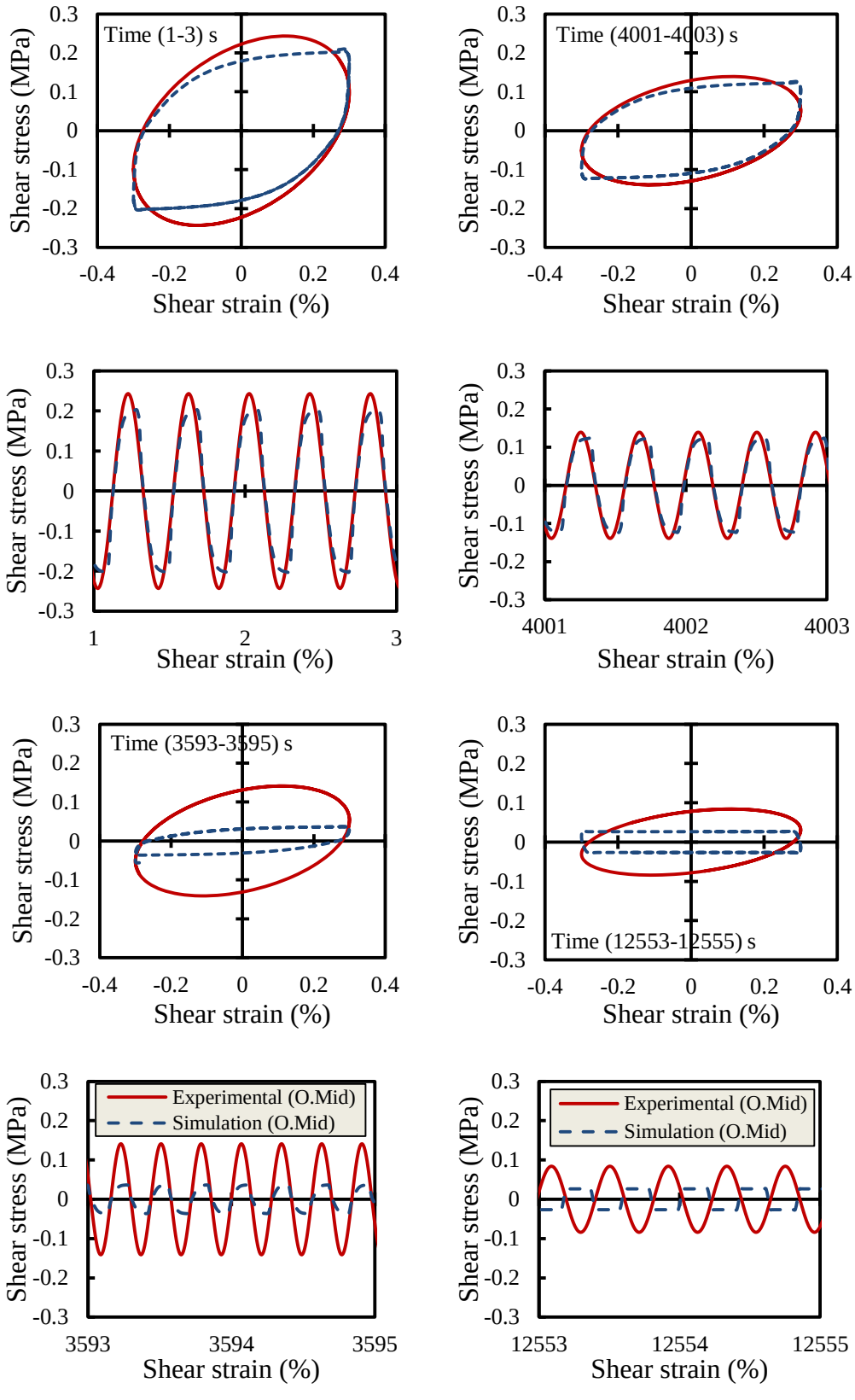

Figure 7- 26: O.Mid sample simulation using Bouc-Wen model of Mid sample for: (a) Phase I and (b) Phase II-III.

In addition, it can be seen that the convergence between simulation and experimental developed to be divergence with time progression, producing under estimation experimental hysteresis loops for both Phase I and Phase II-III. This response is because the Mid sample is shorter than the O.Mid one, and using the Bouc-Wen model in Phase I of the Mid sample will simulate the hysteresis loops of Phase I of the O.Mid one, which is longer than Phase I of the Mid sample; while the Phase II-III model of Mid will simulate Phase II-III for O.Mid, which starts at the mid of Phase II-III for Mid and continues to the end of the O.Mid sample.

More clarification is provided in Figure 7–27, which shows the relationship between complex stiffness modulus against time for simulated and experimental results of Phase I and Phase II-III. Overall, it can be seen that the simulation was very poor and under the prediction for the O.Mid sample while for the U.Mid in Phase I it was good, but was very poor in Phase II-III as well. On the other hand, there is no continuity in the simulated fatigue curves (dash-lines) where they converge at the beginning of Phases I and II and diverge quicker later; also, the degradation of the U.Mid sample in Phase II-III is barely constant, as shown in Figure 7–27.

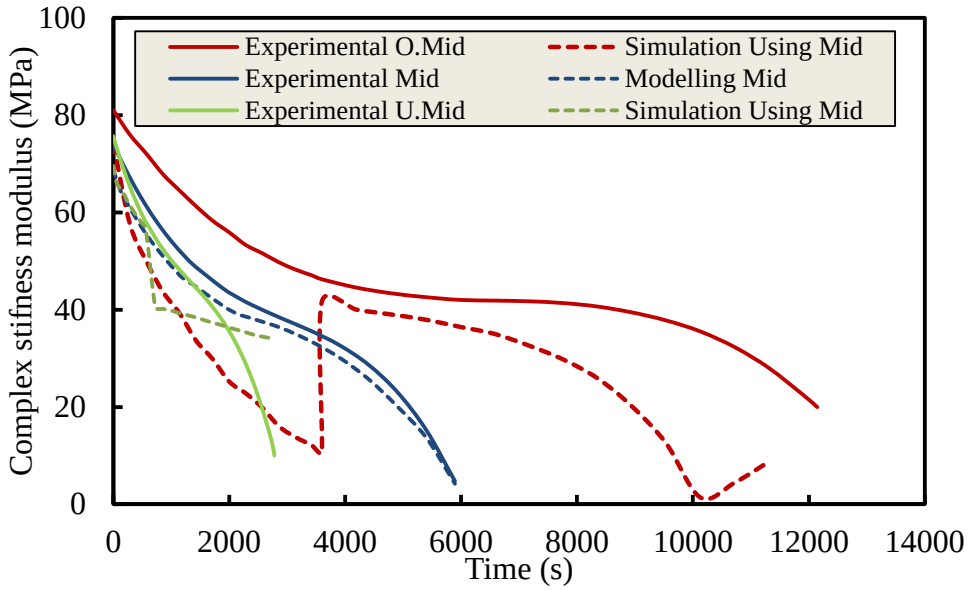

Figure 7- 27: Complex stiffness modulus against time for experimental and modelled O.Mid and U.Mid samples simulated based on Mid sample.

7.8.4.2. Simulation Using the O.Mid Model

The Bouc-Wen models of the O.Mid samples were used to simulate the degraded hysteresis loops of the Mid and U.Mid samples and presented in Figures 7–28 and 7–29. It can be seen that the simulated hysteresis loops are over-predict of the experimental data beyond the initial hysteresis loops for Phase I and Phase II-III in both Mid and U.Mid samples; this is expected because the O.Mid sample has a longer fatigue life than the other samples, irrespective of the variations in the identified Bouc-Wen parameters, which are clear, as detailed previously. On the other hand, the results revealed that the O.Mid model is incapable of simulating the degradation within Phase II-III, which is hardly constant; while the degradation is clear within Phase I but significantly less than the experimental results, as shown in Figure 7–30.

7.8.4.3. Simulation Using the U.Mid Model

In this section, the Bouc-Wen model of U.Mid sample was also used to simulate the degraded hysteresis loops for the Mid and O.Mid samples; and the outcomes are demonstrated in Figures 7–31 and 7–32. As expected, the simulated hysteresis loops were under-predict of the experimental loops beyond the initial loops for Phase I and Phase II-III in both the Mid and O.Mid samples. This is because the U.Mid sample is quite a bit shorter than the Mid and O.Mid samples. The worst point in the U.Mid model is that the solution did not exist at the end of the fatigue life, where the solution stopped at around 4400s and 8500s for Mid and O.Mid respectively, as shown in Figure 7–33. However, the degradation was clear in the simulations but the expectations were still poor and far away from the target; moreover, the fatigue curves were degrading faster and were discontinuous, as shown in the Figure 7–33. The typical discussions presented in the previous sections were on the DBM-G samples, but this behaviour is the same for all other mixes. It is clear that the Bouc-Wen model is more sensitive to the changes in its parameters as a consequence of the variation in the fatigue performance; this is reflected in its performance. In the next section an attempt has been made to use an artificial neural network (ANN) to predict the Bouc-Wen parameters to enhance the performance of this model.

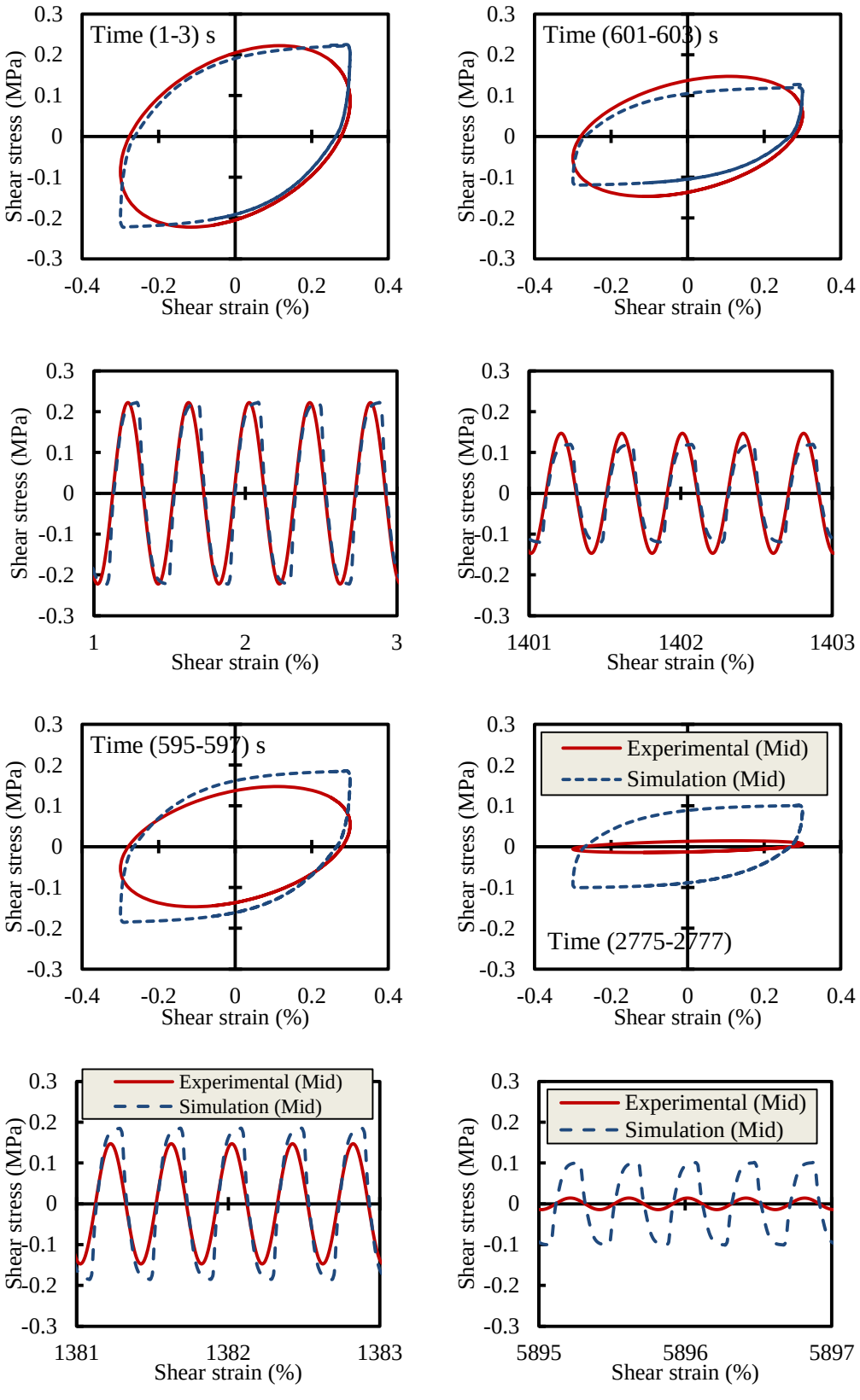

Figure 7- 28: Mid sample simulation using Bouc-Wen model of O.Mid sample for: (a) Phase I and (b) Phase II-III.

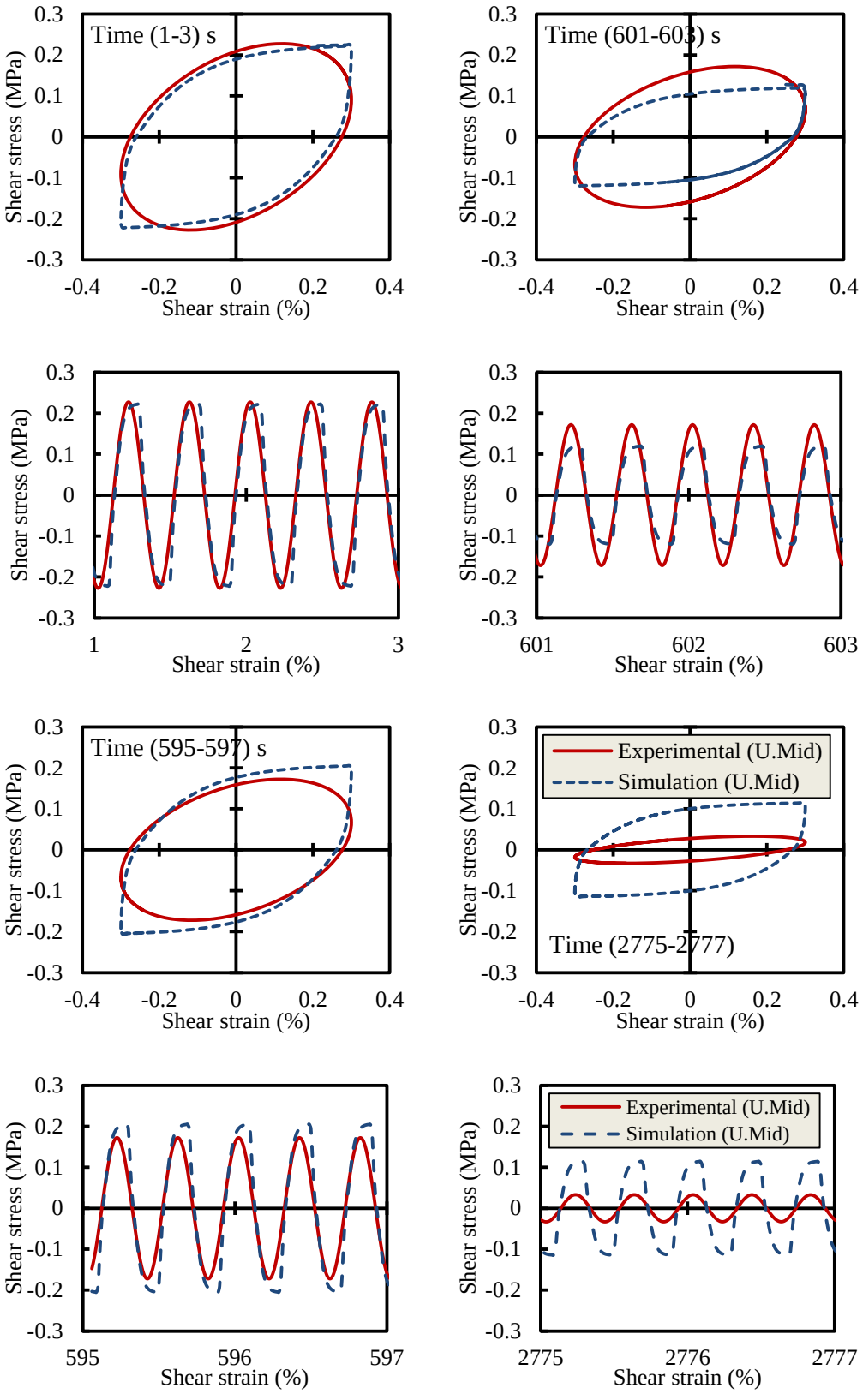

Figure 7- 29: U.Mid sample simulation using Bouc-Wen model of O.Mid sample for: (a) Phase I and (b) Phase II-III.

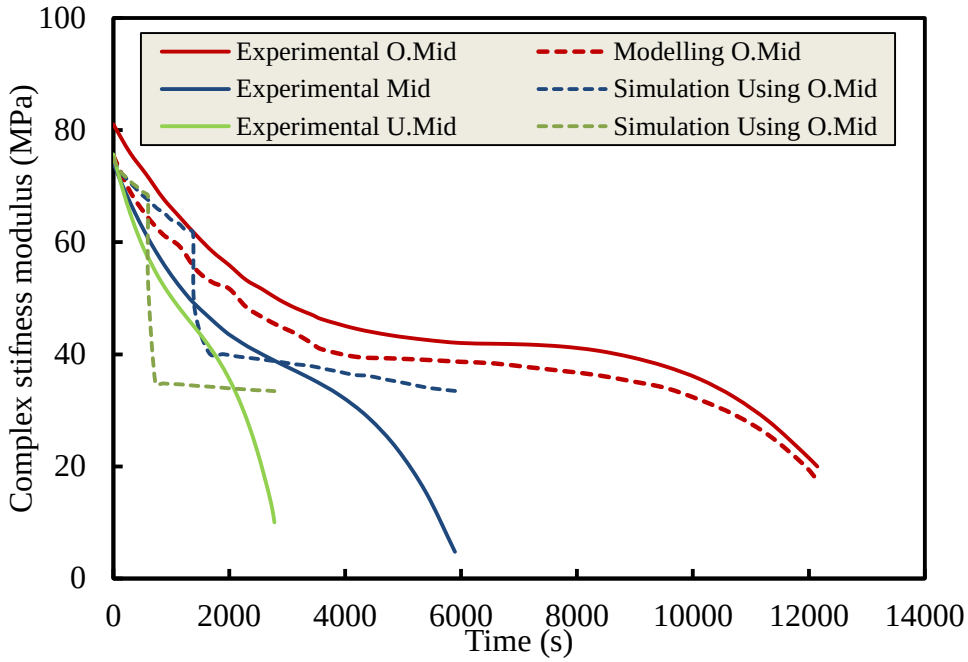

Figure 7- 30: Complex stiffness modulus against time for experimental and modelled of Mid and U.Mid samples simulated based on O.Mid sample.

7.8.5. Improving Bouc-Wen Model Using ANN Technique

7.8.5.1. Non-Degraded Parameters for Phases I and II-III

Phase-I represents a rapid degrading in materials, but it is difficult to determine the terminal point of this phase when Phase II starts. Therefore, excellent correlations were revealed between the non-degraded parameters of Phase I with Phase II-III, as shown in Figures 7–34 and 7–35. It is worth noting that parameters ψ and β take the same trends in distribution along the fitting equations; where, when both fitting equations are extended they are barely identical, as shown in Figure 7–35. However, the fitting equations for both are excellent, but the fitting equation of all data when put together improved significantly to be highly excellent, about 0.99. These fitting equations (Equations 7–15 to 7–17) of non-degraded parameters were used in simulations as seen later in the following sections.

$$A_{II-III} = 0.762A_I - 0.159 \quad (7–15)$$

$$n_{II-III} = 0.976n_I - 0.004 \quad (7–16)$$

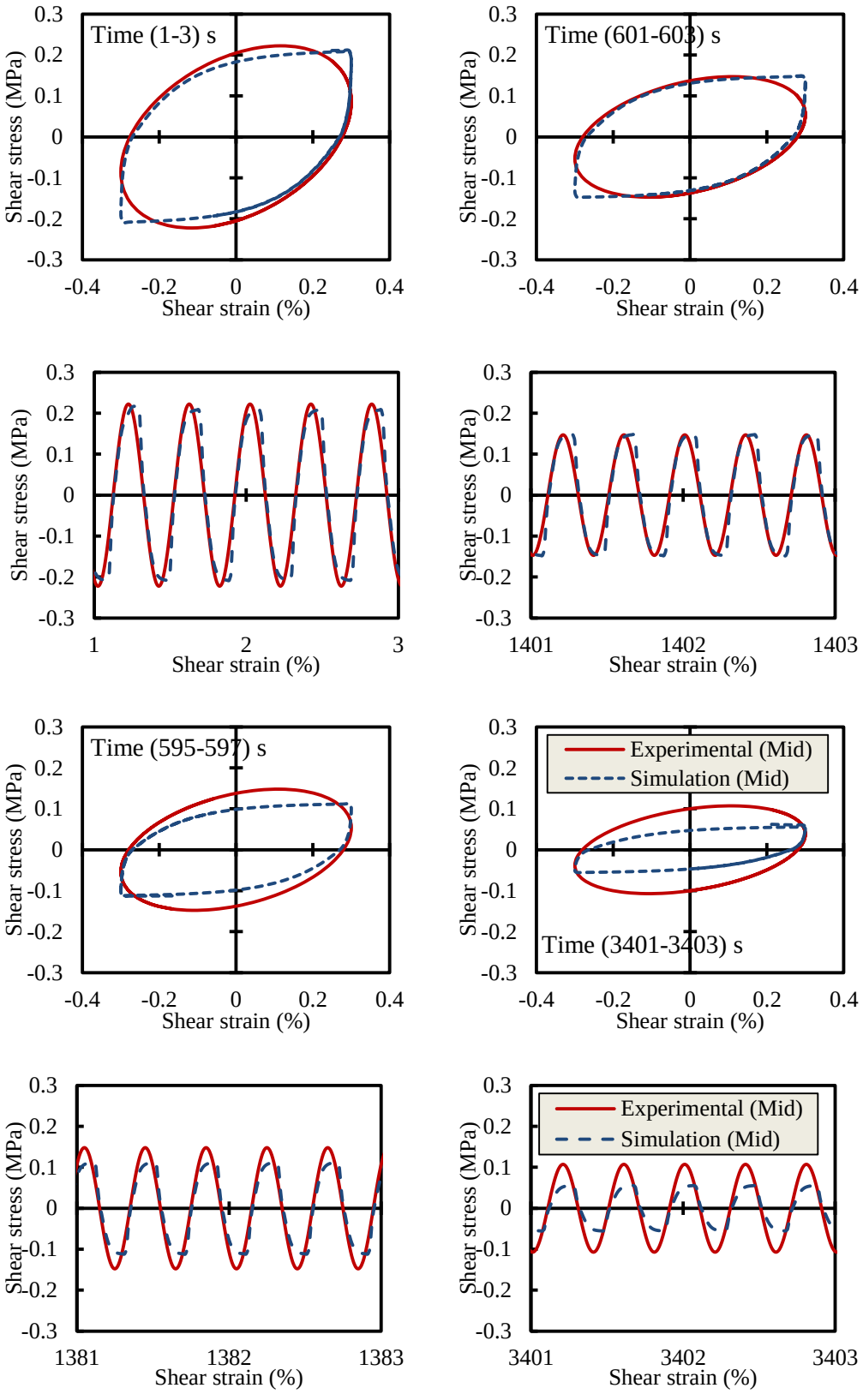

Figure 7- 31: Mid sample simulation using Bouc-Wen model of U.Mid sample for: (a) Phase I and (b) Phase II-III.

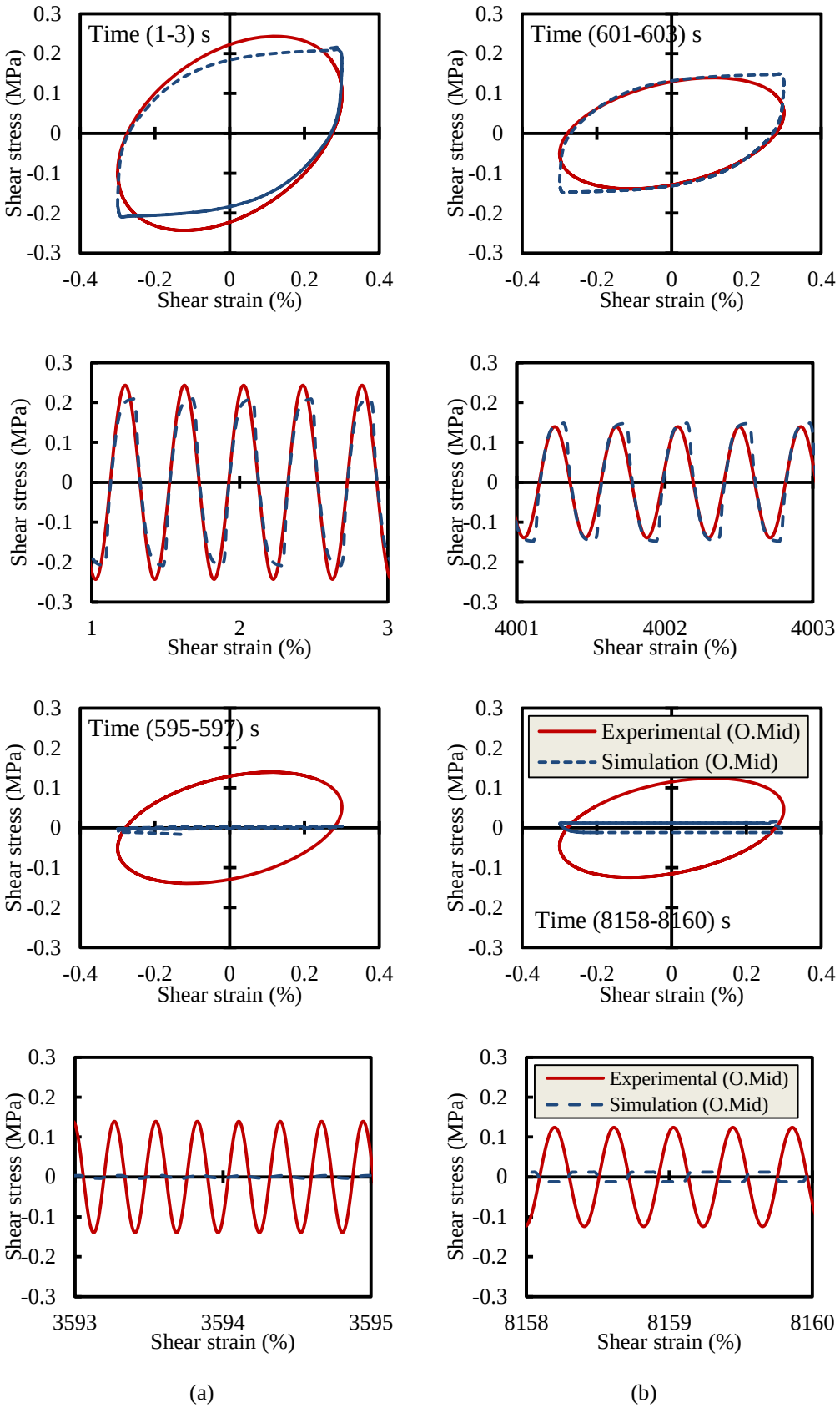

Figure 7- 32: O.Mid sample simulation using Bouc-Wen model of U.Mid sample for: (a) Phase I and (b) Phase II-III.

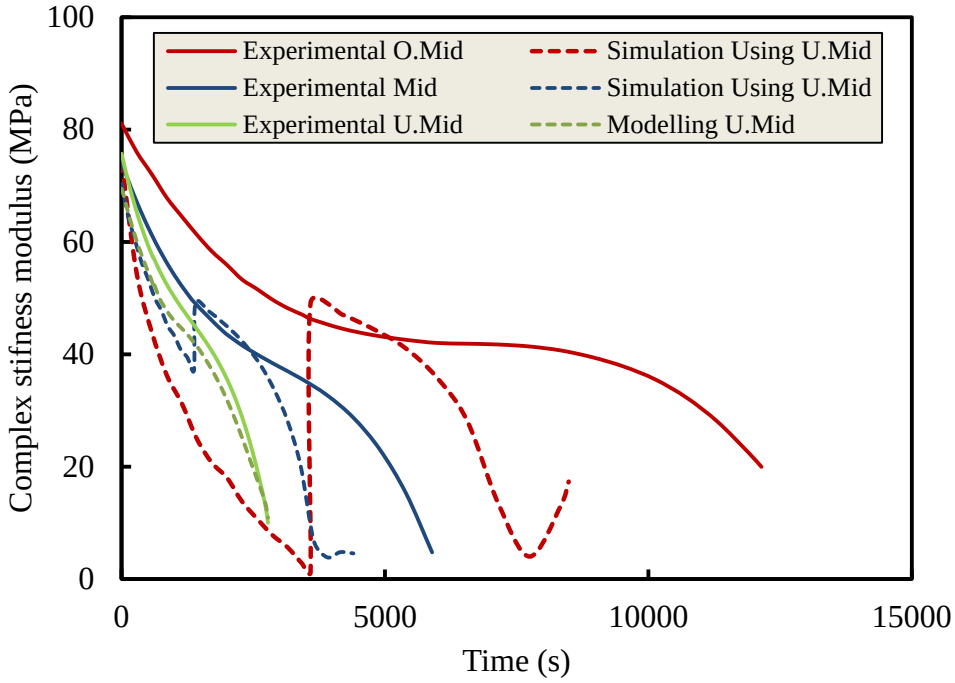

Figure 7- 33: Complex stiffness modulus against time for experimental and modelled of Mid and O.Mid samples simulated based on U.Mid sample

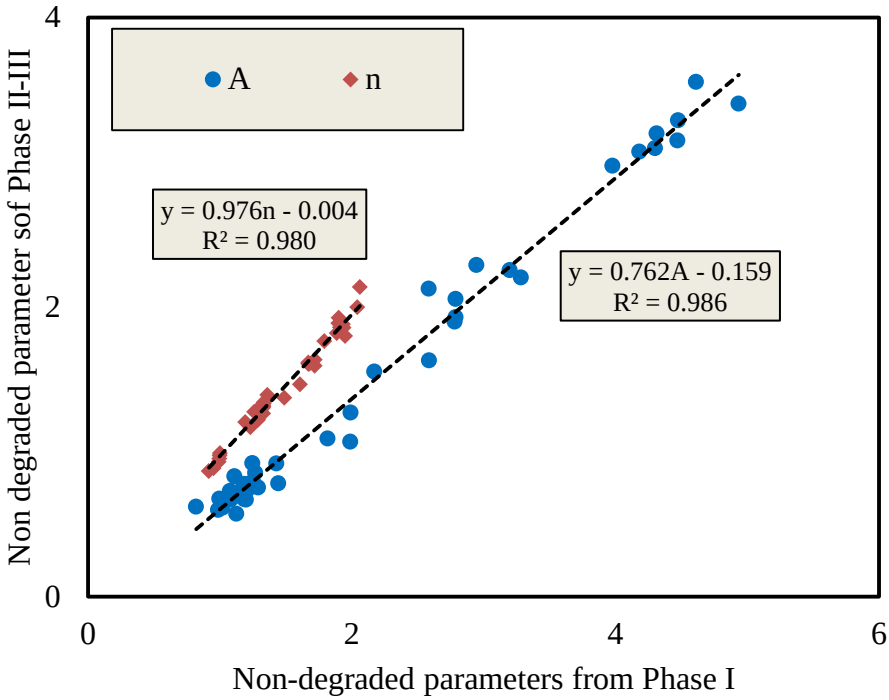

Figure 7- 34: Non-degraded parameters (A and n) of Phase II-III as related to Phase I parameters.

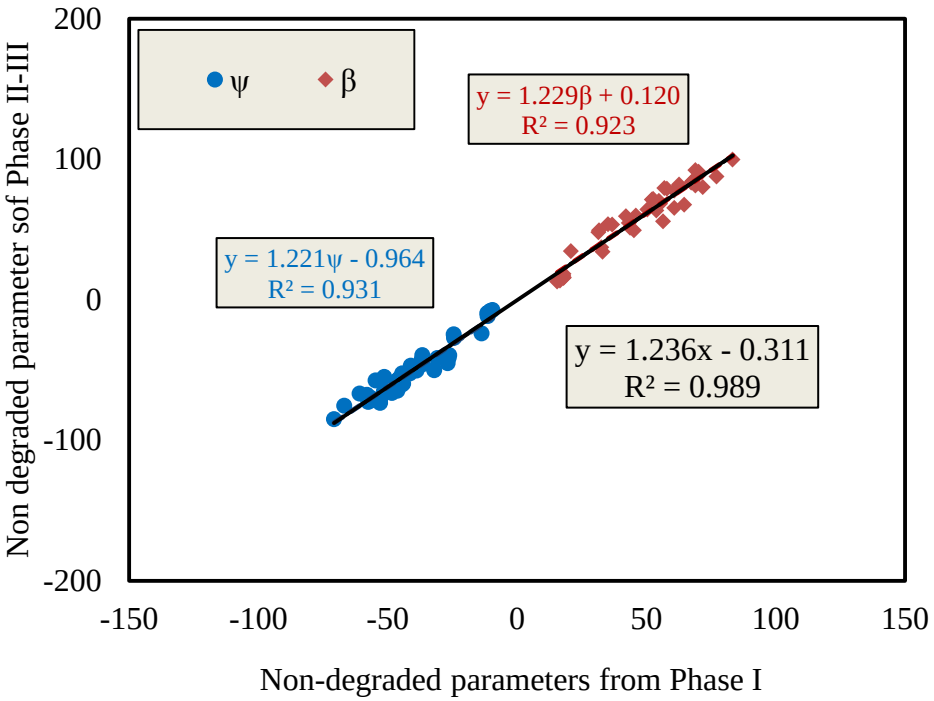

Figure 7- 35: Non-degraded parameters (β and ψ) of Phase II-III as related to Phase I parameters

$$(\beta \; or \; \psi)_{II-III} = 1.236 \; (\beta \; or \; \psi)_I - 0.311 \qquad (7\text{–}17)$$

7.8.5.2. Using ANN in Predicting Degraded Bouc-Wen Parameters

HMA is a viscoelastic composite material where the properties differ from one sample to another and this variation in properties impacts on the fatigue performance; at the end, these variables significantly affected the Bouc-Wen model's performance and parameters, as shown previously.

Herein, an ANN technique was used to develop a model for predicting Bouc-Wen parameters. The process starts from identifying the seven Bouc-Wen parameters for all the tested samples; also, the properties of these samples were collected including: initial complex stiffness modulus (G_o^*), initial phase angle (δ_o), shear stress amplitude (τ), relaxation test coefficients (G_1, m), bulk density (G_{bulk}) and air voids (AV%). Then, the set of data were ready for developing the ANN model; these data were divided randomly into two different groups: one set of the data for training and the other for testing. A multi-layered ANN consisting of input layers, two hidden layers and an output layer was used in modelling; typical ANN

architecture is presented in Figure 7–36. More details about ANN are founded in Chapter V.

The variables in the input layer, as shown in Figure 7–36, are: G_o^*, δo, τ, Gbulk, AV%, G_1 and m. The input layer included the non-degraded parameters as well; these parameters can be identified using the non-degrading Bouc-Wen model (Equation 7–2) for the initial hysteresis loops and used as input variables in the input layer. The objective of the ANN model is to estimate the degraded parameters, δ_A, δ_μ and $\delta_{v,}$ as shown in Figure 7–36. It should be noted that the non-degraded parameters, A, β, ψ, and n, of Phase II-III were calculated using Equations 7–15 to 7–17, as shown previously, in order to be used in the input layer of the ANN model for Phase II-III to predict the degraded parameters of this phase. The architecture of the neural network was selected based on the highest R^2; it was found that the best ANN architecture for developing this model involved two hidden layers with 15 neurones in each layer.

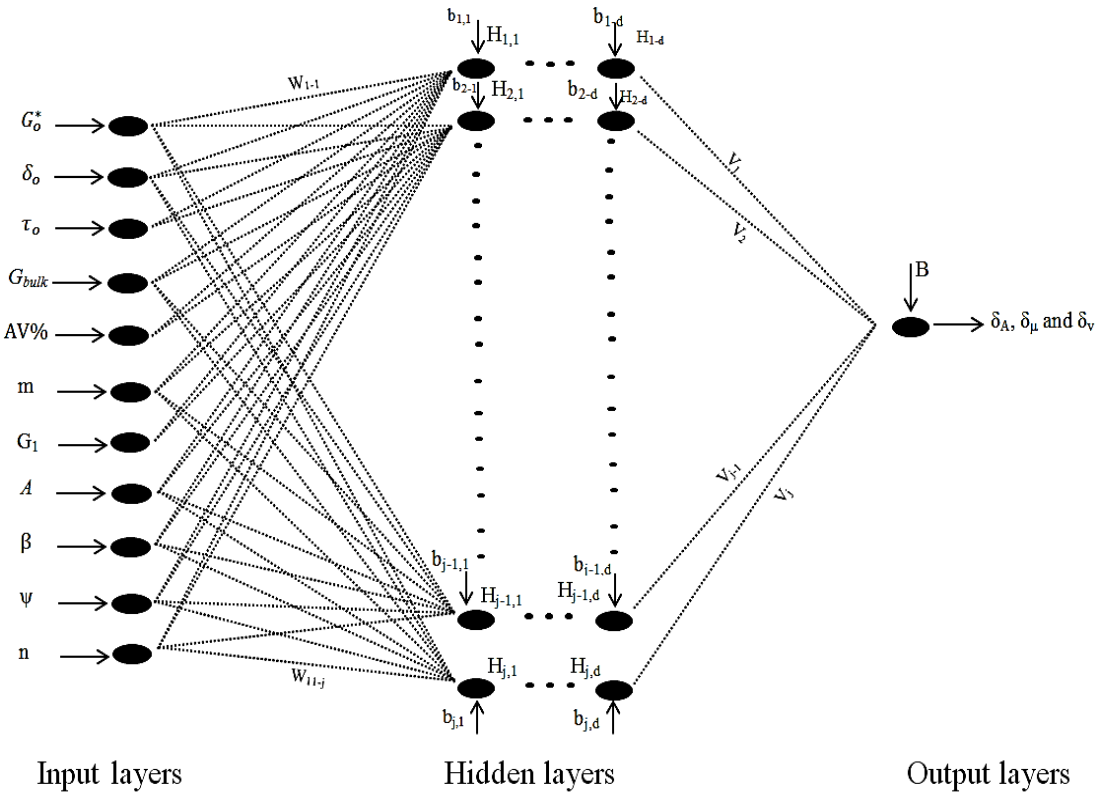

Figure 7- 36: A typical architecture shape for multi-layered ANN to predict degraded parameters: δA, δμ and δv.

In order to develop the ANN model, the data were divided into two main groups: the first group was subdivided into two random sets: a set for training and a set for testing. The second group included five samples; this group was used in the simulation for predicting the degraded parameters using their properties, as shown in Figure 7–37. This aims to produce samples with their degraded parameters to be used later in the Bouc-Wen model to simulate the degraded hysteresis loops, where the random groups make it impossible to obtain samples with their degraded parameters.

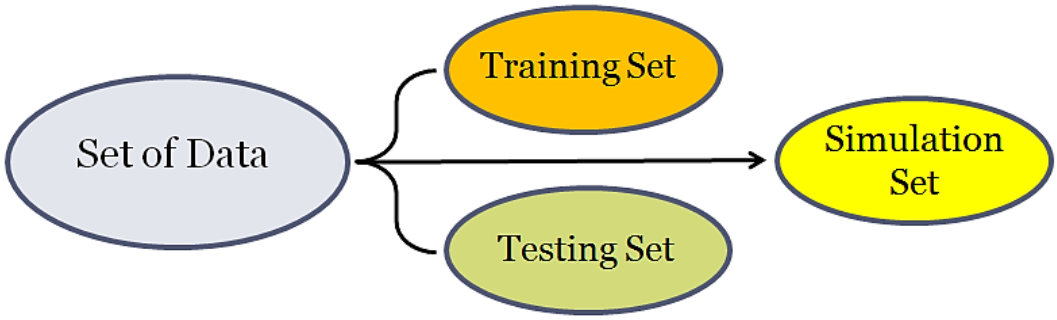

Figure 7- 37: : Data sets for ANN model.

The relationships between the actual and predicted degraded Bouc-Wen parameters of Phase-I and Phase II-III are presented in Figures 7–38 and 7–39. The prediction performance of the trained neural network is acceptable, as is clear from two aspects: firstly, the high correlation in terms of R^2 between actual and predicted values which is calculated for the tested and predicted sets of data of all degraded parameters is good to excellent; secondly, the predicted values of the simulation group are distributed around and nearby the line of quality. Overall, the ANN model demonstrates capability in predicting the degraded parameters based on the input variables in the input layer.

However, this is not the end of story; in the next section the predicted degraded parameters will be used to simulate the degraded hysteresis loops of the five samples using the Bouc-Wen model. This reflects the efficiency of the ANN model in predicting the degraded parameters; moreover, it gives an indication of the sensitivity of the Bouc-Wen model to any small changes in the parameters.

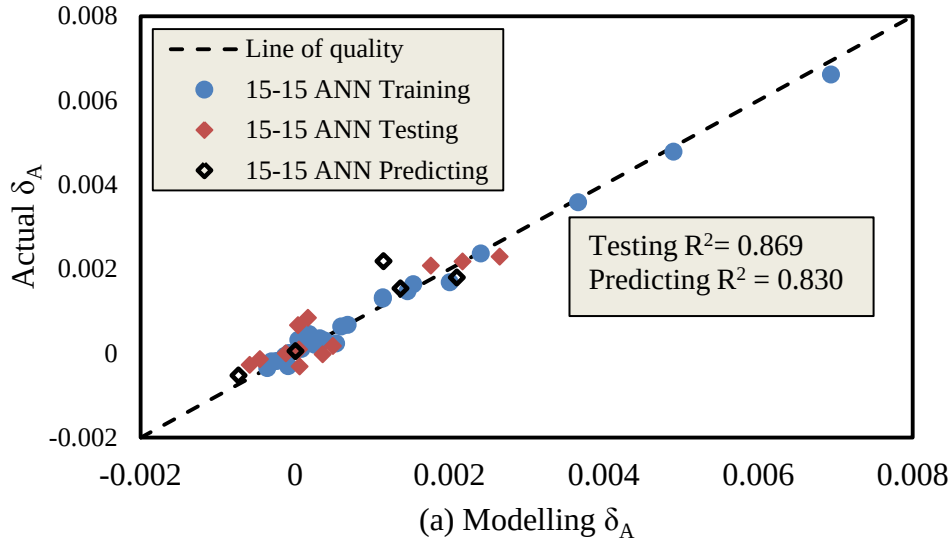

(a) Modelling δ_A

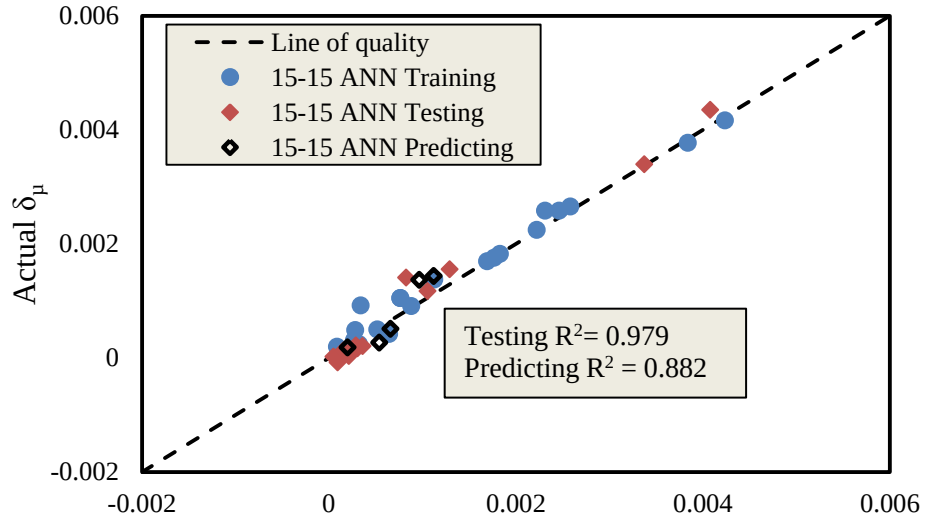

(b) Modelling δ_μ

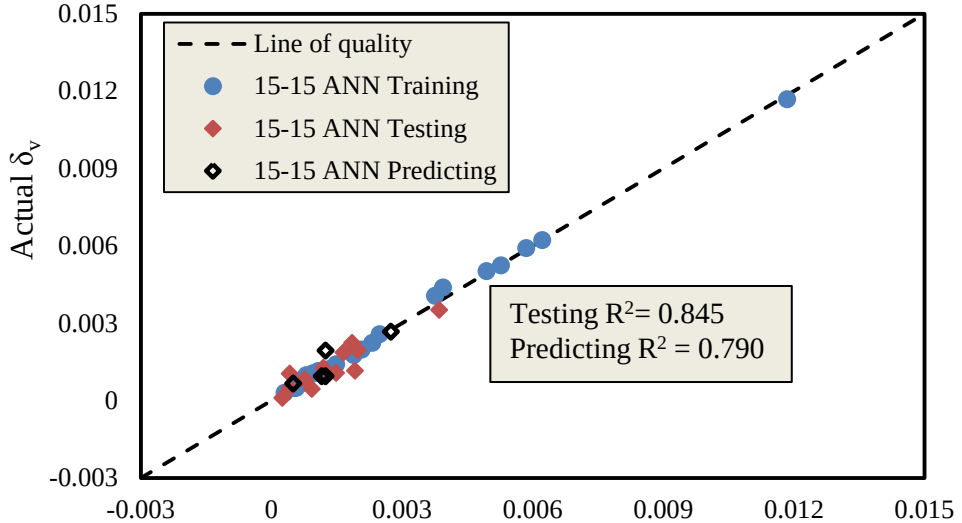

(c) Modelling δ_v

Figure 7- 38: Actual against predicted degraded parameters for Phase I: (a) δA, (b) δμ and (c) δv.

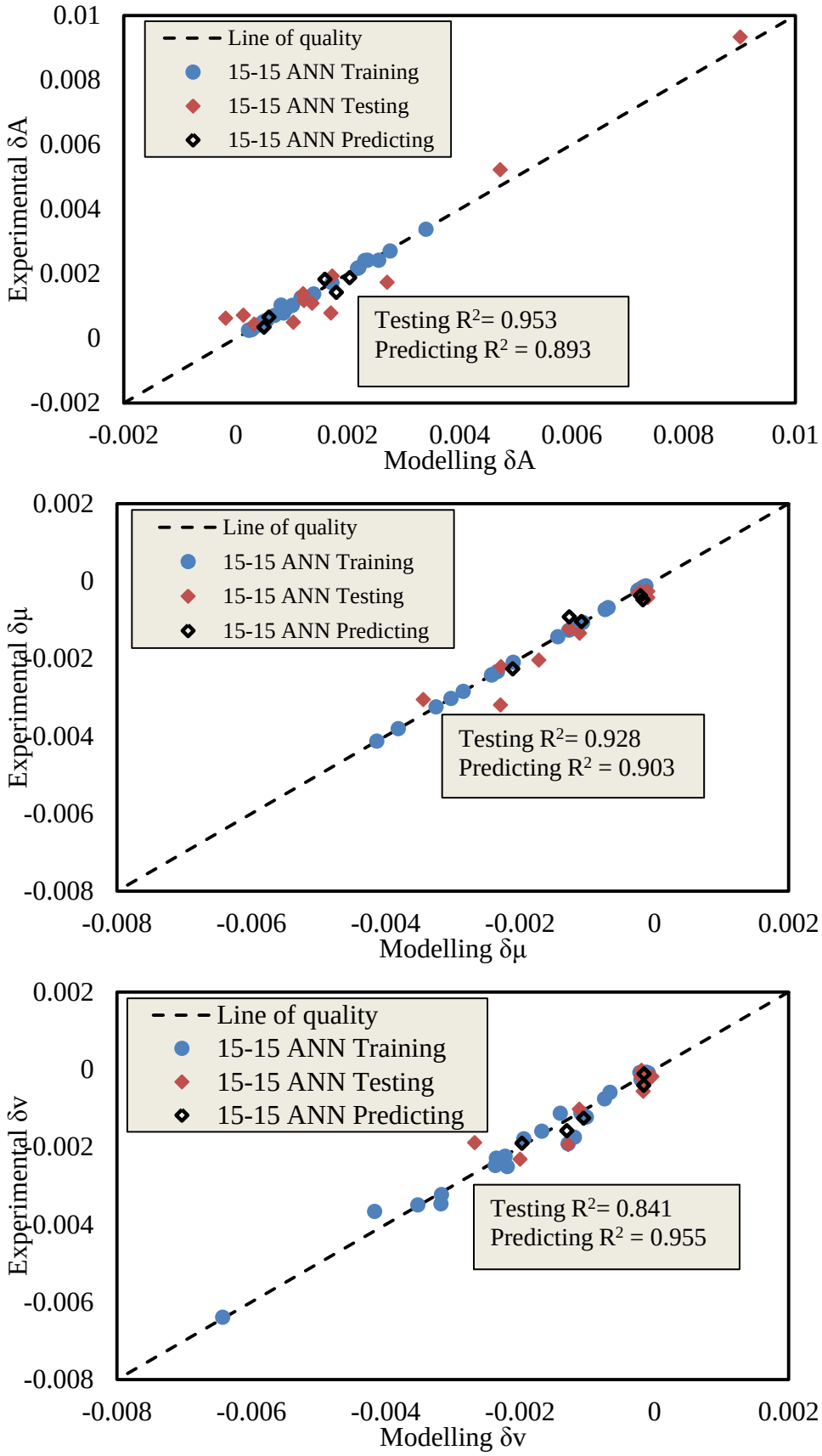

Figure 7- 39: Actual against predicted degraded parameters for Phase II-III: (a) δA, (b) δμ and (c) δv.

7.8.6. Accuracy of the ANN models

Herein, the verification of the ANN model's accuracy was examined, where the predicted degraded parameters, using the ANN model, and non-degraded parameters, using Equation 7–15 to 7–17, were used in the simulation using the Bouc-Wen model. The complex stiffness modulus was calculated for the output of the Bouc-Wen model, as detailed previously, and compared with the actual modulus; this gives an indicator of the accuracy of the ANN model in prediction.

Figure 7–40 demonstrates the complex stiffness modulus for experimental, G^*, and modelled, G^*_z, samples, and differences, D, against time for the five samples selected in the ANN model for predicting (simulation set). The Bouc-Wen model is capable of simulating the degradation in Phase I, as observed from D, which is less than about 12%; however, this model also simulated the degradation in Phase II-III but the accuracy is still poor and away from the actual G^*, as observed from the high D values irrespective of its sign, as shown in Figure 7–40.

Moreover, the Bouc-Wen model showed a disability in the simulation at the end of fatigue life for all samples except sample b, while this property is invisible in the case of Phase I, despite the ANN model exhibiting satisfactory prediction of the degraded parameters for all phases, as demonstrated previously in Figures 7–38 and 7–39.

From these observations, it can be conclude that the Bouc-Wen model is more sensitive to any small changes in the degraded parameters when these parameters are associated with long periods of time; it can be seen from Figures 7–38 and 7–39 that the degraded parameters are very close to the line of quality, which means the differences between actual and predicted parameters are insignificant for Phases I and II-III, while the Bouc-Wen model performed better in Phase I than in Phase II-III, which is relatively longer than Phase I.

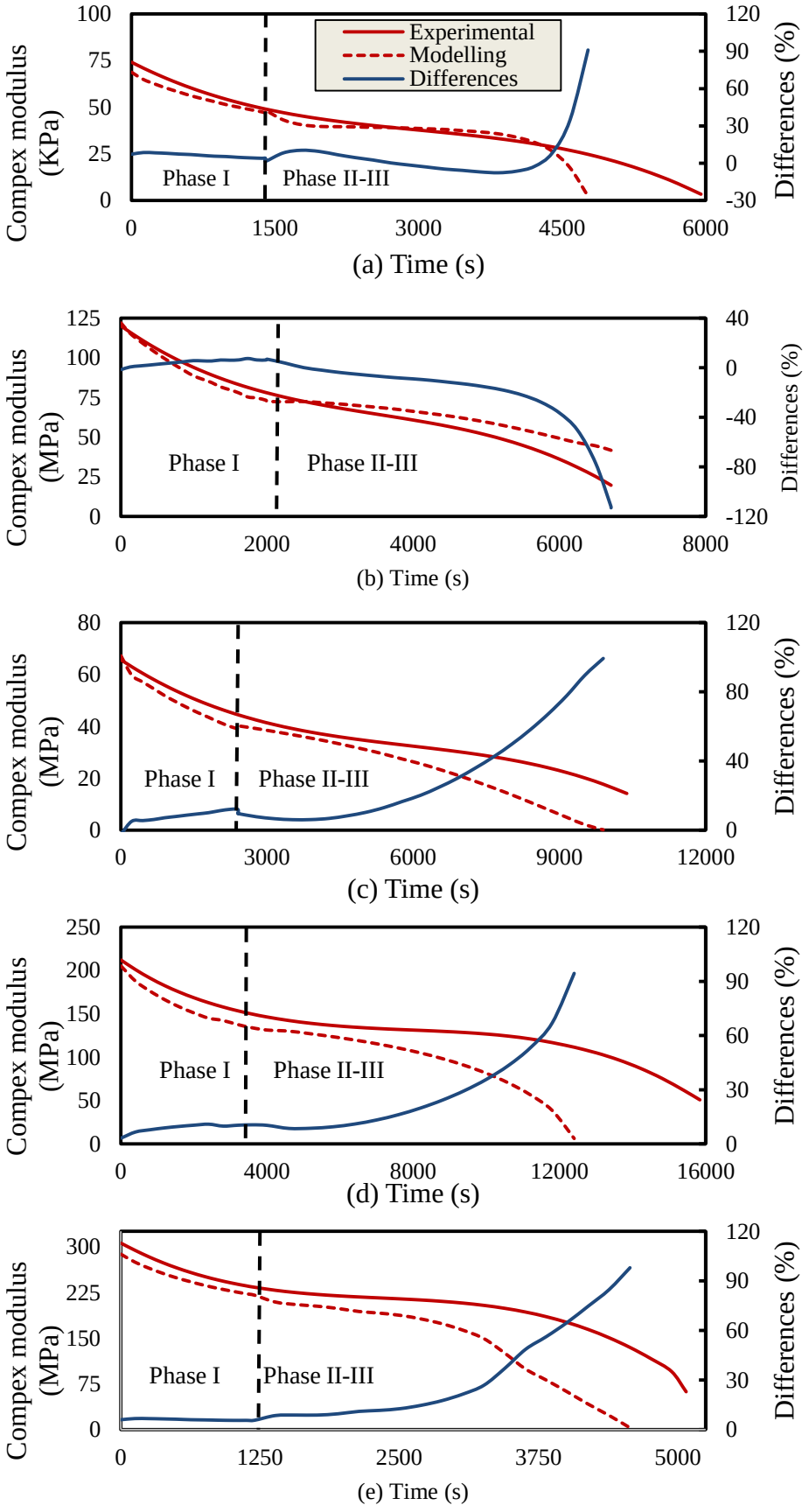

Figure 7- 40: Complex modulus and differences against time for experimental and predicted samples using degraded parameters of the ANN models.

This does not mean that the Bouc-Wen model is incapable of simulation because it has been used in different disciplines, as mentioned previously, but the problem is in the application of this model, as demonstrated from this study. This model displayed capability in modelling the degraded hysteresis loops of HMA samples tested in fatigue, as presented earlier in this chapter, but this ability was poor in the simulation because of the variation in the fatigue results for the tested samples, which reflects the sensitivity of the model to any changes in their degraded parameters in addition to the length of the test.

Generally, ANN seems as a promising technique to enhance the performance of the Bouc-Wen model, but a problem may turn up from the data which requires sufficient data to develop a robust ANN model for predicting Bouc-Wen parameters.

7.9. Summary

From the results presented in this study, the following conclusions have been reached:

1. Fatigue performance of viscoelastic materials is evaluated through the degradation of materials. Several approaches are used to evaluate this degradation, including traditional, energy ratio and dissipated energy approaches. This degrading manifests in viscoelastic materials as hysteresis loops, which are changes in shape, size and slope under load repetitions. The hysteresis loops change from a uniform shape (ellipse) to distorted shapes when the normalised shear modulus decreases to less than 0.35 and 0.2 for the controlled strain and stress test modes respectively, and these values are the second infliction point in the relation of G* vs. N, after which point damage occurs more rapidly.

2. A DSR machine was used to cause fatigue damage in cylindrical samples prepared from HMA and tested in the controlled stress and strain test modes. An approach based on stress-strain relationships was used to produce calculated hysteresis loops for the mixes tested in strain mode due

to the limitations in the memory of the DSR software, which made it impossible to save the real hysteresis loop results during fatigue testing.

3. The Bouc-Wen model is a model that was introduced over the past decades and has been used successfully to model non-linear hysteresis loops of structures under excitation movements. This study represents a successful trial using this model to model the hysteresis loops of viscoelastic materials for samples tested in fatigue using a DSR machine.

4. The solution of the Bouc-Wen model is based on identified parameters that are related to the shape of the loops and the degradation of materials. The experiment results for the hysteresis loops were used to simplify the solution of the model. For this purpose, a non-linear least squares algorithm was used to optimise the solution of the Bouc-Wen model.

5. Two strategies were used to identify Bouc-Wen parameters; these strategies were based on the fatigue phase failure of HMA during fatigue life. Strategy–1 was based on using the hysteresis loops data for all phases (I, II and III) at the same time, while strategy–2 was based on dividing the hysteresis loops into two groups: phase I separately and phases II and III together to identify Bouc-Wen parameters.

6. The results revealed that the capability of the Bouc-Wen model in modelling the hysteresis loops of strategy–2 was better than strategy–1; a better agreement was presented between the experimental and modelled samples. This agreement was clear from the degradation in materials demonstrated by the changes in the hysteresis loop sizes and slopes. In addition, the differences between the modelled and experimental stiffness modulus were in low values.

7. Due to the variation in the fatigue performance of HMA samples as a result of their properties, the Bouc-Wen model was not able to fully simulate the degradation when there were changes in the degraded parameters, δ_A, δ_μ and δ_v. This behaviour reflects the sensitivity of this model to any changes in its parameters, and this is obvious in the long fatigue life.

8. An ANN technique was used to develop models to predict the degraded parameters of the Bouc-Wen model; this technique improved the performance of the Bouc-Wen model especially for Phase I, while its performance in Phase II-III was still poor, despite the degradation simulation being clear. However, the ANN model is a promising technique by which to improve the performance of the Bouc-Wen model, but this step needs sufficient data to create a robust prediction model.

CHAPTER VIII

CHAPTER VIII

8. Accuracy Analysis for Fatigue Parameters and Models

8.1. Introduction

This work included two main parts: experimental and theoretical works. Experimental work presented by using DSR and 2PB techniques in fatigue test with analysis using four parameters, i.e. TA, ER, FI^R and FI_c. TA and ER approaches are common and used by researchers as shown in Chapter II; FI^R and FI_c were developed in this work and introduced as tools for analysing the performance for the first time. Theoretical work included developing three models to predict the fatigue performance of HMA. In this chapter, a comparison was made for the parameters of fatigue analysis; in addition, the accuracy analysis of the prediction models was made to demonstrate the superior model.

8.2. Fatigue Performance Analysis Parameters

Four parameters have been used in this work to analyse the fatigue performance of HMA; two of them are common and well-known parameters called traditional (TA) and energy ratio (ER) approaches; these parameters use the number of cycles to define the fatigue performance. The other two parameters are called fatigue index (FI^R) and fracture index (FI_c); these two parameters were developed based on energy criteria and Paris' law respectively. Four outcomes were used to give a summary about these parameters, as tabulated in Table 8–1. The unit in the TA and ER approaches is the standard unit of fatigue performance, which is number of cycles; in contrast, FI^R and FI_c are indices which were used for evaluating the fatigue performance, so they are unit-less (without units) parameters. TA and ER approaches are very simple parameters; thus, the

requirements are easily obtained from the fatigue test, which are the basic parameters: stiffness modulus and number of cycles. In contrast, FI^R requires more parameters in addition to the linear viscoelastic properties and further calculations for pseudo strain; and in addition to FI^R requirements, FI_c requires a relaxation test, as shown in Table 8–1. FI^R and FI_c are more complicated than TA and ER approaches; however the variation of FI^R and FI_c is relatively low, as revealed from standard errors in the previous chapters. The question then arises as to the possibility of using FI^R and FI_c in pavement design; this point is verified for the TA and ER approaches. However, FI^R and FI_c were used successfully in studying the fatigue performance of HMA, the answer to this question needs to extend the work to include further conditions to develop an approach to use in the design based on these two parameters, FI^R and FI_c. This can be included in the future plan of work.

8.3. Prediction Models

Three models have been used in this study: ANN, fracture and Bouc-Wen; these models have been developed to predict the fatigue performance of HMA samples tested in strain and stress test modes using the DSR technique. The Bouc-Wen model was the worst one, while the other models performed better.

The outcomes of these models have been presented in detail in Chapters V, VI and VII; herein, a simple comparison is introduced to show their superiority in predicting, as presented in Table 8–2.

In this regard, four parameters, R^2, average error, intercept and slope, were used to evaluate the accuracy; these parameters have been interpreted as weights based on their values. For example, the reference magnitude of R^2 is one, and this means there is a perfect correlation between the variables; therefore, R^2 was divided into three scales: excellent, good and fair, based on the R^2 value, and each scale was given a weight, as shown in Table 8–2.

Table 8– 1: Summery of fatigue parameters used in analysis.

Approaches & Parameters	TA	ER	FI^R	FI_c
Unit	Number of cycles	Number of cycles	Unit-less	Unit-less
Requirements	1. Stiffness modulus 2. Number of cycles	1. Stiffness modulus 2. Number of cycles	1. Linear viscoelastic properties 2. Pseudo-strain 3.Fatigue test parameters (stress amplitude, strain amplitude and phase angle)	1. Linear viscoelastic properties 2. Pseudo-strain 3.Fatigue test parameters (stress amplitude, strain amplitude and phase angle) 4. Dissipated pseudo-strain energy. 5. Relaxation test.
Variation	High (standard error)	High (standard error)	Low (standard error)	Low (standard error)
Practical Application	Practically applied	Practically applied	Not applied	Not applied

The average error and intercept have different concepts: the TA and ER were in terms of number of cycles whereas FI^R is non-dimensional parameters between (0 – 1). These parameters were also divided into three scales: excellent, good and fair, based on their values relative to the reference magnitude, which is zero for both average error and intercept; but the threshold in the FI^R case is less than 1, which is relatively very much lower than TA and ER. In addition, each scale was given a specific weight, as detailed in Table 8–2. The last parameter is slope and its reference magnitude is one, as the ideal magnitude; slope was also divided into three scales: excellent, good and fair, according to their values, as shown in Table 8–2.

The weight of each of the used models is presented in Table 8–2; it is clear that the ANN model of the ER-stress mode is the best one with the highest weight, 12, while the ANN models (TA and FI^R) in stress mode with ER-strain mode and TA-strain mode in the fracture model come second at the same weight, which is 11. On the other hand, the ANN mode FI^R-strain mode has a weight of 10, while models TA-strain mode in ANN and ER-strain mode in the fracture model had a weight of 9. The worst models are TA and ER in stress mode of the fracture model, with a weight of 5 and 4 respectively, as detailed in Table 8–2.

Overall, the ANN model is the best one for the stress mode, with a total weight of 23 for TA and ER approaches, while, in the strain mode, the ANN and fracture models achieved the same weight, 20, as a total for TA and ER. Additionally, the ANN model of FI^R in stress was better than in strain, where its weight was 11.

8.4. Summary

Fatigue performance analysis parameters displayed the same ranking order of the mixes but they are distributed from simple parameter such as TA to complex one such FI_c. However, the gain of the complexity was presented by the low variation in the results. The accuracy comparison revealed that ANN of stress' model (TA and ER) was the best one in prediction while fracture model in stress mode model was the worst model in prediction, at the same time other models were in-between this range.

Table 8– 2: A simple comparison of the models.

Models		Bouc-Wen						Fracture						ANN model					
Test Modes		Strain mode			Stress mode			Strain mode			Stress mode			Strain mode			Stress mode		
Reference	Parameters	TA	ER	FI^R	TA	ER	FI^R	TA	ER	FI^R	TA	ER	FI^R	TA	ER	FI^R	TA	ER	FI^R
1.0[a]	R-square	N/A[e]			N/A			0.870	0.748	N/A	0.807	0.763	N/A	0.989	0.981	0.980	0.980	0.994	0.986
								√√	√		√√	√		√√√	√√√	√√√	√√√	√√√	√√√
0.0[b,c]	Average error	N/A			N/A			-42	161	N/A	-14412	13520	N/A	1050	-1432	-0.0045	-637	547	0.00417
								√√√	√√√		√	√		√√	√√	√√√	√√√	√√√	√√√
0.0[b,c]	Intercept	N/A			N/A			-90	1071	N/A	-7054	-4108	N/A	1127	111	0.0759	-1108	754	0.0555
								√√√	√√		√	√		√√	√√√	√√	√√	√√√	√√
1.0[d]	Slope	N/A			N/A			1.003	0.937	N/A	1.441	1.415	N/A	0.889	0.973	1.103	0.956	0.989	1.081
								√√√	√√√		√	√		√√	√√√	√√	√√√	√√√	√√√
Total		N/A			N/A			11	9	N/A	5	4	N/A	9	11	10	11	12	11
Total		N/A			N/A			20		N/A	9		N/A	20		10	23		11

[a] the thresholds are: √√√ when the R-square is excellent (1 to 0.9), √√ when the R-square is good (0.9 to 0.8) and √ when the R-square is less than 0.8 for fair.

[b] the thresholds are: √√√ when average error and intercept is excellent (-1000 to 1000), √√ when average error and intercept is good (-3000 to 3000), √ when average error and intercept greater than ± 3000 is fair.

[c] In the case of FI^R only: √√√ when average error and intercept is excellent (0.05 to -0.05), √√ when average error and intercept is good (-0.1 to 0.1), √ when average error and intercept less than ± 0.1 is fair.

[d] the thresholds are: √√√ when the slope is excellent ($1.1 \geq Slope \geq 0.9$), √√ when the slope is good ($1.2 \geq Slope > 1.1 \cup 0.9 > Slope \geq 0.8$), and √ when the slope is fair ($slope > 1.2 \cup slope < 0.8$).

[e] N/A not applicable.

CHAPTER VIIII

CHAPTER VIIII

9. Conclusions and Recommendations

HMA are composite materials with each component exhibiting different properties. The aggregates' role is a skeleton while filler with bitumen represents mastic to fill the voids and to bond the aggregates together to give more stability in the HMA. Availability of bitumen in the HMA affects its behaviour to act as a viscoelastic material depending on the temperature, where it is elastic at low temperature while viscous at high temperature, and viscoelastic in-between. Extensive work has been performed by researchers to understand this complex behaviour and to enhance its performance. So, in fatigue performance, several criteria were developed to understand this behaviour and to define fatigue life. These criteria were distributed from a simple based on a number of cycles to complicated based on crack developing. Also, several devices were developed to simulate and evaluate the fatigue performance of HMA such as 2PB, 3PB, 4PB, T–C, etc. This study focused on using DSR in evaluating and characterising the fatigue performance of full HMA; at present, DSR is used for FAM only. Therefore, an approach is required to produce small cylindrical samples from HMA to be tested in fatigue using DSR; at the same time, these samples should be representative of the full HMA.

9.1. Conclusions

Based upon the results of the DSR test in both test modes and 2PB test results, the conclusions can be summarised as follow:

- A method was developed and used successfully for preparing full hot mix asphalt DSR samples of 12 mm in diameter and 50 mm in height. This method was based on preparing prismatic beams (50×65×310) mm cut from compacted HMA slab (65×310× 310) mm and then beams cored using

electrical coring machine to extract about 46-43 DSR cylindrical samples from each beam.

- An approached has been developed for selecting a specified DSR samples among a lot of samples prepared using coring technique. This approach was based on the mode and standard deviation values of the bulk density of DSR samples to identify the samples using Equations 3–11 and 3–12, which are suitable to be used for any further work. This approach ensured that selected DSR samples are more representative to the full HMA which represented by prismatic and trapezoidal beams as revealed from the non-significant difference in bulk density between the mode of DSR samples and beams.

- A simple method was devised to arrive at the strain and stress amplitude that should be used in performing the fatigue test in DSR for controlled strain and stress test modes. This method is based on performing the sweep strain and stress amplitude on DSR samples. In strain sweep, the slope of the strain–stress relationship, Equation 3–13, was evaluated and plotted against strain amplitude, and when the slope changed from positive to negative, the value of the strain amplitude was identified as strain amplitude for fatigue test in strain test mode. For stress sweep, the slope of strain response with time was evaluated and plotted against stress amplitudes; at the point when there is a dramatic increase in the relationship, the stress value can be selected at this point, this point can be define when there is divergence from the straight line in the relationship of strain response slope against shear stress amplitude.

- A new fatigue index (FI^R) has been developed based on the concept of pseudo strain energy to be used in evaluating and characterisation the fatigue performance of HMA. Where, stress-pseudostrain hysteresis loops relationship in viscoelastic materials under cyclic loading was used to derive formulas, Equations 3–9 and 3–10, for calculating applied and recovered pseudostrain energy to be used for calculating FI^R using Equation 3–14. The index range is 0–1, where 0 is non-damage and 1 completely damage. Relationship of FI^R against normalized shear modulus showed there is a plateau region between 0.85 to 0.35 and 0.85 to 0.2 of normalised shear

modulus for strain and stress modes test respectively. Beyond 0.35 and 0.2, FI^R increased sharply in both strain and stress test modes respectively.

- The average value of FI^R within plateau region has been used in evaluating the fatigue performance of HMA tested in DSR. Well-known approaches namely traditional approach (TA) and energy ratio approach (ER) were used to verify FI^R results. The analyses demonstrated an agreement of FI^R with these approaches; where the rank of order for all mixes was the same in all approaches in both test modes.

- Two points bending (2PB) technique was performed in strain test mode on trapezoidal samples prepared from HMA in order to verify utilization of DSR instrument. Fatigue analysis was evaluated using the same approaches that have been used in DSR: TA, ER and FI^R. The outcomes of 2PB test emphasised the suitability of using DSR instrument, where the results of the 2PB test agreed with the results of the DSR samples in terms of the rank orders of mixes.

- The variance of the results in this study was checked using error bars in terms of standard error for all approaches in both test modes. The analysis revealed that FI^R displayed a significantly low variation in comparison to the TA and ER approaches for the DSR samples; and this behaviour was emphasised in the 2PB technique too. This confirms the efficiency of using the DSR technique and FI^R approach in fatigue test and performance analysis, and that they are reliable and acceptable.

- The results of the fatigue test for both techniques, 2PB and DSR, confirmed that limestone has a better fatigue performance for both HRA and DBM mixes than granite in both test modes. This is possibly because there are more air voids in the granite mixes in the limestone mixes.

- A comparison study between strain and stress response with stress and strain amplitude derived from the TA approach at 50% of initial stiffness revealed that there is compatibility between them in rank of order. However, the study showed that the response values are not consistent with amplitudes value in fatigue test from a damage and non-damage region perspective, and

this is clear where, in the DBM mixes, the shear stress response was less than the damage value while, in the HRA mixes, the response were at high damage amplitude. Using the shear stress response from the TA approach does not give a fair comparison.

- Rate of damage (m_{II}) was calculated from fatigue curve, G^* vs N, within Phase II; the absolute values of m_{II} demonstrated a trend with N_f, where N_f decreases as $|m_{II}|$ increases in both test modes; but the correlation of $|m_{II}|$ increased significantly when the ratio of N_f to initial G^* was considered. Based on the correlation analysis of m_{II} and several variables from fatigue test and volumetric properties, initial dissipated energy, initial phase angle, and bulk density were selected to develop a model for predicting m_{II}. The predicted m_{II} was used for predicting N_f using N_f/G_0^* relationship for both test modes. The analysis showed that the strain mode model has a more satisfactory prediction than the stress test mode.

From the artificial neural networks (ANN) modelling work, the outcomes can be summarised as follow:

- Regression models have been developed to predict the fatigue life of HMA based on several variables related to mix properties as well as the test conditions. All these regression models are limited based on the amount and variety of the experimental data and the goodness of fit (quality), which is represented by the determination coefficient (R^2).

- The ANN approach, as a new fatigue modelling method was used in this study to create an effective predictive model. The established ANN-based models were able to predict the fatigue life accurately, as evidenced by high R^2 values for the test set of data.

- Experimental data from fatigue tests of cylindrical samples tested in DSR were used to train the neural networks to develop models for predicting the fatigue performance of HMA in terms of number of cycles (N_f and N_1) and FI^R. ANN models were based on parameters from fatigue test (i.e. initial stiffness modulus, initial phase angle, shear strain amplitude, shear stress

amplitude and relaxation test coefficients in addition to volumetric properties of HMA to be the input variables for the ANN.

- The objective of neural networks was developing ANN models based on the fatigue test of modes (strain and stress) to predict fatigue performance. The results revealed an excellent correlation between predicted and actual data for all approaches (N_f, N_1 and FI^R).

- Bias analysis for all ANN models was evaluated based on the typical values of the line of equality because it is considered a perfect model, whereas average error and intercept are zero and the slope is unity. The bias analysis stated that the ANN model for the stress test mode is less accuracy than ANN models of strain test mode.

- The ideal architecture of ANN models was determined after investigating several architectures containing one to two hidden layers with 10, 15 or 20 neurons in each hidden layer. The best ANN model was two hidden layers with 15 neurons based on the high determination coefficient (R^2) between the actual and predicted data.

Based on the fracture model and the analysis results the following conclusions can be drawn:

- A simple fracture model based on a modified Paris' law was introduced and used successfully in analysis the fatigue performance of different asphalt mixes. This model was derived based on the fundamental fatigue parameters represented by the exponential relaxation coefficient (m) and the cumulative dissipated pseudo-strain energy for the matrix, where cracks occur because it is weaker than aggregates in HMA samples.

- Dissipated pseudo strain energy (DPSE) was calculated based on the differences between applied and recovered pseudo-strain energies for cylindrical samples prepared from a variety of asphalt mixes and examined in fatigue using a DSR instrument under strain and stress modes testing. Analysis of the results revealed that a higher DPSE/N ratio indicates lower fatigue life and greater damage.

- The results showed that there is compatibility between the fracture analyses represented by fracture index (FI_c) with other analyses presented in Chapters III and IV using FI^R, TA and ER approaches. In addition, the FI_c results showed better performance analysis in terms of variation than number of cycles.

- Results showed the same conclusions as the previous study (Chapters III and IV): that limestone mixes perform better than granite mixes in both DBM and HRA mixes.

- Models were developed for predicting fatigue performance in terms of number of cycles defined according to traditional (TA) and energy ratio (ER) approaches. These models were based on estimating four parameters (A, B, b and c) extracted from the relationships of FI_c with normalised stiffness modulus (C_N) and DPSE against number of cycles for strain and stress test modes, which were correlated with volumetric and mechanistic properties for developing fatigue models for both test modes, strain and stress.

- The results revealed that the strain model's prediction accuracy was better than that of the stress model, as demonstrated by the bias analysis.

Based on the hysteresis loops characteristics and modelling using Bouc-Wen model; the following outcomes can be concluded:

- The hysteresis loops in viscoelastic materials change in shape, size and slope under load repetitions due to the degrading. This change in loops transforms from a uniform shape (ellipse) to distorted shape when the normalised shear modulus decreases to less than 0.35 and 0.2 for the controlled strain and stress test modes respectively, and these values are the second infliction point in the relation of G* vs. N, after which point damage occurs more rapidly.

- An approach based on stress-strain relationships was used to produce calculated hysteresis loops for the mixes tested in strain mode due to the

limitations in the memory of the DSR software, which made it impossible to save the real hysteresis loop results during fatigue testing.

- The Bouc-Wen model is a model that was introduced over the past decades and has been used successfully to model non-linear hysteresis loops of structures under excitation movements. This study represents a successful trial using this model to model the hysteresis loops of viscoelastic materials for samples tested in fatigue.

- The solution of the Bouc-Wen model is based on identified parameters that are related to the shape of the loops and the degradation of materials. The experiment results for the hysteresis loops were used to simplify the solution of the model. For this purpose, a non-linear least squares algorithm was used to estimate the Bouc-Wen model parameters.

- Two strategies were used to identify Bouc-Wen parameters; these strategies were based on the fatigue phase failure of HMA during fatigue life. Strategy–1 was based on using the hysteresis loops data for all phases (I, II and III) at the same time, while strategy–2 was based on dividing the hysteresis loops into two groups: Phase I separately and Phases II and III together to estimate Bouc-Wen parameters.

- The results revealed that the capability of the Bouc-Wen model in modelling the hysteresis loops of strategy–2 was better than strategy–1; a better agreement was presented between the experimental and modelled samples. This agreement was clear from the degradation in materials demonstrated by the changes in the hysteresis loop sizes and slopes. In addition, the differences between the modelled and experimental stiffness modulus were in low values.

- Due to the variation in the fatigue performance of HMA samples as a result of their properties, the Bouc-Wen model was not able to fully simulate the degradation when there were changes in the degraded parameters, δ_A, δ_μ and δ_v. This behaviour reflects the sensitivity of this model to any changes in its parameters, and this is obvious in the long fatigue life.

- An ANN technique was used to develop models to predict the degraded parameters of the Bouc-Wen model; this technique improved the performance of the Bouc-Wen model especially for Phase I, while its performance in Phase II-III was still poor, despite the degradation simulation being clear.

9.2. Recommendation for Further Work

- The developed approach in this work was limited to the nominal maximum size of aggregates, 10 mm, and two kinds of HMA: DBM and HRA. However, although this is a valid approach, the study needs to be expanded to include aggregate size bigger than 10 mm and other mixes, such as Polymer-modified mixes and cold mixes.

- The approach developed in this study was based on performing a fatigue test using a DSR in torsional technique, and this technique sometimes causes damage in the DSR because of overheating. DSR can be used to perform the fatigue test using tension-compression loading with less probability of damage in the DSR. This approach requires the development of a sequence to apply tension-compression and gather the basic data.

- Potentially, the work could be expanded to include other test conditions: low and high strain and stress amplitudes, different mixes and additives, to evaluate that on the behaviour of FI^R and the possibility of using them in pavement design.

- The study confirmed that the limestone mixes have a better fatigue performance for both HRA and DBM mixes than granite mixes for both techniques: DSR and 2PB. This issue needs to be addressed by studying the interfacial zone between the binder and the aggregate surface in order to give more understanding of this behaviour.

REFERENCES

References

AASHTO 2002. Method for Determining the Fatigue Life of Compacted Hot Mix Asphalt (HMA) Subjected to Repeated Flextural Bending, AASHTO TP8-94.

AASHTO T321-2007. Standard Method of Test for Determining the Fatigue Life of Compacted Hot-Mix-Asphalt Subjected to Repeated Flexural Bending.

Adeli, Hojjat 2001. Neural networks in civil engineering: 1989–2000. *Computer-Aided Civil and Infrastructure Engineering,* 16**,** 126-142.

Airey, Gordon D,Rahimzadeh, Behzad and Collop, Andrew C 2003. Viscoelastic linearity limits for bituminous materials. *Materials and Structures,* 36**,** 643-647.

Al-Khateeb, G. and Shenoy, A. 2004. A Distinctive Fatigue Failure Criterion. *Journal of the Association of Asphalt Paving Technologists,* 73**,** 585-622.

Al Janaideh, Mohammad,Feng, Ying,Rakheja, Subhash,Su, Chun-Yi and Rabbath, C Alain. Hysteresis compensation for smart actuators using inverse generalized Prandtl-Ishlinskii model. American Control Conference, 2009. ACC'09., 2009. IEEE, 307-312.

Andrei, D,Witczak, MW and Mirza, MW 1999. Development of a revised predictive model for the dynamic (complex) modulus of asphalt mixtures. *Development of the 2002 Guide for the Design of New and Rehabilitated Pavement Structures, NCHRP*.

Artamendi, I. and Khalid, H. 2005. Characterization of fatigue damage for paving asphaltic materials. *Fatigue & Fracture of Engineering Materials & Structures,* 28**,** 1113-1118.

ASTM D7460-2008. Standerd Test Method for Determing Fatigue Failure of Compacted Asphalt Concrete Subjected to Repeated Flextural Bending.

Baaj, Hassan,Di Benedetto, Hervé and Chaverot, Pierre 2005. Effect of binder characteristics on fatigue of asphalt pavement using an intrinsic damage approach. *Road Materials and Pavement Design,* 6**,** 147-174.

Baaj, Hassan,Di Benedetto, Herve,Chaverot, Pierre and Partl, MN. Fatigue of mixes: an intrinsic damage approach. Sixth International RILEM Symposium on Performance Testing and Evaluation of Bituminous Materials, 2003. RILEM Publications SARL, 394-400.

Baber, T.T. and Noori, M.N. 1986. Modeling General Hystersis Behavior and Random Vibration Application. *Journal of Vibration, Acoustics, Stress, and Reliability in Design,* 108**,** 411-420.

Baber, T.T. and Noori, M.N.. 1985. Random Vibration of Degrading, Pinching Systems. *Journal of Engineering Mechanics,* 111**,** 1010-1026.

Baber, T.T. and Wen, Y.K. 1981. Random Vibration of Hysteretic, Degrading Systems. *Journal of Engineering Mechanics,* 107**,** 1069-1083.

Baber, Thomas Thaxton and Wen, Yi-Kwei 1980. *Stochastic equivalent linearization for hysteretic, degrading, multistory structures*, B University of Illinois at Urbana-Champaign.

Bari, Javed and Witczak, Matthew W 2006. Development of a New Revised Version of the Witczak E* Predictive Model for Hot Mix Asphalt Mixtures (With Discussion). *Journal of the Association of Asphalt Paving Technologists,* 75.

Basili, M and De Angelis, M 2007. Optimal passive control of adjacent structures interconnected with nonlinear hysteretic devices. *Journal of sound and vibration,* 301**,** 106-125.

Bhasin, Amit,Castelo Branco, Veronica T,Masad, Eyad and Little, Dallas N 2008. Quantitative comparison of energy methods to characterize fatigue in asphalt materials. *Journal of Materials in Civil Engineering,* 21**,** 83-92.

Bhattacharjee, Sudip,Swamy, Aravind Krishna and Daniel, Jo Sias 2009. Application of elastic-viscoelastic correspondence principle to determine fatigue endurance limit of hot-mix asphalt. *Transportation Research Record: Journal of the Transportation Research Board,* 2126**,** 12-18.

Bonnaure, F.,Gravois, A. and Udron, J. A new method for predicting the fatigue life of bituminous mixes. Association of Asphalt Paving Technologists Proceedings, 1980.

Bouc, R. Forced vibration of mechanical systems with hysteresis. Preceedings of the 4th International Conference on Nonlinear Oscillations, Prague, Czechoslovakia, 1967.

Branco, Veronica Teixeira Franco. 2008. *A Unified Method for the Analysis of Nonlinear Viscoelasticity and Fatigue Cracking of Asphalt Mixture Using the Dynamic Mechanical Analyzer*. PhD Dissertation, Texas A&M University.

Brown, S.F. Practical test procedures for mechanical properties of bituminous materials. Proceedings of the Institution of Civil Engineers: Transport, 1995.

BS 597-1 2005. Hot rolled asphalt for roads and other paved areas. *specification for constituent materials and asphalt mixtures.*: British Standard Institution.

BS 4987-1 2005. coated macadam (asphalt concrete) for roads and other paved areas.: British Standard Institution.

BS EN 12697-24 2012. Bituminous mixtures —Test methods for hot mix asphalt *Part 24: Resistance to fatigue.* BSI.

BS EN 12697-26 2012. Bituminous mixtures —Test methods for hot mix asphalt *Part 26: Stiffness.* BSI.

BS EN 12697 2003. Specimen prepared by roller compactor. *Bituminous mixtures-test methods for hot mix asphalt.*: British Standard Instituation.

BS EN 12697 2004. bituminous mixtures-tast methods for hot mix asphalt.: British Standard Institution.

BS PD 6691 2010. Guidence on the use of BS EN 13108 bituminous mixtures - material specifications.: British Stendard Instituation.

Carpenter, S. H. and Shen, S. 2006. Dissipated Energy Approach to Study Hot-Mix Asphalt Healing in Fatigue. *Transportation Research Record,* 1970**,** 178-185.

Ceylan, Halil, Gopalakrishnan, Kasthurirangan, Kim, Sunghwan 2008. Advanced approaches to hot-mix asphalt dynamic modulus prediction. *Canadian Journal of Civil Engineering,* 35**,** 699-707.

Ceylan, Halil,Schwartz, Charles W.,Kim, Sunghwan and Gopalakrishnan, Kasthurirangan 2009. Accuracy of predictive models for dynamic modulus of hot-mix asphalt. *Journal of Materials in Civil Engineering,* 21**,** 286-293.

Cocurullo, A,Airey, GD,Collop, AC and Sangiorgi, C 2008. Indirect tensile versus two-point bending fatigue testing. *Proceedings of the ICE-Transport,* 161**,** 207-220.

Coleman, Bernard D and Hodgdon, Marion L 1986. A constitutive relation for rate-independent hysteresis in ferromagnetically soft materials. *International journal of engineering science,* 24**,** 897-919.

D. Christensen,Richared kim,Dallas Little,Eyad Masad and Kim, Yong-Rak 2009. practical approaches to continuum damage fatigue analysis.

Daniel, J.S.,Bisirri, W. and Kim, Y.R. 2004. Fatigue Evaluation of Asphalt Mixtures Using Dissipated Energy and Viscoelastic Continuum Damage Approaches. *Journal of the Association of Asphalt Paving Technologists,* 73**,** 557-583.

Deacon, John A,Coplantz, John S,Tayebali, Aktarhusein A and Monismith, Carl L 1994. Temperature considerations in asphalt-aggregate mixture analysis and design. *Transportation Research Record*.

Demuth, Howard, Beale, Mark and Hagan, Martin 2009. Neural network toolbox user's guide. The MathWorks. *Inc., Natrick, USA*.

Di Benedetto, H,Ashayer Soltani, A and Chaverot, P 1996. Fatigue damage for bituminous mixtures: a pertinent approach. *Journal of the Association of Asphalt Paving Technologists,* 65.

Di Benedetto, H.,De La Roche, C.,Baaj, H.,Pronk, A. and Lundström, Robert. 2004. Fatigue of bituminous mixtures. *Materials and Structures,* 37**,** 202-216.

Dobson, S,Noori, M,Hou, Z,Dimentberg, M and Baber, T 1997. Modeling and random vibration analysis of SDOF systems with asymmetric hysteresis. *International journal of non-linear mechanics,* 32**,** 669-680.

Dondi, Giulio,Pettinari, Matteo,Sangiorgi, Cesare and Zoorob, Salah E. 2013. Traditional and dissipated energy approaches to compare the 2PB and 4PB flexural methodologies on a worm mix asphalt. *Construction and building Materials,* 47**,** 7.

Foliente, Greg C and Noori, Mohammad N 1996. Equivalent linearization of generally pinching hysteretic degrading systems. *Earthquake Engineering and Structural Dynamics*, 25**,** 611-629.

Gere, James M. 2004. *Mechanics of Materials*, Thomson, 2004.

Ghuzlan, K.A. and Carpenter, S.H. 2000. Energy-derived, damage-based failure criterion for fatigue testing. *Transportation Research Record: Journal of the Transportation Research Board,* 1723**,** 141-149.

Ghuzlan, K.A. and Carpenter, S.H. 2006. Fatigue damage analysis in asphalt concrete mixtures using the dissipated energy approach. *Canadian Journal of Civil Engineering,* 33**,** 890-901.

Haykin, Simon 1999. *Neural networks: a comprehensive foundation,* Prentice Hall PTR.

Hintz, C. and Bahia, H. 2013. Simplification of Linear Amplitude Sweep Test and Specification Parameter. *Transportation Research Record: Journal of the Transportation Research Board,* 2370**,** 10-16.

Huang, C.W.,Masad, E.,Muliana, A.H. and Bahia, H. 2007. Nonlinearly viscoelastic analysis of asphalt mixes subjected to shear loading. *Mechanics of Time-Dependent Materials,* 11**,** 91-110.

Hudson, W Ronald and Kennedy, Thomas William 1968. *An indirect tensile test for stabilized materials,* Center for Highway Research, University of Texas at Austin.

Ikhouane, F.,Mañosa, V. and Rodellar, J. 2004. Bounded and dissipative solutions of the Bouc-Wen model for hysteretic structural systems. *Proceedings of the Amrican Control Conference,* 4**,** 3520-3524.

Ikhouane, Faycal and Rodellar, José 2007. *Systems with hysteresis: analysis, identification and control using the Bouc-Wen model,* Wiley. com.

Ikhouane, Fayçal and Rodellar, José 2005. On the hysteretic Bouc–Wen model. *Nonlinear Dynamics,* 42**,** 79-95.

Ismail, M.,Ikhouane, F. and Rodellar, J. 2009. The hysteresis Bouc-Wen model, a survey. *Archives of Computational Methods in Engineering,* 16**,** 161-188.

Johnson, C.M.,Wen, H. and Bahia, H.U. 2009. Practical Application of Viscoelastic Continuum Damage Theory to Asphalt Binder Fatigue Characterization. *Journal of the Association of Asphalt Paving Technologists,* 78.

Kachanov, L.M. 1958. On time to rupture in creep conditions,. *Proceedings of the USSR Academy of Sciences, Department of Technical.,* 8**,** 26-31.

Kim, Y.R.,Lee, H.J. and Little, D.N. 1997. Fatigue Characterization of Asphalt Concrete Using Viscoelasticity and Continuum Damage Theory (with Discussion). *Journal of the Association of Asphalt Paving Technologists,* 66**,** 520-569.

Kim, Y.R.,Little, D. N. and Lytton., R. L. 2003. Fatigue and Healing Characterization of Asphalt Mixtures. *Journal of Materials in Civil Engineering,* 15**,** 75-83.

Kim, Y.R. and Little, D.N. 2004. Linear Viscoelastic Analysis of Asphalt Mastics. *Journal of Materials in Civil Engineering,* 16**,** 122-132.

Kim, Y.R.,Little, D.N. and Lytton, R.L. 2002. Use of Dynamic Mechanical Analysis (DMA) to Evaluate the Fatigue and Healing Potential of Asphalt Binders in Sand Asphalt Mixtures. *Journal of the Association of Asphalt Paving Technologists,* 71**,** 176-205.

Ktena, A.,Fotiadis, DI,Spanos, PD and Massalas, CV 2001. A Preisach model identification procedure and simulation of hysteresis in ferromagnets and shape-memory alloys. *Physica B: Condensed Matter,* 306**,** 84-90.

Kutay, M Emin,Gibson, Nelson and Youtcheff, Jack 2008. Conventional and Viscoelastic Continuum Damage (VECD)-Based Fatigue Analysis of Polymer Modified Asphalt Pavements (With Discussion). *Journal of the Association of Asphalt Paving Technologists,* 77.

Lampman, Steven R 1996. Fatigue and Fracture, Handbook. *ASM International*.

Larson, Ronald G. 1999. *The structure and rheology of complex fluids*, Oxford university press New York.

Lee, H.J.,Daniel, J.S. and Kim, Y.R. 2000. Continuum damage mechanics-based fatigue model of asphalt concrete. *Journal of Materials in Civil Engineering,* 12**,** 105-112.

Lee, H.J. and Kim, Richared 1998. Viscoelastic constitutive model for asphalt concrete under cyclic loading. *Journal of Engineering Mechanics,* 124**,** 32-40.

Lee, Hyun Jong,Kim, Y Richard and Lee, Seung Woo 2003. Prediction of asphalt mix fatigue life with viscoelastic material properties. *Transportation Research Record: Journal of the Transportation Research Board,* 1832**,** 139-147.

Luo, Xue. 2012. *characterization of fatigue cracking and healing of asphalt mixes.* Doctor of Philosophy, Texas A&M University.

Luo, Xue,Luo, Rong and L. Lytton, Robert 2012. Characterization of Fatigue Damage in Asphalt Mixtures Using Pseudostrain Energy. *Journal of Materials in Civil Engineering,* 25**,** 208-218.

Luo, Xue,Luo, Rong and Lytton, Robert 2013. Modified Paris's Law to Predict Entire Crack Growth in Asphalt Mixtures. *Transportation Research Record: Journal of the Transportation Research Board***,** 54-62.

Macki, Jack W,Nistri, Paolo and Zecca, Pietro 1993. Mathematical models for hysteresis. *SIAM review,* 35**,** 94-123.

Maggiore, C,Airey, G,Di Mino, G,Marsac, P and Di Liberto, M 2012. Fatigue resistance: is it possible having a unique response? *3rd Four Point Bending Conference.* Davis, Californai, USA.

Malvern. *http://www.malvern.com/labeng/products/kinexus* [Online].

Mamlouk, Michael,Souliman, Mena and Zeiada, Waleed. Optimum Testing Conditions to Measure HMA Fatigue and Healing Using Flexural Bending Test. TRB Annual Meeting 2012, 2012.

Masad, E. ,Castelo Branco, VTF.,Little, Dallas N. and Lytton, R. 2008a. A unified method for the analysis of controlled-strain and controlled-stress fatigue testing. *International Journal of Pavement Engineering,* 9**,** 233-246.

Masad, Eyad,Huang, Chien-Wei,Airey, Gordon and Muliana, Anastasia 2008b. Nonlinear viscoelastic analysis of unaged and aged asphalt binders. *Construction and Building Materials,* 22**,** 2170-2179.

Masad, Eyad and Somadevan, Niranjanan 2002. Microstructural finite-element analysis of influence of localized strain distribution on asphalt mix properties. *Journal of engineering mechanics,* 128**,** 1105-1114.

Mayergoyz, Isaak D 2003. *Mathematical models of hysteresis and their applications,* Academic Press.

Menard, Kevin P 1999. *Dynamic mechanical analysis: a practical introduction*, CRC press.

Menard, Kevin P and Bilyeu, Bryan W 2008. *Dynamic mechanical analysis of polymers and rubbers*.

Monismith, C.L. and McLean, D.B 1972. Structural design considerations. *Proceedings of Association of Asphalt Paving Technologists,* 41.

Monismith, CL, Epps, JA, Finn, FN. IMPROVED ASPHALT MIX DESIGN (WITH DISCUSSION). Association of Asphalt Paving Technologists Proc, 1985.

Monismith, CL,Kasianchuk, DA and Epps, JA 1961. Asphalt Mixture Behavior in Repeated Flexure. *Proceedings of Association of Asphalt Paving Technologists,* 30**,** 188-222.

Monismith, CL, Kasianchuk, DA, Epps, JA 1969. Asphalt Mixture Behavior in Repeated Flexure: A Study of an In-Service Pavement Near Morro Bay, California. Report No. TE 67-4. *Univ. of California, Berkeley*.

Mull, MA,Stuart, K and Yehia, A 2002. Fracture resistance characterization of chemically modified crumb rubber asphalt pavement. *Journal of Materials Science,* 37**,** 557-566.

Mun, S. and Lee, H. 2010. Modeling Viscoelastic Crack Growth in Hot-Mix Asphalt Concrete Mixtures Using a Disk-Shaped Compact Tension Test. *Journal of Engineering Mechanics,* 137**,** 431-438.

Nishizawa, Tatsuo,Shimeno, S and Sekiguchi, M. Fatigue analysis of asphalt pavements with thick asphalt mixture layer. Eighth International Conference on Asphalt Pavements, 1997.

Nocedal, Jorge and Wright, S 2006. Numerical optimization, series in operations research and financial engineering. *Springer, New York*.

Oh, JinHyoung and Bernstein, Dennis S 2005. Semilinear Duhem model for rate-independent and rate-dependent hysteresis. *Automatic Control, IEEE Transactions on,* 50**,** 631-645.

Paris, PC and Erdogan, F 1963. A critical analysis of crack propagation laws. *Journal of Basic Engineering,* 85**,** 528.

Park, S.W.,Kim, Y.R. and Schapery, R.A. 1996. A viscoelastic continuum damage model and its application to uniaxial behavior of asphalt concrete. *Mechanics of Materials,* 24**,** 14.

Partl, Manfred N,Bahia, Hussain U,Canestrari, Francesco,de la Roche, Chantal,Di Benedetto, Hervé,Piber, Herald and Sybilski, Dariusz 2013. *Advances in Interlaboratory Testing and Evaluation of Bituminous Materials,* Springer Dordrecht Heidelberg New York London.

Pell, P.S. 1973. characterization of fatigue behaviour in structural design of asphalt concrete pavement to prevent fatigue cracking. *Proc. of Symposium, Highway Research Broad Special Report 140, Washington.*

Pell, PS. Fatigue characteristics of bitumen and bituminous mixes. International Conference on the Structural Design of Asphalt Pavements, 1962.

Pérez-Jiménez, Félix,Valdés, Gonzalo A,Botella, Ramón,Miró, Rodrigo and Martínez, Adriana 2012. Approach to fatigue performance using Fénix

test for asphalt mixtures. *Construction and Building Materials,* 26**,** 372-380.

Pires, J.A. 1996. Stochastic seismic response analysis of soft soil sites. *Nuclear Engineering and Design,* 160**,** 363-377.

Preisach, F. 1935. *Über die magnetize Nachwirkung. Zeitschrift für Physik,* 94**,** 26.

Priddy, Kevin L and Keller, Paul E 2005. *Artificial neural networks: an introduction,* SPIE Press.

Pronk, Adriaan C and Erkens, SMJG 2002. A note on fatigue bending tests using a haversine loading. *Road Materials and Pavement Design,* 3**,** 95-106.

Pronk, Adriaan Cornelis,Poot, MR.,Jacobs, MMJ. and Gelpke, RF. Haversine Fatigue Testing in Controlled Deflection Mode: Is It Possible? Transportation Research Board 89th Annual Meeting, 2010.

Qian, Guo-ping,Liu, Hong-fu,Zheng, Jian-Iong and Jiang, Li-jun 2013. Experiment of Tension-compression Fatigue and Damage for Asphalt Mixtures. *Journal of Highway and Transportation Research and Development (English Edition),* 7**,** 15-21.

Qiang, Li,Jong, Lee Hyun and Woo, Kim Tae 2012. A simple fatigue performance model of asphalt mixtures based on fracture energy. *Construction and Building Materials,* 27**,** 605-611.

Quantao Liu,Erik Schlangen,Martin van de Ven,Gerbert van Bochove and Montfort, Jo van 2012. Evaluation of the induction healing effect of porous asphalt concrete through four point bending fatigue test. *Construction and Building Materials,* 29**,** 403-409.

Reese, Ronald 1997. Properties of aged asphalt binder related to asphalt concrete fatigue life. *Journal of the association of asphalt paving technologists,* 66.

Rice, James R 1986. A path independent integral and the approximate analysis of strain concentration by notches and cracks. *Journal of applied mechanics,* 35**,** 379-386.

Rowe, G.M. 1996. *Application of the Dissipated Energy Cocept to Fatigue Cracking in Asphalt Pavements.* PhD, University of Nottingham.

Rowe, G.M. and Bouldin, M.G. 2000. Improved Techniques to Evalute the Fatigue Resistance of Asphaltic Mixtures. *2nd Eurasphalt & Eurobitume Congress Barcelona,* 81**,** 754-763.

Rowe, GM 1993. Performance of asphalt mixtures in the trapezoidal fatigue test. *Asphalt Paving Technology,* 62**,** 344-344.

Sasani, M. and Popov, E.P. 2001. Seismic energy dissipators for RC panels: analytical studies. *Journal of Engineering Mechanics,* 127**,** 835-843.

Schapery, R.A. 1990. A theory of mechanical behavior of elastic media with growing damage and other changes in structure. *Journal of the Mechanics and Physics of Solids,* 38**,** 215-253.

Schapery, RA 1975. A theory of crack initiation and growth in viscoelastic media. *International Journal of Fracture,* 11**,** 141-159.

Schapery, RA 1978. A method for predicting crack growth in nonhomogeneous viscoelastic media. *International Journal of Fracture,* 14**,** 293-309.

Schapery, RA 1984. Correspondence principles and a generalizedJ integral for large deformation and fracture analysis of viscoelastic media. *International Journal of Fracture,* 25**,** 195-223.

Shell 1978. *Shell Pavement Design Manual—Asphalt Overlays for Road Traffic. Shell International Petroleum Company Ltd.,* London, England.

Shen, S. and Carpenter, S.H. 2005. Application of the Dissipated Energy Concept in Fatigue Endurance Limit Testing. *Transportation Research Record,* 1929**,** 165-173.

Shih, M.H. and Sung, W.P. 2005. A model for hysteretic behavior of rhombic low yield strength steel added damping and stiffness. *Computers and Structures,* 83**,** 895-908.

Shook, JF' Finn, FN, Witczak, MW, Monismith, CL. Thickness Design of Asphalt Pavements–The Asphalt Institute Method. Proceedings, 1982. 17-44.

Shook, JF,Finn, FN,Witczak, MW and Monismith, CL. Thickness Design of Asphalt Pavements–The Asphalt Institute Method. Proceedings, 1982. 17-44.

Si, Z.,Little, DN and Lytton, RL 2002. Characterization of microdamage and healing of asphalt concrete mixtures. *Journal of Materials in Civil Engineering,* 14**,** 461-470.

Song, I.,Little, D.,Masad, E.,Lytton, R.,You, Z.,Rowe, G.,Roque, R.,Kim, R.,Huang, S. and Dongre, R. 2005. Comprehensive Evaluation of Damage in Asphalt Mastics Using X-ray CT, Continuum Mechanics, and Micromechanics. *Journal of the Association of Asphalt Paving Technologists,* 74**,** 885-920.

Song, Junho and Der Kiureghian, Armen 2006. Generalized Bouc–Wen model for highly asymmetric hysteresis. *Journal of engineering mechanics,* 132**,** 610-618.

Spanos, PD and Kougioumtzoglou, IA. Harmonic wavelet-based statistical linearization of the Bouc-Wen hysteretic model. Proceedings of the 11th International Conference on Applications of Statistics and Probability in Civil Engineering, ICASP, 2011. 2649-2656.

Sues, R.H.,Mau, S.T. and Wen, Y.K. 1988. Systemes I dentification of Degading Hysteretic Restoring Forces. *Journal of Engineering Mechanics,* 114**,** 833-847.

Suh, Youngchan,Mun, Sungho and Yeo, Insoo 2010. Fatigue life prediction of asphalt concrete pavement using a harmony search algorithm. *KSCE Journal of Civil Engineering,* 14**,** 725-730.

Tan, Y.,Shan, L.,Richard Kim, Y. and Underwood, B.S. 2012. Healing characteristics of asphalt binder. *Construction and Building Materials,* 27**,** 570-577.

Tayebali, A. A.,Rowe, G. M. and Sousa, J. B. 1992. Fatigue Response of Asphalt-Aggregate Mixtures. *Association of Asphalt Paving Technologists-Proceedings,* 61**,** 333-360.

Thom, Nick 2008. *Principles of Paveent Engineering*, Thomas Telford Publishing Ltd 2008.

Thomas, Papagiannakis A. and Masad, Eyad A. 2008. *Pavement Design and materials*.

Van Dijk and Visser, W. 1975. Practical fatigue characterization of bituminous mixes. *Journal of the association of asphalt paving technologists,* 44**,** 38-72.

Van Dijk and Visser, W. Energy Approach to Fatigue for Pavement Design. Association of Asphalt Paving Technologists Proc, 1977.

Walubita, L.F.,Martin, A.E.,Cleveland, G.S. and Lytton, R.L. 2006. Computation of pseudo strain energy and Paris law fracture coefficients from surface energy and uniaxial strain-controlled tension test data. *International Journal of Pavement Engineering,* 7**,** 167-178.

Wen, Y. K. 1976. Method for random vibration of hysteretic systems. *Journal of Engineering Mechanics,* 102**,** 249-263.

Wen, Yi-Kwei 1986. Stochastic response and damage analysis of inelastic structures. *Probabilistic engineering mechanics,* 1**,** 49-57.

Wen, YK 1989. Methods of random vibration for inelastic structures. *Applied Mechanics Reviews,* 42**,** 39.

Witczak, Matthew,Mamlouk, Michael,Souliman, Mena and Zeiada, Waleed 2013. Laboratory Validation of an Endurance Limit for Asphalt Pavements. *NCHRP Project 9-44A*.

Woldekidan, MF,Huurman, M and Pronk, AC 2013. Linear and Nonlinear Viscoelastic Analysis of Bituminous Mortar. *Transportation Research Record: Journal of the Transportation Research Board,* 2370**,** 53-62.

Woldekidan, MF, Huurman, M and Pronk, AC 2013. Linear and Nonlinear Viscoelastic Analysis of Bituminous Mortar. *Transportation Research Record: Journal of the Transportation Research Board,* 2370**,** 53-62.

Wright, SJ and Nocedal, J 1999. *Numerical optimization*, Springer New York.

Xiao, F., Amirkhanian, S., Juang, C.H. 2009. Prediction of Fatigue Life of Rubberized Asphalt Concrete Mixtures Containing Reclaimed Asphalt Pavement Using Artificial Neural Networks. *Journal of Materials in Civil Engineering,* 21.

Xiao, Feipeng,Amirkhanian, Serji and Juang, C Hsein 2007. Rutting resistance of rubberized asphalt concrete pavements containing reclaimed asphalt pavement mixtures. *Journal of Materials in Civil Engineering,* 19**,** 475-483.

Xue Luo,Rong Luo and Lytton., Robert l. 2013. A modified Paris's law to predict entire crack growth in asphalt mixtures. *TRB 13-2800*.

You, Z and Buttlar, WG 2004. Discrete element modeling to predict the modulus of asphalt concrete mixtures. *Journal of Materials in Civil Engineering,* 16**,** 140-146.

Yu, Jiangmiao and Zou, Guilian 2013. Asphalt Pavement Fatigue Cracking Prediction Model with Mode Factor. *International Journal of Pavement Research & Technology,* 6.

Zeiada, Waleed A,Souliman, Mena I,Kaloush, Kamil E and Mamlouk, Michael 2013. Endurance Limit for HMA Based on Healing Concept

Using Uniaxial Tension-Compression Fatigue Test. *Journal of Materials in Civil Engineering*.

Zhu, X. and Lu, X. 2011. Parametric Identification of Bouc-Wen Model and Its Application in Mild Steel Damper Modeling. *Procedia Engineering,* 14**,** 318-324.

Zollinger, C.J. 2005. *Application of surface energy measurements to evaluate moisture susceptibility of asphalt and aggregates.* MSc Dissertation, Texas A&M University.

Appendix A:

Geometrical properties of end connections and holders

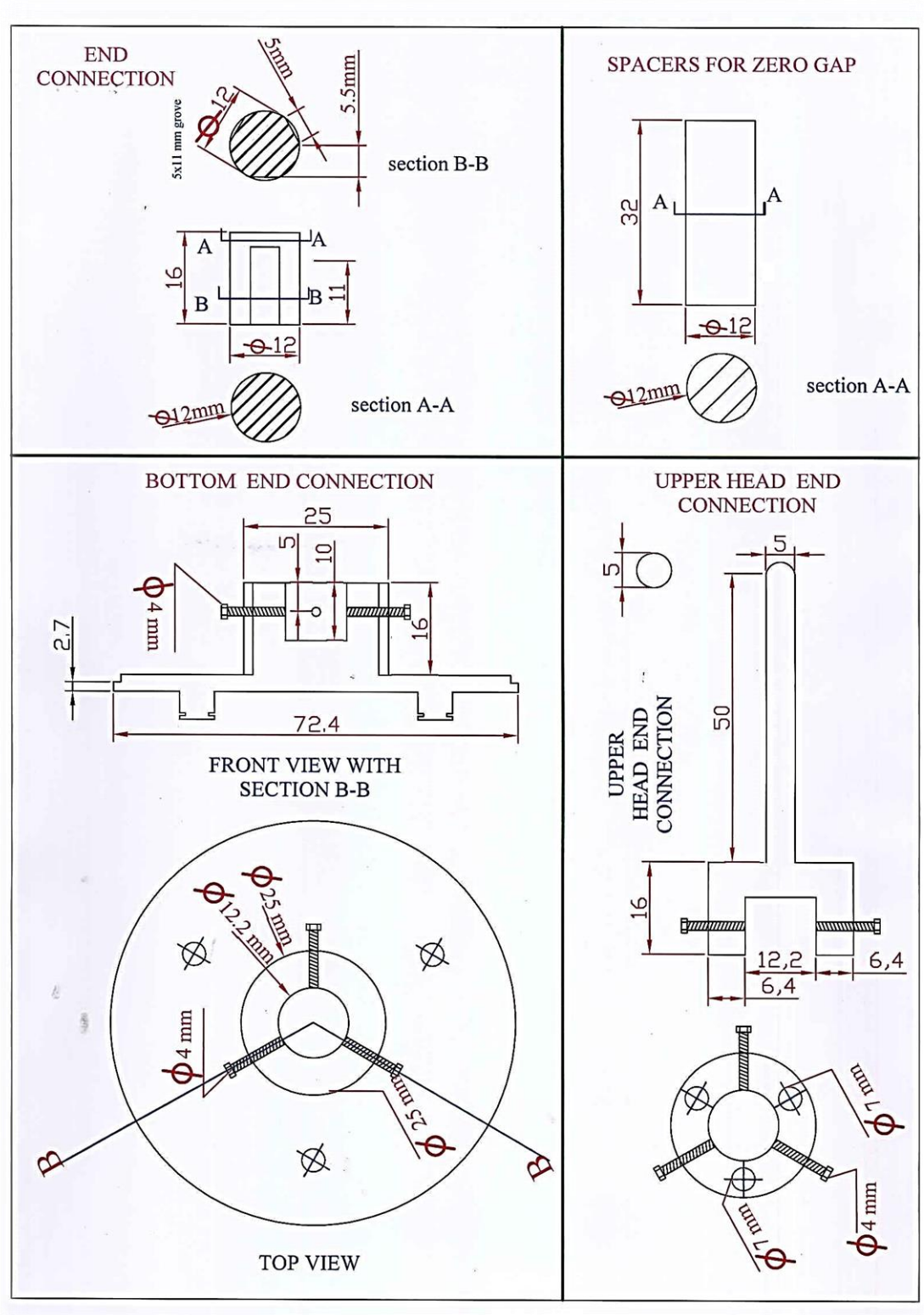

Figure A– 1: Geometrical properties of end connections and holders.

Appendix B

Appendix B-1: Sweep strain amplitude test procedure

Figure B-1 shows the sequences steps for setting DSR sample and running the sweep strain amplitude as follow:

B-1.1. Open the valve of the air supply and switch on the power.

B-1.2. Insert the upper geometry with the top holder and the base plate with bottom holder (Figure A–1) in the specified locations.

B-1.3. Click next to define the geometries and initialise the DSR instrument.

B-1.4. Select the designed sequence from the sequences list in the PC and click on for loading.

B-1.5. Click on the (Start current sequence) button from the tool bars to operate the sequence.

B-1.6. Enter the details of the samples such as (test name, sample code, date and operator). Worthy that the file of data is saved according to these sample code.

B-1.7. Insert the spacer of the zero gap (Figure A-1).

B-1.8. Click next to define the zero gap.

B-1.9. Click next to set the gap (in this sequence define 100 mm) to provide a space for loading the sample.

B-1.10. Remove the spacers.

B-1.11. Loading the sample with end connections (the sample should be glued to the end connections at least 30 minute before testing).

B-1.12. Click next and setting the sample by inserting the end connection in the upper and lower holders. In this case, the gap is selected in the sequence as working gape in order to define exactly the sample height.

B-1.13. Click next to the free rotation to insure there is no any initial loading on the sample during tighten the screws.

B-1.14. Tighten the three screws.

B-1.15. Stick the three thermo caplets to the sample at the top, middle and button and monitor the temperate of the sample using data acquisition unit (instruNet®) as shown in Figures 3–5 and 3–6.

B-1.16. Switch on the temperature control unit and set it at 25^{o}C (Figure 3–4) and install on the base plate around the sample.

B-1.17. Click next and set the temperature of the base plate at 25^{o}C until it arrives to the equilibrium.

B-1.18. Click next to check the amplitude table of the sweep strain amplitude.

B-1.19. Click next to run the oscillation of the amplitude sweep strain.

B-1.20. Stop the sequence and save data in specified folder.

B-1.21. Release the screws, click (Go to top stop) button and remove the sample.

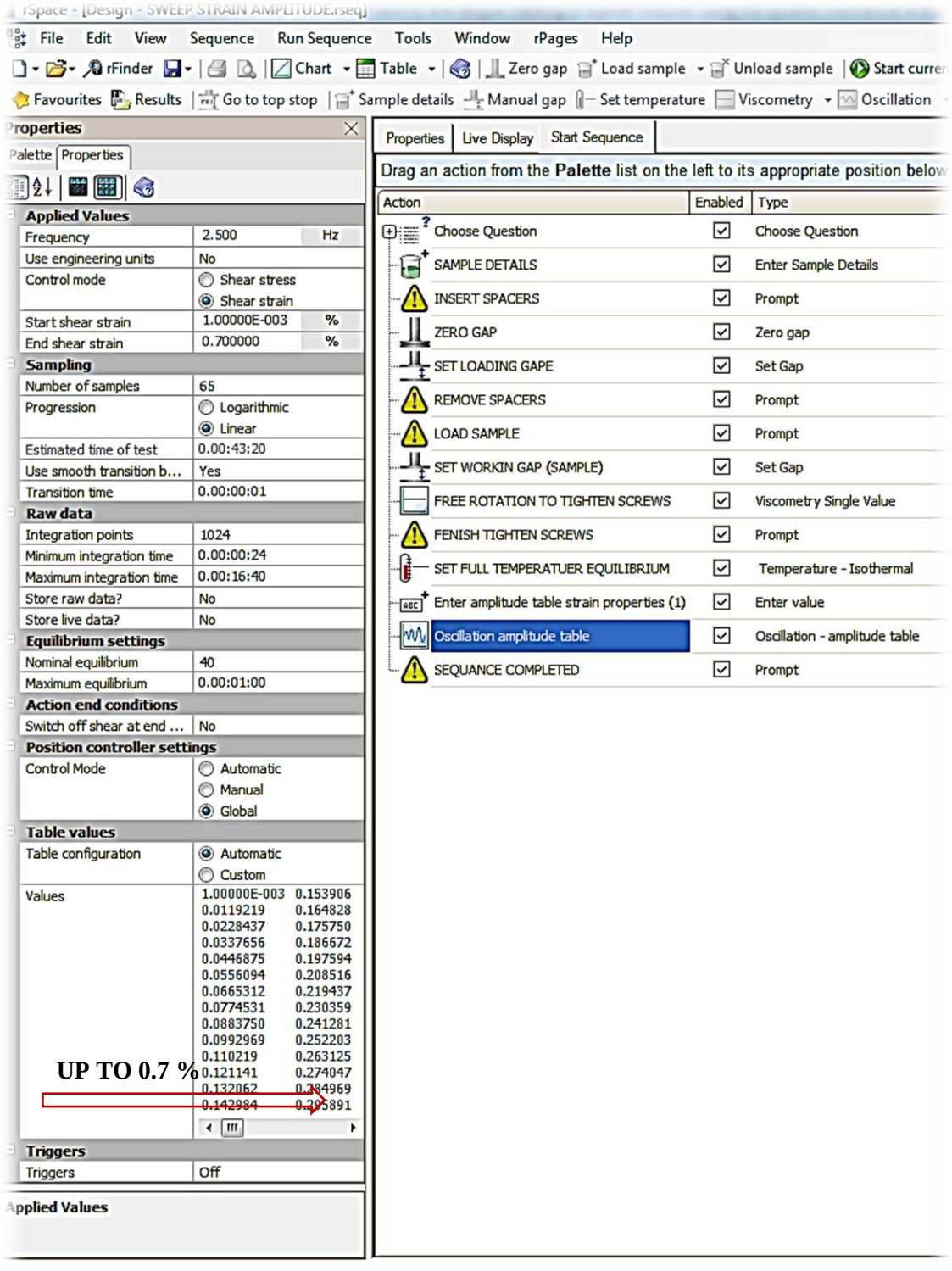

Figure B- 1: DSR-Sequence of sweep strain amplitude test.

Table B- 1: DBM-G samples tested in sweep strain.

ID	G bulk	AV%	ID	G bulk	AV%	ID	G bulk	AV%
DBM-G-1	2.294	7.342	DBM-G-2	2.300	7.097	DBM-G-3	2.347	5.189
γ(%)	τ (Pa)	δ(°)	γ(%)	τ (Pa)	δ(°)	γ(%)	τ (Pa)	δ(°)
0.001	2948	50.070	0.001	2025	48.290	0.001	2663	48.930
0.012	32267	54.170	0.012	20570	54.330	0.012	27200	53.710
0.022	56614	56.150	0.023	36100	56.480	0.022	47750	55.940
0.033	77886	57.560	0.033	49560	57.900	0.033	65670	57.490
0.044	96333	58.660	0.044	62000	59.080	0.044	81600	58.920
0.055	112533	59.630	0.055	73650	59.990	0.055	95620	59.900
0.066	127333	60.250	0.066	83970	60.660	0.066	108600	60.670
0.077	138810	60.990	0.077	94200	61.260	0.076	120000	61.460
0.087	149524	61.440	0.088	103500	61.880	0.087	130700	62.000
0.098	158762	61.840	0.098	112100	62.440	0.098	139200	62.560
0.109	167619	62.370	0.109	120400	62.780	0.109	145700	63.200
0.120	174619	62.810	0.120	128000	63.180	0.120	152300	63.690
0.131	181143	63.140	0.131	135600	63.630	0.131	158900	63.960
0.142	187667	63.600	0.142	142400	63.850	0.142	165300	64.430
0.153	194095	63.960	0.153	146800	64.240	0.153	170600	64.830
0.164	199000	64.150	0.164	151000	64.590	0.164	175600	65.070
0.175	202857	64.410	0.174	155700	64.780	0.175	179900	65.390
0.186	206667	64.640	0.186	160400	65.070	0.185	184000	65.710
0.196	210095	64.800	0.197	165300	65.390	0.196	187300	65.870
0.208	210333	65.070	0.207	169800	65.570	0.207	189300	66.160
0.218	210000	65.310	0.218	174300	65.750	0.218	188500	66.460
0.229	211905	65.470	0.229	178700	66.000	0.229	189700	66.550
0.240	211857	65.650	0.240	182900	66.150	0.240	190300	66.740
0.251	212429	65.800	0.251	186800	66.280	0.251	190900	67.030
0.262	212905	65.810	0.262	190400	66.520	0.262	191100	67.190
0.273	213524	65.960	0.273	194100	66.720	0.272	190900	67.210
0.284	213190	66.070	0.284	197400	66.760	0.284	190400	67.390
0.294	212619	66.210	0.295	196900	67.010	0.295	189500	67.550
0.306	211667	66.300	0.305	197800	67.190	0.305	187500	67.650
0.316	210048	66.570	0.316	199600	67.210	0.317	184100	67.690
0.327	207810	66.630	0.328	201500	67.410	0.328	180000	67.900
0.338	204000	66.680	0.338	203600	67.640	0.338	174900	67.880
0.349	198857	66.820	0.349	205700	67.660	0.349	168400	67.980
0.360	193714	66.890	0.360	207900	67.780	0.361	159800	67.950
0.371	189571	66.960	0.371	209700	67.970	0.372	152700	68.020
0.382	185619	67.140	0.381	211500	68.040	0.382	146300	67.920
0.393	181476	67.260	0.393	213400	68.100	0.394	139200	67.840
0.404	176762	67.210	0.404	215100	68.300	0.405	131700	67.740
0.415	172143	67.380	0.414	215900	68.400	0.415	124200	67.370
0.426	166571	67.520	0.426	213100	68.460	0.427	115400	66.860
0.436	161524	67.510	0.437	212400	68.650	0.438	107200	66.520
0.448	156181	67.560	0.447	212600	68.760	0.448	98780	66.000
0.459	150405	67.810	0.458	213000	68.760	0.460	89550	65.140
0.469	143119	67.750	0.469	213600	68.890	0.471	79750	64.520
0.481	124043	67.880	0.480	214600	68.990	0.481	70400	63.170
0.491	113413	67.980	0.491	215400	68.950	0.493	59350	61.190
0.502	89541	67.880	0.503	216100	69.040	0.504	50240	58.650
0.513	62154	67.880	0.513	216300	69.220	0.514	43570	55.610
0.525	40178	67.920	0.523	216600	69.230	0.526	38070	52.060

Table B- 2: DBM-L samples tested in sweep strain.

ID	G bulk	AV%	ID	G bulk	AV%	ID	G bulk	AV%
DBM-L-1	2.422	2.909	DBM-L-2	2.379	4.653	DBM-L-3	2.436	2.368
γ(%)	τ (Pa)	δ(°)	γ(%)	τ (Pa)	δ(°)	γ(%)	τ (Pa)	δ(°)
0.001	2417	46.140	0.001	3304	43.690	0.001	2827	43.180
0.012	26020	51.960	0.012	31870	50.370	0.012	27970	51.160
0.022	44770	54.350	0.022	54550	52.970	0.022	48160	53.930
0.033	60980	55.940	0.033	74050	54.700	0.033	65330	56.050
0.044	75120	57.250	0.044	91040	56.100	0.044	81020	57.010
0.055	87910	58.160	0.055	105700	57.180	0.055	94340	58.820
0.066	99330	58.950	0.065	118900	57.980	0.066	108500	58.900
0.077	109500	59.810	0.076	130800	58.770	0.076	118100	60.520
0.087	116800	60.480	0.087	141200	59.600	0.087	129400	60.930
0.098	124400	61.000	0.098	150800	60.100	0.098	138500	61.760
0.109	131700	61.660	0.109	158800	60.900	0.109	148200	61.800
0.120	138800	62.160	0.120	166900	61.240	0.120	153800	62.660
0.131	145700	62.520	0.131	171900	61.600	0.131	160700	63.010
0.142	151500	62.940	0.142	176900	62.100	0.142	167500	63.470
0.153	155600	63.410	0.153	182000	62.530	0.153	174000	63.890
0.163	160100	63.770	0.163	186900	62.860	0.163	179900	64.220
0.175	165100	64.050	0.175	191500	63.180	0.175	185700	64.550
0.185	169600	64.450	0.185	195700	63.620	0.185	191700	64.830
0.196	174300	64.820	0.196	199900	63.860	0.196	197200	64.950
0.207	178300	64.990	0.207	203700	64.100	0.207	202200	65.210
0.218	179100	65.480	0.218	207200	64.430	0.218	205500	65.720
0.229	181600	65.780	0.229	207400	64.700	0.229	210400	65.870
0.240	184900	65.860	0.240	208400	64.890	0.240	211800	65.990
0.251	187800	66.120	0.251	209900	65.250	0.251	213700	66.230
0.262	190900	66.390	0.262	211800	65.510	0.261	215900	66.430
0.272	193900	66.540	0.272	213600	65.690	0.273	217800	66.640
0.284	195500	66.740	0.284	215100	66.000	0.284	220600	66.810
0.295	195900	66.950	0.294	216600	66.310	0.294	223000	66.950
0.305	197700	67.060	0.305	218200	66.410	0.305	215700	66.530
0.317	199200	67.260	0.317	219600	66.630	0.317	218400	66.730
0.328	202900	67.220	0.327	221200	66.860	0.327	220700	66.840
0.338	204600	67.550	0.338	221700	66.950	0.338	223500	66.800
0.349	206700	67.620	0.350	219700	67.200	0.349	229300	66.400
0.361	207300	67.770	0.360	219400	67.360	0.360	224800	67.430
0.371	206200	68.000	0.371	219800	67.390	0.371	223300	67.400
0.382	207600	67.890	0.382	220400	67.570	0.382	223600	67.450
0.393	208700	68.030	0.393	221000	67.750	0.393	223100	67.890
0.404	210200	68.230	0.403	221600	67.740	0.403	224800	67.730
0.414	211200	68.310	0.415	222000	67.900	0.415	228400	67.290
0.426	212100	68.460	0.426	222700	68.000	0.425	226200	68.070
0.436	210200	68.720	0.436	222900	68.150	0.435	218800	67.360
0.447	209900	68.760	0.448	223500	68.190	0.447	219800	67.450
0.459	210200	68.870	0.459	220800	68.300	0.458	220800	67.500
0.470	210900	68.930	0.469	218600	68.420	0.469	222200	67.610
0.480	211500	68.950	0.481	217500	68.500	0.480	220500	67.920
0.491	212100	68.870	0.491	216700	68.760	0.492	220800	67.580
0.503	209500	69.060	0.502	216100	68.770	0.502	217100	67.760
0.513	208600	69.080	0.513	215300	68.900	0.512	217200	67.520
0.524	208000	69.140	0.524	214700	68.990	0.524	216100	67.590
0.535	208100	69.250	0.534	213300	69.130	0.535	214000	67.840
0.545	207700	69.390	0.546	212200	69.140	0.545	213400	67.730
0.556	206900	69.430	0.557	210600	69.320	0.557	211800	67.700
0.569	202700	69.720	0.567	208200	69.460	0.568	212200	67.490
0.578	199200	69.790	0.579	202400	69.400	0.578	209800	67.640

0.589	195400	69.770	0.590	197700	69.450	0.589	207600	67.530
0.601	191200	69.850	0.600	193900	69.390	0.601	205700	67.450
0.612	186800	69.800	0.611	189100	69.560	0.611	201900	67.530
0.622	181900	69.520	0.623	186800	69.310	0.622	196800	67.310
0.635	175500	69.390	0.634	182900	69.310	0.634	188800	67.040
0.645	165100	69.120	0.644	176700	69.380	0.644	181300	66.670
0.655	155300	68.550	0.656	171000	69.420	0.655	167300	66.430
0.668	141300	67.860	0.667	160700	69.520	0.670	136100	63.910
0.679	124100	66.660	0.679	142300	69.090	0.685	57800	52.390
0.689	106600	64.500	0.692	111800	68.140	0.685	57800	52.390

Table B- 3: HRA-G samples tested in sweep strain.

ID	G bulk	AV%	ID	G bulk	AV%	ID	G bulk	AV%
HRA-G-1	2.287	4.469	HRA-G-2	2.326	2.866	HRA-G-3	2.298	4.048
γ(%)	τ (Pa)	δ(°)	γ(%)	τ (Pa)	δ(°)	γ(%)	τ (Pa)	δ(°)
0.001	8213	36.130	0.001	9154	33.100	0.001	7271	37.350
0.011	88245	38.830	0.011	95890	36.670	0.011	80600	39.470
0.021	161800	40.170	0.020	174800	38.790	0.021	148800	40.810
0.031	229650	41.500	0.030	247000	40.640	0.031	212300	42.030
0.041	292750	42.870	0.041	313900	42.360	0.041	271600	43.290
0.052	349550	44.000	0.051	375300	43.690	0.052	323800	44.500
0.062	402350	45.040	0.061	433000	44.960	0.062	371700	45.530
0.073	449850	46.120	0.071	483000	46.310	0.073	416700	46.590
0.083	492300	47.000	0.082	525900	47.490	0.083	458700	47.590
0.094	533000	47.840	0.093	568100	48.470	0.093	497900	48.340
0.104	571450	48.830	0.103	608000	49.500	0.104	534900	49.140
0.115	607300	49.630	0.114	645700	50.370	0.115	568900	49.950
0.126	641200	50.230	0.124	681400	51.040	0.125	601000	50.550
0.137	672650	50.950	0.135	714800	51.820	0.136	630500	51.110
0.147	702250	51.600	0.146	746000	52.510	0.147	658500	51.760
0.158	729750	52.070	0.156	775200	52.980	0.157	684300	52.240
0.169	755650	52.740	0.167	802200	53.570	0.168	709100	52.610
0.179	779700	53.360	0.178	827100	54.070	0.179	732300	53.130
0.190	801050	53.770	0.189	850200	54.410	0.190	751900	53.610
0.201	814500	54.200	0.200	868300	54.870	0.201	760700	54.060
0.212	828000	54.720	0.210	886600	55.330	0.212	769400	54.610
0.222	838200	55.100	0.221	894300	55.640	0.222	782100	55.060
0.234	846850	55.570	0.232	899200	56.040	0.233	794500	55.290
0.245	856300	56.100	0.243	907100	56.400	0.244	805500	55.590
0.255	864350	56.470	0.254	913900	56.540	0.255	814800	55.900
0.266	871100	56.650	0.265	919400	56.680	0.266	822800	56.050
0.277	876800	56.980	0.276	924200	56.890	0.277	829400	56.220
0.288	882000	57.190	0.287	927800	56.980	0.288	836200	56.490
0.299	886100	57.260	0.298	931000	56.980	0.298	841200	56.620
0.310	889300	57.570	0.309	933000	57.140	0.309	845600	56.730
0.321	891650	57.830	0.320	934000	57.300	0.321	849300	56.970

0.332	891450	57.890	0.330	931300	57.420	0.331	851600	57.140
0.343	890000	58.010	0.342	927400	57.560	0.342	852600	57.240
0.354	887050	58.210	0.353	921500	57.880	0.354	852600	57.510
0.364	881650	58.270	0.363	912800	58.130	0.364	850500	57.750
0.376	873700	58.360	0.375	900000	58.350	0.375	847400	57.880
0.387	861900	58.580	0.387	881300	58.790	0.387	842500	57.170
0.397	845200	58.660	0.397	855400	59.120	0.397	835000	57.020
0.409	820100	58.910	0.409	815300	59.270	0.408	804900	56.640
0.420	785200	57.520	0.421	759700	59.580	0.420	770700	56.270
0.430	731800	55.270	0.434	669300	58.270	0.431	694300	55.320
0.442	622650	53.890	0.449	470200	54.220	0.442	575100	53.510
0.453	453050	49.140	0.471	156400	49.200	0.454	349700	51.870
0.463	332540	46.910	0.471	156400	43.200	0.465	314600	49.270

Table B- 4: HRA-L samples tested in sweep strain.

ID	G bulk	AV%	ID	G bulk	AV%	ID	G bulk	AV%
HRA-L-1	2.339	2.330	HRA-L-2	2.365	1.252	HRA-L-3	2.326	2.898
γ(%)	τ (Pa)	δ(°)	γ(%)	τ (Pa)	δ(°)	γ(%)	τ (Pa)	δ(°)
0.001	5541	35.540	0.001	6706	35.000	0.001	7137	36.180
0.011	67780	40.390	0.011	68960	39.400	0.011	80160	39.670
0.021	120400	42.920	0.021	123800	41.730	0.021	144700	41.690
0.032	166400	44.820	0.032	172400	43.550	0.031	202300	43.230
0.042	207300	46.450	0.042	216200	45.200	0.042	255100	44.640
0.053	244500	47.730	0.053	256200	46.530	0.052	303800	45.900
0.063	278100	48.820	0.063	293300	47.680	0.063	344900	46.970
0.074	309300	49.950	0.074	327500	48.850	0.073	384200	48.040
0.085	338300	50.860	0.084	359200	49.830	0.084	421200	49.060
0.095	365400	51.590	0.095	389200	50.640	0.094	451900	49.880
0.106	390700	52.420	0.106	416000	51.550	0.105	482900	50.690
0.117	414800	53.130	0.117	433700	52.510	0.116	507500	51.600
0.128	433400	53.710	0.127	452800	53.190	0.127	530800	52.280
0.139	448700	54.470	0.138	471500	53.920	0.138	555600	52.870
0.149	465100	55.100	0.149	483200	54.680	0.148	574100	53.630
0.160	481900	55.530	0.160	492700	55.220	0.159	591900	54.200
0.171	495700	56.100	0.171	506000	55.800	0.170	611800	54.660
0.182	504700	56.700	0.182	515200	56.400	0.181	627800	55.300
0.193	515800	57.110	0.193	521900	56.860	0.191	638200	55.820
0.204	528000	57.580	0.204	531400	57.280	0.202	653400	56.200
0.215	539600	58.100	0.215	534800	57.890	0.213	670200	56.680
0.225	551500	58.410	0.225	540700	58.360	0.224	678100	57.170
0.236	562000	58.760	0.236	545200	58.760	0.235	687000	57.510
0.247	563600	59.300	0.248	547700	59.280	0.246	699300	57.960
0.258	569200	59.650	0.258	552900	59.660	0.257	709500	58.360
0.269	569300	59.920	0.269	552600	60.000	0.268	715500	58.610

0.280	565500	60.310	0.281	554800	60.380	0.279	724700	58.960
0.291	565200	60.570	0.291	551000	60.820	0.290	729000	59.390
0.302	563900	60.860	0.302	550100	61.000	0.300	732600	59.650
0.313	561100	61.270	0.314	546900	61.430	0.312	738600	59.910
0.323	555783	61.580	0.324	540900	61.850	0.323	737400	60.320
0.335	554913	61.750	0.335	538700	62.010	0.333	737600	60.580
0.346	552348	62.070	0.347	529900	62.400	0.345	740500	60.790
0.356	546043	62.370	0.357	523200	62.760	0.356	732700	61.170
0.368	540565	62.570	0.368	517100	62.960	0.366	726200	61.440
0.379	535000	62.870	0.380	508200	63.210	0.378	722300	61.580
0.389	528435	63.110	0.391	497200	63.380	0.389	718200	61.820
0.400	513130	63.210	0.401	476900	63.440	0.399	703300	62.010
0.412	488739	63.420	0.414	436600	62.820	0.411	687500	62.150
0.422	432522	63.660	0.430	329800	59.280	0.422	665000	62.330
0.433	362391	63.780	0.444	203500	52.470	0.433	630000	62.390
0.445	313739	64.000	0.458	115000	45.250	0.445	588100	62.500

Appendix B-2: DSR-Sequence of sweep stress amplitude test

Figures B-2 and B–3 show the sequences steps for setting DSR sample and running the sweep stress amplitude as follow:

B-2.1. Repeat steps B-1.1 to B-1.17.

B-2.2. Click the next to run the sub sequence). This sequence transforms the running of the sequences one time to the (SWEEP STRESS AMPLITUDE) page and continues until finishing the test in the Figure B–3.

B-2.3. Stop the sequence and save the data in specified folder.

B-1.4. Release the screws, click (Go to top stop) button and remove the sample.

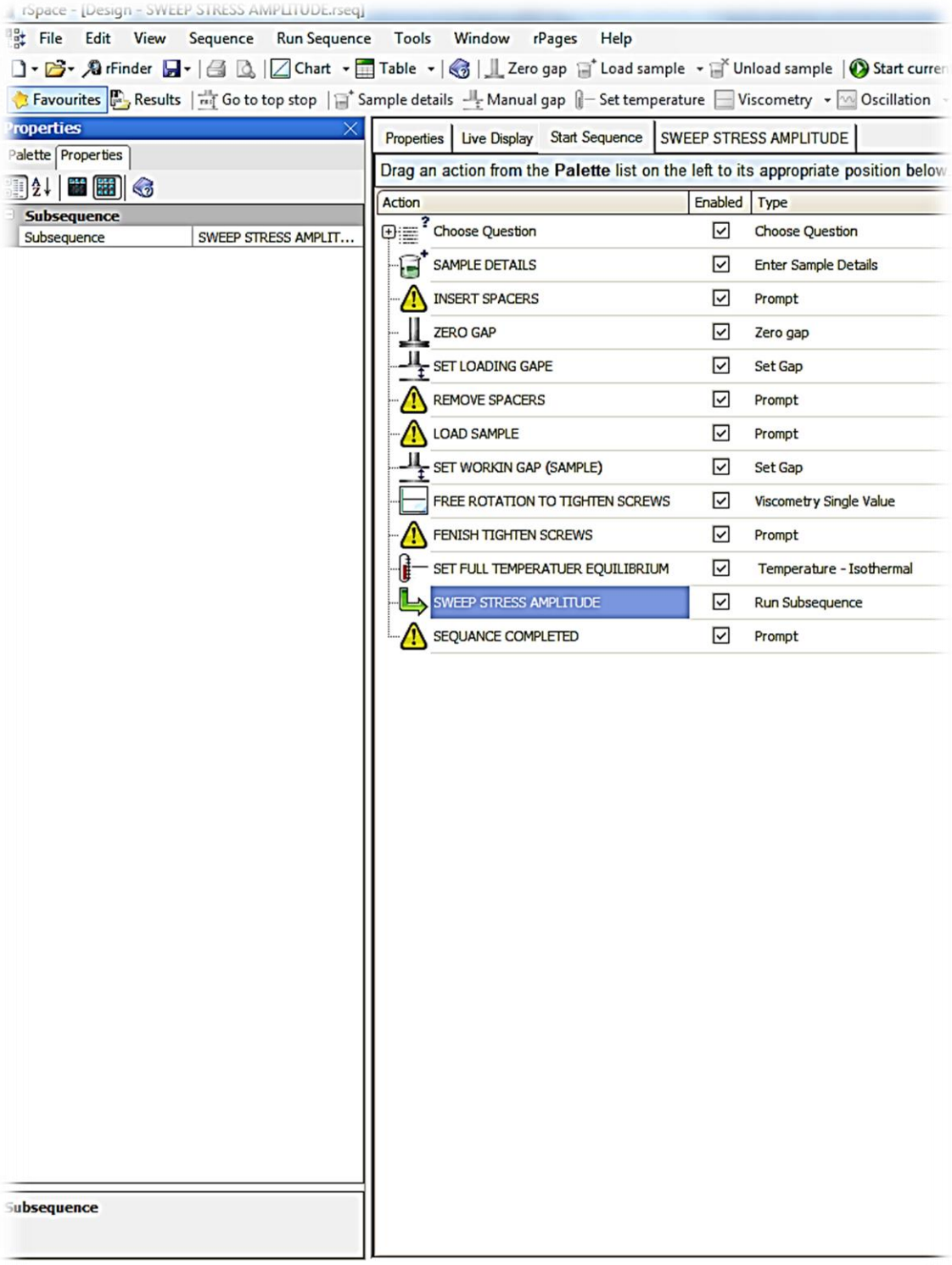

Figure B- 2.1: DSR-Sequence of sweep stress amplitude test

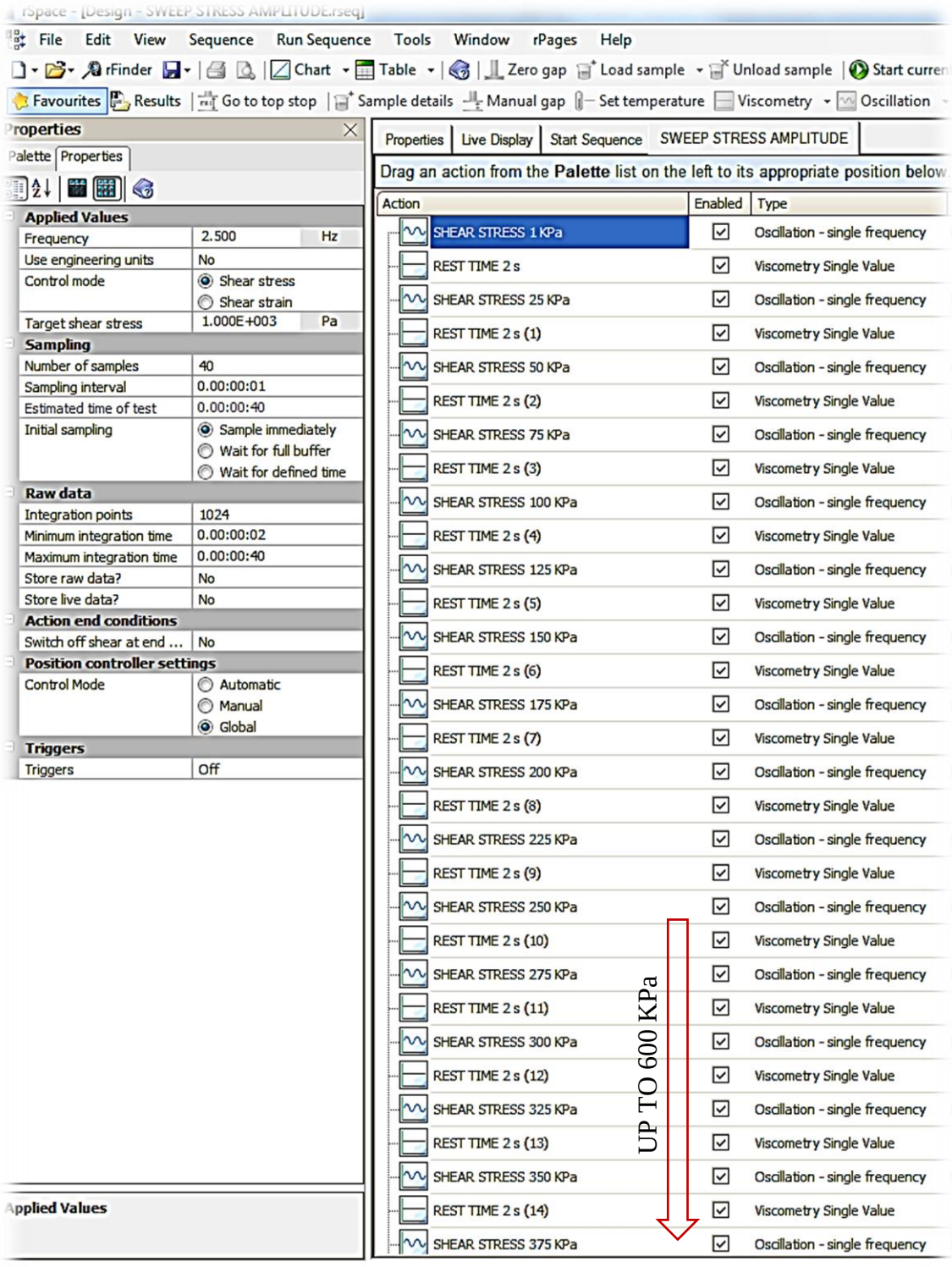

Figure B- 2.2: Sweep stress amplitude test steps.

Table B- 5: DBM-G samples tested in sweep stress.

ID	G bulk	AV%	ID	G bulk	AV%	ID	G bulk	AV%
DBM-G-1	2.342	5.415	DBM-G-2	2.325	6.079	DBM-G-3	2.348	5.146
dγ/dτ	τ (KPa)		dγ/dτ	τ (KPa)		dγ/dτ	τ (KPa)	
1.903E-08	1		1.807E-07	1		7.090E-06	1	
3.687E-05	25		1.520E-05	25		1.402E-06	25	
1.533E-04	50		1.102E-04	50		1.492E-04	50	
9.568E-05	75		5.591E-05	75		1.783E-05	75	
2.276E-04	100		1.773E-04	100		5.958E-05	100	
3.216E-04	125		2.642E-04	125		1.134E-04	125	
4.376E-04	150		3.730E-04	150		1.808E-04	150	
5.955E-04	175		5.084E-04	175		1.604E-04	175	
8.159E-04	200		7.088E-04	200		6.146E-04	200	
8.339E-04	225		1.223E-03	225		3.686E-04	225	
1.896E-03	250		1.630E-03	250		1.115E-03	250	
4.359E-03	275		2.282E-03	275		3.592E-03	275	
1.054E-02	300		9.500E-03	300		1.100E-02	300	

Table B- 6: DBM-L samples tested in sweep stress.

ID	G bulk	AV%	ID	G bulk	AV%	ID	G bulk	AV%
DBM-L-1	2.409	3.441	DBM-L-2	2.377	4.716	DBM-L-3	2.404	3.634
dγ/dτ	τ (KPa)		dγ/dτ	τ (KPa)		dγ/dτ	τ (KPa)	
3.659E-08	1		1.624E-06	1		7.937E-08	1	
1.322E-05	25		1.629E-05	25		6.432E-06	25	
1.046E-04	50		1.005E-04	50		1.366E-05	50	
5.086E-05	75		2.602E-05	75		2.400E-05	75	
1.718E-04	100		2.171E-04	100		7.266E-05	100	
2.568E-04	125		4.210E-04	125		1.226E-04	125	
3.592E-04	150		4.248E-04	150		2.118E-04	150	
4.872E-04	175		6.896E-04	175		2.787E-04	175	
6.504E-04	200		1.012E-03	200		4.304E-04	200	
8.763E-04	225		1.934E-03	225		4.568E-04	225	
1.157E-03	250		6.756E-03	250		6.935E-04	250	
1.563E-03	275		9.200E-03	275		1.006E-03	275	
2.220E-03	300					1.400E-03	300	
3.251E-03	325					2.003E-03	325	
7.171E-03	350					3.176E-03	350	
						5.381E-03	375	
						1.893E-02	400	

Table B- 7: HRA-G samples tested in sweep stress.

ID	G bulk	AV%	ID	G bulk	AV%	ID	G bulk	AV%
HRA-G-1	2.317	3.257	HRA-G-2	2.319	3.137	HRA-G-3	2.315	3.317
dγ/dτ	τ (KPa)		dγ/dτ	τ (KPa)		dγ/dτ	τ (KPa)	
2.415E-08	1		2.490E-08	1		2.466E-08	1	
2.741E-07	25		8.763E-07	25		1.097E-08	25	
1.529E-06	50		1.512E-06	50		1.762E-06	50	
6.581E-07	75		4.092E-06	75		3.327E-06	75	
2.991E-06	100		5.742E-06	100		5.369E-06	100	
4.629E-06	125		9.087E-06	125		1.304E-05	125	
6.534E-06	150		1.148E-05	150		1.887E-05	150	
8.105E-06	175		1.470E-05	175		2.026E-05	175	

1.036E-05	200	1.871E-05	200	2.379E-05	200
1.239E-05	225	2.148E-05	225	2.620E-05	225
1.461E-05	250	2.693E-05	250	3.136E-05	250
1.816E-05	275	3.011E-05	275	3.649E-05	275
2.065E-05	300	3.531E-05	300	4.200E-05	300
2.559E-05	325	3.955E-05	325	4.510E-05	325
2.858E-05	350	4.367E-05	350	5.137E-05	350
3.296E-05	375	4.925E-05	375	5.914E-05	375
4.985E-05	400	5.868E-05	400	6.577E-05	400
6.739E-05	425	7.407E-05	425	7.467E-05	425
6.874E-05	450	7.882E-05	450	8.240E-05	450
7.486E-05	475	9.061E-05	475	8.690E-05	475
8.136E-05	500	9.889E-05	500	8.606E-05	500
9.058E-05	525	1.098E-04	525	1.227E-04	525
1.026E-04	550	1.322E-04	550	2.154E-04	550
2.612E-04	575	2.569E-04	575	4.022E-04	575
3.970E-04	600	3.879E-04	600	5.877E-04	600

Table B- 8: HRA-L samples tested in sweep stress.

ID	G bulk	AV%	ID	G bulk	AV%	ID	G bulk	AV%
HRA-L-1	2.348	1.962	HRA-L-2	2.342	2.240	HRA-L-3	2.344	2.133
dγ/dτ	τ (KPa)		dγ/dτ	τ (KPa)		dγ/dτ	τ (KPa)	
2.087E-08	1		1.869E-07	1		7.966E-09	1	
2.064E-06	25		1.309E-06	25		2.005E-06	25	
1.479E-05	50		6.684E-06	50		9.234E-06	50	
8.476E-06	75		1.022E-05	75		1.996E-05	75	
2.315E-05	100		1.508E-05	100		3.294E-05	100	
3.240E-05	125		2.115E-05	125		4.821E-05	125	
3.436E-05	150		2.189E-05	150		5.233E-05	150	
5.493E-05	175		3.216E-05	175		8.470E-05	175	
7.007E-05	200		3.885E-05	200		1.083E-04	200	
8.412E-05	225		4.766E-05	225		1.318E-04	225	
1.009E-04	250		5.730E-05	250		1.588E-04	250	
1.213E-04	275		6.398E-05	275		1.923E-04	275	
1.432E-04	300		7.361E-05	300		2.212E-04	300	
1.684E-04	325		3.955E-05	325		2.597E-04	325	
1.954E-04	350		4.367E-05	350		3.082E-04	350	
2.235E-04	375		4.925E-05	375		3.748E-04	375	
2.447E-04	400		1.945E-04	400		4.806E-04	400	
2.906E-04	425		1.943E-04	425		5.426E-04	425	
3.422E-04	450		2.116E-04	450		8.240E-05	450	
4.004E-04	475		2.350E-04	475		7.582E-04	475	
4.709E-04	500		2.500E-04	500		9.383E-04	500	
5.473E-04	525		2.700E-04	525		1.298E-03	525	
6.336E-04	550		2.694E-04	550		2.110E-03	550	
7.841E-04	575		4.405E-04	575		0.000E+00	575	
9.773E-04	600		4.700E-04	600		0.000E+00	600	

Appendix B-3: DSR-Sequence of Fatigue test-controlled strain

Figure B-4 shows the sequences steps for setting DSR sample and running the fatigue test in controlled strain test mode as follow:

B-3.1. Repeat steps B-1.1 to B-1.17.

B-3.2. Click next to run the relaxation test. This test is performed at very low strain amplitude (0.002 %) and lasting for 100 s; Figure B-6 demonstrates in details the relaxation test properties.

B-3.3. Move automatically to the next sequence (RESET SAMPLE). This sequence returns the sample to original position before relaxation test.

B-3.4. Move automatically to the next sequence: this sequence gives a rest time. In which loading force is zero for 15 minutes to remove any permanent deformation during relaxation test and (RESET SAMPLE).

B-3.5. Move automatically. Perform fatigue test at low strain amplitude within LVE region to evaluate the linear viscoelastic properties. Strain amplitude is 0.02 % and test duration 120 s. In this period, one point is collected at each 2 s to gathering 60 points at the end of the test using integration points 512.

B-3.6. Move automatically. Perform initial fatigue test at high strain amplitude (Table 3–6) to create the damage. Test lasts for 120 s. during this period one point is collected at each 2 s to gathering 60 points at the end of the test using integration points 512.

B-3.7. Move automatically. Perform initial fatigue test at the same strain amplitude in B-3.6 to produce the initial hysteresis loops. Test lasts for 0.6 s during this period one point is collected at each 0.002 s to gathering 300 points at the end of the test using integration points 512. In this test raw data (torque and angular displacement) are collected to plot the hysteresis loops.

B-3.8. Move automatically. Perform loops sequence (10 times) to perform fatigue test and hysteresis loops test frequently.

B-3.9. Move automatically. Perform fatigue test using strain amplitude in B-3.6 to create the damage. Test lasts for 3600 s. during this period one point is collected at each 2 s to gathering 1800 points at the end of the test using integration points 512.

B-3.10. Move automatically. Perform fatigue test using strain amplitude in B-3.6 to create the damage. Test lasts for 0.6 s during this period one point is collected at each 0.002 s to gathering 300 points at the end of the test using integration points 512. In this test raw data is also collected.

B-3.10. Move automatically. Sequence completed either when the criterion has been verified or completing the number of loops. The criteria defined by the triggers in the sequence properties.

B-3.11. Stop the sequence and save the data in specified folder.

B-3.12. Release the screws, click (Go to top stop) button and remove the sample.

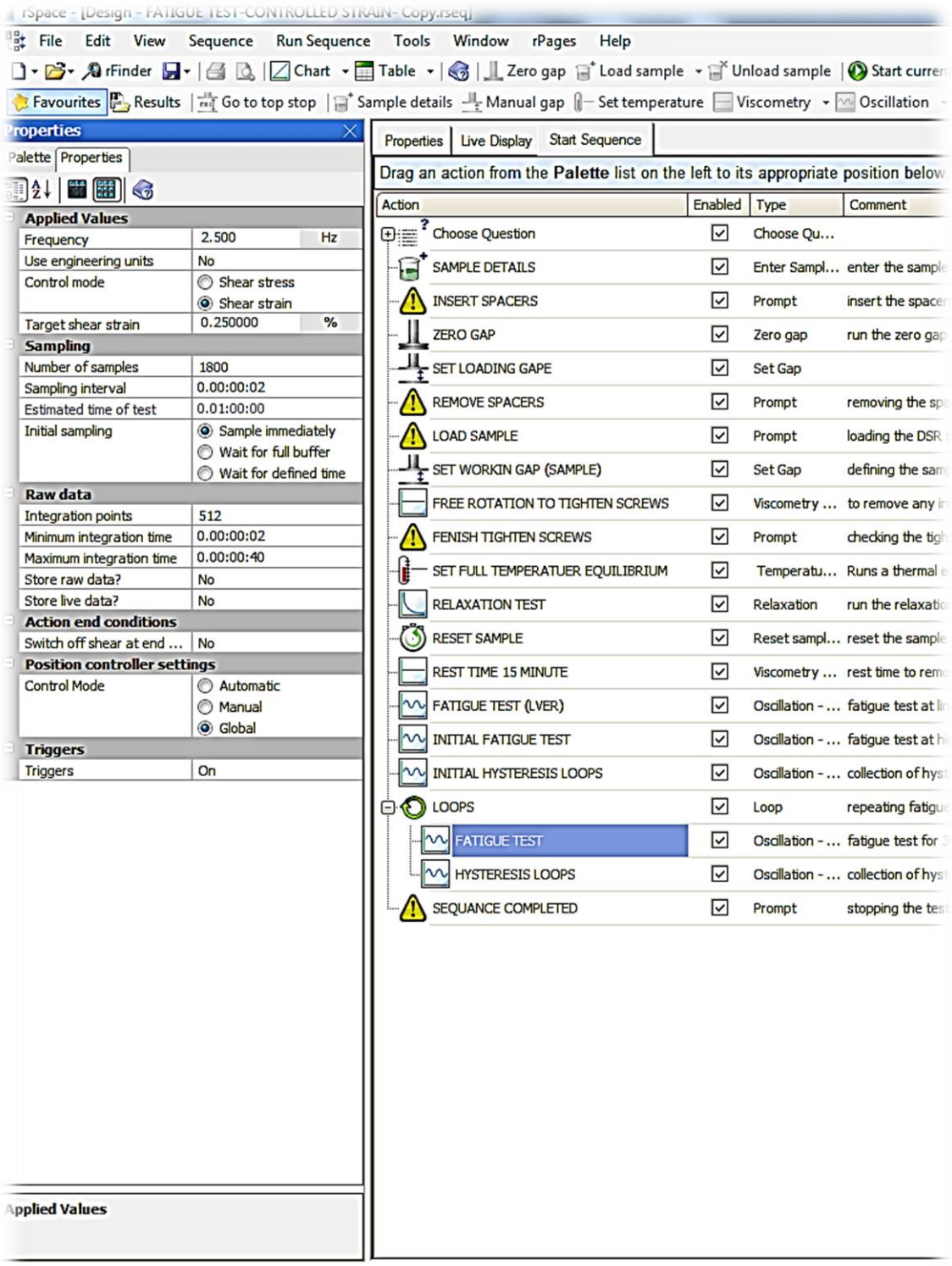

Figure B- 3: DSR sequences for fatigue testing in strain test mode.

Table B- 9: Fatigue data for DBM-G samples tested in strain mode.

ID	DG-1				ID	DG-2				ID	DG-3			
No. cycles	γ(%)	τ(Pa)	G*(Pa)	δ(°)	No. cycles	γ(%)	τ(Pa)	G*(Pa)	δ(°)	No. cycles	γ(%)	τ(Pa)	G*(Pa)	δ(°)
40	0.303	261300	86234778	65.110	40	0.304	249600	82036450	66.640	38	0.303	168800	55674659	69.090
105	0.299	232400	77800170	65.640	115	0.299	221900	74180554	66.620	113	0.299	150200	50199025	69.880
205	0.299	218900	73187204	65.810	240	0.299	207400	69325596	66.710	213	0.299	141700	47383381	70.120
365	0.299	206200	68976129	65.930	415	0.300	197900	66075912	66.800	363	0.299	133200	44556691	70.310
765	0.300	193700	64644240	66.080	715	0.300	185100	61693625	66.930	813	0.299	124800	41746530	70.470
1445	0.301	181100	60252388	66.390	1315	0.301	172800	57477190	67.150	2241	0.299	116800	39076222	70.570
3333	0.299	167400	56071949	66.790	2393	0.299	159500	53362864	67.520	7248	0.299	108300	36186848	70.460
5635	0.299	154400	51692909	67.170	3245	0.299	147300	49335164	67.620	10303	0.300	100600	33581691	70.530
8063	0.299	141900	47474072	67.330	3770	0.299	135100	45194678	67.570	12433	0.299	91590	30638563	70.660
9425	0.299	129100	43140754	67.400	4270	0.299	122800	41034415	67.470	14210	0.300	83550	27894445	70.630
10710	0.299	115800	38778770	67.280	4723	0.299	110600	36970801	67.520	15513	0.300	75260	25126786	70.470
11470	0.299	103200	34517590	67.160	5173	0.299	99050	33075983	67.040	16693	0.299	66770	22321697	70.090
11990	0.299	90390	30222986	66.910	5573	0.300	86000	28678329	67.080	17343	0.299	58360	19498179	69.370
12363	0.300	77500	25845739	66.910	5973	0.300	74450	24817990	65.750	18018	0.299	50200	16762556	68.780
12573	0.300	64380	21434993	65.450	6325	0.299	61080	20399303	63.820	18970	0.299	41590	13896453	66.900
12773	0.300	51740	17230470	64.490	6675	0.300	49390	16486634	60.910	20048	0.299	33330	11136170	65.070
13093	0.299	38400	12823296	60.780	6950	0.299	37550	12542965	56.420	21725	0.299	25010	8360829	62.310
ID	DG-4				ID	DG-5				ID	DG-6			
No. cycles	γ(%)	τ(Pa)	G*(Pa)	δ(°)	No. cycles	γ(%)	τ(Pa)	G*(Pa)	δ(°)	No. cycles	γ(%)	τ(Pa)	G*(Pa)	δ(°)
39	0.303	249200	82126320	66.530	42	0.303	226300	74653700	67.990	39	0.303	252600	83350932	66.480
114	0.299	220800	73880747	66.750	138	0.299	201300	67380528	68.150	115	0.299	224200	74881349	66.930
214	0.299	208800	69865489	66.760	278	0.299	190500	63689796	68.110	215	0.300	212100	70810937	66.980
414	0.300	197000	65730206	66.800	558	0.299	178800	59722431	68.150	440	0.300	200300	66762883	66.950
814	0.300	185100	61624613	66.930	1818	0.301	168200	55961087	68.270	765	0.301	188100	62577557	66.980
1314	0.301	173300	57615522	67.140	5463	0.299	156600	52352695	68.870	1594	0.299	174300	58330405	67.090
2141	0.299	159800	53473431	67.360	8268	0.299	145200	48520979	69.240	3598	0.299	162200	54214129	67.600
3218	0.299	147700	49373389	67.550	10898	0.299	133900	44750281	69.280	6053	0.299	149800	50054465	68.050
4443	0.299	135500	45267311	67.770	13038	0.299	122700	41004973	69.280	8835	0.299	137000	45847612	68.240
5695	0.299	123100	41122844	68.180	14823	0.299	112000	37405776	69.090	12348	0.299	124300	41586928	68.200

7098	0.299	110600	36971913	68.320	15948	0.300	100500	33554470	68.970	15158	0.299	112400	37529591	68.000
8600	0.299	98280	32878032	68.200	17033	0.299	89390	29859172	68.470	18515	0.299	100200	33457547	66.970
9978	0.299	85840	28705574	68.020	18193	0.299	78280	26170886	67.980	20693	0.299	87360	29179819	66.140
11580	0.300	74070	24717931	68.190	19453	0.299	67090	22437752	66.800	22678	0.299	74950	25067393	64.250
13308	0.300	61660	20546758	66.860	21208	0.300	55910	18654700	64.980	23853	0.300	62430	20836671	61.890
14813	0.300	49560	16508389	64.940	22888	0.299	44810	15005140	59.250	24680	0.300	50320	16772439	57.630
16090	0.299	36910	12339117	61.230	24153	0.300	33280	11108960	50.080	25450	0.300	37810	12619865	48.750
ID	DG-7				ID	DG-8				ID	DG-9			
No. cycles	γ(%)	τ(Pa)	G*(Pa)	δ(°)	No. cycles	γ(%)	τ(Pa)	G*(Pa)	δ(°)	No. cycles	γ(%)	τ(Pa)	G*(Pa)	δ(°)
38	0.302	316700	104907150	65.640	38	0.279	244600	87757064	66.390	43	0.266	174000	65468173	67.540
93	0.299	282100	94394234	66.090	57	0.301	237800	78893500	67.325	55	0.306	178900	58435980	68.555
153	0.298	266700	89367990	66.260	83	0.300	224700	74907990	67.420	68	0.300	167600	55825914	68.960
273	0.299	251400	84152599	66.330	153	0.299	210300	70244939	67.550	124	0.300	157500	52525738	69.330
513	0.299	235900	78876272	66.470	298	0.299	197200	65905567	67.590	209	0.300	147000	49062637	69.600
843	0.299	219800	73413494	66.600	663	0.300	184200	61426413	67.710	339	0.300	137200	45798979	69.790
1503	0.300	205200	68299827	66.880	1288	0.300	171300	57050176	67.890	489	0.300	127400	42533160	69.960
2945	0.299	188200	62926939	67.130	2970	0.299	157300	52636334	68.370	749	0.299	117700	39299881	70.060
4328	0.299	172400	57700932	67.540	4488	0.299	144100	48231081	68.840	1134	0.300	108000	36048906	70.130
6733	0.298	156500	52434783	67.870	5845	0.299	131300	43869614	69.250	1604	0.299	98040	32739039	70.230
10188	0.299	141200	47174224	68.250	7298	0.299	118200	39536136	69.380	2274	0.299	88200	29455474	70.340
15810	0.299	125300	41926547	68.450	8655	0.299	105100	35125949	69.170	3050	0.299	78420	26197110	70.520
22300	0.299	109900	36708831	68.520	9578	0.299	91990	30738232	68.800	3690	0.300	68710	22919530	70.780
27100	0.299	94140	31451710	68.530	11063	0.300	78900	26325711	68.170	4235	0.300	58980	19667146	71.140
28800	0.299	78390	26211956	68.430	12815	0.300	65680	21918905	67.270	4580	0.300	49130	16371210	71.390
29400	0.300	62910	20989380	67.820	14578	0.300	52590	17540524	65.380	4920	0.300	39340	13113202	71.510
29850	0.300	47800	15939762	65.480	17358	0.300	39470	13163819	62.130	5345	0.300	29380	9791930	71.560

Table B- 10: Fatigue data for DBM-L samples tested in strain mode.

ID	DL-1				ID	DL-2				ID	DL-3			
No. cycles	γ(%)	τ(Pa)	G*(Pa)	δ(°)	No. cycles	γ(%)	τ(Pa)	G*(Pa)	δ(°)	No. cycles	γ(%)	τ(Pa)	G*(Pa)	δ(°)
36	0.307	214300	69916837	64.060	38	0.306	251500	82114405	67.110	40	0.303	328500	108351832	65.580

98	0.299	188700	63012162	64.430	76	0.300	220500	73392114	68.150	96	0.299	289900	97058124	66.360
158	0.299	179700	60035681	64.590	108	0.300	208700	69567594	68.540	156	0.299	274000	91675589	66.500
398	0.300	167200	55807371	64.810	153	0.300	197900	66044158	68.860	251	0.299	260400	87135763	66.530
1238	0.301	157900	52499111	65.220	243	0.299	184400	61601163	69.200	546	0.300	243600	81234389	66.540
2808	0.299	146600	49028625	67.280	393	0.299	171500	57302282	69.490	1086	0.301	228200	75812442	66.650
4249	0.298	135700	45477243	67.990	528	0.299	160900	53757872	69.700	2920	0.300	211400	70437083	66.870
5741	0.299	125300	41928791	68.410	858	0.299	148100	49491054	69.950	5028	0.299	194100	65021423	67.240
8693	0.299	115600	38656131	68.240	1625	0.299	136000	45471871	70.220	8215	0.299	178200	59519436	67.450
13050	0.299	104800	35004626	67.960	2750	0.299	123700	41393942	70.380	20100	0.298	161800	54216343	67.360
19400	0.299	94370	31523496	67.390	4403	0.299	109500	36569848	70.600	25475	0.300	146100	48740292	67.260
23964	0.299	84110	28103741	67.260	6253	0.299	99150	33110040	70.790	47025	0.299	129600	43324051	65.460
26493	0.299	73070	24426853	67.200	9585	0.300	85760	28626553	71.110	51975	0.299	113600	37950918	64.340
27964	0.299	62780	20979255	66.120	13070	0.299	74030	24719349	71.320	55225	0.299	97100	32488390	63.980
29371	0.300	52520	17511745	64.630	16540	0.299	60770	20300855	71.660	56500	0.299	80770	26997396	61.290
30314	0.299	42040	14038697	61.520	18300	0.300	49500	16521698	72.120	57375	0.299	64980	21696522	57.930
					19968	0.300	36610	12215223	72.330	58700	0.298	48280	16223663	47.100
ID	DL-4				ID	DL-5				ID	DL-6			
No. cycles	γ(%)	τ(Pa)	G*(Pa)	δ(°)	No. cycles	γ(%)	τ(Pa)	G*(Pa)	δ(°)	No. cycles	γ(%)	τ(Pa)	G*(Pa)	δ(°)
38	0.304	224500	73887816	68.490	38	0.317	183300	57799276	69.770	39	0.306	208100	68078396	66.260
113	0.299	199900	66820431	68.520	133	0.300	156500	52210001	70.250	89	0.300	183400	61197795	67.400
213	0.299	188100	62925904	68.560	258	0.299	147400	49243968	70.420	141	0.299	174200	58215602	67.775
463	0.299	176000	58803483	68.630	433	0.300	139400	46541754	70.640	264	0.299	162300	54290015	68.200
1363	0.301	166900	55413710	68.730	808	0.299	129900	43403300	70.820	474	0.299	152500	51026383	68.500
2715	0.300	155000	51717695	69.090	1660	0.299	121000	40489217	71.030	929	0.299	143000	47866750	68.750
4468	0.299	143900	48145447	69.170	3863	0.299	112900	37697167	70.990	1982	0.299	132200	44254749	68.910
6523	0.299	132300	44317599	69.450	5665	0.299	103800	34723500	71.170	6190	0.299	122400	40902939	68.840
8773	0.299	121500	40624854	69.870	7518	0.299	95280	31820140	71.190	17268	0.299	111800	37404940	68.800
11628	0.299	110700	37031214	70.020	9548	0.299	86470	28910740	71.380	26425	0.299	101800	34008492	69.160
15083	0.299	99700	33308054	70.190	11923	0.299	77850	26023299	71.600	33125	0.299	91740	30635041	69.530
17838	0.299	88350	29528151	70.520	15028	0.300	69440	23173393	71.710	38175	0.299	81360	27208154	70.100
20493	0.300	77420	25833792	70.620	17483	0.300	60680	20253266	71.760	46875	0.299	71290	23825916	71.050
22445	0.300	66510	22191230	70.710	19235	0.300	52030	17360289	71.580	49600	0.299	61140	20425754	71.640
24200	0.300	55400	18495828	70.370	21013	0.300	43410	14478542	71.730	51325	0.300	51040	17025251	72.180

25450	0.300	44340	14777242	69.750	22340	0.300	34770	11609000	71.540	53075	0.300	40770	13594214	72.870
27300	0.300	33330	11107149	68.070	23243	0.300	26250	8746035	70.930	54800	0.300	30650	10230546	70.200
ID	DL-7				ID	DL-8				ID	DL-9			
No. cycles	γ(%)	τ(Pa)	G*(Pa)	δ(°)	No. cycles	γ(%)	τ(Pa)	G*(Pa)	δ(°)	No. cycles	γ(%)	τ(Pa)	G*(Pa)	δ(°)
39	0.285	202700	71167255	67.560	38	0.305	212800	69748538	67.070	30	0.260	231500	88933793	65.410
76	0.300	191800	64012709	67.620	113	0.299	188500	62981129	66.810	50	0.302	241950	80063005	66.085
154	0.300	179900	60045727	67.550	188	0.299	178300	59564773	66.720	81	0.299	225600	75355483	66.320
266	0.300	170400	56828035	67.580	338	0.299	166700	55686206	66.700	140	0.299	212800	71213916	66.510
641	0.301	160600	53425414	67.640	563	0.300	157500	52549572	66.540	285	0.299	199700	66752907	66.520
2291	0.302	151100	49955037	68.100	888	0.300	146100	48700812	66.200	495	0.299	186600	62310289	66.590
8260	0.300	139300	46502157	69.150	1288	0.300	136100	45357595	65.970	1120	0.300	173600	57773843	66.570
13703	0.299	127100	42472991	69.690	1690	0.299	124900	41717324	65.700	2111	0.299	159500	53313100	66.700
20273	0.299	116200	38825739	69.870	2115	0.300	114400	38187687	65.540	3808	0.299	146200	48924792	66.900
26025	0.299	106900	35698423	69.710	2490	0.300	103600	34563519	65.270	6008	0.299	132900	44446971	67.230
34200	0.299	96530	32234797	69.230	2915	0.300	93230	31054308	64.600	8205	0.299	119700	40001470	67.410
42050	0.300	85740	28622552	68.410	3393	0.299	83320	27869390	63.980	10863	0.299	106300	35561711	67.140
44200	0.299	75610	25247516	68.010	3918	0.300	72660	24191374	62.210	13555	0.299	93140	31118447	66.560
45700	0.299	64560	21596018	67.160	4468	0.299	63240	21115968	59.480	15538	0.299	79790	26656822	65.510
47125	0.299	54030	18040790	65.930	5270	0.300	51780	17288180	54.740	17055	0.299	66650	22270338	63.740
48250	0.299	41990	14032590	63.430	6473	0.300	42050	14014938	50.710	18308	0.300	53380	17807223	60.460
49025	0.300	32020	10658660	60.520	8250	0.300	30850	10295035	46.020	19848	0.300	39920	13310837	54.080

Table B- 11: Fatigue data for HRA-G samples tested in strain mode.

ID	HG-1				ID	HG-2				ID	HG-3			
No. cycles	γ(%)	τ(Pa)	G*(Pa)	δ(°)	No. cycles	γ(%)	τ(Pa)	G*(Pa)	δ(°)	No. cycles	γ(%)	τ(Pa)	G*(Pa)	δ(°)
56	0.238	882800	370712534	53.130	56	0.231	1013000	438412367	50.050	57	0.241	913600	379772619	53.900
183	0.242	805000	332479762	54.990	139	0.241	953800	395897410	52.660	160	0.242	825800	340795368	55.595
321	0.242	764750	315388787	55.720	234	0.241	896800	372491766	53.860	240	0.243	787600	324574707	56.150
558	0.243	720700	296630749	56.440	401	0.242	849600	351724052	54.560	420	0.243	739000	303955118	56.800
1585	0.244	678400	278402469	57.230	761	0.242	797700	329603583	55.190	662	0.243	692400	284496892	57.380
3810	0.244	635200	260442079	55.620	1241	0.242	744200	306976476	55.410	1342	0.244	648000	266000025	57.640

5073	0.244	590600	241901462	56.265	2183	0.243	692800	285160382	54.590	2705	0.244	602200	246696107	56.900
7460	0.245	544800	222500847	56.600	4928	0.243	641000	263400122	54.400	5108	0.244	557000	228079586	57.180
8950	0.245	499500	203915005	57.300	7490	0.244	588900	241688247	55.060	6913	0.245	513200	209365987	57.880
10678	0.246	454800	185235719	57.870	9915	0.245	536800	219269402	56.250	9235	0.246	465900	189734234	58.690
12055	0.246	410100	166804959	57.680	11898	0.245	484200	197509311	57.390	10478	0.246	420300	171074108	59.150
14660	0.247	365600	148228635	58.300	12620	0.246	432000	175822745	57.920	11118	0.246	373000	151481309	59.170
16888	0.247	321000	129860147	58.940	12980	0.246	380600	154505671	57.980	11643	0.247	329800	133747526	59.050
18415	0.248	275400	111104836	59.350	13200	0.247	321700	130068613	57.260	11963	0.247	282500	114201860	58.070
18868	0.248	228700	92190234	59.050	13320	0.248	272700	109995160	56.310	12243	0.248	234000	94457294	56.060
19005	0.250	184750	73928093	55.480	13420	0.249	224100	89995663	54.660	12483	0.248	185600	74692036	53.260
19070	0.251	142500	56818408	49.820	13500	0.250	167300	66819770	50.000	12685	0.249	142100	57151131	48.700
ID	HG-4				ID	HG-5				ID	HG-6			
No. cycles	γ(%)	τ(Pa)	G*(Pa)	δ(°)	No. cycles	γ(%)	τ(Pa)	G*(Pa)	δ(°)	No. cycles	γ(%)	τ(Pa)	G*(Pa)	δ(°)
56	0.239	929900	389312434	52.900	52	0.242	982000	406573069	53.070	56	0.223	1047000	468577975	47.880
139	0.242	850600	351906401	55.210	137	0.242	881400	364762019	55.810	119	0.241	1018000	421949673	50.820
239	0.242	798600	329738389	56.080	237	0.242	832500	343891739	56.510	195	0.240	954900	397561920	51.955
399	0.243	752400	310089021	56.770	412	0.243	787500	324724860	57.110	360	0.240	900000	374728322	52.950
659	0.243	710800	292404397	57.330	746	0.243	739500	304219581	57.640	780	0.241	848100	351444981	53.600
1159	0.244	662500	272013599	57.830	1508	0.243	690500	283645117	57.790	2340	0.243	797800	328646814	52.610
2221	0.244	615700	251882883	57.650	3470	0.243	643600	264379431	57.170	4323	0.242	738600	305230576	51.120
3463	0.245	572400	233797743	57.050	6060	0.244	595000	243773532	57.290	7175	0.243	682900	281585024	50.690
4603	0.245	521500	212977105	57.300	9528	0.245	546900	223545666	58.070	12128	0.243	626600	257542129	51.560
5245	0.245	476100	194067510	57.460	12255	0.245	498900	203507226	58.710	20058	0.244	571300	234385257	52.530
5885	0.246	431900	175664793	57.680	13433	0.246	449400	182923106	58.980	30800	0.244	514600	210718556	52.740
6425	0.246	383100	155519291	57.440	14570	0.246	399800	162515040	59.180	38625	0.245	458700	187463985	52.420
6865	0.247	336300	136207336	57.180	15220	0.246	350700	142291432	58.800	43425	0.245	402500	164128954	51.250
7245	0.248	287000	115955379	56.620	15445	0.247	301000	121848042	57.590	45825	0.246	345500	140473422	49.260
7565	0.248	242300	97650425	55.220	15595	0.248	253600	102358359	55.770	49075	0.246	288100	117096685	46.490
7848	0.248	194900	78444157	52.640	15735	0.248	202100	81414460	52.730	52950	0.247	231300	93751520	41.320
8148	0.248	145800	58769943	48.350	15898	0.249	152700	61378299	50.090	56975	0.247	174000	70306439	36.450
ID	HG-7				ID	HG-8				ID	HG-9			
No. cycles	γ(%)	τ(Pa)	G*(Pa)	δ(°)	No. cycles	γ(%)	τ(Pa)	G*(Pa)	δ(°)	No. cycles	γ(%)	τ(Pa)	G*(Pa)	δ(°)
56	0.216	1000000	463314739	49.110	59	0.231	991700	429452369	51.180	57	0.225	1046000	463958909	48.970

118	0.241	1015000	420678308	51.600	153	0.241	928800	385813623	53.880	141	0.240	997900	415966719	51.900
189	0.241	949300	394293072	53.220	245	0.241	880200	365343428	54.700	216	0.240	950500	395395853	52.780
298	0.241	895700	371983886	54.330	440	0.242	831900	343952205	55.310	387	0.241	893800	371447807	53.720
536	0.242	839400	347284282	55.470	710	0.242	778600	322216199	56.180	792	0.241	838400	348000780	54.390
836	0.242	786600	324691139	56.300	1010	0.256	769300	300740416	57.330	1871	0.242	785600	324691159	54.500
1656	0.243	731600	301334091	57.260	1822	0.256	714300	279120475	57.430	3118	0.242	729600	301577329	52.990
3758	0.243	676700	278499142	56.500	2865	0.251	645900	256958037	58.450	5900	0.242	674100	278215721	52.470
5778	0.242	617600	254755000	56.310	3933	0.266	634450	238647819	57.020	7808	0.243	620400	255151141	52.960
7440	0.244	564800	231630146	56.950	4248	0.276	596900	216497949	59.060	9205	0.244	565600	231800429	53.390
8940	0.244	509900	208595834	57.730	5630	0.282	546300	193885663	59.460	10213	0.245	510900	208721443	53.750
10463	0.246	455900	185580187	58.390	6155	0.290	500300	172323526	59.960	11188	0.245	456200	185850586	53.430
11663	0.246	399400	162308899	59.010	6425	0.310	462000	149029854	60.190	11898	0.246	399000	162395806	52.580
12645	0.247	343000	138938397	59.400	6590	0.295	380200	129056786	60.940	12348	0.246	343400	139463670	49.650
13205	0.247	286500	115884932	59.500	6860	0.248	265700	107338356	60.970	12588	0.247	287000	116385166	45.770
13565	0.248	229600	92712985	58.990	7325	0.249	214700	86311558	60.880	12678	0.247	254800	103204692	42.730
13805	0.248	173200	69771189	57.780	7625	0.249	160100	64244812	59.440	12755	0.247	222800	90243349	39.500

Table B- 12: Fatigue data for HRA-L samples tested in strain mode.

ID	HL-1				ID	HL-2				ID	HL-3			
No. cycles	γ(%)	τ(Pa)	G*(Pa)	δ(°)	No. cycles	γ(%)	τ(Pa)	G*(Pa)	δ(°)	No. cycles	γ(%)	τ(Pa)	G*(Pa)	δ(°)
56	0.254	684500	268966141	54.740	57	0.259	643700	248720079	56.710	54	0.246	523400	213082118	59.160
208	0.245	591300	241838513	56.900	209	0.245	544200	221951229	58.780	182	0.246	470200	190942612	60.540
358	0.245	559100	228287943	57.590	334	0.245	518350	211217101	59.380	370	0.246	447300	181534828	61.105
758	0.245	527400	215177479	58.380	559	0.246	491000	199803045	60.000	10318	0.246	417000	169557686	61.500
4460	0.244	493900	202098320	59.120	1309	0.246	459900	186883607	60.810	12198	0.247	394500	159803294	61.940
7865	0.246	463400	188373984	59.300	3763	0.246	428000	173973839	61.410	16953	0.247	368000	149191407	62.480
10365	0.245	429100	174890872	60.090	7815	0.246	398300	161633952	61.400	22960	0.247	342300	138441192	62.840
14720	0.247	397300	160992945	60.350	10215	0.246	366900	149353372	61.520	34725	0.247	316300	127914265	63.160
23878	0.247	364300	147690786	61.130	12120	0.247	338100	136826088	61.780	49000	0.247	289700	117201565	62.630
33125	0.247	332300	134587812	61.460	15273	0.247	308300	124620540	62.700	50875	0.247	264300	106962909	62.820
41900	0.248	299400	120926701	61.690	16775	0.248	278000	112190870	62.930	51750	0.248	238000	95977417	63.090

49150	0.248	266500	107538163	61.730	17575	0.248	247100	99464238	63.030	52500	0.248	210200	84773105	63.500
55300	0.247	232600	94050859	60.270	17925	0.249	214700	86283461	62.720	53125	0.248	184700	74500740	63.690
57800	0.248	200300	80769712	59.300	18475	0.249	187200	75170157	62.800	53625	0.248	155000	62465745	63.880
58900	0.248	165800	66835974	57.340	19525	0.249	154700	62015939	62.160	53813	0.248	136750	55044468	63.700
59800	0.248	134500	54147628	54.700	20828	0.249	124400	49883512	60.770	54125	0.248	103100	41499288	63.210
60450	0.249	101200	40641754	48.180	21878	0.249	92130	36976240	57.120	54500	0.249	79430	31876811	62.850
ID	HL-4				ID	HL-5				ID	HL-6			
No. cycles	γ(%)	τ(Pa)	G*(Pa)	δ(°)	No. cycles	γ(%)	τ(Pa)	G*(Pa)	δ(°)	No. cycles	γ(%)	τ(Pa)	G*(Pa)	δ(°)
56	0.250	662100	265075387	56.750	56	0.248	625000	252159494	56.160	56	0.272	742100	273033650	55.240
308	0.245	583800	238667582	58.460	108	0.245	553600	225825532	58.220	283	0.245	604050	246711131	58.115
508	0.245	553800	226045429	59.030	158	0.245	529500	215966424	58.840	508	0.245	569300	232203383	58.870
908	0.245	521100	212445880	59.630	308	0.246	492500	200533398	59.710	858	0.246	535900	218185223	59.530
2057	0.246	489200	199179180	60.510	508	0.246	463000	188491821	60.320	1711	0.245	505100	205857420	60.300
4108	0.245	453800	185484926	60.820	1558	0.246	433100	176147132	61.050	4060	0.245	467300	190955267	60.390
7210	0.244	420900	172202175	60.720	8663	0.246	405500	164700817	60.970	7063	0.245	434500	177368657	60.230
8813	0.246	391900	159380859	60.710	10665	0.246	372600	151178265	61.730	8665	0.246	403200	163704795	60.320
10613	0.245	357900	145810247	61.340	15368	0.247	343100	138827071	61.970	10365	0.246	369300	150205602	60.980
12665	0.247	327100	132606854	61.660	23175	0.247	312200	126184240	62.250	12218	0.247	336300	136356449	61.220
16670	0.248	295400	119339070	62.270	29625	0.247	280800	113505451	62.560	15370	0.247	303100	122608309	61.880
18470	0.247	262600	106116874	62.250	33625	0.248	250200	100987677	62.770	19173	0.248	269400	108821664	62.530
19470	0.248	230600	93052910	61.480	36925	0.248	219100	88242165	62.510	26775	0.248	237300	95636123	62.720
20323	0.248	197400	79614110	60.770	38150	0.248	187900	75744444	61.720	28075	0.248	202500	81650592	63.120
20773	0.248	164500	66206774	58.870	38850	0.248	158500	63837671	60.610	28625	0.249	169300	68055924	63.160
21023	0.249	134000	53850296	56.410	39350	0.249	122300	49074683	57.000	28875	0.249	133500	53653243	62.260
21323	0.249	99870	40088470	53.270	39600	0.250	94540	37866135	52.610	29225	0.249	104000	41787878	62.960
ID	HL-7				ID	HL-8				ID	HL-9			
No. cycles	γ(%)	τ(Pa)	G*(Pa)	δ(°)	No. cycles	γ(%)	τ(Pa)	G*(Pa)	δ(°)	No. cycles	γ(%)	τ(Pa)	G*(Pa)	δ(°)
57	0.249	580700	233184757	55.190	56	0.255	647400	253998894	56.980	56	0.246	551400	224592788	56.270
122	0.246	515550	209688244	56.820	66	0.248	561700	226261113	58.520	149	0.246	496300	201871060	57.880
197	0.246	487450	198112958	57.555	128	0.245	528800	215452438	58.810	284	0.246	466650	189552187	58.605
310	0.246	458800	186310181	58.210	228	0.246	499000	203111390	59.320	509	0.247	442500	179503718	59.200
585	0.246	430700	174785019	58.920	458	0.246	468400	190539727	59.910	1319	0.247	415700	168196770	60.060
1260	0.247	402800	163273248	59.620	1498	0.246	438000	177802315	60.770	3390	0.246	387600	157378647	61.070

3963	0.247	373900	151528046	60.010	4118	0.245	405200	165061674	61.400	10055	0.246	359300	146141863	61.680
7968	0.247	345200	139817087	60.020	6570	0.245	373700	152289436	61.030	13028	0.247	331900	134369750	62.580
13320	0.247	317000	128192685	60.290	9920	0.246	342900	139647399	61.260	30950	0.248	306300	123573339	62.410
17475	0.247	288200	116512704	60.440	11353	0.247	313600	126967161	61.450	46625	0.247	278200	112487668	62.290
20978	0.247	260100	105126164	60.680	13625	0.248	283200	114278797	62.000	58425	0.247	249700	101111948	63.620
24205	0.248	231200	93326283	60.190	29550	0.248	252000	101673169	62.920	62750	0.248	222100	89656592	63.990
26650	0.248	203200	81806177	59.610	31650	0.249	221000	88922509	63.210	64925	0.249	195600	78685359	64.380
28750	0.249	174000	70005472	58.540	32300	0.249	189600	76240415	63.280	66625	0.249	167400	67243499	64.560
30900	0.249	145000	58278572	57.470	32600	0.249	157500	63203262	62.840	68250	0.249	140500	56383811	64.260
33425	0.249	115900	46556842	55.750	32750	0.250	127300	51003850	61.950	69425	0.253	114200	45141552	57.650
35600	0.249	86980	34920788	53.120	32900	0.250	96220	38470765	60.450	70225	0.250	84580	33804551	56.730

Appendix B-4 (DSR-Sequence of Fatigue test-controlled stress)

Figure B-4 shows the sequences steps for setting DSR sample and running the fatigue test in controlled stress test mode as follow:

B-4.1. Repeat steps B-1.1 to B-1.17.

B-4.2. Repeat steps B-3.2 to B-3.4.

B-4.3. Move automatically. Perform fatigue test at low stress amplitude within LVE region to evaluate the linear viscoelastic properties. Stress amplitude is 5 KPa and test duration 120 s. In this period, one point is collected at each 2 s to gathering 60 points at the end of the test using integration points 512.

B-4.4. Move automatically. Perform initial fatigue test at high stress amplitude (Chapter IV) to create the damage. Test lasts for 120 s. during this period one point is collected at each 2 s to gathering 60 points at the end of the test using integration points 512.

B-4.5. Move automatically. Perform initial fatigue test at the same stress amplitude in B-4.4 to produce the initial hysteresis loops. Test lasts for 0.6 s during this period one point is collected at each 0.002 s for gathering 300 points at the end of the test using integration points 512. In this test raw data (torque and angular displacement) are collected to plot the hysteresis loops.

B-4.6. Move automatically. Perform loops sequence (10 times) to perform fatigue test and hysteresis loops test frequently.

B-4.7. Move automatically. Perform fatigue test using stress amplitude in B-4.4 to create the damage. Test lasts for 3600 s. during this period one point is collected at each 2 s to gathering 1800 points at the end of the test using integration points 512.

B-4.8. Move automatically. Perform fatigue test using stress amplitude in B-4.4 to create the damage. Test lasts for 0.6 s during this period one point is collected at each 0.002 s to gathering 300 points at the end of the test using integration points 512. In this test raw data is also collected.

B-4.9. Move automatically. Sequence completed either when the criterion has been verified or completing the number of loops. The criteria defined by the triggers in the sequence properties.

B-4.10. Stop the sequence and save the data in specified folder.

B-4.11. Release the screws, click (Go to top stop) button and remove the sample.

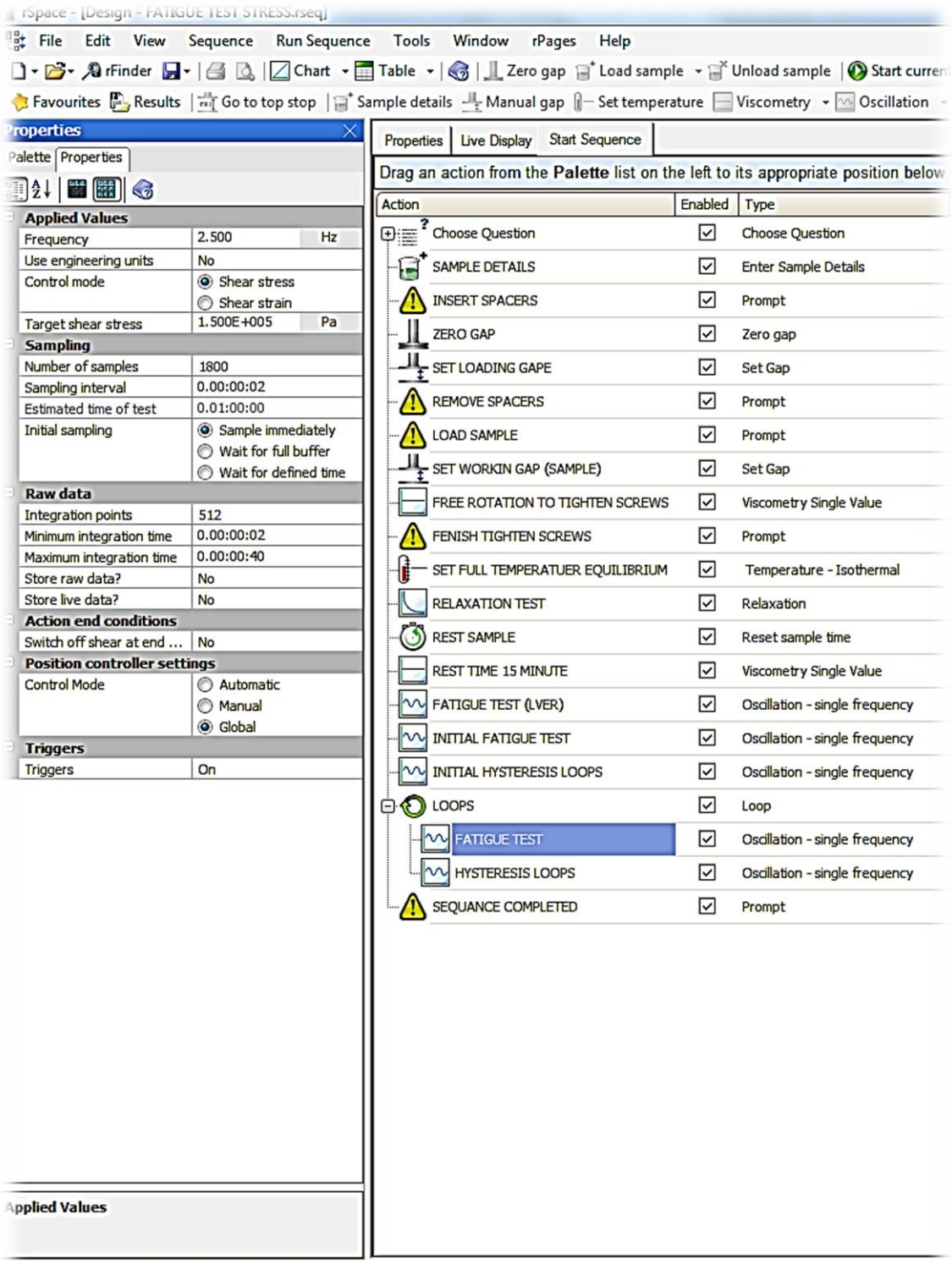

Figure B- 4: DSR sequences for fatigue testing in stress test mode.

Table B- 13: Fatigue data for DBM-G samples tested in stress mode.

ID	DG-1				ID	DG-2				ID	DG-3			
No. cycles	γ(%)	τ(Pa)	G*(Pa)	δ(°)	No. cycles	γ(%)	τ(Pa)	G*(Pa)	δ(°)	No. cycles	γ(%)	τ(Pa)	G*(Pa)	δ(°)
5	0.093	150100	161200000	60.340	10	0.088	150000	170900000	60.650	13	0.099	150100	151100000	61.560
25	0.105	150100	143400000	62.490	50	0.097	150000	154200000	62.350	44	0.110	150100	136200000	63.380
45	0.109	150100	137300000	63.260	113	0.103	150000	145000000	63.140	75	0.116	150100	129300000	64.210
100	0.116	150100	128800000	64.270	238	0.110	150100	136900000	63.550	150	0.124	150100	121400000	65.040
205	0.124	150100	120800000	65.140	450	0.117	150100	128500000	63.910	275	0.132	150100	113800000	65.720
400	0.133	150100	113000000	66.010	850	0.125	150100	119600000	64.340	488	0.142	150100	105900000	66.370
705	0.143	150100	104800000	66.970	1413	0.135	150100	111100000	64.740	813	0.153	150100	98270000	66.970
1105	0.155	150100	96730000	67.960	2175	0.146	150100	102600000	65.170	1288	0.165	150100	90700000	67.480
2210	0.169	150100	88670000	69.340	3100	0.159	150100	94170000	65.590	1963	0.181	150100	83110000	67.940
3485	0.186	150100	80600000	69.440	4138	0.176	150100	85460000	65.900	2838	0.199	150100	75600000	68.430
4590	0.207	150100	72560000	68.470	5200	0.195	150100	76920000	66.350	3875	0.221	150100	68010000	68.830
5875	0.233	150100	64520000	67.600	6388	0.220	150100	68360000	66.840	5038	0.248	150100	60420000	69.390
7090	0.266	150100	56420000	68.430	7563	0.251	150100	59890000	67.550	6350	0.284	150100	52920000	70.130
8755	0.310	150100	48360000	70.910	8625	0.293	150100	51310000	68.170	7650	0.331	150100	45350000	70.600
11030	0.372	150100	40320000	73.340	9725	0.351	150100	42730000	68.680	8725	0.397	150100	37780000	71.450
13405	0.465	150200	32260000	73.210	10875	0.439	150200	34210000	69.300	9338	0.495	150200	30310000	71.960
14605	0.621	150300	24180000	72.220	12063	0.587	150200	25610000	70.440	9444	0.684	150250	22055000	70.495
14775	0.936	150400	16060000	69.490	12288	0.876	150300	17160000	70.570	9478	0.941	150500	16000000	60.110
ID	DG-4				ID	DG-5				ID	DG-6			
No. cycles	γ(%)	τ(Pa)	G*(Pa)	δ(°)	No. cycles	γ(%)	τ(Pa)	G*(Pa)	δ(°)	No. cycles	γ(%)	τ(Pa)	G*(Pa)	δ(°)
13	0.135	150100	111100000	64.000	5	0.147	150100	101900000	63.000	5	0.182	150100	82400000	66.210
44	0.150	150100	99895000	65.600	17	0.163	150100	92180000	64.500	15	0.202	150100	74450000	67.660
81	0.158	150100	94860000	66.220	35	0.172	150100	87090000	65.280	28	0.213	150100	70515000	68.335
144	0.169	150100	88940000	66.970	75	0.184	150100	81490000	66.070	55	0.227	150100	65980000	69.010
231	0.179	150100	83670000	67.590	140	0.196	150100	76590000	66.750	95	0.242	150100	62130000	69.510
381	0.193	150100	77670000	68.260	260	0.210	150100	71390000	67.410	165	0.259	150100	57840000	70.040
569	0.207	150100	72420000	68.860	460	0.226	150100	66280000	68.050	270	0.280	150100	53600000	70.540
844	0.225	150100	66770000	69.570	810	0.245	150100	61150000	68.850	425	0.303	150100	49480000	71.070
1194	0.245	150100	61160000	70.330	1465	0.268	150100	56060000	69.880	655	0.331	150100	45360000	71.640

1631	0.270	150100	55610000	71.110	3005	0.295	150100	50950000	70.400	970	0.364	150100	41240000	72.290
2144	0.300	150100	49990000	71.800	4280	0.327	150100	45870000	69.180	1420	0.405	150100	37100000	73.070
2644	0.337	150100	44540000	72.250	5495	0.368	150200	40760000	68.040	1995	0.456	150100	32960000	73.860
3094	0.386	150100	38890000	72.390	6845	0.421	150200	35680000	68.310	2630	0.520	150200	28860000	74.490
3369	0.451	150200	33300000	72.090	7920	0.491	150200	30570000	69.870	3280	0.608	150200	24720000	74.670
3494	0.544	150200	27630000	70.770	8505	0.589	150200	25490000	70.860	3830	0.730	150200	20590000	74.430
3550	0.665	150300	22635000	65.735	8735	0.739	150300	20340000	70.410	4130	0.910	150300	16510000	73.620
3575	0.968	150700	16410000	51.840	8825	0.968	150400	15550000	65.900	4210	1.205	150500	12490000	68.180
3581	1.188	150900	12700000	47.520	8845	1.374	151000	10990000	50.250	4228	1.868	151400	8203500	49.435
ID	DG-7				ID	DG-8				ID	DG-9			
No. cycles	γ(%)	τ(Pa)	G*(Pa)	δ(°)	No. cycles	γ(%)	τ(Pa)	G*(Pa)	δ(°)	No. cycles	γ(%)	τ(Pa)	G*(Pa)	δ(°)
5	0.149	150100	100400000	64.170	5	0.098	150100	152800000	61.870	5	0.098	150100	152700000	60.890
18	0.166	150100	90270000	65.790	20	0.109	150100	138200000	63.460	20	0.109	150100	137800000	62.550
33	0.175	150100	85545000	66.510	45	0.115	150100	130300000	64.330	45	0.116	150100	129700000	63.410
65	0.187	150100	80260000	67.300	100	0.123	150100	122200000	65.160	95	0.123	150100	122100000	64.170
120	0.199	150100	75350000	67.980	200	0.131	150100	114600000	65.890	190	0.131	150100	114600000	64.920
215	0.214	150100	70290000	68.560	375	0.140	150100	107100000	66.640	370	0.140	150100	107000000	65.730
370	0.230	150100	65360000	69.120	685	0.151	150100	99380000	67.480	735	0.151	150100	99240000	66.680
650	0.249	150100	60270000	69.800	1220	0.164	150100	91690000	68.560	1100	0.164	150100	91630000	67.520
1130	0.272	150100	55220000	70.510	2260	0.179	150100	84050000	69.790	2305	0.179	150100	83970000	68.690
1930	0.299	150100	50200000	70.830	3915	0.196	150100	76390000	69.200	4125	0.197	150100	76360000	67.560
3080	0.332	150100	45180000	70.050	5105	0.218	150100	68780000	67.930	5320	0.218	150100	68710000	66.480
4225	0.374	150200	40170000	68.910	5765	0.246	150100	61140000	67.860	6705	0.246	150100	61070000	66.800
5145	0.427	150200	35150000	68.960	6580	0.281	150100	53500000	68.250	8765	0.281	150100	53450000	69.440
5810	0.498	150200	30140000	69.670	7200	0.327	150100	45880000	69.070	11970	0.328	150100	45820000	70.580
6510	0.598	150200	25100000	70.840	7470	0.393	150100	38230000	69.450	13580	0.393	150200	38170000	69.040
7035	0.747	150300	20100000	71.930	7620	0.491	150200	30620000	68.140	14160	0.491	150200	30590000	68.810
7330	0.996	150300	15090000	71.610	7690	0.659	150400	22820000	62.010	14355	0.652	150300	23050000	67.510
7430	1.522	150700	9900000	64.560	7713	0.944	150750	16065000	46.670	14435	1.001	150800	15070000	46.930

Table B- 14: Fatigue data for DBM-L samples tested in stress mode.

ID	DL-1				ID	DL-2				ID	DL-3			
No. cycles	γ(%)	τ(Pa)	G*(Pa)	δ(°)	No. cycles	γ(%)	τ(Pa)	G*(Pa)	δ(°)	No. cycles	γ(%)	τ(Pa)	G*(Pa)	δ(°)
6	0.126	150100	119100000	62.530	5	0.357	150100	42100000	66.990	7	0.137	150100	109600000	63.560
25	0.139	150100	107900000	63.875	15	0.405	150100	37110000	70.080	19	0.152	150100	98905000	65.065
44	0.147	150100	101900000	64.610	30	0.420	150100	35710000	70.790	30	0.161	150100	93430000	65.850
81	0.158	150100	94770000	65.440	80	0.449	150100	33440000	71.850	52	0.172	150100	87320000	66.690
119	0.167	150000	90090000	65.980	180	0.474	150200	31710000	72.300	82	0.182	150100	82240000	67.310
206	0.181	150100	83040000	66.760	675	0.509	150200	29510000	72.690	135	0.196	150100	76610000	67.990
294	0.193	150000	77900000	67.330	1505	0.549	150200	27340000	72.910	210	0.211	150100	71290000	68.630
456	0.210	150100	71590000	68.080	2720	0.595	150200	25260000	73.190	315	0.227	150100	66080000	69.240
669	0.229	150100	65540000	68.810	4295	0.648	150200	23170000	73.590	473	0.249	150100	60340000	69.890
956	0.252	150100	59590000	69.600	6855	0.713	150200	21060000	73.820	660	0.273	150100	54910000	70.580
1344	0.280	150100	53680000	70.530	12837	0.792	150200	18970000	73.980	908	0.304	150100	49440000	71.270
1719	0.314	150100	47800000	71.410	23292	0.893	150300	16820000	74.250	1215	0.342	150100	43840000	72.010
2269	0.360	150100	41710000	72.380	35612	1.020	150300	14730000	74.560	1500	0.390	150100	38460000	72.770
3069	0.420	150100	35750000	73.050	40687	1.188	150300	12650000	74.450	1815	0.455	150100	32960000	73.680
3944	0.504	150200	29800000	72.840	41267	1.389	150400	10830000	72.810	2115	0.546	150200	27490000	74.380
4619	0.626	150200	24010000	72.400	41282	1.713	150700	8798000	67.590	2333	0.681	150200	22070000	74.620
4931	0.842	150300	17850000	72.230	41317	2.358	151600	6428000	50.640	2434	0.908	150300	16560000	72.620
5000	1.381	150750	11289000	62.110	41338					2460	1.432	150800	10530000	58.270
ID	DL-4				ID	DL-5				ID	DL-6			
No. cycles	γ(%)	τ(Pa)	G*(Pa)	δ(°)	No. cycles	γ(%)	τ(Pa)	G*(Pa)	δ(°)	No. cycles	γ(%)	τ(Pa)	G*(Pa)	δ(°)
7	0.235	150100	63940000	66.530	5	0.101	150100	148900000	61.400	5	0.124	150100	121300000	63.450
19	0.260	150100	57720000	67.735	15	0.112	150100	134500000	62.850	15	0.136	150100	110000000	64.750
30	0.275	150100	54550000	68.330	28	0.118	150100	127200000	63.625	30	0.145	150100	103400000	65.540
52	0.294	150100	51020000	69.040	55	0.126	150100	119000000	64.490	60	0.155	150100	96830000	66.300
82	0.312	150100	48100000	69.500	100	0.134	150100	111900000	65.220	105	0.164	150100	91250000	66.910
135	0.335	150100	44800000	70.030	185	0.144	150100	104300000	65.990	190	0.177	150100	84970000	67.610
210	0.361	150100	41560000	70.500	340	0.155	150100	96890000	66.740	330	0.190	150100	78870000	68.280
315	0.391	150100	38450000	70.980	560	0.168	150100	89350000	67.460	560	0.206	150100	72780000	69.040
465	0.427	150200	35190000	71.480	895	0.183	150100	81890000	68.440	950	0.225	150100	66720000	69.950

675	0.469	150200	32040000	71.990	1685	0.202	150100	74470000	69.730	1570	0.247	150100	60630000	70.990
968	0.522	150200	28790000	72.600	2945	0.224	150100	67010000	70.400	2290	0.275	150100	54580000	71.920
1320	0.587	150200	25610000	73.200	4810	0.252	150100	59560000	68.590	3795	0.309	150100	48540000	71.500
1800	0.671	150200	22390000	73.830	6400	0.288	150100	52110000	68.220	4630	0.353	150100	42490000	70.770
2333	0.783	150200	19190000	74.630	8290	0.336	150100	44670000	70.510	5765	0.413	150200	36390000	70.020
2768	0.939	150300	16010000	75.150	12340	0.403	150100	37240000	71.490	6920	0.495	150200	30330000	70.620
3015	1.171	150300	12840000	74.020	14100	0.504	150200	29780000	70.300	8005	0.619	150200	24270000	72.220
3090	1.564	150700	9639000	64.240	15350	0.673	150200	22340000	71.370	8685	0.826	150300	18190000	73.040
3113	2.123	151700	7145000	42.450	15645	1.002	150500	15010000	66.330	8930	1.239	150400	12130000	71.510
ID	DL-7				ID	DL-8				ID	DL-9			
No. cycles	γ(%)	τ(Pa)	G*(Pa)	δ(°)	No. cycles	γ(%)	τ(Pa)	G*(Pa)	δ(°)	No. cycles	γ(%)	τ(Pa)	G*(Pa)	δ(°)
5	0.249	150100	60180000	67.670	5	0.144	150100	104400000	63.020	5	0.138	150100	108500000	63.700
13	0.278	150100	54080000	68.865	13	0.160	150050	94100000	64.415	15	0.153	150100	98220000	64.870
20	0.295	150100	50940000	69.520	20	0.169	150100	88870000	65.250	28	0.162	150000	92905000	65.525
30	0.310	150100	48390000	70.060	35	0.180	150100	83240000	66.040	55	0.173	150100	86780000	66.300
50	0.332	150100	45180000	70.710	60	0.193	150100	77940000	66.880	95	0.184	150100	81740000	66.910
80	0.356	150100	42140000	71.360	95	0.205	150100	73390000	67.550	170	0.198	150100	75930000	67.570
125	0.383	150100	39150000	71.900	165	0.221	150100	67880000	68.320	285	0.213	150100	70510000	68.270
190	0.415	150100	36210000	72.410	275	0.239	150100	62680000	69.080	460	0.231	150100	65100000	68.890
295	0.455	150100	33030000	72.980	460	0.261	150100	57480000	69.830	720	0.252	150100	59660000	69.740
430	0.499	150200	30120000	73.590	755	0.287	150100	52210000	70.710	1155	0.277	150100	54240000	70.770
630	0.555	150200	27080000	74.040	1180	0.319	150100	47030000	71.670	1880	0.307	150100	48840000	72.050
890	0.624	150200	24080000	74.640	1805	0.359	150100	41760000	72.800	3130	0.346	150100	43400000	72.710
1185	0.712	150200	21090000	75.190	2535	0.411	150100	36560000	73.530	4590	0.395	150100	37990000	71.380
1505	0.831	150200	18070000	75.690	3035	0.479	150200	31370000	73.760	5975	0.461	150200	32550000	70.540
1835	0.998	150300	15050000	76.080	3240	0.575	150200	26100000	73.030	7265	0.554	150200	27130000	71.560
2060	1.244	150300	12080000	75.960	3320	0.712	150300	21110000	69.740	8690	0.692	150200	21700000	73.670
2160	1.626	150500	9257000	73.240	3360	0.946	150700	15920000	52.760	10395	0.923	150200	16280000	68.070
2185	2.522	151900	6023000	46.220	3370	1.400	151200	10800000	40.670	11380	1.378	150300	10910000	59.150

Table B- 15: Fatigue data for HRA-G samples tested in stress mode.

ID	HG-1				ID	HG-2				ID	HG-3			
No. cycles	γ(%)	τ(Pa)	G*(Pa)	δ(°)	No. cycles	γ(%)	τ(Pa)	G*(Pa)	δ(°)	No. cycles	γ(%)	τ(Pa)	G*(Pa)	δ(°)
9	0.071	399000	742672000	60.143	6	0.069	399000	766080000	59.052	9	0.055	399000	961723000	56.286
50	0.079	399000	667660000	63.707	24	0.077	399000	689339000	62.550	32	0.061	399000	866229000	60.103
293	0.084	399133	631484000	65.330	51	0.081	399133	651301000	64.399	69	0.065	399000	817551000	61.685
1098	0.089	399133	594643000	65.409	141	0.087	399133	612864000	66.154	174	0.069	399000	769538000	63.441
1713	0.095	399000	557137000	65.622	948	0.088	399133	574560000	63.792	373	0.074	399000	721259000	64.625
5310	0.102	399133	520030000	66.181	2313	0.099	399133	536256000	67.125	888	0.079	399000	673246000	65.024
9531	0.110	399133	482923000	67.936	4743	0.107	399133	497952000	68.615	1230	0.080	399000	659332566	65.237
15324	0.119	399133	445683000	69.173	5971	0.115	399133	460047000	69.572	1725	0.092	399133	577220000	65.542
22329	0.119	399133	445683000	69.160	9221	0.126	399133	421344000	71.913	2451	0.100	399000	528941000	67.311
30516	0.130	399133	408576000	70.530	17332	0.139	399133	383040000	72.525	3351	0.110	399133	480928000	69.014
61660	0.143	399133	371336000	72.153	48879	0.154	399133	344736000	73.842	5293	0.123	399133	432782000	70.078
73270	0.159	399133	334229000	73.376	70254	0.173	399133	306964000	74.906	8229	0.138	399133	384769000	71.541
77705	0.178	399133	297702750	74.379	71840	0.198	399133	268378171	74.788	15924	0.158	399133	336623000	74.054
80278	0.205	399133	259387478	74.162	73840	0.231	399133	229861883	73.837	18879	0.184	399133	288477000	75.025
82133	0.239	399133	222261768	73.815	75357	0.278	399133	190752271	72.602	20202	0.221	399133	240597000	76.143
83705	0.285	399133	186540284	73.438	76530	0.346	399133	153627047	71.256	20718	0.275	399133	192717000	75.225
84990	0.356	399133	149264632	73.023	77564	0.461	399133	115205699	69.726	20901	0.369	399266	144039000	70.610
86133	0.469	399133	113239635	72.613	78461	0.688	399133	77162094	68.101	20964	0.541	399399	98127400	59.744
86254	0.694	399133	76542534	72.189	79288	1.405	399133	37785403	59.671	20988	0.992	399931	53638900	39.967
ID	HG-4				ID	HG-5				ID	HG-6			
No. cycles	γ(%)	τ(Pa)	G*(Pa)	δ(°)	No. cycles	γ(%)	τ(Pa)	G*(Pa)	δ(°)	No. cycles	γ(%)	τ(Pa)	G*(Pa)	δ(°)
7	0.064	399000	825930000	58.826	9	0.070	398734	752647000	56.232	5	0.097	399000	550088000	58.174
15	0.071	399000	743470000	62.111	25	0.078	399133	678167000	61.020	25	0.107	399133	496755000	61.818
53	0.076	399000	702107000	63.986	80	0.083	399133	640262000	62.537	2020	0.114	399133	467628000	67.817
133	0.080	399000	660744000	65.808	235	0.088	399133	601958000	64.133	3590	0.121	399133	440097000	68.575
390	0.086	399000	619514000	68.229	1755	0.094	399133	564585000	65.862	6105	0.129	399133	412699000	69.639
1200	0.091	399133	582540000	69.000	4900	0.101	399133	526813000	67.125	10870	0.138	399133	385434000	70.610

1431	0.099	399133	537187000	68.256	9315	0.109	399133	489041000	68.562	16665	0.148	399133	357903000	71.847
2943	0.107	399000	495957000	70.251	15285	0.118	399133	451535000	69.931	28135	0.161	399133	330106000	73.177
5724	0.117	399133	454328000	71.581	24505	0.128	399133	413763000	70.995	46010	0.175	399133	302841000	74.453
11229	0.129	399133	413098000	73.070	33455	0.141	399133	376124000	72.405	54890	0.193	399133	275044000	75.757
23409	0.143	399133	371735000	75.118	56670	0.157	399133	338751000	73.682	63160	0.214	399133	247779000	76.901
29721	0.161	399133	330372000	76.528	62000	0.176	399133	300979000	75.065	67970	0.241	399133	220115000	78.377
34628	0.002	399000	289274077	76.355	63075	0.202	399133	263473000	75.690	71060	0.276	399133	192584000	79.587
36528	0.002	399000	247104860	71.637	63575	0.235	399133	226100000	76.063	72795	0.322	399133	165053000	80.970
37980	0.003	399000	206456047	63.304	63710	0.282	399133	188062000	74.773	73390	0.385	399266	137788000	81.808
39228	0.003	399000	165100965	54.863	63785	0.348	399266	152418000	71.780	73538	0.481	399266	110476450	77.951
40310	0.004	399000	124084872	48.213	63840	0.466	399399	113914500	62.736	73570	0.639	399532	83204800	65.769
41288	0.006	399000	82634206	41.496	63868	0.684	399599	79048550	50.873	73593	1.004	399931	53386200	45.732
42178	0.013	399000	41115923	32.253	63900	1.416	400197	37599100	49.902	73610	1.793	400729	29725500	39.514
ID	HG-7				ID	HG-8				ID	HG-9			
No. cycles	γ(%)	τ(Pa)	G*(Pa)	δ(°)	No. cycles	γ(%)	τ(Pa)	G*(Pa)	δ(°)	No. cycles	γ(%)	τ(Pa)	G*(Pa)	δ(°)
9	0.071	399000	743470000	60.355	9	0.065	399000	817152000	59.717	13	0.059	400000	682200000	43.100
25	0.079	399000	669788000	63.508	16	0.073	399000	728175000	60.196	375	0.065	400100	613300000	45.380
44	0.084	399133	632282000	65.316	45	0.076	399000	693994000	61.592	700	0.069	400100	579400000	46.440
122	0.089	399133	594776000	67.099	125	0.081	399133	653961000	63.800	1263	0.073	400100	545600000	47.540
474	0.095	399133	557669000	69.719	258	0.087	399133	612465000	65.769	1913	0.078	400000	511900000	48.470
1010	0.101	399133	523621000	68.801	389	0.093	399133	572033000	67.843	2463	0.084	400100	477500000	49.310
1316	0.110	399133	483189000	69.094	537	0.100	399133	531202000	69.213	3325	0.090	400100	443400000	50.200
1507	0.119	399133	446215000	70.929	1199	0.108	399133	492765000	67.870	4613	0.098	400100	409400000	51.230
1984	0.130	399133	408975000	72.259	1545	0.118	399133	449274000	69.399	6300	0.107	400100	375300000	52.380
4834	0.143	399133	371868000	73.270	3399	0.130	399133	409108000	71.793	8575	0.117	400100	341500000	53.600
5928	0.159	399000	334320062	74.324	5565	0.144	399133	367745000	73.243	12038	0.130	400100	307200000	54.840
6198	0.178	399000	297773662	72.897	10989	0.163	399133	326648000	74.666	16763	0.147	400100	272900000	56.170
6393	0.204	399000	259908644	69.222	20220	0.185	399133	286216000	76.528	24500	0.168	400100	238400000	57.580
6543	0.238	399000	222752628	61.267	27480	0.217	399133	244986000	77.765	32638	0.195	400100	204700000	58.990
6668	0.286	399000	185616616	56.214	30462	0.260	399133	203889000	79.734	36813	0.235	400100	170600000	60.440
6773	0.355	399000	149568872	51.009	33550	0.325	399133	163186652	80.399	37963	0.294	400100	136300000	59.290
6873	0.479	399000	110711043	45.361	37225	0.434	399133	122318337	77.765	38088	0.383	400200	104500000	57.590
6958	0.718	399000	73920057	39.839	42200	0.651	399133	81563369	58.853	38138	0.550	400400	72790000	45.390

Table B- 16: Fatigue data for HRA-L samples tested in stress mode.

ID	HL-1				ID	HL-2				ID	HL-3			
No. cycles	γ(%)	τ(Pa)	G*(Pa)	δ(°)	No. cycles	γ(%)	τ(Pa)	G*(Pa)	δ(°)	No. cycles	γ(%)	τ(Pa)	G*(Pa)	δ(°)
7	0.122	250083	204814416	46.270	6	0.180	250333	139414767	49.660	6	0.115	250584	217410590	48.500
17	0.136	250584	184420389	48.400	19	0.201	250584	124972788	52.710	9	0.129	250521	194915426	48.568
31	0.144	250584	174038751	49.750	40	0.212	250584	118451300	53.810	10	0.137	250584	183128668	49.240
65	0.153	250584	163972884	51.000	109	0.224	250584	111671722	54.790	14	0.145	250500	172880644	50.270
112	0.163	250584	153684868	52.130	273	0.240	250584	104507428	55.710	26	0.154	250584	162989437	51.530
220	0.175	250584	143421036	53.350	858	0.257	250584	97591451	56.720	61	0.165	250584	152114009	52.980
403	0.188	250584	133136166	54.550	4245	0.276	250584	90640899	57.510	146	0.177	250584	141324207	54.410
727	0.204	250584	122914281	55.840	12255	0.300	250584	83637690	58.350	324	0.192	250584	130467541	55.690
1572	0.222	250584	112661199	57.100	23000	0.327	250584	76736383	59.380	616	0.210	250584	119577728	57.110
3202	0.245	250584	102431640	57.890	33525	0.359	250584	69730675	59.890	636	0.228	250584	109724612	58.410
5387	0.272	250584	92198366	59.370	49613	0.399	250584	62772192	60.630	2711	0.256	250584	97834065	57.570
9170	0.306	250584	81953181	60.300	68708	0.449	250584	55772237	61.470	6684	0.288	250584	86976699	59.200
13317	0.349	250584	71729427	61.370	95655	0.513	250584	48808108	62.000	11894	0.329	250584	76094131	60.240
19258	0.408	250584	61467652	62.610	111000	0.599	250667	41827144	62.730	19771	0.384	250584	65217259	61.350
26008	0.489	250584	51216396	64.220	117375	0.719	250667	34867875	63.270	28421	0.461	250584	54363683	62.860
31433	0.612	250584	40960858	65.690	119038	0.896	250667	27980031	61.950	39344	0.576	250667	43481378	64.400
34363	0.816	250667	30711857	66.340	119515	1.192	250834	21047180	54.860	46526	0.767	250667	32677394	61.180
34918	1.222	250751	20525107	63.550	119563	1.723	251168	14579144	39.390	48609	1.154	250751	21726631	47.230
ID	HL-4				ID	HL-5				ID	HL-6			
No. cycles	γ(%)	τ(Pa)	G*(Pa)	δ(°)	No. cycles	γ(%)	τ(Pa)	G*(Pa)	δ(°)	No. cycles	γ(%)	τ(Pa)	G*(Pa)	δ(°)
9	0.171	250584	146519007	50.500	6	0.132	249749	189168972	50.150	15	0.194	250584	129054535	54.420
50	0.190	250584	131888899	53.330	18	0.147	250584	170221226	50.660	170	0.216	250584	115958838	56.200
105	0.201	250584	124434147	54.380	43	0.156	250584	160947984	51.990	339	0.229	250584	109655006	57.070
190	0.214	250584	117246152	55.220	113	0.166	250584	151374280	53.280	725	0.243	250500	103234591	58.170
340	0.228	250584	109897686	56.250	258	0.177	250584	141918009	54.380	1465	0.259	250584	96862532	59.500
628	0.244	250584	102553952	57.390	473	0.189	250584	132415799	55.420	2806	0.277	250584	90336894	58.600
1340	0.263	250500	95230704	58.960	1145	0.204	250584	122955229	56.640	6167	0.298	250584	83951338	59.230
4283	0.285	250584	87927065	58.250	6018	0.221	250584	113513409	57.600	10098	0.324	250584	77445749	60.020
6543	0.311	250584	80582168	59.400	13118	0.241	250584	104074144	58.820	14800	0.353	250584	71029870	60.540

11358	0.342	250584	73244100	59.900	19593	0.265	250584	94620200	59.900	18762	0.388	250584	64542822	61.170
16458	0.380	250584	65940628	60.910	31285	0.294	250584	85140011	60.660	22817	0.431	250584	58097326	62.170
22620	0.428	250584	58593898	62.190	49378	0.331	250584	75685043	61.580	28644	0.480	250584	52169073	61.300
26128	0.489	250667	51291751	61.290	68748	0.378	250584	66221384	62.440	31311	0.555	250584	45161725	63.990
26895	0.570	250667	43977191	62.620	97506	0.442	250584	56741611	63.510	33238	0.647	250667	38729518	64.300
27178	0.681	250667	36786774	62.600	116033	0.530	250584	47305675	64.610	34503	0.778	250667	32226873	64.520
27315	0.856	250751	29305282	61.340	121474	0.662	250667	37837097	65.120	35150	0.963	250751	26033941	62.500
27388	1.140	250876	22012771	54.755	122998	0.884	250751	28370498	64.480	35443	1.283	250834	19545876	60.820
27415	1.746	251210	14386756	38.245	123324	1.322	250918	18976798	53.370	35528	1.974	251210	12728283	45.275
ID	HL-7				ID	HL-8				ID	HL-9			
No. cycles	γ(%)	τ(Pa)	G*(Pa)	δ(°)	No. cycles	γ(%)	τ(Pa)	G*(Pa)	δ(°)	No. cycles	γ(%)	τ(Pa)	G*(Pa)	δ(°)
7	0.129	250166	194431404	47.510	15	0.150	250166	166343423	48.170	15	0.182	250166	137178695	50.990
27	0.143	250584	175352149	50.760	68	0.168	250584	149570062	51.120	48	0.202	250584	123811384	53.700
78	0.151	250584	165425910	52.150	183	0.177	250584	141465779	52.260	109	0.215	250584	116505930	54.710
206	0.161	250500	155617411	53.400	453	0.188	250584	133158236	53.310	259	0.228	250584	109825211	55.670
462	0.172	250584	145864816	54.470	733	0.201	250584	124769540	54.230	808	0.243	250584	102956012	56.520
999	0.184	250584	136119461	55.510	2050	0.215	250584	116445329	55.130	1178	0.261	250584	96052448	57.240
2586	0.198	250584	126448230	56.720	4725	0.232	250584	108150004	56.140	1400	0.281	250584	89188736	57.920
7237	0.215	250584	116667178	57.660	9000	0.251	250584	99843364	57.030	5688	0.304	250584	82297922	58.570
11311	0.234	250584	106935549	58.300	19475	0.274	250584	91515612	57.670	13300	0.332	250584	75492993	59.090
18026	0.258	250584	97227356	59.510	28438	0.301	250584	83197937	58.290	28025	0.365	250584	68603377	59.540
28039	0.286	250584	87494964	60.410	42015	0.335	250584	74908675	59.450	45913	0.406	250584	61729673	60.790
42591	0.322	250584	77772582	61.710	51970	0.376	250584	66565487	60.710	61038	0.457	250584	54849966	61.610
60939	0.368	250584	68089933	62.720	62450	0.430	250584	58218941	61.280	70750	0.521	250667	48071475	61.770
84194	0.430	250584	58332343	63.440	71625	0.502	250667	49914048	62.150	75000	0.609	250667	41153000	61.360
107448	0.515	250584	48624756	64.450	78075	0.603	250667	41588886	62.600	77400	0.731	250667	34288744	59.950
115662	0.644	250667	38895261	65.380	80450	0.753	250667	33293753	62.020	78688	0.913	250751	27460191	53.280
117827	0.859	250667	29168166	65.710	81463	1.004	250751	24975239	58.940	79213	1.215	251001	20652197	39.000
118160	1.295	250834	19362372	57.040	81825	1.508	251001	16648343	46.500	79450	1.640	251168	15319595	38.010

Appendix B-5: DSR-Sequence of Relaxation Test

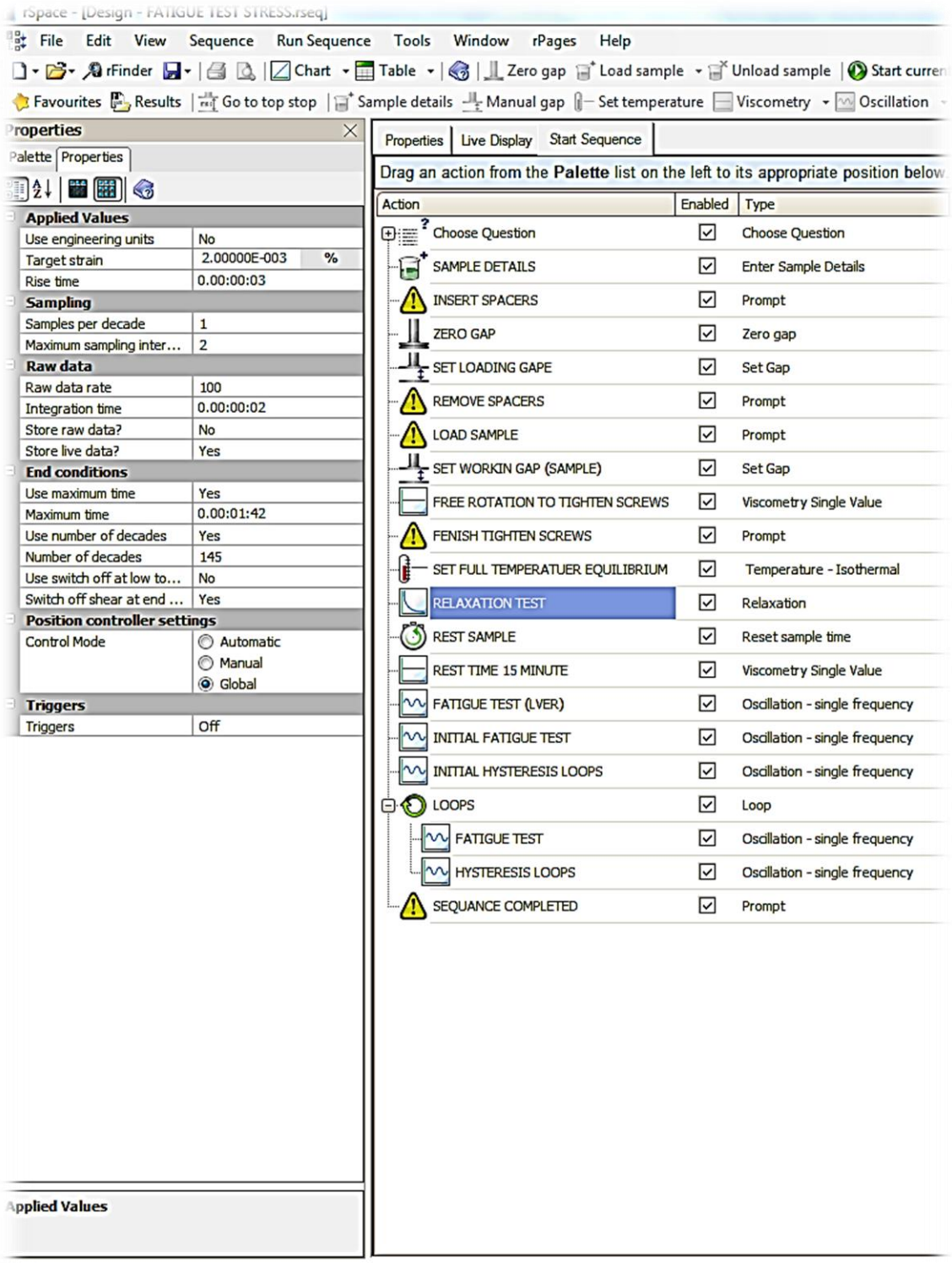

Figure B- 5: DSR sequences for relaxation test.

Table B- 17: Relaxation data for DBM-G samples tested in strain mode.

ID	DG-1	DG-2	DG-3	DG-4	DG-5	DG-6	DG-7	DG-8	DG-9
Time (s)	G*(t) (Pa)	G*(t) (Pa)	G*(t) (Pa)	G*(t) (Pa)	G*(t) (Pa)	G*(t) (Pa)	G*(t) (Pa)	G*(t) (Pa)	G*(t) (Pa)
5	34630000	32310000	23170000	19970000	9803000	31710000	33080000	40590000	30680000
7	23710000	21430000	14340000	13600000	5226000	20430000	22990000	29590000	21720000
9	19430000	18050000	12220000	12430000	5027000	15620000	18010000	22440000	19090000
11	18350000	16770000	11700000	11250000	4407000	15810000	17910000	20830000	17920000
13	18150000	15220000	11090000	11080000	4038000	14340000	16920000	19290000	16790000
15	16000000	14670000	10500000	10660000	3807000	13150000	15830000	18270000	17310000
17	14930000	13790000	9954000	10520000	3537000	13260000	15080000	17530000	16500000
19	13270000	13500000	9597000	9188000	3327000	12980000	14830000	16500000	16100000
21	13380000	12810000	9377000	9793000	3151000	11870000	14290000	16200000	16570000
23	12210000	12130000	9087000	9325000	3005000	12460000	14230000	15940000	16500000
25	11960000	12120000	8860000	8589000	2912000	12040000	13660000	15280000	15730000
27	11520000	11590000	8626000	8569000	2859000	11080000	13560000	15060000	15980000
29	11970000	11040000	8367000	8436000	2696000	12120000	13140000	14640000	16160000
31	11290000	11140000	8157000	8086000	2641000	11180000	13000000	14130000	15950000
33	10750000	10770000	8020000	8670000	2576000	11870000	12700000	14050000	15890000
35	10680000	10400000	7768000	8031000	2477000	11090000	12470000	13940000	16540000
37	10810000	10570000	7701000	7696000	2427000	10790000	12200000	13600000	15580000
39	9974000	10160000	7512000	8051000	2381000	11810000	12060000	13570000	16470000
41	10550000	9928000	7395000	7413000	2319000	11080000	11840000	13290000	16090000
43	10190000	9869000	7318000	7552000	2232000	11880000	11540000	13070000	16260000
45	9441000	9582000	7136000	7783000	2173000	11330000	11430000	13160000	16310000
47	10010000	9207000	7012000	7717000	2139000	11090000	11290000	12630000	16470000
49	9083000	9034000	6949000	7377000	2084000	12220000	11100000	12410000	16940000
51	9235000	9120000	7027000	7059000	2029000	11070000	11130000	12660000	16160000
53	8912000	8777000	6904000	7090000	2003000	11810000	10910000	12400000	16830000
55	8697000	8685000	6761000	7553000	1945000	11880000	10870000	12120000	16790000
57	9117000	8552000	6608000	7290000	1918000	11360000	10600000	11930000	16500000
59	9065000	8193000	6586000	7218000	1868000	12250000	10720000	12110000	17320000
61	8608000	8274000	6511000	6944000	1851000	12360000	10630000	11810000	16860000
63	8794000	8196000	6391000	6723000	1815000	11500000	10600000	11700000	16680000
65	8677000	8061000	6225000	6990000	1826000	12480000	10450000	12000000	17860000
67	8267000	7939000	6176000	6973000	1836000	12420000	10350000	11520000	17440000
69	8397000	7767000	6100000	7123000	1789000	12190000	10230000	11460000	16820000
71	8531000	7606000	5976000	7002000	1771000	13050000	10330000	11350000	17810000
73	8012000	7426000	5854000	6900000	1726000	12580000	10140000	11360000	17890000
75	7910000	7553000	5753000	6586000	1702000	12510000	10090000	11660000	17490000
77	8284000	7483000	5703000	6817000	1678000	13210000	9906000	11510000	17730000
79	8481000	7251000	5677000	7165000	1674000	12580000	9961000	11410000	17650000
81	7838000	7312000	5601000	6624000	1647000	13200000	9875000	11560000	18290000
83	7809000	7267000	5523000	6487000	1620000	12520000	9846000	11200000	17870000
85	8198000	7048000	5520000	6460000	1609000	13260000	9687000	11160000	18880000
87	8393000	7141000	5643000	6409000	1574000	13280000	9618000	11460000	18880000
89	7819000	6860000	5563000	6941000	1566000	12750000	9480000	11130000	
91	7794000	6882000	5439000	6821000	1550000	13780000	9373000	11090000	
93	8075000	7113000	5428000	6597000	1520000	13440000	9463000	11330000	
95	7967000	6920000	5400000	6344000	1461000	12970000	9311000	11000000	
97	8127000	6743000	5360000	6344000	1461000	14040000	9297000	10820000	
99	8038000	6718000	5353000		1439000	13670000	9339000	11370000	
101	7929000	6718000	5282000		1449000	13160000	9060000	11040000	

Table B- 18: Relaxation data for DBM-G samples tested in stress mode.

ID	DG-1	DG-2	DG-3	DG-4	DG-5	DG-6	DG-7	DG-8	DG-9
Time (s)	G*(t) (Pa)	G*(t) (Pa)	G*(t) (Pa)	G*(t) (Pa)	G*(t) (Pa)	G*(t) (Pa)	G*(t) (Pa)	G*(t) (Pa)	G*(t) (Pa)
5	58720000	30360000	37970000	27860000	20010000	12140000	23670000	31610000	44110000
7	54850000	26040000	35020000	23990000	17600000	10970000	20670000	28770000	40150000
9	50220000	21780000	30850000	19560000	14410000	8144000	17240000	25090000	35010000
11	46170000	17800000	27040000	15600000	11460000	4806000	14180000	21700000	30600000
13	41350000	14520000	23530000	12080000	8770000	1927000	11480000	18720000	26910000
15	37840000	11520000	20550000	8923000	6599000	605500	9189000	16020000	23550000
17	34930000	9008000	17970000	6256000	5096000	1038000	7396000	13610000	20590000
19	31850000	7145000	15540000	4263000	4355000	1954000	6253000	11610000	18030000
21	28800000	6000000	13500000	3091000	4164000	2421000	5593000	10000000	15760000
23	26730000	5519000	11910000	2681000	4258000	2409000	5416000	8832000	13810000
25	25070000	5429000	10700000	2838000	4530000	2143000	5402000	8046000	12240000
27	23270000	5687000	9827000	3281000	4708000	1880000	5439000	7628000	11070000
29	21720000	6061000	9314000	3744000	4803000	1725000	5518000	7501000	10190000
31	20490000	6354000	9046000	4135000	4763000	1660000	5501000	7470000	9669000
33	19610000	6573000	8892000	4340000	4620000	1643000	5389000	7530000	9369000
35	18550000	6639000	8880000	4431000	4478000	1637000	5226000	7571000	9155000
37	18200000	6649000	8880000	4369000	4320000	1632000	5062000	7641000	9114000
39	17800000	6577000	8828000	4236000	4162000	1597000	4943000	7639000	9103000
41	17360000	6461000	8819000	4086000	4043000	1546000	4780000	7612000	9108000
43	17280000	6286000	8772000	3847000	3960000	1479000	4647000	7540000	9122000
45	17330000	6231000	8680000	3653000	3867000	1440000	4486000	7436000	9056000
47	17130000	6006000	8530000	3490000	3800000	1400000	4392000	7330000	9032000
49	17180000	5958000	8415000	3343000	3739000	1379000	4242000	7192000	8986000
51	17210000	5856000	8237000	3264000	3695000	1366000	4157000	7089000	8904000
53	17360000	5823000	8070000	3190000	3636000	1351000	4076000	6964000	8753000
55	17420000	5758000	7961000	3120000	3617000	1327000	3974000	6843000	8685000
57	17220000	5716000	7755000	3071000	3557000	1306000	3906000	6716000	8571000
59	17240000	5676000	7582000	3022000	3508000	1304000	3859000	6612000	8389000
61	17550000	5609000	7464000	2962000	3474000	1293000	3776000	6506000	8256000
63	17300000	5640000	7311000	2893000	3450000	1270000	3720000	6453000	8141000
65	17110000	5556000	7227000	2837000	3368000	1253000	3625000	6370000	8025000
67	17240000	5525000	7109000	2772000	3315000	1242000	3574000	6343000	7919000
69	17250000	5487000	6998000	2725000	3294000	1220000	3492000	6264000	7783000
71	17270000	5467000	6893000	2646000	3245000	1183000	3423000	6243000	7663000
73	17100000	5427000	6826000	2599000	3216000	1221000	3345000	6172000	7592000
75	16990000	5361000	6728000	2540000	3207000	1182000	3259000	6140000	7475000
77	17100000	5344000	6680000	2497000	3232000	1145000	3209000	6093000	7384000
79	16880000	5316000	6596000	2469000	3237000	1150000	3177000	6048000	7309000
81	16830000	5304000	6547000	2444000	3200000	1171000	3138000	5986000	7193000
83	16830000	5295000	6462000	2413000	3205000	1188000	3106000	5950000	7092000
85	16820000	5243000	6422000	2380000	3243000	1173000	3055000	5896000	7042000
87	16880000	5223000	6325000	2344000	3150000	1123000	3004000	5848000	6991000
89	16800000	5239000	6292000	2303000	3083000	1104000	2947000	5834000	6924000
91	16500000	5219000	6232000	2271000	2996000	1079000	2899000	5761000	6878000
93	16550000	5183000	6164000	2228000	2985000	1098000	2843000	5712000	6832000
95	16650000	5190000	6112000	2185000	2920000	1066000	2784000	5681000	6765000
97	16650000	5201000	6024000	2135000	2906000	1070000	2769000	5648000	6735000
99	16590000	5164000	6038000	2105000	2877000	1044000	2736000		6692000
101	16540000	5129000	5971000	2066000	2879000	1030000	2734000		6607000

Table B- 19: Relaxation data for DBM-L samples tested in strain mode.

ID	DL-1	DL-2	DL-3	DL-4	DL-5	DL-6	DL-7	DL-8	DL-9
t (s)	G(t)	G(t)	G(t)	G(t)	G(t)	G(t)	G(t)	G(t)	G(t)
5	48820000	18870000	54950000	30120000	40320000	33630000	47950000	35670000	39250000
7	39260000	9791000	45770000	22040000	33670000	21400000	38240000	26110000	29060000
9	28860000	8769000	33220000	17400000	26780000	14680000	27430000	19980000	22030000
11	24210000	8221000	26750000	15730000	22740000	14250000	23560000	17760000	20420000
13	21320000	7412000	23230000	16360000	21480000	13540000	22640000	16850000	19700000
15	20140000	6934000	21440000	14800000	20600000	12800000	22200000	15570000	18600000
17	18610000	6438000	20250000	15170000	19880000	11920000	21770000	14810000	17580000
19	17970000	6110000	18840000	13380000	18320000	11570000	20590000	14060000	16750000
21	16790000	5856000	17720000	12930000	17700000	10930000	20030000	13360000	16260000
23	15720000	5597000	17200000	13230000	16970000	10580000	20000000	12660000	15450000
25	15010000	5246000	15860000	11930000	17010000	10140000	19650000	12010000	14920000
27	13930000	5099000	15010000	12470000	17190000	9948000	18910000	11850000	14140000
29	12870000	4874000	14330000	11440000	16430000	9460000	19060000	11440000	14220000
31	12240000	4765000	13860000	11550000	16410000	9360000	18790000	11030000	13960000
33	12030000	4548000	13680000	11790000	15870000	9183000	18270000	10580000	14160000
35	11680000	4489000	12980000	10650000	15070000	8881000	17760000	10380000	13570000
37	11080000	4350000	12180000	11800000	14900000	8720000	17940000	10080000	13400000
39	10550000	4248000	11720000	10680000	14710000	8399000	18170000	9647000	13500000
41	10410000	4132000	11510000	11190000	14710000	8225000	18080000	9495000	13490000
43	10310000	4100000	11150000	11580000	14660000	8177000	17900000	9206000	13310000
45	10030000	4027000	11130000	10230000	14060000	7988000	17650000	9071000	12810000
47	9535000	3847000	10520000	11330000	13730000	7913000	17670000	8850000	12930000
49	9158000	3751000	10030000	10630000	14150000	7800000	17400000	8615000	12790000
51	8778000	3654000	9885000	10620000	13680000	7584000	17100000	8365000	12690000
53	9040000	3597000	9380000	10600000	13230000	7512000	17120000	8010000	12320000
55	8199000	3496000	9156000	10480000	13700000	7352000	17460000	7936000	12390000
57	8484000	3408000	8823000	10710000	13350000	7412000	17100000	7859000	12310000
59	7997000	3299000	8211000	10380000	13040000	7210000	17140000	7966000	12460000
61	7552000	3244000	7959000	10630000	13220000	7116000	16950000	7906000	12200000
63	7386000	3210000	7610000	9829000	13280000	6997000	16560000	7889000	12240000
65	7051000	3159000	7113000	10790000	12750000	6912000	17520000	7755000	12060000
67	6865000	3031000	6756000	9858000	12910000	6790000	17160000	7713000	11890000
69	6803000	3040000	6672000	10930000	13370000	6743000	17280000	7674000	11710000
71	6511000	3052000	6714000	9855000	13400000	6585000	17290000	7641000	11660000
73	6236000	2984000	6518000	10810000	13350000	6568000	16790000	7738000	11800000
75	6029000	2913000	6132000	10760000	13350000	6508000	16700000	7704000	12020000
77	5753000	2795000	6076000	10180000	12640000	6420000	16790000	7692000	11650000
79	5768000	2783000	6067000	10000000	12390000	6430000	16460000	7761000	11850000
81	5793000	2813000	5599000	10470000	12660000	6325000	16720000	7646000	11540000
83	5621000	2729000	5264000	9416000	12490000	6342000	16770000	7608000	11500000
85	5550000	2698000	5126000	10040000	12750000	6174000	17050000	7465000	11140000
87	5395000	2626000	5202000	10760000	13120000	6182000	17310000	7539000	11400000
89	5048000	2545000	5233000	9837000	12900000	6146000	16890000	7685000	11610000
91	5074000	2562000	5203000	10840000	12660000	6132000	16660000	7645000	11690000
93	4920000	2520000	5148000	9732000	12430000	6128000	17100000	7588000	11570000
95	4842000	2442000	5105000	10160000	12670000	6044000	17160000	7572000	11550000
97	4876000	2371000	4854000	10040000	13110000	6006000	17050000	7630000	11030000
99	4701000	2391000	4649000	10710000	12560000	5911000	17640000	7561000	11260000
101	4568000	2423000	4312000	9841000	12540000	5843000	17580000	7562000	11130000

Table B- 20: Relaxation data for DBM-L samples tested in stress mode.

ID	DL-1	DL-2	DL-3	DL-4	DL-5	DL-6	DL-7	DL-8	DL-9
t (s)	G(t)	G(t)	G(t)	G(t)	G(t)	G(t)	G(t)	G(t)	G(t)
5	33960000	24610000	30620000	35140000	24400000	8954000	19990000	13730000	9898000
7	31210000	20670000	27250000	31390000	21190000	8533000	17330000	11400000	7584000
9	27160000	16560000	23240000	27490000	17370000	6280000	14030000	8674000	4690000
11	23060000	12940000	19580000	23930000	13810000	3625000	10750000	6216000	2194000
13	19520000	9559000	16330000	20650000	10630000	1837000	7611000	4441000	982800
15	16110000	6659000	13340000	17750000	7805000	1660000	4728000	3718000	1087000
17	12960000	4445000	10680000	15160000	5515000	2312000	2370000	3786000	1631000
19	10150000	3084000	8448000	12900000	3871000	2736000	700700	4165000	1947000
21	7673000	2671000	6777000	10950000	2952000	2771000	33720	4510000	1958000
23	5561000	2925000	5618000	9428000	2653000	2600000	320700	4606000	1781000
25	3914000	3381000	4991000	8284000	2737000	2432000	492800	4583000	1592000
27	2742000	3893000	4808000	7526000	2984000	2348000	520200	4497000	1436000
29	1969000	4239000	4936000	7158000	3213000	2344000	434500	4404000	1340000
31	1536000	4398000	5196000	6941000	3341000	2339000	281000	4351000	1292000
33	1369000	4365000	5481000	6923000	3369000	2334000	88700	4307000	1266000
35	1334000	4244000	5676000	7027000	3286000	2316000		4263000	1217000
37	1289000	4115000	5824000	7141000	3125000	2306000		4236000	1176000
39	1241000	3904000	5859000	7214000	2937000	2272000		4195000	1132000
41	1164000	3743000	5805000	7320000	2747000	2262000		4171000	1081000
43	1024000	3586000	5715000	7380000	2566000	2261000		4170000	1057000
45	834400	3369000	5590000	7349000	2403000	2246000		4139000	1024000
47	610300	3344000	5433000	7321000	2264000	2230000		4143000	998500
49	370500	3290000	5280000	7194000	2152000	2223000		4158000	959000
51	122800	3252000	5140000	7122000	2055000	2218000		4095000	919500
53		3209000	5020000	7016000	1988000	2215000		4069000	880900
55		3193000	4951000	6918000	1912000	2216000		4058000	846600
57		3131000	4855000	6821000	1848000	2196000		4024000	826300
59		3109000	4792000	6736000	1795000	2194000		4042000	800900
61		3066000	4736000	6670000	1733000	2187000		4038000	782100
63		3031000	4645000	6561000	1651000	2184000		4060000	756700
65		2960000	4585000	6499000	1581000	2196000		4061000	737500
67		2890000	4535000	6420000	1515000	2200000		4094000	719400
69		2842000	4405000	6316000	1448000	2212000		4075000	700400
71		2808000	4238000	6307000	1381000	2187000		4055000	686800
73		2761000	4295000	6261000	1330000	2188000		4051000	667300
75		2699000	4295000	6215000	1270000	2182000		4037000	639000
77		2685000	4258000	6178000	1206000			4043000	607900
79		2641000	4027000	6083000	1164000			4032000	577200
81		2577000	4244000	6124000	1111000			4046000	591400
83		2580000	4193000	6099000	1060000				609100
85		2563000	4157000	6051000	1001000				599600
87		2535000	4105000	6001000	948200				577600
89		2510000	4105000	5968000	904100				551000
91		2487000	4086000	5944000	862000				516600
93		2449000	4081000	5923000	823200				506900
95		2417000	4085000	5894000	786800				500100
97		2389000	4032000	5853000	746300				467800
99		2370000	3991000	5824000	708500				452200
101		2333000	3912000	5825000	668200				456800

Table B- 21: Relaxation data for HRA-G samples tested in strain mode.

ID	HG-1	HG-2	HG-3	HG-4	HG-5	HG-6	HG-7	HG-8	HG-9
t (s)	G(t)	G(t)	G(t)	G(t)	G(t)	G(t)	G(t)	G(t)	G(t)
5	114000000	115200000	207600000	150300000	172000000	135700000	151600000	104600000	202700000
7	102900000	97840000	196400000	139500000	159700000	126100000	155200000	88370000	178100000
9	87110000	78270000	178300000	124500000	138800000	108700000	126500000	66960000	163200000
11	71140000	61530000	161600000	103300000	118300000	89300000	114100000	47070000	144800000
13	58680000	51080000	139300000	82220000	100900000	73780000	95750000	32930000	128300000
15	51110000	46510000	121400000	72470000	85090000	61190000	79270000	26300000	109800000
17	46720000	47200000	106600000	61600000	74030000	52050000	71600000	25830000	96010000
19	43930000	49310000	94380000	58220000	64130000	49230000	66140000	27040000	85930000
21	43050000	49000000	81820000	53530000	59200000	46300000	56450000	27780000	80040000
23	42270000	49190000	72090000	52180000	54650000	44120000	56090000	27690000	74870000
25	39690000	48870000	69940000	50640000	55510000	43850000	58660000	27340000	69480000
27	38100000	47510000	64360000	50130000	54760000	42040000	56580000	25630000	67500000
29	36730000	46790000	59230000	49690000	52690000	40840000	53960000	25050000	64930000
31	36140000	45340000	58630000	47400000	52250000	38760000	54550000	23720000	66160000
33	35760000	45330000	57640000	46580000	49540000	37710000	57370000	23030000	65290000
35	36540000	44380000	55630000	45440000	50500000	37690000	53980000	22010000	63540000
37	35050000	44590000	51870000	45880000	46440000	36920000	52510000	21960000	61510000
39	33370000	43330000	51000000	44270000	46700000	36390000	55450000	21510000	62220000
41	31780000	43430000	51170000	44300000	44150000	35300000	54490000	21150000	62450000
43	31350000	42720000	48650000	43540000	42270000	34710000	50310000	20980000	60810000
45	30120000	42190000	46060000	42760000	41240000	32900000	51390000	20260000	58120000
47	29570000	41520000	44230000	41460000	41590000	31490000	53590000	20080000	57980000
49	29930000	41410000	45700000	40980000	41280000	30380000	48430000	19680000	57140000
51	30470000	41210000	43470000	40410000	38670000	29700000	49960000	19370000	56960000
53	30280000	40160000	40760000	39960000	39560000	28880000	51470000	18860000	55960000
55	29630000	40410000	40240000	38420000	37170000	28750000	48980000	18620000	54290000
57	29540000	39600000	39850000	37930000	37380000	28970000	48000000	18260000	53770000
59	28450000	39530000	39240000	36520000	37630000	29010000	50500000	17700000	54920000
61	27320000	39000000	37590000	36140000	36700000	28420000	49650000	17700000	54730000
63	26560000	38090000	36390000	35030000	35650000	28720000	48620000	17140000	53410000
65	26190000	38520000	36730000	34060000	35580000	26600000	50730000	17060000	53290000
67	26100000	37740000	35990000	33830000	34240000	26110000	51710000	17260000	52040000
69	25600000	37640000	34150000	32960000	33960000	25200000	48160000	16920000	50690000
71	26450000	37710000	32910000	32270000	34070000	23970000	49190000	16500000	50900000
73	26540000	37130000	34500000	30630000	33750000	23970000	50830000	16380000	53110000
75	26490000	37190000	32630000	30570000	32160000	24150000	46490000	16290000	52680000
77	26210000	36330000	30910000	30030000	31800000	24180000	47530000	16320000	52050000
79	25730000	36470000	30090000	29470000	31000000	24080000	49540000	16020000	50790000
81	25400000	35530000	29590000	29020000	31000000	23770000	47910000	15880000	50760000
83	25670000	35700000	29460000	28400000	31250000	23920000	47210000	15460000	51040000
85	24810000	35700000	29980000	27330000	29880000	23280000	48920000	15220000	52230000
87	23930000	34950000	28750000	27410000	29270000	21890000	48470000	15150000	51400000
89	23350000	34860000	27470000	27150000	29030000	21220000	45540000	15280000	50410000
91	23170000	35060000	26770000	26800000	28640000	21250000	46330000	14890000	49250000
93	22810000	34560000	27050000	26610000	29030000	20780000	48570000	14750000	48520000
95	22510000	34470000	27230000	26330000	27290000	20770000	48470000	14650000	48810000
97	22780000	34460000	25880000	25750000	27250000	21100000	46350000	14670000	49680000
99	23400000	34180000	25060000	25630000	27110000	21120000	47610000	14460000	50490000
101	24130000	33240000	23680000	26220000	27530000	20850000	48650000	14240000	50140000
103	23230000	33780000	23790000	26960000	27240000	20130000	47010000	14270000	48180000

Table B- 22: Relaxation data for HRA-G samples tested in stress mode.

ID	HG-1	HG-2	HG-3	HG-4	HG-5	HG-6	HG-7	HG-8
t (s)	G(t)	G(t)	G(t)	G(t)	G(t)	G(t)	G(t)	G(t)
5	118600000	172900000	268900000	143800000	459900000	111800000	112100000	138300000
7	115200000	156500000	211700000	135800000	381200000	98140000	99960000	126600000
9	106800000	142700000	186200000	126700000	330300000	86470000	87530000	120400000
11	98190000	133600000	162000000	117800000	279400000	78940000	79160000	114200000
13	90940000	122400000	145700000	111300000	251200000	71150000	71950000	105500000
15	84710000	113900000	132300000	104300000	230300000	63880000	65560000	98360000
17	78760000	106500000	122100000	98820000	212800000	57960000	60630000	91680000
19	73110000	100500000	113900000	93760000	199400000	52970000	55720000	86200000
21	68390000	95230000	106700000	88680000	188400000	48280000	51120000	81020000
23	63890000	89860000	100100000	84420000	177300000	43990000	47400000	76550000
25	59530000	85610000	94650000	80290000	167400000	40320000	43280000	72230000
27	55610000	81470000	89160000	76930000	161000000	36620000	39930000	69070000
29	51720000	77550000	84420000	73100000	154300000	33120000	36620000	65220000
31	48120000	73930000	80150000	70010000	147100000	30070000	33530000	62130000
33	44660000	70450000	75900000	66890000	141900000	27360000	30860000	59290000
35	41190000	67270000	72330000	63790000	136500000	24850000	28070000	55970000
37	38040000	64550000	68650000	61140000	131800000	22420000	25860000	53380000
39	34980000	61780000	65500000	58350000	127600000	20270000	24050000	50730000
41	32080000	59190000	62300000	55550000	123600000	18580000	22010000	48410000
43	29220000	56890000	59310000	53150000	119900000	17050000	20530000	46330000
45	26640000	54860000	56840000	51440000	116600000	15760000	19180000	44090000
47	24200000	52820000	54130000	49360000	113600000	14820000	18080000	42200000
49	21840000	50970000	51770000	47350000	110500000	14180000	17430000	40560000
51	19720000	49020000	49670000	45400000	107500000	13840000	16860000	38930000
53	17740000	47630000	47500000	43560000	105200000	13660000	16650000	37200000
55	15900000	46350000	45540000	41860000	102700000	13690000	16630000	36180000
57	14310000	45040000	44800000	40520000	100800000	13820000	16610000	34850000
59	12890000	44130000	43500000	39120000	99060000	14140000	16880000	33730000
61	11660000	42940000	42410000	37850000	96850000	14590000	17150000	32610000
63	10640000	42310000	41400000	36400000	94760000	15070000	17390000	32000000
65	9760000	41560000	40580000	35370000	93070000	15520000	17650000	31020000
67	9030000	41030000	39780000	34320000	91800000	15990000	17880000	30470000
69	8522000	40470000	39270000	33430000	90400000	16320000	18330000	29980000
71	8081000	40200000	38990000	32790000	89620000	16760000	18880000	29590000
73	7817000	40000000	38690000	32080000	88070000	17120000	19030000	29180000
75	7654000	40000000	38570000	31520000	87340000	17410000	19270000	28820000
77	7592000	39720000	38400000	30930000	85940000	17680000	19520000	28770000
79	7589000	39890000	38360000	30600000	85450000	17770000	19540000	28460000
81	7667000	39990000	38480000	30260000	84440000	17970000	19850000	28500000
83	7776000	40000000	38680000	29920000	84080000	18070000	19790000	28360000
85	7948000	40310000	38840000	29620000	83480000	18040000	19780000	28230000
87	8070000	40450000	39230000	29470000	82740000	17980000	19870000	28180000
89	8226000	40620000	39500000	29550000	82880000	17960000	19580000	28200000
91	8408000	40730000	39680000	29740000	82990000	17910000	19423000	28120000
93	8565000	41100000	40000000	29750000	82990000	17700000	19300000	28050000
95	8688000	41010000	40370000	30020000	83290000	17520000	19207000	27950000
97	8781000	41460000	40610000	30210000	83210000	17420000	19194000	27820000
99	8794000	41640000	40890000	30420000	83350000	17440000	19128000	27830000
101	8860000	41780000	41020000	30750000	83290000	17340000	19057000	27740000
103	8931000	41860000	41470000	30850000	83810000	17130000	18988000	27760000
105	8862000	42010000	41530000	30970000	83710000	17060000	18968000	27900000
107	8842000	42160000	41910000	31220000	84280000	16880000	18922000	27640000
109	8796000	42150000	41890000	31300000	84490000	16760000	18843000	27690000
111	8717000	42460000	42350000	31450000	84530000	16880000	18754000	27650000
113	8628000	42440000	42340000	31540000	84570000	16720000	18607000	27490000

115	8481000	42590000	42310000	31500000	85340000	16640000	18495000	27470000
117	8369000	42640000	42590000	31520000	85710000	16610000	18294000	27330000
119	8168000	42710000	42560000	31480000	85520000	16540000	18156000	27300000
121	8030000	42630000	42630000	31620000	85820000	16470000	18033000	27320000
123	7907000	42920000	42670000	31300000	86470000	16420000	17864000	27020000
125	7738000	42900000	42750000	31210000	86660000	16480000	17716000	27010000
127	7590000	42680000	42710000	31170000	86600000	16440000	17539000	26980000
129	7413000	42790000	42720000	31150000	87150000	16420000	17396000	26690000
131	7270000	42850000	42590000	30860000	87310000	16460000	16126000	26600000

Table B- 23: Relaxation data for HRA-L samples tested in strain mode.

ID	HL-1	HL-2	HL-3	HL-4	HL-5	HL-6	HL-7	HL-8	HL-9
Time(s)	G (t) (Pa)	G (t) (Pa)	G (t) (Pa)	G (t) (Pa)	G (t) (Pa)	G (t) (Pa)	G (t) (Pa)	G (t) (Pa)	G (t) (Pa)
5	78050000	108100000	42320000	86910000	78180000	89720000	62160000	69240000	68920000
7	66640000	102100000	27440000	73560000	67150000	79740000	49710000	60020000	56020000
9	50880000	89770000	14850000	57690000	51190000	64210000	33490000	43410000	40600000
11	37110000	76010000	18410000	42680000	38740000	50050000	24130000	34600000	29780000
13	30110000	61530000	19250000	34910000	33220000	40250000	22100000	30840000	24630000
15	28530000	53580000	19090000	32250000	31680000	36110000	22010000	29700000	24360000
17	29260000	48340000	18210000	30770000	30790000	34020000	21630000	28080000	25440000
19	28020000	45630000	17540000	30220000	29890000	33510000	20320000	28090000	24440000
21	26910000	44090000	18910000	29770000	29230000	32350000	18970000	25730000	22220000
23	25790000	41250000	17460000	28570000	27790000	31900000	18040000	25930000	22320000
25	25250000	39920000	18650000	27430000	27130000	30610000	17090000	24440000	21040000
27	23910000	38330000	17360000	26690000	26190000	29270000	16380000	23740000	21880000
29	22650000	36950000	18750000	25900000	25290000	28790000	16040000	23510000	21250000
31	20870000	35430000	18530000	24400000	24750000	27720000	15330000	21920000	19580000
33	19350000	34100000	18750000	23350000	24040000	26670000	14890000	21960000	19450000
35	19340000	33150000	19480000	22830000	23270000	26220000	14320000	21540000	19980000
37	19180000	31920000	17780000	22140000	23210000	25420000	13940000	20650000	19230000
39	19380000	31600000	19860000	22500000	22440000	25210000	13460000	20030000	18780000
41	18900000	31440000	18280000	21880000	22040000	23890000	13250000	19620000	18540000
43	18450000	30150000	19680000	21070000	21790000	23560000	12980000	18870000	18780000
45	18030000	29540000	18830000	20510000	21320000	22720000	12720000	19210000	18440000
47	17300000	28770000	19420000	20580000	20790000	22040000	12150000	19090000	18580000
49	16230000	27840000	19860000	19650000	20730000	22140000	12050000	18560000	18180000
51	16300000	27600000	18650000	19640000	20420000	21620000	11650000	17810000	17470000
53	16030000	27080000	21010000	18930000	19970000	21020000	11410000	17280000	17450000
55	15280000	27120000	19120000	18720000	19680000	20330000	11230000	17440000	17390000
57	15520000	26370000	20700000	18650000	19340000	20520000	10870000	16920000	17790000
59	15130000	26030000	19920000	18170000	19040000	19750000	10740000	16520000	17430000
61	14760000	25400000	20410000	18410000	19090000	19180000	10530000	16590000	17750000
63	14920000	24440000	20350000	17850000	18830000	18960000	10320000	16530000	17200000
65	14360000	23820000	20350000	17820000	18650000	18850000	10290000	16480000	17470000
67	13810000	22910000		17410000	18230000	18040000	10000000	16320000	16860000
69	12970000	22280000		16950000	17940000	18010000	9931000	16020000	17150000
71	12620000	22650000		16700000	17890000	17490000	9696000	15610000	17190000
73	12560000	21820000		16700000	17550000	17600000	9591000	15760000	16830000
75	12390000	21740000		16500000	17400000	17250000	9467000	14900000	16930000
77	12330000	21480000		16550000	17370000	16670000	9279000	14510000	16820000
79	12030000	21380000		16070000	17220000	16770000	9047000	14740000	16770000
81	12100000	21250000		15920000	16950000	16440000	9111000	14690000	15970000
83	12480000	20440000		16220000	17140000	16170000	8919000	14420000	16900000

85	12250000	20380000		15480000	16880000	15920000	8774000	14320000	16060000
87	11770000	20220000		15810000	16660000	15550000	8644000	14200000	16800000
89	12170000	20280000		15780000	16670000	15480000	8398000	14290000	15960000
91	12110000	19470000		15540000	16340000	15170000	8111000	14190000	16050000
93	11870000	19320000		15360000	16440000	14750000	8090000	13440000	16000000
95	11640000	19470000		15450000	16100000	14870000	8091000	13420000	16060000
97	11250000	18840000		15130000	15990000	14720000	8041000	13500000	16440000
99	10760000	19110000		15090000	16060000	14560000	8015000	13810000	16450000
101	11090000	18580000		15010000	15760000	14320000	7846000	13280000	16870000
103	10540000	18350000		15000000	15760000	14100000	7734000	13140000	15860000

Table B- 24: Relaxation data for HRA-L samples tested in stress mode.

ID	HL-1	HL-2	HL-3	HL-4	HL-5	HL-6	HL-7	HL-8	HL-9
Time(s)	G (t) (Pa)	G (t) (Pa)	G (t) (Pa)	G (t) (Pa)	G (t) (Pa)	G (t) (Pa)	G (t) (Pa)	G (t) (Pa)	G (t) (Pa)
5	95500000	98240000	96220000	151600000	43420000	54150000	56150000	121700000	79270000
7	92170000	92370000	91280000	147300000	38320000	50070000	51240000	112100000	74210000
9	86680000	87300000	82730000	136700000	32840000	44320000	44940000	101600000	67030000
11	79970000	82070000	74890000	128200000	28180000	39130000	39270000	91440000	60170000
13	73960000	77160000	68560000	119600000	24010000	34470000	34200000	84370000	54440000
15	69340000	72660000	62930000	112900000	20230000	30430000	29850000	79640000	49810000
17	63840000	68580000	57790000	106800000	16990000	26690000	25800000	72060000	45000000
19	59740000	65000000	53430000	101100000	13960000	23330000	21980000	67320000	41100000
21	56050000	61420000	49460000	97820000	11350000	20190000	18580000	63450000	37510000
23	52310000	58100000	46050000	93660000	9174000	17260000	15390000	59690000	34140000
25	48830000	54910000	42530000	89590000	7489000	14630000	12570000	56160000	31070000
27	45800000	51950000	39510000	86080000	6320000	12260000	10060000	52890000	28160000
29	42740000	49070000	36830000	82440000	5636000	10320000	7964000	50170000	25550000
31	40110000	46280000	34180000	79330000	5318000	8703000	6304000	47460000	23190000
33	37610000	43940000	31690000	75920000	5406000	7418000	5101000	45050000	21080000
35	35240000	41550000	29630000	72740000	5671000	6539000	4303000	42580000	19200000
37	32760000	39390000	27540000	70180000	5893000	5934000	3892000	40710000	17610000
39	30890000	37140000	25820000	67300000	6252000	5591000	3817000	38710000	16290000
41	28850000	34940000	24330000	64590000	6501000	5470000	3944000	37100000	15150000
43	27150000	33190000	22880000	62060000	6649000	5495000	4208000	35550000	14290000
45	25520000	31310000	21930000	59850000	6707000	5589000	4589000	34350000	13680000
47	24170000	29730000	20910000	57560000	6669000	5709000	4877000	33410000	13180000
49	23000000	28200000	20120000	55300000	6549000	5783000	5212000	32550000	12930000
51	21820000	26910000	19580000	53260000	6431000	5833000	5441000	31800000	12780000
53	20990000	25690000	19080000	51500000	6217000	5842000	5563000	31150000	12780000
55	20120000	24630000	18800000	49800000	6090000	5812000	5624000	30880000	12890000
57	19510000	23620000	18470000	48000000	5852000	5756000	5587000	30500000	12960000
59	18650000	22850000	18380000	46460000	5692000	5661000	5532000	30310000	13110000
61	18450000	22140000	18330000	44900000	5523000	5553000	5378000	30290000	13190000
63	17970000	21470000	18310000	43540000	5371000	5412000	5196000	30180000	13210000
65	17610000	20830000	18300000	42350000	5258000	5234000	4964000	30180000	13300000
67	17330000	20330000	18390000	41080000	5159000	5066000	4756000	30340000	13280000
69	17090000	19880000	18320000	39600000	5104000	4849000	4523000	30320000	13230000
71	16680000	19450000	18350000	39160000	5035000	4648000	4315000	30550000	13220000
73	16590000	19130000	18400000	38100000	5006000	4424000	4060000	30750000	13110000
75	16460000	18740000	18360000	37480000	4954000	4220000	3905000	30870000	13050000
77	16240000	18500000	18360000	36730000	4910000	4004000	3707000	30960000	12890000
79	16020000	18260000	18260000	36180000	4849000	3841000	3541000	31150000	12810000
81	15740000	18010000	18350000	35630000	4815000	3654000	3384000	31170000	12680000
83	15590000	17780000	18270000	34930000	4802000	3495000	3266000	31420000	12550000
85	15410000	17650000	18270000	34650000	4721000	3364000	3131000	31500000	12370000
87	15170000	17460000	18200000	34150000	4639000	3259000	3021000	31710000	12240000
89	14970000	17220000	18160000	33810000	4598000	3148000	2894000	31940000	11960000

91	14800000	17120000	18080000	33460000	4559000	3057000	2795000	31770000	11910000
93	14700000	16960000	17940000	33140000	4466000	2979000	2677000	31800000	11670000
95	14480000	16750000	17810000	32800000	4416000	2887000	2574000	31840000	11510000
97	14300000	16460000	17580000	32590000	4375000	2807000	2491000	32010000	11340000
99	14060000	16530000	17310000	32290000	4326000	2718000	2378000	32010000	11190000
101	13940000	16400000	17320000	32100000	4253000	2613000	2315000	31940000	11030000
103	13810000	16210000	17080000	31840000	4209000	2493000	2231000	31800000	10890000
105	13500000	16130000	16930000	31700000	4153000	2384000	2140000	31520000	10730000
107	13220000	16040000	16660000	31570000	4146000	2259000	2066000	31580000	10630000
109	12900000	15730000	16500000	31370000	4121000	2155000	1979000	31700000	10520000
111	12590000	15560000	16220000	31330000	4053000	2052000	1893000	31820000	10460000
113	12350000	15310000	16100000	31240000	4046000	1944000	1801000	31740000	10450000
115	12160000	15120000	15900000	31130000	4113000	1863000	1704000	31880000	10270000
117	11830000	14920000	15830000	31060000	4116000	1768000	1622000	31710000	10190000
119	11610000	14720000	15640000	30950000	4009000	1685000	1531000	31750000	10140000
121	11550000	14460000	15550000	30890000	4013000	1621000	1445000	31800000	10090000

Table B- 25: 2PB data for DBM-G samples.

ID	DBM-G-1					ID	DBM-G-2					ID	DBM-G-3				
No. Cycles	Load (kN)	εσ (KPa)	με	δ (°)	E (MPa)	No. Cycles	Load (kN)	εσ (KPa)	με	δ (°)	E (MPa)	No. Cycles	Load (kN)	εσ (KPa)	με	δ (°)	E (MPa)
100	0.022	450	186	44.552	2416	100	0.023	467	186	48.529	2509	100	0.021	422	206	46.633	2048
400	0.022	431	188	45.545	2296	300	0.022	446	187	49.128	2384	400	0.020	401	206	48.861	1946
26100	0.020	410	188	47.327	2185	21700	0.021	424	188	49.217	2259	1300	0.019	383	206	48.907	1856
121700	0.019	389	189	46.871	2055	43100	0.020	401	188	49.306	2133	7700	0.018	362	207	51.901	1748
242800	0.018	370	191	46.667	1936	95700	0.019	379	189	51.209	2007	41900	0.017	343	208	51.096	1654
515900	0.017	346	191	46.283	1811	234800	0.018	358	190	50.889	1884	89300	0.016	321	209	52.358	1536
789200	0.016	324	192	48.459	1690	492400	0.017	335	191	52.374	1757	160200	0.015	304	210	51.891	1448
966200	0.015	304	193	48.107	1575	719300	0.016	313	192	52.239	1633	386600	0.014	280	210	51.067	1333
1044400	0.014	284	193	47.085	1473	1039800	0.014	289	192	52.102	1503	668800	0.013	261	211	51.106	1238
1086000	0.013	257	194	47.582	1328	1219700	0.013	272	197	52.299	1380	820200	0.012	240	213	55.248	1129
1112400	0.011	235	194	46.692	1208	1466600	0.012	250	199	51.705	1255	977300	0.011	218	213	51.890	1025
1138300	0.010	213	195	47.528	1087	1619000	0.011	225	199	52.696	1128	1132100	0.009	197	213	51.591	923
1179200	0.009	190	196	46.634	969	1725400	0.010	200	199	52.424	1004	1252900	0.008	175	213	53.230	820
1211400	0.008	166	196	46.829	845	1819500	0.008	176	200	52.042	879	1371500	0.007	153	213	54.857	717
1235000	0.007	145	197	45.246	732	1896900	0.007	150	200	51.205	749	1482000	0.006	132	213	53.525	618
1264500	0.005	119	197	44.030	605	1953300	0.006	125	200	50.286	626	1574400	0.005	110	214	55.612	514
1299000	0.004	98	198	44.036	493	2000300	0.004	102	200	49.062	507	1641900	0.004	91	214	50.495	424
1359200	0.003	75	199	40.715	376	2048600	0.003	75	201	48.258	376	1722600	0.003	72	215	38.504	336

Table B- 26: 2PB data for DBM-L samples.

ID	DBM-L-1					ID	DBM-L-2					ID	DBM-L-3				
No. Cycles	Load (kN)	εσ (KPa)	με	δ (°)	E (MPa)	No. Cycles	Load (kN)	εσ (KPa)	με	δ (°)	E (MPa)	No. Cycles	Load (kN)	εσ (KPa)	με	δ (°)	E (MPa)
100	0.020	405	195	53.978	2076	100	0.020	405	195	50.048	2075	100	0.018	366	206	48.299	1780
1100	0.018	369	197	55.219	1875	1100	0.018	371	197	50.602	1887	800	0.017	350	206	50.393	1698
5100	0.017	346	197	55.667	1754	6100	0.017	350	198	51.771	1768	16500	0.016	333	208	50.523	1602
21100	0.016	329	197	57.098	1666	60100	0.016	329	198	52.669	1661	90900	0.016	316	209	51.147	1513
23100	0.016	327	199	57.073	1645	157100	0.015	311	200	52.436	1557	183200	0.015	299	209	52.328	1429
31100	0.016	330	198	56.740	1664	570100	0.014	292	201	51.683	1455	647800	0.014	281	211	51.431	1335
86100	0.015	311	200	56.828	1557	777100	0.013	273	202	53.752	1350	772700	0.013	264	212	50.669	1246
212100	0.014	290	200	57.521	1451	1291100	0.012	255	203	52.912	1253	1433000	0.012	250	214	50.584	1169
545100	0.013	271	201	58.221	1351	1326100	0.012	253	204	52.229	1245	1752100	0.011	229	214	53.155	1067
750100	0.012	253	202	58.032	1256	1688100	0.011	232	203	52.552	1143	2953100	0.010	213	215	52.600	988
938100	0.011	230	202	57.277	1142	1807100	0.011	224	204	52.405	1099	2953400	0.010	212	215	51.848	986
1341100	0.010	211	203	58.026	1039	2343650	0.010	202	210	54.755	964	3346200	0.009	192	216	51.484	888
1521100	0.009	191	203	58.273	940	2491300	0.009	183	210	53.908	872	3461500	0.008	174	216	49.543	804
1578100	0.008	170	203	57.769	835	2571500	0.008	162	210	53.273	773	3564900	0.007	154	217	48.777	711
1651100	0.007	151	203	58.190	741	2678350	0.007	145	211	53.405	686	3705600	0.006	138	218	48.620	631
1715100	0.006	127	204	59.468	623	2724250	0.006	132	211	54.005	623	3733400	0.006	136	218	48.541	623
1772100	0.005	105	204	60.310	518	2812750	0.005	111	211	54.365	528	3853400	0.005	117	218	48.420	537
1807100	0.004	86	204	59.347	420	2858050	0.004	95	211	52.390	446	3909000	0.004	103	218	45.433	471
1808100	0.000	6	31	56.284	209	2906550	0.002	42	125	49.617	283	4005000	0.003	78	219	42.950	357

Table B- 27: 2PB data for HRA-G samples.

ID	HRA-G-1					ID	HRA-G-2					ID	HRA-G-3				
No. Cycles	Load (kN)	εσ (KPa)	με	δ (°)	E (MPa)	No. Cycles	Load (kN)	εσ (KPa)	με	δ (°)	E (MPa)	No. Cycles	Load (kN)	εσ (KPa)	με	δ (°)	E (MPa)
100	0.041	805	190	35.317	4245	100	0.046	917	190	38.352	4831	100	0.041	817	190	38.428	4304
3100	0.039	773	190	36.877	4059	4100	0.044	870	190	38.171	4566	2720	0.039	778	190	39.687	4094
6700	0.037	730	192	37.955	3791	5800	0.042	836	192	40.514	4359	118830	0.037	742	192	41.597	3870
405700	0.035	699	193	38.453	3615	18200	0.040	787	193	40.539	4088	454750	0.036	705	193	43.045	3661
903700	0.033	663	195	39.145	3398	50400	0.038	743	192	43.269	3869	1054510	0.034	665	193	43.022	3445
1545700	0.031	625	196	39.779	3189	145400	0.035	701	193	42.212	3624	1322600	0.031	626	194	43.664	3228
1890700	0.029	584	197	39.293	2973	268400	0.033	654	193	42.349	3383	1530170	0.029	587	195	43.996	3017
2180700	0.027	545	197	39.833	2766	327400	0.030	606	193	43.029	3141	1652400	0.027	545	195	43.959	2802
2372700	0.025	500	198	38.931	2529	351400	0.028	559	193	44.140	2889	1694390	0.025	505	195	44.903	2584
2515700	0.023	465	199	40.578	2340	363400	0.026	516	193	43.708	2676	1736040	0.023	461	195	42.986	2369
2631700	0.021	423	199	40.815	2124	370400	0.023	466	193	43.915	2412	1801150	0.021	419	195	42.462	2155
2730700	0.019	383	201	39.693	1912	375400	0.021	423	193	44.163	2187	1876290	0.019	379	196	46.393	1940
2780700	0.017	343	202	40.309	1702	378400	0.019	376	193	43.077	1945	1926610	0.017	335	194	48.076	1724
2816700	0.015	300	202	39.342	1486	380400	0.016	335	194	45.025	1729	1953640	0.014	293	195	44.581	1507
2848700	0.013	261	204	39.933	1278	383400	0.014	282	193	41.969	1458	1977440	0.012	253	194	37.371	1299
2879700	0.010	218	205	38.787	1062	386400	0.011	234	194	41.282	1208	2025890	0.010	209	194	35.310	1076
2912700	0.008	175	206	39.303	849	388400	0.009	196	194	36.419	1013	2064990	0.008	174	195	34.087	894
2961700	0.006	133	208	32.755	637	401400	0.006	139	193	33.247	717	2124490	0.006	126	196	32.620	647

Table B- 28: 2PB data for HRA-L samples.

ID	HRA-L-1					ID	HRA-L-2					ID	HRA-L-3				
No. Cycles	Load (kN)	εσ (KPa)	με	δ (°)	E (MPa)	No. Cycles	Load (kN)	εσ (KPa)	με	δ (°)	E (MPa)	No. Cycles	Load (kN)	εσ (KPa)	με	δ (°)	E (MPa)
100	0.049	971	179	43.496	5419	100	0.043	847	179	37.808	4728	100	0.040	789	190	39.673	4154
5100	0.045	879	180	44.806	4876	20100	0.039	777	181	42.150	4292	1100	0.038	751	191	40.358	3944
63100	0.042	836	181	47.194	4626	460100	0.037	735	182	42.434	4028	129100	0.036	716	192	42.694	3740
295100	0.040	787	182	48.736	4324	809100	0.035	694	183	44.063	3784	1393000	0.033	650	196	42.869	3322
661100	0.038	743	183	49.358	4066	1475100	0.033	658	186	42.756	3546	2087700	0.031	614	197	43.455	3115
1437100	0.035	700	185	49.088	3794	1659100	0.031	616	185	44.561	3321	2348400	0.029	576	198	45.388	2908
1694100	0.033	658	186	49.851	3542	2154100	0.029	575	187	43.343	3075	3246100	0.027	536	199	45.389	2697
2372100	0.031	621	191	48.355	3253	2257100	0.027	534	188	43.981	2845	3574100	0.025	500	199	43.167	2513
2619100	0.030	590	198	46.582	2984	2291100	0.024	489	188	44.106	2602	3696300	0.023	455	199	43.290	2283
2998100	0.027	545	201	45.913	2709	2319100	0.022	451	189	44.092	2379	3754000	0.021	417	200	43.723	2084
3156100	0.025	494	201	45.860	2453	2353100	0.020	402	189	44.704	2125	3772100	0.019	378	202	43.577	1873
3188100	0.022	437	201	44.440	2170	2382100	0.018	370	191	45.175	1939	3796300	0.017	339	202	43.925	1677
3217100	0.019	385	202	46.275	1908	2414100	0.016	319	193	41.817	1657	3813200	0.014	296	204	44.213	1454
3245100	0.016	331	201	47.179	1643	2447100	0.014	280	194	38.871	1445	3831400	0.013	261	205	42.162	1274
3295100	0.013	272	202	48.542	1350	2513100	0.011	232	195	33.368	1190	3850700	0.010	217	206	41.480	1053
3325100	0.011	227	202	36.719	1124	2582100	0.009	194	197	31.369	985	3868900	0.008	180	207	41.246	871
3358100	0.008	169	202	31.869	838	2634100	0.007	156	198	27.441	790	3900400	0.006	134	209	40.818	641
												3971000	0.004	94	210	36.538	447

Appendix C

Appendix C-1: MATlab code for identifying Bouc-Wen parameters

Main MATlab code for identifying and solving Bouc-Wen model.

```
clear all
close all
%-----------------------------------------------
DATA=xlsread('NF.xlsx',1);% NF is the name of excel file
C1=DATA(:,1);% SHEAR STRESS VALUES z.
C2=DATA(:,2);%SHEAR STRAIN VALUES u.
C3=DATA (:,3);% dt = THE INTERVELS BETWEEN THE POINTS ON THE LOOPS
C4=DATA(:,4);%COMULATIVE TIME IN SEC.
C5=DATA(:,5);%U dot
C6=DATA (:,6);% COMULATIVE ENERGY WITHOUT (1-a)Ki.
C7=DATA(:,7);% ENERGY WITHOUT (1-a)Ki; = STRESS X dt X U dot
Zdot=zeros(length(C1),1); % Z dot1
dy=diff(C1);
dx=diff(C4);
Zdot(1:end-1)=(1/dx(1)).*dy;
Zdot(end)=Zdot(end-1);
for m=1:1:32;
    Ks(m,1)=C1(m,1);
    Ks(m,2)=C1(((length(C1)-32)+m),1);
    Ks(m,3)=C2(m,1);
    Ks(m,4)=C2(((length(C2)-32)+m),1);
end;
Ki=(max(Ks(:,1)))/(max(Ks(:,3)))
Ky=(max(Ks(:,2)))/(max(Ks(:,4)))
alpha=Ky/Ki;% (a)= ALPHA
En = (1-alpha).*Ki.*C6; % ENERGY WITH (1-a)Ki
%-------------------------------------------------------------------------
% Optimization (Identification)approach ------------------------------
%-------------------------------------------------------------------------
x00 = [1 1 1 1 1 1 1] % Starting guess
options = optimoptions('lsqnonlin','MaxFunEvals',6000);%Option to
display output
[xx,resnorm]= lsqnonlin(@(x)
newfundagrstre(x,Zdot,C1,C5,En),x00,options)%Invoke optimizer
% BOUC-WEN PARAMETERS: Alpha, Bita, Gamma, n, dalta_A, dalta_mew AND
Alpha_ID = xx(1);
Bita_ID = xx(2);
Gamma_ID = xx(3);
n_ID = xx(4);
dalta_A=xx(5);
dalta_mew=xx(6);
dalta_v=xx(7);
%-------------------------------------------------------------------------
%SOLUTION OF BOUC-WEN MODEL (DIFFERENTIAL EQUATION)
%-------------------------------------------------------------------------
```

```
Ti=C4(1,1);
tspan= [Ti DATA(end,4)];
x0=C1(1,1);
[t1,response] = ode45(@(t,x)
hystdagrestre1(t,x,Alpha_ID,Bita_ID,Gamma_ID,n_ID,dalta_A,dalta_mew,dal
ta_v,C4,C5,C6,Ki,alpha),tspan,x0);
response_C4=interp1(t1,response,C4,'linear');
subplot (2,1,1)
plot(C4,C1,'-',C4,response_C4,'--');% SHEAR STRESS vs TIME

subplot (2,1,2)
plot(C2,response_C4,'-',C2,C1,'-');% SHEAR STRAIN vs SHEAR STRESS
(hysteresis loops)
```

MATlab code for identifying Bouc-Wen model parameters.

```
function R = newfundagrstre(x,Zdot,C1,C5,En)


R=zeros(length(Zdot),1);
for i=1:length(Zdot);
R(i)=Zdot(i)-
(x(1).*C5(i)/(1+(x(6).*En(i))))+(x(5).*C5(i)*En(i)/(1+(x(6).*En(i))))+x(7)...
*En(i)*C5(i)*(x(2).*(abs(C5(i))/C5(i))*(abs(C1(i))^(x(4)-1))*C1(i)+x(3)...
*(abs(C1(i)))^x(4))/(1+(x(6).*En(i)))+C5(i)*(x(2).*(abs(C5(i))/C5(i))...
*(abs(C1(i))^(x(4)-1))*C1(i)+x(3).*(abs(C1(i)))^x(4))/(1+(x(6).*En(i)));
end
```

MATlab code for solving the differential equation of Bouc-Wen model

```
function x_dot=
hystdagrestre1(t,x,Alpha_ID,Bita_ID,Gamma_ID,n_ID,dalta_A,dalta_mew,

dalta_v,C4,C5,C6,Ki,alpha)
x_dot= zeros(1,1);


x_dot(1)=(Alpha_ID.*interp1(C4,C5,t,'linear')/(1+(dalta_mew.*((1-alpha)...
*Ki.*interp1(C4,C6,t,'linear')))))-((dalta_A.*interp1(C4,C5,t,'linear')...
*((1-alpha).*Ki.*interp1(C4,C6,t,'linear')))/(1+(dalta_mew.*((1-alpha)....
*Ki.*interp1(C4,C6,t,'linear')))))-((dalta_v.*interp1(C4,C5,t,'linear')...
*((1-alpha).*Ki.*interp1(C4,C6,t,'linear')))/(1+(dalta_mew.*((1-alpha)...
*Ki.*interp1(C4,C6,t,'linear')))))*((Bita_ID.*(abs(interp1(C4,C5,t,'linear'))...
/interp1(C4,C5,t,'linear'))*x(1)*((abs(x(1)))^(n_ID -1))+
Gamma_ID.*(abs(x(1)))...
^(n_ID))))-(interp1(C4,C5,t,'linear')/(1+(dalta_mew.*((1-alpha).*Ki...
*interp1(C4,C6,t,'linear')))))*((Bita_ID.*(abs(interp1(C4,C5,t,'linear'))...
```

```
13      /interp1(C4,C5,t,'linear'))*x(1)*((abs(x(1)))^(n_ID -1))+
        Gamma_ID.*(abs(x(1)).^(n_ID))));
14      end
```

Appendix C-3: ANN MATLAB code for predicting fatigue performance

```
1       % Note: open file for input and output
2       for m=1:1:3000% Make an iteration until arrive to the target of (R-sequ.)
3       % Solve an Input-Output Fitting problem with a Neural Network
4       % This script assumes these variables are defined:
5       %   Input - input data.
6       %   Output - target data.
7
8       inputs = Input;
9       targets = Output;
10
11      % Create a Fitting Network
12      hiddenLayerSize =[15 15];% number of hidden layers=========================
13      net = fitnet(hiddenLayerSize);
14      % Choose Input and Output Pre/Post-Processing Functions
15      net.inputs{1}.processFcns = {'removeconstantrows','mapminmax'};
16      net.outputs{2}.processFcns = {'removeconstantrows','mapminmax'};
17      % Setup Division of Data for Training, Validation, Testing
18      % For a list of all data division functions type: help nndivide
19      net.divideFcn = 'dividerand';  % Divide data randomly
20      net.divideMode = 'sample';  % Divide up every sample
21      net.divideParam.trainRatio = 70/100;% training data
22      net.divideParam.valRatio = 15/100; % validation data
23      net.divideParam.testRatio =15/100;% testing data
24      % For help on training function 'trainlm' type: help trainlm
25      % For a list of all training functions type: help nntrain
26      net.trainFcn = 'trainlm';  % for training Levenberg-Marquardt was used
27      % Choose a Performance Function
28      % For a list of all performance functions type: help nnperformance
29      net.performFcn = 'mse';  % Mean squared error
30      % Choose Plot Functions
```

```
% For a list of all plot functions type: help nnplot
net.plotFcns = {'plotperform','plottrainstate','ploterrhist','plotregression', 'plotfit'};

% Train the Network;
[net,tr] = train(net,inputs,targets);

% Test the Network;
outputs = net(inputs);
errors = gsubtract(targets,outputs);
performance = perform(net,targets,outputs);
% Recalculate Training, Validation and Test Performance
trainTargets = targets;% .* tr.trainMask{1};
valTargets = targets;%  .* tr.valMask{1};
testTargets = targets .* tr.testMask{1};
trainPerformance = perform(net,trainTargets,outputs);
valPerformance = perform(net,valTargets,outputs);
testPerformance = perform(net,testTargets,outputs);

%View the Network
%view(net); Note: remove (%) for viewing the network

wb = formwb(net,net.b,net.iw,net.lw);%net.b= baise, net.IW= input weight, net.LW= layer weight.
[b,iw,lw] = separatewb(net,wb);%net.b= baise, net.IW= input weight, net.LW= layer weight.
if regression(targets,outputs)>0.95;% the target of R-square is 0.95
  break;
end
R(m,1)=regression(targets,outputs);
m;
end
% Plots
% Uncomment these lines to enable various plots;
figure, plotperform(tr);
figure, plottrainstate(tr);
figure, plotfit(net,inputs,targets);
```

```
figure, plotregression(targets,outputs);
figure, ploterrhist(errors);
plot (outputs,targets,'o');
performance = perform(net,targets,outputs)
Rs=regression(targets,outputs)
MAX=max(R(:,1))
%-------------------------------------------------------------------------
for I=1:1:length(Input);
DATA(I,1)=Output(1,I);%experimental values
DATA(I,2)=outputs(1,I);%modelled values
end
```

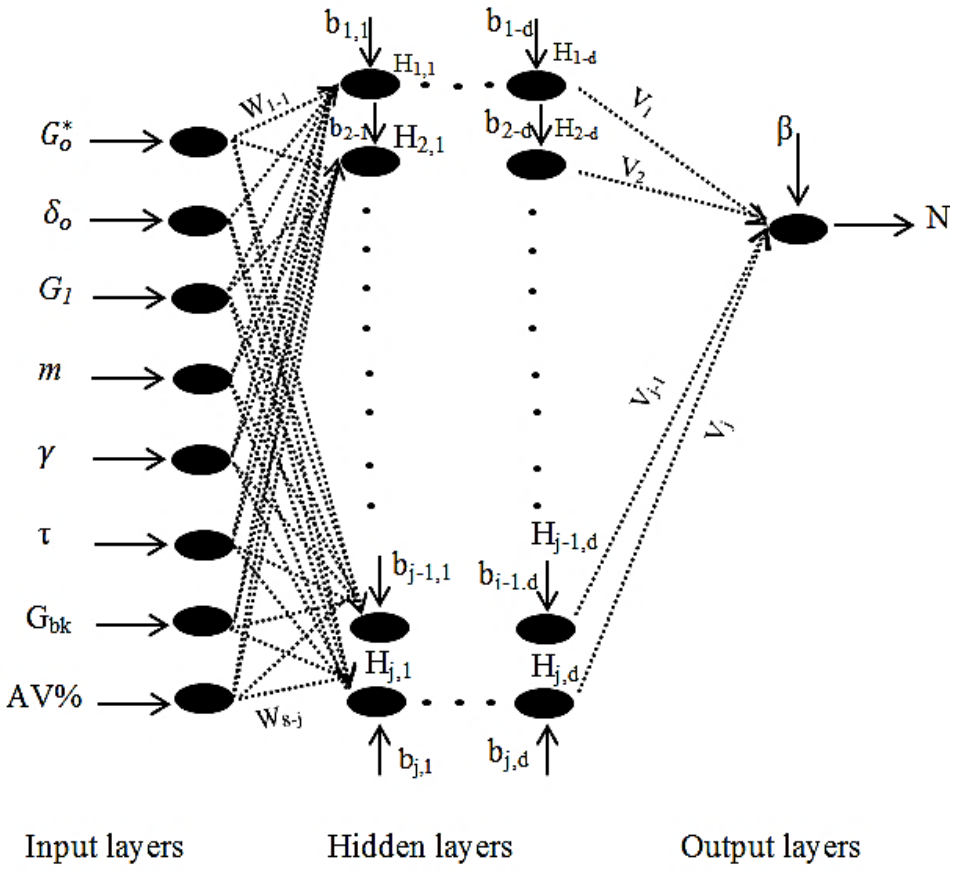

Figure C– 1: Typical architecture of ANN.

Table C– 1: Coefficients of ANN-model for N_f in strain test mode.

Weights of neuron in Input layer							Hidden layers		Weights of neuron in hidden layers													output layers	
G_o^*	δ_o	G_1	m	G_{bulk}	AV%	τ_0	$b_{1\text{-}i}$	$b_{2\text{-}i}$	$H_{1\text{-}i}$	$H_{2\text{-}i}$	$H_{3\text{-}i}$	$H_{4\text{-}i}$	$H_{5\text{-}i}$	$H_{6\text{-}i}$	$H_{7\text{-}i}$	$H_{8\text{-}i}$	$H_{9\text{-}i}$	$H_{10\text{-}i}$	$H_{11\text{-}i}$	$H_{12\text{-}i}$	$H_{13\text{-}i}$	$H_{14\text{-}i}$	$H_{15\text{-}i}$	Weights V_i	Bias (β)
$w_{1\text{-}i}$	$w_{2\text{-}i}$	$w_{3\text{-}i}$	$w_{4\text{-}i}$	$w_{5\text{-}i}$	$w_{6\text{-}i}$	$w_{7\text{-}i}$																			
-0.474	0.688	2.056	1.305	0.914	0.705	-0.450	1.364	-1.728	0.661	-0.051	0.439	-0.133	1.192	0.546	0.686	1.048	-0.072	0.165	-0.007	-0.146	0.379	1.301	0.777	1.149	-0.515
1.004	-1.000	-0.934	-0.378	0.633	0.319	-0.210	-2.752	-1.819	0.051	0.492	0.135	-0.244	0.712	0.684	0.195	0.261	-0.360	-0.001	-0.206	0.081	-0.719	-0.411	-1.152	0.303	–
0.702	-0.626	0.024	-0.244	-0.954	0.196	-1.517	-1.850	1.270	-0.239	-0.264	0.808	-0.828	-0.265	0.496	-0.709	1.121	0.046	0.409	-1.981	1.100	1.197	-0.302	0.115	1.561	–
0.504	0.500	-0.182	1.271	-0.157	1.224	-1.182	-0.929	1.231	-0.523	0.325	-0.357	-1.076	0.194	0.873	-1.230	0.202	1.206	0.338	1.547	0.825	1.108	0.058	-0.131	-0.763	–
0.188	-1.101	1.479	-0.470	-0.690	0.914	1.179	-0.058	0.689	-0.666	-0.359	0.618	-0.515	-0.410	0.774	0.421	0.072	-0.546	0.292	0.769	0.061	-0.599	-0.776	0.401	0.779	–
0.966	-1.713	-0.547	0.553	-0.216	-0.970	0.641	-0.619	-0.017	0.579	-0.057	-0.775	-0.955	-0.141	-0.676	0.542	-1.185	0.658	-0.183	-0.514	-1.015	1.030	0.017	0.163	0.387	–
-0.390	0.761	-0.369	1.168	-0.020	-0.009	-2.655	0.930	0.229	-1.224	-0.574	0.247	-0.639	0.529	-0.531	-1.113	-0.665	0.411	-0.510	1.341	-0.085	0.588	-0.209	-1.234	-0.666	–
0.704	-0.626	0.370	-1.152	-0.934	0.395	0.143	0.115	-0.583	-0.344	0.980	1.089	0.586	0.270	1.233	-0.332	-0.771	-0.111	-0.466	0.865	-0.108	-0.833	0.833	-0.796	-0.237	–
-1.076	0.481	-0.665	-1.319	-0.412	0.148	0.965	-0.101	0.245	-0.143	-0.559	-0.266	0.611	0.281	-0.775	-0.470	0.193	1.100	-0.128	-0.289	-0.418	-0.604	-0.976	0.500	0.961	–
0.218	-1.458	-0.270	0.587	0.429	1.023	-0.089	-1.128	0.630	0.309	-0.731	-0.309	-0.473	0.742	1.265	-0.775	-0.064	-0.941	0.140	-0.375	0.128	0.602	0.436	-0.174	-0.924	–
0.730	1.887	1.255	-0.828	0.757	0.909	0.955	0.789	-0.762	-0.343	0.392	0.393	0.380	-0.137	0.583	0.583	-0.501	0.021	1.260	-0.689	-0.613	-0.607	0.380	0.067	-0.509	–
-0.191	-1.663	-1.235	-0.968	0.517	-0.852	1.365	-0.227	1.964	0.934	-1.095	-0.370	-0.619	0.162	-0.654	-0.317	-0.222	0.457	-0.527	-0.486	0.831	-0.194	-0.406	1.221	0.317	–
0.453	0.738	-1.654	0.966	0.002	0.650	1.902	0.706	-1.354	0.937	0.313	-0.174	-0.139	-0.490	0.298	0.341	-0.701	-0.454	0.658	1.154	-0.884	-0.670	-0.644	-0.624	1.331	–
-0.457	0.471	0.432	2.717	0.676	0.937	1.181	1.357	1.459	0.393	-0.379	-0.119	-0.656	-0.627	-0.515	-0.361	-0.337	0.356	-0.642	0.268	-0.403	-0.511	-0.075	0.471	0.093	–
1.034	0.317	-1.093	0.363	1.266	-1.011	0.669	1.590	1.723	0.619	0.366	-0.240	-0.673	-0.470	-0.427	-0.559	-0.088	0.249	-0.579	0.067	-0.253	-0.161	0.642	0.447	0.377	–

Table C– 2: Coefficients of ANN-model for N1 in strain test mode.

Weights of neuron in Input layer							Hidden layers		Weights of neuron in hidden layers													output layers	
G_o^*	δ_o	G_1	m	G_{bulk}	AV%	τ_0	$b_{1\text{-}i}$	$b_{2\text{-}i}$	$H_{1\text{-}i}$	$H_{2\text{-}i}$	$H_{3\text{-}i}$	$H_{4\text{-}i}$	$H_{5\text{-}i}$	$H_{6\text{-}i}$	$H_{7\text{-}i}$	$H_{8\text{-}i}$	$H_{9\text{-}i}$	$H_{10\text{-}i}$	$H_{11\text{-}i}$	$H_{12\text{-}i}$	$H_{13\text{-}i}$	$H_{14\text{-}i}$	$H_{15\text{-}i}$	Weights V_i	Bias (β)
$w_{1\text{-}i}$	$w_{2\text{-}i}$	$w_{3\text{-}i}$	$w_{4\text{-}i}$	$w_{5\text{-}i}$	$w_{6\text{-}i}$	$w_{7\text{-}i}$																			
-1.318	0.963	-0.424	0.453	0.069	-0.437	-0.522	2.228	-1.163	0.816	0.658	0.478	-0.858	-0.050	-0.433	-0.662	0.638	0.275	-0.272	0.060	-0.461	-1.239	1.022	0.724	-1.033	-0.072
-0.510	-0.577	-1.052	0.811	-1.190	-0.622	0.812	1.420	-1.286	0.449	0.296	-0.824	-0.040	-0.481	-0.678	-0.549	0.261	0.596	0.522	-0.347	0.036	0.996	0.516	-0.312	0.801	–
-0.661	0.317	-0.867	-0.772	-1.109	0.378	0.508	1.902	0.994	-0.746	0.374	0.177	-0.814	-0.729	0.289	0.338	0.669	0.123	-0.387	0.265	-0.057	0.537	-0.327	-0.667	0.159	–
-0.063	1.477	0.227	0.095	2.355	-1.546	-2.115	-1.320	-0.866	0.450	0.745	0.758	1.059	-0.484	-0.272	-0.096	-1.097	-0.157	-0.353	-0.441	-1.316	0.309	-0.030	0.503	1.130	–
-0.912	0.855	-1.497	-0.301	1.104	0.942	-0.246	0.689	1.315	0.281	1.191	0.342	1.183	-0.070	0.193	0.183	-1.113	0.045	-0.418	-0.053	-0.985	-0.123	0.737	0.581	0.872	–
-0.744	1.211	-0.131	0.887	-0.196	1.682	2.187	0.738	-0.187	0.751	0.175	0.502	-0.524	0.393	-0.946	-0.740	-0.858	0.439	-1.218	1.149	0.629	0.153	0.693	0.126	0.846	–
-0.119	-0.634	-1.938	-1.119	-1.080	-0.867	-0.297	1.455	0.062	0.267	-0.194	-0.667	0.546	0.367	0.467	-0.371	0.208	-0.127	-1.004	-0.692	-0.495	-0.733	-0.017	-0.165	1.498	–
1.549	-0.888	2.060	0.581	1.447	-1.592	0.553	-0.220	-0.178	-0.341	-0.853	-0.502	0.728	0.091	2.059	-0.009	-1.453	-2.811	-0.285	-1.147	0.784	-0.490	0.577	0.040	-2.108	–
-1.605	-2.744	-0.157	1.499	-0.828	-1.219	-1.896	0.219	0.494	0.651	-0.074	0.520	-0.259	0.954	-0.589	0.714	-0.862	-0.019	-0.275	-0.655	-1.244	-0.180	0.263	0.996	-0.720	–
-0.819	-0.194	-0.686	1.341	-2.673	0.588	0.947	-0.669	0.660	0.495	-0.315	0.328	0.157	-0.263	-0.393	-0.065	-0.587	-0.221	-0.837	-0.541	0.415	-0.104	0.318	-0.623	0.222	–
1.264	-0.983	0.200	0.594	-2.386	-0.852	0.783	0.204	1.301	0.817	0.134	-0.471	0.975	0.344	-0.988	-0.852	-0.748	0.110	0.192	0.210	-0.265	0.543	0.019	0.552	-0.478	–
0.999	0.812	0.223	0.247	2.968	-0.181	-1.017	1.524	-1.164	-0.322	-0.851	-0.505	-0.569	-0.668	0.279	-0.137	-0.624	0.383	-0.336	0.007	-0.280	-0.294	-0.098	-0.513	0.175	–
-1.034	1.030	0.840	0.231	-1.487	-0.197	-1.769	-1.112	1.258	1.169	-0.507	-0.526	-2.570	-0.107	-0.645	4.271	-1.056	0.026	1.211	-0.602	-1.633	-0.863	-0.311	-0.641	2.058	–
0.516	-0.071	-1.197	-0.743	1.197	-0.532	-1.275	1.658	1.431	0.074	0.481	0.403	0.046	-1.054	-0.707	0.276	-0.634	-0.536	0.292	0.102	-0.817	-1.136	0.525	0.249	-1.369	–
-0.330	1.603	-0.462	-1.490	0.410	-0.885	-0.385	2.052	-1.665	-0.464	0.552	0.312	-1.307	-0.153	-0.810	0.484	-0.538	1.180	0.625	0.188	-0.452	0.429	0.284	-0.638	0.827	–

Table C– 3: Coefficients of ANN-model for FI^R in strain test mode.

Weights of neuron in Input layer							Hidden layers		Weights of neuron in hidden layers														output layers	
G_o^*	δ_o	G_1	m	G_{bulk}	AV%	τ_0	$b_{1\text{-}i}$	$b_{2\text{-}i}$	$H_{1\text{-}i}$	$H_{2\text{-}i}$	$H_{3\text{-}i}$	$H_{4\text{-}i}$	$H_{5\text{-}i}$	$H_{6\text{-}i}$	$H_{7\text{-}i}$	$H_{8\text{-}i}$	$H_{9\text{-}i}$	$H_{10\text{-}i}$	$H_{11\text{-}i}$	$H_{12\text{-}i}$	$H_{13\text{-}i}$	$H_{14\text{-}i}$	$H_{15\text{-}i}$	Weights V_i	Bias (β)
$w_{1\text{-}i}$	$w_{2\text{-}i}$	$w_{3\text{-}i}$	$w_{4\text{-}i}$	$w_{5\text{-}i}$	$w_{6\text{-}i}$	$w_{7\text{-}i}$																		
1.147	-0.068	0.245	0.804	-1.460	-0.331	0.507	-1.939	1.572	-0.060	-0.496	-0.268	-0.691	-0.421	0.266	1.168	-0.281	0.316	-0.466	-0.588	-1.223	0.139	-0.345	-0.866	1.331	0.414
-1.120	-1.099	0.825	0.723	-0.285	-0.131	-0.594	1.739	1.473	-0.427	0.348	0.348	-0.475	0.607	0.065	0.674	0.211	0.488	-0.539	0.183	-0.506	-0.313	0.238	0.254	-0.059	–
0.591	0.954	0.963	0.000	-0.387	-1.346	-0.789	-1.492	1.216	-0.611	0.180	-0.469	-0.889	-0.119	-0.307	0.732	-0.222	-0.620	0.031	0.281	0.249	0.087	0.331	0.196	-1.030	–
0.696	-0.702	0.385	1.166	-1.203	-0.359	-1.064	-0.858	-0.864	0.617	-0.213	-0.642	0.152	-0.507	0.139	0.744	0.358	0.613	-0.401	0.083	-0.152	-0.097	-0.581	0.657	-0.687	–
1.096	0.343	-1.078	0.325	0.134	-0.858	1.016	-1.139	-0.590	-0.153	0.106	0.041	-0.703	-0.965	-0.827	-0.500	-0.048	-0.362	0.487	-0.213	-0.346	-0.531	-0.656	0.481	-0.976	–
0.850	-0.949	0.128	0.768	0.835	-1.025	0.629	-0.470	0.318	-0.216	0.442	-0.391	-0.123	0.327	-0.516	0.540	-1.189	0.071	-0.472	-0.179	-0.479	0.815	-0.526	0.653	0.914	–
-0.280	-0.440	0.790	-1.124	-0.766	-1.394	0.584	0.332	0.158	-0.404	-0.374	0.039	0.089	0.738	0.198	0.156	0.689	0.941	0.072	0.394	0.498	0.684	-0.672	0.177	-0.641	–
-0.951	-1.067	-0.684	-1.241	0.818	-0.391	0.887	0.037	-0.107	0.380	0.537	0.098	0.516	0.240	0.497	0.501	0.506	-0.510	0.235	0.451	0.314	0.521	0.074	0.576	0.062	–
0.726	-1.455	-0.160	-1.133	0.807	-1.061	-0.312	0.367	0.201	0.765	0.140	-0.500	0.006	0.003	-0.701	-0.909	0.709	0.565	0.802	0.383	0.395	0.527	-0.164	0.419	1.142	–
-1.297	-0.741	-0.611	0.901	-0.198	0.716	-0.662	-0.810	-0.555	-0.623	0.038	0.199	-0.497	-0.385	-0.087	-0.555	0.639	-0.683	0.002	0.320	0.856	0.567	0.080	-0.005	0.448	–
-0.041	1.240	-0.113	-1.218	-0.571	-0.345	0.967	1.024	0.693	0.470	-0.152	-0.505	-0.032	0.065	-0.579	-0.307	0.060	0.054	-0.537	0.031	0.613	0.342	-1.016	0.305	0.268	–
-0.295	0.864	0.976	-0.669	1.358	1.155	-0.246	-1.370	0.733	0.860	0.023	-0.238	0.234	-0.083	0.128	-0.388	0.354	-0.053	-0.400	-1.022	-0.030	-0.343	-0.917	0.358	0.754	–
-0.706	-0.481	1.316	-0.257	-0.661	-0.998	-0.049	-1.633	1.155	0.427	-0.366	0.139	-0.420	0.211	-0.321	0.464	-0.649	-0.432	-0.357	-0.203	-0.503	0.710	0.371	-0.640	0.145	–
0.531	1.141	-0.770	1.225	-0.363	0.644	0.606	1.660	1.537	0.545	0.598	-0.029	0.660	0.005	-0.494	0.029	0.196	0.325	-0.290	0.698	0.193	-0.399	-0.534	-0.351	-0.860	–
0.211	-0.793	0.806	1.144	1.176	-1.135	-0.552	1.968	1.686	0.432	-0.260	0.425	0.899	0.491	-0.258	-0.209	0.054	-0.488	-0.253	-0.414	0.588	0.515	0.086	0.755	-1.020	–

Table C– 4: Coefficients of ANN-model for N_f in stress test mode.

Weights of neuron in Input layer							Hidden layers		Weights of neuron in hidden layers														output layers	
G_o^*	δ_o	G_1	m	G_{bulk}	AV%	γ_0	$b_{1\text{-}i}$	$b_{2\text{-}i}$	$H_{1\text{-}i}$	$H_{2\text{-}i}$	$H_{3\text{-}i}$	$H_{4\text{-}i}$	$H_{5\text{-}i}$	$H_{6\text{-}i}$	$H_{7\text{-}i}$	$H_{8\text{-}i}$	$H_{9\text{-}i}$	$H_{10\text{-}i}$	$H_{11\text{-}i}$	$H_{12\text{-}i}$	$H_{13\text{-}i}$	$H_{14\text{-}i}$	$H_{15\text{-}i}$	Weights V_i	Bias (β)
$w_{1\text{-}i}$	$w_{2\text{-}i}$	$w_{3\text{-}i}$	$w_{4\text{-}i}$	$w_{5\text{-}i}$	$w_{6\text{-}i}$	$w_{7\text{-}i}$																		
-0.581	-2.926	-0.240	2.563	0.954	-1.677	1.681	0.653	2.426	-0.584	0.330	-0.731	-0.205	0.713	0.027	0.089	0.479	0.210	0.139	-0.059	-0.654	-0.076	0.372	-0.938	-0.01787	-0.101
0.161	1.986	-1.249	-1.649	1.173	0.584	1.834	0.601	0.731	-1.242	-1.264	0.968	-0.274	-0.569	-0.215	-0.205	-0.457	-0.321	-0.694	-0.433	-1.494	-0.669	-0.517	-0.098	1.296537	–
0.256	0.596	0.680	0.263	0.767	1.572	0.940	-1.673	0.655	-0.398	-1.714	0.250	0.486	-0.625	0.311	1.855	-0.310	0.087	0.265	0.809	-1.581	-0.626	-1.235	0.841	-1.34744	–
-0.691	-1.874	1.858	-0.738	1.889	-3.386	1.196	-2.246	-1.489	0.347	-0.006	0.388	-0.145	-0.541	-0.794	0.682	-1.224	0.450	0.384	-0.345	-0.247	0.101	-0.865	0.273	-0.65381	–
0.627	-0.613	0.205	-0.391	-1.543	-1.048	-0.640	2.229	-0.944	0.245	0.826	0.784	-0.916	-1.145	0.328	-0.155	-0.111	0.545	-0.130	-0.324	-0.348	-0.256	0.143	-0.197	0.466614	–
0.835	-2.144	-0.216	-3.980	-0.059	-0.597	-1.266	1.366	-0.088	-0.521	0.506	-0.355	3.063	0.121	-0.878	0.028	0.830	0.026	-1.396	1.190	0.193	0.179	-0.216	-0.024	1.010419	–
-0.022	3.344	6.766	1.562	-0.241	-0.382	-0.623	1.042	-0.848	0.825	-0.205	0.733	-1.366	-1.173	-0.494	0.525	-0.558	1.189	-1.110	-0.083	0.093	-0.779	-0.180	0.162	-1.45125	–
0.342	-0.121	-1.672	-0.872	-1.089	0.081	-1.783	0.737	-0.908	-1.537	0.183	0.560	-0.675	-0.457	-1.193	2.866	0.236	-0.501	0.717	-0.202	0.006	-0.458	-0.435	0.224	-0.63403	–
-0.171	2.125	1.938	1.396	1.874	-0.285	1.085	-1.948	0.670	2.155	1.529	-0.375	2.064	0.760	-2.101	-1.810	0.220	0.394	-1.817	-1.102	-0.551	0.452	0.356	-0.321	-1.92963	–
-1.000	-1.566	-0.671	1.104	2.676	-4.962	0.567	0.908	0.806	0.615	0.406	-0.301	-0.411	0.060	-0.109	-0.483	0.007	-0.197	-0.348	0.865	0.471	0.618	0.913	0.010	-0.32761	–
-0.276	-0.417	0.279	-3.263	-0.476	-0.739	-0.479	2.296	-1.001	0.321	-0.119	-0.008	0.039	0.395	-0.825	0.961	-0.680	-0.095	-0.234	-0.372	-0.146	0.265	-0.880	0.711	0.398837	–
-0.550	0.168	-0.877	-0.416	0.728	0.527	-1.304	0.099	-1.158	-2.528	0.605	0.031	1.299	0.636	-0.056	1.249	-0.291	-2.064	-0.672	0.683	0.629	-0.014	0.407	0.358	-1.00252	–
0.315	0.110	-0.623	-0.927	-0.494	-1.026	-0.518	2.729	-1.271	0.168	-0.257	0.737	-0.184	-0.512	-0.207	0.882	-0.315	0.663	-0.666	0.308	0.098	-0.603	0.435	-0.230	0.544767	–
1.094	0.839	-0.551	0.028	-0.180	-0.499	-1.367	1.883	1.292	-0.300	-0.222	-0.913	-0.099	1.435	0.036	0.147	0.214	-0.729	0.775	-0.917	0.512	-0.490	-0.672	0.782	0.059732	–
-0.487	0.569	1.035	0.582	0.740	0.921	0.865	-2.123	-1.366	-0.438	-0.101	-0.503	0.615	0.381	0.383	-1.142	0.328	0.247	-0.052	-0.053	1.152	0.915	0.010	-0.937	-2.002	–

Table C– 5: Coefficients of ANN-model for N1 in stress test mode.

Weights of neuron in Input layer							Hidden layers		Weights of neuron in hidden layers													output layers	
G_o^*	δ_o	G_1	m	G_{bulk}	AV%	γ_0	$b_{1\text{-}i}$	$b_{2\text{-}i}$	$H_{1\text{-}i}$	$H_{2\text{-}i}$	$H_{3\text{-}i}$	$H_{4\text{-}i}$	$H_{5\text{-}i}$	$H_{6\text{-}i}$	$H_{7\text{-}i}$	$H_{8\text{-}i}$	$H_{9\text{-}i}$	$H_{10\text{-}i}$	$H_{11\text{-}i}$	$H_{12\text{-}i}$	$H_{13\text{-}i}$	$H_{14\text{-}i}$	$H_{15\text{-}i}$	Weights V_i	Bias (β)
$w_{1\text{-}i}$	$w_{2\text{-}i}$	$w_{3\text{-}i}$	$w_{4\text{-}i}$	$w_{5\text{-}i}$	$w_{6\text{-}i}$	$w_{7\text{-}i}$																			
0.255	0.985	-0.949	0.699	0.932	-1.104	-0.291	-1.980	1.755	-0.354	-0.045	0.252	-1.000	0.589	-0.467	0.264	0.080	-0.182	-0.632	1.014	0.737	0.089	-0.569	0.583	1.066194	-0.563
0.334	-1.474	-0.997	-0.551	-0.433	-1.158	-0.938	-1.856	-1.427	0.566	-0.716	-0.100	-0.459	0.496	0.129	0.568	-0.344	-0.468	0.127	-0.279	-0.094	0.700	0.401	0.613	1.20295	–
0.144	-1.891	-0.044	0.184	-0.423	0.795	-0.734	-1.436	-1.327	0.540	-0.630	0.461	-0.281	-0.376	-0.080	-0.631	0.324	-0.023	-0.564	0.493	-0.199	-0.310	-0.438	0.480	0.919263	–
0.020	0.295	-1.831	0.391	-1.121	0.291	1.399	0.993	1.040	-0.767	-0.085	-0.307	0.407	0.162	-0.802	-0.363	-0.085	0.921	-0.041	0.094	-0.046	-0.191	-0.319	0.024	-0.01166	–
0.240	1.259	-0.367	-1.105	0.919	0.642	0.372	-0.726	-0.716	0.506	-0.456	-0.646	0.413	0.029	-0.350	-0.289	0.031	-0.331	-0.010	0.579	0.338	-0.126	-0.337	0.815	-0.69512	–
-0.482	-1.123	0.285	1.801	-1.197	-0.881	0.650	0.524	0.515	-0.163	-0.178	-0.588	-0.419	-0.257	0.532	0.531	-0.333	0.473	0.298	0.042	-0.730	0.354	-0.641	0.284	-0.31994	–
0.293	1.069	0.138	-1.680	0.455	1.530	-0.752	-0.173	-0.183	0.663	0.705	-0.289	0.089	-0.203	0.316	0.087	-0.632	0.103	-0.668	0.095	0.597	-0.364	-0.213	-0.494	-0.25693	–
-0.096	1.121	1.527	0.350	0.649	-1.250	-0.361	-0.188	0.147	0.586	-0.471	0.465	-0.312	-0.235	-1.045	-0.694	-0.289	-0.079	0.520	-0.216	-0.722	-0.145	0.529	-0.531	-1.10067	–
0.853	-0.975	0.751	-0.913	-0.694	0.423	-0.758	0.202	-0.133	-0.415	0.570	-0.565	-0.460	-0.172	-0.426	-0.336	-0.558	0.463	0.392	0.302	-0.430	-0.667	-0.126	0.408	-0.69666	–
0.737	-1.098	0.281	-0.944	-0.384	-1.066	-0.435	0.410	0.581	0.621	-0.776	-0.259	-1.035	-0.016	-0.567	-0.209	0.347	-0.260	-0.422	0.611	1.116	0.027	-0.573	-0.536	-1.2103	–
-0.666	-0.975	1.252	-0.402	-0.187	-0.739	-0.918	-1.183	0.736	0.429	-0.395	-0.526	-0.339	0.176	-0.952	-0.701	-0.390	0.412	-0.087	0.022	0.193	0.540	-0.616	0.490	-0.9199	–
-0.156	-0.375	1.674	0.353	-0.083	1.617	-0.423	-0.969	-0.947	-0.268	-0.372	-0.272	-0.060	-0.680	0.114	-0.048	0.139	0.528	0.547	-0.115	-0.096	-0.073	-0.236	-0.482	0.444242	–
1.154	-0.604	0.048	0.798	0.989	-0.283	0.539	1.601	1.194	0.615	-0.301	-0.099	-0.028	-0.652	-0.805	1.130	-0.353	-0.494	-0.106	-0.490	-0.462	-0.171	0.161	-0.226	0.781762	–
-0.167	0.775	0.984	-0.137	0.141	-1.217	-0.917	-1.827	-1.543	0.040	-0.609	0.686	-0.684	-0.084	-0.658	-0.811	-1.058	0.370	0.738	0.262	0.001	-0.391	0.286	-0.267	-1.45204	–
-1.089	-0.588	-0.501	-0.763	0.592	0.635	-0.858	-2.078	1.672	0.494	-0.530	-0.739	-0.789	-0.631	1.096	-0.693	-0.280	0.062	-0.193	0.511	0.820	-0.037	0.633	-0.334	1.251408	–

Table C– 6: Coefficients of ANN-model for FI^R in stress test mode.

Weights of neuron in Input layer							Hidden layers		Weights of neuron in hidden layers													output layers	
G_o^*	δ_o	G_1	m	G_{bulk}	AV%	γ_0	$b_{1\text{-}i}$	$b_{2\text{-}i}$	$H_{1\text{-}i}$	$H_{2\text{-}i}$	$H_{3\text{-}i}$	$H_{4\text{-}i}$	$H_{5\text{-}i}$	$H_{6\text{-}i}$	$H_{7\text{-}i}$	$H_{8\text{-}i}$	$H_{9\text{-}i}$	$H_{10\text{-}i}$	$H_{11\text{-}i}$	$H_{12\text{-}i}$	$H_{13\text{-}i}$	$H_{14\text{-}i}$	$H_{15\text{-}i}$	Weights V_i	Bias (β)
$w_{1\text{-}i}$	$w_{2\text{-}i}$	$w_{3\text{-}i}$	$w_{4\text{-}i}$	$w_{5\text{-}i}$	$w_{6\text{-}i}$	$w_{7\text{-}i}$																			
0.556	0.882	-0.594	-0.906	-1.083	-0.042	0.959	-2.006	1.725	-0.565	-0.235	-0.536	0.281	0.380	-0.102	-0.704	-0.169	-0.521	-0.298	-0.331	-0.587	-0.477	0.409	-0.422	0.553241	0.431
-1.380	-0.687	1.082	0.689	0.410	-0.928	0.197	1.648	1.417	-0.462	-0.221	0.159	-0.569	-0.038	-0.391	0.549	-0.497	-0.222	0.662	-0.740	-0.452	0.574	0.142	-0.340	-0.35127	–
0.201	-0.987	1.071	0.850	-0.771	0.982	-0.380	-1.500	1.089	-0.369	0.936	-0.543	0.787	0.082	0.850	0.344	0.154	0.013	-0.420	-0.691	-0.677	0.654	0.280	0.241	1.071261	–
0.239	-0.255	0.400	1.221	0.701	0.587	1.249	-1.260	0.914	-0.610	0.234	-0.497	0.252	0.345	0.610	-0.310	0.617	0.505	0.460	0.721	0.176	-0.237	-0.017	0.325	0.459766	–
0.308	-1.265	-0.006	-1.164	0.508	0.653	0.564	-0.838	0.618	-0.374	-0.273	0.164	0.822	-0.810	-0.158	0.167	0.700	0.175	-0.177	-0.487	0.492	-0.525	-0.192	0.053	1.024775	–
-0.509	-1.109	1.600	-0.446	0.891	0.420	-0.693	0.378	-0.406	0.199	-0.633	0.103	-0.521	-0.702	-0.940	-0.254	-0.135	0.599	0.576	-0.682	0.126	-0.689	1.040	-0.372	-1.22614	–
1.220	-0.618	0.842	-0.941	0.531	1.008	-0.961	-0.339	-0.261	0.709	-0.109	-0.617	0.897	0.413	-0.041	-0.314	-0.134	-0.339	-0.301	0.417	-0.542	0.067	0.078	0.396	0.021793	–
-0.843	0.037	-0.935	0.598	1.276	0.732	-0.458	-0.245	0.164	0.038	0.002	-0.345	0.340	-0.434	0.514	-0.190	-0.125	-0.709	0.508	-0.398	0.678	0.255	0.668	0.577	-0.23626	–
-0.908	-0.417	0.044	-1.314	0.164	-0.953	1.179	-0.269	-0.134	-0.678	-0.330	-0.551	-0.114	-0.569	0.361	0.462	0.676	0.034	0.004	0.102	0.528	-0.696	-0.691	-0.381	-0.83465	–
1.142	0.821	-0.183	-0.218	0.868	-1.723	-0.101	0.516	0.541	0.292	0.551	0.440	-0.010	-0.546	-0.362	-1.077	0.617	0.399	-0.019	0.769	-0.681	0.396	0.482	-0.406	-1.27297	–
-1.332	-1.031	-0.805	0.104	-0.945	0.770	-0.238	-0.874	-0.826	-0.089	0.653	-0.330	0.162	0.456	0.382	-0.798	0.684	0.165	0.197	-0.359	0.057	-0.508	0.596	-0.431	0.604041	–
-0.479	0.140	-0.471	0.916	0.986	0.467	-1.219	-1.150	1.006	0.430	0.544	-0.493	-0.695	-0.038	0.669	0.392	0.265	0.484	0.393	-0.302	0.399	-0.101	-0.382	-0.376	-0.18497	–
-0.210	0.000	-0.870	0.433	-1.018	-0.928	1.129	-1.510	-1.236	-0.276	0.500	-0.862	0.210	0.234	0.194	-0.028	0.912	0.828	-0.658	-0.072	0.155	-0.576	0.234	0.484	1.001477	–
0.913	1.320	0.354	-0.603	-0.476	-1.176	0.939	1.457	1.438	0.628	0.379	-0.493	0.062	0.224	0.609	0.437	0.666	0.112	0.054	-0.188	0.031	-0.709	-0.552	0.411	-0.37502	–
-1.227	1.385	-0.495	0.100	1.144	0.225	0.543	-1.966	1.885	-0.016	0.553	-0.357	0.470	0.469	-0.106	0.853	-0.413	0.496	0.273	0.177	0.158	0.377	0.285	-0.264	-0.73336	–

Table C– 7: Coefficients of ANN-model for N_f @ 15% in independent test mode.

Weights of neuron in Input layer						Hidden layers		Weights of neuron in hidden layers														output layers	
G_o^*	δ_o	G_1	m	G_{bulk}	AV%	$b_{1\text{-}i}$	$b_{2\text{-}i}$	$H_{1\text{-}i}$	$H_{2\text{-}i}$	$H_{3\text{-}i}$	$H_{4\text{-}i}$	$H_{5\text{-}i}$	$H_{6\text{-}i}$	$H_{7\text{-}i}$	$H_{8\text{-}i}$	$H_{9\text{-}i}$	$H_{10\text{-}i}$	$H_{11\text{-}i}$	$H_{12\text{-}i}$	$H_{13\text{-}i}$	$H_{14\text{-}i}$	$H_{15\text{-}i}$	Weights V_i	Bias (β)
$w_{1\text{-}i}$	$w_{2\text{-}i}$	$w_{3\text{-}i}$	$w_{4\text{-}i}$	$w_{5\text{-}i}$	$w_{6\text{-}i}$																		
-0.548	1.585	0.763	-1.378	-0.270	-0.080	2.108	-1.230	0.738	0.417	-1.219	1.405	-0.364	1.125	-0.438	0.623	0.140	-0.342	0.888	-1.370	0.210	0.364	-0.463	0.912	-0.066
0.796	-0.985	1.962	0.549	-0.448	1.165	-1.597	-1.585	0.431	0.554	-0.021	-0.203	-0.419	-0.301	-0.087	1.244	0.005	1.303	0.105	0.235	0.063	-0.073	0.238	0.728	–
0.293	0.196	-0.477	-3.007	-1.105	1.615	-1.889	-1.079	0.465	0.596	-1.194	-0.055	1.643	0.472	0.149	-1.226	-1.603	0.376	-0.734	1.499	1.371	0.734	-0.323	2.385	–
0.081	1.552	-1.952	-2.024	-1.780	-0.272	-1.357	1.336	-0.433	0.193	-0.497	1.172	-1.060	-0.589	-0.458	-0.869	-1.678	0.133	0.050	-0.042	-0.775	0.008	-2.229	-1.412	–
-0.520	2.579	0.361	0.268	-2.840	0.785	-0.511	-0.483	0.215	0.322	1.421	1.364	0.920	0.247	0.662	0.315	0.977	-0.186	-0.423	-1.337	0.225	0.059	-1.188	-1.236	–
-0.646	-0.060	-0.948	0.928	0.881	-0.130	1.169	-0.151	0.692	-0.920	0.642	-0.302	-2.425	0.666	0.100	-0.511	0.624	-0.500	0.335	-0.001	-0.360	-0.199	0.160	1.273	–
-0.365	-0.962	-1.837	-0.514	1.024	1.012	0.049	0.117	-0.680	0.113	0.487	0.371	0.805	-0.152	-0.572	0.139	0.680	-0.049	0.336	0.605	0.371	-0.287	-0.310	0.170	–
-0.177	-0.435	-2.102	-1.882	-0.263	-1.092	0.528	0.496	0.623	0.442	0.091	-1.369	0.085	-0.249	-1.026	0.002	-0.630	-0.588	0.434	-0.591	-0.498	-0.136	0.145	-1.955	–
0.181	-1.150	-1.705	2.054	0.823	0.234	-0.879	-0.113	-0.292	0.530	-0.708	1.558	0.113	-0.054	-0.628	0.210	-0.605	-0.646	0.356	1.227	1.757	0.043	-0.424	-2.037	–
0.920	0.775	1.269	-0.504	0.504	1.734	-0.144	1.201	1.079	-0.950	-0.834	0.351	0.185	1.099	0.025	0.011	-0.328	-0.009	-0.654	1.177	1.353	0.715	0.135	-1.020	–
1.803	0.525	1.993	1.197	-1.476	0.367	1.050	0.686	0.781	-0.186	0.141	-0.416	-0.755	0.068	0.101	-0.459	-0.267	-0.408	0.752	0.470	-0.686	0.402	0.335	0.577	–
-0.884	0.016	1.773	-2.308	0.485	-0.360	-0.928	-1.183	-1.076	0.223	-0.846	0.036	-0.261	0.417	0.439	-0.026	0.967	-0.464	-0.018	-0.219	-0.530	-0.503	1.436	-0.948	–
-1.615	0.506	1.592	0.862	-0.133	-1.235	-0.504	1.243	0.174	-0.837	0.360	-0.780	-0.139	-0.038	1.193	-0.935	-0.227	0.347	0.535	0.245	-0.604	-0.236	-0.940	0.107	–
0.018	-1.232	-1.434	0.682	-0.458	-0.250	2.005	-1.450	-0.354	-0.043	0.516	0.528	-0.145	0.089	-0.046	-0.420	0.616	0.591	0.624	-0.283	0.352	0.644	-0.475	0.135	–
1.528	-0.832	1.206	-0.438	-2.995	0.691	2.394	1.937	0.108	0.117	0.148	-0.159	-0.019	0.359	0.731	0.741	-0.551	0.120	-0.333	-0.520	0.261	0.828	0.511	0.163	–

Table C– 8: Coefficients of ANN-model for Nf @ 50% in independent test mode.

Weights of neuron in Input layer						Hidden layers		Weights of neuron in hidden layers														output layers	
G_o^*	δ_o	G_1	m	G_{bulk}	AV%	$b_{1\text{-}i}$	$b_{2\text{-}i}$	$H_{1\text{-}i}$	$H_{2\text{-}i}$	$H_{3\text{-}i}$	$H_{4\text{-}i}$	$H_{5\text{-}i}$	$H_{6\text{-}i}$	$H_{7\text{-}i}$	$H_{8\text{-}i}$	$H_{9\text{-}i}$	$H_{10\text{-}i}$	$H_{11\text{-}i}$	$H_{12\text{-}i}$	$H_{13\text{-}i}$	$H_{14\text{-}i}$	$H_{15\text{-}i}$	Weights V_i	Bias (β)
$w_{1\text{-}i}$	$w_{2\text{-}i}$	$w_{3\text{-}i}$	$w_{4\text{-}i}$	$w_{5\text{-}i}$	$w_{6\text{-}i}$																		
-0.562	-1.082	0.606	-1.116	0.248	0.565	2.736	-2.105	0.214	0.344	-0.261	-0.195	0.247	-1.163	-0.520	-0.290	-0.298	-0.221	1.045	0.867	-1.520	-0.160	0.550	-1.890	1.267
0.627	0.647	0.849	1.423	-0.786	0.513	-1.982	-0.651	0.798	-0.093	0.377	-0.755	1.180	-1.178	2.573	-0.702	1.799	-1.644	0.538	0.185	1.436	1.880	0.566	-2.472	–
0.215	-0.470	-0.316	-2.110	0.240	-0.065	1.710	1.144	-0.555	-0.314	-0.325	0.382	1.195	1.977	0.324	-1.118	-0.403	-1.432	0.051	0.762	-0.632	0.340	-0.531	-1.769	–
1.085	1.249	-0.576	1.403	0.752	0.806	-1.232	-1.027	0.406	-0.216	0.357	-0.383	-0.034	-0.405	-1.430	1.964	-0.484	-0.115	1.075	-0.112	0.115	0.196	0.371	-2.358	–
1.543	0.712	-1.469	-1.164	0.685	1.155	-1.226	0.456	-1.266	0.621	-0.832	0.812	-0.209	0.454	2.073	0.807	0.131	-0.748	0.231	-0.445	-0.731	-0.801	-0.273	0.286	–
-1.017	0.715	0.491	1.835	0.891	1.777	0.437	-0.278	0.778	-0.629	0.015	-0.823	1.151	-0.872	0.384	-0.161	-0.543	-1.714	-0.203	-0.132	-1.700	-1.670	-0.580	-2.534	–
-0.046	0.743	1.422	2.768	1.508	0.770	0.339	-0.327	-0.040	0.327	-0.022	0.413	-0.395	0.762	0.699	1.149	1.455	0.509	-0.845	0.551	1.208	0.081	-0.499	1.156	–
-0.610	2.115	2.300	0.822	-1.398	-0.201	0.584	-0.144	-0.706	-0.427	-0.409	0.128	0.209	-0.572	-0.399	0.793	-0.134	0.057	0.371	-0.141	0.077	-0.461	0.604	-0.581	–
-0.209	1.223	0.025	0.193	0.301	-0.048	1.051	0.335	0.462	0.396	-0.436	-0.199	0.162	0.245	0.138	-0.411	-0.437	-0.276	-0.325	1.294	1.038	-0.170	-0.577	0.273	–
-1.652	1.728	2.736	-1.079	1.299	1.052	-1.439	0.967	0.875	-0.755	-0.104	1.071	-0.552	0.249	-0.283	-1.191	-0.290	-2.025	0.450	-0.983	0.895	-0.728	0.046	1.756	–
0.438	-0.292	0.321	1.004	-0.478	-1.523	0.142	-0.702	-0.267	-0.099	-0.504	-0.028	0.498	0.166	-0.070	0.096	0.785	1.474	-0.260	-0.253	-0.975	-0.917	0.223	1.049	–
-1.219	0.737	-1.334	-0.044	-1.096	0.514	-0.840	-0.607	0.259	-0.462	0.435	-0.575	-0.943	0.331	-0.029	-1.397	1.166	0.310	-0.572	-0.751	-0.266	0.303	0.106	0.483	–
0.384	-0.346	-1.862	-1.541	-3.849	2.449	-0.664	-1.313	-0.239	0.226	-0.785	-0.058	-0.420	-0.253	0.850	-0.119	-0.182	0.952	0.034	-0.151	-0.379	-0.083	0.432	0.280	–
-0.419	2.550	-0.920	1.637	1.973	0.403	-2.371	-1.747	-0.769	-0.003	0.316	0.321	-1.008	0.074	-1.493	-0.038	-0.584	1.569	-0.614	0.533	-1.336	0.242	0.634	0.901	–
-0.789	-0.746	2.425	-0.541	-1.232	0.134	-2.030	-1.605	-0.021	0.494	-0.187	-0.072	-0.945	1.348	0.243	-0.785	0.079	1.038	-0.996	1.302	0.384	-0.316	-0.576	-1.544	–

Table C– 9: Coefficients of ANN-model for FI^R independent test mode.

Weights of neuron in Input layer						Hidden layers		Weights of neuron in hidden layers														output layers	
G_o^*	δ_o	G_1	m	G_{bulk}	AV%	$b_{1\text{-}i}$	$b_{2\text{-}i}$	$H_{1\text{-}i}$	$H_{2\text{-}i}$	$H_{3\text{-}i}$	$H_{4\text{-}i}$	$H_{5\text{-}i}$	$H_{6\text{-}i}$	$H_{7\text{-}i}$	$H_{8\text{-}i}$	$H_{9\text{-}i}$	$H_{10\text{-}i}$	$H_{11\text{-}i}$	$H_{12\text{-}i}$	$H_{13\text{-}i}$	$H_{14\text{-}i}$	$H_{15\text{-}i}$	Weights	Bias
$w_{1\text{-}i}$	$w_{2\text{-}i}$	$w_{3\text{-}i}$	$w_{4\text{-}i}$	$w_{5\text{-}i}$	$w_{6\text{-}i}$																		V_i	(β)
0.717	1.139	-0.388	1.188	-0.470	1.191	-2.149	-1.678	0.395	-0.446	0.260	-0.434	-0.865	0.008	-0.765	-0.031	-0.440	-0.272	-0.438	0.297	0.187	0.474	0.246	0.620	0.168
-1.081	0.668	0.255	-0.059	1.657	-1.123	1.705	1.467	-0.094	0.629	-0.293	-0.490	0.454	-0.456	-0.115	-0.527	0.429	0.130	-0.386	-0.333	-0.812	-0.806	0.345	-0.558	–
-1.131	-1.263	-0.114	1.579	0.222	0.622	1.613	-1.031	0.287	0.716	-0.221	0.113	-0.011	0.635	-0.320	-0.545	0.371	0.144	0.895	0.214	0.111	0.707	-0.527	-1.110	–
-0.232	-0.854	-0.125	0.230	-2.313	-0.886	1.972	-0.934	0.121	-0.152	0.140	0.254	-0.774	-0.262	0.195	-0.548	0.021	-0.287	-0.792	0.567	0.236	0.453	-0.673	-0.322	–
-2.226	0.105	-0.070	-1.277	0.025	0.568	0.862	0.660	-0.531	-0.122	-0.838	1.086	-0.706	-0.416	0.353	-0.870	0.147	0.965	0.856	-0.272	0.001	-0.305	-0.239	1.381	–
1.124	1.492	-0.560	-0.226	1.780	-0.197	-0.822	-0.528	0.074	0.099	0.174	0.184	-0.543	0.688	-1.062	-0.420	0.692	-0.367	-0.532	-0.536	0.574	-0.646	-0.141	0.692	–
-0.788	1.471	2.088	-0.243	2.024	0.090	0.450	0.156	-0.012	0.051	0.459	-0.254	-0.298	-0.325	-0.587	0.271	-0.908	-0.030	0.423	0.886	0.016	-0.046	0.668	0.886	–
-0.348	-1.795	-0.857	-0.513	1.247	-1.124	-0.267	0.247	0.067	0.126	0.334	-0.148	0.081	-0.521	-0.150	-0.555	-1.095	1.265	0.766	0.254	0.276	1.133	0.136	-1.342	–
-0.761	-1.323	-0.159	1.129	-1.760	-0.439	-0.662	-0.239	-0.475	0.522	0.266	0.576	0.257	0.656	0.466	0.575	0.046	0.097	0.667	0.028	-0.631	0.003	0.052	-0.108	–
0.754	0.803	0.725	0.289	-1.551	2.151	0.815	-0.607	-0.422	0.623	-0.368	0.862	-0.233	-1.059	-0.523	0.977	0.219	-0.786	-0.480	0.375	1.648	1.086	-0.360	1.859	–
0.954	-0.087	-1.200	0.931	1.442	-1.055	1.041	0.510	0.647	0.648	-0.917	-1.121	1.379	-0.386	0.061	-0.325	-0.186	-0.267	0.859	-0.112	0.355	1.300	-0.041	2.007	–
-1.478	-0.361	-0.157	-0.843	1.538	1.120	-1.284	-0.925	-0.303	-0.628	0.414	1.116	-0.088	-0.405	1.294	-0.492	-0.089	0.576	0.044	1.243	-0.147	-0.350	0.283	1.551	–
1.795	0.702	0.369	1.262	0.127	-1.108	1.731	1.221	0.198	-0.009	0.547	-0.002	-0.602	-0.460	-1.718	-0.255	0.411	-0.454	0.594	-0.425	0.339	0.104	-0.036	-1.401	–
0.089	0.318	1.675	1.289	1.067	1.711	2.113	-1.229	-0.484	0.413	0.382	0.439	0.085	0.806	0.818	-1.186	-0.819	-0.838	0.705	-0.633	0.690	-0.108	0.561	-1.275	–
0.940	-0.503	-0.625	-1.509	0.892	0.775	2.105	-1.654	-0.314	0.813	0.323	-0.421	0.117	-0.439	-0.302	0.826	-0.091	0.490	-0.297	0.781	-0.416	-0.407	-0.452	0.674	–

Publications

- "Fatigue Performance of Hot Mix Asphalt Tested in Controlled Stress Mode Using Dynamic Shear Rheometer", accepted in International Journal of Pavement Engineering, DOI: 10.1080/10298436.2016.1172707.

- "A Simple Fracture Model for Hot Mix Asphalt Based on Fundamental Fatigue Parameters" accepted in the 8th RILEM International Conference on Mechanisms of Cracking and Debonding in Pavements, June 7-9, 2016- Nantes, France.

- "Modelling the Hysteresis Loops of Hot Mix Asphalt" accepted in the 8th RILEM International Conference on Mechanisms of Cracking and Debonding in Pavements, June 7-9, 2016- Nantes, France.

- "A New Approach in Fatigue Testing and Evaluation of Hot Mix Asphalt Using a Dynamic Shear Rheometer" paper accepted to be published in Proceedings of the 6th International Conference Bituminous Mixtures and Pavements Thessaloniki, Greece, 10-12 June 2015.50